TESIS DE LA UNIVERSIDAD
DE ZARAGOZA
2023
3

Javier Escuer Gracia

Computational modelling of endovascular drug-delivery devices to better understand their performance

Director/es
Martínez Barca, Miguel Ángel

http://zaguan.unizar.es/collection/Tesis

ISSN 2254-7606

Prensas de la Universidad
Universidad Zaragoza

© Universidad de Zaragoza
Servicio de Publicaciones

ISSN 2254-7606

Tesis Doctoral

COMPUTATIONAL MODELLING OF ENDOVASCULAR DRUG-DELIVERY DEVICES TO BETTER UNDERSTAND THEIR PERFORMANCE

Autor

Javier Escuer Gracia

Director/es

Martínez Barca, Miguel Ángel

UNIVERSIDAD DE ZARAGOZA
Escuela de Doctorado

Programa de Doctorado en Ingeniería Mecánica

2022

Repositorio de la Universidad de Zaragoza – Zaguan http://zaguan.unizar.es

Computational modelling of endovascular drug-delivery devices to better understand their performance

Thesis by

Javier Escuer Gracia

Faculty Advisors

Prof. Miguel Ángel Martínez Barca
Prof. Estefanía Peña Baquedano

Doctoral Degree in *Mechanical Engineering*

Escuela de Ingeniería y Arquitectura (EINA)
Universidad de Zaragoza
Zaragoza, April 2022

A mis padres,
a Jara,
a Javi

Compendium of publications

This Doctoral Thesis is a compendium of four publications previously published in various international scientific journals in order to qualify for the title of Doctor in Mechanical Engineering by the University of Zaragoza, according to the agreement of June 26, 2020 of the Governing Council approving the Regulations on Doctoral Theses. According to this regulation, the first page of this document includes the compendium of publications in chronological order together with the Journal Impact Factor (JIF) of each scientific journal.

1. Escuer J., Martínez M.A., McGinty S., Peña E. (2019). Mathematical modelling of the restenosis process after stent implantation. *Journal of the Royal Society Interface* 16(157), 20190313. https://doi.org/10.1098/rsif.2019.0313.
   JIF(2019): 3.748 (Q2: 19/71 Multidisciplinary Sciences).
2. Escuer J., Cebollero M., Peña E., McGinty S., Martínez M.A. (2020). How does stent expansion alter drug transport properties of the arterial wall? *Journal of the Mechanical Behavior of Biomedical Materials*, 104, 103610.
   https://doi.org/10.1016/j.jmbbm.2019.103610.
   JIF (2020): 3.902 (Q2: 32/89 Biomedical Engineering).
3. Escuer J., Aznar I., McCormick C., Peña E., McGinty S., Martínez M.A. (2021). Influence of vessel curvature and plaque composition on drug transport in the arterial wall following drug-eluting stent implantation. *Biomechanics and Modeling in Mechanobiology* 20:767–786.
   https://doi.org/10.1007/s10237-020-01415-3.
   JIF (2020): 2.963 (Q3: 36/71 Biomedical Engineering).
4. Escuer J., Fensterseifer Schmidt A., Peña E., Martínez M.A., McGinty S. (2022). Mathematical modelling of endovascular drug delivery: balloons versus stents. *International Journal of Pharmaceutics*, 121742. In press.
   https://doi.org/10.1016/j.ijpharm.2022.121742.
   JIF (2020): 5.875 (Q1: 32/276 Pharmacology & Pharmacy).

Acknowledgements

After many years, this period of my life is finally coming to an end. It has been a period of productive learning, not only scientifically, but also on a personal level. For this reason, I would like to thank all those who have been by my side, in one way or another, in this equally long and intense journey.

First of all, I would like to thank the assistance and support of my thesis supervisors, Miguel Ángel and Fany, for trusting me and giving me the opportunity to undertake this research. Thank you for pointing me in the right direction many times and for all the fruitful discussions over these years. I would like to extend my thanks to Begoña Calvo for introducing me to the world of research.

I would like to specially thank Sean McGinty, responsible of my research stay in the University of Glasgow. Many thanks for the opportunity to work with you during this time. You have been like a third supervisor for me and without your help this would not have been possible. I have certainly enjoyed the collaboration and the experience in Glasgow and in Scotland. Thank you also to my online PhD collegues of The University of Glasgow, Ally and André, for their help and collaboration in completing this work.

I also want to thank Claire Conway for welcoming me in the National University of Ireland Galway. Thank for kindly offering me all your valuable knowledge and specially for making my stay in Galway a great experience.

I do not want to forget all the PhD colleagues I have had over these years who have made going to work every morning easier. It was great to share this time with you all.

Last but not least, millions of thanks to my parents, Ángel and Pili, who, without understanding very well what kind of world I had got into, feel very proud and happy. Thank you for your unconditional support and for your help in my decisions throughout my life and for transmitting to me your values of perseverance and hard work. I most certainly would not be here without you and that is something I will never forget. Thanks also to my sister, Mariángel, and the rest of my family, family in law and friends who have shown me their support during all these years. A special mention to the youngest members of the family, who are able to bring a smile to my face even in the hardest moments.

Finally, I would like to express my deepest and most sincere gratitude to Jara. My wife, my partner, my friend, my everything. Thank you for your endless patience, for supporting me in every possible way and for being by my side every step of the way. I am convinced that this work has been possible thanks to your trust and support. And of course, I would like to dedicate this work to my son Javi who has made this last part of the journey even more exciting! He gives us his joy and strength every day to be better people. Jara, Javi, I am back.

To all of them, thank you!.

Huesca, 23th April 2022.

Agradecimientos

Después de muchos años, este periodo de mi vida llega a su fin. Ha sido un periodo de productivo aprendizaje, no sólo científico, sino también a nivel personal. Por ello, me gustaría dar las gracias a todos los que han estado a mi lado, de una u otra manera, en este viaje tan largo e intenso.

En primer lugar, quiero agradecer la ayuda y el apoyo de mis directores de tesis, Miguel Ángel y Fany, por confiar en mí y darme la oportunidad de desarrollar esta investigación. Gracias por guiarme muchas veces en la dirección correcta y por todas las fructíferas discusiones a lo largo de estos años. Me gustaría extender mi agradecimiento a Begoña Calvo por introducirme en el mundo de la investigación.

Me gustaría agradecer especialmente a Sean McGinty, responsable de mi estancia de investigación en la Universidad de Glasgow. Muchas gracias por la oportunidad de trabajar contigo durante este tiempo. Has sido como un tercer supervisor para mí en muchos momentos y sin tu ayuda esto no habría sido posible. Sin duda he disfrutado de la colaboración y de la experiencia en Glasgow y en Escocia. Gracias también a mis compañeros 'online' de doctorado de la Universidad de Galsgow, Ally y André, por su ayuda y colaboración para completar este trabajo.

También quiero dar las gracias a Claire Conway por acogerme en la National University of Ireland Galway. Gracias por ofrecerme amablemente todos tus valiosos conocimientos y, especialmente, por hacer de mi estancia en Galway una gran experiencia.

No quiero olvidar a todos los compañeros de doctorado que he tenido a lo largo de estos años y que han hecho más fácil el ir a trabajar cada mañana. Ha sido estupendo compartir este tiempo con todos vosotros.

Por último, pero no menos importante, millones de gracias a mis padres, Ángel y Pili, que sin entender muy bien en qué mundo me había metido, se sienten muy orgullosos y felices. Gracias por vuestro apoyo incondicional y por vuestra ayuda en mis decisiones a lo largo de mi vida y por transmitirme vuestros valores de perseverancia y trabajo. Sin duda no estaría aquí sin vosotros y eso es algo que nunca olvidaré. Gracias también a mi hermana, Mariángel, y al resto de mi familia y amigos que me han mostrado su apoyo durante todos estos años. Una mención especial a los más pequeños de la casa, que son capaces de sacarme una sonrisa incluso en los momentos más duros.

Por último, quiero expresar mi más profundo y sincero agradecimiento a Jara. Mi mujer, mi compañera, mi amiga, mi todo. Gracias por tu infinita paciencia, por apoyarme en todo lo posible y por estar a mi lado en todo momento. Estoy convencido de que este trabajo ha sido posible gracias a tu confianza y apoyo. Y por supuesto, me gustaría dedicar este trabajo a mi hijo Javi que ha hecho que esta última parte del camino sea todavía más emocionante y que nos transmite alegría y fuerza cada día para ser mejores personas. Jara, Javi, estoy de vuelta.

A todos ellos, ¡gracias!.

Huesca, 23 de abril de 2022.

Abstract

Coronary artery disease (CAD) remain the leading cause of mortality in the world. Atherosclerosis is the major contributor of coronary artery disease (CAD) and it is characterized by build-up of plaque (atheroma) due to the abnormal accumulation of cholesterol and other lipids, macrophages, connective tissue, calcium and other substances in the inner lining of the arterial walls. This causes a progressive narrowing (stenosis) of the vessel that leads to the partial or total reduction of the blood flow through the coronary arteries to the heart muscle. Moreover, the possible rupture of an atherosclerotic plaque can lead to the formation of blood clots (thrombi) which, directed towards target organs such as the heart or brain, can cause myocardial infarctions, strokes or even death.

The most common treatment for obstructive CAD is percutaneous coronary intervention (PCI) where a stent is deployed to widen the artery and restore blood flow. However, in-stent restenosis (ISR), a gradual luminal re-narrowing mainly due to the vessel wall injury induced by the device, is the major clinical limitation of this technique. With the advent of drug-eluting stents (DESs), the incidence of ISR has been dramatically reduced. While DESs work well in the majority of cases, their permanency in the vessel is associated with delayed healing of the vessel and thrombosis risk, with most patients receiving an expensive and prolonged course of dual antiplatelet therapy. Moreover, if ISR occurs, it is not feasible to remove the original stent and insert a new one, which complicates the repeat revascularisation strategy, leading many clinical groups to consider the use of drug-coated balloons (DCBs) as an alternative as an attractive alternative to DESs for the treatment of CAD in certain anatomical conditions. In particular, DCBs may be used in the treatment of ISR, where it is not feasible to insert a further DES. Moreover, DCBs are becoming increasingly interesting in the context of treating small de novo lesions. A key potential advantage of deploying a DCB over a DES is the lack of permanency. However, this may potentially be a disadvantage, where the brief period of deployment associated with DCBs presents only a short window for drug to be delivered.

Complementary to the wide variety of physiological and clinical studies, the use of computational (*in silico*) modelling and simulation for endovascular devices has emerged as a powerful technique that can contribute to address some of the limitations of often difficult and expensive experimental analysis, with models focusing on different areas: structural mechanics and computational fluid dynamics (CFD), drug elution kinetics, uptake and subsequent redistribution within the arterial tissue and arterial healing response.

However, the literature is lacking computational models that adequately take into account both the influence of mechanical deformation on drug transport. Therefore, a comprehensive study of the effect of stent deployment on the drug transport properties of a multilayer porous arterial wall was provided. This model incorporated the state-of-the art description of the mechanical properties of arterial tissue through an anisotropic, hyperelastic material model and included a nonlinear saturable binding model to describe drug transport in the arterial wall. Relationships between mechanical force generated through device expansion and alteration in diffusion within the arterial wall were established and different simulations to elucidate the impact of such alterations in spatio-temporal drug release and tissue uptake were performed. Mechanical deformation of the arterial wall results in modified drug transport properties and tissue drug concentrations, highlighting the importance of coupling solid mechanics with drug transport.

Existing drug transport models generally have two common limitations: typically neglect the significant geometrical variability of the arteries and do not incorporate the existence of disease state. Focused on these limitations, a computational study of the impact of the curvature of the coronary artery and the heterogeneous composition of the atherosclerotic plaque on drug transport in the arterial wall following DES implantation was provided. The results demonstrate that arterial curvature and plaque composition have important influences on the spatio-temporal distribution of drug, with potential implications in terms of effectiveness of the treatment.

Despite the plethora of models that consider DESs, there are only a handful of *in silico* models focused on DCBs, each with their own set of strengths and limitations. The most comprehensive model of DCB delivery, transport and retention to date has been developed in this Thesis. The model incorporated two nonlinear phases of binding (specific and non-specific) and included the influence of advection, within a multilayer arterial wall. This framework was used to simulate drug delivery from different types of balloon platform, explore the influence of DCB application time, compare DCB delivery of two different drugs (sirolimus and paclitaxel) and compare simulations of DESs vs DCBs to explore if there are any potential benefits, in terms of safety and efficacy, of treating small de novo lesions with a DCB vs a DES. The results highlighted the pros and cons of each device and indicated the potential for designing a DCB that gives rise to sufficiently similar safety and efficacy indicators as current commercial DESs.

Finally, a continuum mechanobiological model was proposed to describe the complex restenosis process following the insertion of a stent into a coronary artery, in terms of densities/concentrations of important species such as growth factors, matrix metalloproteinases, extracellular matrix (ECM), contractile and synthetic smooth muscle cells (SMCs) and endothelial cells (ECs). Diffusion–reaction equations were used for modelling the mass balance between species in the arterial wall and experimental data from the literature were used in order to estimate model parameters.

The results suggested that the arterial wall response was driven by the damage area, proliferation of SMCs and the collagen turnover. Tissue growth was defined as a result of the change over time of ECs, SMCs and ECM, and model predictions in terms of percentage of stenosis were in good agreement with clinical data.

To summarize, this PhD Thesis provides a research study on several aspects related to drug-delivery endovascular devices in arteries. All the models presented in this Thesis could serve as a powerful tool for the pre-clinical evaluation and to provide some insights on the design of newer endovascular devices much more efficient and safer.

Keywords: Biomechanics; Atherosclerosis; Arterial wall; Endovascular devices; Drug-eluting stent; Drug-coated balloon; Drug delivery; In-stent restenosis; Finite element method; Computational modelling; Stent deployment; Mechanical expansion; Hyperelastic models; Arterial healing.

Sinopsis

La enfermedad arterial coronaria sigue siendo la principal causa de mortalidad en el mundo. La aterosclerosis es la principal causa de enfermedad coronaria y se caracteriza por la acumulación de placa (ateroma) debida a la acumulación anormal de colesterol y otros lípidos, macrófagos, tejido conectivo, calcio y otras sustancias en la pared arterial. Esto provoca un estrechamiento (estenosis) progresivo del vaso que conduce a la reducción parcial o total del flujo sanguíneo a través de las arterias coronarias hacia el corazón. Además, la posible rotura de una placa aterosclerótica puede dar lugar a la formación de coágulos de sangre (trombos) que, dirigidos hacia órganos diana como el corazón o el cerebro, pueden causar infartos de miocardio, accidentes cerebrovasculares o incluso la muerte.

El tratamiento más habitual de la enfermeda coronaria obstructiva es la intervención coronaria percutánea (ICP), en la que se coloca un stent para ensanchar la luz del vaso y restablecer el flujo sanguíneo. Sin embargo, la principal limitación clínica de esta técnica es la reestenosis intra-stent (RIS), un re-estrechamiento gradual del lumen debido principalmente a la lesión producida en la pared del vaso inducida por el dispositivo tras su implantación. Con la llegada de los stents liberadores de fármacos o stents farmacoactivos (SFAs), la incidencia de la RIS se ha reducido drásticamente. Aunque los SFAs funcionan bien en la mayoría de los casos, su permanencia en el vaso se asocia a un retraso en la cicatrización del mismo y al riesgo de trombosis. Además, la mayoría de los pacientes han de recibir un tratamiento antiplaquetario caro y prolongado. Además, si se produce RIS, no es factible retirar el stent original e insertar uno nuevo en el mismo lugar, lo que complica la estrategia de revascularización, conduciendo a muchos grupos clínicos a considerar el uso de balones farmacoactivos (BFAs) como una alternativa atractiva a los SFAs para el tratamiento de la enfermedad coronaria en determinadas condiciones anatómicas. En particular, los BFAs pueden utilizarse en el tratamiento de la RIS cuando no es factible insertar otro SFA. Además, los BFAs son cada vez más interesantes en el contexto del tratamiento de pequeñas lesiones de novo. Una de las principales ventajas potenciales de la implantación de un BFA frente a un SFA es que no tienen permanencia en el vaso. Sin embargo, esto puede ser una desventaja, ya que el breve período de aplicación asociado a estos dispositivos presenta solamente una corta ventana para la administración del fármaco.

Como complemento a la gran variedad de estudios fisiológicos y clínicos, el uso del modelado y la simulación computacional (*in silico*) para los dispositivos endovasculares ha surgido como una potente técnica que puede contribuir a abordar algunas de las limitaciones de los a menudo difíciles y costosos análisis experimentales, con modelos centrados en diferentes áreas: mecánica estructural y dinámica de fluidos computacional (CFD), cinética de liberación del fármaco, captación y posterior redistribución en el tejido arterial y respuesta de cicatrización arterial.

Sin embargo, la literatura carece de modelos computacionales que tengan en cuenta adecuadamente la influencia de la deformación mecánica en el transporte del fármaco. Por lo tanto, se realizó un estudio exhaustivo del efecto del despliegue del stent en las propiedades de transporte de fármacos de la pared arterial, considerada porosa y multicapa. Este modelo incorporó la descripción más avanzada de las propiedades mecánicas del tejido arterial a través de un modelo de material anisotrópico e hiperelástico e incluyó un modelo de unión saturable no lineal para describir el transporte de fármaco en la pared. Se establecieron relaciones entre la fuerza mecánica generada a través de la expansión del dispositivo y la alteración de la difusión en la pared arterial y se realizaron diferentes simulaciones para dilucidar el impacto de dichas alteraciones en la liberación espacio-temporal del fármaco y la subsecuente captación del tejido. La deformación mecánica de la pared arterial dio lugar a la modificación de las propiedades de transporte del fármaco y de las concentraciones de droga en el tejido, poniendo de manifiesto la importancia de acoplar la mecánica de sólidos con el transporte del fármaco.

Los modelos de transporte de fármacos existentes suelen tener dos limitaciones comunes: normalmente descuidan la importante variabilidad geométrica de las arterias y no incorporan la existencia del estado de enfermedad. Teniendo en cuenta estas dos limitaciones, se presentó un estudio computacional del impacto de la curvatura de la arteria coronaria y la composición heterogénea de la placa aterosclerótica en el transporte de fármacos en la pared arterial tras la implantación de un SFA. Los resultados demuestran que la curvatura de la arteria y la composición de la placa tienen importantes influencias en la distribución espacio-temporal del fármaco, con posibles implicaciones en términos de eficacia del tratamiento.

A pesar de la gran cantidad de modelos que tienen en cuenta los SFAs, sólo existen un pequeño número de modelos *in silico* centrados en los BFAs, cada uno con su propio conjunto de puntos fuertes y limitaciones. En esta tesis se ha desarrollado el modelo más completo hasta la fecha sobre la administración, el transporte y la retención de fármaco desde un BFA. El modelo incorpora dos fases no lineales de unión (específica y no específica) e incluye la influencia de la convección en una pared arterial multicapa. Este marco se utilizó para simular la administración de fármacos desde diferentes tipos de plataformas de balones, explorar la influencia del tiempo de aplicación del BFA, comparar la administración del BFA recubierto con dos fármacos diferentes (sirolimus y paclitaxel) y comparar las simulaciones de los SFAs frente a los BFAs para explorar si existe algún beneficio potencial, en términos de seguridad y eficacia, en el tratamiento de pequeñas lesiones de novo con un BFA frente a un SFA. Los resultados pusieron de manifiesto los ventajas y desventajas de cada dispositivo e indicaron la posibilidad de diseñar un BFA que diera lugar a indicadores de seguridad y eficacia suficientemente similares a los actuales SFA comerciales.

Por último, se propuso un modelo mecanobiológico continuo para describir el complejo proceso de RIS en una arteria coronaria, en términos de densidades/concentraciones de diferentes especies biológicas como los factores de crecimiento, las metaloproteasas, la matriz extracelular, las células musculares lisas (CMLs) contráctiles y sintéticas y las células endoteliales. Se utilizaron ecuaciones de difusión-reacción para modelar el equilibrio de masas entre especies en la pared arterial y se emplearon datos experimentales de la literatura para estimar los parámetros del modelo. Los resultados sugieren que la respuesta de la pared arterial está determinada por el área de daño, la proliferación de las CMLs y el recambio de colágeno. El crecimiento del tejido se definió como resultado de la variación temporal de las células endoteliales, las CMLs y la matriz extracelular, y las predicciones del modelo en términos de porcentaje de estenosis coincidieron con datos clínicos de la literatura.

En resumen, esta tesis doctoral ofrece una investigación sobre varios aspectos relacionados con los dispositivos endovasculares de administración de fármacos en las arterias. Todos los modelos presentados en esta Tesis podrían servir como una poderosa herramienta para la evaluación preclínica y para proporcionar algunas ideas sobre el diseño de nuevos dispositivos endovasculares mucho más eficientes y seguros.

Palabras clave: Biomecánica; Aterosclerosis; Pared arterial; Dispositivos intravasculares; Stent farmacoactivo; Liberación de fármacos; Restenosis intra-stent; Método de elementos finitos; Modelado computacional; Expansión mecánica; Modelos hiperelásticos; Cicatrización arterial.

Contents

List of Figures

List of Tables

CHAPTER 1

Motivation, objectives and outline

The motivation of this work is mainly founded on the high social and economical impact of cardiovascular diseases. The main objectives and a brief description of the contents of this Thesis are also included in this Chapter.

Contents

1.1 Motivation

Cardiovascular diseases (CVDs) remain the leading cause of mortality in the world [Tsao et al., 2022; Timmis et al., 2022]. In Europe, approximately 4.1 million deaths (accounting for just under 2.2 million deaths in females and just over 1.9 million deaths in males) were attributed to CVDs (Fig. 1.1) in the most recent year of available data (2019), with coronary heart disease (CHD), 38% of all CVD deaths in females and 44% in males, and stroke, 26% of all CVD deaths in females and 21% in males, the primary culprits [Timmis et al., 2022]. In 2015, the European Heart Network estimated CVDs cost the European Union (EU) economy 210 billion euros. This remains the most recent estimate of the economic burden of CVDs in EU countries [Timmis et al., 2022].

In the particular case of Spain, there were 493,776 deaths in 2020, 75,073 more than in the previous year (17.9% more) mainly because of the COVID-19 pandemic (Fig. 1.2). The group of diseases of the circulatory system remained the leading cause

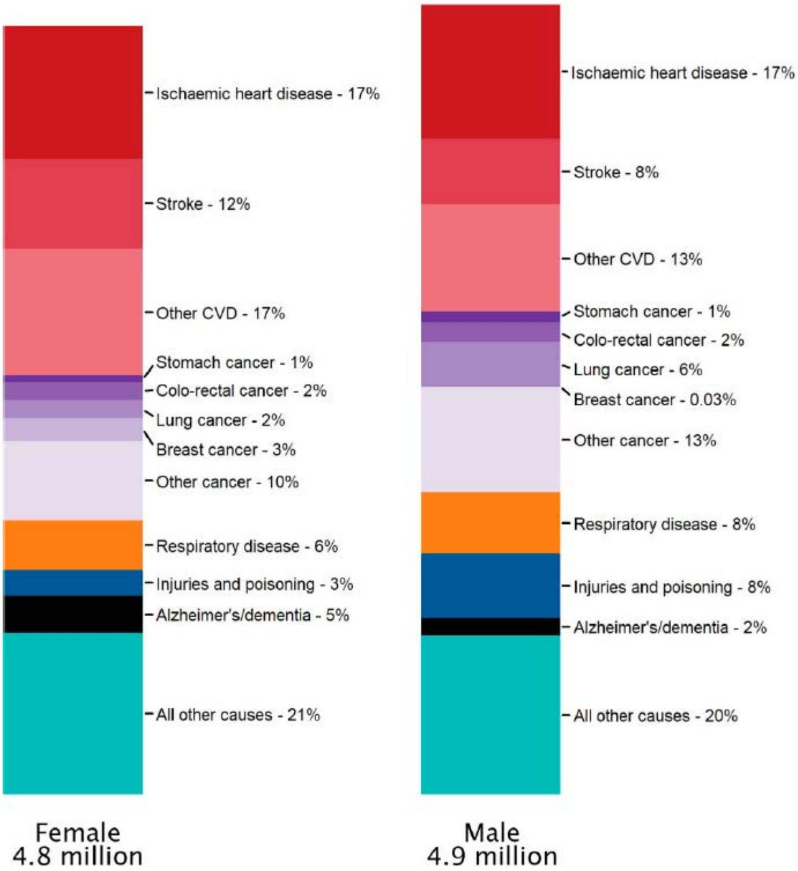

Figure 1.1. *National causes of death in females and males in European Society of Cardiology (ESC) member countries [Timmis et al., 2022].*

of death with 24.3% of the total deaths, followed by tumours (22.8%). Infectious diseases, which include identified COVID-19 viruses and suspected COVID-19, were the third cause of death (16.4% of the total).

Atherosclerosis is the major contributor of coronary artery disease (CAD) and it is characterized by build-up of plaque (atheroma) due to the abnormal accumulation of cholesterol and other lipids, large inflammatory cells called macrophages, connective tissue, calcium and other substances in the inner lining of the arterial walls, causing a progressive narrowing (stenosis) of the vessel that leads to the partial or total reduction of the blood flow through the coronary arteries to the heart muscle. Moreover, the possible rupture of an atherosclerotic plaque can lead to the formation of blood clots (thrombi) which, directed towards target organs such as the heart or brain, can cause myocardial infarctions, strokes or even death [Libby et al., 2002].

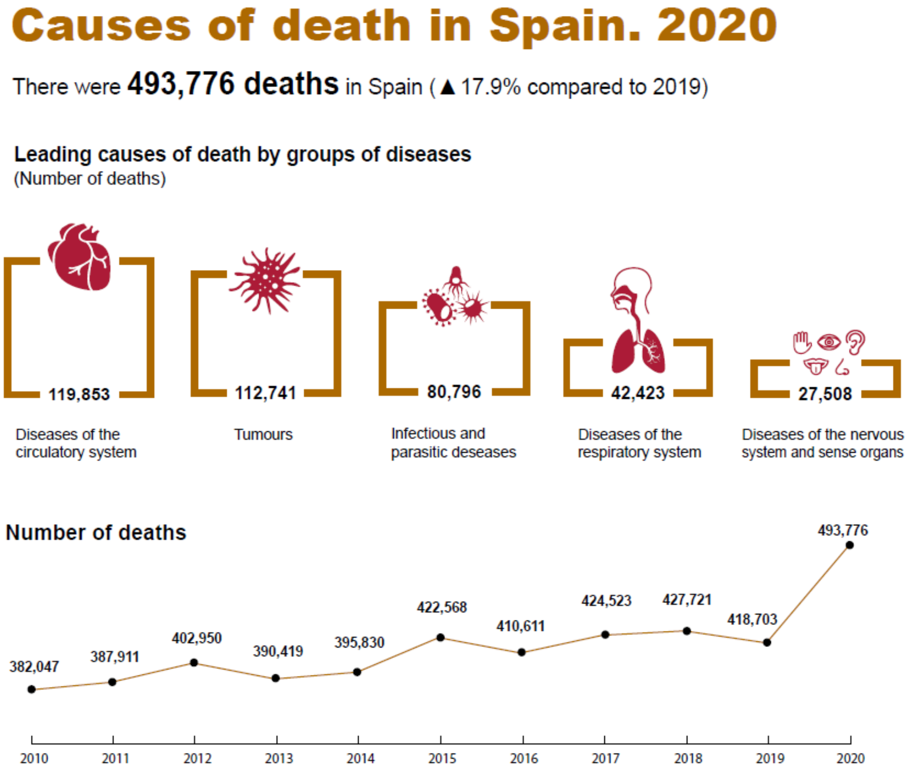

Figure 1.2. *Causes of death in Spain in 2020. Source: Instituto Nacional de Estadistica (INE) / National Statistics Institute of Spain [INE, 2021].*

The current therapeutic alternatives to treat atherosclerotic lesions are pharmacological treatment and strict control of risk factors, conventional (invasive) surgery and minimally invasive endovascular techniques, such as coronary angioplasty, where a prosthetic device is introduced into the artery by means of a catheter without the need of a conventional intervention. Coronary angioplasty, also called percutaneous transluminal coronary angioplasty (PTCA) or percutaneous coronary intervention (PCI), was initially performed without stent insertion [Dotter and Judkins, 1964; Grüntzig, 1978]. In a balloon angioplasty, the device is delivered to the site of vessel narrowing via a catheter inserted in an artery. The balloon is then inflated at high pressure for a few seconds, compressing the atherosclerotic plaque and expanding the vessel, restoring lumen size, and hence improving blood flow (revascularization). After that, the device is retrieved again by catheterization. However, its success was hindered by the inherent limitations of acute vessel closure and elastic recoil in the short term and negative vascular remodelling (late recoil) and neointimal proliferation in the longer term [Bauters and Isner, 1997].

Coronary artery stents were, therefore, developed to overcome these limitations, by scaffolding the balloon-dilated artery, sealing the dissection flaps and preventing late recoil. The vast majority of PCI procedures performed currently involve balloon angioplasty and stent deployment [Iqbal et al., 2013]. However, despite outstanding clinical improvements, together with acute stent thrombosis (ST), neointimal hyperplasia growth and late remodelling of the vessel that led to new complication of in-stent restenosis (ISR), continued to be reported as major limitations of this technique [Alfonso et al., 2014]. Indeed, mid- and long-term clinical follow-up of patients with bare metal stents (BMSs) implanted revealed substantial ISR rates of 20-30% [Hoffmann et al., 1996]. This led to several attempts to minimize restenosis rates, optimizing stent performance in terms of geometrical design, manufacturing methods, materials, delivery procedure and expansion methods. When mechanical updates did not address the problems of ISR encountered with BMSs, researchers considered pharmacological solutions through the use of stents coated with antiproliferative substances.

With the advent of drug-eluting stents (DESs), the incidence of restenosis has been dramatically reduced [Buccheri et al., 2016]. However, despite revolutionary success reducing the rates of ISR and associated clinical events, the use of DES with durable polymers did not prove to be a definitive solution for the treatment of CAD. Their permanency in the artery is associated with delayed healing of the vessel and thrombosis risk, with most patients receiving an expensive and prolonged course of dual antiplatelet therapy [Byrne et al., 2015b]. Moreover, if ISR occurs, it is not feasible to remove the original stent and insert a new one, which complicates the repeat revascularisation strategy, leading many clinical groups to consider the use of drug-coated balloons (DCBs) as an alternative as an attractive alternative to DESs for the treatment of CAD in certain anatomical conditions. In particular, DCBs may be used in the treatment of ISR, where it is not feasible to insert a further DES [Scheller et al., 2006]. Moreover, DCBs are becoming increasingly interesting in the context of treating small de novo lesions [Jeger et al., 2018]. A key potential advantage of deploying a DCB over a DES is the lack of permanency. However, this may potentially be a disadvantage, where the brief period of deployment associated with DCBs presents only a short window for drug to be delivered.

Complementary to the wide variety of physiological and clinical studies, the use of computational (*in silico*) modelling and simulation for endovascular devices has emerged as a powerful technique that can contribute to address some of the limitations of often difficult and expensive experimental analysis, with models focussing on different areas: structural mechanics and computational fluid dynamics (CFD), drug elution kinetics, uptake and subsequent redistribution within the arterial tissue and arterial healing response. The relative flexibility of numerical methods to conduct parametric studies of the different variables involved in the endovascular devices design can be translated into a reduction of time and cost in terms of device design and fabrication. To model the interaction of the device with the arterial wall, the biomechanical properties of the tissue must be perfectly known. Within the physiological domain, constitutive models attempt to capture the (visco)elastic behaviour of cardiovascular tissues, incorporating structure-related parameters into their mathematical definition. It should also be noted that during some surgical interventions, such as coronary angioplasty, the loads to which vascular tissue is subjected during surgical interventions are much higher than those corresponding to physiological conditions, therefore, numerical simulations must consider theories of damage and (visco)plasticity, among others.

Therefore, more efforts are needed to develop more advanced models of endovascular devices implanted in arteries under healthy and pathological conditions for a better understanding of their performance and can help to design personalised endovascular devices much more efficient and safe. This models must take into account all the mechanical and behavioural features that characterise them, in order to make the models as realistic as possible. This is the main motivation of this Thesis.

1.2 Objectives

Based on the motivation previously explained, the main objective of this Thesis is to advance in the development of mathematical and computational models for the study of drug transport and retention in the arterial tissue in order to better understand the performance of newer and more efficient drug delivery devices.

In addition to the overall objective set out above, some of the partial objectives are itemized here:

- To develop newer computational models of fluid flow and drug transport in healthy coronary arteries released from different endovascular devices (stent and balloon) using a commercial finite element tool such as COMSOL Multiphysics (COMSOL AB, Burlington, MA, USA). The models will incorporate two nonlinear phases of drug binding (specific and nonspecific) in the tissue and include the influence of diffusion and advection within a multilayer arterial wall.
- To analyse the influence of the mechanical expansion of the device on drug transport properties of the arterial wall in order to establish relationships between mechanical deformation generated through device expansion and alteration in diffusion and convection within the arterial wall. To carry out simulations to elucidate the impact of such alterations on spatio-temporal drug release and tissue uptake profiles.
- To study the impact of the variability of the coronary artery geometry on drug transport in the blood flow and in the arterial tissue, performing a series of simulations to elucidate the effect of arterial curvature on spatio-temporal drug uptake within tissue.
- To investigate the effect of the atherosclerotic plaque heterogeneity on the overall

distribution of drug in the vessel wall. Plaque will be idealised as a fibrous cap with a core which may be lipid, necrotic or calcified, depending on the lesion considered.

- To simulate drug delivery from different types of balloon platform, explore the influence of DCB application time, and try to elucidate the importance on release kinetics of elevated pressure during drug-coated balloon (DCB) application. DCBs obstruct the artery during delivery, so inflating for longer than necessary could therefore have serious consequences for the patient. This tiny time window for drug delivery makes DCB design specially challenging.
- To compare simulations of drug-eluting stents (DESs) and DCBs in order to explore if there are any potential benefits, in terms of safety and efficacy, of treating small de novo lesions with a DCB vs a DES. DESs tends to release drug in a controlled and sustained fashion over a period of weeks or months, which is thought to be broadly consistent with the healing time of the artery following device deployment. However, DCBs typically transfer drug rapidly to the arterial wall during a short application period of the order of a minute.
- To analyse the effect of the choice of drug (sirolimus and paclitaxel). An important aspect in the performance of any endovascular device is the drug release profile. If too much drug is delivered to the blood and the tissue then toxicity can arise, whereas if too little drug is delivered then could either be completely ineffective or result in drug action waning before healing is complete. Of course, this therapeutic window varies between drugs and between patients and most probably with time after implantation too.
- To establish a methodology for modelling the restenosis process after stent implantation (in-stent restenosis, ISR) in order to better understand the biological species and processes involved. To develop a mathematical and computational continuum model based on reaction-diffusion equations which successfully captures the main characteristics of the ISR in a coronary artery.

This is a Thesis mainly based on computational modelling, although logically using experimental data obtained from the literature. To reach the goals above exposed, the following strategy have been adopted throughout the evolution of this Thesis:

- Problem statement. In this case, the problem has been raised by clinicians who have observed undesirable outcomes in the treatment of atherosclerosis using endovascular devices.
- Choice of the main physical effects to be modelled in the different problems posed: drug transport released from endovascular devices in healthy and pathological vessels, mechanical expansion of endovascular devices and in-stent restenotic growth.
- Choice of mathematical equations to reproduce the physical effects to be simulated.

- Review of mathematical and computational models existing in the literature that will serve as a basis for the new models developed by the researcher. Selection of the valid aspects for our problems and modification of the necessary elements of the existing models.
- Fitting parameters of the developed models using experimental data, mainly found in the existing literature.
- Implementation of the computational models in a commercial finite element software such as COMSOL Multiphysics (COMSOL AB, Burlington, MA, USA) and ABAQUS (Dassault Systèmes Simulia Corp., Johnston, RI, USA).
- Application of the computational models developed to get answers to the main clinical issues raised. For example, analysis of the influence of different drugs, the effect of the drugs in different concentrations and in different types of vessels, comparison of the effect of drug release from different endovascular devices, coupling mechanical and drug transport models, etc.
- Drawing clinical conclusions based on the numerical results obtained.

1.3 Thesis outline

This Thesis is presented as a compendium of publications and this document, therefore, complies with the requirements established by the University of Zaragoza, following the Agreement of the of the Governing Council of the University that approves the Regulations on Doctoral Thesis and where thesis developed as a compendium of publications are contemplated. In the first page of this document it has been specified that this Thesis was developed by a compendium of publications and the complete references of each work that constitute the body of the thesis have been listed.

This Thesis consists of the following structure:

- The motivation, research objectives and outline following in this work are presented in **Chapter 1**.
- **Chapter 2**, entitled ***Introduction***, exposes the main features of the vascular system. Special emphasis is put in the description of the vessel wall structure of large and medium-sized arteries, as well as in their classification as a function of their physiological role and composition. The most mechanically relevant features of blood vessels is also presented. A review of the state-of-the-art in cardiovascular modelling is provided. In particular, the constitutive laws most frequently used in the modelling of the vessel wall are presented. After that, a general view of the the importance of the clinical problems studied in this work and the main treatment techniques is exposed. The chapter is completed with a general description of the state-of-the-art of mathematical

and computational modelling in the research of endovascular devices. All these concepts are important for understanding the results and scope of this Thesis.

- In **Chapter 3**, entitled ***Published works***, the works that comprise the compendium of publications are included.
- Finally, in **Chapter 4**, entitled ***Discussion and Conclusions***, an overall discussion of this work is provided. The original contributions of this Thesis, as well as the specific and final conclusions and the future lines of work are also described.

To conclude, an Appendix with an extensive summary in Spanish language of the work developed is included.

CHAPTER

2

Introduction

To fully understand the implications of this Thesis, in this introductory chapter, a brief summary of the main features and functions of the vascular system is presented. Blood vessels are classified as a function of their composition and physiological role, and their main mechanically relevant characteristics are presented. Next, the state-of-the-art in constitutive modelling for passive behaviour of the arteries is briefly exposed. Afterwards, the mechanisms of atherosclerosis are described and an exhaustive description of the main techniques to treat advanced atherosclerotic lesions is presented. Finally, a literature review in mathematical and computational modelling in endovascular devices research is addressed. This review led to identification some of the research gaps which have been studied in this Thesis.

Contents

2.1 An overview of the cardiovascular system

The cardiovascular system, also called circulatory system, is an organ system whose primary function is to pump blood through a complex network of blood vessels to all parts of the body by the action of the heart. This process provides every body cells with necessary substances, such as oxygen, nutrients and hormones, and removes waste products, such as carbon dioxide, urea and lactic acid, from those same cells.

Circulation of the blood can be subdivided into two distinctive pathways which start and end at the heart: the pulmonary circuit and the systemic circuit. The pulmonary circuit moves blood to and from the lungs. It transports deoxygenated (poor-content oxygen) blood to the lungs to absorb oxygen and release carbon dioxide (CO_2). The oxygenated (high-content oxygen) blood then flows back to the heart. The systemic circuit carries blood to and from the rest of the body. It sends oxygenated blood out to cells and returns deoxygenated blood back to the heart.

The vascular tree consists of three main classes of blood vessels:

- Arteries constitute a branching system of high-pressure blood vessels which usually transports oxygenated blood away from the heart to all other tissues and organs. Pulmonary arteries and umbilical arteries (in case of fetal circulation) are the exception to this rule since these arteries carry deoxygenated blood from the heart to the organs that oxygenate it. As they enter peripheral tissues, arteries branch repeatedly and decrease in diameter (each branch is smaller in diameter than the preceding one). The smallest arterial branches are called arterioles.
- Veins transport blood from peripheral tissues back to the heart. Most veins carry deoxygenated blood. The exceptions are the pulmonary veins (and umbilical veins in case of fetal circulation). The superior and inferior venae cavae carry deoxygenated blood from the upper and lower systemic circulation, respectively. The pulmonary veins carry oxygen rich blood from the lungs to the heart. The smallest venous branches are called venules.
- Capillaries are microscopic blood vessels that connect arterioles with venules. Blood passing through capillaries gives up the oxygen and nutrients carried to this point by the arteries and picks up waste and CO_2 as it enters veins. Veins lead away from the capillaries as tiny vessels and increase in size until they join the superior and inferior venae cavae as they return to the heart. The extremely thin walls of capillaries facilitate passage of oxygen and nutrients to cell bodies and the removal of accumulated waste and CO_2.

Arteries and veins share the same general features, but the walls of arteries are much thicker because of the higher pressure of the blood that flows through them.

2.2 The structure of the arterial wall

The arteries are generally categorized into two types: elastic and muscular arteries. Elastic arteries, such as the aorta, main pulmonary artery, common carotid and common iliac arteries, tend to be vessels with large diameters where the media layer contains both smooth muscle cells (SMCs) and larger numbers of collagen and elastin filaments. Muscular arteries, such as the coronary, cerebral, femoral and renal arteries,

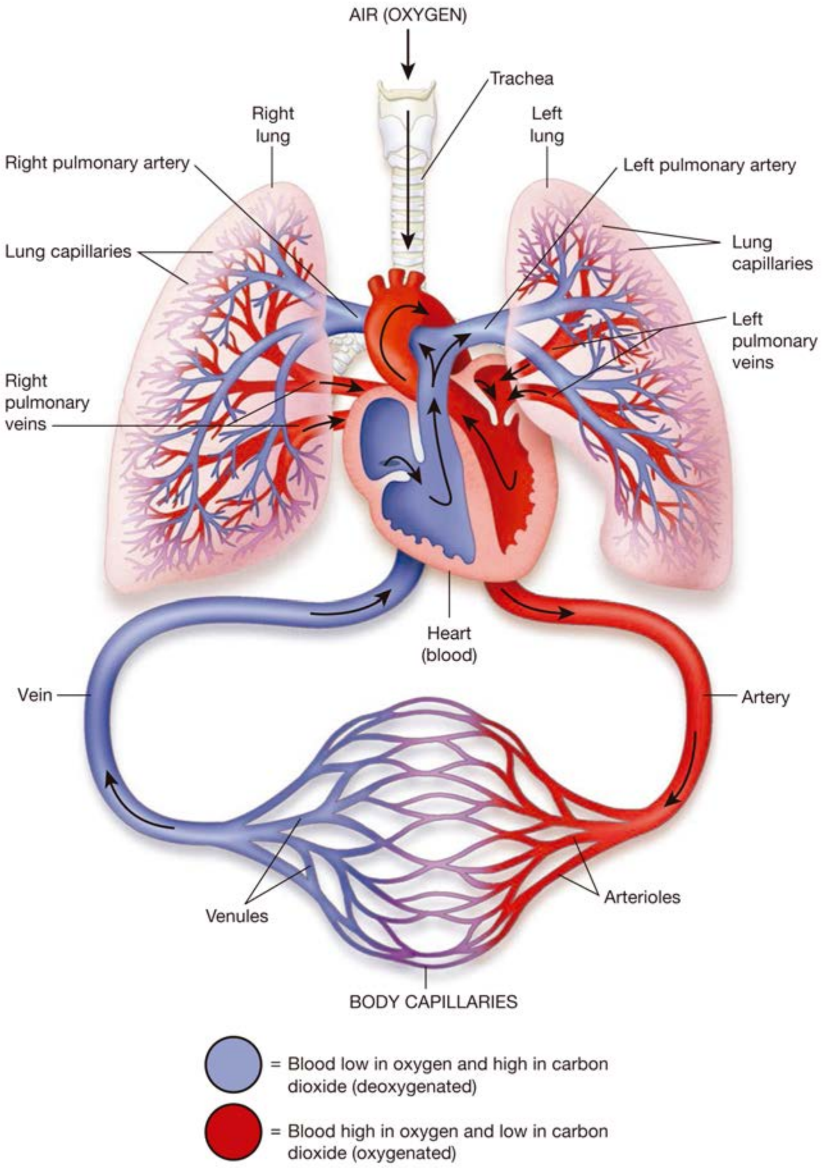

Figure 2.1. *Schematic overview of the cardiovascular system. The black arrows indicate the direction of blood flow [Wingerd, 2009].*

are medium-sized vessels that decrease in diameter as they approach the periphery, and in which the media layer is less elastic (contain fewer elastic fibres) and contain more SMCs [Rhodin, 1980].

Regardless of the category, the healthy wall of an artery is a complex structure

Table 2.1
Main differences between arteries and veins.

	Arteries	**Veins**
Direction of blood flow	From the heart to the body	Back to the heart
Velocity of blood flow	Fast	Slow
Oxygen concentration	Carry oxygenated blood (except pulmonary artery)	Carry deoxygenated blood (except pulmonary vein)
Pressure	High	Low
Anatomy	Thick outer walls Elastic and muscular	Thin outer walls Less elastic
Lumen	Narrow	Wide
Location	Deeper in the body	Closer to the skin
Valves	No	Yes
Main disease	Atherosclerosis	Thrombosis

that consists in three distinct concentric layers (also called tunicas). Going from the lumen to the outer wall we find the intima, the media and finally the adventitia:

- The **intima** (tunica intima) is the innermost layer of the arterial tissue. It is composed of the following structures: endothelium (ET), a single layer of endothelial cells (ECs) lining the vessel wall which constitutes a selective barrier against blood plasma lipids, lipoproteins and other molecules; a thin basal membrane; and the subendothelial space (SES), a thin layer of connective tissue which is mainly composed of collagenous bundles, elastic fibrils, SMCs, and perhaps some fibroblast [Rhodin, 1980]. Although this arterial layer has multiple parts, in healthy young individuals these tissue components contribute minimally to the thickness of the vessel wall [Tortora and Derrickson, 2018] and, from the mechanical perspective, its contribution is practically negligible. However, the thickness and stiffness of the SES varies with age and disease, making that its mechanical contribution may become significant [Holzapfel et al., 2000].
- The **media** layer (tunica media) is the middle layer of the vessel wall. It is a relatively thick layer comprised of concentric layers of SMCs embedded within an extracellular matrix (ECM) composed of a network of collagen and elastin fibres [Robertson and Watton, 2013], and delineated by elastic laminae. The number of elastic laminae decreases toward the periphery, i.e. as the muscular arteries are reached. In most arteries, the media is separated from the intima and adventitia by the internal elastic lamina (IEL) and external elastic lamina (EEL), respectively. In muscular arteries the IEL and EEL are much more prominent, whereas in elastic arteries they are hardly distinguishable from the regular elastic laminae [Holzapfel et al., 2000]. From the mechanical point of view, the media is the most significant layer in a healthy artery.
- The **adventitia** (tunica externa) is the outermost layer of the arterial wall consisting mainly of a sparse population of fibroblasts, collagen fibres, some

elastin fibres and nerves. In large arteries, this layer also gives rise to the vasa vasorum: a network of small blood vessels that supply oxygen and nutrients to the cells of the vessel wall [Wagenseil and Mecham, 2009], as well as removing waste products. The thickness of the adventitia varies considerably depending on the type (elastic or muscular), physiological function and location of the blood vessel [Rhodin, 1980; Holzapfel et al., 2000]. For example, the adventitia is thicker in muscular arteries than in elastic arteries, often occupying approximately the half of the arterial wall.

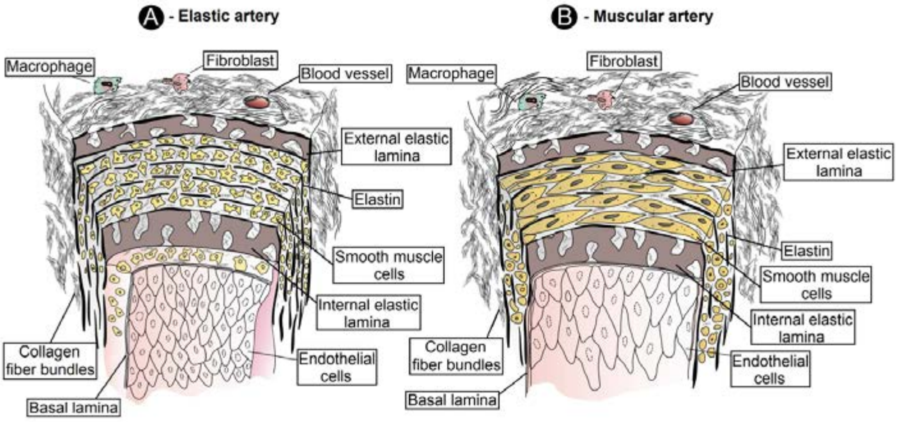

Figure 2.2. *Schematic representation of the arterial wall. Adapted from Rhodin [1980].*

2.3 Mechanical properties of the arterial tissue

The microstructural composition of the vessels wall, detailed in the previous section, has several implications which have to be taken into account as precursor to the formulation of sophisticated constitutive laws trying to capture the mechanical behaviour of those vessels. This is necessary to study the endovascular devices expansion in order to analyse the damage caused by the them in the tissue.

2.3.1 Active and passive response

The mechanical behaviour of the arterial tissue is governed by both a passive contribution, which is fundamentally from the elastin (at low pressures) and collagen (at high pressures) combination [Roach and Burton, 1957], and an active contribution related to the SMCs [Holzapfel and Ogden, 2018]. Consistent with histology, this mechanical response exhibited in both states is highly dependent on its location along the vascular tree [Humphrey, 1995].

However, as other living tissues, the vascular tissue shows an active behaviour which is related to its capability, not only to change its properties in response to environmental changes, but also to react to external stimuli and exerted forces (i.e. arterial growth and remodelling). For example, a main function of this active behaviour in the arterial system is carried out by the smooth muscle cells in the medial layer, which can relax or contract in order to modify the vessel diameter, regulating the amount of blood sent to each organ [Humphrey, 2002], and the extracellular matrix turnover [Holzapfel and Ogden, 2010]. Another typical examples of active behaviour are the heart contraction which pumps blood into the vascular system by means of the contraction of the myocardial tissue [Taber and Perucchio, 2000] and vessel wall growth due to hypertension.

Several models including the active behaviour of vascular tissues are found in the literature (see for example [Holzapfel and Ogden, 2010] for a detailed review of active material models up to 2010 and [Holzapfel and Ogden, 2018] for more recent approaches). However, only the passive response of the arterial tissue has been considered in this Thesis. Therefore, the constitutive equations and arterial mechanical models presented in following sections and chapters neglect the active response.

2.3.2 Anisotropy

The existence of preferred orientations for some of the microstructural components forming the vessels wall leads to the appearance of a marked anisotropic macroscopic behaviour. Specifically, anisotropy in arteries is associated to the preferred orientation of the collagen fibres, SMCs or the elastin network in the different tissue layers. In the intima, the collagen fibre orientation is not uniform through the layer thickness. For example, five separate layers with differently aligned families are observed in coronary arteries [Gasser et al., 2006]. The distinct families of collagen fibres in this layer are characterized by large deviations of individual collagen fibres from the mean orientations. There is also elastin present in the subendothelial space, which is arranged in a 3D network of elastic fibres [Rhodin, 1980]. In the media layer, the elastin, bundles of collagen fibres and SMCs and their interconnections constitute a continuous fibrous helix. This helix has a small pitch so that within the media it is almost circumferentially oriented. Moreover, experimental studies [Canham et al., 1989] demonstrated that collagen, about 30% of type I and 70% of type III, and SMCs in this layer were consistently circumferentially and coherently aligned [Gasser et al., 2006]. Furthermore, it is worth noting that the fibres average orientation exhibits certain radial component [Rhodin, 1980]. Concerning the adventitia, its microstructure is dispersed, which makes it difficult to determine a preferred orientation [Gasser et al., 2006]. Experimental studies [Canham et al., 1989], showed that collagen fibres, primarily of type I, form two helically arranged families, within which the individual collagen fibres have a large deviation from their mean orientations.

In order to try to reproduce the particular microstructure of the arterial tissue, a feasible possibility, which is widely accepted in arterial mechanics, is to assume in each layer of the tissue two directions of anisotropy helically oriented at $\pm\beta$ degrees relative to the circumferential direction [Holzapfel et al., 2000, 2002]. This assumption considers that the varying fibres orientation in each layer is mimicked by assuming a homogeneous orientation, which is frequently assumed constant across the whole thickness. Regarding the orientation angle, for example, histological images of the three layers of a human aorta [Holzapfel, 2006] showed a variation of the collagen fiber alignment angle through the wall thickness: intimal, medial and adventitial samples showed mean collagen fiber angles of 18.8º, 37.8º and 58.9º, respectively (Fig. 2.3). Concerning the radial component of the mean orientations of the families of collagen fibres, it is not usually taken into account in this approach [Holzapfel et al., 2000; Gasser et al., 2006]. The inclusion of certain dispersion with respect to the main anisotropy direction can partially compensate this lacking [Holzapfel et al., 2005b; Gasser et al., 2006; Alastrué et al., 2009]. In this Thesis, this approach has been assumed for modelling the arterial layers in the work entitled *How does stent expansion alter drug transport properties of the arterial wall?* (see Section 3.1 in Chapter 3).

2.3.3 Incompressibility

Additionally to cells and connective tissue, the arterial wall has an important amount of intracellular and extracellular water which ranges approximately from 70 to 80% per wet weight [Humphrey, 1995]. Based on histology, therefore, an artery can be classified mechanically as a ”mixture-composite” with a solid part composed of elastin, collagen and smooth muscle cells and a fluid part which is fundamentally an extracellular aqueous solution.

The high water content of the arterial tissue justifies the usual assumption in arterial mechanics that it is almost incompressible. Although this is not strictly true, due in part to certain movements of fluid in and out of the arterial wall induced by stress gradients [Chuong and Fung, 1984], volume is preserved and arteries undergo isochoric deformations under a wide variety of loads and, specifically, under physiological loads [Humphrey, 1995]. The assumption of incompressibility of the arterial wall, which has been also assumed in this Thesis, is therefore a reasonable assumption and it is supported by other experimental studies [Lawton, 1954; Carew et al., 1968; Dobrin and Rovick, 1969].

This approach has important consequences for the interpretation of experimental data and simplifies theoretical analysis of arterial tissue, allowing for the formulation of constitutive laws based only on isochoric invariants and reducing the required number

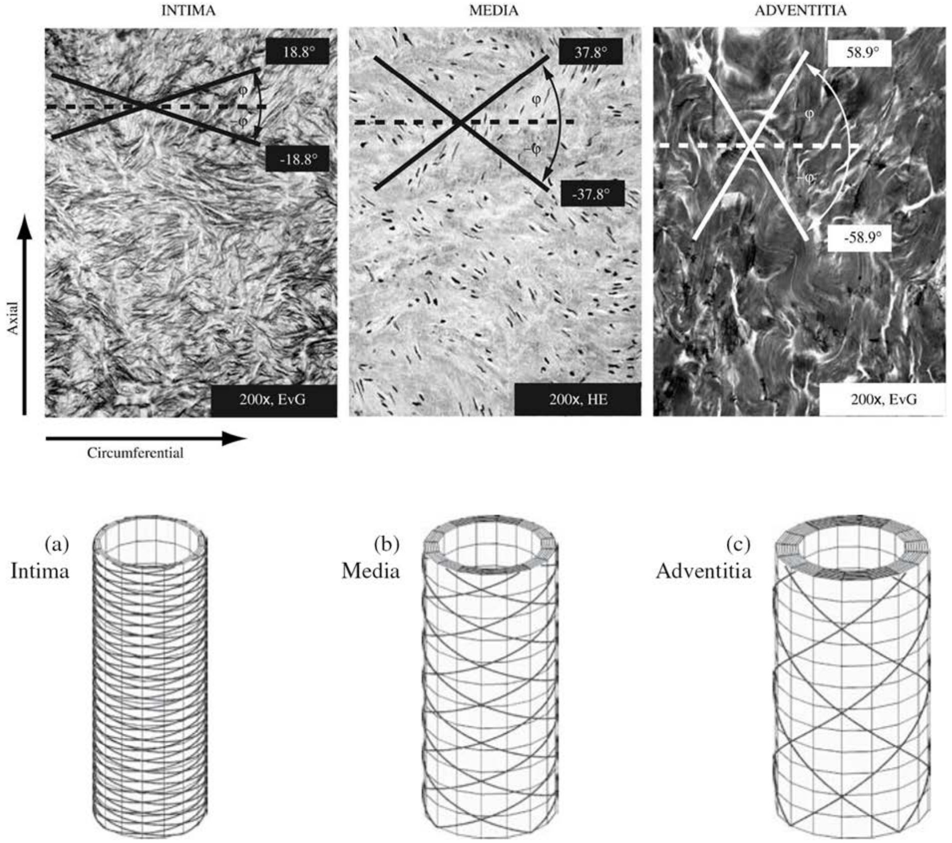

Figure 2.3. *Upper: Histological images (3 mm thick sections) of an intimal, medial and adventitial strips with circumferential orientation. Collagen fibres appear as relatively straight lines in the intima and as wavy structures in the adventitia. In the media layer, nuclei of SMCs, which appear as black dashes or dots, depending on their orientations and radial positions, indicate preferred orientations of the tissue [Holzapfel, 2006]. Lower: Tube-like artery showing the collagen fibre orientations at biological equilibrium projected on (a) the intima, (b) the media and (c) the adventitia [Holzapfel, 2008].*

of material parameters [Nolan and McGarry, 2016].

2.3.4 Residual stresses

The presence of residual stresses in the blood vessels wall is one of the most important features of vascular tissues. Residual stresses are defined as those stresses that exist in the vessels in the absence of externally applied loads [Humphrey, 1995].

Arteries are therefore pre-stressed, i.e. in their load-free configuration they are still under tension and compression. This is fact is revealed when a cut is performed on an arterial segment in an unloaded configuration. Then, considering a cut in the radial direction, the vessel shortens (or lengthens) releasing part of the residual stresses in the longitudinal direction. Also when a cut is performed in the longitudinal direction, usually on a short vessel ring, it springs open releasing the residual stresses associated to the circumferential direction.

Bergel [1960] is considered the first author to allude to residual stress in arteries. However, it was Fung [1983] and Vaishnav and Vossoughi [1983] who initiated the study of residual stress and deformation in arteries. This was followed by the pioneering works by Chuong and Fung [1986] and Takamizawa and Hayashi [1987], which are some of the earliest insights into the mechanical effect and important implications of residual stresses in arteries, showing that they play a key role in the mechanical behaviour of arteries maintaining the homeostatic state of stress *in vivo* and contributing to the adaptation to altered conditions in their mechanobiological environment [Cardamone et al., 2009], including pathological changes such as disease or injury.

Moreover, several experimental studies [Holzapfel et al., 2007; Sommer et al., 2010; Peña et al., 2015] have revealed the presence of different residual strains patterns for the different layers of the arterial tissue, with predominant residual deformations in circumferential or axial direction depending on the layer, highlighting that residual stresses in arteries are highly layer-specific and axially dependent [Holzapfel et al., 2007].

2.4 Constitutive modelling of the arterial wall

The mechanical behaviour of soft biological tissues has been widely studied in the last decades, and this is particularly the case for arterial wall tissue. A brief review of the most widely used constitutive laws in the modelling of the passive elastic behaviour of blood vessels is presented this section. The active behaviour of the arterial tissue has been omitted in this review. For further details about the constitutive modelling of both the passive and the active behaviour of the arterial tissue, the reader is referred to different publications [Holzapfel et al., 2000; Vito and Dixon, 2003; Kalita and Schaefer, 2008; Holzapfel and Ogden, 2010; Gasser, 2017, 2021].

2.4.1 Isotropic models

The behaviour of the different layers of the arterial tissue is highly anisotropic due to the structural arrangement of collagen fibres. However, there are many isotropic strain energy functions (SEF) proposed in the literature to characterize the mechanical response of the arterial wall. Due to vascular tissue and rubber share some common mechanical properties, constitutive models that were originally proposed for rubber, have also been widely used to describe the vessel wall.

The neo-Hookean model [Treloar, 1943a,b] is the simplest form of all commonly used hyperelastic models and has been chosen in several works to model vascular tissue in order to reduce computational complexity as it requires optimization of only one coefficient per material. The SEF of this model is expressed as:

$$\Psi = c_{10} \left[I_1 - 3 \right] . \tag{2.1}$$

where $I_1 = \mathrm{tr}\,(\boldsymbol{C})$ denotes the first invariant of the right Cauchy-Green deformation tensor [Spencer, 1971], $\boldsymbol{C}$, and the constant $c_{10} > 0$ is a material parameter. The well-known Mooney-Rivlin constitutive model [Mooney, 1940; Rivlin, 1948] is able to reproduce a wider range of mechanical non-linear behaviours and it has been also used to model vascular tissue. The SEF for an incompressible Mooney-Rivlin material is a linear combination of the first and the second invariant of $\boldsymbol{C}$, and it is as follows:

$$\Psi = c_{10} \left[I_1 - 3 \right] + c_{01} \left[I_2 - 3 \right] \tag{2.2}$$

where c_{10} and c_{01} are empirically determined material constants and I_2 is the second invariant of the right Cauchy-Green deformation tensor, which is defined as $I_2 = \frac{1}{2}\left[\left[\mathrm{tr}\,(\boldsymbol{C}) \right]^2 + \mathrm{tr}\left(\boldsymbol{C}^2 \right) \right]$. If $c_{01} = 0$ the neo-Hookean model is obtained. Both the neo-Hookean model and the Mooney-Rivlin model are also special cases of the polynomial model introduced by Rivlin and Saunders [1951], which was developed as a Taylor series expansion of $(I_1 - 3)$ and $(I_2 - 3)$:

$$\Psi = \sum_{i,j=1}^{N} c_{ij} \left[I_1 - 3 \right]^i \left[I_2 - 3 \right]^j . \tag{2.3}$$

where c_{ij} are material parameters, with $c_{00} = 0$. Neo-Hookean and Mooney-Rivlin expressions are obtained with $N = 1$ and appropriate choices of the parameters c_{ij}. Another hyperelastic model based on a series expansion but that only depends on the first invariant is the Yeoh model, firstly introduced in 1990 and slightly modified in 1993 [Yeoh, 1990, 1993]:

$$\Psi = \sum_{i=1}^{3} c_{i0} \left[I_1 - 3 \right]^i . \tag{2.4}$$

where the series is truncated after the first three terms ($N = 3$). However, a slightly more generalized expression of the Yeoh hyperelastic model, which includes N terms, is used nowadays:

$$\Psi = \sum_{i=1}^{N} c_{i0} \left[I_1 - 3 \right]^i . \tag{2.5}$$

This model is also known as reduced polynomial model. Note that given the case $N = 1$, the Yeoh model reduces to the neo-Hookean model.

In contrast to other purely phenomenological descriptions that originally have been proposed for rubber, constitutive models that have especially been developed for vascular tissue include exponential terms in their respective SEFs. One of these models was developed by Demiray [1972], whose most noticeable characteristic is the exponential dependence on the first invariant I_1 which helps to mimic the characteristic stiffening of the vascular tissue:

$$\Psi = \frac{a}{2\,b} \left[\exp\left(b \left[I_1 - 3 \right] \right) - 1 \right] . \tag{2.6}$$

where the constants a has stress units, whereas b is dimensionless. This SEF was modified several years later [Demiray et al., 1988] by including a neo-Hookean term and the quadratic dependence of the term $[I_1 - 3]$ in Eq. 2.6. With these modifications, the new form results as follows:

$$\Psi = \mu \left[I_1 - 3 \right] + \frac{a}{2\,b} \left[\exp\left(b \left[I_1 - 3 \right]^2 \right) - 1 \right] . \tag{2.7}$$

where μ has stress units.

Regarding the phenomenological constitutive models based on the principal stretches, Valanis and Landel [1967] proposed a SEF of the following form:

$$\Psi = \sum_{i=1}^{3} f\left(\lambda_i \right) . \tag{2.8}$$

where λ_1, λ_2, λ_3 are the principal stretch ratios [Fung, 1993]. This expression is known as the Valanis-Landel model and the total SEF is additively decomposed on functions solely depending on one of the principal stretches. Another model which is naturally expressed as a function of the principal stretches was formulated by Ogden [1972]. The Ogden model is a versatile expression that can describe the mechanical behavior of a wide variety of hyperelastic materials including rubbers, polymers and biological tissues when subjected to high strains, which is written as follows:

$$\Psi = \sum_{i=1}^{N} \frac{2\,\mu_i}{\alpha_i} \left[\lambda_1^{\alpha_i} + \lambda_2^{\alpha_i} + \lambda_3^{\alpha_i} - 3 \right] , \tag{2.9}$$

where each μ_i and α_i is a material constant. For practical purposes, Eq. 2.9 is restricted to a finite number of terms (normally N is taken as 3), while, for consistency with the classical theory, the following requirement must be satisfied:

$$\mu = \sum_{i=1}^{N} \mu_i \, \alpha_i, \tag{2.10}$$

where μ is the shear modulus of the material. Hence, the first part of the Ogden's SEF depends only on $I_1 = \lambda_1^2 + \lambda_2^2 + \lambda_3^2$ and $I_2 = \lambda_1\lambda_2 + \lambda_1\lambda_3 + \lambda_2\lambda_3$. However, it is not possible to explicitly express this function as a function of the invariants. Note that for particular values of the material parameters, the Ogden model reduces to the Mooney-Rivlin model for $N = 2$, ($\alpha_1 = 2$ and $\alpha_2 = -2$) and to the neo-Hookean model for $N = 1$ and $\alpha_1 = 2$.

Regarding the micromechanical models, the eight-chain model, also known as the Arruda-Boyce model [Arruda and Boyce, 1993], assumes a representative network structure represented by eight chains that are positioned on the diagonals of a unit cubic cell from the center of the cube to its corners. The SEF for this model is dependent on the first invariant only and is expressed as follows:

$$\Psi = \mu \sum_{i=1}^{5} \frac{A_i}{\lambda_{\mathrm{m}}^{2i-1}} \left[I_1^i - 3^i \right] \tag{2.11}$$

where μ is the initial modulus and λ_{m} is the limiting chain stretch, i.e. the value of the chain stretch when the chain length reaches its fully extended state. Using the first five terms of the inverse Langevin function, the coefficients A_i are the following: $A_1 = 1/2$, $A_2 = 1/20$, $A_3 = 11/1050$, $A_4 = 19/7000$ and $A_5 = 519/673750$.

2.4.2 Anisotropic models

Considering the tube-like shape exhibited by the blood vessels, most of these non-structural anisotropic functions are usually expressed in cylindrical coordinates, so the radial, circumferential and longitudinal characteristic directions are explicitly included in the SEF.

A two dimensional form of the SEF using a polynomial function of the Green-Lagrange strain tensor, $\boldsymbol{E}$, with seven parameters was proposed by Vaishnav et al. [1973], which is written as follows:

$$\begin{aligned} \Psi = {} & c_1 \, E_{\Theta\Theta}^2 + c_2 \, E_{\Theta\Theta} E_{ZZ} + c_3 \, E_{ZZ}^2 + c_4 \, E_{\Theta\Theta}^3 \\ & + c_5 \, E_{\Theta\Theta}^2 E_{ZZ} + c_6 \, E_{\Theta\Theta} E_{ZZ}^2 + c_7 \, E_{ZZ}^3, \end{aligned} \tag{2.12}$$

where each c_i is a stress-like material parameter and $E_{\Theta\Theta}$ and E_{ZZ} are components of the modified Green–Lagrange strain tensor in the circumferential and axial directions, respectively. This expression represented the first attempt to describe the anisotropic mechanical response of arteries [Holzapfel et al., 2000] and clearly set the standard for work in arterial mechanics [Humphrey, 1995]. However, its applicability is limited.

One of the most extensively used constitutive laws of this type for arteries was formulated by Fung et al. [1979], assuming the following 2D exponential form:

$$\Psi = c\left[\exp(Q) - 1\right], \tag{2.13}$$

where c is a model constant and Q is a function of the components of the Green-Lagrange strain tensor within the local cylindrical coordinate system given by:

$$Q = b_1 E_{\Theta\Theta}^2 + b_2 E_{ZZ}^2 + 2 b_3 E_{\Theta\Theta} E_{ZZ} \tag{2.14}$$

where b_i, $i = 1, \cdots, 3$ are non-dimensional material parameters. The limitation of this SEF is its 2D formulation which cannot describe a 3D anisotropic problem such as a thick-walled cylindrical tube under inflation or torsion [Holzapfel et al., 2000]. To overcome this limitation, Chuong and Fung [1983] later suggested the following 3D exponential SEF, assuming the material to be incompressible, homogeneous and cylindrically orthotropic [Humphrey, 1995]:

$$\Psi = c \exp(Q), \tag{2.15}$$

with

$$\begin{aligned} Q =\, & b_1 E_{\Theta\Theta}^2 + b_2 E_{ZZ}^2 + b_3 E_{RR}^2 \\ & + 2 b_4 E_{\Theta\Theta} E_{ZZ} + 2 b_5 E_{ZZ} E_{RR} + 2 b_6 E_{RR} E_{\Theta\Theta}, \end{aligned} \tag{2.16}$$

where b_i, $i = 1, \cdots, 6$ are dimensionless parameters which characterize the material and $E_{\Theta\Theta}$, E_{ZZ} and E_{RR} are components of the modified Green–Lagrange strain tensor in the circumferential, longitudinal and radial directions, respectively [Chuong and Fung, 1983]. This last expression for Q was later fully completed in a more general form by Humphrey [1995], including the shear terms, although these result naturally from their assumed material symmetry:

$$\begin{aligned} Q =\, & b_1 E_{\Theta\Theta}^2 + b_2 E_{ZZ}^2 + b_3 E_{RR}^2 \\ & + 2 b_4 E_{\Theta\Theta} E_{ZZ} + 2 b_5 E_{ZZ} E_{RR} + 2 b_6 E_{RR} E_{\Theta\Theta} \\ & + b_7 E_{\Theta Z}^2 + b_8 E_{RZ}^2 + b_9 E_{R\Theta}^2, \end{aligned} \tag{2.17}$$

where b_i, $i = 1, \cdots, 9$ are dimensional parameters, and $E_{\Theta Z}$, E_{RZ} and $E_{R\Theta}$ are the Green-Lagrangian shear strains. Finally, Humphrey and Na [2002] proposed a generalization of the non-dimensional function Q proposed by Chuong and Fung [1983]:

$$\begin{aligned} Q =& c_1\, E_{\Theta\Theta}^2 \;+\; c_2\, E_{ZZ}^2 \;+\; c_3\, E_{RR}^2 \\ &+ 2\, c_4\, E_{\Theta\Theta} E_{ZZ} \;+\; 2\, c_5\, E_{ZZ} E_{RR} \;+\; 2\, c_6\, E_{RR} E_{\Theta\Theta} \\ &+ c_7 \left[E_{R\Theta}^2 + E_{\Theta R}^2\right] \;+\; c_8 \left[E_{\Theta Z}^2 + E_{Z\Theta}^2\right] \;+\; c_9 \left[E_{ZR}^2 + E_{RZ}^2\right], \end{aligned} \tag{2.18}$$

As alternative to the exponential form proposed by Fung et al. [1979], Takamizawa and Hayashi [1987] suggested a logarithmic expression of the SEF, as follows:

$$\Psi \;=\; -c\, \ln\left(1 - Q\right), \tag{2.19}$$

with

$$Q \;=\; \frac{1}{2}\, b_1\, E_{\Theta\Theta}^2 \;+\; \frac{1}{2}\, b_2\, E_{ZZ}^2 \;+\; b_3\, E_{\Theta}\, E_{Z}, \tag{2.20}$$

where the stress valued coefficient, c, and the dimensionless coefficients b_1, b_2 and b_3 characterize the mechanical properties of the material [Takamizawa and Hayashi, 1987]. An innovative approach for the modelling of the arterial tissue was proposed by Holzapfel and Weizsäcker [1998], where the SEF was decoupled into two terms as follows:

$$\Psi \;= \Psi_{\text{iso}} \;+\; \Psi_{\text{aniso}} \tag{2.21}$$

$$\Psi \;=\; c_1\, \left[I_1 - 3\right] \;+\; c_2\, \left[\exp\left(Q\right) - 1\right], \tag{2.22}$$

where c_1 and c_2 are stress-like parameters. The first term of the potential, Ψ_{iso}, represents the isotropic contribution to the total SEF specified by the classical neo-Hookean material, whereas the second term, Ψ_{aniso}, represents the anisotropic contribution specified by the model proposed by Fung et al. [1979], previously shown (see Eq. 2.13).

Holzapfel et al. [2000] developed a model specifically designed for the arterial wall including two directions of anisotropy. From the engineering point of view, each layer is considered as a composite reinforced by two families of collagen fibres which are arranged in symmetrical spirals (i.e. helically distributed). They assume that each layer responds with similar mechanical characteristics and they therefore use the same form of SEF (but with a different set of material parameters) for each layer of the tissue. They considered the (classical) neo-Hookean model to determine the isotropic response in each layer and an exponential function to represent the collagen fibres contribution, the latter mainly motivated by the strong stiffening effect of each layer of the tissue shown at high pressures.

$$\Psi = \mu\left(I_1 - 3\right) + \frac{k_1}{2k_2} \sum_{\alpha=4,6} \left[\exp\left\{k_2\left[I_\alpha - 1\right]^2\right\} - 1\right], \tag{2.23}$$

where I_1 characterizes the isotropic mechanical response of the arterial elastin [Gundiah et al., 2009; Lillie et al., 2010], an important constituent of the ground substance of the ECM, while the invariants $I_4 \geq 1$ and $I_6 \geq 1$ characterize the mechanical response in the preferential directions of the fibers/cells. Assuming that the anisotropy directions are helically oriented at $\pm\beta$ degrees with respect to the circumferential direction, the invariants I_4 and I_6 can also be expressed as a function of the main stretches:

$$I_4 = \lambda_1^2 \cos^2 \beta_1 + \lambda_2^2 \sin^2 \beta_1, \qquad I_6 = \lambda_1^2 \cos^2 \beta_2 + \lambda_2^2 \sin^2 \beta_2. \tag{2.24}$$

where $\beta_1 = \beta$ and $\beta_2 = -\beta$ [Holzapfel et al., 2000]. Moreover, it has been assumed that the strain energy corresponding to the anisotropic terms only contributes to the global mechanical response of the tissue when stretched (i.e. $I_4 > 1$ and $I_6 > 1$) and that the tissue does not bear any load when compressed. Finally, the parameters $\mu > 0$ and $k_1 > 0$ are stress-like material constants defining the isotropic matrix response and the layer stiffness of collagen fibres, respectively, whereas $k_2 > 0$ is a dimensionless parameter related to the progressivity of fibre stiffening behaviour during deformation. For the reminder of this Thesis, we refer to this SEF as Holzapfel-Gasser-Ogden (HGO) model. The HGO model [Holzapfel et al., 2000] was modified in order to take into account the dispersion of the collagen fibres around the anisotropy directions characterized by the invariants I_4 and I_6 [Holzapfel et al., 2005a,b]. The SEF of this model is defined as follows:

$$\Psi = \mu\,(I_1 - 3) + \frac{k_1}{2k_2} \sum_{\alpha=4,6} \left[\exp\left\{ k_2\,(1-\rho)\,[I_1 - 1]^2 + \rho\,[I_\alpha - 1]^2 \right\} - 1 \right], \tag{2.25}$$

where the parameter $\rho \in (0,\, 1)$, which has a purely phenomenological basis, allows to regulate the degree of anisotropy between full isotropy and full alignment (transverse isotropy) and is therefore a measure of dispersion in the fibre orientation. When $\rho = 1$ an ideal alignment of collagen fibres is obtained, while a value of $\rho = 0$ corresponds to an isotropic distribution, obtaining the SEF proposed by Demiray [1972]. However, the ρ parameter does not have a real physical meaning and can not be computed from fibre distribution experimental data. For the reminder of this Thesis, we refer to this model as ρ model.

Based on the previous HGO model [Holzapfel et al., 2000], the model proposed by Gasser et al. [2006], also referred as Gasser-Ogden-Holzapfel (GOH) model, incorporates and additional scalar structure parameter, κ, which characterizes the dispersion of each fibre family orientation and describes its degree of anisotropy. In this model, the SEF is given by the following expression:

$$\Psi = \mu\,(I_1 - 3) + \frac{k_1}{2k_2} \sum_{\alpha=4,6} \left[\exp\left\{ k_2\,[\kappa I_1 + (1 - 3\kappa) I_\alpha - 1]^2 \right\} - 1 \right], \tag{2.26}$$

where $\kappa \in (0,\, \frac{1}{3})$. Contrary to the SEF of the ρ model, where ρ basically couples the invariants I_1 and I_4 (or I_1 and I_6), a structurally consistent derivation, where the structural components of the vessel wall are reflected by associated entities in the formulation, leads to the derivation of κ. Specifically, this parameter is a result of considering the fibres oriented following the von Mises orientation density function and can be obtained directly from experimental data. Thus, when $\kappa = 0$, the fibres are perfectly aligned (no dispersion) and when $\kappa = 1/3$ the fibres are randomly distributed and the material becomes isotropic.

During the development of this Thesis, the SEFs proposed by Yeoh [1993] and Gasser et al. [2006] have been used to characterize the mechanical properties of the arterial tissue in the works entitled *Mathematical modelling of the restenosis process after stent implantation* (see Section 3.4 in Chapter 3) and *How does stent expansion alter drug transport properties of the arterial wall?* (see Section 3.1 in Chapter 3), respectively. In both works, model parameters were calibrated against the experimental data reported by Holzapfel et al. [2005b].

2.5 Atherosclerosis

Atherosclerosis is a complex progressive pathological process that is not entirely understood. It is, however, reasonably well established that the phenomenon is characterized by build-up of plaque (atheroma) due to abnormal accumulation of cholesterol and other lipids, calcium, large inflammatory cells called macrophages, connective tissue and other substances, in the inner lining of the arterial walls. These fatty deposits cause luminal narrowing (stenosis), rupture or erosion of the arterial wall, hardening of the arteries and loss of their elasticity, which leads to an eventually or complete reduction in the blood flow through the vessels (Fig. 2.4). Nevertheless, the most serious damage occurs when the plaque becomes fragile and ruptures (vulnerable plaque). Plaque rupture causes the formation of blood clots (thrombi) that can obstruct blood flow to the heart (causing coronary heart disease, including stable angina and heart attacks), brain (causing ischemic stroke) or lower extremities (causing peripheral vascular disease) [Libby et al., 2002; Bentzon et al., 2014].

2.5.1 Localization of atherosclerotic plaque

Atherosclerotic lesions are distributed irregularly throughout the vasculature. Some vessels are characteristically spared, whereas other sites within the vascular tree frequently harbor lesions [Frangos et al., 1999; VanderLaan et al., 2004]. However, atherosclerotic lesions do not occur at random sites. Atherosclerosis occurs mainly in larger and medium size arteries, which involves an abnormal accumulation of high molecular weight lipoprotein in the arterial wall [Tarbell, 2003]. The coronary arteries, the major branches of the aortic arch, the visceral arterial branches of the abdominal

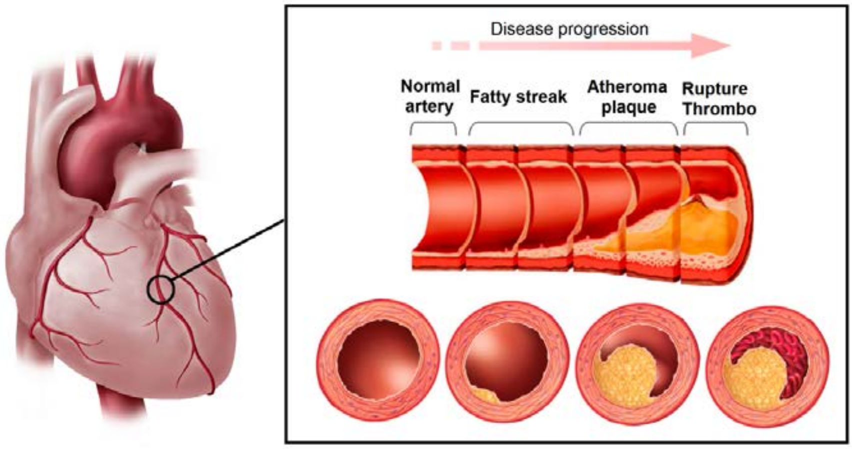

Figure 2.4. *Illustration showing the natural progression of atherosclerosis in a coronary artery [Cilla et al., 2014].*

aorta, the distal abdominal aorta and its ileofemoral branches are high-susceptibility sites for the localization of atherosclerotic lesions, accounting for most of the clinical manifestations of the disease in humans [DeBakey et al., 1985].

These predominant sites are thought to be conditioned by hemodynamic parameters, being particularly associated with regions of low velocity and wall shear stress, oscillatory flow or turbulent flow [VanderLaan et al., 2004]. The coronary arteries have a complex geometric configuration of branchings and curves and undergo mechanical torsions during the normal cardiac cycle; this may help explain the propensity for these vessels to develop clinically significant disease. The left coronary artery bifurcation into left anterior descending and circumflex branches has a particular predilection for plaque formation [Frangos et al., 1999]. Thus, the disease tends to be localized in regions of the outer walls of bifurcations and the inner walls of curved segments where fluid shear stress is altered from its normal patterns [Tarbell, 2003].

2.5.2 Atherosclerosis risk factors

Although cardiovascular diseases caused by atherosclerosis do not typically manifest before middle age, pathological data have shown that the disease process begins early in life making primary prevention efforts necessary from childhood [WHO, 2007]. It therefore seems eminently reasonable to initiate a healthy lifestyle training in childhood to promote improved cardiovascular health in adult life [Williams et al., 2002].

Various risk factors are associated with atherosclerosis, which can be divided into immutable and modifiable risk factors [Herrington et al., 2016]. Immutable risk factors, that can not be controlled include the following:

- Age: as the body ages, the risk for atherosclerosis increases and genetic or lifestyle factors cause plaque to gradually build in the arteries. By middle age or older, enough plaque has built up to cause signs or symptoms. For men, the risk increases after age 45, while in women, the risk increases after age 55.
- Family history of early heart disease.
- Gender: generally, men have a greater risk of heart disease than women, and they have heart attacks earlier in life. Moreover, even after menopause, when the death rate from heart disease increases for women, is still lower than the death rate for men.

Some other risk factors can be modified, treated or controlled through lifestyle changes or by taking medicine. Risk factors for atherosclerosis we have control over are [Rafieian-Kopaei et al., 2014]:

- Unhealthy blood cholesterol levels (hypercholesterolemia or hyperlipidemia): this includes high low density lipoprotein (LDL) cholesterol, sometimes called 'bad' cholesterol, and low high density lipoprotein (HDL) cholesterol, sometimes called 'good' cholesterol.
- High blood pressure (hypertension): blood pressure is considered high if it stays at or above 140/90 mmHg over a period of time.
- Smoking: this can damage and tighten blood vessels, raise cholesterol levels, and raise blood pressure. Furthermore, smoking also does not allow enough oxygen to reach the body tissues.
- Overweight or obesity: overweight is having extra body weight from muscle, bone, fat, and/or water. Obesity is having a high amount of extra body fat.
- Lack of physical activity or sedentary lifestyle: lack of activity can worsen other risk factors for atherosclerosis.
- Insulin resistance: insulin is a hormone that helps move blood sugar into cells where it is used and insulin resistance occurs when the body cannot use its own insulin properly.
- Diabetes mellitus: a disease in which the body blood sugar level is high (hyperglycemia) because the body does not make enough insulin or does not use its insulin properly.
- Alcohol consumption: heavy drinking can damage the heart muscle and worsen other risk factors for atherosclerosis.
- Stress: research shows that the most commonly reported trigger for a heart attack is an emotionally upsetting event particularly one involving anger.

- Sleep apnoea: a disorder in which the breathing stops or gets very shallow while a person is sleeping. Untreated sleep apnoea can raise the chances of high blood pressure, diabetes, and even a heart attack or stroke.

In addition, scientists continue to study other possible risk factors for atherosclerosis. A number of risk factors have been proposed during the past several decades to help identify high-risk individuals [Hackam and Anand, 2003] allowing a steady, but gradual progression toward precision medicine. Indeed, the generation of data in this area of research is explosive and when combined with new technologies and techniques provides the potential for more refined, targeted approaches to cardiovascular medicine [Thomas and Lip, 2017]. In particular, clinical interest has focused on lipid parameters including triglycerides, lipoprotein (a) (Lp(a)), apolipoprotein A-I (Apo A-I), and apolipoprotein B-100 (Apo B-100); on inflammatory biomarkers such as C-Reactive Protein (CRP) and fibrinogen; and on nutritional markers associated with premature atherothrombosis, such as total plasma homocysteine [Ridker et al., 2001; Fruchart et al., 2004]. The combination of traditional risk factors and the so-called novel risk factors is expected to facilitate the assessment of patient global risk, thereby allowing optimal use of diagnostic and therapeutic efforts in high risk subjects [Fruchart et al., 2004].

2.5.3 Diagnosis and treatment of atherosclerotic lesions

2.5.3.1 Diagnosis

Atherosclerotic plaques develop over a long period of time before symptoms appear and in 50% of the population it is asymptomatic. Early detection and follow up of vulnerable plaque are a major challenge to prevent acute coronary syndromes (ACS) and cardiac events [Bom et al., 2017]. In recent years, cardiovascular research has sought potential clinical strategies to overcome the limited ability to detect high risk plaques and eventually guide targeted therapy [MacNeill et al., 2003]. Imaging techniques that enable visualization of structural and morphologic characteristics of the atherosclerotic plaque may be helpful to identify the characteristics of the vulnerable plaque *in vivo* and subsequently predict clinical outcome.

Several methods have been used to evaluate the extent and location of atherosclerotic lesions which detect indicators of atherosclerosis such as classical risk factors. Conventional vascular imaging technologies, which either assess morphological characteristics of plaques or functional properties, rely on observation of luminal narrowing (stenosis) for the detection of atherosclerotic plaques. These technologies are either invasive, as with coronary X-ray angiography and intravascular ultrasound (IVUS), or noninvasive as with magnetic resonance imaging (MRI), duplex ultrasound and carotid intimal medial thickness (CIMT) measurements. Preferably, imaging of atherosclerosis is performed non-invasively to minimize potential damage to the patient due to the imaging procedure itself [MacNeill et al., 2003]. Each of these techniques has strengths and weaknesses for imaging atherosclerosis, and none have yet been determined to be the definitive diagnostic tool for atherosclerotic plaque detection.

2.5.3.2 Treatment of atherosclerotic lesions

Certain lifestyle changes, such as eating a healthy diet and exercising, are generally the first-line treatment for people diagnosed with atherosclerosis. But sometimes, medication or surgical procedures may be needed. The most important treatment methods can be categorized into:

- Non-surgical or pharmacological treatments.
- Extensive (or invasive) surgical treatments.
- Minimally invasive treatments.

Regarding the non-surgical treatments, which are used only in case of asymptomatic stenosis, many different types and combinations of drugs are available to slow or reverse the progression of atherosclerosis. Statins are widely prescribed for LDL cholesterol lowering in the primary and secondary prevention of cardiovascular disease [Bonetti et al., 2003]. Moreover, recent clinical studies suggest that statins have other beneficial effects since they are directly involved in restoring or improving endothelial function, attenuating vascular remodeling, inhibiting vascular inflammatory response, and perhaps, stabilizing atherosclerotic plaques [Zhou and Liao, 2010; Ward et al., 2019]. Another common type of cholesterol-lowering medication is a cholesterol absorption inhibitor called Ezetimibe (Zetia) [Patel et al., 2003]. The pharmacological effect of the Ezetimibe is complementary to that of the statins. Blood thinners are another type of medication used to prevent blood clots from forming in patients at high risk for diseases of the heart and blood vessels. The two main types of blood thinners are anticoagulants, which include heparin and warfarin, and antiplatelet drugs, such as aspirin and clopidogrel.

Sometimes, though, more aggressive treatment is needed and narrowed arteries have to be reopened with one of two treatments: bypass surgery or coronary angioplasty. Traditional treatment strategies for coronary heart disease were limited to coronary artery bypass graft surgery (CABG), known widely as open-heart surgery Diodato and Chedrawy [2014]; Melly et al. [2018]. This type of surgery involves redirecting blood flow around blocked arteries in the heart using a healthy blood vessel taken from another part of the body. However, this was, and to some extent still is, a notoriously dangerous procedure with many associated risks. Some of the possible complications include transient ischemic attacks, internal bleeding and infection as well as neurological damage and stroke. Despite the fact that the surgery has improved through the years, with an increased survival rate, the risk factor is definitely higher in the case of older people and those with related medical conditions of a serious nature

[McGinty, 2010].

In response to the risk of invasive procedures, the treatment of CAD was transformed by the introduction of coronary angioplasty, also called percutaneous transluminal coronary angioplasty (PTCA) or percutaneous coronary intervention (PCI), which remains the focus of intensive research and development. Coronary angioplasty was conceptually described by Dotter and Judkins [1964] and first performed in a conscious human by Andreas Gruntzig in 1977 [Grüntzig, 1978]. The angioplasty procedures performed initially were without stent deployment, a technique that is now referred as Plain Old Balloon Angioplasty (POBA). The process involves delivering a balloon to the site of vessel narrowing via a catheter inserted in an artery. The balloon is then inflated under pressure compressing the atherosclerotic plaque and expanding the vessel, restoring lumen size, and hence improving blood flow [McCormick, 2018a].

There is no dispute that POBA revolutionized the treatment of CAD. However, its success was hindered by the inherent limitations of acute vessel closure and elastic recoil in the short term and negative vascular remodeling (late recoil) and neointimal proliferation in the longer term [Bauters and Isner, 1997]. Coronary artery stents were, therefore, developed to overcome these limitations, by scaffolding the balloon-dilated artery, sealing the dissection flaps and preventing late recoil. The vast majority of PCI procedures performed currently involve balloon angioplasty and stent deployment [Iqbal et al., 2013].

2.6 Endovascular devices: stents and balloons

Stents can be classified into three large families: bare metal stents (BMSs), drug-eluting stents (DESs) and bioresorbable vascular scaffolds (BRSs). Moreover, drug-coated balloons (DCBs) have emerged as an attractive alternative to DESs for the treatment of CAD in certain anatomical conditions. Each of these devices are described in detail in the following subsections.

2.6.1 Bare metal stents (BMSs)

The initial era of POBA (1970-1980) was later replaced by the implantation of bare metal stents (BMS) (1980–1999). Wallstent® (Schneider AG, Lausanne, Switzerland) was the first BMS implanted in a human coronary artery in 1986 [Iqbal et al., 2013]. It was a self-expanding platform comprising a stainless steel wire-mesh structure developed by Sigwart and Puel [Sigwart et al., 1987]. Schatz and co-workers developed the Palmaz-Schatz® (Johnson & Johnson, Warren, NJ, USA) stent in 1987, the first stent approved by the Food and Drug Administration (FDA) in the USA. This stainless steel, slotted tube device overcame some of the practical limitations of the

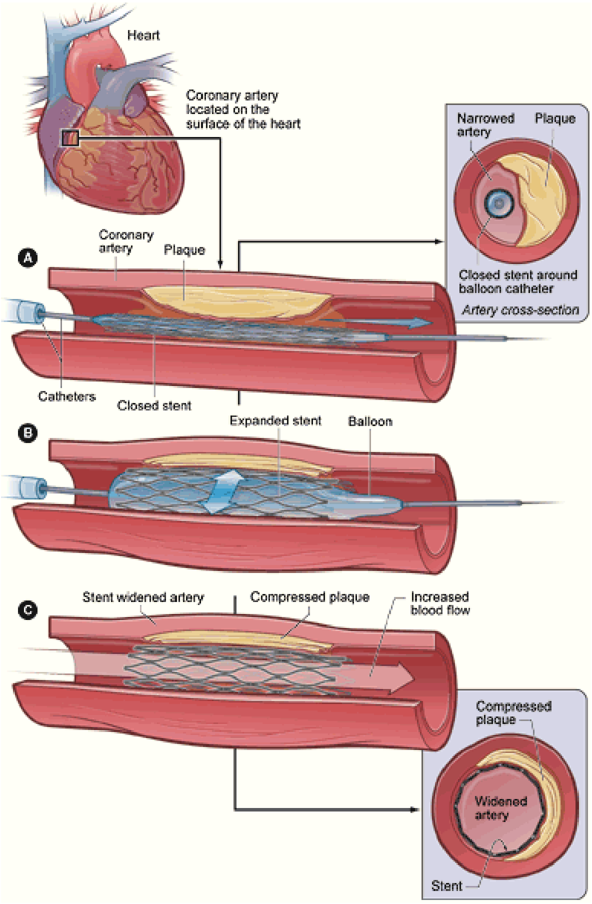

Figure 2.5. *Illustration of a percutaneous coronary intervention (PCI). In A, the deflated balloon with the unexpanded stent is inserted into the narrowed coronary artery is shown. In B, the balloon is inflated at high pressure for a few seconds expanding the stent and compressing the atheroclerotic plaque. The widened artery with the stent implanted is shown in C. The balloon and the catheter have been retrieved again. The blood flow has been restored. (Source: US National Heart Lung and Blood Institute.)*

original Wallstent® by using an alternative deployment mechanism, through the use of balloon expansion and it was one of the most studied and widely used stent in 1990s. In fact, almost all coronary stents are balloon-mounted in this way nowadays. Many other BMS were subsequently developed and received FDA-approval in early 1990s, e.g. Flexstent® (Cook Cardiology, Indianapolis, IN, USA), Wiktor® (Medtronic, Minneapolis, MN, USA), Micro® (Applied Vascular Engineering, Santa Rosa, CA, USA), Cordis® (Cordis Coorporation - Johnson & Johnson, Warren, NJ, USA) and Multi-link® (Advanced Cardiovascular Systems, Santa Clara, CA, USA).

In 1993, two landmark trials, the Belgium Netherlands Stent Arterial Revascularization Therapies Study (BENESTENT) [Serruys et al., 1994] and the North American Stent Restenosis Study (STRESS) [Fischman et al., 1994], demonstrated superiority of the bare metal stents (BMS) over POBA since the use of these stents reduced early elastic recoil and restenosis observed with balloon angioplasty [Iqbal et al., 2013]. After the publication of these studies, the use of coronary stents increased exponentially over the next few years and by 1999, coronary stenting was performed in 84.2% of PCI procedures [Serruys et al., 2006].

However, despite outstanding clinical improvements, together with acute stent thrombosis (ST), neointimal hyperplasia growth and late remodeling of the vessel that led to new complication of in-stent restenosis (ISR), result of smooth muscle cell (SMC) migration and proliferation and extracellular matrix (ECM) deposition directly linked to stent implantation [Costa and Simon, 2005], continued to be reported as major limitations of this technique. Indeed, mid- and long-term clinical follow-up of patients with BMS implanted revealed substantial ISR rates of 20-30% [Hoffmann et al., 1996]. This led to several attempts to minimize restenosis rates, optimizing stent performance in terms of geometrical design, manufacturing methods, materials, delivery procedure and expansion methods. When mechanical updates did not address the problems of ISR encountered with BMS, researchers considered pharmacological solutions through the use of stents coated with antiproliferative substances. The reader is referred to Section 3.4 (*Mathematical modelling of the restenosis process after stent implantation*) of this Thesis for a comprehensive description of the mechanisms involved in the ISR process.

2.6.2 Drug-eluting stents (DESs)

Drug-eluting stents (DESs) were developed to specifically solve the issue of ISR encountered with BMS. They typically consist of three key components that together contribute to the overall safety and efficacy of the device: the metallic stent platform (normally they use the most advanced BMS platform available at the time of their development), the drug to inhibit the cell proliferation that causes restenosis and the drug delivery coating technology [McCormick, 2018a]. A number of different drugs have been used to date in the design of DES. However, the majority of them have contained either the drug paclitaxel, sirolimus and other limus derivatives (e.g. everolimus, zotarolimus, biolimus, novolimus, tacrolimus, myolimus and amphilimus).

2.6.2.1 First generation of DESs

The first DES implanted in human was performed by J. Eduardo Sousa in Brazil in 1999, reporting minimal ISR rates through to 12-month clinical follow-up [Sousa et al., 2001a,b]. This research culminated in the development and commercial launch

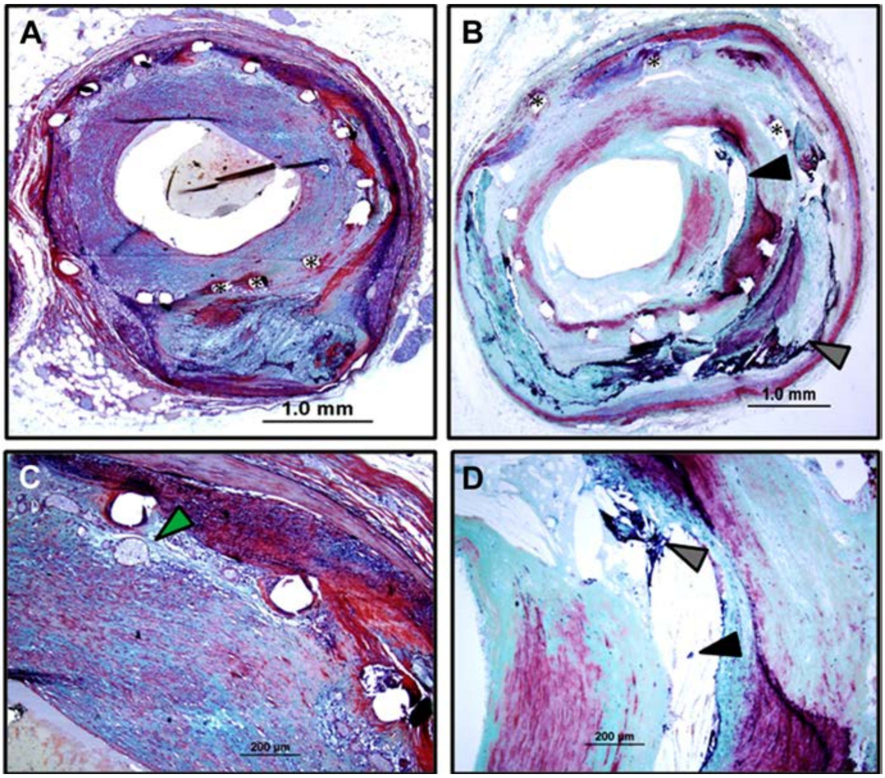

Figure 2.6. *Medical images of ISR within a bare-metal stent (A and C) and a drug-eluting stent (B and D), both implanted 5 years antemortem. In the BMS, the dominant pathology is SMC-rich neointimal hyperplasia. There is also some chronic inflammation with neovascularization around stent struts (green arrowhead). In the DES, there is presence of neoatherosclerosis with formation of a necrotic core (black arrowheads) and calcification (grey arrowheads) [Alfonso et al., 2014].*

Table 2.2
A brief overview concerning drugs used in endovascular devices.

Drug	Molecular formula	Molecular weight (Da)
Paclitaxel	$C_{47}H_{51}NO_{14}$	853.9
Sirolimus	$C_{51}H_{79}NO_{13}$	914.2
Everolimus	$C_{53}H_{83}NO_{14}$	958.2
Zotarolimus	$C_{52}H_{79}N_5O_{12}$	966.2
Biolimus A9 (Umirolimus)	$C_{55}H_{87}NO_{14}$	986.3
Novolimus	$C_{50}H_{77}NO_{13}$	900.1
Myolimus	$C_{51}H_{81}NO_{12}$	900.0
Tacrolimus	$C_{44}H_{69}NO_{12}$	804.0

of the Cypher® (Cordis Coorporation - Johnson & Johnson, Warren, NJ, USA) stent, which was finally approved for clinical use in Europe (CE mark) in 2002. In the United States of America (USA), Cypher® stent received the approval of the Food and Drug Administration (FDA) for treatment of patients one year later. It consisted of a 140 μm 316L stainless steel stent coated with a permanent polymer containing the pharmacological agent sirolimus (rapamycin). Sirolimus and paclitaxel were the two antiproliferative agents initially used in first-generation DESs. It is well documented that these drugs inhibit cell growth in a dose-dependent manner *in vitro* [Axel et al., 1997; Oberhoff et al., 2002; Wessely et al., 2006], entering the cell membrane through rapid diffusion [Oberhoff et al., 2002]. Sirolimus is a natural product discovered in the 1960s in Rapa Nui, the native name of the Easter Island (Chile), inspiring the compound's well-known common name of rapamycin. This immunosuppressive hydrophobic substance targets the FK506-binding protein 12 (FKBP12), a member of the immunophilin family of proteins. The resulting complex, rapamycin-FKBP12, specifically interacts with the mammalian target of rapamycin (mTOR), interrupting the cell cycle progression in the G1-S phase [Marx et al., 1995]. Moreover, it was experimentally demonstrated that rapamycin blocks human SMC migration [Poon et al., 1996]. These findings suggested that it might be ideal for reducing SMC proliferation and migration in the development of restenosis after stent implantation. Cypher® stent was tested in numerous randomized controlled trials (RCTs) showing a significant reduction in the incidence of ISR and target vessel revascularization compared with BMS [Sousa et al., 2003a; Iqbal et al., 2013].

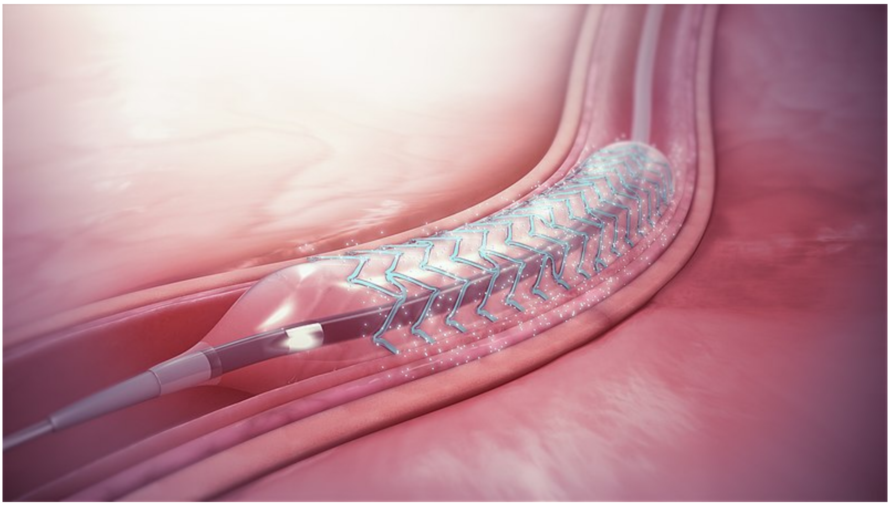

Figure 2.7. *Illustration of a coronary stent eluting out the drug in the blood vessel.*

The Taxus® Express™ (Boston Scientific, Natick, MA, USA) stent was developed almost simultaneously with the Cypher® stent, which received the FDA-approval for commercial and clinical use approximately one year later than its competitor. It consisted of a 132 μm 316L stainless steel stent design with a with a drug/polymer coating formulation consisting of paclitaxel (Fig. 2.8) and a proprietary polymer carrier technology called Translute™, which was specifically developed for the Taxus® stent. Paclitaxel was first isolated in 1971 from the bark of Pacific yew tree [Costa and Simon, 2005]. Like sirolimus, it is a hydrophobic compound able to inhibit vascular SMC migration and proliferation [Creel et al., 2000; Heldman et al., 2001]. Moreover, paclitaxel inhibits neointimal growth by binding specifically to the β subunit of tubulin present on microtubules [Axel et al., 1997; Oberhoff et al., 2002; Costa and Simon, 2005], resulting in cell cycle arrest in the G0-G1 and G2-M phases, making it ideal for the prevention and treatment of human coronary restenosis [Heldman et al., 2001; Martin and Boyle, 2011]. Again, several RCTs confirmed Taxus® stent efficacy against BMS [Sousa et al., 2003b; Iqbal et al., 2013]. This paclitaxel-eluting stent (PES) was subsequently replaced by the Taxus® Liberté™ (Boston Scientific, Natick, MA, USA) which used the same polymer and drug dose but with a thinner strut platform (97 μm vs 132 μm) providing a more uniform drug distribution [Garg and Serruys, 2010].

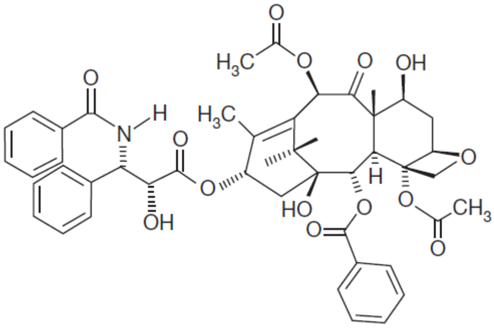

Figure 2.8. *The chemical structure of the antiproliferative substance paclitaxel, which is obtained from the Pacific Yew tree, Taxus brevifolia [Garg and Serruys, 2010].*

The biological effects of the drugs used in DES are fundamental, but, finally, the residence time of the drug in the tissue will determine the effect and toxicity [Levin et al., 2004]. The hydrophobicity of drugs plays a crucial role in local distribution of drugs eluted from stents [Hwang et al., 2001; O'Connell et al., 2010]. Both sirolimus and paclitaxel are small hydrophobic compounds [Creel et al., 2000; Levin et al., 2004], i.e. exhibit poor solubility in water. These drugs lead to higher arterial wall retention than drugs with hydrophilic ('water-loving' [McNaught et al., 1997]) nature such as dextran or heparin [Creel et al., 2000; Hwang et al., 2001; Hwang and Edelman, 2002], which cannot stay in the tissue for more than a few minutes after release and have no effect on intimal hyperplasia when eluted from a stent [Levin et al., 2004].

However, despite revolutionary success reducing the rates of ISR and associated clinical events [Moses et al., 2003], first generation DES did not prove to be a definitive

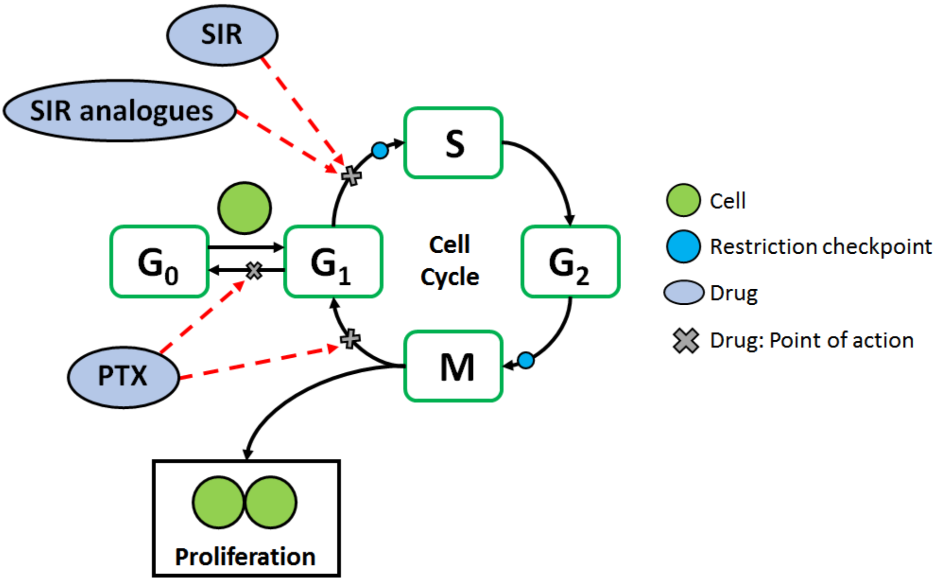

Figure 2.9. *Schematic depicting the specific locations where drug (sirolimus, SIR, and derivatives, and paclitaxel, PTX) targets the cell cycle to impede mitosis. Adapted from McQueen et al. [2021].*

solution for coronary artery disease. In 2006, a potential safety issue emerged with numerous meta-analyses and data registries associating DES with the increased risk of late ST [McFadden et al., 2004; Nordmann et al., 2006; Camenzind et al., 2007], possible related to delayed endothelialization by the anti-proliferative substances or delayed hypersensitivity reaction to the polymer in DES [Iqbal et al., 2013]. The concern of potentially fatal ST with the first generation of DES stimulated many clinical studies furthering research into the mechanism of ST and development of novel antiplatelet agents, better polymers and newer generation DES.

2.6.2.2 Second generation of DESs

The first generation BMS were generally comprised of 316L stainless steel, since this material is radio-opaque and provides adequate radial strength to maintain arterial scaffolding with minimal acute recoil. Alternatives to stainless steel material are stiffer chromium-based alloys (cobalt-chromium, Co-Cr, or platinum-chromium, Pt-Cr) [Stefanini and Holmes Jr, 2013], which exhibit superior radial strength and improved radio-opacity and conformability, refining the stent platform architecture with thinner struts that may reduce restenosis. These thinner struts, typically around 80-90 μm, can also lead to a reduction in device profile and, therefore, an improvement in stent deliverability to the target lesion [Garg and Serruys, 2010].

Second generation of DES uses the newer BMS stent platforms described above and also incorporates novel drugs and more biocompatible polymers. Concerning the drugs used, first generation DES used primarily paclitaxel and sirolimus. Several clinical analysis showed that sirolimus has better kinetics and wider therapeutic window than paclitaxel. Moreover, paclitaxel has possible higher risk of cytotoxicity. These are the main reasons why sirolimus-eluting stents are superior to paclitaxel-eluting stents in terms of a significant reduction of the risk of reintervention and late stent thrombosis [Schömig et al., 2007]. The anti-restenotic efficacy of sirolimus is the reason why new generation DES commonly elute limus compounds (everolimus, zotarolimus, umirolimus, biolimus, novolimus and amphilimus) [Lee and de la Torre Hernandez, 2018; McKavanagh et al., 2018] and they remain dominant in the latest DES designs that are emerging [McCormick, 2018a]. These sirolimus analogues differ in terms of lipophilicity, molecular weight (Table 2.2), structure, binding capability and performance.

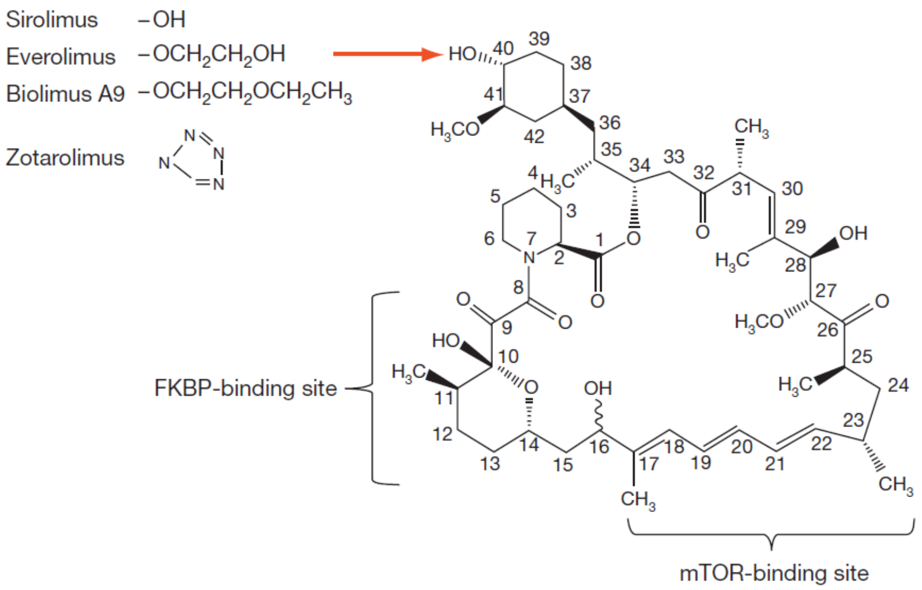

Figure 2.10. *The chemical structure of the 'limus' family of antiproliferative agents. The different agents are derived following modifications to the macrocylic ring as shown [Garg and Serruys, 2010].*

Everolimus is a hydroxyethyl derivative of sirolimus and works similarly by inhibiting mTOR. It is a licensed product for use in oncology, transplant medicine and coronary stents. The everolimus-eluting stent (EES) consists of the Multilink™ Vision Co-Cr strut platform (81 μm) with a nonerodable biocompatible polymer [Garg and Serruys, 2010]. This stent was commercially available as the Xience®

V (Abbott Vascular, Santa Clara, CA, USA) or Promus® and Promus® Element (Boston Scientific, Natick, MA, USA) as part of a co-marketing agreement. EESs have been shown to be superior, both in efficacy and in safety, to the first generation DES, reducing vascular inflammation and promoting better endothelialization [Stone et al., 2008, 2010]. Another common commercial options of DES in the market are the zotarolimus-eluting stents (ZES). Zotarolimus is a semi-synthetic derivative of sirolimus, designed specifically for use in stents, with the Endeavor®, Resolute™ and Resolute™ Integrity (Medtronic Cardiovascular, Santa Rosa, CA, USA) stents as its maximum exponents [McCormick, 2018a]. They use the Driver™ Co-Cr strut platform (91 μm) with a permanent biostatic and biocompatible polymer [Garg and Serruys, 2010]. They have been shown to be non-inferior to everolimus [Serruys et al., 2010].

The safety and efficacy of second generation DES have been assessed in numerous RCTs [Serruys et al., 2010], showing significant reductions in rates of death or myocardial infarction (MI), target lesion revascularization and ST compared with first-generation DESs [Iqbal et al., 2013]. Given these clinical advances, second-generation DESs have become the most widely used DES worldwide and they are accepted as the percutaneous treatment of choice for CAD, totally replacing BMS and first-generation DES [Tomberli et al., 2018]. However, despite the major technical refinements, concerns persist about their long-term safety. Late and very late ST (LST/VLST) declined with an incidence of less than 1% at 5 years, which is lower than that of BMS but still represents an ongoing safety concern because of the need to continue dual antiplatelet therapy (DAPT) for one year and beyond. The persistence of late events and the attempt to minimize the duration and intensity of the DAPT have sparked the development of newer generation of devices.

2.6.2.3 Biodegradable-polymer DESs (BP-DESs)

It has been hypothesised that permanent polymers used in the first generation DES led to persistent vessel wall inflammation and delayed vascular healing, which contributed to ST and delayed ISR. Although the durable polymers currently used in DES are less thrombogenic, a safety concern remains about their long term response. This is why considerable efforts has been made in the coatings and polymers research field.

Modern biodegradable polymeric coatings, are generally made of lactic or glycolic acids, e.g. polylactic acid (PLA), poly-L-lactic acid (PLLA), poly-D,L-lactic acid (PDLLA), polyglycolic acid (PGA), and polylactic-co-glycolic acid (PLGA), facilitating drug delivery to the arterial tissue and being fully resorbed by hydrolysis after drug release without causing any long-term issues [Lee and de la Torre Hernandez, 2018]. Differences in BPs induce a varying rate of drug release, polymer degradation time (normally from 3 to 15 months) [Nezami et al., 2021] and different impact on endothelial function, smooth muscle cells growth, and thrombogenicity [Tomberli et al., 2018]. The most widely studied DESs with biodegradable polymers elute Biolimus A9. Biolimus A9 (also known as umirolimus), is another semi-synthetic analogue of sirolimus, similar in potency to sirolimus but ten times more lipophilic. For example, some trials of biolimus-eluting BioMatrix® (Biosensors International, Singapore) stent have shown promising results [Windecker et al., 2008]. The Synergy® stent (Boston Scientific, Natick, Massachusetts, USA) is based on a 74 μm thick thick Pt-Cr stent platform which releases everolimus from an ultrathin abluminal biodegradable PLGA polymer coating of 4 μm thickness, which is resorbed during a period of 3-4 months. The Orsiro® stent (Biotronik AG, Buelach, Switzerland) is another common commercial example of BP-DES which consists of a 60 μm thick Co-Cr platform which releases sirolimus from biodegradable PLLA polymer coating which is resorbed during a period of approximately 2 years.

Despite theoretical advantages and the promising outcomes of using BPs in newer-generation DES, showing lower rates of VLST than first-generation DESs and non-inferiority in terms of efficacy and safety compared with second-generation DESs [Stefanini et al., 2012], more extended research and further RCTs need to be conducted before their widespread clinical application [Tomberli et al., 2018; Lee and de la Torre Hernandez, 2018].

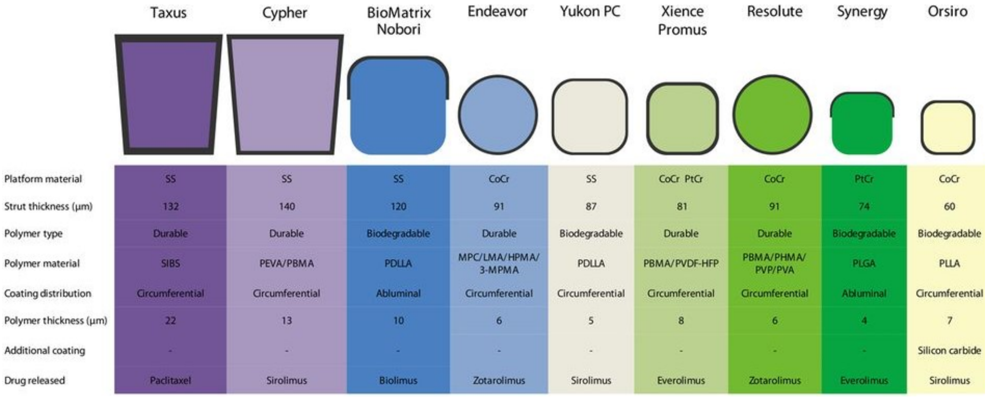

	Taxus	Cypher	BioMatrix Nobori	Endeavor	Yukon PC	Xience Promus	Resolute	Synergy	Orsiro
Platform material	SS	SS	SS	CoCr	SS	CoCr PtCr	CoCr	PtCr	CoCr
Strut thickness (μm)	132	140	120	91	87	81	91	74	60
Polymer type	Durable	Durable	Biodegradable	Durable	Biodegradable	Durable	Durable	Biodegradable	Biodegradable
Polymer material	SIBS	PEVA/PBMA	PDLLA	MPC/LMA/HPMA/ 3-MPMA	PDLLA	PBMA/PVDF-HFP	PBMA/PHMA/ PVP/PVA	PLGA	PLLA
Coating distribution	Circumferential	Circumferential	Abluminal	Circumferential	Circumferential	Circumferential	Circumferential	Abluminal	Circumferential
Polymer thickness (μm)	22	13	10	6	5	8	6	4	7
Additional coating	-	-	-	-	-	-	-	-	Silicon carbide
Drug released	Paclitaxel	Sirolimus	Biolimus	Zotarolimus	Sirolimus	Everolimus	Zotarolimus	Everolimus	Sirolimus

Figure 2.11. *Design characteristics of representative DESs with durable or biodegradable polymer coatings. SS, stainless steel; Co-Cr, cobalt chromium; Pt-Cr, platinum chromium; SIBS, poly(styrene-b-isobutylene-b-styrene); PEVA, poly-ethylene-co-vinyl acetate; PBMA, poly n-butyl methacrylate; PVDF-HFP, co-polymer of vinylidene fluoride and hexafluoropropylene; MPC, methacryloyloxyethyl phosphorylcholine; LMA, lauryl methacrylate; HPMA, hydroxypropyl methacrylate; 3-MPMA, trimethoxysilylpropyl methacrylate; PVP, polyvinyl pyrrolidinone; PHMA, polyhexyl methacrylate; PVA, polyvinyl acetate; PLGA, poly-lactic co-glycolic acid; PLLA, poly-L-lactic acid; PDLLA, poly-D, L-lactic acid. [Stefanini et al., 2014].*

2.6.2.4 Polymer-free DESs (PF-DESs)

The development of completely polymer-free DESs (PF-DESs) is a significant alternative to avoid the long-term undesirable effects of durable and BP stent coatings [Iqbal et al., 2013; McCormick, 2018a; Lee and de la Torre Hernandez, 2018; Nezami et al., 2021]. Therefore, due to the absence of polymer, these stents must incorporate other mechanisms and technologies to control drug release from the device surface and must ensure that the stent platform material is biocompatible [McGinty et al., 2015b].

To date, several PF-DESs have been developed and some of them have reached the market. Depending on the approach considered in the design of these devices, they can be divided into four categories: macroporous, microporous, nanoporous and smooth surface [McGinty et al., 2015b]. Examples of stents with pores at the macroscale, essentially holes or slotted grooves in the body of the device to inlay the drug, include the Janus® Flex (Carbostent and Implantable DevicesCID, Saluggia, Italy) PF tacrolimus-eluting stent, Conor® (Conor Medsystems - Jhonson & Jhonson, Warren, NJ, USA) PF-SES, CoStar™ (Conor Medsystems - Jhonson & Jhonson, Warren, NJ, USA) PF-PES and Nevo™ (Cordis Corporation - Jhonson & Jhonson, Warren, NJ, USA) PF-SES. Microporous PF-DESs consist of a modified rough surface of pits and holes whose size is of the order of 1-2 μm. These pits are then loaded with drug to provide controlled drug release [McGinty et al., 2015b; McCormick, 2018a]. One of the first microporous stents to be approved for use was the Yukon® (Translumina Therapeutics, New Delhi, Delhi, India) PF-SES. A more recent microporous PF-DES that is showing particularly impressive clinical results is the BioFreedom™ (Biosensors International, Singapore) PF biolimus-eluting stent. The high lipophilicity of Biolimus A9 may be an important factor in the impressive clinical results that have been reported for this stent [McCormick, 2018a]. Some nanoporous systems for drug delivery from stents have also been investigated [Vo et al., 2018].

PF-DES are out of the scope of this Thesis. The author refers the reader to other published reviews [Abizaid and Costa Jr, 2010; McCormick, 2018b] for further details on these stents.

2.6.3 Bioresorbable stents (BRSs)

The latest category of coronary stents considered in this review is fully bioresorbable stents (BRSs). The basic rationale for such stents is that the stent disappears once its main function had been served, having potential (and theoretical) clinical benefits [Sotomi et al., 2017; McCormick, 2018a; Nezami et al., 2021]: (i) reduction in long-term adverse clinical events related with the present of permanent materials (metallic stents and durable polymers) in the arterial tissue; (ii) restoration of the natural vasoactivity, physiological shear stress and healthy mechanotransduction of the treated vessel through bioresorption; (iii) facilitation of subsequent revascularization strategies that may be required in a future, which is extremely important for younger adult patients and children in particular; (iv) elimination of stiffening and straightening of the vessel at the site of device implantation; (v) reduction of the risk of in-device neoatherosclerosis (vi) reduction of the risk of ISR and ST caused by inflammatory responses to stent implantation, shortening also the DAPT administration time and associated bleeding risks.

Several BRSs have been introduced by a number of manufacturers during the last years. They are frequently made of polymer or metallic alloys. Igaki-Tamai® (Igaki Medical Planning Company, Kyoto, Japan), a fully bioresorbable scaffold made of PLLA, with no drug coating was the first device of this kind to be evaluated in humans [Iqbal et al., 2013]. However, the leading biodegradable polymer platform for which there is most extensive clinical data is the Absorb™ bioresorbable vascular scaffold (BVS) stent (Abbott Vascular, Santa Clara, CA, USA). It was the first BRS with the FDA-approval (March 2016), although it is currently off the market due to low commercial sales. The stent was also made of PLLA with a coating of PDLLA to provide diffusion-controlled release of the antiproliferative drug everolimus. The strut thickness was 150 μm, similar to the level used within early BMS and DES designs [McCormick, 2018a]. Another BRS is the novolimus-eluting DESolve™ Nx stent (Elixir Medical Corporation, Milpitas, CA, USA), which uses a similar polymer and strut thickness to the Absorb™ BVS. It got the CE mark in May 2014. DESolve™ Cx (Elixir Medical Corporation, Milpitas, CA, USA) is another novolimus-eluting stent with a strut thickness of 120 μm. Among the metal-based alloy BRSs, the Magmaris™ (Biotronik AG, Buelach, Switzerland) stent is a metallic, sirolimus-eluting magnesium-based BRS with an open cell design and a strut thickness 150 μm.

However, the initial enthusiasm that greeted the generally positive results from early clinical trials [Serruys et al., 2015] of these stents has now given way to increasing safety concern since several adverse clinical outcomes have been reported, highlighting that further research is still required in this field until a true therapy option for treating coronary artery disease is provided. Finally, the optimal combination of biodegradability, stent alloy, design, strut thickness, polymer, and drug all combined will determine the safety of DES.

BRSs are out of the scope of this Thesis. The author refers the reader to other published reviews [Ang et al., 2018; Zheng, 2018] for further details on these stents.

2.6.4 Drug-coated balloons (DCBs)

The most common treatment for obstructive CAD is the implantation of a permanent DES. While DESs work well in the majority of cases [Byrne et al., 2015a], their permanency is associated with delayed healing of the vessel and thrombosis risk, even with second-generation DES, with most patients receiving an expensive and prolonged course of dual antiplatelet therapy (DAPT) [Byrne et al., 2015b]. Moreover, if ISR occurs, it is not feasible to remove the original stent and insert a new one, which complicates the repeat revascularisation strategy. Drug-coated balloons (DCBs) have emerged as an attractive alternative to DESs for the treatment of CAD in certain anatomical conditions where permanent devices performed less successfully (Fig. 2.12). In particular, DCBs may be used in the treatment of ISR, where it is not feasible to insert a further DES [Scheller et al., 2004, 2006], peripheral arterial disease (PAD) [Tepe et al., 2008; Byrne et al., 2014; Tepe et al., 2015; Cortese et al., 2016] and atherosclerosis in coronary bifurcations [Jeger et al., 2020; Nezami et al., 2021]. Moreover, DCBs are becoming increasingly attractive in the context of treating de novo lesions, particularly in small coronary vessels [Jeger et al., 2018].

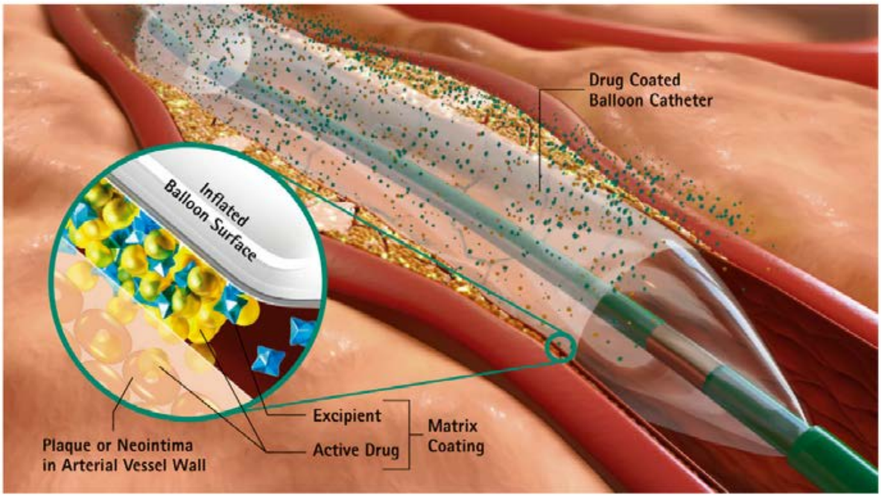

Figure 2.12. *Drug-Coated Balloon Technique and Mechanism of Action [Jeger et al., 2020].*

A key potential advantage of deploying a DCB over a DES is the lack of permanency. However, this may potentially be a disadvantage, where the brief period of deployment associated with DCBs presents only a short window for drug to be delivered. Specifically, while DCBs typically transfer drug rapidly to the arterial wall during a short application period of the order of a minute [Cortese and Bertoletti, 2012], DESs usually offer sustained drug release over a period of weeks or months. It is therefore of interest to explore how the different time scales of delivery between DCBs and DESs influence drug delivery and retention.

Current commercial DESs almost exclusively elute limus compounds [Lee and de la Torre Hernandez, 2018]. While the first and most of the current DCBs eluted paclitaxel [Scheller et al., 2004, 2006; Byrne et al., 2014], thought to be advantageous given the short drug delivery window [Bozsak et al., 2014], more recent efforts have considered different formulations of limus analogues in new generation of DCBs eluting balloons (e.g. utilising nanoparticle-based delivery) [Gray and Granada, 2010; Sojitra et al., 2013; Iyer et al., 2019]. How the differing physico-chemical properties of these commonly used therapeutic compounds influences the success of DCB treatment remains to be resolved [McQueen et al., 2021].

Due to clinical studies have not revealed convincing results to support the application of DCBs to treat stenosed de novo coronary lesions, and satisfactory outcome with regard to treating both BMS and DES coronary ISR [Scheller et al., 2008; Alfonso et al., 2014; Byrne et al., 2014], this strategy has been limited in clinics for the management ISR [Neumann et al., 2019]. Based on several clinical observations, the European Society of Cardiology (ESC) recommended equally the use of DES or DCB to treat coronary ISR [Nezami et al., 2021]. However, the necessity of a new permanent device limits the attractiveness of repeat DES implantation compared with the use of a DCB. As a result, many clinicians prefer the use of DCBs over DES in patients presenting first ISR, reserving the use of a new DES for those with subsequent recurrences after DCB treatment [Jeger et al., 2020].

In contrast to de novo coronary lesions treatment, where current DESs revealed significant superiority to DCBs, for treating de novo peripheral atherosclerosis there is no definite argument with regard to superiority of stenting compared with balloon angioplasty. This motivated clinicians and researchers to consider DEB therapy as a serious alternative option to treat PAD.

2.7 Mathematical and computational modelling in endovascular devices research

Mathematical and computational (*in silico*) modelling for coronary stents has emerged as a powerful technique that can contribute to addressing some of the limitations of often difficult and expensive experimental analysis [Conway et al., 2012; McGinty and Pontrelli, 2016]. Such research has predominantly focused on three key areas [McQueen et al., 2021]:

- Structural mechanics and computational fluid dynamics (CFD).
- Drug elution kinetics, uptake and retention in tissue.
- Arterial healing response.

A brief review with the state-of-the-art of mathematical and computational models of each key area is presented in the following subsections.

2.7.1 Computational modelling of arterial wall mechanics and balloon and stent deployment

Due to strong links between levels of vascular injury induced during device deployment and ISR rates and in order to investigate the mechanical behaviour of balloons and coronary stents [Martin and Boyle, 2011], computational models to evaluate deployment of an endovascular device inside a vessel can provide useful insights into the stress-strain response that the device induces within the arterial tissue and how device design factors contribute to mechanical performance *in vivo*. Optimized stent designs and deployment techniques can assist in minimizing injury, facilitate recovery, and inhibit adverse biological reactions [Karanasiou et al., 2017].

Numerous *in silico* studies, based on finite element analysis, with different levels of complexity have been performed during the last two decades to investigate geometrical and material properties of stents, different deployment strategies, effects of arterial curvature, the use of patient-specific geometries or the inclusion of stenosis and atherosclerotic tissue, to cite some examples [Migliavacca et al., 2004; Lally et al., 2005; Holzapfel et al., 2005b; Kiousis et al., 2007; Gijsen et al., 2008; Pericevic et al., 2009; Zahedmanesh et al., 2010; Mortier et al., 2010; García et al., 2012; Conway et al., 2012, 2014; Schiavone et al., 2014; Schiavone and Zhao, 2016; Chiastra et al., 2016; Conway et al., 2017; Morris et al., 2018; Zhao et al., 2021]. However, these models do not adequately account for drug-transfer from the device.

The results obtained by the earlier studies are discussed in more detail in the publication proposed by Martin and Boyle [2011]. See also for example Morlacchi and Migliavacca [2013] and Karanasiou et al. [2017] for other extensive reviews on this topic. Furthermore, we invite the reader to refer to the specific articles mentioned in this subsection for full details about these models.

2.7.2 Computational modelling of drug transport from endovascular devices

In the context of drug transport modelling, mathematical and computational analysis contribute to a better understanding of drug-release from medical devices and subsequent transport in the biological environment, aiming to guide the development of a next generation of endovascular devices with more favourable safety and efficacy [Escuer et al., 2022]. In particular, there is rich literature on mathematical and computational modelling of DESs. Early studies uncovered that stent drug kinetics are governed by physiological transport forces (diffusion and advection) [Hwang et al., 2001], arterial ultrastructures [Hwang and Edelman, 2002] and the drug physicochemical properties [Hwang et al., 2003], providing mechanistic explanations for the superior results that were observed with stents coated with lipophilic vs hydrophilic compounds.

In the last two decades, a large number of mathematical and computational studies have been developed to describe the transport of drug eluted from stents in arteries adopting either well-defined one-dimensional (1D) simplifications despite the complex physics and biology that underpins these processes [Pontrelli and de Monte, 2007; Tzafriri et al., 2009; McGinty et al., 2010; Pontrelli and de Monte, 2010; d'Errico et al., 2015; McGinty et al., 2015a; McGinty and Pontrelli, 2016; McKittrick et al., 2019], two-dimensional (2D) approaches [Zunino, 2004; Mongrain et al., 2005, 2007; Vairo et al., 2010; Bozsak et al., 2014; Denny and Walsh, 2014a,b; Bozsak et al., 2015; Ferreira et al., 2017, 2018; Tzafriri et al., 2018; Mandal and Mandal, 2018; Escuer et al., 2020, 2021], or three-dimensional (3D) formulations [Migliavacca et al., 2007; Zunino et al., 2009; Feenstra and Taylor, 2009; Cutrì et al., 2013].

However, despite the plethora of models that consider DESs, there are only a handful of mathematical and computational models that focus on DCBs [Kolachalama et al., 2013; Kolandaivelu et al., 2015; Mandal et al., 2016; Sarifuddin and Mandal, 2018; Tzafriri et al., 2019; Anbalakan et al., 2021; Colombo et al., 2021; Jain et al., 2022; Escuer et al., 2022], each with their own set of strengths and limitations (see Table 2.3). Commonalities between these models include the assumptions that drug is transported by diffusion within the arterial wall and that drug binding plays a key role in drug distribution and retention. However, the level of complexity of the binding model, the influence of other transport processes such as advection of drug due to radially outwards plasma flow and how the drug source is incorporated, is handled differently between the models. It is appreciated that, in reality, blood is a complex non-Newtonian fluid and that blood flow is in fact pulsatile. However, the focus of this kind of models is usually on drug distribution in arterial tissue, rather than on accurately reproducing flow patterns in the arterial lumen. Regardless of the flow model employed, drug released into the lumen is expected to be rapidly cleared by the blood [Zunino, 2004]. When drug transport is not the primary focus of the study, other flow models have been considered, with the Carreau model among the most popular. For the reasons above, the additional complexity that arises from this model is unlikely to markedly affect the results of interest. Regarding pulsatility, there is experimental evidence which shows that pulsatility contributes minimally to drug deposition for a well-apposed device [O'Brien et al., 2013]. Moreover, the time dependence mainly due to the cardiac pulsatile flow is usually neglected in these models since the pulsatile nature of the blood flow is characterized by much smaller temporal scales than the temporal scale of the advection–diffusion-reaction processes which govern drug transport within the arterial wall. Therefore, according to the current state of the art models which couples luminal flow with drug release from endovascular devices and subsequent tissue binding [Bozsak et al., 2014; Ferreira et al., 2018; Escuer et al., 2020, 2021], blood is modelled as a steady, incompressible Newtonian fluid governed by the steady Navier-Stokes equations and the continuity equation. The only existing models to date that incorporate the multilayer nature of the arterial wall have very recently been presented by Jain et al. [2022] and Escuer

Table 2.3
Summary of the existing models of DCB kinetics, highlighting key considerations and limitations. Adapted from Escuer et al. [2022].

Reference	Drug source	Binding model	Advection included?	Disease included?	Dimension	Multilayer?
Kolachalama et al. [2013]	Flux	One phase, nonlinear	No	No	1D	No
Kolandaivelu et al. [2015]	Flux	One phase, nonlinear	No	No	2D	No
Mandal et al. [2016]	Flux	One phase, nonlinear	No	Yes	2D	No
Sarifuddin and Mandal [2018]	Flux	One phase, nonlinear	Yes	Yes	2D	No
Tzafriri et al. [2019]	Flux	Two phases, nonlinear	No	No	1D	No
Anbalakan et al. [2021]	Flux	Two phases, nonlinear	Yes	Yes	2D	No
Colombo et al. [2021]	Constant	One phase, nonlinear	No	Yes	3D	No
Jain et al. [2022]	Constant	One phase, nonlinear	Yes	No	1D	Yes
Escuer et al. [2022]	Flux	Two phases, nonlinear	Yes	No	2D-axi	Yes

et al. [2022]. However, the primary goal of the work presented by Jain et al. [2022] was to provide an analytical solution, necessitating simplifications in other aspects (dimensionality and linearity of the binding model).

2.7.2.1 Modelling drug release from the stent coating

Modelling drug release is not an area of research exclusive to DESs, therefore mathematical and computational models of drug release from DESs incorporate well-established ideas from other applications [McGinty, 2014]. In line with the existing literature, most models assume that drug release from DESs comprising non-erodible polymers (first and second generation DESs) is governed purely by diffusion satisfying a linear diffusion equation [Zunino, 2004; Pontrelli and de Monte, 2007; McGinty et al., 2010; Vairo et al., 2010; Bozsak et al., 2014, 2015; Escuer et al., 2020, 2021]:

$$\frac{\partial c_c}{\partial t} = \nabla \cdot (\boldsymbol{D}_c \nabla c_c), \tag{2.27}$$

where c_c (r, z, t) is the volume-averaged concentration of free drug eluted from the stent coating and; $\boldsymbol{D}_c$ represents the effective drug diffusion coefficient within the polymer, usually assumed to be constant and isotropic. At t = 0, the drug is assumed to be completely contained within the polymer coating in dissolved phase (free drug) at uniform concentration, derived from the drug loading mass. However, depending on the physical and chemical characteristics of the polymeric coating and of the drug (newer generation DESs), it may be necessary to also account for other phenomena such as dissolution [McGinty et al., 2015a; McGinty and Pontrelli, 2016], degradation [Prabhu and Hossainy, 2007; Rossi et al., 2012; Zhu and Braatz, 2014, 2015; Ferreira et al., 2017, 2018] or erosion [Formaggia et al., 2010; Zhu and Braatz, 2015]. In the case of polymer-free stents, it is less clear how the sustained release is obtained and how this may be modelled [McGinty et al., 2015b; Vo et al., 2018]. We invite the reader to refer to the specific articles for full details about these models.

2.7.2.2 Modelling drug release from the balloon

Drug delivery from the DCB is typically modelled as either a constant concentration for the duration of balloon application [Colombo et al., 2021; Jain et al., 2022] or a time-dependent flux prescribed at the lumen-tissue interface to approximate the releasable portion of drug from the device during inflation [Kolachalama et al., 2013; Kolandaivelu et al., 2015; Mandal et al., 2016; Sarifuddin and Mandal, 2018; Tzafriri et al., 2019; Anbalakan et al., 2021; Escuer et al., 2022]. Regarding the latter approach, two different flux expressions can be found in the literature that have been parameterised on experimental data. The first is provided by Kolachalama et al. [2013] who considered a zotarolimus-eluting balloon, while the second is provided by Anbalakan et al. [2021] who considered a sirolimus-eluting balloon. The same expression is used to describe the flux, J_{DCB}, in each case:

$$J_{DCB} = \frac{kA}{M_w} \exp\left(-kt\right), \quad t \leq t_0, \tag{2.28}$$

where k and A are empirically estimated constants, M_w is the molecular weight of the drug considered and t is the time. Whilst the same form of expression is used in both cases, the inferred parameter values are quite different, resulting in a substantial difference in the overall influx of drug [Escuer et al., 2022].

2.7.2.3 Modelling drug transport in the blood flow

Some models couple blood flow with drug release from endovascular devices and subsequent tissue binding [Bozsak et al., 2014, 2015; Escuer et al., 2020, 2021]. They usually consider blood as a steady, incompressible Newtonian fluid governed by the steady Navier-Stokes equations and the continuity equation:

$$\rho_b(\boldsymbol{u}_l \cdot \nabla)\boldsymbol{u}_l = -\nabla p_l + \mu_b \nabla^2 \boldsymbol{u}_l, \tag{2.29}$$

where $\boldsymbol{u}_l$ and p_l are the velocity vector field and the pressure field of the blood flow in the lumen, respectively, and ρ_b and μ_b are the density and the dynamic viscosity of the blood, respectively. The operators ∇ and ∇^2 are the gradient and the Laplacian, respectively. These models usually consider an inlet Poiseuille velocity profile and outlet fixed pressure boundary conditions. It is well-known that, in reality, blood is a complex non-Newtonian fluid and that blood flow is in fact pulsatile. However, the focus of this kind of models is usually on drug distribution in arterial tissue, rather than on accurately reproducing flow patterns in the arterial lumen. Regardless of the flow model employed, drug released into the lumen is expected to be rapidly cleared by the blood [Zunino, 2004]. When drug transport is not the primary focus of the study, other flow models have been considered, with the Carreau model among the most popular. However, the additional complexity that arises from this model is unlikely to markedly affect the results of interest. Regarding pulsatility, there is experimental evidence which shows that pulsatility contributes minimally to drug deposition for a well-apposed device [O'Brien et al., 2013]. Moreover, the time dependence mainly due to the cardiac pulsatile flow is usually neglected in these models since the pulsatile nature of the blood flow is characterized by much smaller temporal scales than the temporal scale of the advection–diffusion-reaction processes which govern drug transport within the arterial wall.

Drug transport inside the arterial lumen is modelled as a time-dependent advection-diffusion process:

$$\frac{\partial c_l}{\partial t} + \boldsymbol{u}_l \cdot \nabla c_l = \nabla \cdot (\boldsymbol{D}_l \nabla c_l), \tag{2.30}$$

where $c_l\ (r, z, t)$ is the drug concentration within the fluid domain; $\boldsymbol{D}_l$ is the diffusivity of the drug in the blood, normally considered to be constant and isotropic; and $\boldsymbol{u}_l$ is the blood flow velocity calculated by Eq. (2.29).

2.7.2.4 Modelling drug transport through the arterial wall

The healthy arterial wall is usually modelled as a multi-layered structure organised in three porous layers: subendothelial space (SES), media and adventitia. Due to the porous nature of the tissue, the flow field through the different regions of the arterial wall in response to the transmural pressure gradient is calculated using Darcy's law and the continuity equation:

$$\boldsymbol{u}_j = \frac{K_i}{\mu_p} \nabla p_i, \qquad\qquad \nabla \cdot \boldsymbol{u}_i = 0 \tag{2.31}$$

where the subscript j denote the different layers of the tissue, $\boldsymbol{u}_j$ is the transmural velocity vector field; K_j is the Darcian permeability; μ_p is the dynamic viscosity of the plasma and; p_j is the pressure field. In the most advanced existing models, the endothelium, internal and external elastic laminae are treated as semipermeable membranes between the different layers of the tissue and the fluid flux across them is described by the Kedem-Katchalsky equations [Kedem and Katchalsky, 1958].

The processes that govern mass transport through the arterial wall are diffusion, convection and binding (reaction) [McGinty, 2014]. Therefore, drug transport could be described by an advection–diffusion–reaction equation of the following form:

$$\frac{\partial c_j}{\partial t} + \frac{\gamma_j}{\phi_j}\boldsymbol{u}_j \cdot \nabla c_j = \nabla \cdot (\boldsymbol{D}_j \nabla c_j) - R_j \tag{2.32}$$

where $c_j\ (r,z,t)$, γ_j, ϕ_j, $\boldsymbol{u}_j$ and $\boldsymbol{D}_j$ refer to the dissolved drug concentration, hindrance coefficients, porosities, transmural fluid velocities calculated by Eq. (2.31) and diffusion coefficient tensor in each layer of the tissue. The different composition of each layer results in differing porosities, diffusion coefficients [Creel et al., 2000; Hwang et al., 2001; Levin et al., 2004] and binding properties. The term R_j represents the binding reaction which may take several forms [McGinty, 2014].

While the convective and diffusive element of the drug transport is well established, the precise form of modelling binding is controversial [McGinty, 2014]. Some authors assumed equilibrium models, through a partition coefficient which defines the equilibrium ratio of bound drug within the tissue with respect to drug dissolved in the fluid [McGinty et al., 2010; Vairo et al., 2010; Horner et al., 2010; Abraham et al., 2013], while others have considered simple loss terms which accounts for consumption of drug in the system [Zunino, 2004; Pontrelli and de Monte, 2007, 2009, 2010]. However, non-linear saturable reversible binding models is currently the well-accepted approach [Tzafriri et al., 2009; Bozsak et al., 2014, 2015], with some authors highlighting the importance of taking into account binding to specific receptors and binding to non-specific sites (general extracellular matrix sites) as two separate phases [Tzafriri et al., 2012; McGinty and Pontrelli, 2016; McKittrick et al., 2019; Escuer et al., 2020, 2021], with saturation of specific receptors being strongly linked to efficacy at least for sirolimus-eluting stents. Therefore, for this approach the resulting reaction term, R_j, may be written as:

$$R_j = \frac{\partial b_j^{ns}}{\partial t} + \frac{\partial b_j^{s}}{\partial t}, \tag{2.33}$$

with

$$\frac{\partial b_j^{ns}}{\partial t} = k_{on,j}^{ns} c_j (b_{max,j}^{ns} - b_j^{ns}) - k_{off,j}^{ns} b_j^{ns}, \tag{2.34}$$

$$\frac{\partial b_j^{s}}{\partial t} = k_{on,j}^{s} c_j (b_{max,j}^{s} - b_j^{s}) - k_{off,j}^{s} b_j^{s}. \tag{2.35}$$

where the superscripts s and ns denotes specific and non-specific binding, respectively. This reaction model is able to define three different states of the drug in the tissue: drug dissolved in the plasma, $c_j\ (r,z,t)$, drug bound to specific binding sites (target receptors), $b_j^s\ (r,z,t)$, and drug bound to non-specific binding sites (general ECM sites), $b_j^{ns}\ (r,z,t)$. The binding rate constants (forward reaction rates) are given by $k_{on,j}^{s}$ and $k_{on,j}^{ns}$ whereas the unbinding rate constants (reverse reaction rates) are given by $k_{off,j}^{s}$ and $k_{off,j}^{ns}$. The parameters $b_{max,j}^{s}$ and $b_{max,j}^{ns}$ are the maximum density of binding sites. Analogous to the fluid flux, discontinuity of solute flux across the semipermeable membranes is also governed by the Kedem-Katchalsky equations [Kedem and Katchalsky, 1958] in the most advanced existing models. Due to the lack of binding data available in the literature for the different regions of the arterial tissue, this reaction model is only considered in the media layer and, in some models where the pathology is considered, in the atheroscletoric tissue Escuer et al. [2021].

2.7.2.5 Other modelling considerations

These models generally consider an intact vessel with diffusion, advection and binding dictating the transport of drugs within the blood flow and the respective wall layers. There are a limited number of studies that attempt to incorporate both the mechanics of arterial tissue and drug transport. For example, in their 3D models, Migliavacca et al. [2007] and Cutrì et al. [2013] included drug transport in an arterial wall deformed by their own previous simulations of stent deployment, but neither model relates the drug transport parameters to the level of deformation. Feenstra and Taylor [2009] through a porohyperelastic-transport approach, calculated the geometry, porosity field and interstitial fluid velocity directly from a simulation of stent deployment and used these within a model of drug transport in the arterial wall consisting of three distinct layers. In this sense, tissue porosity and the contribution to drug transport of advection were not assumed a priori. However, this model assumed a linear drug reaction and drug diffusion coefficients that did not vary with deformation. Denny and Walsh [2014a,b] modelled the influence of strut compression on local diffusivity through simulations of the compression of an idealised arterial wall by an idealised unit cell model of a stent, but their model did not adequately account for the effects of nonlinear binding of drug. Finally, Ferreira et al. [2017, 2018] developed a linear viscoelastic model to explore how drug diffusion may be hindered in the presence of atherosclerotic plaque, but do not account for mechanical deformation of the arterial wall as a result of stent deployment.

Moreover, the vast majority of these models generally consider a healthy straight vessel geometry, i.e. do not take into account the considerable geometrical variability of the coronary artery (curved regions, branching, etc.) which is associated with alterations in the local haemodynamics, playing an important role in the localisation of the atherosclerotic lesions [Frangos et al., 1999; Tarbell, 2003]. The influence of coronary arterial curvature on mass transport was previously investigated for other macromolecules such as low-density lipoproteins (LDL), showing different average concentrations of LDL in curved arteries compared with straight arteries [Caputo et al., 2013; Wang and Vafai, 2015]. However, to the best of our knowledge, in terms of drug transport there are only a very limited number of computational approaches available in the literature that take into account complex arterial geometries [Hossain et al., 2012; Cutrì et al., 2013], but they are not specifically focussed on the effect of the curvature of the vessel on tissue uptake and retention of drug.

There is growing evidence that atherosclerotic plaque composition may well have an impact on drug distribution within diseased tissue [McKittrick et al., 2016]. However, very few of the computational models of drug transport in arteries from the available literature incorporate the existence of disease state [Vairo et al., 2010; McGinty et al., 2010; Hossain et al., 2012; Ferreira et al., 2017, 2018; Mandal and Mandal, 2018]. Of the models that do, for instance, Vairo et al. [2010] assumed a porous homogeneous plaque between the device and the healthy tissue considering a 2D axisymmetric geometry, but the process of binding was described in terms of equilibrium conditions. Hossain et al. [2012] performed several simulations on a 3D patient-specific geometry of a bifurcation of a two-layered coronary artery with a plaque in order to analyse the effect of both artery and plaque heterogeneity on drug transport. However, a first-order reaction kinetics model was adopted to account for possible drug binding. Mandal and Mandal [2018] also present a 2D axisymmetric model and take into consideration the binding and unbinding processes to describe the interaction of the drug with the healthy and unhealthy tissue, but the porous nature of the arterial wall was not fully taken into account. Finally, Ferreira et al. used different 2D geometries to investigate the impact of local plaque composition [Ferreira et al., 2017] and plaque eccentricity on drug distribution [Ferreira et al., 2018], but like most other existing drug transport models [Vairo et al., 2010; Tzafriri et al., 2012; Cutrì et al., 2013; McGinty and Pontrelli, 2015, 2016; Ferreira et al., 2017; Mandal and Mandal, 2018; Ferreira et al., 2018; McKittrick et al., 2019] the arterial wall is modelled as a single layer, limiting the interpretation of the results.

This literature review included in this section led to the identification of some major gaps in endovascular devices research, some of which have been addressed during the development of this Thesis (see Chapter 3). However, whilst drug release and subsequent distribution within the arterial tissue has been modelled extensively, in increasingly sophisticated modelling frameworks, the consequent effect of spatio-temporal drug levels on SMCs behaviour has largely been neglected, which is somewhat surprising given the key role that SMCs play in neointimal hyperplasia formation and the overall arterial healing response. The reader is referred to the work recently published by McQueen et al. [2021], in which the author of this Thesis has participated as co-author, for a series of mathematical models of varying complexity developed to detail the action of drug on SMC growth.

2.7.3 Computational modelling of in-stent restenosis (ISR)

In recent years, mechanobiological models have emerged to relate mechanics to the complex response of different biological systems. They can be grouped into two categories: (a) discrete cell-based models, such as cellular automata (CA) or agent-based models (ABMs), in some cases combining with finite-element analysis; and (b) continuum models, which usually can be formulated in terms of systems of ordinary differential equations (ODEs) or partial differential equations (PDEs).

2.7.3.1 Discrete cell-based models

CA and ABM models can be defined as rule-based models that take a bottom-up approach. Each individual cell is modelled explicitly based on a set of rules of behaviour that are defined for it, and the global system behaviour emerges through the local interactions among the cells based on the defined rules of behaviour at the cell level. Although the differences between CA and ABM are marginal, the main difference is that a lattice point must be defined for CA while ABM can be lattice free, meaning that cells can be at any location in the computational domain [Hwang et al., 2009; Zahedmanesh and Lally, 2012].

A series of discrete models can be found in the literature to simulate the healing response of the arterial tissue following stent implantation. For example, Evans et al. [2008] highlighted the importance of using a multiscale approach to describe computationally the main physical and biological processes implicated in ISR, introducing the concept of the complex autonoma (CxA) models, based on a hierarchical aggregation of coupled CA and ABMs. Boyle et al. demonstrated that nonlinear growth could be simulated with a cell-centred model [Boyle et al., 2010] and simulated ISR by modelling a combination of injury and inflammation with SMCs represented as discrete agents [Boyle et al., 2011, 2013]. Zahedmanesh et al. developed an 2D ABM coupled with the finite element method (FEM) to investigate the dynamics of SMCs growth in vascular tissue engineering scaffolds [Zahedmanesh and Lally, 2012] and an ABM of ISR which allows a quantitative evaluation of the ECM turnover after stent-induced vascular injury [Zahedmanesh et al., 2014]. The previous works of Tahir et al. [2011, 2013, 2014] were based on ABMs fully coupled with blood flow to simulate the process of ISR, where the ISR final growth response owing to injury and the role of re-endothelialization on ISR were analysed. However, these models did not incorporate the SMC migration through the internal elastic lamina (IEL) and instead, a broken IEL layer was always used to estimate the injury. To cover these gaps, Tahir et al. [2015] focused on the initial phase after stenting and developed a cellular Potts model (CPM) of a 2D stented artery which permitted both the migration through the IEL fenestrae and proliferation of cells at the same time, which makes it a better choice for simulating the initial phases of ISR. They hypothesized that deeper stent deployment allows easier migration of SMCs into the lumen and the development of neointimal tissue due to SMC proliferation heavily depends on the number of initial migrated cells within the first few hours or days, which form an initial condition for the later phase of the vascular repair. Most recently, Keshavarzian et al. [2018] developed a coupled 3D ABM-FEM computational framework to simulate arterial growth and remodelling following transient increases in blood pressure and changes in production of various soluble factors (e.g., growth factors and proteases). Zun et al. [2017] presented a fully-coupled 3D multiscale model of ISR in a straight cylindrical vessel, with blood flow simulations coupled to an agent-based SMC proliferation model demonstrating qualitative agreement with *in vivo* experimental data of porcine coronary arteries. Nolan and Lally [2018] investigated the mechanism behind damage-induced cell proliferation using a ABM-FE approach in a 2D circumferential section of a stented artery, through the comparison of two earlier models from their research group [Boyle et al., 2013; Zahedmanesh et al., 2014]. Li et al. [2019], developed a fully coupled 2D ABM-FE framework to simulate the progression of the ISR that bi-directionally links FE stress calculations to the changing cell geometry. Zun et al. [2019] extended their previous 3D model including ECM production applied to stent geometries reconstructed from micro-CT scans of stents deployed in curved coronary arteries, significantly increasing the computational costs of the model, although contributing to increased accuracy of the predictions. Finally, the latest work by Zun et al. [2021] involved coupling of a previously developed 2D ABM of ISR [Tahir et al., 2014] to a 1D pulsatile coronary blood flow model, also previously developed, and investigated the impact of blood flow dynamics on the physiology of restenosis. Very recently, Corti et al. [2022] presented a multiscale framework consisting of a computational fluid dynamics (CFD) simulation coupled with an ABM, that integrates the effects of local haemodynamics and monocyte gene expression on cellular dynamics to simulate ISR in a patient-specific geometry of stented human superficial femoral artery. See Corti et al. [2021] for an extensive review on computational multiscale agent-based modeling frameworks of vascular remodeling.

2.7.3.2 Continuum models

The most common alternative to ABMs is continuum models. In contrast to discrete models where cell behaviour is usually described by a set of rules, continuum models offer a mechanistic description, featuring physical parameters which may in principle be measured. Moreover, they are usually based on several coupled ODEs/PDEs, therefore, model equations provide insight into the relationship among the components of the system. In addition, continuum models often have lower computational cost than ABMs, and naturally allow for modelling evolution of species and coupling with the mechanical aspects of the problem.

Rachev et al. [2000] proposed a theoretical continuum model to describe the main mechanisms of the coupled deformation and stress-induced arterial tissue thickening observed at the regions close to an implanted stent, comparing the results obtained with experimental data documented in the available literature [Hoffmann et al., 1996]. However, this phenomenological model does not take into account, for example, the mechanisms implicated in the SMC proliferation or the ECM synthesis. Other continuum mathematical biological models typically comprise a series of ODEs/PDEs to capture the spatio-temporal evolution of the species of interest (e.g., growth factors, cells, ECM components, etc.), and thus the subsequent tissue remodeling, in response to fluid or mechanical stimuli [Corti et al., 2021]. Continuum models have been developed to describe different phenomena such as vein graft adaptation [Budu-Grajdeanu et al., 2008; Casarin et al., 2017], atherosclerotic plaque formation [Calvez et al., 2009; Ibragimov et al., 2010; El Khatib et al., 2012; Filipovic et al., 2013; Cilla et al., 2014; Watson et al., 2018, 2020; Pleouras et al., 2020], fibrotic tissue formation surrounding medical implants [Su et al., 2011; Nicolás et al., 2015], arterial physiopathology [Marino et al., 2017], the complex healing process in soft biological tissues [Gierig et al., 2021] and ISR [Lally and Prendergast, 2006; Fereidoonnezhad et al., 2017; Cheng and Zhang, 2019; Escuer et al., 2019; He et al., 2020; Maes et al., 2021].

Focus on the use of continuum models to simulate the response of the artery to stenting, literature is much more limited when compared with cell-based models [Boland et al., 2019]. For example, Lally and Prendergast [2006] adopted a damage-adaptive finite element approach to simulate ISR using damage as a stimulus variable related to the stress levels induced within the tissue by three different stent designs. The relationship between stress and damage was determined from fatigue tests on harvested porcine coronary tissue. Fereidoonnezhad et al. [2017] proposed a continuum microstructurally–based damage–induced growth model, which takes into account the cellular changes in the arterial wall caused by stent-induced injury, including vascular smooth muscle cell migration and proliferation. Based on the theory of volumetric finite growth, the deformation gradient was multiplicatively decomposed into an elastic and a growth part. They implemented the model into the commercial FE software ABAQUS (Dassault Systèmes Simulia Corp., Johnston, RI, USA) via a user-defined material subroutine (UMAT), which was verified against the results obtained from a MATLAB (Mathworks, Natick, MA, USA) code. Then, the model was applied to simulate the development of restenosis after angioplasty, and the results matched clinical observations qualitatively. Cheng and Zhang [2019] presented a growth model to simulate the arterial wall remodelling after stenting similar to the one proposed by Fereidoonnezhad et al. [2017], but its growth factor was linked to the stress instead of the damage. Their results suggested that the volumetric growth of the arterial tissue tended to even out, lowering both the overall stress and the stress concentration. Moreover, the residual stresses were shown to have significant impact on the results of artery tissue growth. Escuer et al. [2019] developed another damage-related volumetric growth model to predict ISR, in terms of densities/concentrations of important species such as growth factors (GFs), matrix metalloproteinases (MMP), extracellular matrix (ECM), contractile and synthetic SMCs and endothelial cells (ECs). In this model, the initial damage stimulus induced by stenting triggered the biological response characterized by EC denudation and subsequent repopulation, and the dynamics of GFs and MMP, which in turn affected the production and degradation of ECM, with effects on SMC contractile to synthetic switching and on the following SMC activity [Corti et al., 2021]. The results suggested that the arterial wall response was driven by the damage area, proliferation of SMCs and the collagen turnover. Tissue growth was defined as a result of the change over time of ECs, SMCs and ECM. Also in this case, the model predictions in terms of percentage of stenosis were in good agreement with clinical data Nobuyoshi et al. [1988]. See Section 3.4 in Chapter 3 for further details about this work.

Most recently, He et al. [2020] considered stenting-induced damage in the media layer of the arterial wall and developed an anisotropic damage-dependent growth model to predict the rate of ISR. Although the model proposed by Escuer et al. [2019] is a more biofidelic approach to capturing the mechanobiological phenomena of the restenosis process after stenting, Maes et al. [2021] proposed a predictive FE model of restenosis, using the homogenized constrained mixture modelling framework designed to model growth and remodelling in soft tissues [Humphrey and Rajagopal, 2002], allowing a direct connection between mechanical quantities and SMCs growth. Manjunatha et al. [2022a] developed an analogous model to the one presented by Escuer et al. [2019] for the prediction and quantification of the after-effects of stent implantation, considering one of the significant GFs and its effect on constituents of the arterial tissue. Finally, Manjunatha et al. [2022b] also proposed a fully-coupled Lagrangian FE framework which replicates the process of ISR observed after stent implantation in a coronary artery based on coupled advection-reaction-diffusion equations and continuum mechanical modelling. Key differences to the work of Escuer et al. [2019] lie in the capturing of chemotactic and haptotactic movement of SMCs, the incorporation of anisotropic growth, and the FE formulation itself.

Each of the models mentioned in this section has their own set of strengths and limitations. A better understanding and mathematical description of chemical, biological and mechanobiological processes involved in ISR will further improve the clinical relevance of these models.

CHAPTER

3

Publications

This thesis is presented as a compendium of four research papers. The works that comprise the compendium of publications are included in this Chapter.

Contents

3.1 Work 1: How does stent expansion alter drug transport properties of the arterial wall?

In this work, we provide the most comprehensive study to date of the effect of stent mechanical expansion on the drug transport properties of a three-layer arterial wall. Our model incorporates the state-of-the art description of the mechanical properties of the arterial wall through an anisotropic, hyperelastic material model and includes a nonlinear saturable binding model to describe drug transport in the arterial tissue. We establish relationships between mechanical force generated through device expansion and alteration in diffusion within the arterial wall and perform simulations to elucidate the impact of such alterations in spatio-temporal drug release and tissue uptake. Mechanical deformation of the arterial wall results in modified drug transport properties and tissue drug concentrations, highlighting the importance of coupling solid mechanics with drug transport.

Contents lists available at ScienceDirect

Journal of the Mechanical Behavior of Biomedical Materials

ELSEVIER

How does stent expansion alter drug transport properties of the arterial wall?

Javier Escuer, Martina Cebollero, Estefanía Peña, Sean McGinty, Miguel A. Martínez

ARTICLE INFO

ABSTRACT

1. Introduction

Escuer J., Cebollero M., Peña E., McGinty S., Martínez M.A. (2020).
Journal of the Mechanical Behavior of Biomedical Materials 104, 103610.
JIF (2020) = 3.902 (Q2: 32/89 Biomedical Engineering).

journal of the mechanical behavior of biomedical materials 104 (2020) 103610

Contents lists available at ScienceDirect

Journal of the Mechanical Behavior of Biomedical Materials

journal homepage: http://www.elsevier.com/locate/jmbbm

How does stent expansion alter drug transport properties of the arterial wall?

Javier Escuer[a], Martina Cebollero[a], Estefanía Peña[a,b], Sean McGinty[c], Miguel A. Martínez[a,b,*]

[a] Aragón Institute for Engineering Research (I3A), University of Zaragoza, Spain
[b] Biomedical Research Networking Center in Bioengineering, Biomaterials and Nanomedicine (CIBER-BBN), Spain
[c] Division of Biomedical Engineering, University of Glasgow, Glasgow, UK

ARTICLE INFO

Keywords:
Drug-eluting stent
Mechanical expansion
Drug transport
Arterial wall
Coupling mechanics-drug transport
Anisotropic hyperelastic material

ABSTRACT

Stents have become the most successful device to treat advanced atherosclerotic lesions. However, one of the main issues with these interventions is the development of restenosis. The coating of stents with antiproliferative substances to reduce this effect is now standard, although such drugs can also delay re-endothelialization of the intima. The drug release strategy is therefore a key determinant of drug-eluting stent efficacy. Many mathematical models describing drug transport in arteries have been developed and, usually separately, models describing the mechanics of arterial tissue have been devised. However, the literature is lacking a comprehensive model that adequately takes into account both the mechanical deformation of the porous arterial wall and the resulting impact on drug transport properties. In this paper, we provide the most comprehensive study to date of the effect of stent mechanical expansion on the drug transport properties of a three-layer arterial wall. Our model incorporates the state-of-the art description of the mechanical properties of arterial tissue though an anisotropic, hyperelastic material model and includes a nonlinear saturable binding model to describe drug transport in the arterial wall. We establish relationships between mechanical force generated through device expansion and alteration in diffusion within the arterial wall and perform simulations to elucidate the impact of such alterations in spatio-temporal drug release and tissue uptake. Mechanical deformation of the arterial wall results in modified drug transport properties and tissue drug concentrations, highlighting the importance of coupling solid mechanics with drug transport.

1. Introduction

Coronary heart disease (CHD) is the leading cause of death worldwide (Naghavi et al., 2017). CHD is attributed to atherosclerosis, the hardening and narrowing of the arterial lumen due to the build-up of cholesterol and fatty deposits on the inner wall of the vessel. This in turn reduces blood flow through the coronary arteries to the heart muscle.

Stent implantation has become the most successful strategy in the treatment of CHD by percutaneous coronary intervention (PCI). However, in-stent restenosis (ISR), a gradual luminal re-narrowing mainly due to the vessel wall injury induced by the device, is the major clinical limitation of this technique (Alfonso et al., 2014). The introduction of drug-eluting stents (DES), which release antiproliferative substances into the arterial tissue has contributed to the dramatic reduction in incidence of ISR to less than 10% (Buccheri et al., 2016). However, the risk of developing late or very-late stent thrombosis (ST) is typically higher with the use of DES compared with bare-metal stents, and given the high mortality rates associated with ST, this issue remains an important safety concern that needs to be addressed (Alfonso et al., 2014; Byrne et al., 2015).

The use of computational (*in silico*) modelling and simulation for coronary stents has emerged as a powerful technique that can contribute to addressing some of the limitations of often difficult and expensive experimental analysis (Conway et al., 2012; McGinty and Pontrelli, 2016). In terms of simulating the deployment of a stent inside a coronary artery, these models can provide useful insights into the stress-strain response that the device induces within the arterial tissue and how stent design factors contribute to mechanical performance *in vivo*. In the literature, several *in silico* studies with different levels of complexity have been performed to investigate geometrical and material properties of stents, different deployment strategies, effects of arterial curvature, the use of patient-specific geometries and the inclusion of stenosis and

---

[*] Corresponding author. Mechanical Engineering Department, c/ María de Luna s/n 50018, Zaragoza, Spain.
E-mail address: miguelam@unizar.es (M.A. Martínez).

https://doi.org/10.1016/j.jmbbm.2019.103610
Received 12 November 2019; Received in revised form 23 December 2019; Accepted 29 December 2019
Available online 7 January 2020
1751-6161/© 2020 Elsevier Ltd. All rights reserved.

Table 1

(a) Material parameters of the Gasser et al. (2006) strain energy function (SEF) for the different layers of the arterial wall. The normalised root mean square error (NRMSE) is a measure of the accuracy of the fit. (b) Coefficients of the elasto-plastic material model used to describe the behaviour of the stent struts. (c) Values of the bilinear elasto-plastic model parameters for the phosphorylcholine polymer coating.

a. ARTERIAL WALL

Material	Model	μ (kPa)	k_1 (kPa)	k_2 (−)	κ (−)	β (°)	NRMSE	Reference
Intima	Gasser et al. (Gasser et al., 2006)	26.16	10485.17	20.00	0.165	50.02	0.0249	fitted to (Holzapfel et al., 2005b)
Media	Gasser et al. (Gasser et al., 2006)	1.93	149.10	51.74	0.262	37.47	0.0157	fitted to (Holzapfel et al., 2005b)
Adventitia	Gasser et al. (Gasser et al., 2006)	8.17	695.61	604.79	0.265	60.33	0.0298	fitted to (Holzapfel et al., 2005b)

b. STENT STRUTS

Material	Model	E (MPa)	ν (−)	σ_y (MPa)	σ_u (MPa)	ε_u (−)	Reference
Stainless steel 316L	Elasto-plastic	$2{\cdot}10^5$	0.28	264	584	0.247	(Conway et al., 2012; McGarry et al., 2004)

c. STENT COATING

Material	Model	E (MPa)	ν	σ_y (MPa)	E_t (MPa)	Reference
PC-based polymer	Bilinear elastic	240	0.5	16	7.7	(Hopkins et al., 2010; Schiavone et al., 2014)

atherosclerotic tissue (Conway et al., 2012, 2014; Migliavacca et al., 2005; Lally et al., 2005; Kiousis et al., 2007; Zahedmanesh et al., 2010; García et al., 2012). However, these models do not adequately account for drug-transfer from a DES.

In the context of drug transport modelling, computational analysis can contribute to a better understanding of drug-release and binding mechanisms in arteries, aiming to guide the development of a next generation of DES with more favourable safety and efficacy (McGinty, 2014). A large number of computational studies have been developed in the last decade for this purpose, adopting either well-defined one-dimensional simplifications (McGinty and Pontrelli, 2016; Pontrelli and de Monte, 2007; Tzafriri et al., 2009; Pontrelli and de Monte, 2010; McGinty et al., 2010; d'Errico et al., 2015; McGinty and Pontrelli, 2015; McKittrick et al., 2019), or two-dimensional (Zunino, 2004; Mongrain et al., 2005, 2007; Vairo et al., 2010; Bozsak et al., 2014, 2015; Denny and Walsh, 2014a, 2014b; Ferreira et al., 2017, 2018; Tzafriri et al., 2018) and three-dimensional formulations (Migliavacca et al., 2007; Zunino et al., 2009; Feenstra and Taylor, 2009; Cutrì et al., 2013). These models generally consider an intact vessel with diffusion, advection and binding dictating the transport of drugs within the blood flow and the respective wall layers. However, these models do not take account of the influence of mechanical deformation on drug transport. In terms of modelling the drug binding process in the arterial wall, a nonlinear saturable reversible binding model is currently the well-accepted approach (Tzafriri et al., 2009; Bozsak et al., 2014, 2015). The precise form of modelling binding is controversial, however, with some authors highlighting the importance of taking into account binding to specific receptors and binding to non-specific sites (general extracellular matrix sites) as two separate phases (McGinty and Pontrelli, 2016; Tzafriri et al., 2012). In terms of modelling drug dynamics within the stent coating, although most models assume that drug transport is governed purely by diffusion (Vairo et al., 2010; Bozsak et al., 2014, 2015), depending on the physical and chemical characteristics of the polymeric coating and of the drug, it may be necessary to also account for other phenomena such as dissolution (McGinty and Pontrelli, 2015, 2016), degradation (Ferreira et al., 2017, 2018; Zhu and Braatz, 2015) or erosion (Zhu and Braatz, 2015).

There are a limited number of studies that attempt to incorporate both the mechanics of arterial tissue and drug transport. For example, in their 3D models, Migliavacca et al. (2007) and Cutrì et al. (2013) include drug transport in an arterial wall deformed by their simulations of stent deployment, but neither model relates the drug transport parameters to the level of deformation. Ferreira et al., 2017, 2018 use a linear visco-elastic model to explore how drug diffusion may be hindered in the presence of atherosclerotic plaque, but do not account for mechanical deformation of the arterial wall as a result of stent deployment. Feenstra and Taylor (2009), through a porohyperelastic-transport approach, calculate the geometry, porosity field and interstitial fluid velocity directly from a simulation of stent deployment and use these within a model of drug transport in the arterial wall consisting of three distinct layers. In this sense, tissue porosity and the contribution to drug transport of advection are not assumed *a priori*. However, this model assumes a linear drug reaction and drug diffusion coefficients that do not vary with deformation. Denny et al. (Denny and Walsh, 2014a, 2014b) do model the influence of strut compression on local diffusivity (Denny and Walsh, 2014a, 2014b) through simulations of the compression of an idealised arterial wall by an idealised unit cell model of a stent, but their model does not adequately account for the effects of nonlinear binding of drug.

In this paper, we provide the most comprehensive study to date of the effect of stent mechanical expansion on the drug transport properties of a three-layer arterial wall. Our model incorporates the state-of-the art description of the mechanical properties of arterial tissue through an anisotropic, hyperelastic material model and includes a nonlinear saturable binding model to describe drug transport in the arterial wall. We establish relationships between mechanical force generated through device expansion and alteration in diffusion within the arterial wall and perform simulations to elucidate the impact of such alterations on spatio-temporal drug release and tissue uptake.

1.1. *Outline*

We start with a discussion of the mechanical aspect of the problem and present the material models employed to describe the stent-induced deformation of arterial tissue. We then derive expressions for the arterial drug diffusion coefficients as a function of deformation (Section 2.2). This is followed by a description of the drug transport model in the lumen, where blood flow is described by the steady Navier-Stokes equations, and in the multi-layer anisotropic porous tissue of the arterial wall, where Darcy's law is used to calculate the plasma filtration through the tissue and advection-diffusion-reaction equations are used to model the drug dynamics (Section 2.3). A detailed description of the computational geometry and the implementation of the model equations is provided in Section 2.4. The key results are presented in Section 3, along with a discussion of their significance. Finally, in Section 4 and 5 we reiterate the limitations of our work and provide some final conclusions, respectively.

2. Material and methods

2.1. *Mechanical model*

2.1.1. *Modelling the arterial wall*

We consider the arterial wall to be composed of three distinct layers:

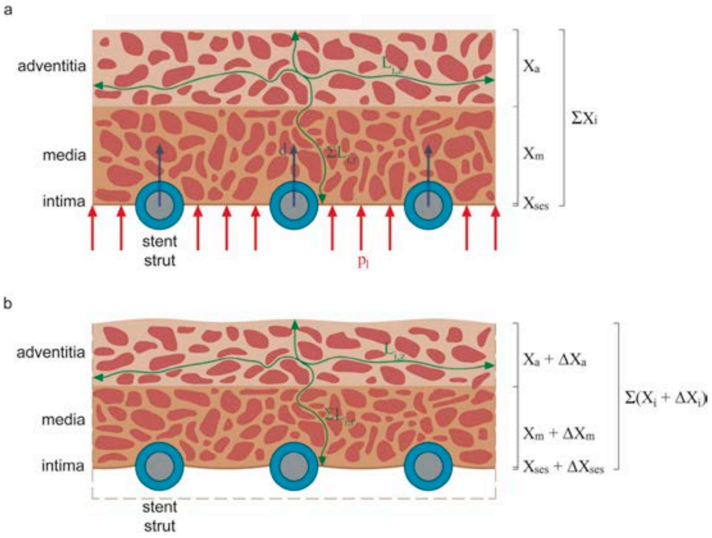

Fig. 1. Schematic showing the influence of stent expansion on tortuosity. (a) Prior to stent expansion, the tortuous path length in the radial direction through the three layers of the tissue is given by $\sum L_{i,r}$, while the path length in the longitudinal is given by $L_{i,z}$, where the subscript $i = \{ses, m, a\}$ denotes the subendothelial space of the intima, the media and the adventitia, respectively. The total thickness of the wall is given by $\sum X_i$. (b) After stent expansion, the total deformed thickness of the wall is $\sum(X_i + \Delta X_i)$, where $\Delta X_i > 0$ denotes elongation and $\Delta X_i < 0$ contraction.

the intima, the media and the adventitia. Each individual layer is modelled as an anisotropic, hyperelastic and incompressible material (Carew et al., 1968; Holzapfel et al., 2005a) and reinforced by two families of collagen fibres, following the model proposed by Gasser et al. (2006). In this model, the strain-energy function (SEF) is given by:

$$\Psi = \mu(I_1 - 3) + \sum_{\alpha=4,6} \frac{k_1}{2k_2} \left[\exp\left\{ k_2 [\kappa I_1 + (1 - 3\kappa) I_\alpha - 1]^2 \right\} - 1 \right], \tag{1}$$

where $I_1 = \mathrm{tr}(\mathbf{C})$ represents the first invariant of the right Cauchy-Green deformation tensor (Spencer, 1971), **C**, characterizing the isotropic mechanical response of the elastin (Gundiah et al., 2009; Lillie et al., 2010) while $I_4 \geq 1$ and $I_6 \geq 1$ characterize the mechanical response in the preferential directions of the fibers/cells (Holzapfel et al., 2005a). The material parameters $\mu > 0$ and $k_1 > 0$ have the dimension of stress whereas $k_2 > 0$ and $0 \leq \kappa \leq 1/3$, that characterizes the level of dispersion of the collagen orientations, are dimensionless. When $\kappa = 0$ the fibres are perfectly aligned (no dispersion) and when $\kappa = 1/3$ the fibres are randomly distributed and the material becomes isotropic. Assuming that the anisotropy directions are helically oriented at $\pm\beta$ degrees with respect to the longitudinal direction, the invariants I_4 and I_6 can also be expressed as a function of the main stretches:

$$\begin{aligned} I_4 &= \lambda_1^2 \cos^2\beta_1 + \lambda_2^2 \sin^2\beta_1, \\ I_6 &= \lambda_1^2 \cos^2\beta_2 + \lambda_2^2 \sin^2\beta_2. \end{aligned} \tag{2}$$

where $\beta_1 = \beta$ and $\beta_2 = -\beta$ (Holzapfel et al., 2000). Moreover, it has been assumed that the strain energy corresponding to the anisotropic terms only contributes to the global mechanical response of the tissue when stretched, that is $I_4 > 1$ and $I_6 > 1$, and that the tissue does not bear any load when compressed. The model parameters were calibrated against the experimental data reported by Holzapfel et al. (2005a) and shown in Table 1. Notice that all tissues have been considered as incompressible for this material parameter identification, i.e. with volume ratio $J = \det \mathbf{F} = 1$, where **F** is the deformation gradient tensor.

2.1.2. *Modelling stent struts and stent coating*

The stent struts are modelled as an elasto-plastic material with a Young's modulus, E, of 200 GPa and Poisson's ratio, ν, of 0.28, representative of biomedical grade stainless steel alloy 316L (Conway et al., 2012). The plasticity is described by isotropic hardening J_2 flow theory with the tensile stress-strain curves taken from the literature (McGarry et al., 2004), including a yield strength, σ_y, of 264 MPa and a ultimate tensile strength (UTS), σ_u, of 584 MPa at an engineering plastic strain of 0.247. The stent coating is modelled as a nonlinear elastic material with bilinear behaviour simulating a phosphorylcholine (PC)-based polymer coating with a Young's modulus of 240 MPa, a Poisson's ratio of 0.5, a yield strength of 16 MPa and a tangent modulus, E_t, of 7.7 MPa (Hopkins et al., 2010; Schiavone et al., 2014).

2.2. *Derivation of arterial diffusion coefficients as a function of deformation*

In a porous media, as in the case of the arterial wall, diffusion of species takes place over a tortuous path that depends on the material structure (O'Connell and Walsh, 2012). The influence of the porosity coupled with the tortuous nature of the arterial tissue results in the so-called effective diffusivity or effective diffusion coefficient, D, which is defined as (Cussler, 2009):

$$D = \frac{\varphi}{\tau} D_{free}, \tag{3}$$

where φ is the porosity, τ represents the tortuosity and D_{free} is the species free diffusivity which is determined by the Stokes-Einstein equation (Cussler, 2009):

$$D_{free} = \frac{k_B T}{6\pi\mu R}, \tag{4}$$

where T is the absolute temperature, k_B is the Boltzmann's constant, μ is the dynamic viscosity of the solvent (plasma) and R is the hydrodynamic solute (drug) radius. Due to the heterogeneous structure of the arterial wall, the effective diffusion coefficient will be different for each layer of the tissue (O'Connell et al., 2010). Moreover, there is experimental evidence to suggest that diffusion within each layer is anisotropic (Hwang and Edelman, 2002; Levin et al., 2004). Tortuosity can be estimated by the ratio between the average pore path length, L, to the straight distance between the ends of the pore path, X, as: $\tau = L/X$ (O'Connell et al., 2010). Although the pore pathways in the arterial tissue runs through different 3D planes, since we consider a 2D axisymmetric model in this work, we consider diffusion in the radial and longitudinal directions only. It is assumed that after stent implantation the arterial wall is

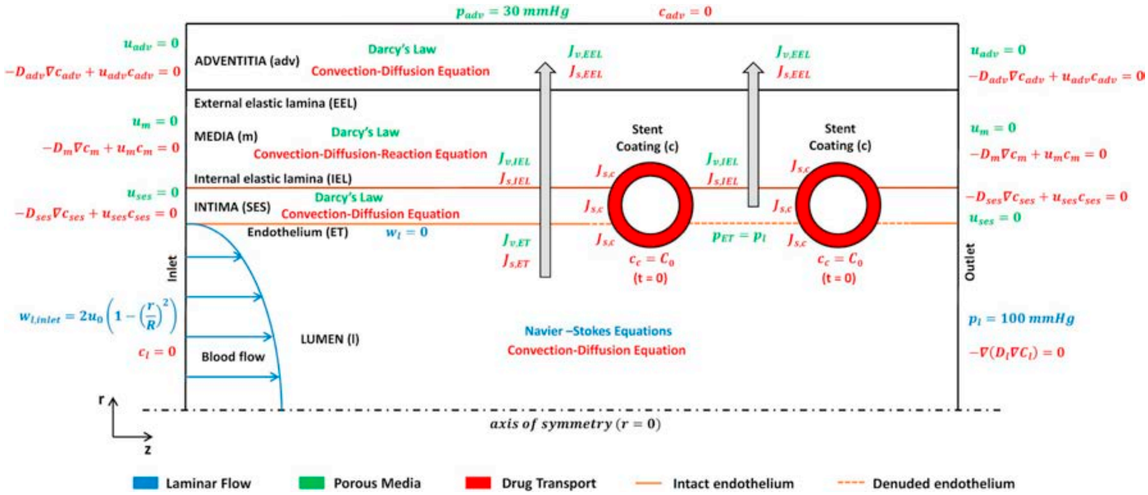

Fig. 2. Schematic showing boundary conditions of the drug transport model.

radially compressed by the stent struts, leading to changes in tortuosity, and therefore in arterial diffusivity, in both radial and longitudinal directions (Denny and Walsh, 2014b; O'Connell and Walsh, 2010). Fig. 1 shows how stenting theoretically affects the tortuous path in both directions. The stent expansion will also cause local changes to porosity in the arterial tissue. However, these local variations are not taken into account in the analysis framework presented assuming that the overall porosity in each layer is constant. In the radial direction, a variation in the thickness of each layer of the arterial wall (X_i) is observed, resulting in an increase in tortuosity in that direction:

$$\tau_{i,r} = \frac{L_{i,r}}{X_i + \Delta X_i}, \tag{5}$$

where the subscript $i = \{ses, m, a\}$ denotes the subendothelial space of the intima, the media and the adventitia, respectively; the subscript r denotes the radial direction; $L_{i,r}$ is the length of the pore path in each layer, which is assumed to remain constant (O'Connell et al., 2010) and; ΔX_i represents the change in each wall layer thickness and is positive for an increase but negative for a decrease in thickness. The definition of radial strain, $\varepsilon_{i,r} = \Delta X_i / X_i$, is used to relate the tortuosity after compression in the radial direction in each layer of the tissue, $\tau_{i,r}$, to the uncompressed wall tortuosity, $\tau^0_{i,r}$, as follows:

$$\frac{\tau^0_{i,r}}{\tau_{i,r}} = \frac{L_{i,r}/X_i}{L_{i,r}/(X_i + \Delta X_i)} = 1 + \varepsilon_{i,r}, \tag{6}$$

By relating Eqs. (3) and (6), we can establish a ratio between the initial effective diffusion coefficient, $D^0_{i,r}$, and the effective diffusivity after compression, $D_{i,r}$, in radial direction:

$$\frac{D^0_{i,r}}{D_{i,r}} = \frac{1}{1 + \varepsilon_{i,r}}. \tag{7}$$

Following the same reasoning, we can obtain a relationship between the initial effective diffusivity in the uncompressed wall longitudinal direction, $D^0_{i,z}$, and the effective diffusivity after compression in that direction, $D_{i,z}$, through the longitudinal strain, $\varepsilon_{i,z}$, and finally define an anisotropic diffusion tensor after stenting for each layer of the tissue, $\mathbf{D}_i$, as:

$$\mathbf{D}_i = \begin{pmatrix} D_{i,r} & 0 \\ 0 & D_{i,z} \end{pmatrix} = \begin{pmatrix} D^0_{i,r}(1 + \varepsilon_{i,r}) & 0 \\ 0 & D^0_{i,z}(1 + \varepsilon_{i,z}) \end{pmatrix}, \tag{8}$$

where the subscript z refers to the longitudinal direction. Due to stenting, the arterial wall experiences compressive strain ($\varepsilon_{i,r} < 0$) in the radial direction and tensile strain ($\varepsilon_{i,z} > 0$) in the longitudinal direction, therefore, Eq. (8) shows that the magnitude of the effective diffusivity in the tissue after stent deployment is lower than the uncompressed value in the radial direction and higher than the uncompressed value in the longitudinal one. This assumption is in agreement with the experimental data reported in Levin et al. (2004), where it is shown that the radial diffusivity of paclitaxel and sirolimus in the arterial wall in the radial direction is lower than in circumferential and longitudinal directions.

2.3. Drug transport model

2.3.1. Modelling blood flow

The blood flow is modelled as a Newtonian fluid and assumed to be steady, laminar and incompressible, described by the stationary Navier-Stokes equations and the continuity equation:

$$\rho_b(\boldsymbol{u}_l \cdot \nabla)\boldsymbol{u}_l = -\nabla p_l + \mu_b \nabla^2 \boldsymbol{u}_l, \tag{9}$$

$$\nabla \cdot \boldsymbol{u}_l = 0, \tag{10}$$

where $\boldsymbol{u}_l$ is the lumen velocity vector, p_l is the pressure in the lumen, μ_b is the blood dynamic viscosity and ρ_b is the blood density. A laminar Poiseuille velocity profile is imposed at the inlet of the arterial lumen, $\Gamma_{l,inlet}$:

$$w_{l,inlet} = 2u_0\left(1 - \left(\frac{r}{r_l}\right)^2\right), \tag{11}$$

where $w_{l,inlet}$ denotes the longitudinal component of the blood velocity in the lumen at the inlet, u_0 is the mean blood velocity computed considering a Reynolds number of $Re_l = 400$ (Formaggia et al., 2010), r_l is the internal radius of the artery at the inlet (unstented region) and r is the radial coordinate. At the outlet of the lumen, $\Gamma_{l,outlet}$, a pressure value of 100 mmHg (13.3 kPa) is fixed (Ai and Vafai, 2006). Moreover, a no-slip boundary condition ($w_l = 0$) was considered at the lumen-arterial wall interface, Γ_{et}. In this work, the pulsatile nature of the blood flow is neglected in agreement with previous models (Mongrain et al., 2005, 2007; Vairo et al., 2010; Bozsak et al., 2014).

Table 2
List of parameters related to the drug transport model.

Parameter	Description	Value	Reference
Δp	Pressure difference between lumen and adventitia	70 mmHg	Meyer et al. (1996)
Re_l	Lumenal Reynolds number	400	Formaggia et al. (2010)
ρ_b	Blood density	1060 $kg{\cdot}m^{-3}$	Bozsak et al. (2014)
ρ_p	Plasma density	1060 $kg{\cdot}m^{-3}$	Bozsak et al. (2014)
μ_b	Blood dynamic viscosity	$3.5 \cdot 10^{-3}$ Pa·s	Karner et al. (2001)
μ_p	Plasma dynamic viscosity	$7.2 \cdot 10^{-4}$ Pa·s	Zunino (2004)
ρ_i	Density of wet arterial tissue	983 $kg{\cdot}m^{-3}$	Tzafriri et al. (2012)
φ_{ses}	Porosity of the intima	0.983	Ai and Vafai (2006)
φ_m	Porosity of the media	0.258	Ai and Vafai (2006)
φ_a	Porosity of the adventitia	0.85	d'Errico et al. (2015)
γ_{ses}	Hindrance coefficient in the intima	1	Calculated from (Bozsak et al., 2014)
γ_m	Hindrance coefficient in the media	0.845	Calculated from (Curry, 1984; Formaggia et al., 2010; Bozsak et al., 2014)
γ_a	Hindrance coefficient in the adventia	1	Estimated
κ_{ses}	Darcy permeability in the intima	$2.2{\cdot}10^{-16}$ m^2	Ai and Vafai (2006)
κ_m	Darcy permeability in the media	$2{\cdot}10^{-18}$ m^2	Zunino (2004)
κ_a	Darcy permeability in the adventitia	$2{\cdot}10^{-18}$ m^2	Vairo et al. (2010)
$L_{p,et}$	Hydraulic conductivity of endothelium	$2.2{\cdot}10^{-12}$ $m^2{\cdot}s{\cdot}kg^{-1}$	Bozsak et al. (2014)
$L_{p,iel}$	Hydraulic conductivity of IEL	$2.2{\cdot}10^{-9}$ $m^2{\cdot}s{\cdot}kg^{-1}$	Bozsak et al. (2014)
$L_{p,eel}$	Hydraulic conductivity of EEL	$2.2{\cdot}10^{-9}$ $m^2{\cdot}s{\cdot}kg^{-1}$	Estimated
M_0	Drug dose in the coating	150 μg	Estimated
D_c	Effective diffusion coefficient in the coating	10^{-13} $m^2{\cdot}s^{-1}$	Mongrain et al. (2005)
SIROLIMUS			
D_l	Effective diffusion coefficient in the lumen	$4.1{\cdot}10^{-12}$ $m^2{\cdot}s^{-1}$	Bozsak et al. (2014)
D_{ses}	Effective diffusion coefficient in the intima	$1.67{\cdot}10^{-11}$ $m^2{\cdot}s^{-1}$	Bozsak et al. (2014)
$D_{m,r}$	Effective radial diffusion coefficient in the media	$7{\cdot}10^{-12}$ $m^2{\cdot}s^{-1}$	Levin et al. (2004)
$D_{m,z}$	Effective axial diffusion coefficient in the media	$4{\cdot}10^{-11}$ $m^2{\cdot}s^{-1}$	Levin et al. (2004)
D_a	Effective diffusion coefficient in the adventitia	$4{\cdot}10^{-12}$ $m^2{\cdot}s^{-1}$	Estimated
P_{et}	Permeability of endothelium	$3.6{\cdot}10^{-6}$ $m{\cdot}s^{-1}$	Bozsak et al. (2014)
P_{iel}	Permeability of IEL	$9.6{\cdot}10^{-6}$ $m{\cdot}s^{-1}$	Bozsak et al. (2014)
P_{eel}	Permeability of EEL	$9.6{\cdot}10^{-6}$ $m{\cdot}s^{-1}$	Estimated
s_{et}	Sieving coefficient in the endothelium	0.855	Bozsak et al. (2014)
s_{iel}	Sieving coefficient in the IEL	1	Bozsak et al. (2014)
s_{eel}	Sieving coefficient in the EEL	1	Estimated
K_d	Equilibrium dissociation constant	$2.6{\cdot}10^{-3}$ $mol{\cdot}m^{-3}$	Tzafriri et al. (2009)
k_{on}	Drug binding rate constant	2 $m^3{\cdot}mol^{-1}{\cdot}s^{-1}$	Tzafriri et al. (2009)
k_{off}	Drug unbinding rate constant	$5.2{\cdot}10^{-3}$ s^{-1}	McGinty and Pontrelli (2016)
b_{max}	Total binding site density	0.366 $mol{\cdot}m^{-3}$	Tzafriri et al. (2009)
MW_{sir}	Molecular weight	914.172 $g{\cdot}mol^{-1}$	Levin et al. (2004)
PACLITAXEL			
D_l	Effective diffusion coefficient in the lumen	$4.2{\cdot}10^{-12}$ $m^2{\cdot}s^{-1}$	Bozsak et al. (2014)
D_{ses}	Effective diffusion coefficient in the intima	$1.7{\cdot}10^{-11}$ $m^2{\cdot}s^{-1}$	Bozsak et al. (2014)
$D_{m,r}$	Effective radial diffusion coefficient in the media	$2{\cdot}10^{-12}$ $m^2{\cdot}s^{-1}$	Levin et al. (2004)
$D_{m,z}$	Effective axial diffusion coefficient in the media	$5{\cdot}10^{-11}$ $m^2{\cdot}s^{-1}$	Levin et al. (2004)
D_a	Effective diffusion coefficient in the adventitia	$4{\cdot}10^{-12}$ $m^2{\cdot}s^{-1}$	Vairo et al. (2010)
P_{et}	Permeability of endothelium	$3{\cdot}10^{-6}$ $m{\cdot}s^{-1}$	Bozsak et al. (2014)
P_{iel}	Permeability of IEL	$9.8{\cdot}10^{-6}$ $m{\cdot}s^{-1}$	Bozsak et al. (2014)
P_{eel}	Permeability of EEL	$9.8{\cdot}10^{-6}$ $m{\cdot}s^{-1}$	Estimated
s_{et}	Sieving coefficient in the endothelium	0.86	Bozsak et al. (2014)
s_{iel}	Sieving coefficient in the IEL	1	Bozsak et al. (2014)
s_{eel}	Sieving coefficient in the EEL	1	Estimated
K_d	Equilibrium dissociation constant	$3.1{\cdot}10^{-3}$ $mol{\cdot}m^{-3}$	Tzafriri et al. (2009)
k_{on}	Drug binding rate constant	0.17 $m^3{\cdot}mol^{-1}{\cdot}s^{-1}$	Calculated from (Tzafriri et al., 2009)
k_{off}	Drug unbinding rate constant	$5.27{\cdot}10^{-4}$ s^{-1}	Calculated from (Tzafriri et al., 2009)
b_{max}	Total binding site density	0.127 $mol{\cdot}m^{-3}$	Tzafriri et al. (2009)
MW_{ptx}	Molecular weight	853.906 $g{\cdot}mol^{-1}$	Levin et al. (2004)

2.3.2. *Modelling the porous media*

The coronary artery wall consists of three porous layers and the transmural velocity vector field in each layer, $\boldsymbol{u}_i$, is computed by Darcy's law, constrained with the solenoidal condition on $\boldsymbol{u}_i$ arising from the mass conservation law for an incompressible flow (Vairo et al., 2010; Migliavacca et al., 2007):

$$\boldsymbol{u}_i = \frac{\kappa_i}{\mu_p}\nabla p_i, \qquad \nabla\cdot\boldsymbol{u}_i = 0 \tag{12}$$

where the subscript $i = \{ses, m, a\}$ denotes the subendothelial space of the intima, the media or the adventitia, respectively; κ_i is the Darcian permeability of each layer of the arterial wall; μ_p is the dynamic viscosity of the blood plasma and; p_i is the pressure within each layer of the tissue. Finally, to mathematically model the fluid volume flux across the semipermeable membranes between layers, we used the well-known Kedem-Katchalsky equations (Kedem and Katchalsky, 1958):

$$J_{v,j} = L_{p,j}\left(\Delta p_j - \varsigma_{d,j}\Delta\pi_j\right), \tag{13}$$

where the subscript $j = \{et, iel, eel\}$ denotes the endothelium, the internal or the external elastic lamina, respectively; $L_{p,j}$ is the hydraulic conductivity of each membrane considered; Δp_j is the pressure difference across the semipermeable membrane; $\varsigma_{d,j}$ is the Staverman osmotic reflection coefficient and; $\Delta\pi_j$ is the osmotic pressure differential across the membranes. Neglecting the contribution due to osmosis (Formaggia

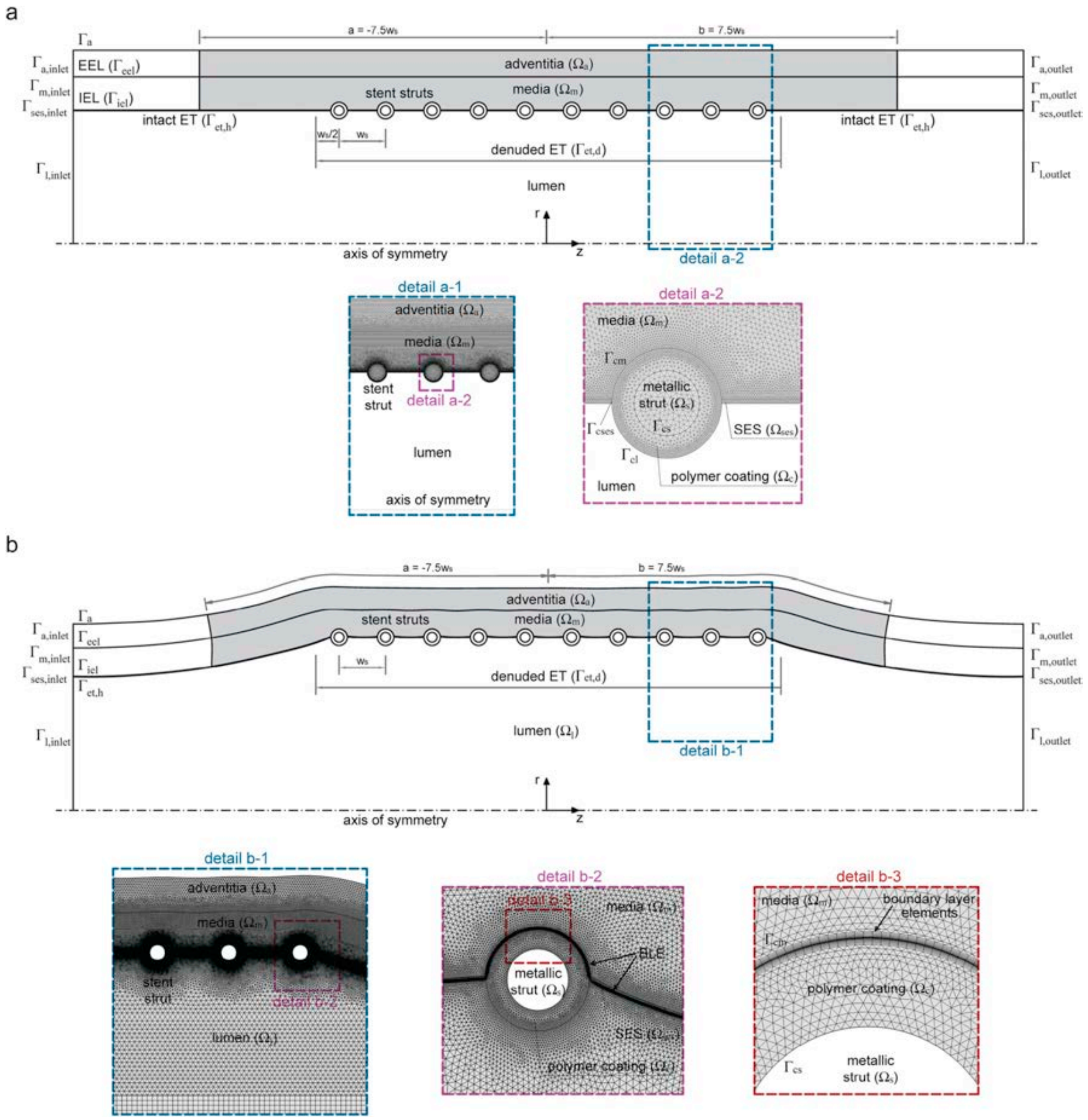

Fig. 3. The 3D arterial geometry is assumed to be axisymmetric and therefore a 2D representation is considered in this work. (a) Overall longitudinal section view of the pre-stressed arterial segment with a DES implanted. In details a-1 and a-2 a detailed view of the finite element (FE) mesh used in the mechanical model is shown. (b) Overall longitudinal section view of the arterial segment after stent deployment. In details b-1, b-2 and b-3 a detailed view of the FE mesh used in the drug transport analysis. In both subfigures, the therapeutic domain (target area for drug transport) considered to compute all the variables of the model is shaded in grey and it was defined as the domain that extends in $a < z < b$ with the origin of the computational geometry placed between the two central struts and where $a = -7.5w_s$ and $b = 7.5w_s$. In this figure, Ω_l defines the vessel lumen, Ω_{ses} the SES, Ω_m the media, Ω_a the adventitia, Ω_s the metallic stent struts and Ω_c the stent coating. The boundaries Γ_{et}, Γ_{iel}, Γ_{eel} define the endothelium, internal and external elastic laminae, respectively; Γ_a the outer boundary of the arterial wall; Γ_{cl}, Γ_{cses}, Γ_{cm} and Γ_{cs} the interface between the stent coating and blood, SES, media and metallic strut, respectively; $\Gamma_{l,inlet}$ and $\Gamma_{l,outlet}$ the inlet and outlet boundaries of the lumen, respectively and; $\Gamma_{i,inlet}$ and $\Gamma_{i,outlet}$ the inlet and outlet boundaries of the wall layers with respect to the blood flow, respectively.

Table 3
List of parameters related to the geometrical model prior to stent expansion.

Parameter	Description	Value	Reference
r_l	Lumen radius	2.0 mm	Dodge et al. (1992)
δ_{ses}	Intima thickness	0.01 mm	Karner et al. (2001)
δ_m	Media thickness	0.5 mm	Migliavacca et al. (2007)
δ_a	Adventitia thickness	0.4 mm	Creel et al. (2000)
d_{strut}	Strut diameter	0.15 mm	Mongrain et al. (2005)
δ_p	Polymeric coating thickness	0.05 mm	Mongrain et al. (2005)
w_s	Interstrut distance	0.7 mm	Mongrain et al. (2005)

Table 4
Summary of the five different cases considered in the simulations. In each case, the initial drug loading is 150 μg.

Case	Description	Pressurised artery?	Lumen radius in stented region	Lumen radius in unstented region
(i)	Uncoupled	No	2.0 mm	2.0 mm
(ii)	0% expansion	Yes (P = 100 mmHg)	2.0 mm	2.0 mm
(iii)	10% expansion	Yes (P = 100 mmHg)	2.2 mm	2.0 mm
(iv)	20% expansion	Yes (P = 100 mmHg)	2.4 mm	2.0 mm
(v)	30% expansion	Yes (P = 100 mmHg)	2.6 mm	2.0 mm

et al., 2010; Bozsak et al., 2014), we can formulate the flux J_v for each membrane considered:

$$J_{v,et} = L_{p,et}\Delta p_{et} = L_{p,et}(p_l - p_{ses}), \tag{14}$$

$$J_{v,iel} = L_{p,iel}\Delta p_{iel} = L_{p,iel}(p_{ses} - p_m) \tag{15}$$

and

$$J_{v,eel} = L_{p,eel}\Delta p_{eel} = L_{p,eel}(p_m - p_a). \tag{16}$$

In this work, it is assumed that the endothelium is completely denuded due to stent placement in regions between struts and upstream and downstream of the stent over a distance that is one half of the interstrut spacing, measured from the stent strut centers (Bozsak et al., 2014, 2015). Outside of these regions the endothelium is assumed to be intact. In denuded regions, the flux $J_{v,et}$ simplifies to continuity of pressure ($p_l = p_{ses}$). A zero-flow condition, $-\boldsymbol{n}_i\cdot\boldsymbol{u}_i = 0$, where $\boldsymbol{n}_i$ is the unit outward normal vector to the corresponding exterior boundary, is imposed to the left and right wall boundaries, $\Gamma_{i,inlet}$ and $\Gamma_{i,outlet}$, respectively (sufficiently far from the therapeutic domain so that these boundary conditions have no effect on the results). At the perivascular side (outer boundary of the arterial wall, Γ_a), a pressure of 30 mmHg (Ai and Vafai, 2006) is applied in order to impose a pressure gradient of 70 mmHg (Meyer et al., 1996) between the inner and the outer surface of the tissue. We refer the reader to Fig. 2 for a diagrammatic representation of the boundary conditions.

2.3.3. Modelling drug transport within the stent coating

We consider durable polymer-coated stents and assume that drug release is governed by diffusion:

$$\frac{\partial c_c}{\partial t} = \nabla\cdot(\boldsymbol{D}_c\nabla c_c), \tag{17}$$

where $c_c(r,z,t)$ is the concentration of dissolved (free) drug in the coating and $\boldsymbol{D}_c$ is the effective diffusion coefficient of the drug through the porous polymer. We assume that initially all the drug exists in dissolved form in the polymer coating at concentration C_0, calculated as M_0/V_c, where M_0 is the initial mass of drug within the coating and V_c is the volume of the coating. Continuity of concentration and flux, $J_{s,c}$, of free drug across the outer boundary of the polymeric stent coating is prescribed:

$$J_{s,c} = (-\boldsymbol{D}_c\nabla c_c)\cdot\boldsymbol{n}_c = -(-\boldsymbol{D}_k\nabla c_k + \boldsymbol{u}_k c_k)\cdot\boldsymbol{n}_k, \qquad c_c = c_k, \tag{18}$$

where the subscript $k = \{l, ses, m\}$ represents the lumen, the SES and the media, respectively. Finally, a zero-flux condition, $-\boldsymbol{n}_c\cdot(-\boldsymbol{D}_c\nabla c_c) = 0$ is imposed at the interface between the metallic strut and the polymer coating.

2.3.4. Modelling drug transport within the lumen and the arterial wall

Drug transport in the lumen is described by the unsteady advection-diffusion equation:

$$\frac{\partial c_l}{\partial t} + \boldsymbol{u}_l\cdot\nabla c_l = \nabla\cdot(\boldsymbol{D}_l\nabla c_l), \tag{19}$$

where $c_l(r,z,t)$ is the concentration of drug in the lumen, $\boldsymbol{D}_l$ is the diffusion coefficient and $\boldsymbol{u}_l$ is the velocity of the blood flow in the lumen computed by the steady Navier-Stokes equations. The advection-diffusion equation is also used to model the drug transport in the intima and the adventitia:

$$\frac{\partial c_{ses}}{\partial t} + \frac{\gamma_{ses}}{\varphi_{ses}}\boldsymbol{u}_{ses}\cdot\nabla c_{ses} = \nabla\cdot(\boldsymbol{D}_{ses}\nabla c_{ses}), \tag{20}$$

$$\frac{\partial c_a}{\partial t} + \frac{\gamma_a}{\varphi_a}\boldsymbol{u}_a\cdot\nabla c_a = \nabla\cdot(\boldsymbol{D}_a\nabla c_a), \tag{21}$$

and the advection-diffusion-reaction equation is used to model the drug transport in the media:

$$\frac{\partial c_m}{\partial t} + \frac{\gamma_m}{\varphi_m}\boldsymbol{u}_m\cdot\nabla c_m = \nabla\cdot(\boldsymbol{D}_m\nabla c_m) - \frac{\partial b_m}{\partial t}, \tag{22}$$

$$\frac{\partial b_m}{\partial t} = k_{on}c_m(b_{max} - b_m) - k_{off}b_m, \tag{23}$$

where $c_i(r,z,t)$ denotes the volume-averaged concentration of free drug in layer i, $\gamma_i \le 1$ is the hindrance coefficient, φ_i is the porosity, $\boldsymbol{u}_i$ is the transmural velocity in the porous layers computed by Darcy's law and $\boldsymbol{D}_i$ is the diffusion tensor in each layer of the arterial wall. For the media layer, we consider a non-linear saturable reversible binding model (Eq. (23)) to describe drug interactions with the tissue (Tzafriri et al., 2009; Bozsak et al., 2014; Kolachalama et al., 2013; McGinty et al., 2015). This model allows one to define two different states of the drug in the media layer: drug dissolved in the plasma (free drug, $c_m(r,z,t)$) and drug bound

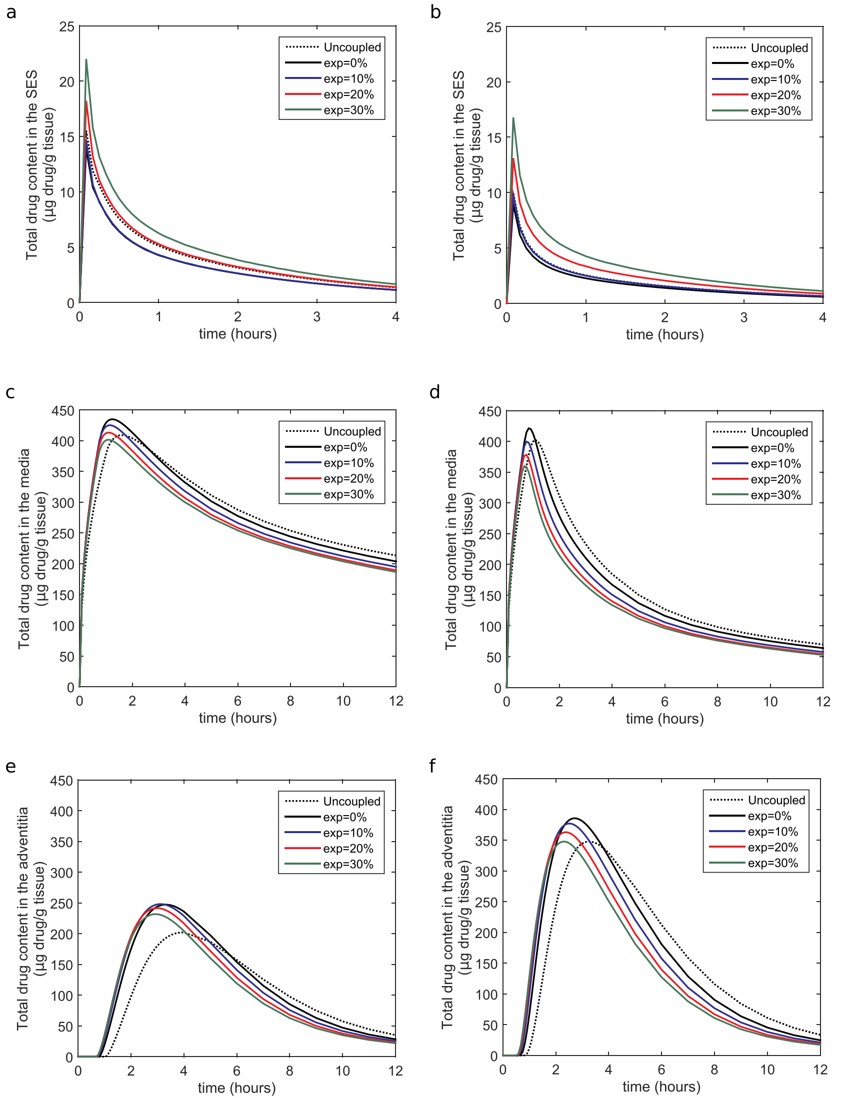

Fig. 4. Content of sirolimus (a, c, e) and paclitaxel (b, d, f) in each layer of the arterial wall (presented as μg drug per g of tissue). In the SES and the adventitia, drug content corresponds exclusively to free drug and in the media layer corresponds to free plus bound drug. Notice that the scales of the x- and y-axis in (a) and (b) are different from the rest of the subfigures. The results are shown for the uncoupled model and for luminal diameter expansions of $0-30\%$ for the coupled model.

to binding sites, $b_m(r,z,t)$. The parameters k_{on} and k_{off} are the association (binding) and dissociation (unbinding) rate constants, respectively, and b_{max} is the maximum density of binding sites. The rate constants are related through the equilibrium dissociation constant, K_d, which is defined as $K_d = k_{off}/k_{on}$.

The discontinuity of solute flux, J_s, across the endothelium and internal and external elastic laminae is governed by the Kedem-Katchalsky equations:

$$J_{s,j} = P_j \Delta c_j + s_j \overline{c}_j J_{v,j} \tag{24}$$

where P_j is the permeability of each semipermeable membrane, Δc_j is the solute concentration differential, s_j is the sieving coefficient and $\overline{c}_j$ is computed as the weighted average of the concentrations on either side of the membrane (Levitt, 1975):

$$\overline{c}_{et} = \frac{1}{2}(c_l + c_{ses}) + \frac{s_{et} J_{v,et}}{12 P_{et}}(c_l - c_{ses}), \tag{25}$$

$$\overline{c}_{iel} = \frac{1}{2}(c_{ses} + c_m) + \frac{s_{iel} J_{v,iel}}{12 P_{iel}}(c_{ses} - c_m) \tag{26}$$

$$\overline{c}_{eel} = \frac{1}{2}(c_m + c_{adv}) + \frac{s_{eel} J_{v,eel}}{12 P_{eel}}(c_m - c_{adv}). \tag{27}$$

Zero drug concentration, $c_l = 0$, and outflow, $-\boldsymbol{n}_l \cdot (-\boldsymbol{D}_l \nabla c_l) = 0$, conditions are imposed at the inlet and outlet boundaries in the lumen, respectively. Following Vairo et al. (2010), the upstream and downstream boundaries of the tissue are subjected to a zero-flux condition: $-$

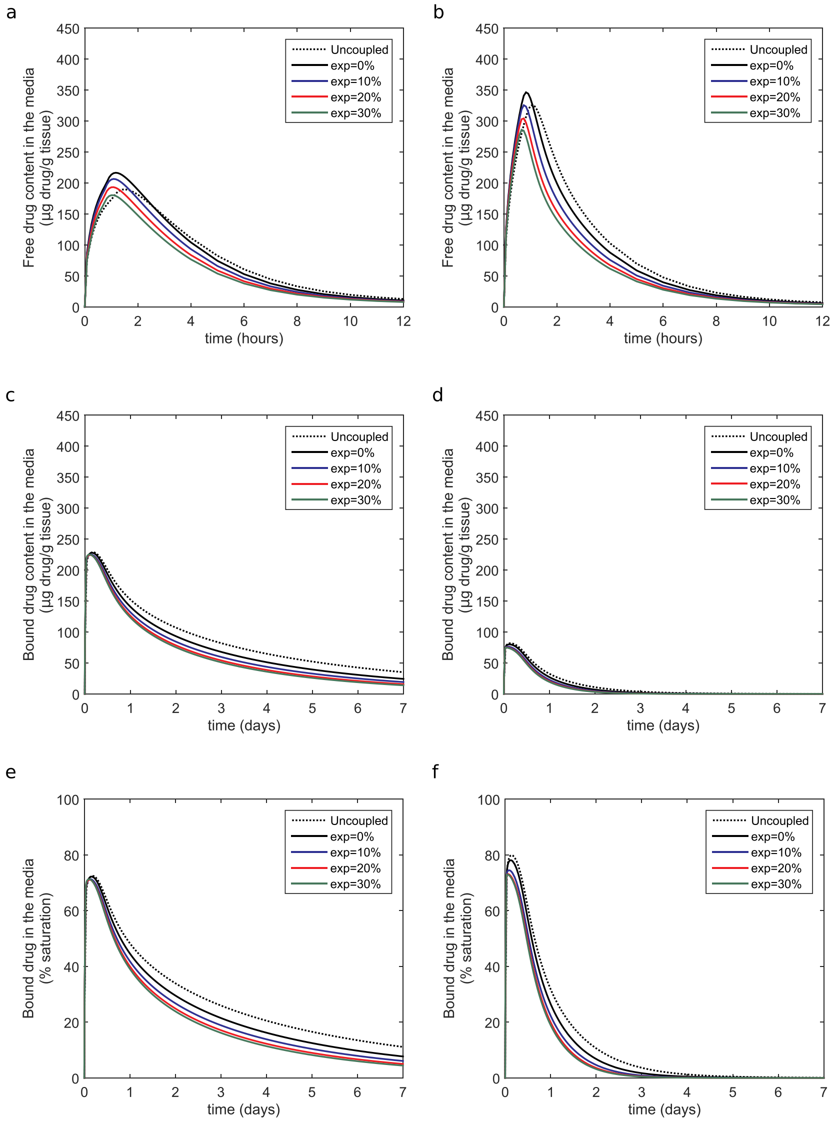

Fig. 5. Content of free sirolimus (a) and paclitaxel (b) in the media layer of the arterial wall (presented as μg drug per g of tissue). Content of bound of sirolimus (c) and paclitaxel (d) in the media (presented as μg drug per g of tissue). Binding site % saturation as a function of time for sirolimus (e) and paclitaxel (f) in the media. Note the different scales on the x- and y-axes. The results are shown for the uncoupled model and for luminal diameter expansions of $0-30\%$ for the coupled model.

$\boldsymbol{n}_i\cdot(-\boldsymbol{D}_i\nabla c_i+\boldsymbol{u}_i c_i)=0$. Finally, a perfect sink condition, $c_a = 0$, was applied at the perivascular wall for the free drug. All governing equations and boundary conditions involved in the computational model have been summarised in Fig. 2.

2.3.5. Drug transport model parameters

The majority of DES to date have contained either the drug paclitaxel, sirolimus or a sirolimus analogue. Sirolimus and analogues are anti-proliferative compounds that target the FK-binding protein 12 (FKBP12). This complex subsequently binds to the mammalian target of rapamycin (mTOR) and thereby interrupts the cell cycle in the G1-S phase. Paclitaxel is also an anti-proliferative compound; however, it inhibits neointimal growth by binding with and stabilising microtubules, resulting in cell-cycle arrest in the G0-G1 and G2-M phases (Martin and Boyle, 2011). In this work we consider both sirolimus and paclitaxel. Wherever possible, the model input parameters for sirolimus and paclitaxel are derived from experimental data available in the literature and are summarised in Table 2.

2.4. Computational model

To analyse the effect of the mechanical expansion of DES on drug transport, an idealised numerical model is developed that accounts for the changes in the tortuosity of the arterial wall as a result of strut compression.

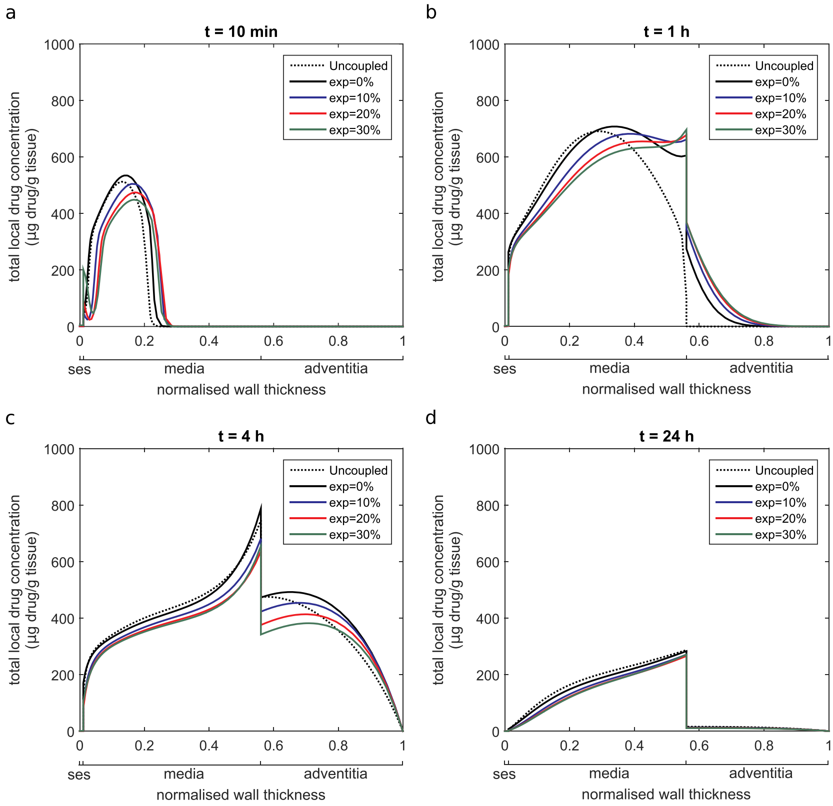

Fig. 6. Spatially varying profiles of total (free plus bound) local concentration of sirolimus in the tissue (presented as μg drug per g of tissue) at 10 min (a), 1 h (b), 4 h (c) and 1 day (d) after stent implantation. The results are shown for the uncoupled model and for luminal diameter expansions of $0-30\%$ for the coupled model in a radial section between the middle struts.

2.4.1. *Model geometry*

We consider initially a 2D-axisymmetric geometry of an idealised straight segment of a coronary artery where a DES is implanted (Fig. 3a). This geometry is similar to that introduced by Mongrain et al. (2005) and subsequently used by Vairo et al. (2010) and Bozsak et al. (2014). The arterial wall is modelled as a three-layered structure with the sub-endothelial space (SES) of the intima, the media and the adventitia defined as different domains (Ω_{ses}, Ω_m and Ω_a, respectively), while the endothelium (ET), internal elastic lamina (IEL) and external elastic lamina (EEL) are treated as interfacial semipermeable membranes (Γ_{et}, Γ_{iel} and Γ_{eel}, respectively). The lumen radius, r_l, and the thickness of each layer of the tissue prior to stent expansion, δ_i, are listed in Table 3. The DES is represented by 10 polymer-coated metallic circular struts each of 0.25 mm total diameter, including a coating thickness, δ_p, of 50 μm, and separated by a centre-to-centre distance of 0.7 mm. A half-embedment configuration of the stent struts into the arterial wall is taken into account.

2.4.2. *Numerical methods*

The commercially available software COMSOL Multiphysics 5.3a (COMSOL AB, Burlington, MA, USA) was used to create the finite element (FE) mesh and to numerically solve the coupled stent expansion/drug transport model detailed in Section 2. Three consecutive modelling steps were performed: (1) a stationary mechanical analysis was run in order to simulate the stent deployment, (2) starting from the deformed geometry computed in (1), a stationary analysis of blood flow dynamics and plasma filtration was carried out, and finally (3) a time-dependent drug transfer analysis was performed, which was coupled with the data calculated in previous steps such as the strain response of the vessel wall and the luminal and transmural flow. A sensitivity analysis was previously conducted in order to investigate the influence of the mesh and time step size on the results (data not shown). Different tests were made and mesh and time step independence was assumed when there was less than 1% difference in the temporal evolution of the total drug content in the media layer of the arterial wall for successive mesh and time step refinements. The computational domains were spatially discretized using a combination of triangular and quadrilateral elements, resulting in an overall mixed mesh with approximately 350,000 elements. Lagrange P3-P2 elements were used to discretize the blood dynamics problem and quadratic Lagrange elements were use to numerically approximate the mechanical, porous media and drug transport problems. A direct linear solver (MUMPS) was used to solve the stationary problems with a tolerance for the relative error of the solution of 10^{-3}. The backward differentiation formula (BDF) method was the implicit method used for the time discretization of the transient drug transport problem, with variable order of accuracy varying from one (also known as the backward Euler method) to five in order to obtain better stability and variable time step size. The maximum time-step size was restricted to 1 h. The relative and absolute tolerances were set to 10^{-3} and 10^{-4}, respectively. The resulting system of time-dependent partial differential equations (PDEs) were solved using a direct linear solver (PARDISO) with a nested dissection preordering algorithm. The computation time of the total simulation (the three steps described in Section 2.4.2) for each expansion case performed on 8 cores of an Intel®

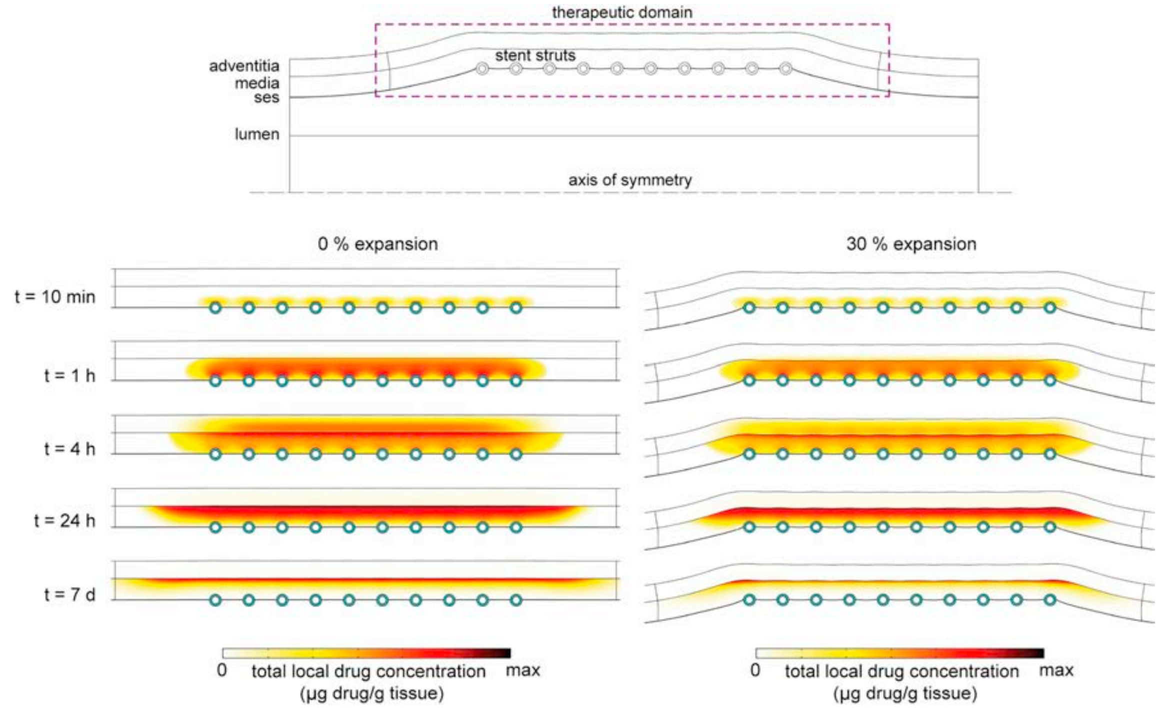

Fig. 7. Spatial variation of sirolimus at five different time points (t = 10 min, t = 1 h, t = 4 h, t = 24 h and t = 7 days) for the 0% (left) and 30% (right) expansion cases. For each time point the same colour scale is used for the 0% and 30% expansion cases. The maximum values of total local concentration of sirolimus chosen for each time point are presented as μg drug per g of tissue and they are the following: at t = 10 min, max = 2722.67 μg drug/g tissue; at t = 1 h, max = 1102.44 μg drug/g tissue; at t = 4 h, max = 795.74 μg drug/g tissue; at t = 24 h, max = 283.79 μg drug/g tissue and; at t = 7 d, max = 89.76 μg drug/g tissue. A comparison between spatial distribution in the tissue of sirolimus and paclitaxel for each expansion case and the corresponding tables with the maximum values at each time point may be found in the supplementary material.

Core™ i7-4770 CPU @ 3.40 GHz processor is about 6 h.

3. Results and discussion

In what follows, we will consider results related to five different cases: (i) uncoupled (ii) 0% expansion (iii) 10% expansion (iv) 20% expansion and (v) 30% expansion, as summarised in Table 4. In each case, the initial drug loading in the stent coating is fixed to 150 μg. In the *uncoupled* case, we consider a straight unpressurised arterial geometry: this is essentially an extension of the model of Bozsak et al. (2014) that now includes the adventitia layer. In the *0 % expansion model* the artery is now pressurised, causing a reduction in thickness of the arterial tissue, but overexpansion of the vessel caused by the stent is not considered. The remaining cases simulate a pressurised artery as well as a further deformation over the stented portion due to expansion of the stent. With the exception of case (i), all of our simulations result in changes to drug transport parameters as outlined in Section 2.

In order to compare results between the different cases, we will consider the temporal profiles of drug content and spatial profiles of local drug concentration in tissue. The total drug content in each layer of the tissue (presented as μg drug per g of tissue) at any instant is calculated as (Tzafriri et al., 2012; McKittrick et al., 2019):

$$DC_i(t) = \frac{MW_{drug}}{V_i \rho_i} \int_{V_i} (c_i + b_i) dV_i, \tag{28}$$

where V_i is the volume of layer i, that falls within the therapeutic domain considering $a < z < b$, with the origin of the computational geometry placed between the two central struts and with $a = -7.5w_s$ and $b = 7.5w_s$, where w_s is the interstrut distance (see Fig. 3); MW_{drug} is the molecular weight of the drug (sirolimus or paclitaxel) and; ρ_i is the density of wet arterial layer tissue. In the absence of experimental data on a layer-specific basis, we assume a constant density across the three arterial wall layers (see Table 2). Moreover, since binding site saturation has been linked with efficacy (Tzafriri et al., 2012; McKittrick et al., 2019) we further calculate the % of binding sites that are saturated as a function of time:

$$Binding\ sites\ \%\ saturation(t) = \frac{100}{V_i b_{max}} \int_{V_i} b_i \, dV_i. \tag{29}$$

Note that in this model, binding is only considered in the media layer, therefore the % saturation in the SES and in the adventitia will be zero.

In Fig. 4 we plot temporal profiles of drug content (DC) of two drugs, sirolimus or paclitaxel, within each layer of the arterial wall for cases (i)-(v). The plots show that, in the media and the adventitia, the peak DC decreases with stent expansion, however in the SES, the peak DC increases with the level of expansion. The time that the peak DC occurs increases sequentially moving from the SES to the adventitia and there is a short delay before drug enters the adventitia, consistent with the time taken for drug to traverse the media. Similar trends are observed between sirolimus and paclitaxel, although the values of DC differ as a result of drug-specific binding and transport parameters. Interestingly, the DC of sirolimus is higher than paclitaxel in the SES and media, but lower in the adventitia.

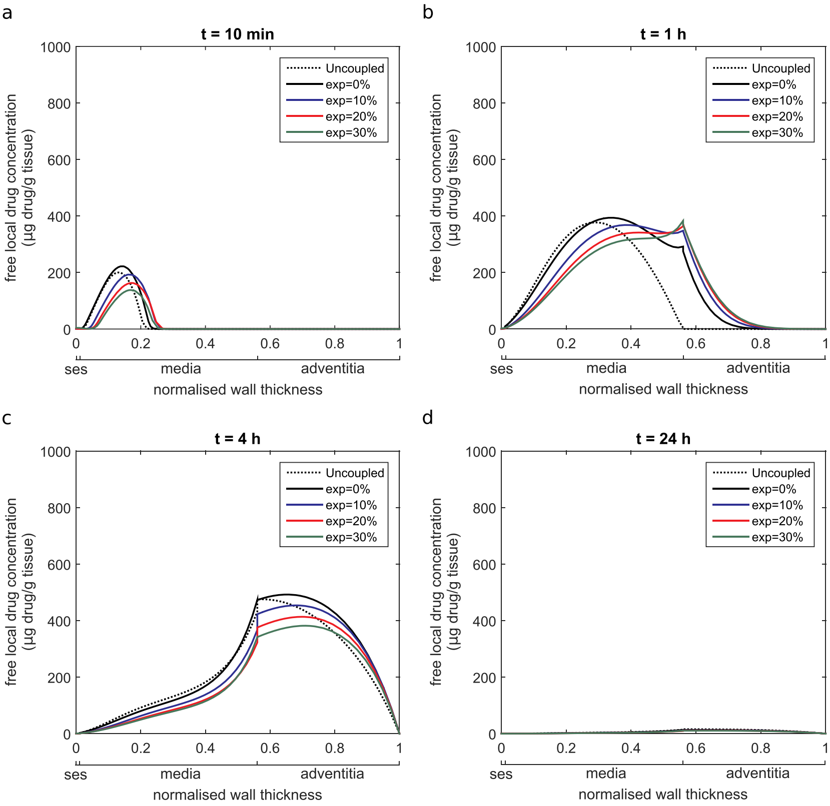

Fig. 8. Spatially varying profiles of free local concentration of sirolimus in the tissue (presented as μg drug per g of tissue) at 10 min (a), 1 h (b), 4 h (c) and 1 day (d) after stent implantation. The results are shown for the uncoupled model and for luminal diameter expansions of $0 - 30\%$ for the coupled model in a radial section between the middle struts.

In Fig. 5 we separate-out free DC from bound DC in the media for each drug. We observe that, for each drug, the peak free DC decreases with level of expansion while there is a negligible effect on peak bound DC. The implication is that expansion has a more pronounced effect on media free drug concentrations. High levels of binding site saturation are achieved for both sirolimus (≈ 70%) and paclitaxel (≈ 75–80%) rapidly, before a steady decline in saturation levels with time. The decline is more rapid for paclitaxel. Figs. 4–5 demonstrate that the effect of stent expansion on drug transport in the arterial wall is dependent not only on the specific layer in question, but also on the particular drug. Generally speaking, the effect of expansion is more prominent in the case of paclitaxel, particularly so in the adventitia layer of the arterial wall.

While DC provides a useful gross measure to effect comparisons, it is also important to consider the impact of local drug concentrations, which are linked to the biological effect of the drug, in order to assess whether drug concentrations locally are at therapeutic (and not toxic) levels. The study of local drug concentrations is also relevant for the design of effective drug delivery modalities (Hwang et al., 2001). In Fig. 6 we display spatially-varying profiles of total (free plus bound) local sirolimus concentration in the arterial wall, calculated as $(c_i + b_i)\frac{MW_{drug}}{\rho_i}$, at four different times across a radial section between the middle struts (i.e. between the 5th and 6th struts). The greatest differences between the four cases are observed at early times, where the peak sirolimus local concentration decreases with level of expansion. When the drug reaches the media/adventitia boundary, there is a sharp jump in the spatial profiles resulting from the contrast in material properties between the layers, described through the Kedem-Katchalsky equations. As time progresses, the higher drug retention in the media layer is evident compared with the adventitia. Our model also enables us to generate 2D plots of local drug concentration.

In Fig. 7 we show the spatial distribution of the total local concentration of sirolimus in the therapeutic domain at various time points across 7 days for the 0% and 30% expansion cases. The five time points after stent implantation shown are: t = 10 min, t = 1 h, t = 4 h, t = 24 h and t = 7 days. We observe that at early times the concentration is higher close to the stent struts and relatively lower close to the lumen between struts. After 1 h of the stent implantation, the plots show the drug progression through the media layer with time and after 4 h the concentration distribution pattern in the arterial wall is more homogeneous. After 1 day, the concentration level of drug in the tissue has already dropped approximately by an order of magnitude in the media and is almost 40 times lower in the adventitia compared to the maximum concentration reached in this layer. After a week, the concentration level in the media is approximately 20 times lower than the maximum concentration value. In general, similar trends are observed for both cases of expansion, but with lower levels of concentration when expansion increases. A comparison between the spatial distribution in the tissue of sirolimus and paclitaxel for each expansion case and the corresponding tables with the maximum values at each time point may be found in the supplementary material.

In Figs. 8–10 we separate-out the free and bound local sirolimus concentration. From these plots we deduce that, in the early stages, the

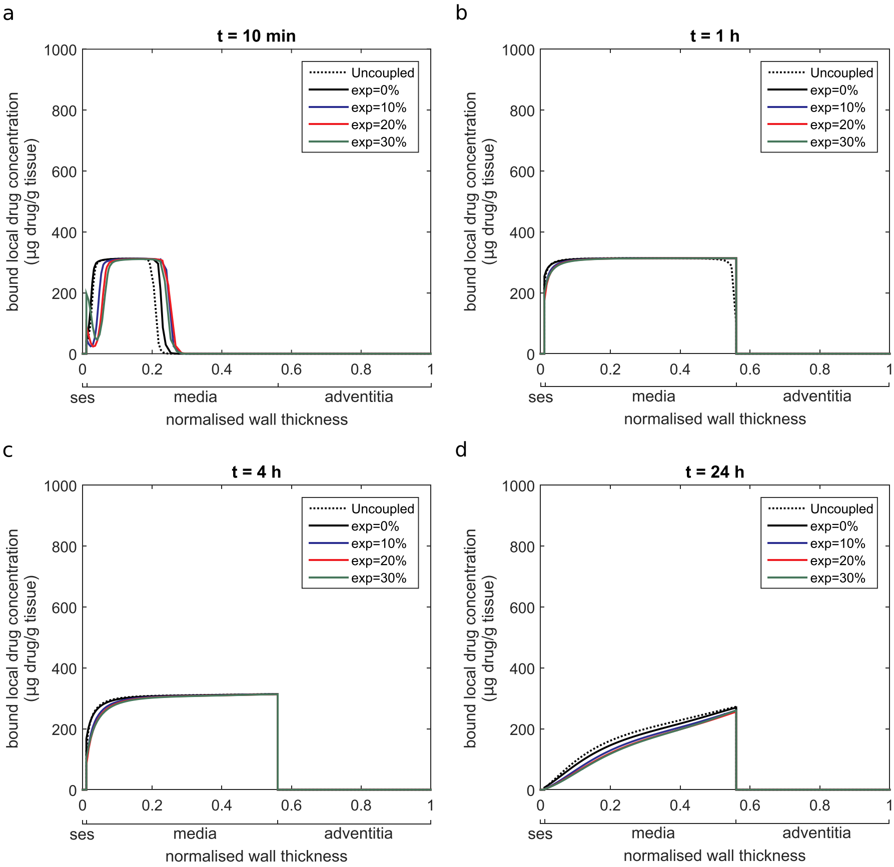

Fig. 9. Spatially varying profiles of local bound concentration of sirolimus in the tissue at 10 min (a), 1 h (b), 4 h (c) and 1 day (d) after stent implantation. The results are shown for the uncoupled model and for luminal diameter expansions of $0-30\%$ for the coupled model in a radial section between the middle struts.

total local drug concentration profiles are characterized by rapid infiltration of drug into the SES followed by rapid diffusion into the media (these early profiles are governed by the free local drug concentration). However, as time progresses, the total local drug concentration profiles are dominated by the bound local drug concentration. There is little difference between binding site saturation levels as we increase level of expansion. However, at early times, expansion has the effect of leading to binding site saturation deeper into the wall.

In order to probe this further, in Figs. 11 and 12 we present plots showing how the radial and longitudinal diffusion coefficients (D_r and D_z, respectively), magnitude of the radial component of flow (u_r) and radial Peclet number ($Pe_r = u_r\delta_m/D_r$) vary across the media layer for the various levels of expansion considered. Fig. 11a confirms that as we increase the level of expansion, we decrease the radial diffusion coefficient, with differences greater closer to the intima. The dependence of the longitudinal diffusion coefficient on expansion is more complex, increasing with expansion close to the intima before decreasing with expansion close to the adventitia as can be seen in Fig. 11b. The level of expansion also has an influence on the resulting flow-field in the tissue (Fig. 12a): higher radial flow speed is observed with increasing levels of expansion. When we consider the radial Peclet number (Fig. 12b) we observe a similar profile to that of radial flow speed (Fig. 12a), confirming that transport across the wall, in all cases, is dominated by advection. Therefore, despite the relatively modest reduction in radial diffusion coefficient with expansion, it is primarily advection driven by the pressure gradient across the wall that governs radial drug transport. These findings support the relatively modest variation in temporal and spatial profiles of content of drug in Figs. 4–10. Importantly, we note that given the low value of the radial Peclet number (of order 1), a relatively small change to the flow field could tip the balance back in favour of diffusion, and in this case the observed changes in drug diffusion as a result of mechanical expansion will be of more significance. Similar trends are observed for paclitaxel, but with greater differences between cases (i)-(v). The corresponding plots for paclitaxel may be found in the supplementary material.

4. Limitations

We would like to emphasize that there are a number of limitations in this work, as we now discuss. Regarding the geometry of the model, a 2D axisymmetric geometry corresponding to an idealised representation of a straight segment of a healthy coronary artery has been considered in this study. This could be improved using more realistic geometries of arteries (curved segments, bifurcations or directly 3D patient-specific geometries obtained from medical images) and devices (i.e. complex geometries of commercial DES). However, such models considerably increase the computational cost of the simulations and detract from the key objective which was to study the effect of coupling mechanics-drug transport. Moreover, there is growing evidence that disease composition may well have an impact on drug release and subsequent tissue

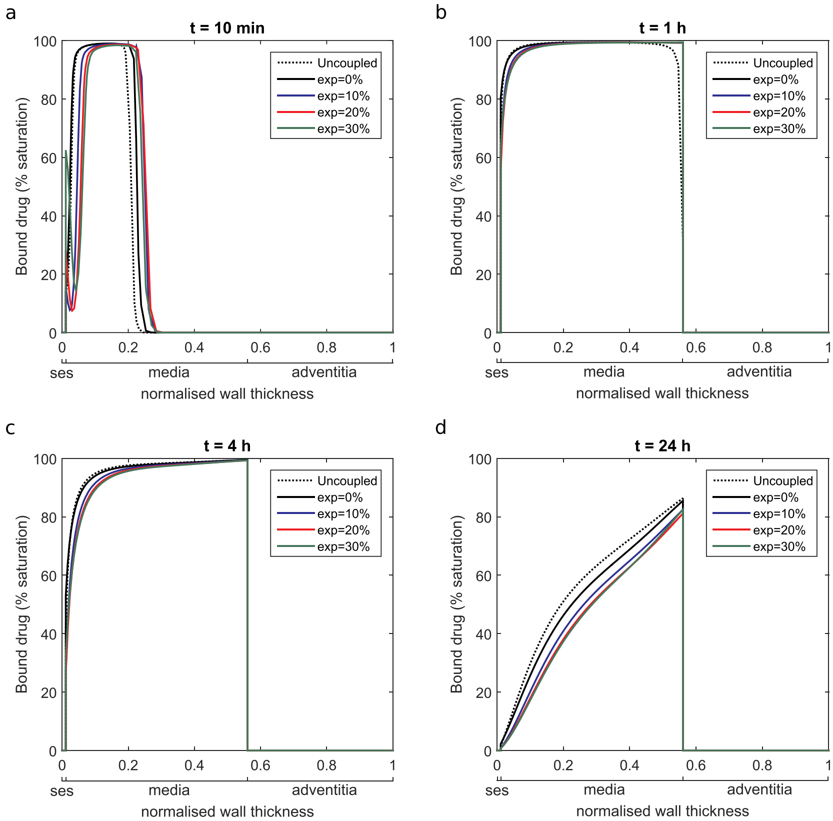

Fig. 10. Spatially varying profiles of binding site % saturation in the tissue at 10 min (a), 1 h (b), 4 h (c) and 1 day (d) after stent implantation, calculated as $\frac{b_i}{b_{max}} \cdot 100$. The results are shown for the uncoupled model and for luminal diameter expansions of $0 - 30\%$ for the coupled model in a radial section between the middle struts.

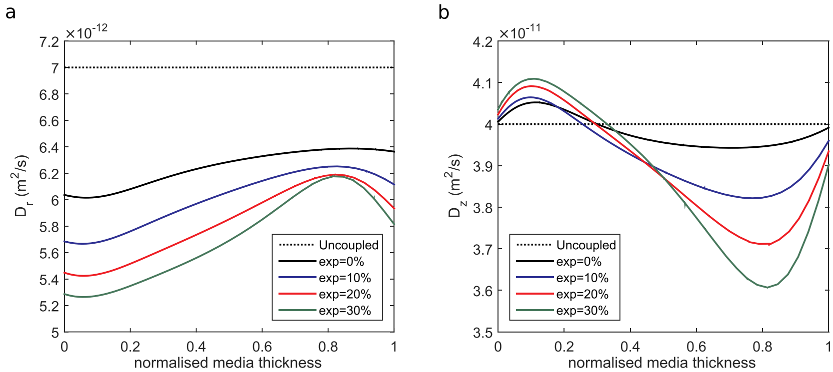

Fig. 11. Radial (a) and longitudinal (b) diffusion coefficients variation of sirolimus in the media layer of the arterial wall. The results are shown for the uncoupled model and for luminal diameter expansions of $0 - 30\%$ for the coupled model. In both subfigures the radial line is drawn between the middle struts.

distribution (McKittrick et al., 2016), however in line with most of the computational models of drug transport in arteries published in the literature, we neglect the existence of atheroma plaque in this work.

The large number of parameters involved in the model were obtained from existing experimental data or other computational models. These data are taken from different species and may not be representative of the corresponding parameters in human tissue. Moreover, there is a lack of transport and reaction parameters for the adventitia layer, therefore these parameters had to be estimated.

Our proposed description of the blood flow (steady Newtonian with inlet Poiseuille velocity profile and outlet fixed pressure boundary conditions) aligns with the current state of the art model which couples luminal flow with drug release from stents and tissue binding (Bozsak et al., 2014), as well as many other groups in the field (Mongrain et al.,

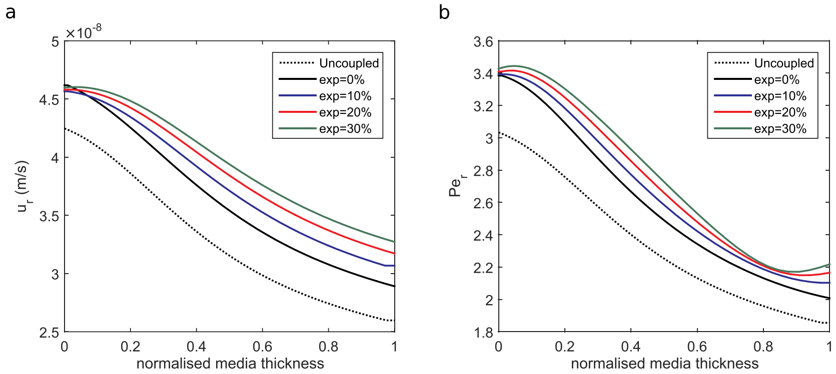

Fig. 12. (a) Radial component of flow in the media. (b) Radial Peclet number variation for sirolimus in the media layer of the arterial wall. The results are shown for the uncoupled model and for luminal diameter expansions of $0 - 30\%$ for the coupled model. In both subfigures the radial line is drawn between the middle struts.

2005, 2007; Vairo et al., 2010; Bozsak et al., 2014). Whilst we accept that in reality we will have pulsatile flow, we point out that the focus of this study is on drug distribution in arterial tissue, rather than on accurately reproducing flow patterns in the lumen. We cite evidence from the literature which shows that ‘pulsatility contributes minimally to drug deposition for a well-apposed strut’ (O’Brien et al., 2013). Moreover, the pulsatile flow is characterized by much smaller temporal scales than the temporal scale of the advection-diffusion-reaction processes which govern drug transport within the arterial wall, therefore, the time dependence mainly due to the cardiac pulsatile flow was finally neglected in this work.

In terms of modelling drug transport within the stent coating, in line with the vast majority of models in the literature, a simple diffusion model is considered in this work. However, depending on the particular stent, drug and coating under consideration, more complex nonlinear models that accounts for the combined effects of diffusion, dissolution and solubility in the polymer coating (McGinty and Pontrelli, 2015) may be required in order to describe drug release from the stent. In the literature we can find a wide range for diffusion coefficients of the drug in the polymeric coating of the stent, representing the range from fast-to slow-release kinetics. These values range from 10^{-13} to 10^{-17} $m^2 \cdot s^{-1}$ (Bozsak et al., 2014). Moreover, there are a large number of stents on the market ranging from durable polymer coated stents, to polymer free and biodegradable stents and the release kinetics can vary considerably between these different types. In this work, we assume a typical fast-release stent taking a diffusion coefficient of 10^{-13} $m^2 \cdot s^{-1}$ in all simulations.

In terms of modelling drug transport within the arterial wall, a single phase nonlinear saturable reversible binding model is taken into account. Therefore, in this model we do not take into account the effect of binding as two separate phases (drug bound to specific receptors and non-specific general extracellular matrix sites), the benefits and drawbacks of which are discussed in (McGinty and Pontrelli, 2016). In order to simulate stent deployment, vessel pressurization and displacement have been performed in a single computation step. A more realistic and challenging approach would be to perform this in two separate stages.

Finally, we appreciate the importance of validating computational models such as ours against experimental data. However, to the best of our knowledge, there is a lack of experimental tests in the available literature that relate the level of deformation due to stenting, and the consequent modification of material properties of the tissue, with the drug content within the arterial wall. We would hope that this work would inspire the generation of suitable experimental data to validate the work.

5. Conclusions

In this paper, we have provided a comprehensive study of the effect of stent mechanical expansion on the drug transport properties of a three-layer arterial wall described as an anisotropic, hyperelastic material. We have established relationships between mechanical force generated through device expansion and alteration in drug diffusion coefficients within the arterial wall and performed simulations to quantify the impact of such alterations on spatio-temporal drug release and tissue uptake. Our findings demonstrate that mechanical expansion can have an influence on the effective diffusion coefficients of drugs in arterial tissue, with the overall influence on drug transport through the arterial wall dependent on the radial Peclet number that is derived from these diffusion coefficients. Since current computational models typically make use of drug diffusion coefficients that have been derived from static tissue experiments (i.e. not subjected to mechanical expansion), these models are likely to be under- or over-estimating drug transport and retention in arterial tissue. Finally, we remark that our findings may also be of importance to other forms of localised arterial drug delivery, such as through drug coated balloons (DCBs). The key difference with DCBs would appear to be a time-varying dependence on drug transport parameters, coinciding with inflation and deflation of the balloon.

Declaration of competing interest

The authors declare that they have no known competing financial interests or personal relationships that could have appeared to influence the work reported in this paper.

CRediT authorship contribution statement

Javier Escuer: Conceptualization, Methodology, Formal analysis, Writing - original draft, Visualization. **Martina Cebollero:** Methodology, Formal analysis. **Estefanía Peña:** Conceptualization, Methodology, Resources, Writing - original draft, Supervision, Project administration, Funding acquisition. **Sean McGinty:** Conceptualization, Methodology, Writing - original draft, Supervision. **Miguel A. Martínez:** Conceptualization, Methodology, Resources, Writing - original draft, Supervision, Project administration, Funding acquisition.

Acknowledgments

Financial support for this research was provided by the Spanish Ministry of Economy and Competitiveness through research project DPI2016-76630-C2-1-R and grant number BES-2014-069737; the Department of Industry and Innovation (Government of Aragón) through the research group Grant T24-17R (Fondo Social Europeo) and research project LMP121-18 and; the Instituto de Salud Carlos III (ISCIII) through the CIBER initiative.

Appendix A. Supplementary data

Supplementary data to this article can be found online at https://doi.org/10.1016/j.jmbbm.2019.103610.

References

Ai, L., Vafai, K., 2006. A coupling model for macromolecule transport in a stenosed arterial wall. Int. J. Heat Mass Transf. 49 (9–10), 1568–1591.

Alfonso, F., Byrne, R.A., Rivero, F., Kastrati, A., 2014. Current treatment of in-stent restenosis. J. Am. Coll. Cardiol. 63 (24), 2659–2673.

Bozsak, F., Chomaz, J.M., Barakat, A.I., 2014. Modeling the transport of drugs eluted from stents: physical phenomena driving drug distribution in the arterial wall. Biomechanics Model. Mechanobiol. 13 (2), 327–347.

Bozsak, F., Gonzalez-Rodriguez, D., Sternberger, Z., Belitz, P., Bewley, T., Chomaz, J.M., et al., 2015. Optimization of drug delivery by drug-eluting stents. PLoS One 10 (6), e0130182.

Buccheri, D., Piraino, D., Andolina, G., Cortese, B., 2016. Understanding and managing in-stent restenosis: a review of clinical data, from pathogenesis to treatment. J. Thorac. Dis. 8 (10), E1150.

Byrne, R.A., Joner, M., Kastrati, A., 2015. Stent thrombosis and restenosis: what have we learned and where are we going? The Andreas Grüntzig Lecture ESC 2014. Eur. Heart J. 36 (47), 3320–3331.

Carew, T.E., Vaishnav, R.N., Patel, D.J., 1968. Compressibility of the arterial wall. Circ. Res. 23 (1), 61–68.

Conway, C., Sharif, F., McGarry, J., McHugh, P., 2012. A computational test-bed to assess coronary stent implantation mechanics using a population-specific approach. Cardiovasc. Eng. Technol. 3 (4), 374–387.

Conway, C., McGarry, J., McHugh, P., 2014. Modelling of atherosclerotic plaque for use in a computational test-bed for stent angioplasty. Ann. Biomed. Eng. 42 (12), 2425–2439.

Creel, C.J., Lovich, M.A., Edelman, E.R., 2000. Arterial paclitaxel distribution and deposition. Circ. Res. 86 (8), 879–884.

Curry, F.R.E., 1984. Mechanics and thermodynamics of transcapillary exchante. Handb. Physiol. 309–374.

Cussler, E.L., 2009. Diffusion: Mass Transfer in Fluid Systems. Cambridge university press.

Cutrì, E., Zunino, P., Morlacchi, S., Chiastra, C., Migliavacca, F., 2013. Drug delivery patterns for different stenting techniques in coronary bifurcations: a comparative computational study. Biomechanics Model. Mechanobiol. 12 (4), 657–669.

Denny, W.J., Walsh, M.T., 2014a. Numerical modelling of mass transport in an arterial wall with anisotropic transport properties. J. Biomech. 47 (1), 168–177.

Denny, W.J., Walsh, M.T., 2014b. Numerical modelling of the physical factors that affect mass transport in the vasculature at early time periods. Med. Eng. Phys. 36 (3), 308–317.

Dodge Jr., J.T., Brown, B.G., Bolson, E.L., Dodge, H.T., 1992. Lumen diameter of normal human coronary arteries. Influence of age, sex, anatomic variation, and left ventricular hypertrophy or dilation. Circulation 86 (1), 232–246.

d'Errico, M., Sammarco, P., Vairo, G., 2015. Analytical modeling of drug dynamics induced by eluting stents in the coronary multi-layered curved domain. Math. Biosci. 267, 79–96.

Feenstra, P.H., Taylor, C.A., 2009. Drug transport in artery walls: a sequential porohyperelastic-transport approach. Comput. Methods Biomech. Biomed. Eng. 12 (3), 263–276.

Ferreira, J.A., Gonçalves, L., Naghipoor, J., de Oliveira, P., Rabczuk, T., 2017. The influence of atherosclerotic plaques on the pharmacokinetics of a drug eluted from bioabsorbable stents. Math. Biosci. 283, 71–83.

Ferreira, J.A., Gonçalves, L., Naghipoor, J., de Oliveira, P., Rabczuk, T., 2018. The effect of plaque eccentricity on blood hemodynamics and drug release in a stented artery. Med. Eng. Phys. 60, 47–60.

Formaggia, L., Quarteroni, A., Veneziani, A., 2010. In: Formaggia, L., Quarteroni, A., Veneziani, A. (Eds.), Cardiovascular Mathematics: Modeling and Simulation of the Circulatory System, vol. 1. Springer Science & Business Media.

García, A., Peña, E., Martínez, M., 2012. Influence of geometrical parameters on radial force during self-expanding stent deployment. Application for a variable radial stiffness stent. J. Mech. Behav. Biomed. Mater. 10, 166–175.

Gasser, T.C., Ogden, R.W., Holzapfel, G.A., 2006. Hyperelastic modelling of arterial layers with distributed collagen fibre orientations. J. R. Soc. Interface 3 (6), 15–35.

Gundiah, N., Ratcliffe, M.B., Pruitt, L.A., 2009. The biomechanics of arterial elastin. J. Mech. Behav. Biomed. Mater. 2 (3), 288–296.

Holzapfel, G.A., Gasser, T.C., Ogden, R.W., 2000. A new constitutive framework for arterial wall mechanics and a comparative study of material models. J. Elast. Phys. Sci. Solids 61 (1–3), 1–48.

Holzapfel, G.A., Stadler, M., Gasser, T.C., 2005a. Changes in the mechanical environment of stenotic arteries during interaction with stents: computational assessment of parametric stent designs. J. Biomech. Eng. 127 (1), 166–180.

Holzapfel, G.A., Sommer, G., Gasser, C.T., Regitnig, P., 2005b. Determination of layer-specific mechanical properties of human coronary arteries with nonatherosclerotic intimal thickening and related constitutive modeling. Am. J. Physiol. Heart Circ. Physiol. 289 (5), H2048–H2058.

Hopkins, C., McHugh, P., McGarry, J., 2010. Computational investigation of the delamination of polymer coatings during stent deployment. Ann. Biomed. Eng. 38 (7), 2263–2273.

Hwang, C.W., Edelman, E.R., 2002. Arterial ultrastructure influences transport of locally delivered drugs. Circ. Res. 90 (7), 826–832.

Hwang, C.W., Wu, D., Edelman, E.R., 2001. Physiological transport forces govern drug distribution for stent-based delivery. Circulation 104 (5), 600–605.

Karner, G., Perktold, K., Zehentner, H.P., 2001. Computational modeling of macromolecule transport in the arterial wall. Comput. Methods Biomech. Biomed. Eng. 4 (6), 491–504.

Kedem, O., Katchalsky, A., 1958. Thermodynamic analysis of the permeability of biological membranes to non-electrolytes. Biochim. Biophys. Acta 27, 229–246.

Kiousis, D.E., Gasser, T.C., Holzapfel, G.A., 2007. A numerical model to study the interaction of vascular stents with human atherosclerotic lesions. Ann. Biomed. Eng. 35 (11), 1857–1869.

Kolachalama, V.B., Pacetti, S.D., Franses, J.W., Stankus, J.J., Zhao, H.Q., Shazly, T., et al., 2013. Mechanisms of tissue uptake and retention in zotarolimus-coated balloon therapy. Circulation 127 (20), 2047–2055.

Lally, C., Dolan, F., Prendergast, P., 2005. Cardiovascular stent design and vessel stresses: a finite element analysis. J. Biomech. 38 (8), 1574–1581.

Levin, A.D., Vukmirovic, N., Hwang, C.W., Edelman, E.R., 2004. Specific binding to intracellular proteins determines arterial transport properties for rapamycin and paclitaxel. Proc. Natl. Acad. Sci. U. S. A. 101 (25), 9463–9467.

Levitt, D.G., 1975. General continuum analysis of transport through pores. I. Proof of Onsager's reciprocity postulate for uniform pore. Biophys. J. 15 (6), 533–551.

Lillie, M., Shadwick, R., Gosline, J., 2010. Mechanical anisotropy of inflated elastic tissue from the pig aorta. J. Biomech. 43 (11), 2070–2078.

Martin, D.M., Boyle, F.J., 2011. Drug-eluting stents for coronary artery disease: a review. Med. Eng. Phys. 33 (2), 148–163.

McGarry, J., O'Donnell, B., McHugh, P., McGarry, J., 2004. Analysis of the mechanical performance of a cardiovascular stent design based on micromechanical modelling. Comput. Mater. Sci. 31 (3–4), 421–438.

McGinty, S., 2014. A decade of modelling drug release from arterial stents. Math. Biosci. 257, 80–90.

McGinty, S., Pontrelli, G., 2015. A general model of coupled drug release and tissue absorption for drug delivery devices. J. Control. Release 217, 327–336.

McGinty, S., Pontrelli, G., 2016. On the role of specific drug binding in modelling arterial eluting stents. J. Math. Chem. 54 (4), 967–976.

McGinty, S., McKee, S., Wadsworth, R.M., McCormick, C., 2010. Modelling drug-eluting stents. Math. Med. Biol.: J. IMA 28 (1), 1–29.

McGinty, S., McKee, S., McCormick, C., Wheel, M., 2015. Release mechanism and parameter estimation in drug-eluting stent systems: analytical solutions of drug release and tissue transport. Math. Med. Biol.: J. IMA 32 (2), 163–186.

McKittrick, C., Kennedy, S., Oldroyd, K., McGinty, S., McCormick, C., 2016. Modelling the impact of atherosclerosis on drug release and distribution from coronary stents. Ann. Biomed. Eng. 44 (2), 477–487.

McKittrick, C., McKee, S., Kennedy, S., Oldroyd, K., Wheel, M., Pontrelli, G., et al., 2019. Combining mathematical modelling with in vitro experiments to predict in vivo drug-eluting stent performance. J. Control. Release 303, 151–161.

Meyer, G., Merval, R., Tedgui, A., 1996. Effects of pressure-induced stretch and convection on low-density lipoprotein and albumin uptake in the rabbit aortic wall. Circ. Res. 79 (3), 532–540.

Migliavacca, F., Petrini, L., Montanari, V., Quagliana, I., Auricchio, F., Dubini, G., 2005. A predictive study of the mechanical behaviour of coronary stents by computer modelling. Med. Eng. Phys. 27 (1), 13–18.

Migliavacca, F., Gervaso, F., Prosi, M., Zunino, P., Minisini, S., Formaggia, L., et al., 2007. Expansion and drug elution model of a coronary stent. Comput. Methods Biomech. Biomed. Eng. 10 (1), 63–73.

Mongrain, R., Leask, R., Brunette, J., Faik, I., Bulman-Feleming, N., Nguyen, T., 2005. Numerical modeling of coronary drug eluting stents. Stud. Health Technol. Inform. 113, 443–458.

Mongrain, R., Faik, I., Leask, R.L., Rodés-Cabau, J., Larose, É., Bertrand, O.F., 2007. Effects of diffusion coefficients and struts apposition using numerical simulations for drug eluting coronary stents. J. Biomech. Eng. 129 (5), 733–742.

Naghavi, M., Abajobir, A.A., Abbafati, C., Abbas, K.M., Abd-Allah, F., Abera, S.F., et al., 2017. Global, regional, and national age-sex specific mortality for 264 causes of death, 1980–2016: a systematic analysis for the Global Burden of Disease Study 2016. The Lancet 390 (10100), 1151–1210.

O'Brien, C.C., Kolachalama, V.B., Barber, T.J., Simmons, A., Edelman, E.R., 2013. Impact of flow pulsatility on arterial drug distribution in stent-based therapy. J. Control. Release 168 (2), 115–124.

O'Connell, B.M., Walsh, M.T., 2010. Demonstrating the influence of compression on artery wall mass transport. Ann. Biomed. Eng. 38 (4), 1354–1366.

O'Connell, B.M., Walsh, M.T., 2012. Arterial mass transport behaviour of drugs from drug eluting stents. In: Biomedical Science, Engineering and Technology. IntechOpen.

O'Connell, B.M., McGloughlin, T.M., Walsh, M.T., 2010. Factors that affect mass transport from drug eluting stents into the artery wall. Biomed. Eng. Online 9 (1), 15.

Pontrelli, G., de Monte, F., 2007. Mass diffusion through two-layer porous media: an application to the drug-eluting stent. Int. J. Heat Mass Transf. 50 (17–18), 3658–3669.

Pontrelli, G., de Monte, F., 2010. A multi-layer porous wall model for coronary drug-eluting stents. Int. J. Heat Mass Transf. 53 (19–20), 3629–3637.

Schiavone, A., Zhao, L., Abdel-Wahab, A.A., 2014. Effects of material, coating, design and plaque composition on stent deployment inside a stenotic artery-finite element simulation. Mater. Sci. Eng. C 42, 479–488.

Spencer, A., 1971. Part III. Theory of invariants. Continuum Phys. 1, 239–353.

Tzafriri, A.R., Levin, A.D., Edelman, E.R., 2009. Diffusion-limited binding explains binary dose response for local arterial and tumour drug delivery. Cell Prolif 42 (3), 348–363.

Tzafriri, A.R., Groothuis, A., Price, G.S., Edelman, E.R., 2012. Stent elution rate determines drug deposition and receptor-mediated effects. J. Control. Release 161 (3), 918–926.

Tzafriri, A.R., Garcia-Polite, F., Li, X., Keating, J., Balaguer, J.M., Zani, B., et al., 2018. Defining drug and target protein distributions after stent-based drug release: durable versus deployable coatings. J. Control. Release 274, 102–108.

Vairo, G., Cioffi, M., Cottone, R., Dubini, G., Migliavacca, F., 2010. Drug release from coronary eluting stents: a multidomain approach. J. Biomech. 43 (8), 1580–1589.

Zahedmanesh, H., Kelly, D.J., Lally, C., 2010. Simulation of a balloon expandable stent in a realistic coronary artery: determination of the optimum modelling strategy. J. Biomech. 43 (11), 2126–2132.

Zhu, X., Braatz, R.D., 2015. A mechanistic model for drug release in PLGA biodegradable stent coatings coupled with polymer degradation and erosion. J. Biomed. Mater. Res. A 103 (7), 2269–2279.

Zunino, P., 2004. Multidimensional pharmacokinetic models applied to the design of drug-eluting stents. Cardiovasc. Eng.: Int. J. 4 (2), 181–191.

Zunino, P., D'Angelo, C., Petrini, L., Vergara, C., Capelli, C., Migliavacca, F., 2009. Numerical simulation of drug eluting coronary stents: mechanics, fluid dynamics and drug release. Comput. Methods Appl. Mech. Eng. 198 (45–46), 3633–3644.

Supplementary Online Material for How Does Stent Expansion Alter Drug Transport Properties of the Arterial Wall?

Javier Escuer [a] Martina Cebollero [a] Estefanía Peña [a,b] Sean McGinty [c]
Miguel A. Martínez [a,b,*]

[a] *Aragón Institute for Engineering Research (I3A), University of Zaragoza, Spain*

[b] *Biomedical Research Networking Center in Bioengineering, Biomaterials and Nanomedicine (CIBER-BBN), Spain.*

[c] *Division of Biomedical Engineering, University of Glasgow, Glasgow, UK*

This document includes the following sections:

- S1. Supplemental figures
- S2. Supplemental tables

S1 Suplemental figures

The corresponding spatially varying profiles of total, free and bound local concentration of paclitaxel in the arterial wall at four different time points are shown in this section (Figs. S1-S4). Moreover, we show a comparison between the 2D spatial variation of sirolimus and paclitaxel at five time points after stent implantation for each expansion case (Figs. S5-S9). Finally, we present plots showing a comparison between sirolimus and paclitaxel of how the radial and longitudinal diffusion coefficients (D_r and D_z, respectively) and radial Peclet number vary across the media layer for the different levels of expansion considered (Figs. S10-S11).

[Fig. 1 about here.]

[Fig. 2 about here.]

---

[*] Corresponding author. Miguel A. Martínez. Mechanical Engineering Department. c/ María de Luna s/n 50018. Zaragoza. Spain. Tel.: +34 876555252; Fax: +34 976762578
Email address: `miguelam@unizar.es` (Miguel A. Martínez).

[Fig. 3 about here.]

[Fig. 4 about here.]

[Fig. 5 about here.]

[Fig. 6 about here.]

[Fig. 7 about here.]

[Fig. 8 about here.]

[Fig. 9 about here.]

[Fig. 10 about here.]

[Fig. 11 about here.]

S2 Suplemental tables

The maximum values of local concentrations in each layer at five different time points, presented as μg drug (sirolimus or paclitaxel) per g of tissue, for the uncoupled model and for each expansion case are shown in the following tables.

[Table 1 about here.]

[Table 2 about here.]

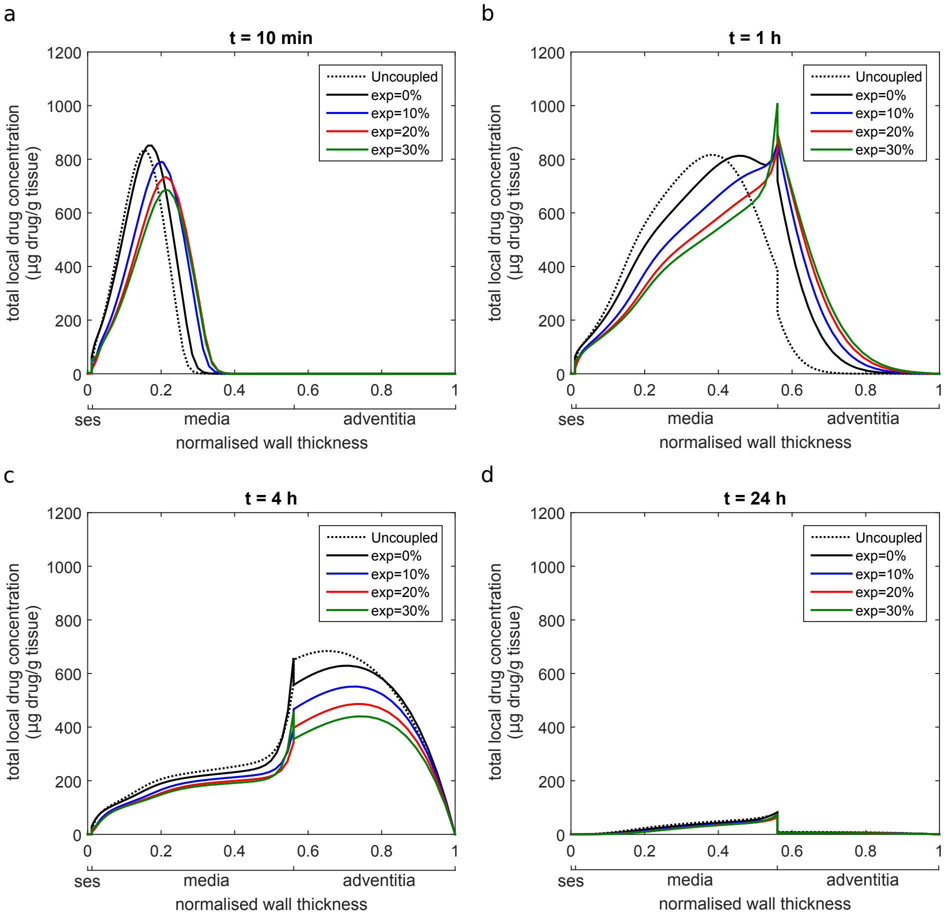

Fig. S1. Spatially varying profiles of total (free plus bound) local concentration of paclitaxel in the tissue (presented as μg drug per g of tissue) at 10 min (a), 1 hour (b), 4 hours (c) and 1 day (d) after stent implantation. The results are shown for the uncoupled model and for luminal diameter expansions of $0-30\%$ for the coupled model in a radial section between the middle struts.

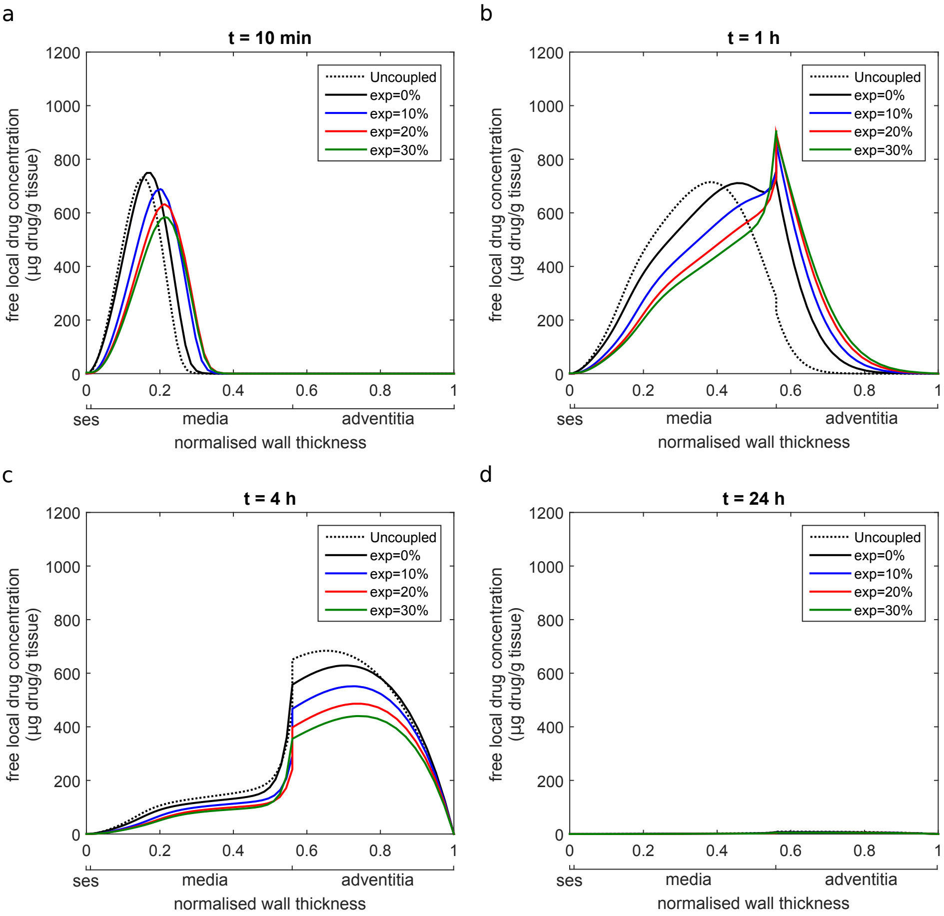

Fig. S2. Spatially varying profiles of free local concentration of paclitaxel in the tissue (presented as μg drug per g of tissue) at 10 min (a), 1 hour (b), 4 hours (c) and 1 day (d) after stent implantation. The results are shown for the uncoupled model and for luminal diameter expansions of $0 - 30\%$ for the coupled model in a radial section between the middle struts.

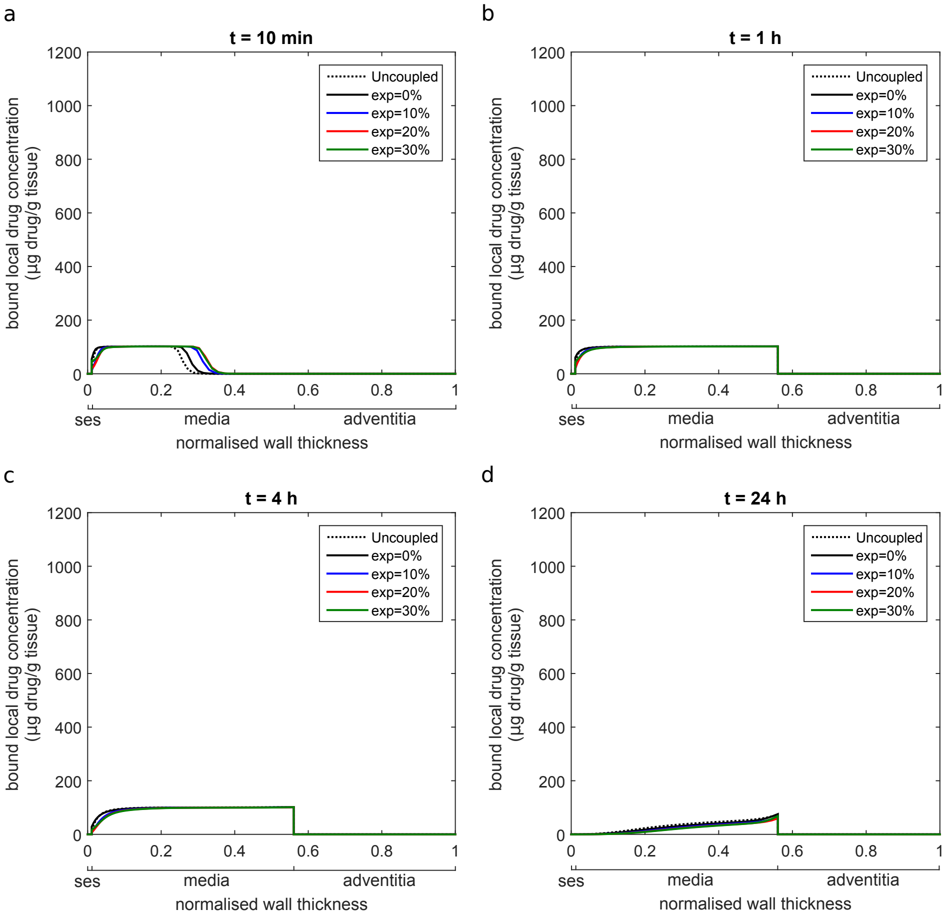

Fig. S3. Spatially varying profiles of bound local concentration of paclitaxel in the tissue (presented as μg drug per g of tissue) at 10 min (a), 1 hour (b), 4 hours (c) and 1 day (d) after stent implantation. The results are shown for the uncoupled model and for luminal diameter expansions of $0 - 30\%$ for the coupled model in a radial section between the middle struts.

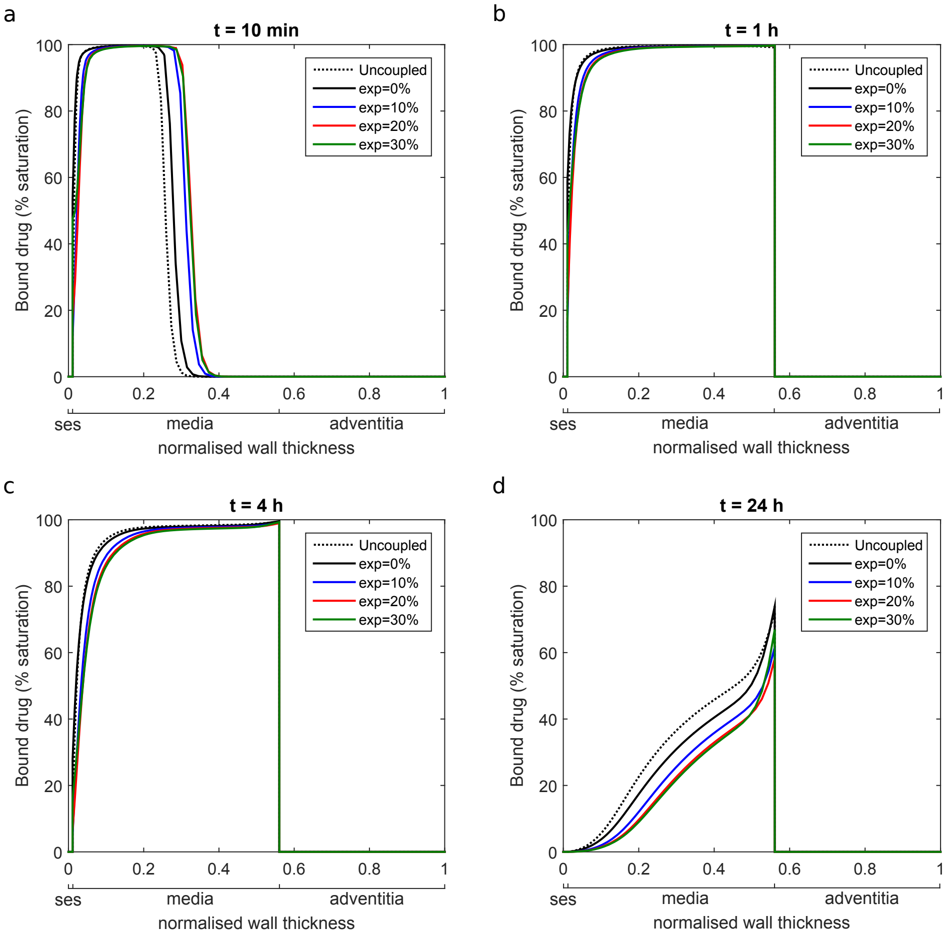

Fig. S4. Spatially varying profiles of binding sites % saturation in the tissue at 10 min (a), 1 hour (b), 4 hours (c) and 1 day (d) after stent implantation, calculated as $\frac{b_i}{b_{max}} \cdot 100$. The results are shown for the uncoupled model and for luminal diameter expansions of $0 - 30\%$ for the coupled model in a radial section between the middle struts.

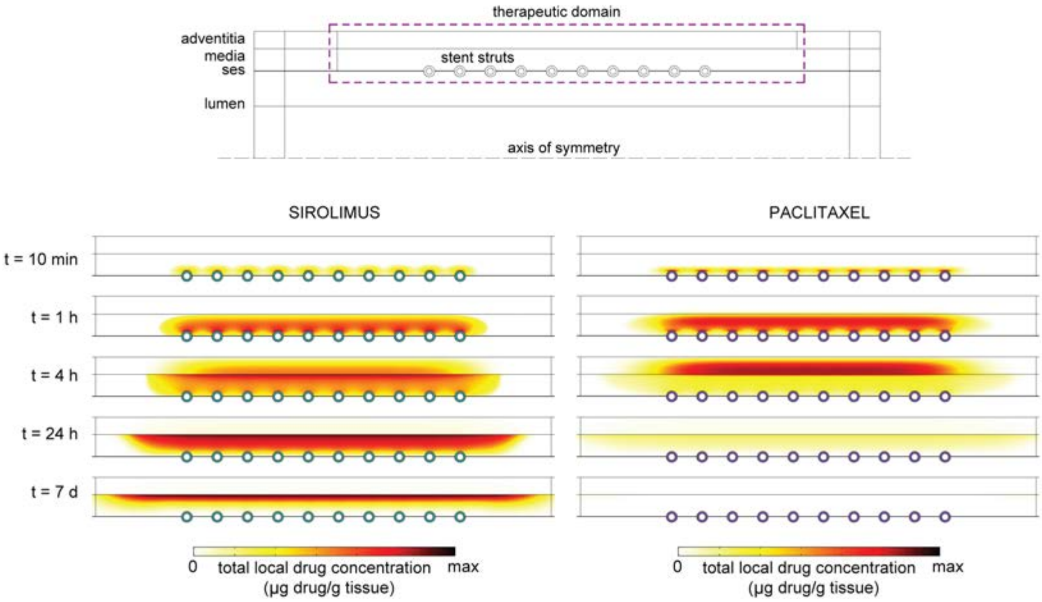

Fig. S5. Comparison between the spatial variation of sirolimus and paclitaxel at five different time points after stent implantation for the uncoupled model. The maximum values of total local drug concentration chosen for each time point are presented as μg drug per g of tissue and they are the following: at t = 10 min, max = 2722.67 μg drug/g tissue; at t = 1 h, max = 1102.44 μg drug/g tissue; at t = 4 h, max = 795.74 μg drug/g tissue; at t = 24 h, max = 283.79 μg drug/g tissue and; at t = 7 d, max = 89.76 μg drug/g tissue (see bold values in Tables S1-S2). Note that the 'max' value in color legend is the same for paclitaxel and siroliumus for the same time point.

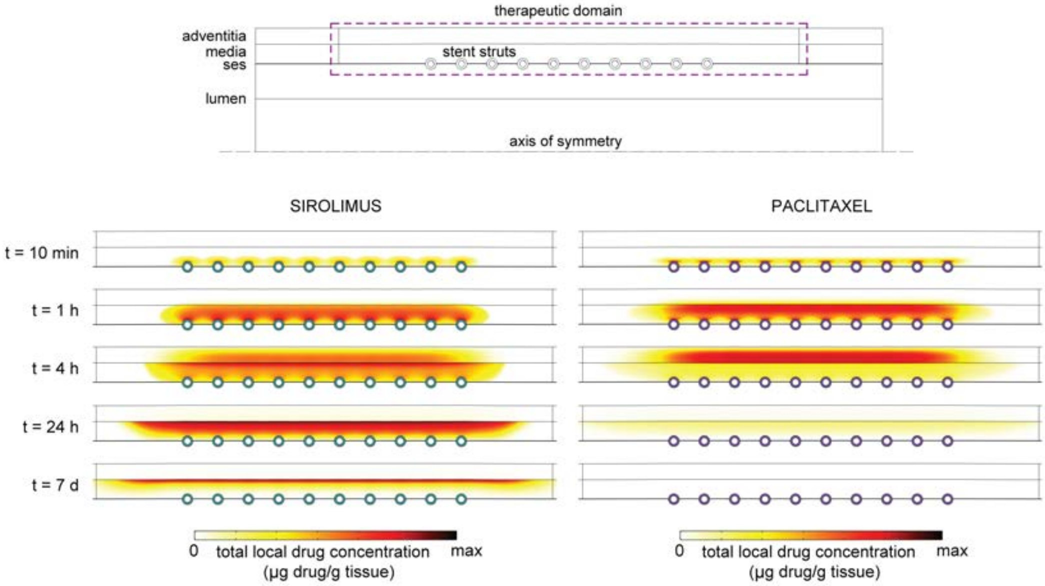

Fig. S6. Comparison between the spatial variation of sirolimus and paclitaxel at five different time points after stent implantation for the 0 % expansion case. The maximum values of total local drug concentration chosen for each time point are presented as μg drug per g of tissue and they are the following: at t = 10 min, max = 2722.67 μg drug/g tissue; at t = 1 h, max = 1102.44 μg drug/g tissue; at t = 4 h, max = 795.74 μg drug/g tissue; at t = 24 h, max = 283.79 μg drug/g tissue and; at t = 7 d, max = 89.76 μg drug/g tissue (see bold values in Tables S1-S2). Note that the 'max' value in color legend is the same for paclitaxel and siroliumus for the same time point.

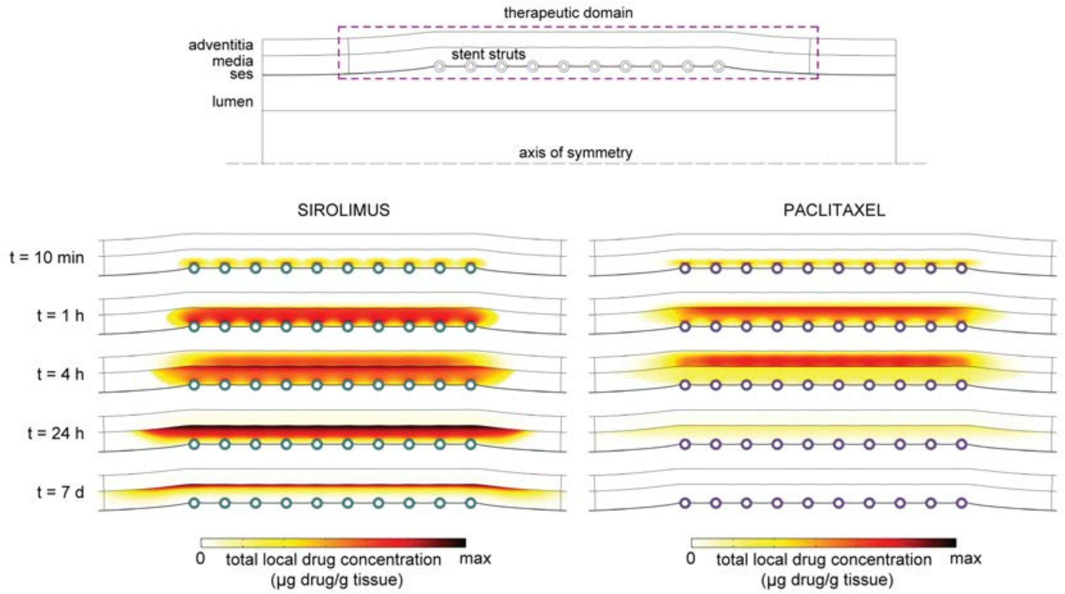

Fig. S7. Comparison between the spatial variation of sirolimus and paclitaxel at five different time points after stent implantation for the 10 % expansion case. The maximum values of total local drug concentration chosen for each time point are presented as μg drug per g of tissue and they are the following: at t = 10 min, max = 2722.67 μg drug/g tissue; at t = 1 h, max = 1102.44 μg drug/g tissue; at t = 4 h, max = 795.74 μg drug/g tissue; at t = 24 h, max = 283.79 μg drug/g tissue and; at t = 7 d, max = 89.76 μg drug/g tissue (see bold values in Tables S1-S2). Note that the 'max' value in color legend is the same for paclitaxel and siroliumus for the same time point.

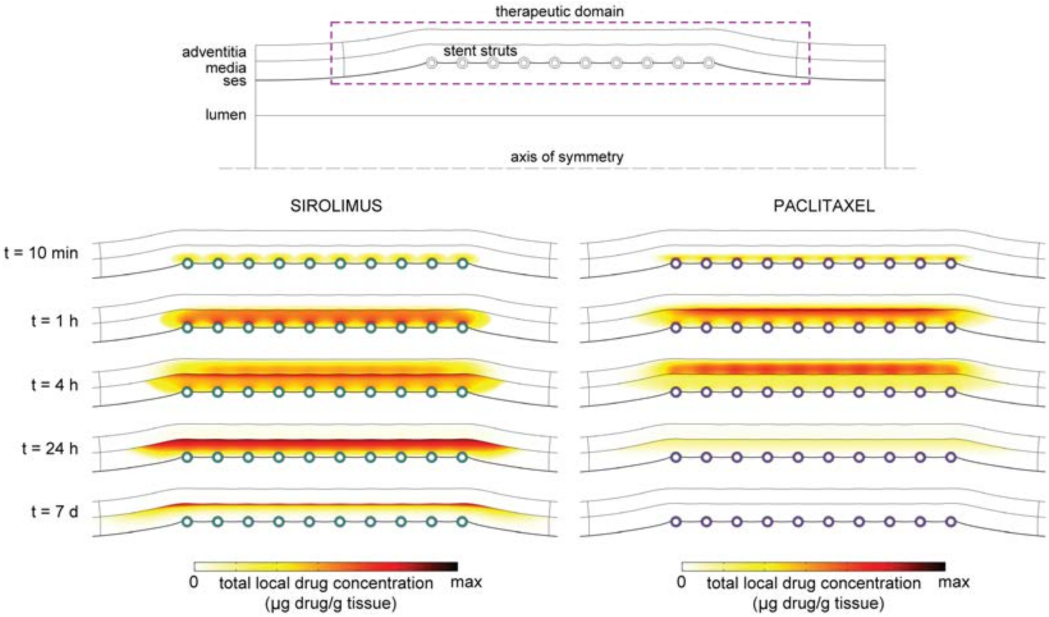

Fig. S8. Comparison between the spatial variation of sirolimus and paclitaxel at five different time points after stent implantation for the 20 % expansion case. The maximum values of total local drug concentration chosen for each time point are presented as μg drug per g of tissue and they are the following: at t = 10 min, max = 2722.67 μg drug/g tissue; at t = 1 h, max = 1102.44 μg drug/g tissue; at t = 4 h, max = 795.74 μg drug/g tissue; at t = 24 h, max = 283.79 μg drug/g tissue and; at t = 7 d, max = 89.76 μg drug/g tissue (see bold values in Tables S1-S2). Note that the 'max' value in color legend is the same for paclitaxel and siroliumus for the same time point.

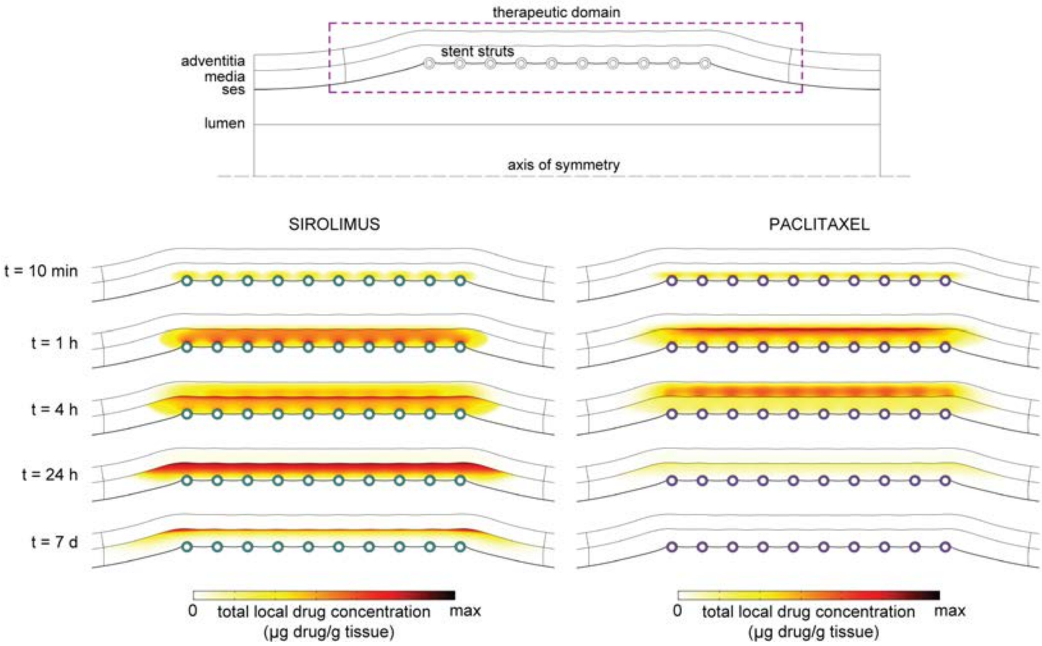

Fig. S9. Comparison between the spatial variation of sirolimus and paclitaxel at five different time points after stent implantation for the 30 % expansion case. The maximum values of total local drug concentration chosen for each time point are presented as μg drug per g of tissue and they are the following: at t = 10 min, max = 2722.67 μg drug/g tissue; at t = 1 h, max = 1102.44 μg drug/g tissue; at t = 4 h, max = 795.74 μg drug/g tissue; at t = 24 h, max = 283.79 μg drug/g tissue and; at t = 7 d, max = 89.76 μg drug/g tissue (see bold values in Tables S1-S2). Note that the 'max' value in color legend is the same for paclitaxel and siroliumus for the same time point.

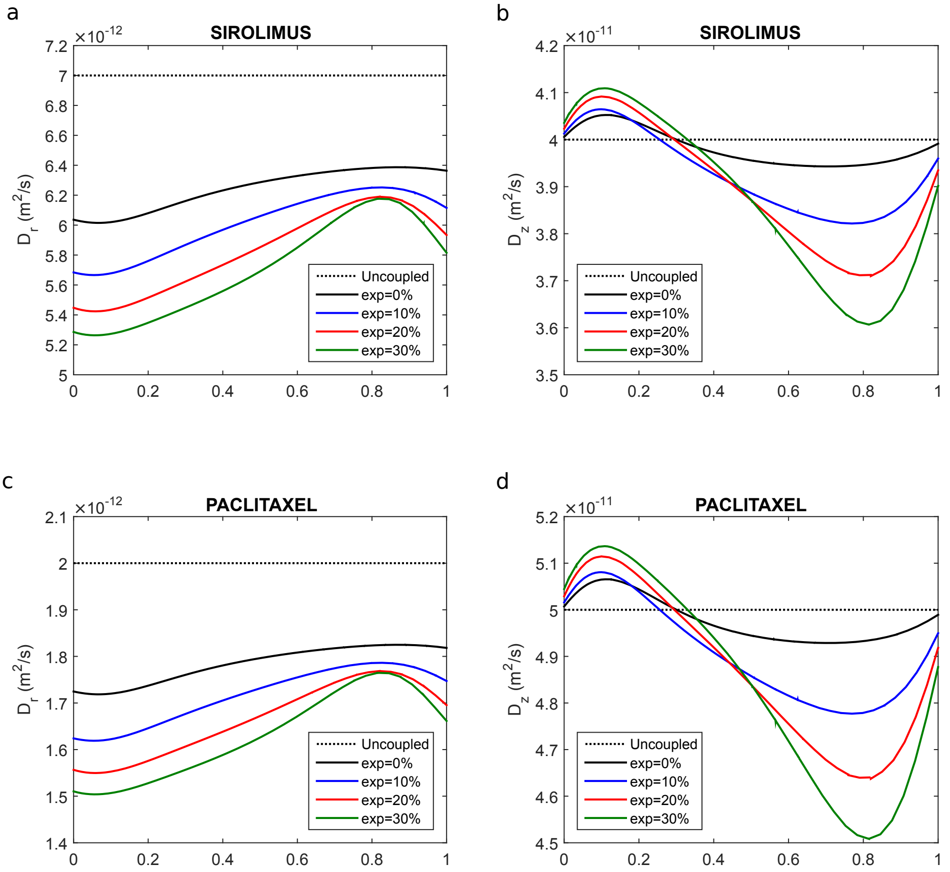

Fig. S10. Radial and longitudinal diffusion coefficient (D_r and D_z, respectively) variation of sirolimus (a, b) and paclitaxel (c, d) in the media layer of the arterial wall. The results are shown for the uncoupled model and for luminal diameter expansions of $0-30\%$ for the coupled model. The radial line is drawn between the middle struts.

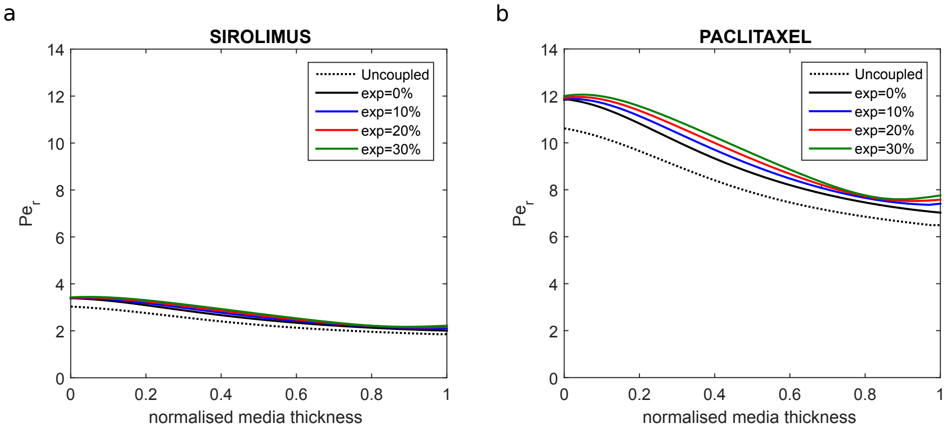

Fig. S11. Radial Peclet number variation for sirolimus (a) and paclitaxel (b) in the media layer of the arterial wall. The results are shown for the uncoupled model and for luminal diameter expansions of $0 - 30\%$ for the coupled model. The radial line is drawn between the middle struts.

(i) UNCOUPLED CASE (Sirolimus)

max. value at	t = 10 min	t = 1 h	t = 4 h	t = 24 h	t = 7 d
Total local concentration in the SES	240.00	89.72	23.20	$4.17\cdot10^{-2}$	$2.04\cdot10^{-3}$
Free local concentration in the media	1559.48	750.45	476.91	15.64	1.27
Bound local concentration in the media	314.70	314.70	314.17	276.08	114.60
Total local concentration in the media	1874.68	1065.16	791.08	291.72	115.88
Total local concentration in the adventitia	$6.61\cdot10^{-19}$	0.433	475.49	15.56	1.26

(ii) 0 % EXPANSION CASE (Sirolimus)

max. value at	t = 10 min	t = 1 h	t = 4 h	t = 24 h	t = 7 d
Total local concentration in the SES	215.52	79.82	20.61	$2.76\cdot10^{-2}$	$1.34\cdot10^{-3}$
Free local concentration in the media	1648.91	761.21	481.56	13.39	0.87
Bound local concentration in the media	315.22	314.72	314.18	270.39	88.88
Total local concentration in the media	1964.13	1075.93	**795.74**	**283.79**	**89.76**
Total local concentration in the adventitia	$1.48\cdot10^{-15}$	274.97	496.94	13.32	0.87

(ii) 10 % EXPANSION CASE (Sirolimus)

max. value at	t = 10 min	t = 1 h	t = 4 h	t = 24 h	t = 7 d
Total local concentration in the SES	253.18	93.46	24.17	$4.12\cdot10^{-2}$	$7.42\cdot10^{-4}$
Free local concentration in the media	1519.25	701.00	446.13	12.59	0.82
Bound local concentration in the media	315.18	314.64	314.06	267.95	84.75
Total local concentration in the media	1834.43	1015.64	760.20	280.54	85.57
Total local concentration in the adventitia	$2.96\cdot10^{-14}$	346.06	466.75	12.52	0.81

(ii) 20 % EXPANSION CASE (Sirolimus)

max. value at	t = 10 min	t = 1 h	t = 4 h	t = 24 h	t = 7 d
Total local concentration in the SES	317.22	116.87	30.35	$7.03\cdot10^{-2}$	$8.16\cdot10^{-4}$
Free local concentration in the media	1402.83	645.86	409.43	12.17	0.81
Bound local concentration in the media	315.14	314.55	313.92	266.59	84.47
Total local concentration in the media	1717.98	960.42	723.36	278.77	85.29
Total local concentration in the adventitia	$1.27\cdot10^{-13}$	370.51	432.15	12.10	0.81

(ii) 30 % EXPANSION CASE (Sirolimus)

max. value at	t = 10 min	t = 1 h	t = 4 h	t = 24 h	t = 7 d
Total local concentration in the SES	307.89	113.57	29.33	$9.18\cdot10^{-2}$	$1.30\cdot10^{-3}$
Free local concentration in the media	1297.68	599.28	379.67	12.23	0.81
Bound local concentration in the media	315.10	314.47	313.79	266.79	84.54
Total local concentration in the media	1612.78	913.75	693.46	279.03	85.36
Total local concentration in the adventitia	$3.22\cdot10^{-13}$	367.74	402.43	12.15	0.81

Table S1

Maximum local sirolimus concentration in each layer of the arterial wall (presented as μg sirolimus per g of tissue) for the uncoupled model and for each expansion case at five different time points after stent implantation. The local drug content in each layer of the tissue is calculated as $(c_i + b_i)\frac{MW_{drug}}{\rho_i}$. Bold values in this table for a given time indicate that the maximum sirolimus concentration was greater than the maximum paclitaxel concentration at the same time. Bold values correspond to the 'max' values in the legend in Fig. 7 of the main document and Figs. S5-S9 in this supplementary material.

(i) UNCOUPLED CASE (Paclitaxel)

max. value at	t = 10 min	t = 1 h	t = 4 h	t = 24 h	t = 7 d
Total local concentration in the SES	208.87	77.03	19.86	$4.06{\cdot}10^{-3}$	$1.31{\cdot}10^{-6}$
Free local concentration in the media	2513.17	997.11	696.90	9.43	$6.46{\cdot}10^{-2}$
Bound local concentration in the media	109.41	109.23	109.11	85.53	2.61
Total local concentration in the media	2622.58	1106.34	806.01	94.96	2.68
Total local concentration in the adventitia	$1.08{\cdot}10^{-13}$	243.62	732.08	9.40	$6.41{\cdot}10^{-2}$

(ii) 0 % EXPANSION CASE (Paclitaxel)

max. value at	t = 10 min	t = 1 h	t = 4 h	t = 24 h	t = 7 d
Total local concentration in the SES	194.59	71.86	18.52	$3.63{\cdot}10^{-3}$	$3.57{\cdot}10^{-7}$
Free local concentration in the media	2613.26	974.75	618.71	7.70	$2.51{\cdot}10^{-2}$
Bound local concentration in the media	109.41	109.22	109.05	81.60	1.03
Total local concentration in the media	**2722.67**	1083.98	727.77	89.31	1.06
Total local concentration in the adventitia	$6.00{\cdot}10^{-11}$	770.59	684.81	7.67	$2.49{\cdot}10^{-2}$

(ii) 10 % EXPANSION CASE (Paclitaxel)

max. value at	t = 10 min	t = 1 h	t = 4 h	t = 24 h	t = 7 d
Total local concentration in the SES	244.12	90.09	23.22	$4.59{\cdot}10^{-3}$	$4.65{\cdot}10^{-8}$
Free local concentration in the media	2404.38	955.52	560.80	7.53	$4.57{\cdot}10^{-3}$
Bound local concentration in the media	109.40	109.22	109.01	81.13	0.19
Total local concentration in the media	2513.79	1064.74	669.81	88.67	0.194
Total local concentration in the adventitia	$3.58{\cdot}10^{-8}$	919.14	621.66	12.52	$4.54{\cdot}10^{-3}$

(ii) 20 % EXPANSION CASE (Paclitaxel)

max. value at	t = 10 min	t = 1 h	t = 4 h	t = 24 h	t = 7 d
Total local concentration in the SES	303.78	111.53	28.76	$6.22{\cdot}10^{-3}$	$8.89{\cdot}10^{-8}$
Free local concentration in the media	2220.36	991.98	511.81	7.93	$1.37{\cdot}10^{-3}$
Bound local concentration in the media	109.39	109.23	108.96	82.18	$5.75{\cdot}10^{-2}$
Total local concentration in the media	2329.76	1101.21	620.77	90.11	$5.89{\cdot}10^{-2}$
Total local concentration in the adventitia	$2.20{\cdot}10^{-5}$	958.84	564.97	7.86	$1.36{\cdot}10^{-3}$

(ii) 30 % EXPANSION CASE (Paclitaxel)

max. value at	t = 10 min	t = 1 h	t = 4 h	t = 24 h	t = 7 d
Total local concentration in the SES	303.54	111.75	28.81	$7.08{\cdot}10^{-3}$	$6.98{\cdot}10^{-7}$
Free local concentration in the media	2057.77	993.20	476.51	8.08	$1.79{\cdot}10^{-3}$
Bound local concentration in the media	109.38	109.23	108.91	82.56	$7.51{\cdot}10^{-2}$
Total local concentration in the media	2167.15	**1102.44**	585.43	90.65	$7.68{\cdot}10^{-2}$
Total local concentration in the adventitia	$6.12{\cdot}10^{-4}$	960.30	519.59	8.01	$1.77{\cdot}10^{-3}$

Table S2
Maximum local paclitaxel concentration in each layer of the arterial wall (presented as μg paclitaxel per g of tissue) for the uncoupled model and for each expansion case at five different time points after stent implantation. The local drug content in each layer of the tissue is calculated as $\frac{(c_i+b_i)MW_{drug}}{\rho_i}$. Bold values in this table for a given time indicate that the maximum paclitaxel concentration was greater than the maximum sirolimus concentration at the same time. Bold values correspond to the 'max' values in the legend in Fig. 7 of the main document and Figs. S5-S9 in this supplementary material.

3.2 Work 2: Influence of vessel curvature and plaque composition on drug transport in the arterial wall following drug-eluting stent implantation

In this work, we provide a comprehensive investigation of the influence of arterial curvature and plaque composition on drug transport in the arterial wall following drug-eluting stent (DES) implantation. The arterial wall is considered as a three-layered structure including the subendothelial space, the media and the adventitia, with porous membranes separating them (endothelium, internal and external elastic lamina). Blood flow is modelled by the Navier–Stokes equations, while Darcy's law is used to calculate plasma filtration through the porous layers. Our findings demonstrate that arterial curvature and plaque composition have important influences on the spatio-temporal distribution of drug, with potential implications in terms of effectiveness of the treatment. Since the majority of computational models to date tend to neglect these features, these models are likely to be under- or over-estimating drug uptake and redistribution in arterial tissue.

Biomechanics and Modeling in Mechanobiology (2021) 20:767–786
https://doi.org/10.1007/s10237-020-01415-3

ORIGINAL PAPER

Influence of vessel curvature and plaque composition on drug transport in the arterial wall following drug-eluting stent implantation

Javier Escuer[1] · Irene Aznar[1] · Christopher McCormick[2] · Estefania Peña[1,3] · Sean McGinty[4] · Miguel A. Martínez[1,3,5]

Received: 2 May 2020 / Accepted: 21 December 2020 / Published online: 3 February 2021
© The Author(s), under exclusive licence to Springer-Verlag GmbH, DE part of Springer Nature 2021

Abstract
In the last decade, many computational models have been developed to describe the transport of drug eluted from stents and the subsequent uptake into arterial tissue. Each of these models has its own set of limitations: for example, models typically employ simplified stent and arterial geometries, some models assume a homogeneous arterial wall, and others neglect the influence of blood flow and plasma filtration on the drug transport process. In this study, we focus on two common limitations. Specifically, we provide a comprehensive investigation of the influence of arterial curvature and plaque composition on drug transport in the arterial wall following drug-eluting stent implantation. The arterial wall is considered as a three-layered structure including the subendothelial space, the media and the adventitia, with porous membranes separating them (endothelium, internal and external elastic lamina). Blood flow is modelled by the Navier–Stokes equations, while Darcy's law is used to calculate plasma filtration through the porous layers. Our findings demonstrate that arterial curvature and plaque composition have important influences on the spatiotemporal distribution of drug, with potential implications in terms of effectiveness of the treatment. Since the majority of computational models tend to neglect these features, these models are likely to be under- or over-estimating drug uptake and redistribution in arterial tissue.

Keywords Drug transport · Drug-eluting stents · Arterial wall · Curvature · Atheroma plaque

1 Introduction

Coronary artery disease (CAD) is the leading cause of death globally (Roth et al. 2018). Atherosclerosis is the major contributor of CAD and results from the abnormal accumulation of fat, cholesterol, macrophages, calcium and other substances inside the vessel, leading to the partial or total reduction of the blood flow through the coronary arteries to the heart muscle.

Coronary angioplasty with stenting has revolutionised the treatment of advanced atherosclerotic lesions in arteries. However, in-stent restenosis (ISR), a gradual luminal re-narrowing mainly due to the response to vessel wall injury induced by the device, is the major clinical limitation of this technique (Alfonso et al. 2014). The advent of drug-eluting stents (DES), which release antiproliferative substances into the arterial tissue and improved stent designs, has contributed to substantially reduce the occurrence of ISR compared with bare metal stents (BMS). However, ISR still remains a significant clinical and technological challenge. Moreover, an increased risk of developing late or very late stent thrombosis (LST/VLST) following DES implantation, which has been associated with high rates of mortality, has emerged as a major safety concern (Alfonso et al. 2014; Byrne et al. 2015).

Computational modelling and numerical simulation have risen as a fundamental tool in the investigation of medical

---

Supplementary Information The online version contains supplementary material available at https://doi.org/10.1007/s10237-020-01415-3.

Miguel A. Martínez
miguelam@unizar.es

[1] Aragón Institute for Engineering Research (I3A), University of Zaragoza, Zaragoza, Spain
[2] Department of Biomedical Engineering, University of Strathclyde, Glasgow, UK
[3] Biomedical Research Networking Center in Bioengineering, Biomaterials and Nanomedicine (CIBER-BBN), Zaragoza, Spain
[4] Division of Biomedical Engineering, University of Glasgow, Glasgow, UK
[5] María de Luna, 3, 50018 Zaragoza, Spain

Escuer J., Aznar I., McCormick C., Peña E., McGinty S., Martínez M.A. (2021).
Biomechanics and Modeling in Mechanobiology 20:767–786.
JIF (2020) = 2.963 (Q3: 36/71 Biomedical Engineering).

Biomechanics and Modeling in Mechanobiology (2021) 20:767–786
https://doi.org/10.1007/s10237-020-01415-3

ORIGINAL PAPER

Influence of vessel curvature and plaque composition on drug transport in the arterial wall following drug-eluting stent implantation

Javier Escuer[1] · Irene Aznar[1] · Christopher McCormick[2] · Estefanía Peña[1,3] · Sean McGinty[4] · Miguel A. Martínez[1,3,5]

Received: 2 May 2020 / Accepted: 21 December 2020 / Published online: 3 February 2021
© The Author(s), under exclusive licence to Springer-Verlag GmbH, DE part of Springer Nature 2021

Abstract

In the last decade, many computational models have been developed to describe the transport of drug eluted from stents and the subsequent uptake into arterial tissue. Each of these models has its own set of limitations: for example, models typically employ simplified stent and arterial geometries, some models assume a homogeneous arterial wall, and others neglect the influence of blood flow and plasma filtration on the drug transport process. In this study, we focus on two common limitations. Specifically, we provide a comprehensive investigation of the influence of arterial curvature and plaque composition on drug transport in the arterial wall following drug-eluting stent implantation. The arterial wall is considered as a three-layered structure including the subendothelial space, the media and the adventitia, with porous membranes separating them (endothelium, internal and external elastic lamina). Blood flow is modelled by the Navier–Stokes equations, while Darcy's law is used to calculate plasma filtration through the porous layers. Our findings demonstrate that arterial curvature and plaque composition have important influences on the spatiotemporal distribution of drug, with potential implications in terms of effectiveness of the treatment. Since the majority of computational models tend to neglect these features, these models are likely to be under- or over-estimating drug uptake and redistribution in arterial tissue.

Keywords Drug transport · Drug-eluting stents · Arterial wall · Curvature · Atheroma plaque

1 Introduction

Coronary artery disease (CAD) is the leading cause of death globally (Roth et al. 2018). Atherosclerosis is the major contributor of CAD and results from the abnormal accumulation of fat, cholesterol, macrophages, calcium and other substances inside the vessel, leading to the partial or total reduction of the blood flow through the coronary arteries to the heart muscle.

Coronary angioplasty with stenting has revolutionised the treatment of advanced atherosclerotic lesions in arteries. However, in-stent restenosis (ISR), a gradual luminal re-narrowing mainly due to the response to vessel wall injury induced by the device, is the major clinical limitation of this technique (Alfonso et al. 2014). The advent of drug-eluting stents (DES), which release antiproliferative substances into the arterial tissue and improved stent designs, has contributed to substantially reduce the occurrence of ISR compared with bare metal stents (BMS). However, ISR still remains a significant clinical and technological challenge. Moreover, an increased risk of developing late or very late stent thrombosis (LST/VLST) following DES implantation, which has been associated with high rates of mortality, has emerged as a major safety concern (Alfonso et al. 2014; Byrne et al. 2015).

Computational modelling and numerical simulation have risen as a fundamental tool in the investigation of medical

---

Supplementary Information The online version contains supplementary material available at. https://doi.org/10.1007/s10237-020-01415-3.

✉ Miguel A. Martínez
miguelam@unizar.es

[1] Aragón Institute for Engineering Research (I3A), University of Zaragoza, Zaragoza, Spain

[2] Department of Biomedical Engineering, University of Strathclyde, Glasgow, UK

[3] Biomedical Research Networking Center in Bioengineering, Biomaterials and Nanomedicine (CIBER-BBN), Zaragoza, Spain

[4] Division of Biomedical Engineering, University of Glasgow, Glasgow, UK

[5] María de Luna, 3, 50018 Zaragoza, Spain

devices, helping to address some of the limitations of often difficult, expensive and extremely variable experimental/clinical tests. In the particular case of DES, computational analysis has enhanced the understanding of the factors which govern drug release from the device and drug binding and redistribution within the arterial wall. Such efforts are helping in the development of a safer and more effective new generation of DES.

In the last decade, a large number of computational studies have been developed to describe the transport of drug eluted from stents in arteries (e.g. Vairo et al. 2010; McGinty et al. 2010; Tzafriri et al. 2012; Bozsak et al. 2014; McGinty and Pontrelli 2015, 2016; Ferreira et al. 2017, 2018; Mandal and Mandal 2018; McKittrick et al. 2019). These models generally consider a healthy straight vessel geometry with diffusive, advective and binding processes governing the transport of the drug within the blood flow and through the respective porous layers of the arterial wall. However, such models do not take into account the considerable geometrical variability of the coronary artery (curved regions, branching, etc.) which is associated with alterations in the local haemodynamics, playing an important role in the localisation of the atherosclerotic lesions (Frangos et al. 1999; Tarbell 2003). The influence of coronary arterial curvature on mass transport has previously been investigated for other macromolecules such as low-density lipoproteins (LDL), showing different average concentrations of LDL in curved arteries compared with straight arteries (Caputo et al. 2013; Wang and Vafai 2015). However, to the best of our knowledge, in terms of drug transport there are only a very limited number of computational approaches available in the literature that take into account complex arterial geometries (Hossain et al. 2012; Cutrì et al. 2013), but they are not specifically focussed on the effect of the curvature of the vessel on tissue uptake and retention of drug.

Moreover, there is growing evidence that plaque composition may well have an impact on drug distribution within diseased tissue (McKittrick et al. 2016). However, very few of the computational models of drug transport in arteries from the available literature incorporate the existence of disease state (Vairo et al. 2010; McGinty et al. 2010; Hossain et al. 2012; Ferreira et al. 2017, 2018; Mandal and Mandal 2018). Of the models that do, for instance, Vairo et al. (2010) assume a porous homogeneous plaque between the device and the healthy tissue in their 2D axisymmetric geometry, but the process of binding is described in terms of equilibrium conditions. Hossain et al. (2012) perform several simulations on a 3D patient-specific geometry of a bifurcation of a two-layered coronary artery with a plaque in order to analyse the effect of both artery and plaque heterogeneity on drug transport. However, a first-order reaction kinetics model was adopted to account for possible drug binding. Mandal and Mandal (2018) also present a 2D axisymmetric model and take into consideration the binding and unbinding processes to describe the interaction of the drug with the healthy and unhealthy tissue, but the porous nature of the arterial wall is not fully taken into account. Finally, Ferreira et al. use different 2D geometries to investigate the impact of local plaque composition (Ferreira et al. 2017) and plaque eccentricity on drug distribution (Ferreira et al. 2018), but like most other drug transport models (Vairo et al. 2010; Tzafriri et al. 2012; Cutrì et al. 2013; McGinty and Pontrelli 2015, 2016; Ferreira et al. 2017; Mandal and Mandal 2018; Ferreira et al. 2018; McKittrick et al. 2019) the arterial wall is modelled as a single layer, limiting the interpretation of the results.

In this work, we provide a comprehensive computational study of the impact of the variability of the coronary artery geometry on drug transport in the blood flow and in the arterial wall. In particular, we perform a series of simulations to elucidate the effect of arterial curvature on spatiotemporal drug uptake within tissue. Computations are also carried out on an idealised curved coronary artery geometry under diseased conditions, simulated by the presence of an atherosclerotic plaque between DES and tissue, and the effect of the plaque heterogeneity on the overall drug distribution is investigated. Our model incorporates the generally accepted nonlinear saturable reversible binding model (Tzafriri et al. 2012; McGinty and Pontrelli 2016; McKittrick et al. 2019) to describe the reversible reaction of the free drug molecules.

The paper is organised as follows. We start with a description of how we model blood flow in the lumen (Sect. 2.1.1), followed by plasma filtration through the tissue (Sect. 2.1.2). We then present equations to describe drug release from the stent and subsequent transport in the arterial wall under healthy and diseased conditions (Sects. 2.1.3 and 2.1.4). A detailed description of the computational geometry and the implementation of the model equations in a commercial finite element software is provided in Sect. 2.2. We then proceed to show the key results of the different simulations performed in Sect. 3. Finally, we present a discussion of the significance of the results in Sect. 4, highlighting the limitations and assumptions of the model.

2 Material and methods

2.1 Governing equations

2.1.1 Modelling blood flow

In this work, blood is modelled as an incompressible Newtonian fluid governed by the steady Navier–Stokes equations and the continuity equation:

$$\rho_b(\boldsymbol{u}_l \cdot \nabla)\boldsymbol{u}_l = -\nabla p_l + \mu_b \nabla^2 \boldsymbol{u}_l, \quad \nabla \cdot \boldsymbol{u}_l = 0 \tag{1}$$

where $\boldsymbol{u}_l$ and p_l are the velocity vector field and the pressure field of the blood flow in the lumen, respectively, and ρ_b and μ_b are the density and the dynamic viscosity of the blood, respectively. At the inlet of the lumen, $\Gamma_{l,\text{inlet}}$, a fully developed parabolic velocity profile is prescribed:

$$w_{l,\text{inlet}} = u_{max}\left(1 - \left(\frac{r}{r_l}\right)^2\right), \tag{2}$$

where w_l is the axial component of the blood velocity in the lumen; u_{max} is the centreline velocity for a typical value of the Reynolds number ($Re_l = \rho_b u_0 (2r_l)/\mu_b$) in the coronary artery of 400 corresponding to laminar flow (Formaggia et al. 2010); r is the radial position; u_0 is the mean velocity; and r_l is the internal radius of the artery. A constant pressure of 100 mmHg is considered at the lumen outlet, $\Gamma_{l,\text{outlet}}$ (Ai and Vafai 2006). Moreover, the no-slip condition ($w_l = 0$) is prescribed at the endothelium, Γ_{et} (Vairo et al. 2010; Bozsak et al. 2014; Escuer et al. 2020). We refer the reader to Fig. 1 for a schematic summarising the governing equations and the boundary conditions involved in the computational model.

2.1.2 Modelling porous media

The healthy arterial wall is modelled as a multi-layered structure organised in three porous layers: subendothelial space (SES), media and adventitia. The plaque is also assumed to behave as a porous medium. Although it is well known that atherosclerotic plaque composition is highly heterogeneous, in this work plaque is idealised as a fibrous cap with a core which may be lipid, necrotic or calcified, depending on the lesion considered. Due to the porous nature of the tissue, the flow field through the different regions of the arterial wall is calculated using Darcy's law and the continuity equation:

$$\boldsymbol{u}_i = \frac{K_i}{\mu_p} \nabla p_i, \quad \nabla \cdot \boldsymbol{u}_i = 0 \tag{3}$$

where the subscript $i = \{i_1, i_2\}$ denotes the healthy and unhealthy tissue regions, respectively; $i_1 = \{ses, m, a\}$ denotes the SES, the media and the adventitia, respectively; $i_2 = \{pfc, pc\}$ denotes the plaque's fibrous cap and the core of the plaque, respectively; $\boldsymbol{u}_i$ is the transmural velocity vector field; K_i is the Darcian permeability; μ_p is the dynamic viscosity of the plasma; and p_i is the pressure field. The endothelium (ET), and internal and external elastic laminae (IEL and EEL, respectively) are treated as semipermeable membranes, and the fluid flux across them, $J_{v,j}$, is described by the Kedem–Katchalsky equations (Kedem and Katchalsky 1958). Neglecting the osmotic contribution as an approximation (Formaggia et al. 2010; Bozsak et al. 2014; Escuer et al. 2020), the Kedem–Katchalsky equations for fluid flux can be simplified as:

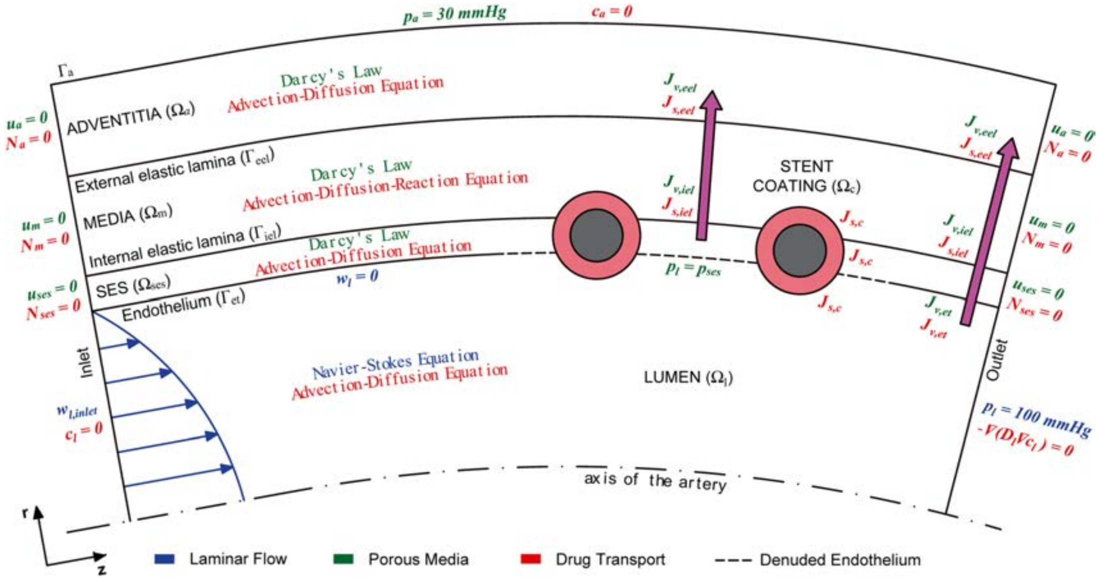

Fig. 1 Schematic summarising the governing equations and the boundary conditions of the computational model

$$J_{v,j} = L_{p,j}\Delta p_j, \tag{4}$$

where the subscript $j = \{et, etp, iel, ielp, eel\}$ denotes the semipermeable membranes considered: the lumen–SES interface (et), the lumen–plaque interface (etp), the SES–media interface (iel), the plaque–media interface (ielp) and the media–adventitia interface (eel), respectively; $L_{p,j}$ is the membrane hydraulic conductivity; and Δp_j the pressure drop across each semipermeable membrane. The equations for the flux J_v, corresponding to each boundary, are shown in Supplementary Material.

Due to the stent implantation, the endothelium is assumed to be denuded between stent struts and in zones distal and proximal to the stent over a distance that is one half of the interstrut spacing (ISS) measured from the respective stent strut centres (Bozsak et al. 2014) (Fig. 2). Outside of these regions, the endothelium is assumed to be intact. In denuded regions, the volume flux across the endothelium simplifies to continuity of pressure, i.e. $p_l = p_{ses}$ under healthy conditions or $p_l = p_{pfc}$ in the presence of plaque in the outer wall of the artery. At the longitudinal wall boundaries, $\Gamma_{i_1,inlet}$ and $\Gamma_{i_1,outlet}$, in agreement with Bozsak et al. (2014), Escuer et al. (2020), a zero-flow condition, $-\boldsymbol{n}_{i_1} \cdot \boldsymbol{u}_{i_1} = 0$, where $\boldsymbol{n}_{i_1}$ is the unit outward normal vector to the corresponding exterior boundary, is imposed. This choice of boundary condition is justified by the fact that we are interested in computing drug concentrations only within the therapeutic domain, while these boundaries are imposed sufficiently far upstream and downstream of the stented region. Moreover, it is assumed that the plasma cannot penetrate the surface of the polymer coating. At the perivascular side, Γ_a, a constant pressure of 30 mmHg (Ai and Vafai 2006) is applied in order to set a physiologically realistic pressure drop of 70 mmHg between the lumen and the outer surface of the tissue (Meyer et al. 1996).

2.1.3 Modelling drug release from the stent coating

Drug release from a DES with non-erodible polymeric coating is modelled as a diffusion dominated process satisfying a simple diffusion equation (McGinty 2014):

$$\frac{\partial c_c}{\partial t} = \nabla \cdot (\boldsymbol{D}_c \nabla c_c), \tag{5}$$

where $c_c(r, z, t)$ is the volume-averaged concentration of free drug eluted from the stent coating and $\boldsymbol{D}_c$ represents the diffusivity of the considered drug in the polymer. At t = 0, the drug is assumed to be completely contained within the polymer coating in dissolved phase (free drug) at uniform concentration, C_0. Continuity of drug concentration and mass flux is prescribed across the outer boundary of the polymeric stent coating, Γ_{ck}:

$$c_c = c_k, \tag{6}$$

$$(-\boldsymbol{D}_c \nabla c_c) \cdot \boldsymbol{n}_c = -(-\boldsymbol{D}_k \nabla c_k + \boldsymbol{u}_k c_k) \cdot \boldsymbol{n}_k, \tag{7}$$

where the subscript $k = \{l, pfc, m\}$ represents the lumen, the fibrous cap of the plaque and the media, respectively. Finally, we assume that the metallic strut is impermeable to the drug, and therefore, a zero-flux condition, $-\boldsymbol{n_c} \cdot (-\boldsymbol{D}_c \nabla c_c) = 0$, through the boundary surface between the metallic strut and the polymer coating, is imposed.

2.1.4 Modelling drug transport within the lumen and the arterial wall

Drug transport inside the arterial lumen is modelled as a time-dependent advection–diffusion process:

$$\frac{\partial c_l}{\partial t} + \boldsymbol{u}_l \cdot \nabla c_l = \nabla \cdot (\boldsymbol{D}_l \nabla c_l), \tag{8}$$

where $c_l(r, z, t)$ is the drug concentration within the fluid domain; $\boldsymbol{D}_l$ is the isotropic diffusivity of the drug in the blood; and $\boldsymbol{u}_l$ is the blood flow velocity calculated by Eq. (1). Likewise, drug transport processes in the SES and the adventitia may be written as:

$$\frac{\partial c_{ses}}{\partial t} + \frac{\gamma_{ses}}{\phi_{ses}} u_{ses} \cdot \nabla c_{ses} = \nabla \cdot (D_{ses} \nabla c_{ses}), \tag{9}$$

$$\frac{\partial c_a}{\partial t} + \frac{\gamma_a}{\phi_a} u_a \cdot \nabla c_a = \nabla \cdot (D_a \nabla c_a), \tag{10}$$

where the subscripts *ses* and *a* denote the SES and the adventitia, respectively, and γ, ϕ, $\boldsymbol{u}$, $\boldsymbol{D}$ and $c(r, z, t)$ refer to the hindrance coefficients, porosities, transmural fluid velocities calculated by Eq. (3), diffusion coefficients and dissolved drug concentrations within the respective domains. In the media and plaque regions, drug dynamics are governed by the advection–diffusion–reaction equation:

$$\frac{\partial c_m}{\partial t} + \frac{\gamma_m}{\phi_m} \boldsymbol{u}_m \cdot \nabla c_m = \nabla \cdot (\boldsymbol{D}_m \nabla c_m) - \frac{\partial b^{ns}_m}{\partial t} - \frac{\partial b^{s}_m}{\partial t}, \tag{11}$$

$$\frac{\partial b^{ns}_m}{\partial t} = k^{ns}_{on} c_m (b^{ns}_{max,m} - b^{ns}_m) - k^{ns}_{off} b^{ns}_m, \tag{12}$$

$$\frac{\partial b^{s}_m}{\partial t} = k^{s}_{on} c_m (b^{s}_{max,m} - b^{s}_m) - k^{s}_{off} b^{s}_m. \tag{13}$$

$$\frac{\partial c_{i_2}}{\partial t} + \frac{\gamma_{i_2}}{\phi_{i_2}} \boldsymbol{u}_{i_2} \cdot \nabla c_{i_2} = \nabla \cdot (\boldsymbol{D}_{i_2} \nabla c_{i_2}) - \frac{\partial b_{i_2}}{\partial t}, \tag{14}$$

$$\frac{\partial b_{i_2}}{\partial t} = k^{ns}_{on} c_{i_2}(b_{max,i_2} - b_{i_2}) - k^{ns}_{off} b_{i_2}, \tag{15}$$

where the subscripts m and i_2 denote parameters and variables with respect to the media and plaque layers, respectively, and superscripts s and ns denote specific and non-specific binding, respectively. Equations (12) and (13) describe a nonlinear saturable reversible binding model to adequately account for the drug binding process in the media (Tzafriri et al. 2012; McGinty and Pontrelli 2016; McKittrick et al. 2019). This reaction model is able to define three different states of the drug in the media layer: drug dissolved in the plasma, $c_m(r, z, t)$, drug bound to specific binding sites (target receptors), $b^s_m(r, z, t)$, and drug bound to non-specific binding sites (general ECM sites), $b^{ns}_m(r, z, t)$. Due to the lack of binding data available in the literature for the plaque, we have considered a single phase nonlinear saturable reversible binding model in these regions, Eq. (15), and only two different states of the drug can be defined: drug dissolved in the plasma, $ci2(r, z, t)$, and drug bound to components of plaque, $bi2(r, z, t)$. The binding rate constants (forward reaction rates) are given by k^s_{on} and k^{ns}_{on}, whereas the unbinding rate constants (reverse reaction rates) are given by k^s_{off} and k^{ns}_{off}. In the plaque regions, these are assumed to take the same values as the non-specific rates in the media. The rate constants are related through the equilibrium dissociation constants, K^s_d and K^{ns}_d, which are defined as $K^s_d = k^s_{off}/k^s_{on}$ and $K^{ns}_d = k^{ns}_{off}/k^{ns}_{on}$. The parameters $b^s_{max,m}$, $b^{ns}_{max,m}$ and b_{max,i_2} are the maximum density of binding sites in the media (specific and non-specific) and in the plaque region, respectively. Discontinuity of solute flux across the semipermeable membranes, $J_{s,j}$, is governed by the Kedem–Katchalsky equations (Kedem and Katchalsky 1958):

$$J_{s,j} = P_j \Delta c_j + s_j \bar{c}_j J_{v,j}, \tag{16}$$

where P_j is the permeability of each semipermeable membrane; Δc_j is the solute concentration difference; s_j is the sieving coefficient; and $\bar{c}_j$ is the weighted average concentration on either side of the corresponding membrane (Levitt 1975). The equations for the flux J_s corresponding to each boundary are shown in Supplementary Material. Continuity of flux and concentration is assumed on the fibrous cap–plaque core interface, Γ_p. Note that when a calcified lesion is considered in the simulations, the plaque core is assumed to be impermeable to all species present in adjacent regions. This assumption is in agreement with Ferreira et al. (2017) and echoes Tzafriri et al. (2017) where it was found that, at least for paclitaxel, diffusion in dense and calcified plaque is significantly hindered, potentially up to 300-fold. In the lumen, a zero-drug-concentration boundary condition is applied at the inlet, $c_l = 0$, and an outflow condition, $-\boldsymbol{n}_l \cdot (-\boldsymbol{D}_l \nabla c_l) = 0$, is applied at the outlet. Following Vairo et al. (2010), the upstream and downstream boundaries of the tissue are subjected to a zero-flux condition: $-\boldsymbol{n}_{i_1} \cdot \boldsymbol{N}_{i_1} = -\boldsymbol{n}_{i_1} \cdot (-\boldsymbol{D}_{i_1} \nabla c_{i_1} + \boldsymbol{u}_{i_1} c_{i_1}) = 0$. Finally, a perfect sink condition for the free drug is applied at the perivascular side, $c_a = 0$ (Bozsak et al. 2014; Escuer et al. 2020).

2.2 Computational model

2.2.1 Geometry of the model

Several 2D computational models corresponding to idealised longitudinal sections of segments of coronary arteries have been considered in this work as a first step for performing a comprehensive analysis of the influence of arterial curvature and plaque composition on drug transport within the arterial wall. To study the effect of the arterial curvature, six different geometries of a healthy coronary artery containing a DES have been analysed: one corresponding to a straight segment and the remaining five corresponding to curved segments of varying curvature. The curvature of a vessel can be defined by the curvature ratio, κ, which is calculated as (Santamarina et al. 1998):

$$\kappa = \frac{r_l}{R}, \tag{17}$$

where r_l is the lumen radius and R is the curvature radius of the vessel measured in the centreline of the artery. The average curvature ratio of a coronary artery is approximately 0.1 (Jayarama 2006), but varies greatly depending on the particular location, lying in the range of 0.02–0.5 (Santamarina et al. 1998). In Fig. 2a, the geometry for the case with average curvature ratio is shown. Moreover, to investigate the impact of plaque composition, a stenosed curved segment (with $\kappa = 0.1$) of a coronary artery with an eccentric

Table 1 List of the geometrical parameters related to the computational models

Parameter	Description	Value (mm)	References
r_l	Lumen radius	1.5	Mongrain et al. (2005)
δ_{ses}	Intima thickness	0.01	Karner et al. (2001)
δ_m	Media thickness	0.5	Vairo et al. (2010)
δ_a	Adventitia thickness	0.4	Creel et al. (2000)
d_{strut}	Metallic strut diameter	0.15	Mongrain et al. (2005)
δ_p	Polymeric coating thickness	0.05	Mongrain et al. (2005)

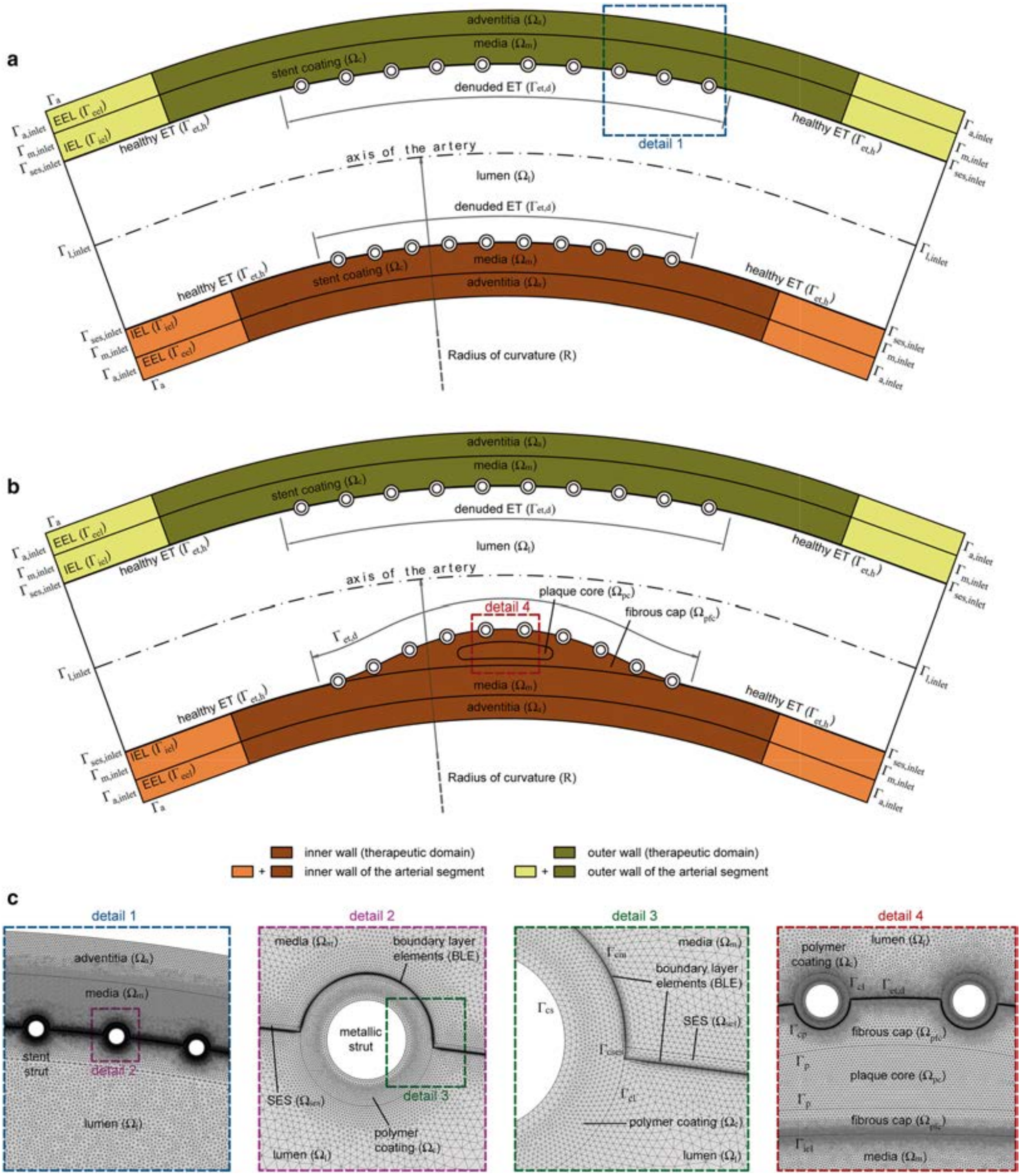

Fig. 2 **a** Overall longitudinal section view of a curved segment of a coronary artery with average curvature ($\kappa = 0.1$) where a DES was implanted. **b** Overall longitudinal section view of a stenosed curved segment of a coronary artery with average curvature ($\kappa = 0.1$ Jayarama 2006) with an atherosclerotic plaque located between the DES and the media. In both cases (healthy and unhealthy), the stent struts are assumed to be half-embedded in the tissue. The target areas for drug transport, also called therapeutic domains, considered to compute all the variables involved in the model are shaded in dark green for the outer wall and in dark brown for the inner wall. These domains are defined as three times the interstrut distance measured in the centreline of the artery (2.1 mm) (Bozsak et al. 2014; Escuer et al. 2020) and then projected radially to each wall. **c** Detailed view of the finite element (FE) mesh used in the computations. As shown in the figure, domains are represented by Ω and boundaries by Γ. Ω_l defines the arterial lumen; Ω_{ses} the SES; Ω_m the media layer; Ω_a the adventitia; Ω_{pfc} the fibrous cap of the plaque; Ω_{pc} the plaque core; and Ω_c the polymeric coating of the stent. Γ_{et} defines the endothelium; Γ_{iel} the internal elastic lamina; Γ_{eel} the external elastic lamina; Γ_a the perivascular side of the vessel; Γ_{cl} the stent coating–lumen interface; Γ_{cses} the coating–SES interface; Γ_{cm} the coating–media interface; Γ_{cs} the coating–metallic strut interface; $\Gamma_{l,inlet}$ and $\Gamma_{l,outlet}$ the inlet and outlet boundaries of the lumen, respectively; and $\Gamma_{i_1,inlet}$ and $\Gamma_{i_1,outlet}$ the inlet and outlet boundaries of the healthy tissue, respectively

atherosclerotic plaque located between the DES and the media layer within the inner wall of the vessel has been taken into account (Fig. 2b). The length of the arterial segments remains constant in all cases studied. A schematic showing the geometry of all investigated cases is shown in Fig. 3. The healthy arterial wall is modelled as a three-layered structure with the subendothelial space (SES), the media and the adventitia defined as distinct domains (Ω_{ses}, Ω_m and Ω_a, respectively), while the endothelium, Γ_{et}, the internal elastic lamina, Γ_{iel}, and the external elastic lamina, Γ_{eel}, are modelled as semipermeable membranes of negligible thickness between these layers. The plaque is composed of two different domains: fibrous cap, Ω_{pfc}, and core, Ω_{pc}. The length of the plaque (approximately 6 mm) and the percentage of diameter stenosis (20 %) correspond to values within the range found in the literature (Hossain et al. 2012; Rozie et al. 2009; Kosa et al. 1999; Kern et al. 1999). The device is represented by ten circular struts half-embedded the tissue in all simulations. The ISS in each case will change with the curvature of the segment, with the centre of each strut being projected radially. This means that the ISS will be different for the inner and outer walls and will be also affected by the presence of the plaque. The lumen geometry was extended at both ends (not shown in Figs. 2 and 3) by a length equivalent to five diameters, in order to obtain a fully developed flow near the DES and to avoid effects associated with the constraints applied at the inlet and the outlet boundaries, thereby reducing their influence on the results (Chiastra et al. 2014). Parameters related to the computational geometry, such as the internal artery radius, r_l; layer thicknesses, δ_i; metallic strut diameter, d_{strut}; and polymer thickness, δ_p, are taken from the existing literature and are listed in Table 1.

2.2.2 Numerical methods

The commercial finite element (FE) package COMSOL Multiphysics 5.3a (COMSOL AB, Burlington, MA, USA) was used to build the mesh and to numerically solve the governing equations described in Sect. 2 for the different cases considered. The computational analysis was conducted in two steps: (1) a stationary analysis of blood flow dynamics and plasma filtration and (2) a time-dependent drug transport analysis coupled with the solutions of luminal and transmural flow computed in the previous step. A sensitivity analysis was carried out in order to evaluate the influence of the mesh and time step size on the solution. Mesh density and time step independence was assumed when there was less than 1% difference in the time-varying profiles of normalised mean concentration (NMC) in the media layer after several mesh and time step refinements. The computational domains were discretised in space using triangular elements, resulting in an overall mesh with approximately 885,000 elements in case of healthy conditions (geometries without plaque) and more than 950,000 elements under pathological conditions. The discretisation employs Lagrange P3–P2 elements for the blood dynamics problem and quadratic Lagrange elements for the porous media and drug dynamics problems, respectively. Details of the mesh used in the different regions of the computational model are illustrated in Fig. 2c. A direct linear solver (MUMPS) was used to solve the stationary step with a tolerance for the relative error of the solution of 10^{-3}. The backward differentiation formula (BDF) method was used for the time discretisation of the transient step, with variable order of accuracy between 1 and 5 and variable time step size. The relative and absolute tolerance was set to 10^{-3} and 10^{-4}, respectively. The resulting system of time-dependent partial differential equations (PDEs) is solved using a direct linear solver (PARDISO) with a nested dissection preordering algorithm. Using 14 cores of an Intel® Core^{TM} i9-10940X CPU @ 3.30 GHz processor, the computation time for each of the 9 cases varies between 15 and 20 h.

2.2.3 Model parameters

To date, the drugs most widely used in drug-eluting stents are sirolimus and its analogues such as everolimus or zotarolimus. Sirolimus and derivatives are antiproliferative agents that target the FK506 binding protein 12 (FKBP12). This complex subsequently binds to the mammalian target of rapamycin (mTOR) and therefore interrupts the cell cycle from the G1 to the S phase (Martin and Boyle 2011). In the numerical simulations, sirolimus has been considered. Wherever possible, transport and binding parameters for sirolimus and physiological parameters related to the blood flow and porous media have been obtained from existing published experimental data. The values of these model parameters are given in Table 2.

2.2.4 Summary of investigated cases

We start by simulating the straight artery model (corresponding to $\kappa = 0$) and then we simulate five different curvature ratios ranging from $\kappa = 0.025$ to $\kappa = 0.4$. Finally, in order to analyse the impact of atherosclerotic plaques on curved vessels on drug transport, three different types of plaque, varying the composition of the core (fibrotic, lipid or calcified core), are compared for the case of average arterial curvature ($\kappa = 0.1$). The list of cases simulated are summarised in Table 3. In all cases, we assume an initial drug concentration in the stent coating, C_0, of 100 mol m^{-3} (Bozsak et al. 2014).

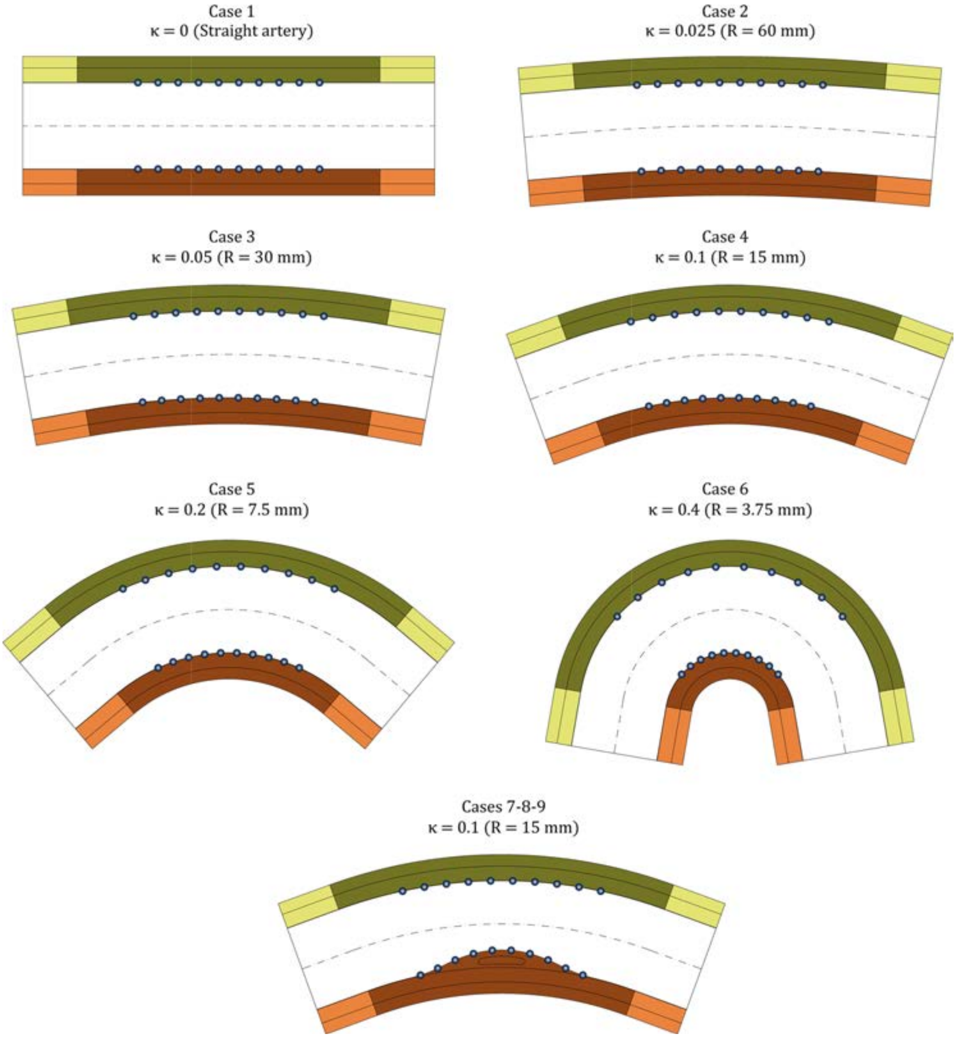

Fig. 3 Schematic showing the geometry of all investigated cases

2.3 Analysis of the results

In order to enable comparisons between the different cases (Table 3), we will show the time-varying profiles of normalised mean concentration (NMC) and spatially varying profiles of normalised local concentration (NLC). These results are typically shown over the first 12–24 h since this is where the largest differences have been observed for the parameter values simulated. However, we also show 2D results over 7 days. In Supplementary Material, we extend the results to 30 days. Furthermore, we also calculate the percentage of binding sites that are saturated as a function of time, a quantity strongly linked with efficacy, and display the results over 30 days. The results presented in this work are focussed on the drug distribution in the arterial wall since the drug concentration in the blood is typically 3–4 orders of magnitude lower than in the tissue (Fig. S23 of Supplementary Material).

2.3.1 Normalised mean concentration (NMC)

The total NMC in each region of the curved artery at any time point is evaluated by averaging the total concentration over its respective spatial domain as follows:

Table 2 List of model parameters

Parameter	Description	Value	References
Δp	Pressure difference across the arterial wall	70 mmHg	Meyer et al. (1996)
Re_l	Lumenal Reynolds number	400	Formaggia et al. (2010)
ρ_b	Blood density	1060 kg m^{-3}	LaDisa et al. (2003)
ρ_p	Plasma density	1060 kg m^{-3}	Bozsak et al. (2014)
μ_b	Blood dynamic viscosity	3.5×10^{-3} Pa s	Karner and Perktold (2000)
μ_p	Plasma dynamic viscosity	7.2×10^{-4} Pa s	Zunino (2004)
ϕ_{ses}	Porosity of the intima	0.983	Ai and Vafai (2006)
ϕ_m	Porosity of the media	0.258	Ai and Vafai (2006)
ϕ_a	Porosity of the adventitia	0.85	Lovich and Edelman (1996)
ϕ_{pfc}	Porosity of the fibrous cap	0.75	Ferreira et al. (2017)
ϕ_{pc}	Porosity of the plaque core (fibrotic)	0.75	Ferreira et al. (2017)
ϕ_{pc}	Porosity of the plaque core (lipid)	0.5	Naghipoor and Rabczuk (2017)
ϕ_{pc}	Porosity of the plaque core (calcified)	0	Ferreira et al. (2017)
γ_{ses}	Hindrance coefficient in the intima	1	Escuer et al. (2020)
γ_m	Hindrance coefficient in the media	0.845	Escuer et al. (2020)
γ_a	Hindrance coefficient in the adventitia	1	Escuer et al. (2020)
γ_{i_2}	Hindrance coefficient in the plaque	1	Estimated
κ_{ses}	Darcy permeability in the intima	2.2×10^{-16} m^2	Ai and Vafai (2006)
κ_m	Darcy permeability in the media	2×10^{-18} m^2	Zunino (2004)
κ_a	Darcy permeability in the adventitia	2×10^{-18} m^2	Vairo et al. (2010)
κ_{pfc}	Darcy permeability in the fibrous cap	10^{-20} m^2	Ferreira et al. (2018)
κ_{pc}	Darcy permeability in the plaque core (fibrotic)	10^{-20} m^2	Ferreira et al. (2018)
κ_{pc}	Darcy permeability in the plaque core (lipid)	10^{-20} m^2	Ferreira et al. (2018)
κ_{pc}	Darcy permeability in the plaque core (calcified)	0 m^2	Ferreira et al. (2017)
$L_{p,et}$	Hydraulic conductivity of endothelium	2.2×10^{-12} m^2 s kg^{-1}	Bozsak et al. (2014)
$L_{p,iel}$	Hydraulic conductivity of IEL	2.2×10^{-9} m^2 s kg^{-1}	Bozsak et al. (2014)
$L_{p,eel}$	Hydraulic conductivity of EEL	2.2×10^{-9} m^2 s kg^{-1}	Escuer et al. (2020)
C_0	Initial concentration in the polymeric coating	100 mol m^{-3}	Bozsak et al. (2014)
D_c	Effective diffusion coefficient in the coating	10^{-13} m^2 s^{-1}	Mongrain et al. (2005)
D_l	Effective diffusion coefficient in the lumen	4.1×10^{-12} m^2 s^{-1}	Bozsak et al. (2014)
D_{ses}	Effective diffusion coefficient in the intima	1.67×10^{-11} m^2 s^{-1}	Bozsak et al. (2014)
$D_{m,r}$	Effective radial diffusion coefficient in the media	7×10^{-12} m^2 s^{-1}	Levin et al. (2004)
$D_{m,z}$	Effective axial diffusion coefficient in the media	4×10^{-11} m^2 s^{-1}	Levin et al. (2004)
D_a	Effective diffusion coefficient in the adventitia	4×10^{-12} m^2 s^{-1}	Escuer et al. (2020)
D_{pfc}	Effective diffusion coefficient in the fibrous cap	6.23×10^{-12} m^2 s^{-1}	Hossain et al. (2012)
D_{pc}	Effective diffusion coefficient in the plaque core (fibrotic)	6.23×10^{-12} m^2 s^{-1}	Hossain et al. (2012)
D_{pc}	Effective diffusion coefficient in the plaque core (lipid)	6.23×10^{-12} m^2 s^{-1}	Hossain et al. (2012)
D_{pc}	Effective diffusion coefficient in the plaque core (calcified)	0 m^2 s^{-1}	Ferreira et al. (2017)
P_{et}	Permeability of ET	3.6×10^{-6} m s^{-1}	Bozsak et al. (2014)
P_{iel}	Permeability of IEL	9.6×10^{-6} m s^{-1}	Bozsak et al. (2014)
P_{eel}	Permeability of EEL	9.6×10^{-6} m s^{-1}	Escuer et al. (2020)
s_{et}	Sieving coefficient in the ET	0.855	Bozsak et al. (2014)
s_{iel}	Sieving coefficient in the IEL	1	Bozsak et al. (2014)
s_{eel}	Sieving coefficient in the EEL	1	Escuer et al. (2020)
K_d^{ns}	Non-specific equilibrium dissociation constant	2.6×10^{-3} mol m^{-3}	Tzafriri et al. (2009)
k_{on}^{ns}	Non-specific drug binding rate constant	2 m^3 mol^{-1} s^{-1}	Tzafriri et al. (2009)
k_{off}^{ns}	Non-specific drug unbinding rate constant	5.2×10^{-3} s^{-1}	McGinty and Pontrelli (2016)
$b_{max,m}^{ns}$	Non-specific binding site density in the media	0.363 mol m^{-3}	Tzafriri et al. (2012)

Table 2 (continued)

Parameter	Description	Value	References
K_d^s	Specific equilibrium dissociation constant	2×10^{-7} mol m^{-3}	Bierer et al. (1990)
k_{on}^s	Specific drug binding rate constant	800 m^3 mol^{-1} s^{-1}	Wear and Walkinshaw (2007)
k_{off}^s	Specific drug unbinding rate constant	1.6×10^{-4} s^{-1}	McGinty and Pontrelli (2016)
$b_{max,m}^s$	Specific binding site density in the media	0.0033 mol m^{-3}	Tzafriri et al. (2012)
$b_{max,pfc}$	Total binding site density in the fibrous cap	0.03 mol m^{-3}	Ferreira et al. (2018)
$b_{max,pc}$	Total binding site density in the plaque core (fibrotic)	0.03 mol m^{-3}	Ferreira et al. (2018)
$b_{max,pc}$	Total binding site density in the plaque core (lipid)	0.366 mol m^{-3}	Estimated
$b_{max,pc}$	Total binding site density in the plaque core (calcified)	0 mol m^{-3}	Estimated

$$\text{Total NMC}_i(t) = \frac{1}{A_i \cdot C_0} \int_{A_i} \left(c_i + b_i^s + b_i^{ns}\right) \mathrm{d}A, \tag{18}$$

where A_i is the area of the region i that falls within the therapeutic domain considered. The free and bound NMC (both specific and non-specific) of drug in each domain of the arterial wall at any time point are evaluated by averaging the free and bound (specific, S, and non-specific, NS) concentration over its respective spatial domain as follows:

$$\text{Free NMC}_i\ (t) = \frac{1}{A_i \cdot C_0} \int_{A_i} c_i\ \mathrm{d}A, \tag{19}$$

$$\text{S Bound NMC}_i\ (t) = \frac{1}{A_i \cdot C_0} \int_{A_i} b_i^s\ \mathrm{d}A. \tag{20}$$

$$\text{NS Bound NMC}_i\ (t) = \frac{1}{A_i \cdot C_0} \int_{A_i} b_i^{ns}\ \mathrm{d}A. \tag{21}$$

Table 3 Summary of the different cases considered in the simulations. In each case, the initial concentration of drug in the polymeric coating of the stent is fixed to 100 mol m^{-3} (Bozsak et al. 2014)

Case	Radius of curvature (R)	Curvature (κ)	Plaque?
Case 1	∞	0	No
Case 2	60 mm	0.025	No
Case 3	30 mm	0.05	No
Case 4	15 mm	0.1	No
Case 5	7.5 mm	0.2	No
Case 6	3.75 mm	0.4	No
Case 7	15 mm	0.1	Yes (Fibrotic core)
Case 8	15 mm	0.1	Yes (Lipid core)
Case 9	15 mm	0.1	Yes (Calcified core)

2.3.2 Normalised local concentration (NLC)

The total, free and bound NLC in each region of the curved artery are calculated as follows:

$$\text{Total NLC}_i = (c_i + b_i^s + b_i^{ns})/C_0, \tag{22}$$

$$\text{Free NLC}_i = c_i/C_0, \tag{23}$$

$$\text{S Bound NLC}_i = b_i^s/C_0, \tag{24}$$

$$\text{NS Bound NLC}_i = b_i^{ns}/C_0. \tag{25}$$

2.3.3 Binding sites % saturation (% BSS)

The binding site % saturation as a function of time is calculated as (McKittrick et al. 2019):

$$\%\ \text{SBSS}\ (t) = \frac{100}{A_i \cdot b_{max,i}^s} \int_{A_i} b_i^s\ \mathrm{d}A_i. \tag{26}$$

$$\%\ \text{NSBSS}\ (t) = \frac{100}{A_i \cdot b_{max,i}^{ns}} \int_{A_i} b_i^{ns}\ \mathrm{d}A_i. \tag{27}$$

Note that the interaction between the drug and the tissue is only considered in the media and in the plaque regions; therefore, the bound NMC, the bound NLC and the % BSS in the SES and in the adventitia are zero by definition. Moreover, binding is not modelled as separated phases in the plaque; therefore, in these regions the bound NMC and the bound NLC refer to total bound drug and % BSS refers to general binding sites.

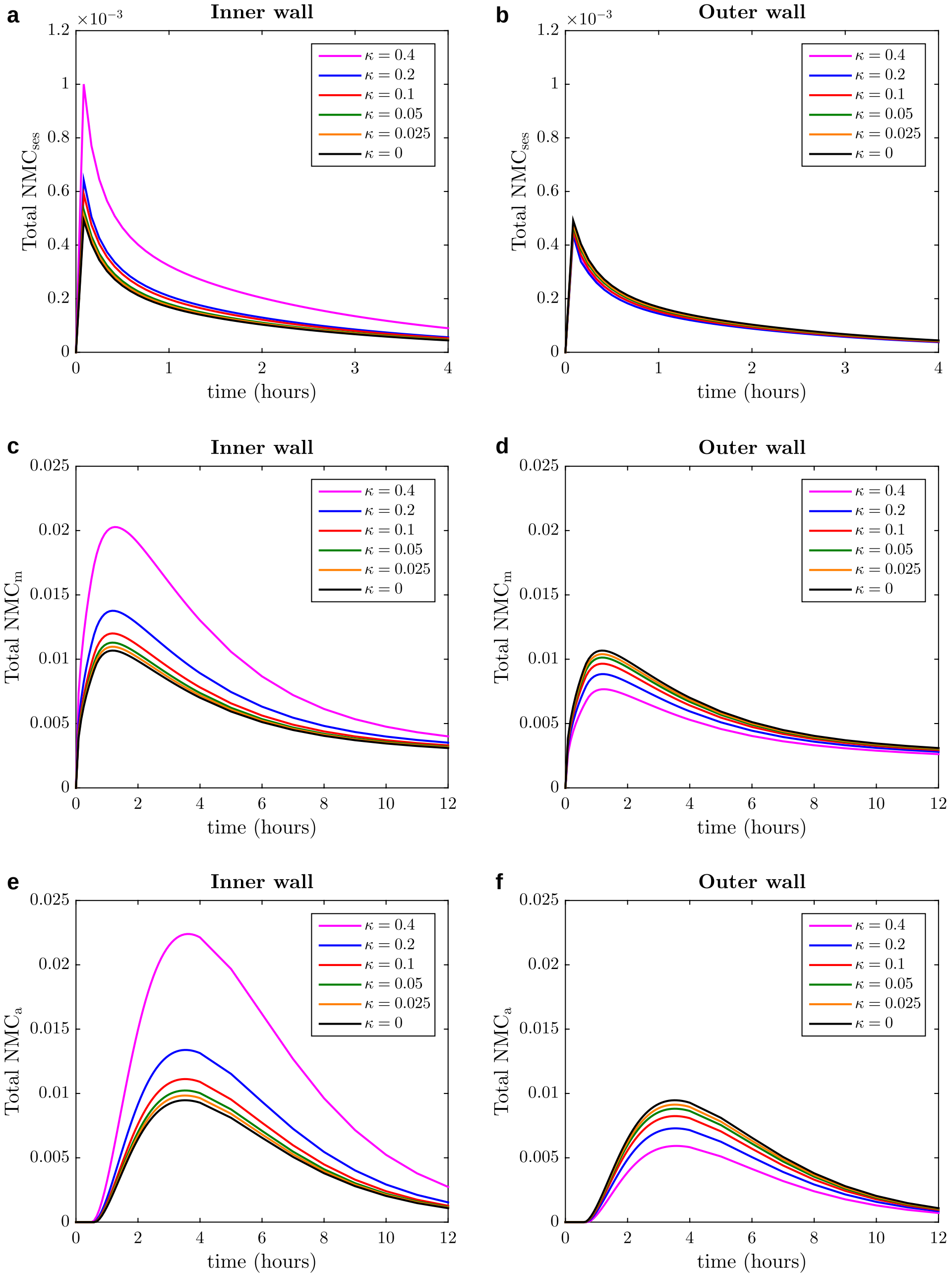

Fig. 4 Time-varying profiles of total normalised mean concentration (NMC) of sirolimus in each layer of the inner and outer walls of the artery: SES (**a**, **b**); media (**c**, **d**); and adventitia (**e**, **f**). The results are shown for the straight model ($\kappa = 0$) and for five different degrees of arterial curvature ($\kappa = 0.025 - 0.4$). Notice that the scales of x- and y-axes for the NMC in the SES (**a**, **b**) are different from the rest of the subfigures

3 Results

3.1 Effect of arterial curvature

The temporal variation of NMC of sirolimus within each layer of the arterial wall, obtained for the simulations corresponding to the straight artery ($\kappa = 0$) and five different degrees of curvature ($\kappa = 0.025 - 0.4$) under healthy conditions (without plaque) is displayed in Fig. 4. Firstly, our results show that the inner wall is more sensitive to changes in κ than the outer wall. Specifically, there is a greater difference between NMC profiles when κ is varied in the inner wall compared with the outer wall. Interestingly, in the inner wall the total NMC in each layer increases with increasing κ, yet in the outer wall the reverse trend is observed.

Since binding is only considered in the media, in Fig. 5 we separate out free NMC from bound NMC (specific and non-specific) in this layer. From these plots it is evident that, for both the inner and outer walls, differences in total NMC as κ is varied are primarily as a result of differences in free NMC, i.e. there is little variation in bound drug NMC as κ is varied. However, there is a clear trend for higher binding site saturation levels in the inner wall with increasing κ, with the opposite trend observed in the outer wall (Fig. 6).

In Fig. 7, we display spatially varying profiles of total NLC of sirolimus in the arterial wall at four different times after stent implantation in a radial section between the middle struts (struts 5 and 6 in each wall). Similar trends are observed as with NMC, i.e. an increase in NLC with increasing κ in the inner wall and the reverse trend in the outer wall. At early times (10 mins), the differences are most notable in the media layer, while at intermediate times (1–4 h), where the drug has reached the adventitia, these trends are observed across the entire arterial wall. Interestingly, at later times (24 h) the NLC concentrations are virtually indistinguishable. In Fig. 8, we also show 2D results over 7 days for curvature ratios of $\kappa = 0.1$ (average curvature) and $\kappa = 0.4$ (maximum curvature). The corresponding plots for the spatially varying profiles of free and bound (specific and non-specific) NLC and binding site % saturation levels, supporting the idea that differences between the inner and outer walls are driven by differences in free drug concentrations, may be found in Supplementary Material (Figs. S3–S7).

In Fig. 8, we plot the spatial variation of total NLC across the inner wall tissue domain and compare $\kappa = 0.1$ with $\kappa = 0.4$ for the first 7 days. This plot shows clear differences in drug deposition, with the higher curvature leading to higher NLC of drug, with the effect most prominent at early times.

3.2 Effect of plaque composition

The time-varying profiles of total NMC of drug for four regions of the inner wall (fibrous cap, plaque core, media and adventitia) of a stented curved segment of an artery ($\kappa = 0.1$) under pathological conditions are illustrated in Fig. 9. The results are shown for three different plaque core compositions: fibrotic, lipid and calcified. Figure 9a displays the total NMC in the fibrous cap, assuming different compositions of plaque core. We observe that the NMC profile is similar regardless of whether the plaque core is fibrotic or lipid, but when the core is considered calcified the peak NMC is approximately 13% greater and the NMC profile tracks slightly below the fibrotic and lipid core cases beyond day 5. This is likely due to the impenetrable nature of the calcification. Figure 9b clearly shows that the plaque composition impacts on the total NMC of drug within the plaque, with a lipid core giving rise to higher NMC levels than a fibrotic core. When we probe the split between free and bound drug (Figs. S14b–S15b), we find that the higher NMC in the lipid core is primarily as a result of the higher levels of bound drug, following the higher density of drug binding sites. Since the model assumes that calcified plaque is impenetrable to drug, the total NMC is zero by definition. Figure 9c and 9d shows not only that the presence of plaque significantly influences the time-varying total NMC of drug within the media and adventitia, respectively, but also that the composition of the plaque core leads to modest variation in the total NMC of drug within these layers. The presence of the plaque leads to a delay and reduction in magnitude of the peak NMC of drug in the media; however, the plaque appears to act as source for drug, ensuring that NMC drug levels in the media are maintained at higher levels for longer. While there is a slight delay in peak bound drug NMC in the media (Figs. S15c–S15d), receptors and ECM binding sites are saturated at higher levels for longer in the case of the presence of plaque (Fig. S16). The corresponding spatially varying profiles of total NLC of sirolimus within the plaque and arterial wall at four different times after stent implantation are shown in Fig. 10. The rest of the figures for the temporal profiles of NMC and binding site % saturation (Figs. S14–S16) and for the spatially varying profiles of NLC (Figs. S17–S21) may be found in Supplementary Material.

4 Discussion

This study has yielded a number of interesting points that we wish to emphasise. Our results clearly demonstrate that curvature leads to the asymmetric distribution of drug in the arterial wall, with the level of asymmetry

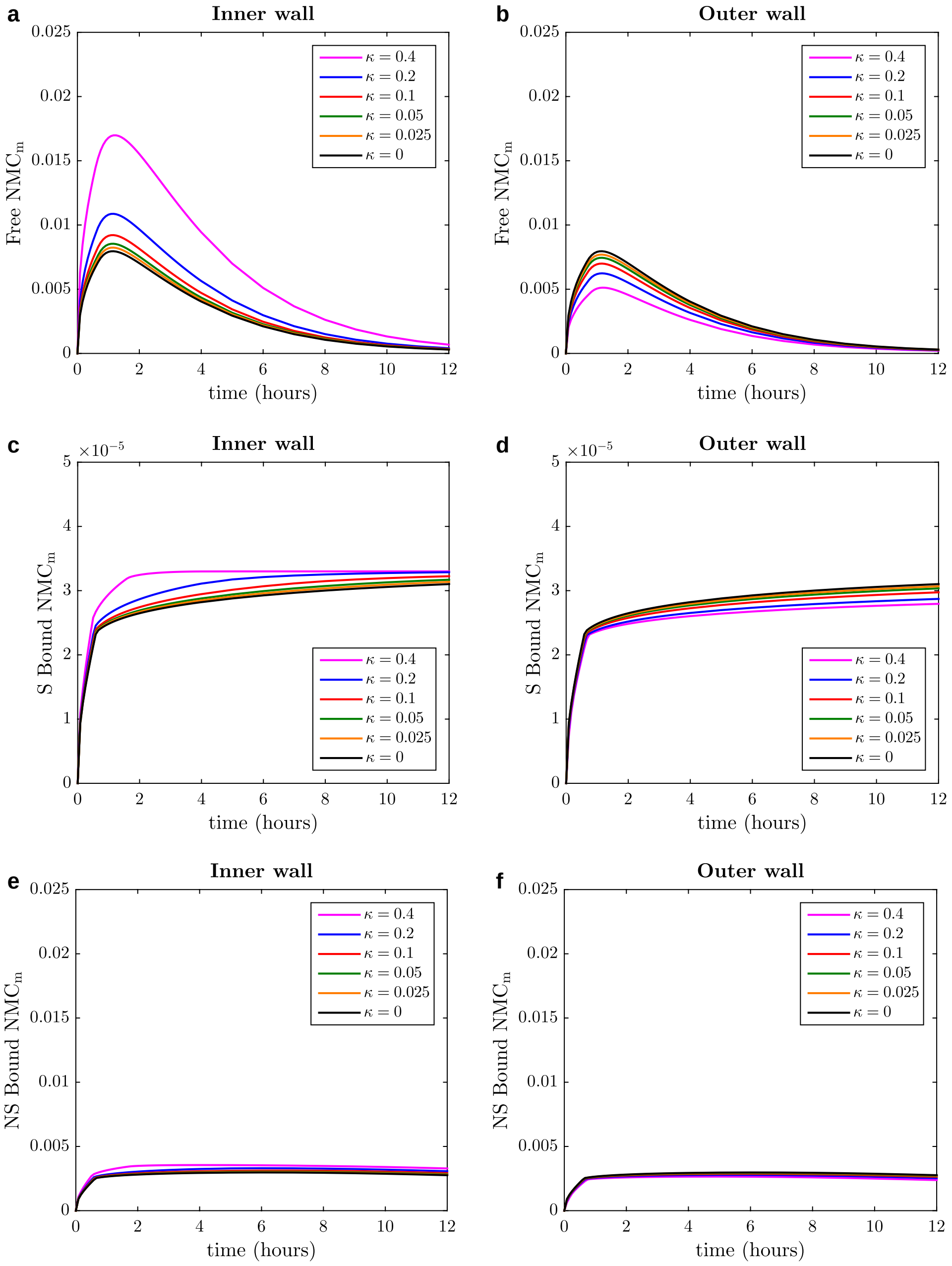

Fig. 5 Time-varying profiles of free NMC (**a**, **b**), specific (S) bound NMC (**c**, **d**) and non-specific (NS) bound NMC (**e**, **f**) of sirolimus in the media layer of the inner and outer walls of the artery, respectively. The results are shown for the straight model ($\kappa = 0$) and for five different degrees of arterial curvature ($\kappa = 0.025 - 0.4$). Notice that the scales of y-axes for the specific (S) bound NMC (**c**, **d**) are different from the rest of the subfigures

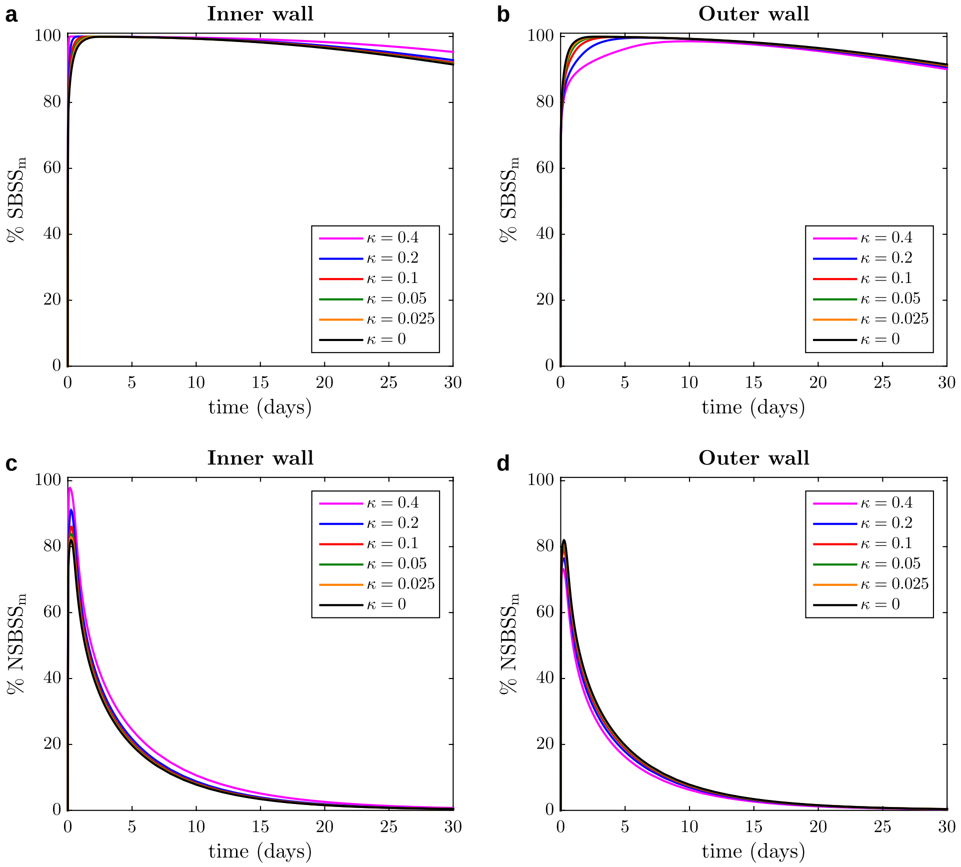

Fig. 6 Specific (target receptor) and non-specific (ECM) binding site % saturation in the media layer of the inner and outer walls of the artery as a function of time, respectively. The results are shown for the straight model ($\kappa = 0$) and for five different degrees of arterial curvature ($\kappa = 0.025 - 0.4$)

highly dependent on the level of curvature. Specifically, with increasing curvature, more of the drug ‘partitions’ into the inner wall. We have established (Supplementary Material) that the total mass of drug delivered to the wall is consistent, regardless of level of curvature, and that the level of curvature does not influence the drug release rate. To probe this further, we calculated the Dean number ($De_l = Re_l\sqrt{\kappa}$) for the flow in the curved vessel and Peclet number for transport in the wall under healthy conditions. There is a nonlinear increase in Dean number with curvature and consequent asymmetry in the fluid flow pattern in the lumen (Figs. S24 and S25 of Supplementary Material, respectively). In Fig. S26 of Supplementary Material, we plot the magnitude of the radial component of the plasma filtration velocity and the radial Peclet number ($Pe_{r,i1} = u_{r,i1}\delta_{i1}/D_{r,i1}$) across the inner and outer walls of the artery, respectively, for the different cases of curvature. These plots suggest that curvature has the effect of increasing the radial Peclet number in the inner wall more than in the outer wall, as a result of increased plasma filtration. This asymmetric distribution, as a result of fluid forces, is likely to be exacerbated in more realistic patient-specific geometries. The implication of this finding for stent manufacturers is that care should be taken when considering the drug loading on the stent, since this asymmetric drug distribution could, in theory at least, result in insufficient drug concentrations reaching the outer wall, while the concentrations reaching the inner wall could be too high. The consequence for the patient could well be asymmetric neointimal growth as part of the healing process. While it is now possible to reconstruct patient-specific 3D lumen geometries (Chiastra et al. 2018), further work is required to develop robust methods for accurate reconstruction of the wall that discriminates between different components

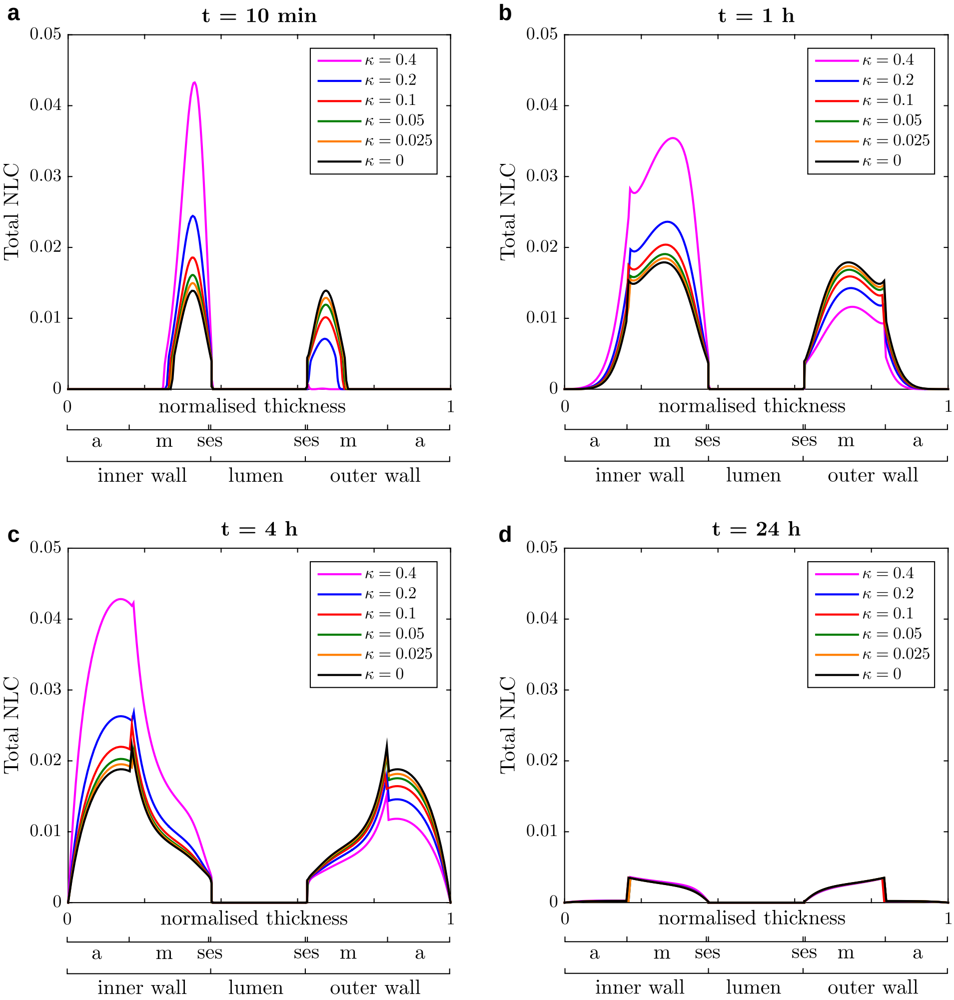

Fig. 7 Spatially varying profiles of total normalised local concentration (NLC) of sirolimus in the tissue, calculated as $(c_i + b_i^s + b_i^{ns})/C_0$, at 10 min (**a**), 1 h (**b**), 4 h (**c**) and 1 day (**d**) after stent implantation. The results are shown for the straight model ($\kappa = 0$) and for five different degrees of arterial curvature ($\kappa = 0.025 - 0.4$) in a radial section between the middle stent struts. Note that lumen diameter is not drawn to scale

of tissue and plaque. Even when such methodologies are available, a severe limitation is accurate characterisation of tissue and plaque properties.

Plaque core composition influences drug concentrations within the plaque core itself, owing to the differing density of binding sites. Our results suggest that lipidic plaques give rise to higher drug concentrations than fibrotic plaques, while calcified plaques are impenetrable to drug as per our model assumptions. The impenetrability of calcified plaque has potentially important implications and, if large enough in extent, may act as a significant barrier to drug reaching the arterial tissue where proliferating and migrating cells reside. Indeed, Tzafriri et al. (2017) demonstrated that calcified plaque limits intravascular drug delivery and found that controlled orbital atherectomy can lead to improved drug delivery. Our results suggest that the presence of plaque, regardless of the composition of the core, can slightly delay receptor saturation in the media, a quantity that has widely been associated with efficacy (e.g. Tzafriri et al. 2012; McKittrick et al. 2019). Perhaps more importantly, our results indicate that plaque can act as a source of drug ensuring that decline in

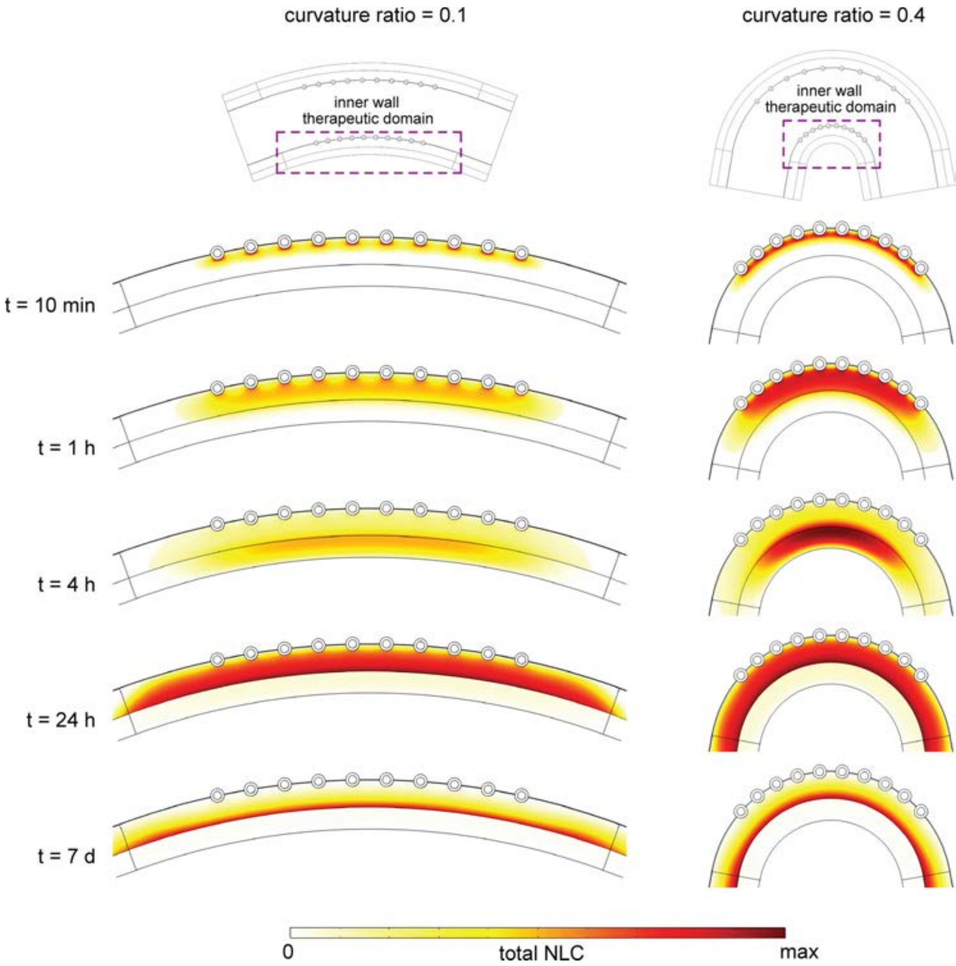

Fig. 8 Spatial variation of total NLC of sirolimus, calculated as $(c_i + b_i^s + b_i^{ns})/C_0$, within the inner wall of the artery at five different time points (t = 10 min, t = 1 h, t = 4 h, t = 24 h and t = 7 days) for curvature ratios of $\kappa = 0.1$ (average curvature ratio) and $\kappa = 0.4$, respectively. For each time point, the same colour scale is used for both cases of curvature. The maximum values of total NLC of drug chosen for each time point are the following: max = 6.23×10^{-2} at t = 10 min; max = 4.16×10^{-2} at t = 1 h; max = 4.56×10^{-2} at t = 4 h; max = 3.65×10^{-3} at t = 24 h; and max = 1.74×10^{-3} at t = 7 days. Tables with the maximum values at each time point may be found in Section S4 of Supplementary Material

receptor saturation is significantly reduced compared with the healthy case. This is in agreement with the somewhat simpler one-dimensional model devised by McGinty et al. (2010) who noted that the plaque may act as a reservoir for drug. The implication is that in diseased states, binding sites may well be saturated for longer, i.e. patients receive an effective drug dose for longer. However, these findings differ from those reported in the work of Tzafriri et al. (2010), where it was found, somewhat counterintuitively, that drug content in human aortae inversely correlated with lipid content. One potential explanation provided, specifically for paclitaxel, was the displacement of tubulin-expressing cells by lipid pools, potentially important given paclitaxel's ability to bind specifically to tubulin. Since our findings reveal that drug distribution and retention is dependent on plaque composition, stent manufacturers

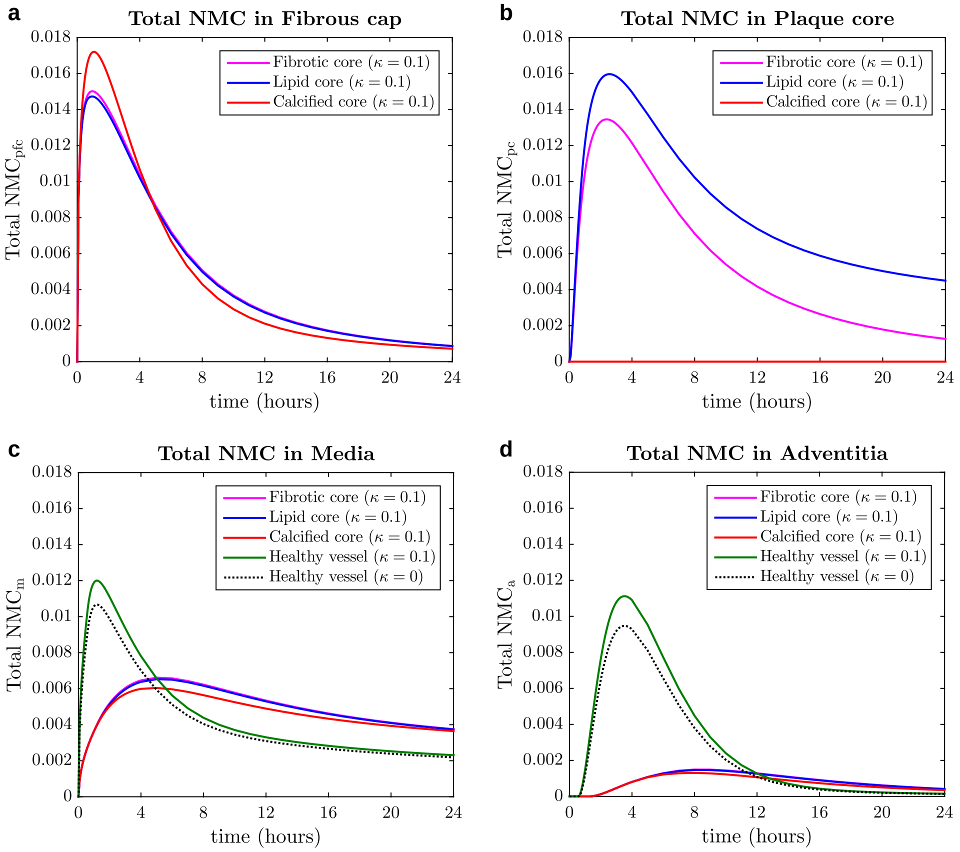

Fig. 9 Time-varying profiles of the total NMC of sirolimus in the fibrous cap (**a**), plaque core (**b**), media (**c**) and adventitia (**d**) within the inner wall of the artery for a curvature ratio of $\kappa = 0.1$ (average curvature ratio). The results are shown for three different plaque core compositions: fibrotic, lipid and calcified. In case of the media and adventitia, the results are also shown for the straight model ($\kappa = 0$) and for a curvature ratio of $\kappa = 0.1$, both under healthy conditions (i.e. healthy vessel without plaque)

are advised to consider that a 'one-size-fits-all' stent drug dose may not be adequate for all patients, and could, at least in part, be contributing to differences in outcome from patient to patient that are observed clinically.

4.1 Limitations of this work

We should emphasise that the results in the present paper are heavily dependent on the model parameter values and binding model employed for the different types of plaque. This is primarily because there is a lack of data available in the literature for the different components of plaque to fully parametrise such a model. We have taken the majority of our plaque parameter values from the literature, but necessarily have had to estimate some of them (Table 2). Given the paucity of data on drug transport and binding properties of atherosclerotic plaque, despite the obvious importance and relevance to the condition being treated by stents, there is an urgent need for further research in this area so that models such as the one presented here may be furnished with the most realistic and reliable parameter values. This is the key limitation of the present work, although we now comprehensively discuss the remaining limitations.

We have employed a simplified 2D coronary artery model with curvature in this study. Our plaque geometry is also a simplification. The geometry we have chosen is based on Lee and Libby (1997) and incorporates the general features of human atherosclerotic plaque: a core that can be either lipid, fibrous or calcified, surrounded by fibrous tissue. What tends to be observed clinically are plaques consisting of multiple material components, in often complex geometrical

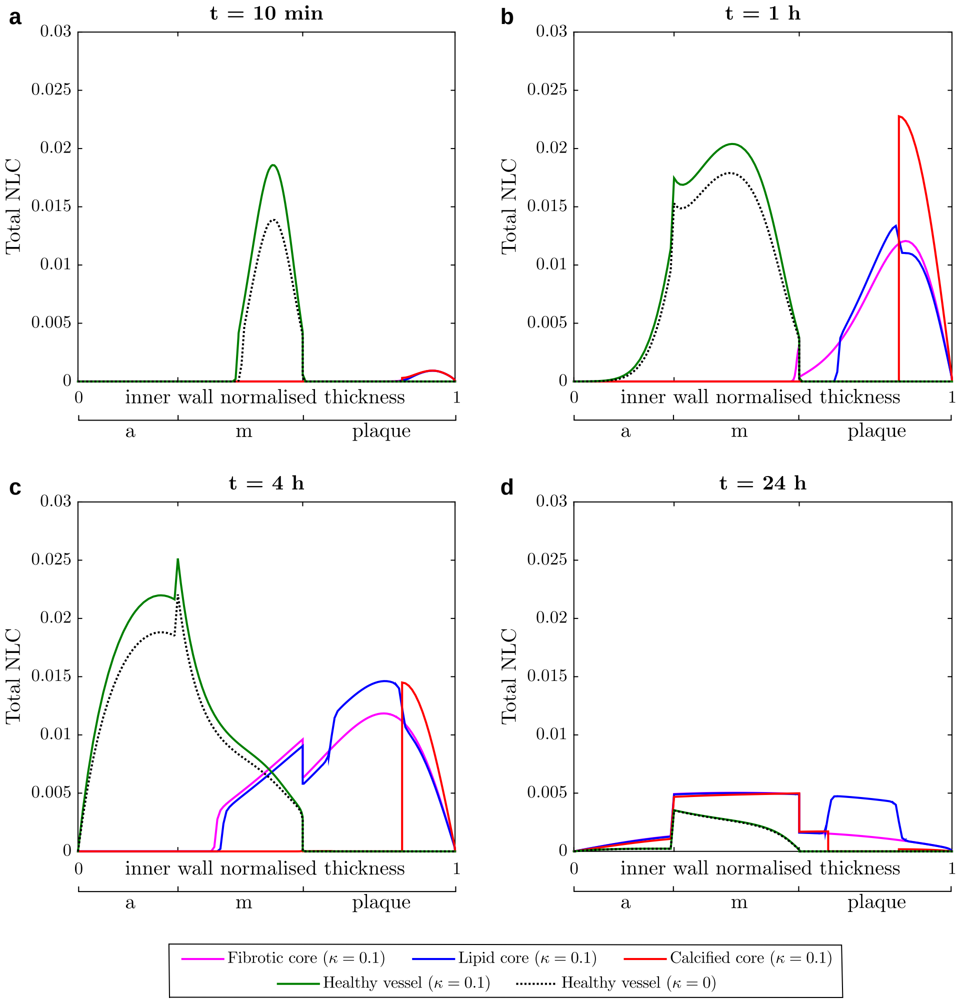

Fig. 10 Spatially varying profiles of total NLC of sirolimus, calculated as $(c_i + b_i^s + b_i^{ns})/C_0$, in the inner wall of the artery at 10 min **a**, 1 h **b**, 4 h **c** and 1 day **d** after stent implantation in a radial section between the middle stent struts. The results are shown for three different plaque core compositions: fibrotic, lipid and calcified for a curvature ratio of $\kappa = 0.1$ (average curvature ratio). Moreover, the results for the straight model ($\kappa = 0$) and for a curvature ratio of $\kappa = 0.1$, both under healthy conditions (i.e. healthy vessel without plaque) are shown

configurations, with vulnerable plaques in particular typically displaying a thin fibrous cap separating a lipid rich core from the lumen. The plaque composition, structure and geometry in reality are patient-specific, with each of these likely to affect drug distribution.

While 3D patient-specific models are now common when considering haemodynamics in stented arteries, these models often neglect, or do not adequately consider the state of the art in terms of modelling drug release and retention. There are many aspects related to drug release and subsequent redistribution in tissue that we do not fully understand, which is why the majority of models focussing on the drug kinetics are still considering lower-dimensional models. In this work, we focussed on two of these aspects, curvature and plaque composition, with our results providing evidence to support the investigation of a 3D patient-specific model in the future.

In this work, the complex geometry of the stent is simplified to ten equally spaced circular struts. We have verified that using square struts with the same coating area and drug loading gives rise to results that are almost indistinguishable. We appreciate that there are a variety of stents on the market of varying strut size, coating thickness and drug loading. Comparing these aspects was not the focus of this study, although we note that varying each of these aspects will have an impact on the results.

In terms of modelling drug release from the stent coating, a simple diffusion model is considered in this work in line with a large number of mathematical and computational models in the existing literature. The diffusion coefficient we have selected is at the upper end of the range considered in the literature and implies fast release kinetics. However, depending on the particular stent, drug and coating under consideration, a more complex nonlinear model that accounts for the combined effects of diffusion, dissolution and solubility in the polymer coating may be required in order to describe drug release from the device (McGinty and Pontrelli 2015).

4.2 Conclusions

In this paper, we have provided a comprehensive study of the influence of the vessel curvature and plaque composition on drug transport within the arterial wall, described as a multi-layered anisotropic structure, under healthy and pathological conditions. We have performed 2D idealised simulations to quantify the impact of such geometrical and compositional variation on spatiotemporal uptake of drug in tissue. Our findings demonstrate that arterial curvature and plaque composition have important influences on the spatiotemporal distribution of drug, with potential implications in terms of effectiveness of the treatment. Since the majority of computational models tend to neglect these features, these models are likely to be under- or over-estimating drug uptake and redistribution in arterial tissue.

Acknowledgements This work was funded by the Spanish Ministry of Economy, Industry and Competitiveness through research Project No. DPI2016-76630-C2-1-R and Grant No. BES-2014-069737; the Department of Industry and Innovation (Government of Aragon) through research group Grant No. T24-17R (Fondo Social Europeo) and research Project No. LMP121-18; and the Carlos III Health Institute (ISCIII) through the CIBER initiative. Dr. McGinty acknowledges funding provided by EPSRC (Grant No. EP/S030875/1).

Compliance with ethical standards

Conflict of interest The authors declare that they have no conflict of interest.

References

Ai L, Vafai K (2006) A coupling model for macromolecule transport in a stenosed arterial wall. Int J Heat Mass Transf 49(9–10):1568–1591

Alfonso F, Byrne RA, Rivero F, Kastrati A (2014) Current treatment of in-stent restenosis. J Am Coll Cardiol 63(24):2659–2673

Bierer BE, Mattila PS, Standaert RF, Herzenberg LA, Burakoff SJ, Crabtree G, Schreiber SL (1990) Two distinct signal transmission pathways in t lymphocytes are inhibited by complexes formed between an immunophilin and either fk506 or rapamycin. Proc Nat Acad Sci 87(23):9231–9235

Bozsak F, Chomaz JM, Barakat AI (2014) Modeling the transport of drugs eluted from stents: physical phenomena driving drug distribution in the arterial wall. Biomech Model Mechanobiol 13(2):327–347

Byrne RA, Joner M, Kastrati A (2015) Stent thrombosis and restenosis: what have we learned and where are we going? the andreas grüntzig lecture esc 2014. Eur Heart J 36(47):3320–3331

Caputo M, Chiastra C, Cianciolo C, Cutrì E, Dubini G, Gunn J, Keller B, Migliavacca F, Zunino P (2013) Simulation of oxygen transfer in stented arteries and correlation with in-stent restenosis. Int J Numer Methods Biomed Eng 29(12):1373–1387

Chiastra C, Migliavacca F, Martínez MÁ, Malvè M (2014) On the necessity of modelling fluidstructure interaction for stented coronary arteries. J Mech Behav Biomed Mater 34:217–230

Chiastra C, Migliori S, Burzotta F, Dubini G, Migliavacca F (2018) Patient-specific modeling of stented coronary arteries reconstructed from optical coherence tomography: towards a widespread clinical use of fluid dynamics analyses. J Cardiovasc Transl Res 11(2):156–172

Creel CJ, Lovich MA, Edelman ER (2000) Arterial paclitaxel distribution and deposition. Circ Res 86(8):879–884

Cutrì E, Zunino P, Morlacchi S, Chiastra C, Migliavacca F (2013) Drug delivery patterns for different stenting techniques in coronary bifurcations: a comparative computational study. Biomech Model Mechanobiol 12(4):657–669

Escuer J, Cebollero M, Peña E, McGinty S, Martínez MA (2020) How does stent expansion alter drug transport properties of the arterial wall? J Mech Behav Biomed Mater 104:103610. https://pubmed.ncbi.nlm.nih.gov/32174384/

Ferreira JA, Gonçalves L, Naghipoor J, de Oliveira P, Rabczuk T (2017) The influence of atherosclerotic plaques on the pharmacokinetics of a drug eluted from bioabsorbable stents. Math Biosci 283:71–83

Ferreira JA, Gonçalves L, Naghipoor J, de Oliveira P, Rabczuk T (2018) The effect of plaque eccentricity on blood hemodynamics and drug release in a stented artery. Med Eng Phys 60:47–60

Formaggia L, Quarteroni A, Veneziani A (2010) Cardiovascular mathematics: modeling and simulation of the circulatory system, vol 1. Springer, Berlin

Frangos SG, Gahtan V, Sumpio B (1999) Localization of atherosclerosis: role of hemodynamics. Arch Surg 134(10):1142–1149

Hossain SS, Hossainy SF, Bazilevs Y, Calo VM, Hughes TJ (2012) Mathematical modeling of coupled drug and drug-encapsulated nanoparticle transport in patient-specific coronary artery walls. Comput Mech 49(2):213–242

Jayarama G (2006) Flow in tubes with complicated geometries with special application to blood flow in large arteries. In: Misra JC (ed) Biomathematics: modelling and simulation. World Scientific, Singapore, pp 279–304. https://www.worldscientific.com/worldscibooks/10.1142/5058

Karner G, Perktold K (2000) Effect of endothelial injury and increased blood pressure on albumin accumulation in the arterial wall: a numerical study. J Biomech 33(6):709–715

Karner G, Perktold K, Zehentner HP (2001) Computational modeling of macromolecule transport in the arterial wall. Comput Methods Biomech Biomed Eng 4(6):491–504

Kedem O, Katchalsky A (1958) Thermodynamic analysis of the permeability of biological membranes to non-electrolytes. Biochim Biophys Acta 27:229–246

Kern MJ, Puri S, Bach RG, Donohue TJ, Dupouy P, Caracciolo EA, Craig WR, Aguirre F, Aptecar E, Wolford TL et al (1999) Abnormal coronary flow velocity reserve after coronary artery stenting in patients: role of relative coronary reserve to assess potential mechanisms. Circulation 100(25):2491–2498

Kosa I, Blasini R, Schneider-Eicke J, Dickfeld T, Neumann FJ, Ziegler S, Matsunari I, Neverve J, Schömig A, Schwaiger M (1999) Early recovery of coronary flow reserve after stent implantation as assessed by positron emission tomography. J Am Coll Cardiol 34(4):1036–1041

LaDisa JF, Guler I, Olson LE, Hettrick DA, Kersten JR, Warltier DC, Pagel PS (2003) Three-dimensional computational fluid dynamics modeling of alterations in coronary wall shear stress produced by stent implantation. Ann Biomed Eng 31(8):972–980

Lee RT, Libby P (1997) The unstable atheroma. Arterioscler Thromb Vasc Biol 17(10):1859–1867

Levin AD, Vukmirovic N, Hwang CW, Edelman ER (2004) Specific binding to intracellular proteins determines arterial transport properties for rapamycin and paclitaxel. Proc Nat Acad Sci USA 101(25):9463–9467

Levitt DG (1975) General continuum analysis of transport through pores. I. Proof of onsager's reciprocity postulate for uniform pore. Biophys J 15(6):533–551

Lovich MA, Edelman ER (1996) Computational simulations of local vascular heparin deposition and distribution. Am J Physiol Heart Circ Physiol 271(5):H2014–H2024

Mandal AP, Mandal PK (2018) Distribution and retention of drug through an idealised atherosclerotic plaque eluted from a half-embedded stent. Int J Dyn Control 6(3):1183–1193

Martin DM, Boyle FJ (2011) Drug-eluting stents for coronary artery disease: a review. Med Eng Phys 33(2):148–163

McGinty S (2014) A decade of modelling drug release from arterial stents. Math Biosci 257:80–90

McGinty S, Pontrelli G (2015) A general model of coupled drug release and tissue absorption for drug delivery devices. J Control Release 217:327–336

McGinty S, Pontrelli G (2016) On the role of specific drug binding in modelling arterial eluting stents. J Math Chem 54(4):967–976

McGinty S, McKee S, Wadsworth RM, McCormick C (2010) Modelling drug-eluting stents. Math Med Biol J IMA 28(1):1–29

McKittrick C, Kennedy S, Oldroyd K, McGinty S, McCormick C (2016) Modelling the impact of atherosclerosis on drug release and distribution from coronary stents. Ann Biomed Eng 44(2):477–487

McKittrick CM, McKee S, Kennedy S, Oldroyd K, Wheel M, Pontrelli G, Dixon S, McGinty S, McCormick C (2019) Combining mathematical modelling with in vitro experiments to predict in vivo drug-eluting stent performance. J Control Release 303:151–161

Meyer G, Merval R, Tedgui A (1996) Effects of pressure-induced stretch and convection on low-density lipoprotein and albumin uptake in the rabbit aortic wall. Circ Res 79(3):532–540

Mongrain R, Leask R, Brunette J, Faik I, Bulman-Feleming N, Nguyen T (2005) Numerical modeling of coronary drug eluting stents. Stud Health Technol Inf 113:443–458

Naghipoor J, Rabczuk T (2017) A mechanistic model for drug release from plga-based drug eluting stent: a computational study. Comput Biol Med 90:15–22

Roth GA, Abate D, Abate KH, Abay SM, Abbafati C, Abbasi N, Abbastabar H, Abd-Allah F, Abdela J, Abdelalim A et al (2018) Global, regional, and national age-sex-specific mortality for 282 causes of death in 195 countries and territories, 1980–2017: a systematic analysis for the global burden of disease study 2017. The Lancet 392(10159):1736–1788

Rozie S, De Weert T, De Monyé C, Homburg P, Tanghe H, Dippel D, Van der Lugt A (2009) Atherosclerotic plaque volume and composition in symptomatic carotid arteries assessed with multidetector ct angiography; relationship with severity of stenosis and cardiovascular risk factors. Eur Radiol 19(9):2294–2301

Santamarina A, Weydahl E, Siegel JM, Moore JE (1998) Computational analysis of flow in a curved tube model of the coronary arteries: effects of time-varying curvature. Ann Biomed Eng 26(6):944–954

Tarbell JM (2003) Mass transport in arteries and the localization of atherosclerosis. Annu Rev Biomed Eng 5(1):79–118

Tzafriri AR, Levin AD, Edelman ER (2009) Diffusion-limited binding explains binary dose response for local arterial and tumour drug delivery. Cell Prolif 42(3):348–363

Tzafriri AR, Vukmirovic N, Kolachalama VB, Astafieva I, Edelman ER (2010) Lesion complexity determines arterial drug distribution after local drug delivery. J Control Release 142(3):332–338

Tzafriri AR, Groothuis A, Price GS, Edelman ER (2012) Stent elution rate determines drug deposition and receptor-mediated effects. J Control Release 161(3):918–926

Tzafriri AR, Garcia-Polite F, Zani B, Stanley J, Muraj B, Knutson J, Kohler R, Markham P, Nikanorov A, Edelman ER (2017) Calcified plaque modification alters local drug delivery in the treatment of peripheral atherosclerosis. J Control Release 264:203–210

Vairo G, Cioffi M, Cottone R, Dubini G, Migliavacca F (2010) Drug release from coronary eluting stents: a multidomain approach. J Biomech 43(8):1580–1589

Wang S, Vafai K (2015) Analysis of low density lipoprotein (ldl) transport within a curved artery. Ann Biomed Eng 43(7):1571–1584

Wear MA, Walkinshaw MD (2007) Determination of the rate constants for the fk506 binding protein/rapamycin interaction using surface plasmon resonance: An alternative sensor surface for ni2+-nitrilotriacetic acid immobilization of his-tagged proteins. Anal Biochem 371(2):250–252

Zunino P (2004) Multidimensional pharmacokinetic models applied to the design of drug-eluting stents. Cardiovasc Eng Int J 4(2):181–191

Publisher's Note Springer Nature remains neutral with regard to jurisdictional claims in published maps and institutional affiliations.

Noname manuscript No.
(will be inserted by the editor)

Supplementary Online Material for Influence of Vessel Curvature and Plaque Composition on Drug Transport in the Arterial Wall following Drug-eluting Stent Implantation

Javier Escuer · Irene Aznar · Christopher McCormick · Estefanía Peña · Sean McGinty · Miguel A. Martínez

Received: date / Accepted: date

This document includes the following sections:

- S1. Limitations of this work
- S2. Supplemental equations
- S3. Supplemental figures
- S4. Supplemental tables

S1 Limitations of this work

We would like to note that the present work has a number of limitations, as we now discuss. Regarding the geometry of the model, 2D geometries corresponding to idealised representations of longitudinal sections of a coronary artery under healthy and pathological conditions have been considered in this study instead of more realistic 3D patient-specific geometries obtained from medical images. It should be noted that a 2D-axisymmetric approach, normally used for straight vessel geometries, cannot be taken into account here since this study focuses on arterial segments with curvature. We did a comparative analysis of the results obtained between considering a 2D or a 2D-axysimmetric representation of a straight artery segment and we verified that the results revealed that although the magnitudes of drug concentration in the respective wall layers varies slightly, the overall behaviour and the conclusions drawn are quite similar (results not shown). We have also considered a simple representation of the device instead of a 3D complex shape corresponding to commercial designs of DES. Such realistic models in 3D significantly increase the computational cost of the numerical analysis performed and detract from the key objective of this work which was to study the influence of the vessel curvature and plaque composition on drug transport in the tissue. In regard to the parameters involved in the computational model, the vast majority were obtained from existing experimental data or other computational models. The problem is that these data are taken from different species and may not be representative of the corresponding parameters in human tissue. Moreover, there is a lack of appropriate transport and reaction parameters for the adventitia layer and for the atherosclerotic plaque, therefore these parameters had to be estimated. In terms of modelling drug release from the stent coating, a simple diffusion model is considered in this work in line with a large number of mathematical and computational models in the existing literature. However, depending on the particular stent, drug and coating under consideration, a

---

J. Escuer
Aragón Institute for Engineering Research (I3A), University of Zaragoza, Spain.

I. Aznar
Aragón Institute for Engineering Research (I3A), University of Zaragoza, Spain.

C. McCormick
Department of Biomedical Engineering, University of Strathclyde, Glasgow, UK.

E. Peña
Aragón Institute for Engineering Research (I3A), University of Zaragoza, Spain.
Biomedical Research Networking Center in Bioengineering, Biomaterials and Nanomedicine (CIBER-BBN), Spain.

S. McGinty
Division of Biomedical Engineering, University of Glasgow, Glasgow, UK.

M. A. Martínez
Aragón Institute for Engineering Research (I3A), University of Zaragoza, Spain.
Biomedical Research Networking Center in Bioengineering, Biomaterials and Nanomedicine (CIBER-BBN), Spain.
María de Luna, 3. E-50018 Zaragoza (Spain).
E-mail: miguelam@unizar.es

more complex nonlinear model that accounts for the combined effects of diffusion, dissolution and solubility in the polymer coating may be required in order to describe drug release from the device [McGinty and Pontrelli, 2015]. Furthermore, in terms of modelling drug transport within the arterial wall, a single phase nonlinear saturable reversible binding model is taken into account. Therefore, in this model we do not take into consideration the effect of binding as two separate phases (drug bound to specific receptors and non-specific general extracellular matrix sites), the benefits and drawbacks of which are discussed in McGinty and Pontrelli [2016].

S2 Supplemental equations

S2.1 Kedem-Katchalsky equations for fluid flux

Endothelium (ET), internal and external elastic laminae (IEL and EEL, respectively) are treated as semipermeable membranes and the fluid flux across them, $J_{v,j}$, is described by the Kedem-Katchalsky equations [Kedem and Katchalsky, 1958]. Neglecting the osmotic contribution as an approximation [Formaggia et al., 2010; Bozsak et al., 2014; Escuer et al., 2020], the Kedem-Katchalsky equations for fluid flux can be simplified as:

$$J_{v,j} = L_{p,j} \Delta p_j, \tag{1}$$

where the subscript $j = \{et, etp, iel, ielp, eel\}$ denotes the semipermeable membranes considered: the lumen-SES interface (et), the lumen-plaque interface (etp), the SES-media interface (iel), the plaque-media interface (ielp) and the media-adventitia interface (eel), respectively; $L_{p,j}$ is the membrane hydraulic conductivity and; Δp_j the pressure drop across each semipermeable membrane. Therefore, the volume flux J_v for each membrane in case of healthy conditions (without plaque) in both inner and outer walls of the artery can be formulated as follows:

$$J_{v,et} = L_{p,et} \Delta p_{et} = L_{p,et}(p_l - p_{ses}), \tag{2}$$

$$J_{v,iel} = L_{p,iel} \Delta p_{iel} = L_{p,iel}(p_{ses} - p_m), \tag{3}$$

$$J_{v,eel} = L_{p,eel} \Delta p_{eel} = L_{p,eel}(p_m - p_a), \tag{4}$$

where l, ses, m and a denote the lumen, subendothelial space, media and adventitia, respectively. In the case of presence of plaque in the inner wall of the artery, the volume flux J_v in the boundaries corresponding to the plaque can be formulated as follows:

$$J_{v,etp} = L_{p,et} \Delta p_{etp} = L_{p,et}(p_l - p_{pfc}), \tag{5}$$

$$J_{v,ielp} = L_{p,iel} \Delta p_{iel} = L_{p,iel}(p_{pfc} - p_m), \tag{6}$$

where pfc denotes the plaque fibrous cap. In regions where the endothelium is considered denuded, the volume flux $J_{v,et}$ simplifies to continuity of pressure, i.e. $p_l = p_{ses}$ under healthy conditions or $p_l = p_{pfc}$ under unhealthy conditions.

S2.2 Kedem-Katchalsky equations for solute flux

Discontinuity of solute flux across the semipermeable membranes, $J_{s,j}$, is also governed by the Kedem-Katchalsky equations [Kedem and Katchalsky, 1958]:

$$J_{s,j} = P_j \Delta c_j + s_j \bar{c}_j J_{v,j}, \tag{7}$$

where P_j is the permeability of each semipermeable membrane; Δc_j is the solute concentration difference; s_j is the sieving coefficient and; $\bar{c}_j$ is the weighted average concentration on either side of the corresponding membrane computed as [Levitt, 1975; Bozsak et al., 2014; Escuer et al., 2020]:

$$\bar{c}_{et} = \frac{1}{2}(c_l + c_{ses}) + \frac{s_{et} J_{v,et}}{12 P_{et}}(c_l - c_{ses}), \tag{8}$$

$$\bar{c}_{etp} = \frac{1}{2}(c_l + c_{pfc}) + \frac{s_{et} J_{v,etp}}{12 P_{et}}(c_l - c_{pfc}), \tag{9}$$

$$\bar{c}_{iel} = \frac{1}{2}(c_{ses} + c_m) + \frac{s_{iel} J_{v,iel}}{12 P_{iel}}(c_{ses} - c_m), \tag{10}$$

$$\bar{c}_{ielp} = \frac{1}{2}(c_{pfc} + c_m) + \frac{s_{iel} J_{v,ielp}}{12 P_{iel}}(c_{pfc} - c_m), \tag{11}$$

$$\bar{c}_{eel} = \frac{1}{2}(c_m + c_{adv}) + \frac{s_{eel} J_{v,eel}}{12 P_{eel}}(c_m - c_{adv}). \tag{12}$$

Therefore, the solute flux J_s for each membrane in case of healthy conditions (without plaque) in both inner and outer walls of the artery can be formulated as follows:

$$J_{s,et} = P_{et}(c_l - c_{ses}) + s_{et} \bar{c}_{et} J_{v,et}, \tag{13}$$

$$J_{s,iel} = P_{iel}(c_{ses} - c_m) + s_{iel} \bar{c}_{iel} J_{v,iel}, \tag{14}$$

$$J_{s,eel} = P_{eel}(c_m - c_a) + s_{eel} \bar{c}_{eel} J_{v,eel}. \tag{15}$$

In the case of presence of plaque in the inner wall of the artery, the volume flux J_v in the boundaries corresponding to the plaque can be formulated as follows:

$$J_{s,etp} = P_{et}(c_l - c_{pfc}) + s_{et} \bar{c}_{etp} J_{v,etp}, \tag{16}$$

$$J_{s,ielp} = P_{iel}(c_{pfc} - c_m) + s_{iel} \bar{c}_{ielp} J_{v,ielp}. \tag{17}$$

S2.3 Normalised mean concentration (NMC)

The total NMC in each region of the curved artery at any time point is evaluated by averaging the total concentration over its respective spatial domain as follows [Bozsak et al., 2014]:

$$Total\ NMC_i\ (t) = \frac{1}{A_i \cdot C_0} \int_{A_i} (c_i + b_i)\, dA, \quad (18)$$

where the subscript $i = \{i_1, i_2\}$ denotes the healthy and unhealthy tissue regions, respectively; $i_1 = \{ses, m, a\}$ denotes the SES, the media and the adventitia, respectively; $i_2 = \{pfc, pc\}$ denotes the plaque's fibrous cap and the core of the plaque, respectively, and; A_i is the area of the region i, that falls within the therapeutic domain considered. The free and bound NMC of drug in each domain of the arterial wall at any time point are evaluated by averaging the free and bound concentration over its respective spatial domain as follows:

$$Free\ NMC_i\ (t) = \frac{1}{A_i \cdot C_0} \int_{A_i} c_i\ dA, \quad (19)$$

$$Bound\ NMC_i\ (t) = \frac{1}{A_i \cdot C_0} \int_{A_i} b_i\ dA. \quad (20)$$

Note that the interaction between the drug and the tissue is only considered in the media and in the plaque region, therefore the bound NMC in the SES and in the adventitia is zero by definition.

S2.4 Binding sites % saturation

The percentage of binding sites that are saturated as a function of time is calculated as [McKittrick et al., 2019]:

$$Binding\ sites\ \%\ sat.\ (t) = \frac{100}{A_i \cdot b_{max,i}} \int_{A_i} b_i\ dA_i, \quad (21)$$

where $b_{max,i}$ is the maximum density of binding sites in each region of the arterial wall. Note that the interaction between the drug and the tissue is only considered in the media and in the plaque region, therefore the % saturation in the SES and in the adventitia is zero by definition.

S3 Suplemental figures

The corresponding spatially varying profiles of free and bound normalised local concentration (NLC) of sirolimus, calculated as c_i/C_0 and b_i/C_0, respectively, are shown in this section at four different time points: 10 minutes, 1 hour, 4 hour and 1 day after stent implantation (Figs. S1 - S2). Six cases of arterial curvature are compared under healthy arterial wall conditions. The results are shown in a radial section between the middle struts. These figures complement the results presented in Figs. 5 and 6 in the *Results* section of the main document, which are related with the study of the effect of vessel curvature on spatial drug distribution in the tissue.

[Fig. 1 about here.]

[Fig. 2 about here.]

[Fig. 3 about here.]

To study the local concentrations throughout the different regions of the arterial wall, not only in representative sections such as a radial section between the middle stent struts, our model also enables us to generate useful 2D plots of the spatial distribution of drug for the first 7 days after DES implantation. In Fig. S4 we compare the spatial distribution of the drug for two curvature ratios ($\kappa = 0.1$ and $\kappa = 0.4$) in the outer wall of the artery. This figure complement the results presented in Fig. 6 of the main document where we plot the spatial variation of total NLC across the inner wall tissue domain showing clear differences in drug deposition, with the higher curvature leading to higher NLC of drug, with the effect most prominent at early times.

[Fig. 4 about here.]

In the rest of figures of this section (Figs. S5 - S9) the spatial variations of total NLC of sirolimus at five different time points for each curvature ratio (from $\kappa = 0.025$ to $\kappa = 0.4$) in the inner and the outer wall are shown.

[Fig. 5 about here.]

[Fig. 6 about here.]

[Fig. 7 about here.]

[Fig. 8 about here.]

[Fig. 9 about here.]

Regarding the analysis of the influence of plaque composition on drug transport within the arterial wall, the temporal distribution of the free and bound NMC of drug in four different regions of the inner wall of the artery are shown in Figs. S10 and S11, respectively. Such regions are: fibrous cap, plaque core, media and adventitia. Three different plaque core compositions are compared: fibrotic, lipid and calcified. In Fig. S12, we also show the results corresponding to the percentage of binding sites that are saturated as a function of time.

[Fig. 10 about here.]

[Fig. 11 about here.]

[Fig. 12 about here.]

We also represent the spatially-varying profiles of free and bound NLC of sirolimus and the binding site % saturation, calculated as $(b_i/b_{max,i})\cdot 100$, in the inner wall of the artery at four different time points (Figs. S13 - S15). The results are shown for three different plaque core compositions: fibrotic, lipid and calcified for a curvature ratio of $\kappa = 0.1$ (average curvature ratio). Moreover, the results for the straight model ($\kappa = 0$) and for a curvature ratio of $\kappa = 0.1$, both under healthy conditions (i.e. healthy vessel without plaque) are shown.

[Fig. 13 about here.]

[Fig. 14 about here.]

[Fig. 15 about here.]

We also show the spatial distribution of the NLC of sirolimus in the inner wall of the artery under unhealthy conditions (in presence of plaque) at five time points for a curvature ratio of $\kappa = 0.1$. (Fig. S16). Figs. S10 - S16 complement the results presented in Figs. 7 and 8 which can be found in the *Results* section of the main document.

[Fig. 16 about here.]

Finally, we calculated the following non-dimensional parameters: the Dean number ($De_l = Re_l\sqrt{\kappa}$) for the flow in the curved vessel and the radial Peclet number ($Pe_{r,i1} = u_{r,i1}\delta_{i1}/D_{r,i1}$) for transport in the wall. It can be noted a nonlinear increase in Dean number with curvature (Fig. S17) and consequent asymmetry in the fluid flow pattern in the lumen (Fig. S18). In Fig. S19 we plot the magnitude of the radial component of the plasma filtration velocity and the radial Peclet number across the inner and outer walls of the artery, respectively, for the different cases of curvature considered under healthy conditions.

[Fig. 17 about here.]

[Fig. 18 about here.]

[Fig. 19 about here.]

S4 Suplemental tables

The maximum values of normalised local concentrations (NLC) in each region of the tissue at five different time points for the different cases simulated are shown in the following tables (Tables S1 and S2).

[Table 1 about here.]

[Table 2 about here.]

Acknowledgements This work was funded by the Spanish Ministry of Economy, Industry and Competitiveness through research project number DPI2016-76630-C2-1-R and grant number BES-2014-069737; the Department of Industry and Innovation (Government of Aragon) through research group grant number T24-17R (Fondo Social Europeo) and research project number LMP121-18 and; the Carlos III Health Institute (ISCIII) through the CIBER initiative. Dr. McGinty acknowledges funding provided by EPSRC (Grant number EP/S030875/1).

Conflict of interest The authors declare that they have no conflict of interest.

References

Bozsak F, Chomaz JM, Barakat AI (2014) Modeling the transport of drugs eluted from stents: physical phenomena driving drug distribution in the arterial wall. Biomechanics and Modeling in Mechanobiology 13(2):327–347

Escuer J, Cebollero M, Peña E, McGinty S, Martínez MA (2020) How does stent expansion alter drug transport properties of the arterial wall? Journal of the Mechanical Behavior of Biomedical Materials p 103610

Formaggia L, Quarteroni A, Veneziani A (2010) Cardiovascular Mathematics: Modeling and simulation of the circulatory system, vol 1. Springer Science & Business Media

Kedem O, Katchalsky A (1958) Thermodynamic analysis of the permeability of biological membranes to non-electrolytes. Biochimica et Biophysica Acta 27:229–246

Levitt DG (1975) General continuum analysis of transport through pores. i. proof of onsager's reciprocity postulate for uniform pore. Biophysical Journal 15(6):533–551

McGinty S, Pontrelli G (2015) A general model of coupled drug release and tissue absorption for drug delivery devices. Journal of Controlled Release 217:327–336

McGinty S, Pontrelli G (2016) On the role of specific drug binding in modelling arterial eluting stents. Journal of Mathematical Chemistry 54(4):967–976

McKittrick CM, McKee S, Kennedy S, Oldroyd K, Wheel M, Pontrelli G, Dixon S, McGinty S, McCormick C (2019) Combining mathematical modelling with in vitro experiments to predict in vivo drug-eluting stent performance. Journal of Controlled Release 303:151–161

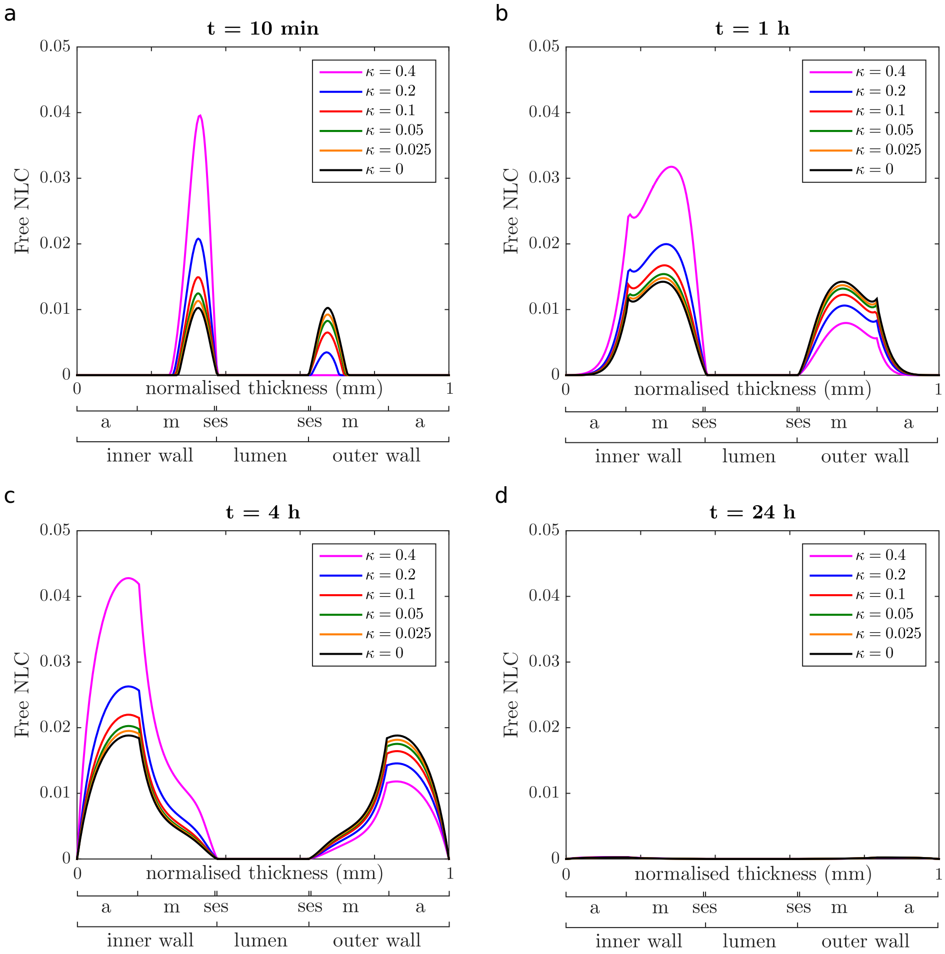

Fig. S1 Spatially varying profiles of free normalised local concentration (NLC) of sirolimus in the tissue, calculated as c_i/C_0, at 10 min (a), 1 hour (b), 4 hours (c) and 1 day (d) after stent implantation. The results are shown for the straight model ($\kappa = 0$) and for five different degrees of arterial curvature ($\kappa = 0.025 - 0.4$) in a radial section between the middle stent struts. Note that lumen diameter is not drawn to scale.

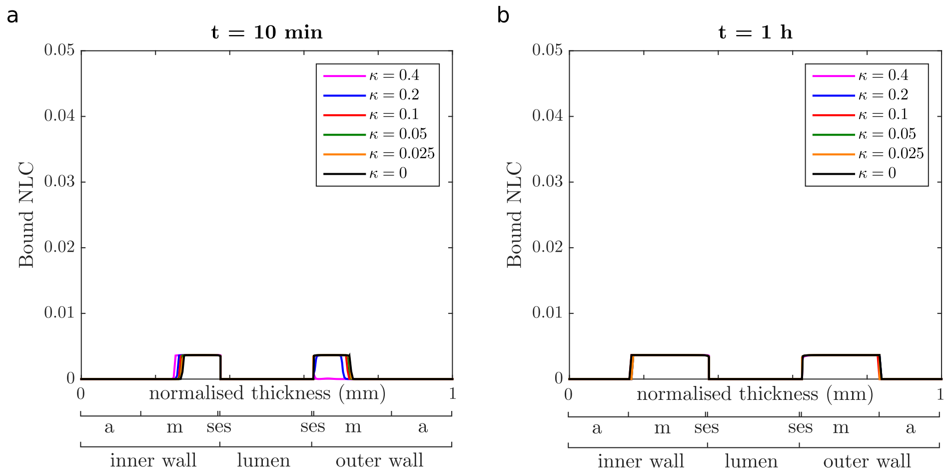

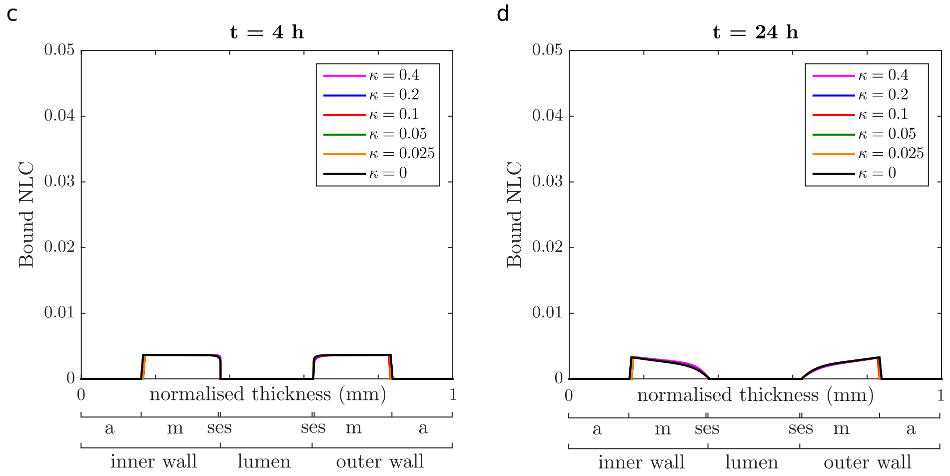

Fig. S2 Spatially varying profiles of bound normalised local concentration (NLC) of sirolimus in the tissue, calculated as b_i/C_0, at 10 min (a), 1 hour (b), 4 hours (c) and 1 day (d) after stent implantation. The results are shown for the straight model ($\kappa = 0$) and for five different degrees of arterial curvature ($\kappa = 0.025 - 0.4$) in a radial section between the middle stent struts. Note that lumen diameter is not drawn to scale.

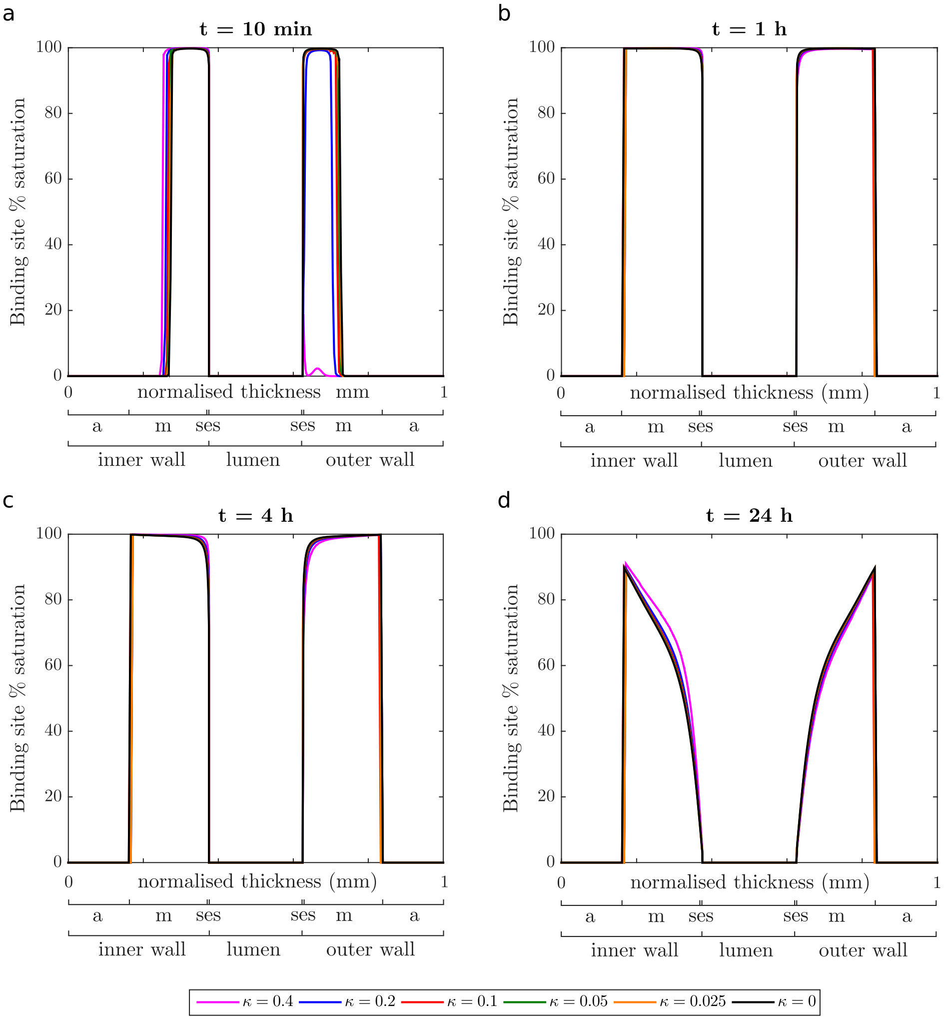

Fig. S3 Spatially varying profiles of binding site % saturation of sirolimus in the tissue, calculated as $b_i/C_0 \cdot 100$, at 10 min (a), 1 hour (b), 4 hours (c) and 1 day (d) after stent implantation. The results are shown for the straight model ($\kappa = 0$) and for five different degrees of arterial curvature ($\kappa = 0.025 - 0.4$) in a radial section between the middle stent struts. Note that lumen diameter is not drawn to scale.

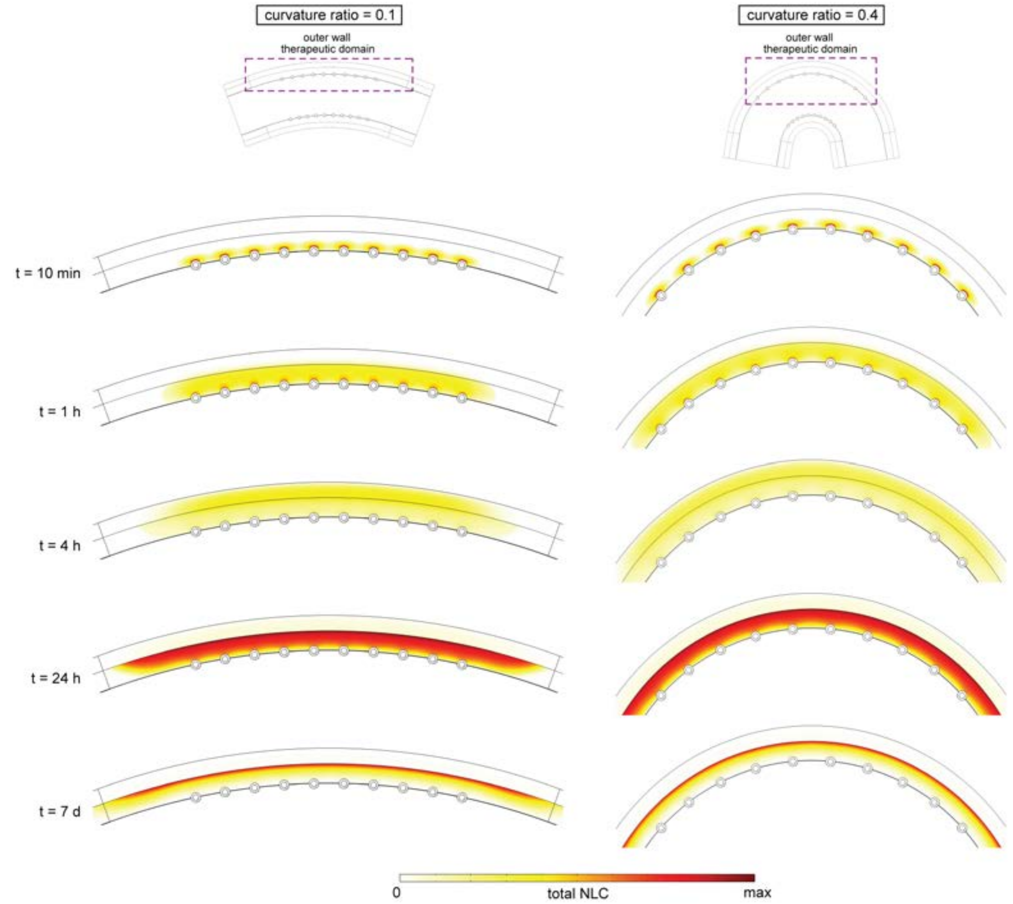

Fig. S4 Spatial variation of total NLC of sirolimus within the outer wall of the artery at five different time points (t = 10 min, t = 1 hour, t = 4 hours, t = 24 hours and t = 7 days) for curvature ratios of $\kappa = 0.1$ (average curvature ratio) and $\kappa = 0.4$, respectively. For each time point the same colour scale is used for both cases. The maximum values of total NLC of sirolimus for each time point are the following: at t = 10 min, max = $6.23 \cdot 10^{-2}$; at t = 1 h, max = $4.16 \cdot 10^{-2}$; at t = 4 h, max = $4.27 \cdot 10^{-2}$; at t = 24 h, max = $3.65 \cdot 10^{-3}$ and; at t = 7 d, max = $1.73 \cdot 10^{-3}$. Tables with the maximum values at each time point for all cases considered may be found in Section S4 (Table S1) of this supplementary material.

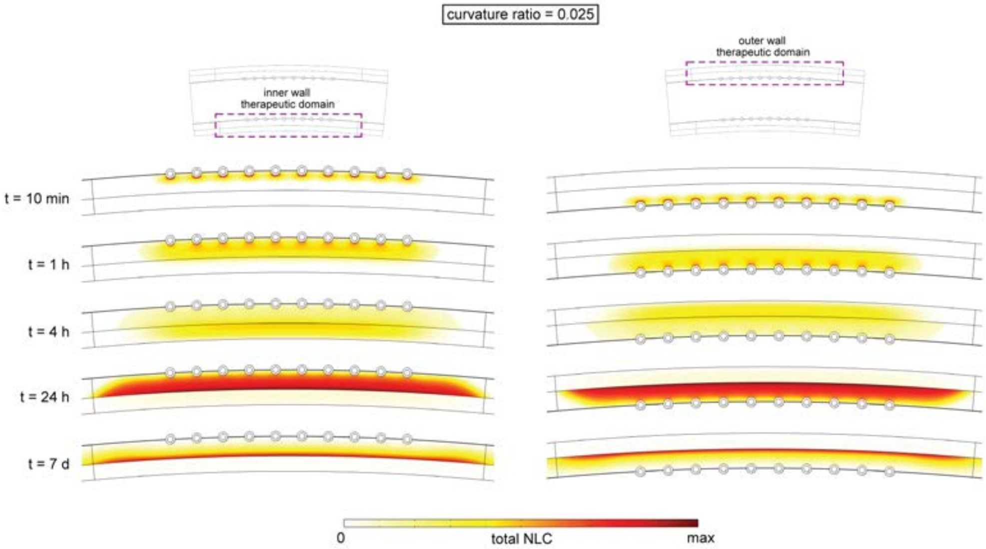

Fig. S5 Spatial variation of total NLC of sirolimus at five different time points (t = 10 min, t = 1 hour, t = 4 hours, t = 24 hours and t = 7 days) for a curvature ratio of $\kappa = 0.025$ in the inner and the outer wall, respectively. For each time point the same colour scale is used for both cases. The maximum values of total NLC of sirolimus for each time point are the following: at t = 10 min, max $= 6.23 \cdot 10^{-2}$; at t = 1 h, max $= 4.16 \cdot 10^{-2}$; at t = 4 h, max $= 4.27 \cdot 10^{-2}$; at t = 24 h, max $= 3.65 \cdot 10^{-3}$ and; at t = 7 d, max $= 1.73 \cdot 10^{-3}$. Tables with the maximum values at each time point for all cases considered may be found in Section S4 (Table S1) of this supplementary material.

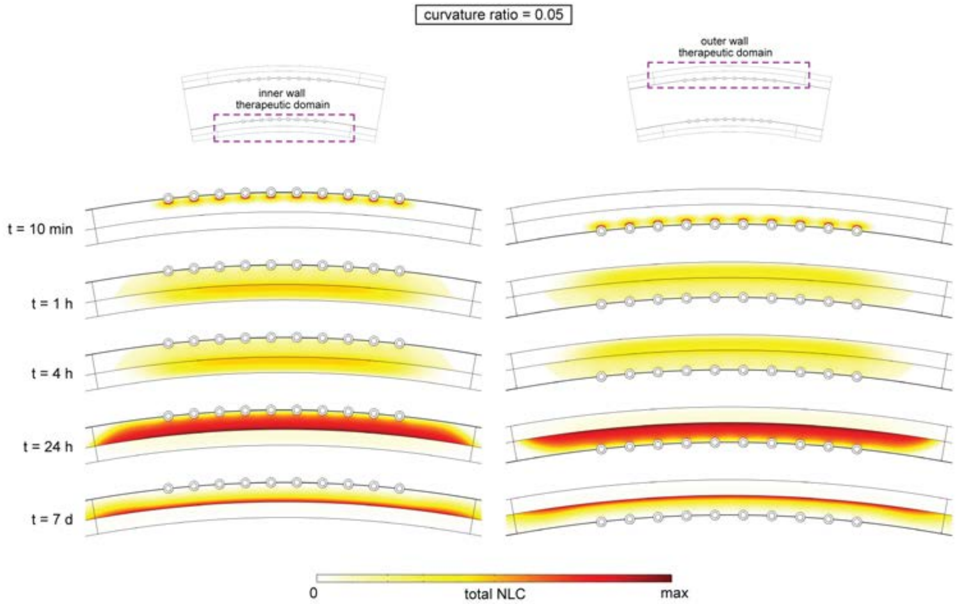

Fig. S6 Spatial variation of total NLC of sirolimus at five different time points (t = 10 min, t = 1 hour, t = 4 hours, t = 24 hours and t = 7 days) for a curvature ratio of $\kappa = 0.05$ in the inner and the outer wall, respectively. For each time point the same colour scale is used for both cases. The maximum values of total NLC of sirolimus for each time point are the following: at t = 10 min, max $= 6.23 \cdot 10^{-2}$; at t = 1 h, max $= 4.16 \cdot 10^{-2}$; at t = 4 h, max $= 4.27 \cdot 10^{-2}$; at t = 24 h, max $= 3.65 \cdot 10^{-3}$ and; at t = 7 d, max $= 1.73 \cdot 10^{-3}$. Tables with the maximum values at each time point for all cases considered may be found in Section S4 (Table S1) of this supplementary material.

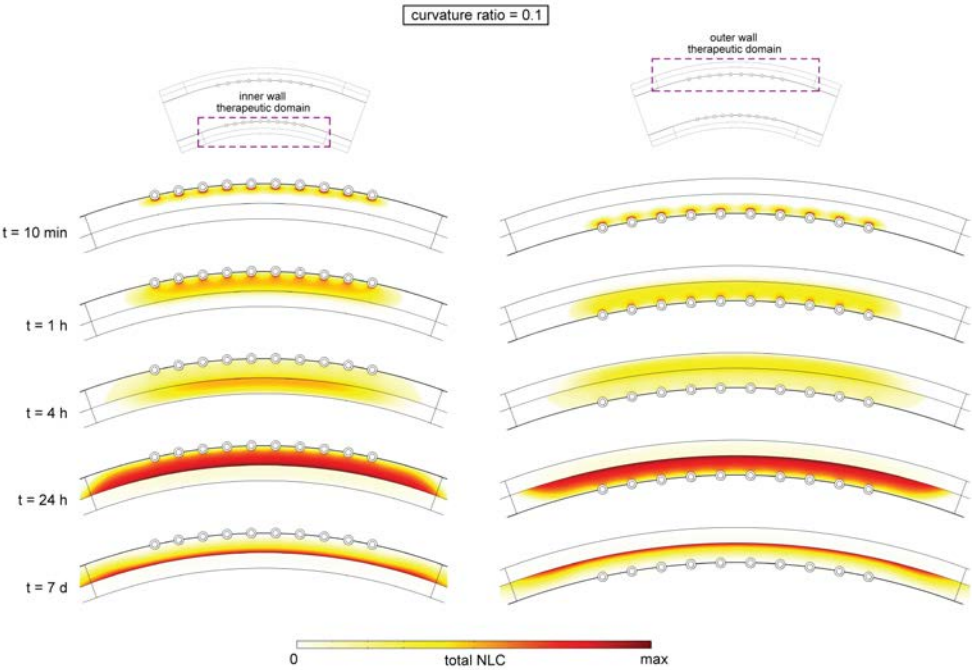

Fig. S7 Spatial variation of total NLC of sirolimus at five different time points (t = 10 min, t = 1 hour, t = 4 hours, t = 24 hours and t = 7 days) for a curvature ratio of $\kappa = 0.1$ (average curvature ratio) in the inner and the outer wall, respectively. For each time point the same colour scale is used for both cases. The maximum values of total NLC of sirolimus for each time point are the following: at t = 10 min, max = $6.23 \cdot 10^{-2}$; at t = 1 h, max = $4.16 \cdot 10^{-2}$; at t = 4 h, max = $4.27 \cdot 10^{-2}$; at t = 24 h, max = $3.65 \cdot 10^{-3}$ and; at t = 7 d, max = $1.73 \cdot 10^{-3}$. Tables with the maximum values at each time point for all cases considered may be found in Section S4 (Table S1) of this supplementary material.

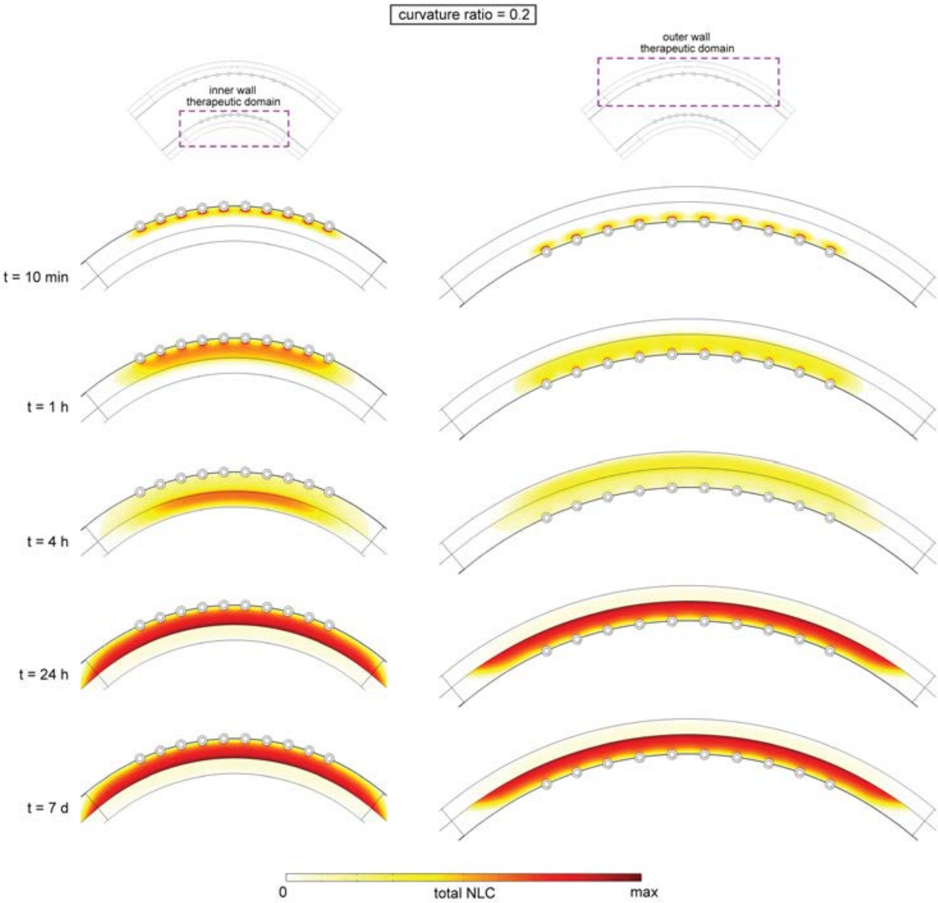

Fig. S8 Spatial variation of total NLC of sirolimus at five different time points (t = 10 min, t = 1 hour, t = 4 hours, t = 24 hours and t = 7 days) for a curvature ratio of $\kappa = 0.2$ in the inner and the outer wall, respectively. For each time point the same colour scale is used for both cases. The maximum values of total NLC of sirolimus for each time point are the following: at t = 10 min, max $= 6.23 \cdot 10^{-2}$; at t = 1 h, max $= 4.16 \cdot 10^{-2}$; at t = 4 h, max $= 4.27 \cdot 10^{-2}$; at t = 24 h, max $= 3.65 \cdot 10^{-3}$ and; at t = 7 d, max $= 1.73 \cdot 10^{-3}$. Tables with the maximum values at each time point for all cases considered may be found in Section S4 (Table S1) of this supplementary material.

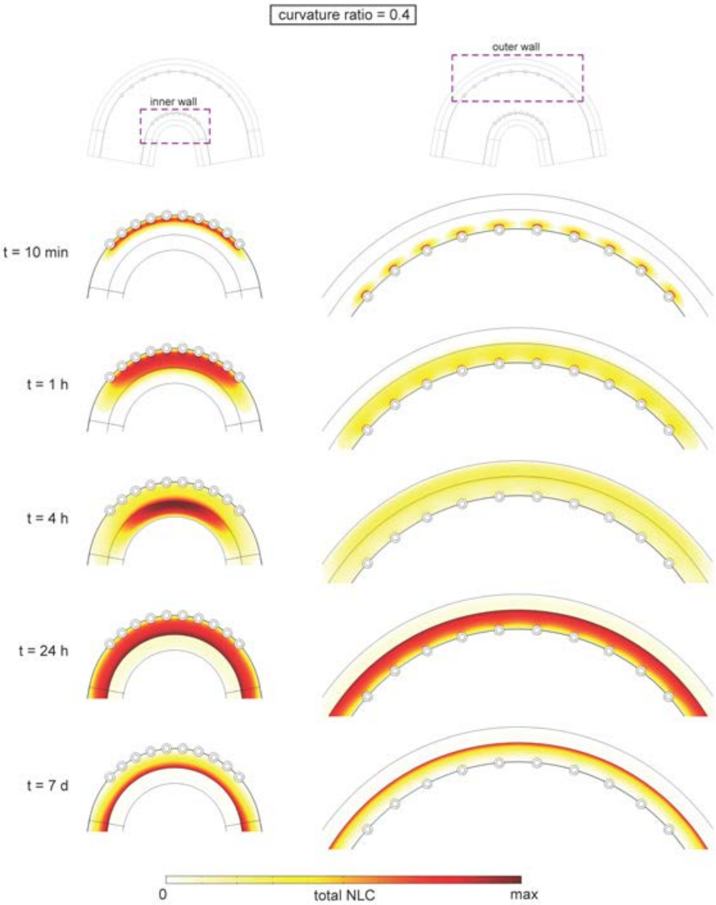

Fig. S9 Spatial variation of total NLC of sirolimus at five different time points (t = 10 min, t = 1 hour, t = 4 hours, t = 24 hours and t = 7 days) for a curvature ratio of $\kappa = 0.4$ in the inner and the outer wall, respectively. For each time point the same colour scale is used for both cases. The maximum values of total NLC of sirolimus for each time point are the following: at t = 10 min, max $= 6.23 \cdot 10^{-2}$; at t = 1 h, max $= 4.16 \cdot 10^{-2}$; at t = 4 h, max $= 4.27 \cdot 10^{-2}$; at t = 24 h, max $= 3.65 \cdot 10^{-3}$ and; at t = 7 d, max $= 1.73 \cdot 10^{-3}$. Tables with the maximum values at each time point for all cases considered may be found in Section S4 (Table S1) of this supplementary material.

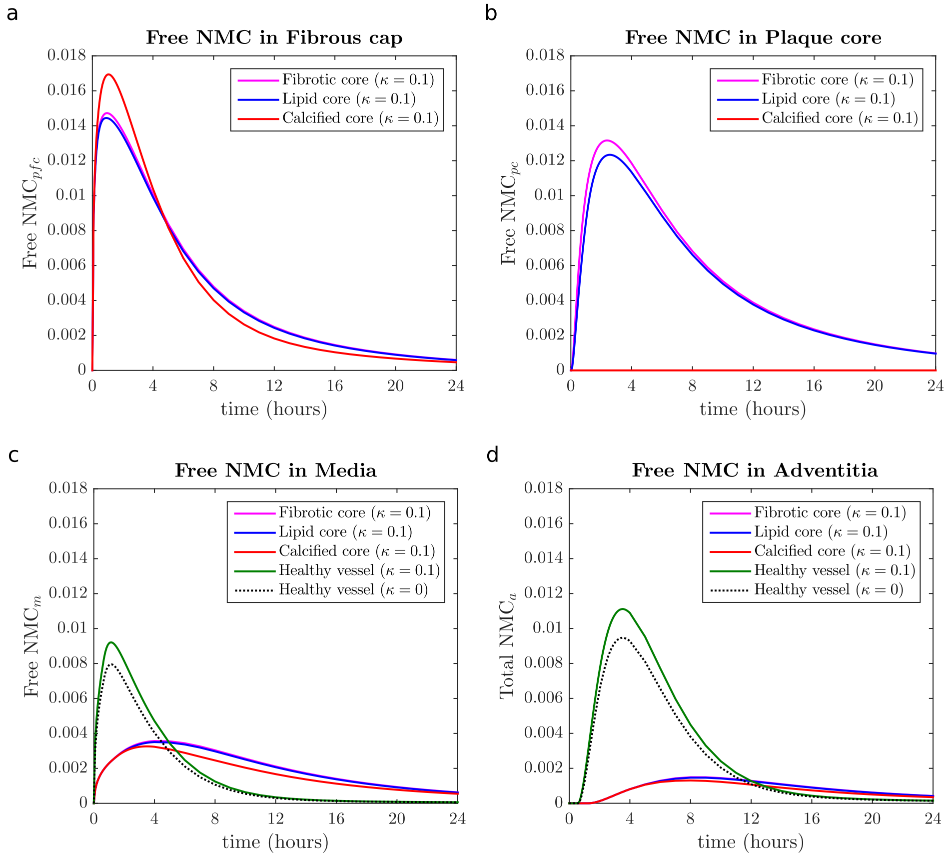

Fig. S10 Temporal distribution of the free NMC of sirolimus in the fibrous cap (a), plaque core (b), media (c) and adventitia (d) within the inner wall of the artery for a curvature ratio of $\kappa = 0.1$ (average curvature ratio). The results are shown for three different plaque core compositions: fibrotic, lipid and calcified. In case of the media and adventitia, the results are also shown for the straight model ($\kappa = 0$) and for a curvature ratio of $\kappa = 0.1$, both under healthy conditions (i.e. healthy vessel without plaque).

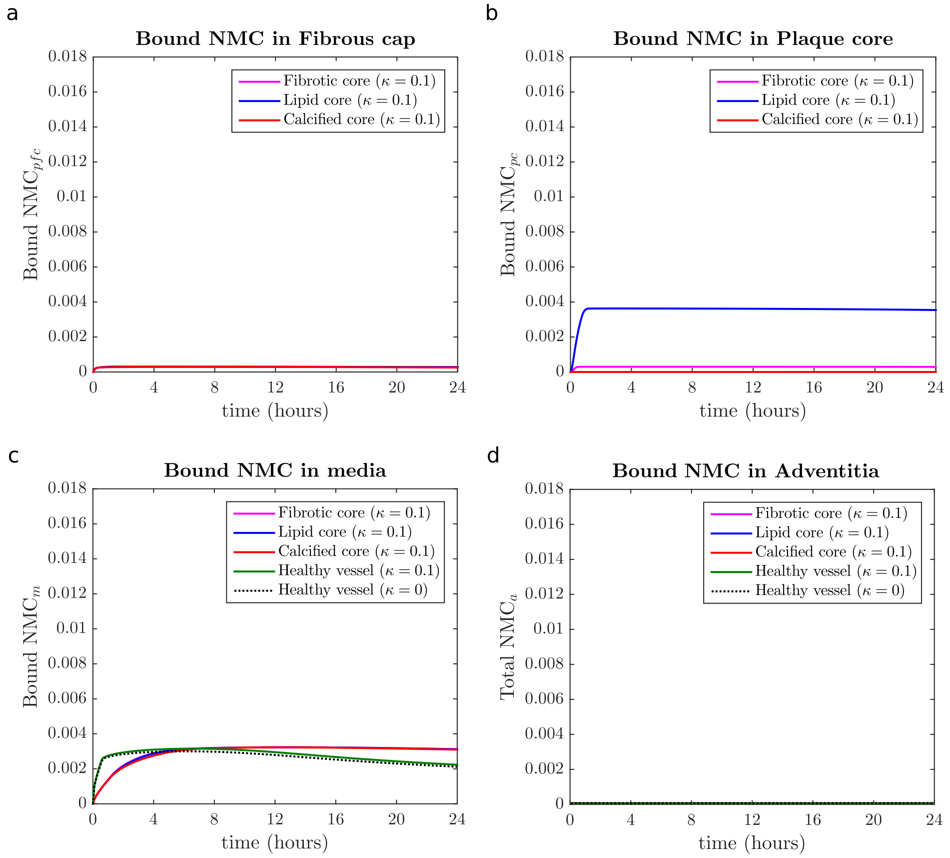

Fig. S11 Temporal distribution of the bound NMC of sirolimus in the fibrous cap (a), plaque core (b), media (c) and adventitia (d) within the inner wall of the artery for a curvature ratio of $\kappa = 0.1$ (average curvature ratio). The results are shown for three different plaque core compositions: fibrotic, lipid and calcified. In case of the media and adventitia, the results are also shown for the straight model ($\kappa = 0$) and for a curvature ratio of $\kappa = 0.1$, both under healthy conditions (i.e. healthy vessel without plaque).

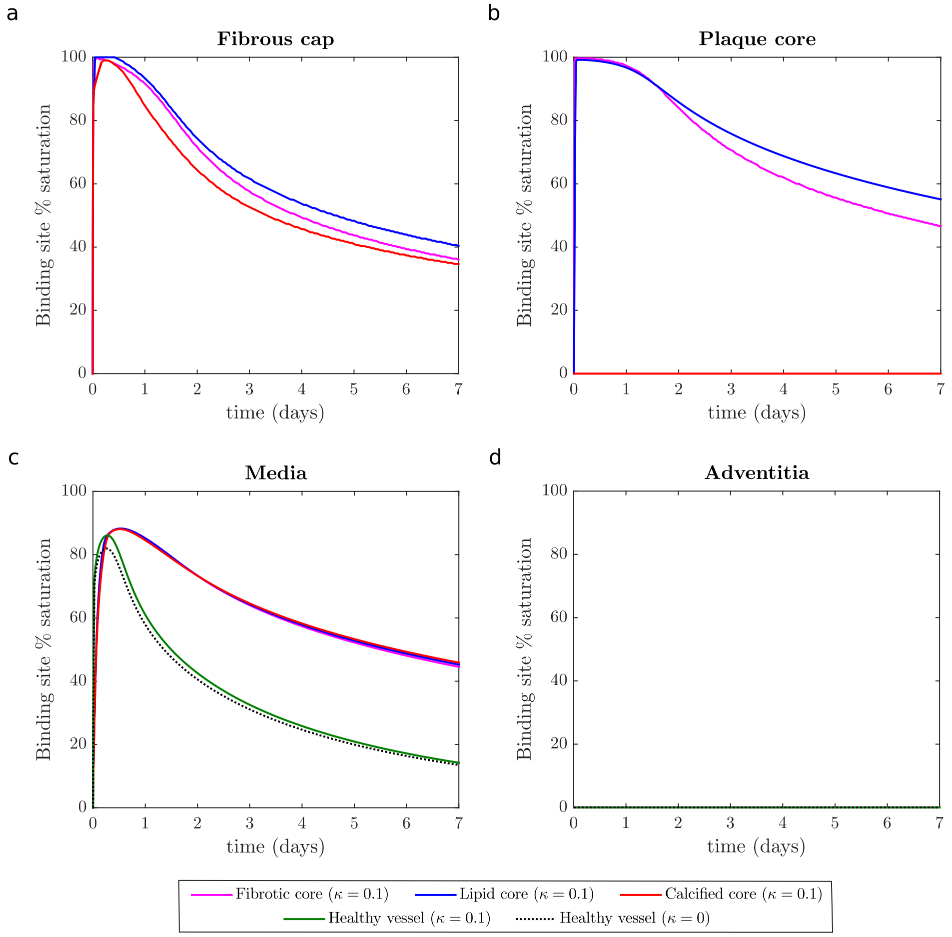

Fig. S12 Temporal distribution of the binding site % saturation in the fibrous cap (a), plaque core (b), media (c) and adventitia (d) within the inner wall of the artery for a curvature ratio of $\kappa = 0.1$ (average curvature ratio). The results are shown for three different plaque core compositions: fibrotic, lipid and calcified. In case of the media and adventitia, the results are also shown for the straight model ($\kappa = 0$) and for a curvature ratio of $\kappa = 0.1$, both under healthy conditions (i.e. healthy vessel without plaque).

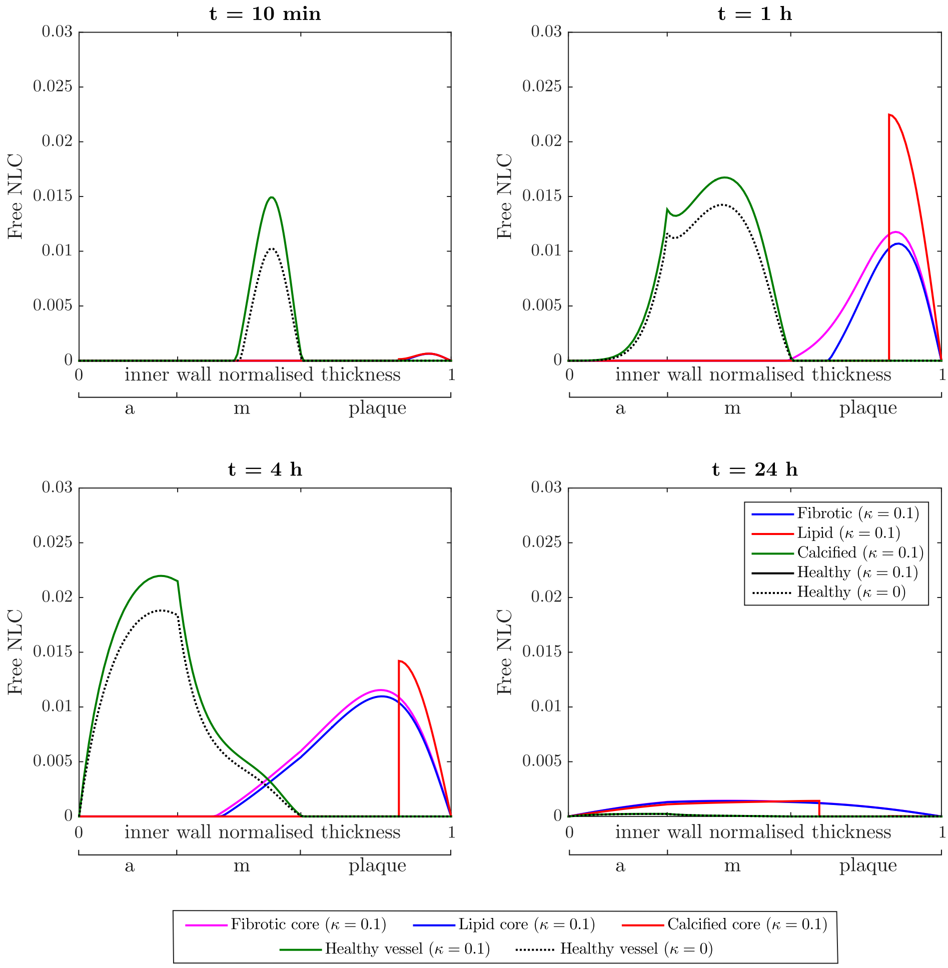

Fig. S13 Spatially varying profiles of free NLC of sirolimus, calculated as c_i/C_0, in the inner wall of the artery at 10 min (a), 1 hour (b), 4 hours (c) and 1 day (d) after stent implantation in a radial section between the middle stent struts. The results are shown for three different plaque core compositions: fibrotic, lipid and calcified for a curvature ratio of $\kappa = 0.1$ (average curvature ratio). Moreover, the results for the straight model ($\kappa = 0$) and for a curvature ratio of $\kappa = 0.1$, both under healthy conditions (i.e. healthy vessel without plaque) are shown.

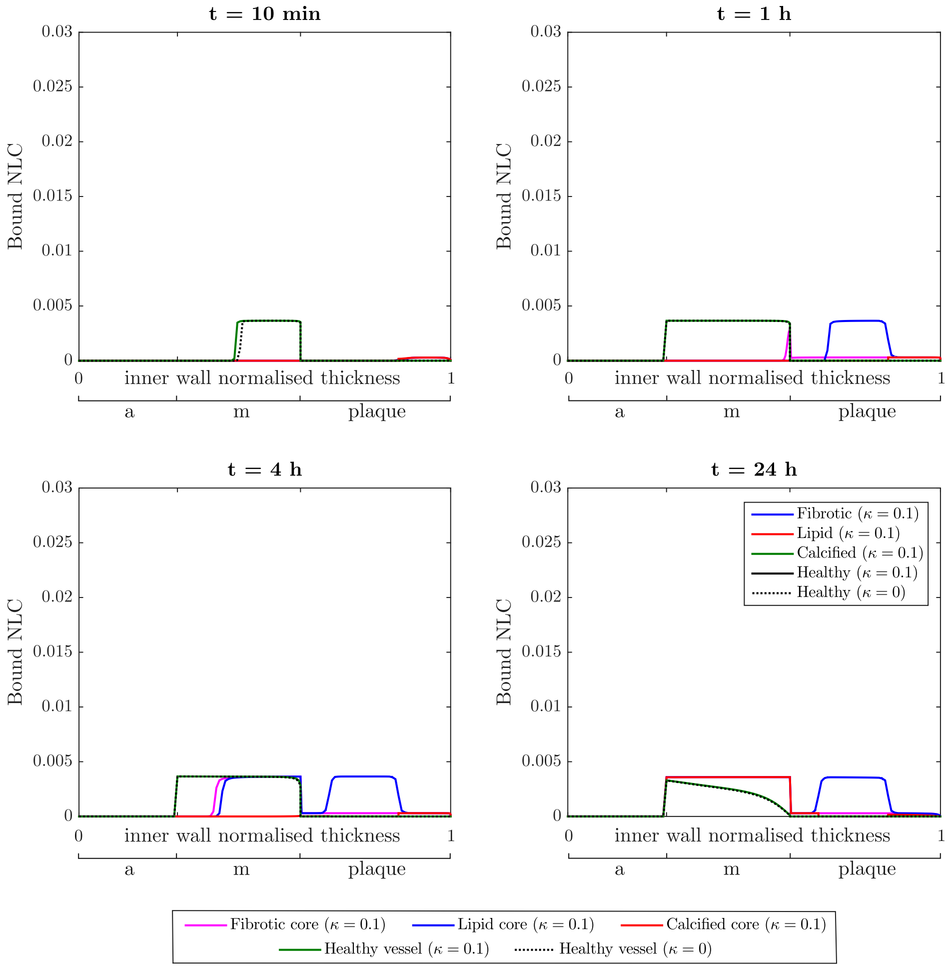

Fig. S14 Spatially varying profiles of bound NLC of sirolimus, calculated as b_i/C_0, in the inner wall of the artery at 10 min (a), 1 hour (b), 4 hours (c) and 1 day (d) after stent implantation in a radial section between the middle stent struts. The results are shown for three different plaque core compositions: fibrotic, lipid and calcified for a curvature ratio of $\kappa = 0.1$ (average curvature ratio). Moreover, the results for the straight model ($\kappa = 0$) and for a curvature ratio of $\kappa = 0.1$, both under healthy conditions (i.e. healthy vessel without plaque) are shown.

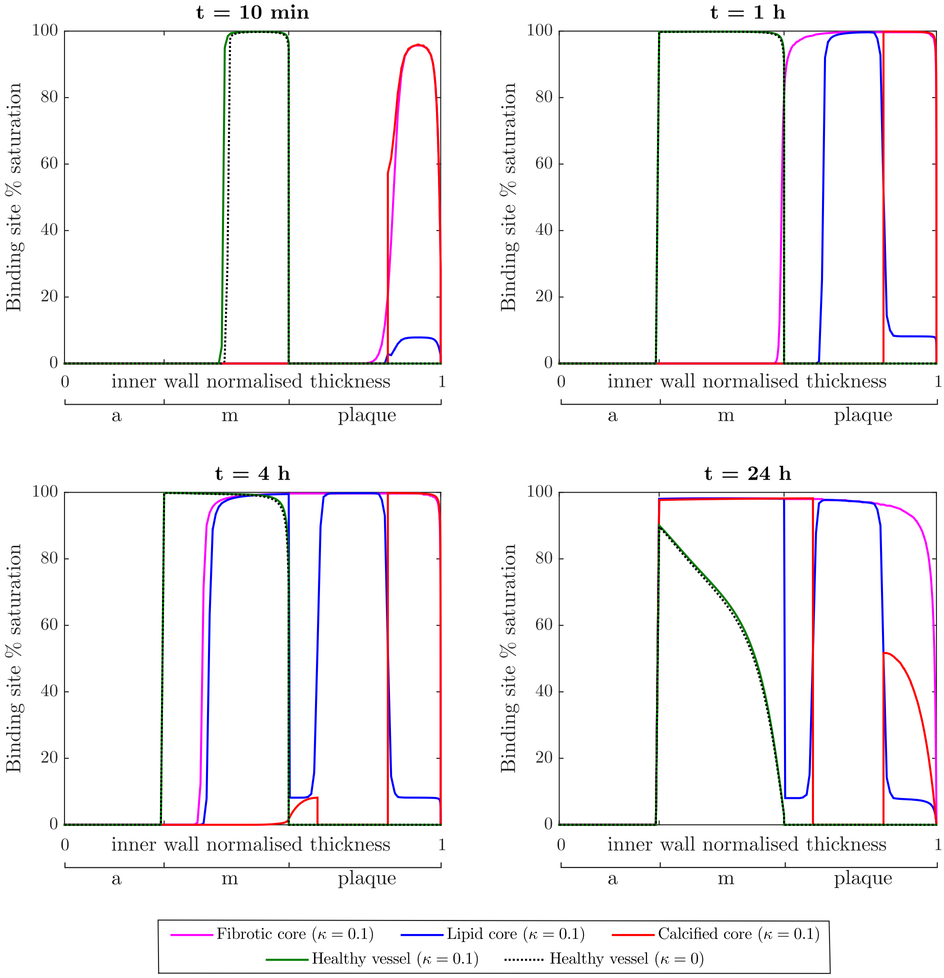

Fig. S15 Spatially varying profiles of binding site % saturation in the inner wall of the artery, calculated as $(b_i/b_{max,i}) \cdot 100$, at 10 min (a), 1 hour (b), 4 hours (c) and 1 day (d) after stent implantation in a radial section between the middle stent struts. The results are shown for three different plaque core compositions: fibrotic, lipid and calcified for a curvature ratio of $\kappa = 0.1$ (average curvature ratio). Moreover, the results for the straight model ($\kappa = 0$) and for a curvature ratio of $\kappa = 0.1$, both under healthy conditions (i.e. healthy vessel without plaque) are shown.

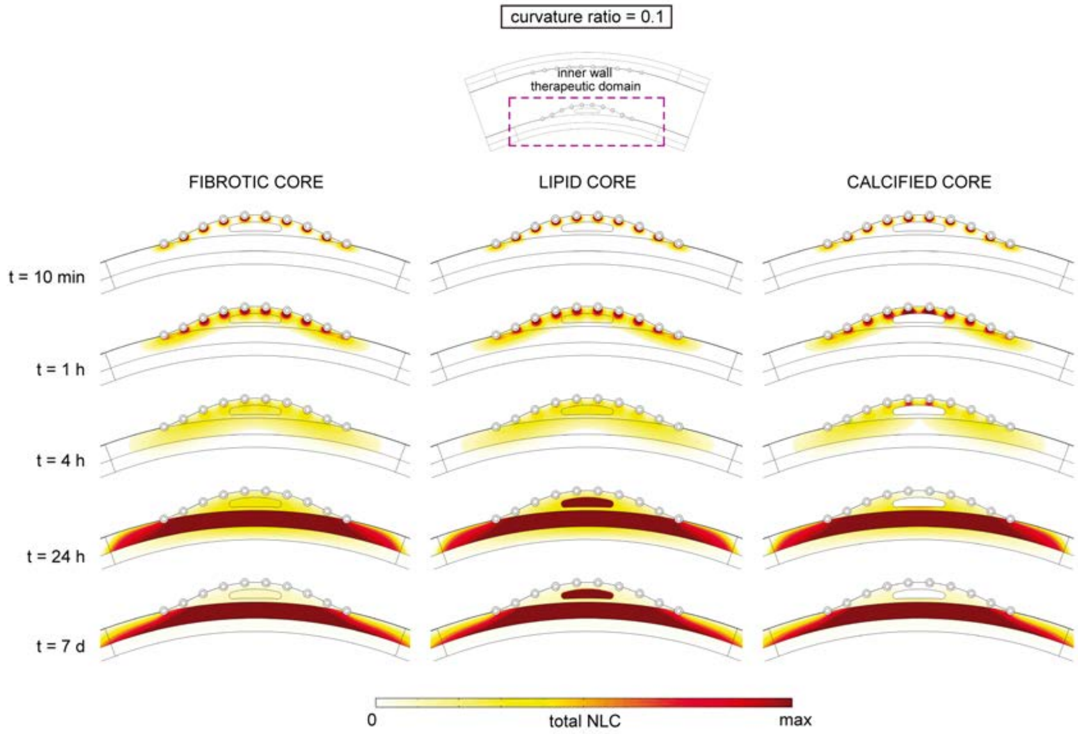

Fig. S16 Spatial variation of total NLC of sirolimus at five different time points (t = 10 min, t = 1 hour, t = 4 hours, t = 24 hours and t = 7 days) for a curvature ratio of $\kappa = 0.1$ in the inner wall of the artery under unhealthy conditions (in presence of plaque). For each time point the same colour scale is used for both cases. The maximum values of total NLC of sirolimus for each time point are the following: at t = 10 min, max = $9.17 \cdot 10^{-2}$; at t = 1 h, max = $8.47 \cdot 10^{-2}$; at t = 4 h, max = $3.55 \cdot 10^{-2}$; at t = 24 h, max = $5.03 \cdot 10^{-3}$ and; at t = 7 d, max = $2.52 \cdot 10^{-3}$. Tables with the maximum values at each time point for all cases considered may be found in Section S4 (Table S2) of this supplementary material.

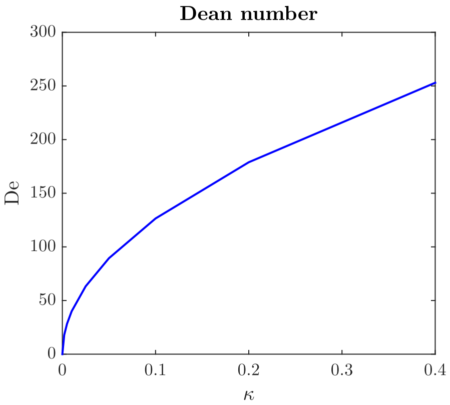

Fig. S17 Variation of the Dean number (De) for the flow in the straight artery ($\kappa = 0$) and in the curved vessel ($\kappa = 0.025 - 0.4$).

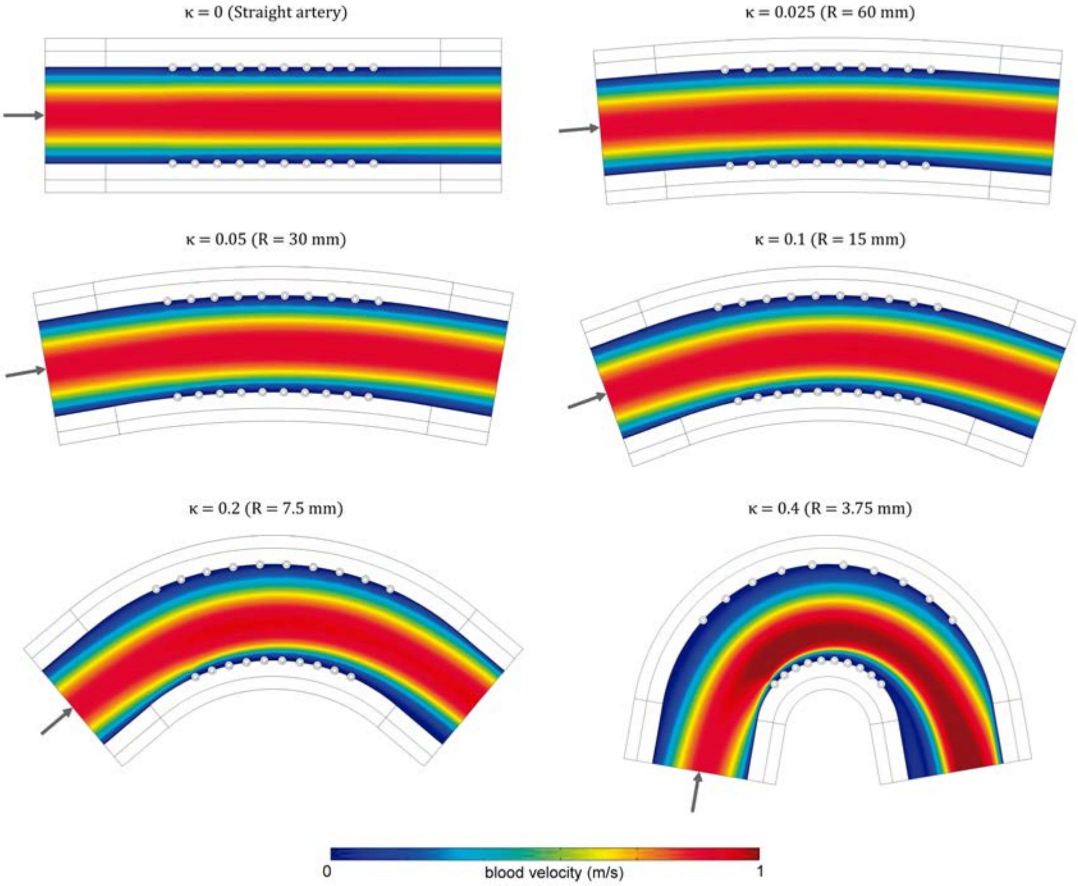

Fig. S18 Fuid flow pattern in the lumen for the straight artery ($\kappa = 0$) and for five different degrees of arterial curvature ($\kappa = 0.025 - 0.4$). The arrow indicates the inlet.

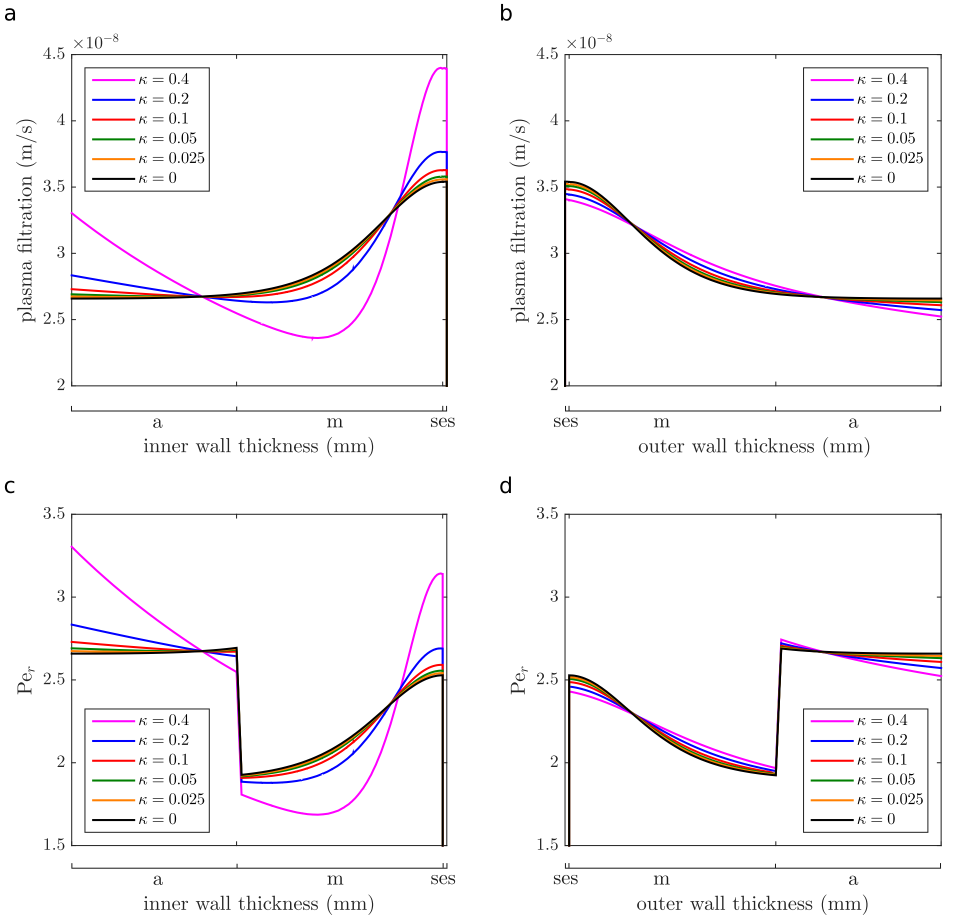

Fig. S19 Magnitude of the radial component of the plasma filtration (a, b) and radial Peclet number variation (c, d) in the inner and the outer wall of the artery. The results are shown for the healthy straight model ($\kappa = 0$) and for five different degrees of arterial curvature ($\kappa = 0.025 - 0.4$) in a radial section between the middle stent struts.

Table S1 Maximum normalised local concentration (NLC) of sirolimus, calculated as $(c_i + b_i)/C_0$, in each layer of the arterial wall for the straight segment ($\kappa = 0$) and for five different cases of arterial curvature ($\kappa = 0.025 - 0.4$) under healthy conditions (without plaque), at five different time points after stent implantation. Bold values in this table for a given time indicate the absolute maximum NLC of sirolimus in every case at the same time. They correspond to the 'max' values which appear in the legend in Figs. S4 - S9 which can be found in this supplementary material.

CASE 1. Healthy arterial wall. Straight segment ($\kappa = 0$)

max. value at	t = 10 min	t = 1 h	t = 4 h	t = 24 h	t = 7 d
Total NLC in the SES (c_{ses})	$7.00\cdot10^{-3}$	$2.64\cdot10^{-3}$	$6.84\cdot10^{-4}$	$9.71\cdot10^{-7}$	$4.86\cdot10^{-8}$
Free NLC in the media (c_m)	$4.89\cdot10^{-2}$	$2.48\cdot10^{-2}$	$1.84\cdot10^{-2}$	$2.25\cdot10^{-4}$	$1.68\cdot10^{-5}$
Bound NLC in the media (b_m)	$3.66\cdot10^{-3}$	$3.66\cdot10^{-3}$	$3.65\cdot10^{-3}$	$3.28\cdot10^{-3}$	$1.44\cdot10^{-3}$
Total NLC in the media ($c_m + b_m$)	$5.26\cdot10^{-2}$	$2.85\cdot10^{-2}$	$2.21\cdot10^{-2}$	$3.51\cdot10^{-3}$	$1.46\cdot10^{-3}$
Total NLC in the adventitia (c_a)	$2.62\cdot10^{-21}$	$1.11\cdot10^{-2}$	$1.18\cdot10^{-2}$	$2.26\cdot10^{-4}$	$1.67\cdot10^{-5}$

CASE 2. Healthy arterial wall. Curved segment ($\kappa = 0.025$)

max. value at	t = 10 min	t = 1 h	t = 4 h	t = 24 h	t = 7 d
Total NLC in the SES (c_{ses})	$7.14\cdot10^{-3}$	$2.69\cdot10^{-3}$	$6.97\cdot10^{-4}$	$9.87\cdot10^{-7}$	$4.99\cdot10^{-8}$
Free NLC in the media (c_m)	$4.89\cdot10^{-2}$	$2.51\cdot10^{-2}$	$1.90\cdot10^{-2}$	$2.27\cdot10^{-4}$	$1.69\cdot10^{-5}$
Bound NLC in the media (b_m)	$3.66\cdot10^{-3}$	$3.66\cdot10^{-3}$	$3.66\cdot10^{-3}$	$3.28\cdot10^{-3}$	$1.44\cdot10^{-3}$
Total NLC in the media ($c_m + b_m$)	$5.26\cdot10^{-2}$	$2.88\cdot10^{-2}$	$2.27\cdot10^{-2}$	$3.51\cdot10^{-3}$	$1.46\cdot10^{-3}$
Total NLC in the adventitia (c_a)	$2.71\cdot10^{-21}$	$1.15\cdot10^{-2}$	$1.95\cdot10^{-2}$	$2.27\cdot10^{-4}$	$1.68\cdot10^{-5}$

CASE 3. Healthy arterial wall. Curved segment ($\kappa = 0.05$)

max. value at	t = 10 min	t = 1 h	t = 4 h	t = 24 h	t = 7 d
Total NLC in the SES (c_{ses})	$7.07\cdot10^{-3}$	$2.66\cdot10^{-3}$	$6.88\cdot10^{-4}$	$9.83\cdot10^{-7}$	$5.13\cdot10^{-8}$
Free NLC in the media (c_m)	$4.90\cdot10^{-2}$	$2.54\cdot10^{-2}$	$1.98\cdot10^{-2}$	$2.29\cdot10^{-4}$	$1.70\cdot10^{-5}$
Bound NLC in the media (b_m)	$3.66\cdot10^{-3}$	$3.66\cdot10^{-3}$	$3.66\cdot10^{-3}$	$3.29\cdot10^{-3}$	$1.45\cdot10^{-3}$
Total NLC in the media ($c_m + b_m$)	$5.27\cdot10^{-2}$	$2.91\cdot10^{-2}$	$2.35\cdot10^{-2}$	$3.52\cdot10^{-3}$	$1.47\cdot10^{-3}$
Total NLC in the adventitia (c_a)	$2.55\cdot10^{-21}$	$1.21\cdot10^{-2}$	$2.02\cdot10^{-2}$	$2.30\cdot10^{-4}$	$1.69\cdot10^{-5}$

CASE 4. Healthy arterial wall. Curved segment ($\kappa = 0.1$)

max. value at	t = 10 min	t = 1 h	t = 4 h	t = 24 h	t = 7 d
Total NLC in the SES (c_{ses})	$7.20\cdot10^{-3}$	$2.70\cdot10^{-3}$	$6.99\cdot10^{-4}$	$9.98\cdot10^{-7}$	$5.45\cdot10^{-8}$
Free NLC in the media (c_m)	$4.93\cdot10^{-2}$	$2.62\cdot10^{-2}$	$2.14\cdot10^{-2}$	$2.34\cdot10^{-4}$	$1.74\cdot10^{-5}$
Bound NLC in the media (b_m)	$3.66\cdot10^{-3}$	$3.66\cdot10^{-3}$	$3.66\cdot10^{-3}$	$3.30\cdot10^{-3}$	$1.47\cdot10^{-3}$
Total NLC in the media ($c_m + b_m$)	$5.30\cdot10^{-2}$	$2.99\cdot10^{-2}$	$2.51\cdot10^{-2}$	$3.53\cdot10^{-3}$	$1.49\cdot10^{-3}$
Total NLC in the adventitia (c_a)	$2.55\cdot10^{-21}$	$1.32\cdot10^{-2}$	$2.19\cdot10^{-2}$	$2.35\cdot10^{-4}$	$1.73\cdot10^{-5}$

CASE 5. Healthy arterial wall. Curved segment ($\kappa = 0.2$)

max. value at	t = 10 min	t = 1 h	t = 4 h	t = 24 h	t = 7 d
Total NLC in the SES (c_{ses})	$7.75\cdot10^{-3}$	$2.89\cdot10^{-3}$	$7.49\cdot10^{-4}$	$1.24\cdot10^{-6}$	$1.01\cdot10^{-7}$
Free NLC in the media (c_m)	$5.04\cdot10^{-2}$	$2.83\cdot10^{-2}$	$2.57\cdot10^{-2}$	$2.46\cdot10^{-4}$	$1.82\cdot10^{-5}$
Bound NLC in the media (b_m)	$3.66\cdot10^{-3}$	$3.66\cdot10^{-3}$	$3.66\cdot10^{-3}$	$3.31\cdot10^{-3}$	$1.51\cdot10^{-3}$
Total NLC in the media ($c_m + b_m$)	$5.41\cdot10^{-2}$	$3.20\cdot10^{-2}$	$2.94\cdot10^{-2}$	$3.56\cdot10^{-3}$	$1.53\cdot10^{-3}$
Total NLC in the adventitia (c_a)	$2.60\cdot10^{-21}$	$1.58\cdot10^{-2}$	$2.62\cdot10^{-2}$	$2.48\cdot10^{-4}$	$1.81\cdot10^{-5}$

CASE 6. Healthy arterial wall. Curved segment ($\kappa = 0.4$)

max. value at	t = 10 min	t = 1 h	t = 4 h	t = 24 h	t = 7 d
Total NLC in the SES (c_{ses})	$9.98\cdot10^{-3}$	$3.68\cdot10^{-3}$	$9.51\cdot10^{-4}$	$1.38\cdot10^{-6}$	$1.08\cdot10^{-7}$
Free NLC in the media (c_m)	$5.86\cdot10^{-2}$	$3.79\cdot10^{-2}$	$3.19\cdot10^{-2}$	$2.89\cdot10^{-4}$	$2.27\cdot10^{-5}$
Bound NLC in the media (b_m)	$3.66\cdot10^{-3}$	$3.66\cdot10^{-3}$	$3.66\cdot10^{-3}$	$3.36\cdot10^{-3}$	$1.71\cdot10^{-3}$
Total NLC in the media ($c_m + b_m$)	$\mathbf{6.23 \cdot 10^{-2}}$	$\mathbf{4.16 \cdot 10^{-2}}$	$4.16\cdot10^{-2}$	$\mathbf{3.65 \cdot 10^{-3}}$	$\mathbf{1.73 \cdot 10^{-3}}$
Total NLC in the adventitia (c_a)	$1.50\cdot10^{-20}$	$2.41\cdot10^{-2}$	$\mathbf{4.27 \cdot 10^{-2}}$	$2.95\cdot10^{-4}$	$2.25\cdot10^{-5}$

Table S2 Maximum total normalised local concentration (NLC) of sirolimus, calculated as $(c_i+b_i)/C_0$, in each region of the diseased arterial wall (with plaque) in a curved segment ($\kappa = 0.1$), at five different time points after stent implantation. Bold values in this table for a given time indicate the absolute maximum NLC of sirolimus in every case at the same time. They correspond to the 'max' values which appear in the legend in Fig. S16 which can be found in this supplementary material.

CASE 7. Diseased arterial wall (Fibrotic core). Curved segment ($\kappa = 0.1$)

max. value at	t = 10 min	t = 1 h	t = 4 h	t = 24 h	t = 7 d
Total NLC in the SES (c_{ses})	$6.64\cdot10^{-3}$	$2.49\cdot10^{-3}$	$6.45\cdot10^{-4}$	$5.63\cdot10^{-6}$	$3.42\cdot10^{-7}$
Free NLC in the plaque (c_{i2})	$8.75\cdot10^{-2}$	$5.76\cdot10^{-2}$	$2.37\cdot10^{-2}$	$1.34\cdot10^{-3}$	$3.63\cdot10^{-5}$
Bound NLC in the plaque (b_{i2})	$3.00\cdot10^{-4}$	$3.00\cdot10^{-4}$	$3.00\cdot10^{-4}$	$2.94\cdot10^{-4}$	$1.74\cdot10^{-4}$
Total NLC in the plaque ($c_{i2} + b_{i2}$)	$8.78\cdot10^{-2}$	$5.79\cdot10^{-2}$	$2.40\cdot10^{-2}$	$1.63\cdot10^{-3}$	$2.10\cdot10^{-4}$
Free NLC in the media (c_m)	$4.89\cdot10^{-2}$	$3.17\cdot10^{-2}$	$1.60\cdot10^{-2}$	$1.44\cdot10^{-3}$	$4.31\cdot10^{-5}$
Bound NLC in the media (b_m)	$3.66\cdot10^{-3}$	$3.66\cdot10^{-3}$	$3.66\cdot10^{-3}$	$3.59\cdot10^{-3}$	$2.28\cdot10^{-3}$
Total NLC in the media ($c_m + b_m$)	$5.26\cdot10^{-2}$	$3.54\cdot10^{-2}$	$1.97\cdot10^{-2}$	$\mathbf{5.03 \cdot 10^{-3}}$	$2.32\cdot10^{-3}$
Total NLC in the adventitia (c_a)	$2.36\cdot10^{-21}$	$9.34\cdot10^{-3}$	$1.63\cdot10^{-2}$	$1.32\cdot10^{-3}$	$3.80\cdot10^{-5}$

CASE 8. Diseased arterial wall (Lipid core). Curved segment ($\kappa = 0.1$)

max. value at	t = 10 min	t = 1 h	t = 4 h	t = 24 h	t = 7 d
Total NLC in the SES (c_{ses})	$6.64\cdot10^{-3}$	$2.49\cdot10^{-3}$	$6.45\cdot10^{-4}$	$5.58\cdot10^{-6}$	$3.43\cdot10^{-7}$
Free NLC in the plaque (c_{i2})	$8.75\cdot10^{-2}$	$5.76\cdot10^{-2}$	$2.37\cdot10^{-2}$	$1.31\cdot10^{-3}$	$4.38\cdot10^{-5}$
Bound NLC in the plaque (b_{i2})	$3.66\cdot10^{-3}$	$3.66\cdot10^{-3}$	$3.66\cdot10^{-3}$	$3.58\cdot10^{-3}$	$2.20\cdot10^{-3}$
Total NLC in the plaque ($c_{i2} + b_{i2}$)	$9.12\cdot10^{-2}$	$6.13\cdot10^{-2}$	$2.74\cdot10^{-2}$	$4.89\cdot10^{-3}$	$2.24\cdot10^{-3}$
Free NLC in the media (c_m)	$4.89\cdot10^{-2}$	$3.17\cdot10^{-2}$	$1.60\cdot10^{-2}$	$1.40\cdot10^{-3}$	$4.71\cdot10^{-5}$
Bound NLC in the media (b_m)	$3.66\cdot10^{-3}$	$3.66\cdot10^{-3}$	$3.65\cdot10^{-3}$	$3.59\cdot10^{-3}$	$2.36\cdot10^{-3}$
Total NLC in the media ($c_m + b_m$)	$5.26\cdot10^{-2}$	$3.54\cdot10^{-2}$	$1.97\cdot10^{-2}$	$4.99\cdot10^{-3}$	$2.36\cdot10^{-3}$
Total NLC in the adventitia (c_a)	$2.36\cdot10^{-21}$	$9.35\cdot10^{-3}$	$1.63\cdot10^{-2}$	$1.29\cdot10^{-3}$	$4.06\cdot10^{-5}$

CASE 9. Diseased arterial wall (Calcified core). Curved segment ($\kappa = 0.1$)

max. value at	t = 10 min	t = 1 h	t = 4 h	t = 24 h	t = 7 d
Total NLC in the SES (c_{ses})	$6.64\cdot10^{-3}$	$2.49\cdot10^{-3}$	$6.45\cdot10^{-4}$	$5.55\cdot10^{-6}$	$3.43\cdot10^{-7}$
Free NLC in the plaque (c_{i2})	$9.14\cdot10^{-2}$	$8.44\cdot10^{-2}$	$3.52\cdot10^{-2}$	$1.42\cdot10^{-3}$	$5.37\cdot10^{-5}$
Bound NLC in the plaque (b_{i2})	$3.00\cdot10^{-4}$	$3.00\cdot10^{-4}$	$3.00\cdot10^{-4}$	$2.94\cdot10^{-4}$	$2.02\cdot10^{-4}$
Total NLC in the plaque ($c_{i2} + b_{i2}$)	$\mathbf{9.17 \cdot 10^{-2}}$	$\mathbf{8.47 \cdot 10^{-2}}$	$\mathbf{3.55 \cdot 10^{-2}}$	$1.71\cdot10^{-3}$	$2.56\cdot10^{-4}$
Free NLC in the media (c_m)	$4.89\cdot10^{-2}$	$3.17\cdot10^{-2}$	$1.60\cdot10^{-2}$	$1.39\cdot10^{-3}$	$5.37\cdot10^{-5}$
Bound NLC in the media (b_m)	$3.66\cdot10^{-3}$	$3.66\cdot10^{-3}$	$3.65\cdot10^{-3}$	$3.59\cdot10^{-3}$	$2.47\cdot10^{-3}$
Total NLC in the media ($c_m + b_m$)	$5.26\cdot10^{-2}$	$3.54\cdot10^{-2}$	$1.97\cdot10^{-2}$	$4.98\cdot10^{-3}$	$\mathbf{2.52 \cdot 10^{-3}}$
Total NLC in the adventitia (c_a)	$2.39\cdot10^{-21}$	$9.35\cdot10^{-3}$	$1.63\cdot10^{-2}$	$1.10\cdot10^{-3}$	$4.28\cdot10^{-5}$

3.3 Work 3: Mathematical modelling of endovascular drug delivery: balloons versus stents

The purpose of this work is to provide a computational model that allows drug delivery from drug-coated balloons (DCBs) and drug-eluting stents (DESs) to be investigated and compared. We present a comprehensive computational framework that employs a 2D-axisymmetric geometry, incorporates two nonlinear phases of drug binding (specific and nonspecific) and includes the influence of diffusion and advection, within a multilayer arterial wall. We utilise this framework to: (i) simulate drug delivery from different types of balloon platform; (ii) explore the influence of DCB application time; (iii) elucidate the importance on release kinetics of elevated pressure during DCB application; (iv) compare DCB delivery of two different drugs (sirolimus and paclitaxel) and; (v) compare simulations of DESs versus DCBs. Key measures of comparison are related to safety (drug content in tissue, DC) and efficacy (specific binding site saturation, %SBSS) markers. Our results highlight the pros and cons of each device in terms of DC and % SBSS levels achieved and, moreover, indicate the potential for designing a DCB that gives rise to sufficiently similar safety and efficacy indicators as current commercial DESs.

International Journal of Pharmaceutics

Mathematical modelling of endovascular drug delivery: Balloons versus stents

Javier Escuer, André Fensterseifer Schmidt, Estefanía Peña, Miguel A. Martínez, Sean McGinty

Escuer J., Fensterseifer Schmidt A., Peña E., Martínez M.A., McGinty S. (2022).
International Journal of Pharmaceutics, 121742.
JIF (2020) = 5.875 (Q1: 37/276 Pharmacology & Pharmacy).

Contents lists available at ScienceDirect

International Journal of Pharmaceutics

journal homepage: www.elsevier.com/locate/ijpharm

Mathematical modelling of endovascular drug delivery: Balloons versus stents

Javier Escuer[a], André Fensterseifer Schmidt[b], Estefanía Peña[a,c], Miguel A. Martínez[a,c], Sean McGinty[b,d,*]

[a] Aragón Institute for Engineering Research (I3A), University of Zaragoza, Spain
[b] Division of Biomedical Engineering, University of Glasgow, Glasgow, UK
[c] Biomedical Research Networking Center in Bioengineering, Biomaterials and Nanomedicine (CIBER-BBN), Spain
[d] Glasgow Computational Engineering Centre, Division of Infrastructure and Environment, University of Glasgow, Glasgow, UK

ARTICLE INFO

Keywords:
Pharmacokinetics
Drug-coated balloons
Drug-eluting stents
Computational modelling

ABSTRACT

The most common treatment for obstructive coronary artery disease (CAD) is the implantation of a permanent drug-eluting stent (DES). Not only has this permanency been associated with delayed healing of the artery, but it also poses challenges when treating subsequent re-narrowing due to in-stent restenosis (ISR). Drug-coated balloons (DCBs) provide a potential solution to each of these issues. While their use has been primarily limited to treating ISR, in recent years, DCBs have emerged as an attractive potential alternative to DESs for the treatment of certain de novo lesions. However, there remain a number of concerns related to the safety and efficacy of these devices. Firstly, unlike DESs, DCBs necessitate a very short drug delivery window, favouring a higher drug loading. Secondly, while the majority of coronary DCBs in Europe are coated with paclitaxel, the potential mortality signal raised with paclitaxel DCBs in peripheral interventions has shifted efforts towards the development of limus-eluting balloons. The purpose of this paper is to provide a computational model that allows drug delivery from DCBs and DESs to be investigated and compared. We present a comprehensive computational framework that employs a 2D-axisymmetric geometry, incorporates two nonlinear phases of drug binding (specific and non-specific) and includes the influence of diffusion and advection, within a multilayer arterial wall. We utilise this framework to (i) simulate drug delivery from different types of balloon platform; (ii) explore the influence of DCB application time; (iii) elucidate the importance on release kinetics of elevated pressure during DCB application; (iv) compare DCB delivery of two different drugs (sirolimus and paclitaxel) and; (v) compare simulations of DESs versus DCBs. Key measures of comparison are related to safety (drug content in tissue, *DC*) and efficacy (specific binding site saturation, %*SBSS*) markers. Our results highlight the pros and cons of each device in terms of *DC* and %*SBSS* levels achieved and, moreover, indicate the potential for designing a DCB that gives rise to sufficiently similar safety and efficacy indicators as current commercial DESs.

1. Introduction

Coronary artery disease (CAD) is the leading cause of death globally (Roth et al., 2018). The most common treatment for obstructive CAD is percutaneous coronary intervention (PCI) where a stent is deployed to widen the artery and restore blood flow. Nowadays, the vast majority of stents deliver drug to the arterial wall (so-called drug-eluting stents [DESs]) to counteract the inflammatory response following deployment, with the aim of preventing excessive neointimal regrowth, known as restenosis. While DESs work well in the majority of cases (Byrne et al., 2015), their permanency is associated with delayed healing of the vessel and thrombosis risk, with most patients receiving an expensive and prolonged course of dual antiplatelet therapy (Byrne et al., 2015). Moreover, if in-stent restenosis (ISR) occurs, it is not feasible to remove the original stent and insert a new one, which complicates the repeat revascularisation strategy.

Drug-coated balloons (DCBs) have emerged as an attractive alternative to DESs for the treatment of CAD in certain anatomical conditions. In particular, DCBs may be used in the treatment of ISR, where it is not feasible to insert a further DES (Scheller et al., 2006). Moreover,

---

* Corresponding author at: Division of Biomedical Engineering, University of Glasgow, Glasgow, UK.
E-mail address: sean.mcginty@glasgow.ac.uk (S. McGinty).

https://doi.org/10.1016/j.ijpharm.2022.121742
Received 26 February 2022; Received in revised form 3 April 2022; Accepted 8 April 2022

DCBs are becoming increasingly interesting in the context of treating small de novo lesions (Jeger et al., 2018). A key potential advantage of deploying a DCB over a DES is the lack of permanency. However, this may potentially be a disadvantage, where the brief period of deployment associated with DCBs presents only a short window for drug to be delivered. Specifically, while DCBs typically transfer drug rapidly to the arterial wall during a short application period of the order of 1 min (Cortese and Bertoletti, 2011; Heilmann et al., 2010), DESs usually offer sustained drug release over a period of weeks or months. It is therefore of interest to explore how the different time scales of delivery between DCBs and DESs influence drug delivery and retention. Current commercial DESs almost exclusively elute limus compounds (Lee and Torre Hernandez, 2018). While the first DCBs eluted paclitaxel (Scheller et al., 2006), thought to be advantageous given the short drug delivery window (Bozsak et al., 2014), more recent efforts have considered different formulations of limus-eluting balloons (e.g. utilising nanoparticle technology) (Sojitra et al., 2013). How the differing physico-chemical properties of these commonly used compounds influences the success of DCB treatment remains to be resolved (McQueen et al., 2021).

Mathematical and computational modelling has emerged as a powerful tool to simulate drug release from medical devices and subsequent transport in the biological environment. In particular, there is rich literature on mathematical and computational modelling of DESs (McGinty, 2014). Such analysis has uncovered that stent drug kinetics are governed by physiological transport forces (diffusion and advection) (Hwang et al., 2001), arterial ultrastructures (Hwang and Edelman, 2002) and the drug physicochemical properties (Hwang et al., 2003). These early studies provided mechanistic explanations for the superior results that were observed with stents coated with lipophilic vs hydrophilic compounds, while more recent work has highlighted the importance of including two phases of nonlinear drug binding (specific and non-specific) within the models (Tzafriri et al., 2009; Tzafriri et al., 2012; McKittrick et al., 2019), with saturation of specific receptors being strongly linked to efficacy, at least for sirolimus-eluting stents. It is notable that, despite the complex physics and biology that underpins these models, they were simplified in the sense that they considered only one spatial dimension. The most advanced models of DES kinetics now include multiple layers of the arterial wall in more realistic, but still idealised, 2D-axisymmetric models (Escuer et al., 2021).

Despite the plethora of models that consider DESs, there are only a handful of mathematical and computational models that focus on DCBs (Kolachalama et al., 2013; Mandal et al., 2016; Sarifuddin and Mandal, 2018; Tzafriri et al., 2019; Anbalakan et al., 2021; Colombo et al., 2021; Jain et al., 2022), each with their own set of strengths and limitations (Table 1). Commonalities between these models include the assumptions that drug is transported by diffusion within the arterial wall and that drug binding plays a key role in drug distribution and retention. However, the level of complexity of the binding model, the influence of other transport processes such as advection, and how the drug source is incorporated, is handled differently between the models. Moreover, the models range from 1D to 3D and while some incorporate disease (either heterogeneous (Sarifuddin and Mandal, 2018) or homogeneous (Anbalakan et al., 2021; Colombo et al., 2021)), some do not. The only existing model that incorporates the multilayer nature of the arterial wall has very recently been presented by (Jain et al., 2022). However, their primary goal was to provide an analytical solution, necessitating simplifications in other aspects (dimensionality and linearity of the binding model).

In this paper we present the most comprehensive model of DCB delivery, transport and retention to date. We employ a 2D-axisymmetric geometry, incorporate two nonlinear phases of binding (specific and non-specific) and include the influence of advection, within a multilayer arterial wall. We utilise this framework to (i) simulate drug delivery from different types of balloon platform (Kolachalama et al., 2013; Anbalakan et al., 2021); (ii) explore the influence of DCB application time; (iii) elucidate the importance on release kinetics of elevated pressure during DCB application; (iv) compare DCB delivery of two different drugs (sirolimus [SIR] and paclitaxel [PTX]) and; (v) compare simulations of DESs vs DCBs to explore if there are any potential benefits, in terms of safety and efficacy, of treating small de novo lesions with a DCB vs a DES.

2. Methodology

2.1. Geometrical Model

We consider two different 2D-axisymmetric geometries corresponding to idealised straight sections of coronary arteries where either a DCB is deployed or a DES with non-erodible polymeric coating is implanted (Fig. 1). In each case, a lesion length of 7 mm is assumed (Bozsak et al., 2014), while we calculate drug concentrations within an extended therapeutic domain of 10.5 mm in length. A three-layer arterial wall is considered, including the subendothelial space (SES), media and adventitia.

To model drug delivery from a DCB, we impose a flux condition on the lumen-tissue interface across the lesion, while drug delivery from a DES is assumed to occur from ten struts half-embedded in the arterial wall (Bozsak et al., 2014; Escuer et al., 2021). Drug transport within the arterial wall is governed by advection-diffusion-reaction equations, which we parameterise on a layer-specific basis. It is noteworthy that the flow field within the porous tissue is governed by Darcy's law, driven by the pressure gradient between the lumen and the perivascular tissue. In existing state-of-the-art models of drug kinetics following stenting (Bozsak et al., 2014; Escuer et al., 2020; Escuer et al., 2021), the pressure in the lumen is commonly calculated by solving the steady Navier–-Stokes and continuity equations, while drug transport within the lumen is typically modelled through an advection–diffusion equation. Under these conditions, our preliminary simulations (See Supplementary Material S1) indicated that the pressure along the lumen-wall interface is approximately constant. Moreover, they indicated that advection–diffusion of drug within the lumen leads to essentially zero drug concentration in the lumen. In other words, the lumen effectively acts as

Table 1
Summary of the existing models of DCB kinetics, highlighting key considerations and limitations.

Reference	Drug source	Binding model	Advection included?	Disease included?	Dimension	Multilayer?
(Kolachalama et al., 2013)	Flux	One phase, nonlinear	No	No	1D	No
(Sarifuddin and Mandal, 2018)	Flux	One phase, nonlinear	Yes	Yes	2D	No
(Tzafriri et al., 2019)	Flux	Two phases, nonlinear	No	No	1D	No
(Anbalakan et al., 2021)	Flux	Two phases, nonlinear	Yes	Yes	2D	No
(Colombo et al., 2021)	Constant	One phase, nonlinear	No	Yes	3D	No
(Jain et al., 2022)	Constant	One phase, linear	Yes	No	1D	Yes

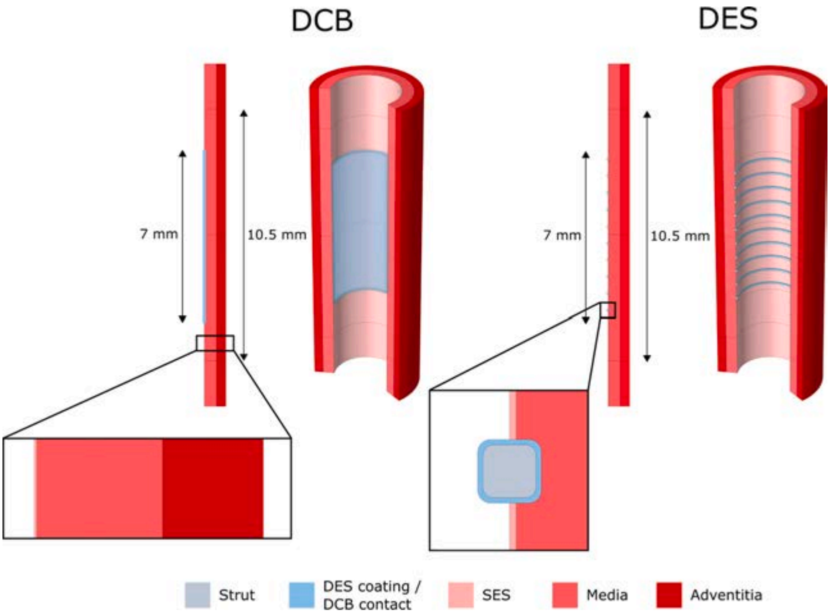

Fig. 1. Schematic summarising the geometric model employed for the DCB (left) and the DES (right). SES: subendothelial space. In each case, a lesion length of 7 mm is assumed, while we calculate drug concentrations within an extended therapeutic domain of 10.5 mm in length.

a sink for drug. Taken together, these findings allow us to significantly reduce the complexity of the model: through symmetry, we only need to solve our model equations on half the arterial wall domain. The pressure calculated from our preliminary simulations is used to define the pressure gradient (and consequently the advective term) in Darcy's law, while an infinite sink condition is assumed for drug in contact with the lumen.

2.2. Governing equations

2.2.1. Modelling drug release from the DCB and DES

We adopt two distinct approaches to modelling drug release from the DCB and the DES. As observed in Table 1, existing models of drug delivery from DCBs either prescribe a flux at the lumen-tissue interface or impose a constant drug concentration for the duration of balloon application. During the period of balloon application ($t \leqslant t_0$) we adopt the former approach, utilising two different flux expressions from the literature that have been parameterised on experimental data. The first is provided by (Kolachalama et al., 2013) who considered a zotarolimus-eluting balloon, while the second is provided by (Anbalakan et al., 2021) who considered a sirolimus-eluting balloon. The same expression is used to describe the flux, J_{DCB}, in each case,

$$J_{DCB} = \frac{kA}{M_w}\exp(-kt), \quad t \leqslant t_0, \tag{1}$$

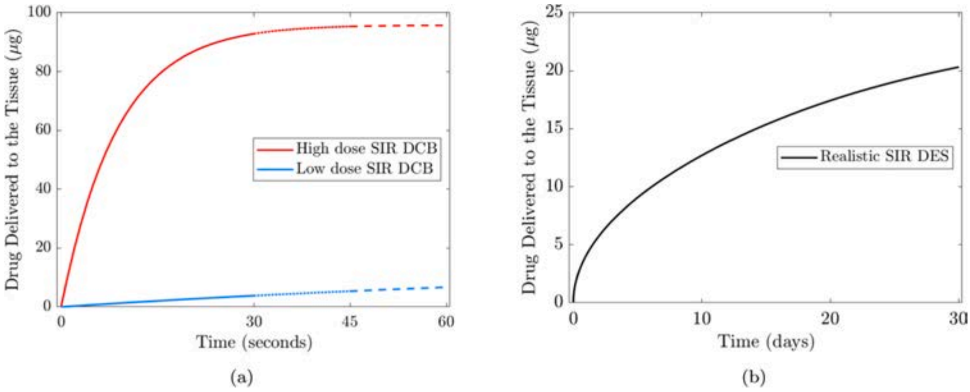

Fig. 2. Drug mass delivered to the arterial wall (a) Low dose and high dose sirolimus (SIR) DCB delivery, showing 30 s, 45 s and 60 s application times (different line styles). Simulations employ Eq. 1 with $k = 0.009221\ \mathrm{s}^{-1}$, $A = 0.24\ \mu\mathrm{g/mm}^2$ for the low dose flux expression (Kolachalama et al., 2013) and $k = 0.1135\ \mathrm{s}^{-1}$, $A = 1.4618\ \mu\mathrm{g/mm}^2$ for the high dose flux expression (Anbalakan et al., 2021). (b) SIR delivered to tissue from a realistic DES based on XIENCE V® (Abbott Laboratories, Abbott Park, IL, USA) drug release kinetics, with total drug loading of $M_{DES}^0 = 50\ \mu g$, strut thickness of $81\mu\mathrm{m}$, coating thickness of $L_{poly} = 8\ \mu\mathrm{m}$ and drug coating diffusion coefficient of $D_{DES} = 1.5 \times 10^{-17}\ \mathrm{m}^2\mathrm{s}^{-1}$.

where k and A are empirically estimated constants, M_w is the molecular weight of the drug and t is the time. Whilst the same form of expression is used, the inferred parameter values are quite different, resulting in a substantial difference in the overall influx of drug. To effect comparison between the respective flux expressions, we assume k and A are drug-independent and utilise the molecular weight, M_w, of sirolimus in Eq. 1. The mass of drug delivered to the tissue over 60 s is then found to vary from $6.7\,\mu$g to $96.3\,\mu$g using the (Kolachalama et al., 2013) and (Anbalakan et al., 2021) fluxes, respectively (Fig. 2a). This discrepancy is likely due to the differing excipients used (proprietary and polyethylene oxide, respectively) and, to a lesser extent, the physicochemical properties of the drugs. While both the mass of drug delivered and the shape of the flux vary, for the remainder of this paper we refer to the flux expression provided by (Kolachalama et al., 2013) as *low dose* while we refer to the flux expression provided by (Anbalakan et al., 2021) as *high dose*.

Following balloon removal ($t > t_0$), the flux boundary condition (1) is replaced with a sink boundary condition for drug ($c_{DCB} = 0$), to be consistent with our observation (see Supplementary Material S1.3) that any drug at the lumen-wall interface is washed away by the blood. Note that the imposition of such a boundary condition assumes that balloon coating adherence to the tissue is negligible, since this would potentially act as a reservoir for more sustained drug release. Such a mechanism has been reported in the literature for certain drug/excipient combinations (Chang et al., 2019; Tzafriri et al., 2020).

In line with the existing literature (McGinty, 2014), drug release from a DES with non-erodible polymeric coating is modelled as a diffusion dominated process satisfying a linear diffusion equation:

$$\frac{\partial c_{DES}}{\partial t} = \nabla\cdot(D_{DES}\nabla c_{DES}), \tag{2}$$

where $c_{DES}\ (r,z,t)$ is the volume-averaged concentration of drug within the stent coating and D_{DES} represents the effective drug diffusion coefficient within the polymer, assumed to be constant and isotropic. At $t = 0$, the drug is assumed to be completely contained within the polymer coating in dissolved phase (free drug) at uniform concentration, C_0, derived from the drug loading mass. The strut shape, strut thickness, coating thickness L_{poly}, drug mass loading M^0_{DES} and drug diffusion coefficient (Fig. 2b) are based upon XIENCE V® (Abbott Laboratories, Abbott Park, IL, USA) which releases approximately 80% of its drug load within 30 days (Perkins et al., 2009).

2.2.2. *Modelling drug transport within the arterial wall*

The arterial wall is modelled as a multilayered structure organised in three porous layers: SES, media and adventitia. Due to the porous nature of the tissue, the flow field through the different regions of the arterial wall is calculated using Darcy's law and the continuity equation:

$$\boldsymbol{u}_i = \frac{K_i}{\mu_p}\nabla p_i,\ \ \nabla\cdot\boldsymbol{u}_i = 0, \tag{3}$$

where the subscript $i = \{ses, m, a\}$ denotes the SES, the media and the adventitia, respectively; $\boldsymbol{u}_i$ is the transmural velocity vector field; K_i is the Darcian permeability; μ_p is the dynamic viscosity of the plasma; and p_i is the pressure field. The endothelium (ET), internal and external elastic laminae (IEL and EEL, respectively) are treated as semipermeable membranes and the fluid flux across them, $J_{v,j}$, is described by the Kedem-Katchalsky equations (Kedem and Katchalsky, 1958). Neglecting the osmotic contribution as an approximation (Formaggia et al., 2010; Bozsak et al., 2014; Bozsak et al., 2015; Escuer et al., 2020; Escuer et al., 2021), the Kedem-Katchalsky equations for fluid flux can be simplified as:

$$J_{v,j} = L_{p,j}\Delta p_j, \tag{4}$$

where the subscript $j = \{et, iel, eel\}$ denotes the endothelium (lumen-SES interface), the internal elastic lamina (SES-media interface) and the external elastic lamina (media-adventitia interface), respectively; $L_{p,j}$ is the membrane hydraulic conductivity and; Δp_j the pressure drop across each semipermeable membrane. The equations for the flux J_v, corresponding to each boundary, are shown in the Supplementary Material (S2).

Due to DCB and DES deployment, the endothelium is assumed to be denuded across the lesion length of 7 mm and, in the case of the DES, between struts and a distance corresponding to half of the interstrut spacing (ISS) proximal and distal to the lesion (Bozsak et al., 2014). Outside of these regions the endothelium is assumed to be intact. In denuded regions, the volume flux across the endothelium simplifies to continuity of pressure, i.e. $p_l = p_{ses}$, where the subscript l denotes the lumen. Upstream of the lesion, we impose a zero-flow condition at the longitudinal boundaries, $U_i := -\boldsymbol{n}_i\cdot\boldsymbol{u}_i = 0$, where $\boldsymbol{n}_i$ is the unit outward normal vector to the corresponding exterior boundary, in agreement with previous studies (Bozsak et al., 2014; Escuer et al., 2020). This choice of boundary condition is justified by the fact that we are interested in computing drug concentrations only within the therapeutic domain while these boundaries are imposed sufficiently far upstream and downstream of the lesion. Similar conditions are applied at the axis of symmetry at the midpoint of the lesion. Moreover, it is assumed that the plasma cannot penetrate the surface of the DES polymer coating. At the lumen and perivascular tissue, constant pressures of 100 mmHg (derived from our prelimary simulations, see Supplementary Material S1.3) and 30 mmHg (Ai and Vafai, 2006) are considered, emulating a physiologically realistic pressure drop of 70 mmHg (Meyer et al., 1996). However, during the period of DCB inflation ('*inf*'), we consider an increased pressure of $p_{inf} = 8$ atm (Anbalakan et al., 2021) across the denuded region, corresponding to the pressure at which balloons are typically inflated during angioplasty:

$$p_{ses} = \begin{cases} p_{inf}, & t \leqslant t_0 \\ p_l, & t > t_0. \end{cases} \tag{5}$$

Drug transport within the SES and the adventitia may be written as advection–diffusion equations:

$$\frac{\partial c_{ses}}{\partial t} + \frac{\gamma_{ses}}{\phi_{ses}}\boldsymbol{u}_{ses}\cdot\nabla c_{ses} = \nabla\cdot(\boldsymbol{D}_{ses}\nabla c_{ses}), \tag{6}$$

$$\frac{\partial c_a}{\partial t} + \frac{\gamma_a}{\phi_a}\boldsymbol{u}_a\cdot\nabla c_a = \nabla\cdot(\boldsymbol{D}_a\nabla c_a). \tag{7}$$

The parameters $\gamma, \phi, \boldsymbol{u}, \boldsymbol{D}$ and $c(r,z,t)$ refer to the hindrance coefficients, porosities, transmural fluid velocities calculated by Eq. (3), diffusivity tensors and dissolved drug concentrations within the respective domains. Within the media, in addition to advection and diffusion, drug binding processes are thought to strongly influence drug transport and retention. Therefore, we incorporate state-of-the-art two-phase nonlinear saturable binding kinetics, distinguishing between drug bound specifically to target receptors (s) and non-specifically to extracellular matrix (ECM) components (ns). The resulting advection–diffusion-reaction equation within the media is:

$$\frac{\partial c_m}{\partial t} + \frac{\gamma_m}{\phi_m}\boldsymbol{u}_m\cdot\nabla c_m = \nabla\cdot(\boldsymbol{D}_m\nabla c_m) - \frac{\partial b^{ns}_m}{\partial t} - \frac{\partial b^{s}_m}{\partial t}, \tag{8}$$

$$\frac{\partial b^{ns}_m}{\partial t} = k^{ns}_{on}c_m(b^{ns}_{max,m} - b^{ns}_m) - k^{ns}_{off}b^{ns}_m, \tag{9}$$

$$\frac{\partial b^{s}_m}{\partial t} = k^{s}_{on}c_m(b^{s}_{max,m} - b^{s}_m) - k^{s}_{off}b^{s}_m, \tag{10}$$

where $b^s_m(r,z,t)$ and $b^{ns}_m(r,z,t)$ denote the concentration of drug bound specifically and non-specifically, with respective binding on and binding off rates given by $k^s_{on}, k^{ns}_{on}, k^s_{off}$ and k^{ns}_{off}. The parameters $b^s_{max,m}, b^{ns}_{max,m}$ denote, respectively, the maximum density of specific and non-specific binding sites within the media. Discontinuity of solute flux across the semipermeable membranes, $J_{s,j}$, is governed by the Kedem-Katchalsky equations (Kedem and Katchalsky, 1958):

$$J_{s,j} = P_j \Delta c_j + s_j \overline{c}_j J_{v,j} \tag{11}$$

where P_j is the permeability of each semipermeable membrane; Δc_j is the solute concentration difference; s_j is the sieving coefficient and; $\overline{c}_j$ is the weighted average concentration on either side of the corresponding membrane (Levitt, 1975). The equations for the flux J_s corresponding to each boundary are shown in the Supplementary Material (S2). The upstream tissue boundary (Vairo et al., 2010) and symmetry plane at the centre of the lesion are subjected to zero-flux conditions: $N_i := -\boldsymbol{n}_i\cdot(-\boldsymbol{D}_i\nabla c_i + \boldsymbol{u}_i c_i) = 0$. A perfect sink condition for the free drug is applied at the perivascular side, $c_a = 0$ (Bozsak et al., 2014; Escuer et al., 2020) and in the case of the DES also at the lumen, $c_{ses} = 0$. In the case of the DES, continuity of drug concentration and mass flux is prescribed across the outer boundary of the polymeric stent coating:

$$c_{DES} = c_k, \tag{12}$$

$$J_{s,DES} = \left(-\boldsymbol{D}_{DES}\nabla c_{DES}\right)\cdot\boldsymbol{n}_{DES} = -\left(-\boldsymbol{D}_k\nabla c_k + \boldsymbol{u}_k c_k\right)\cdot\boldsymbol{n}_k, \quad k = \{ses, m\}. \tag{13}$$

Finally, we assume a perfect sink at the interface between the stent struts and the lumen ($c_{DES} = 0$) and that the metallic DES struts are imper-

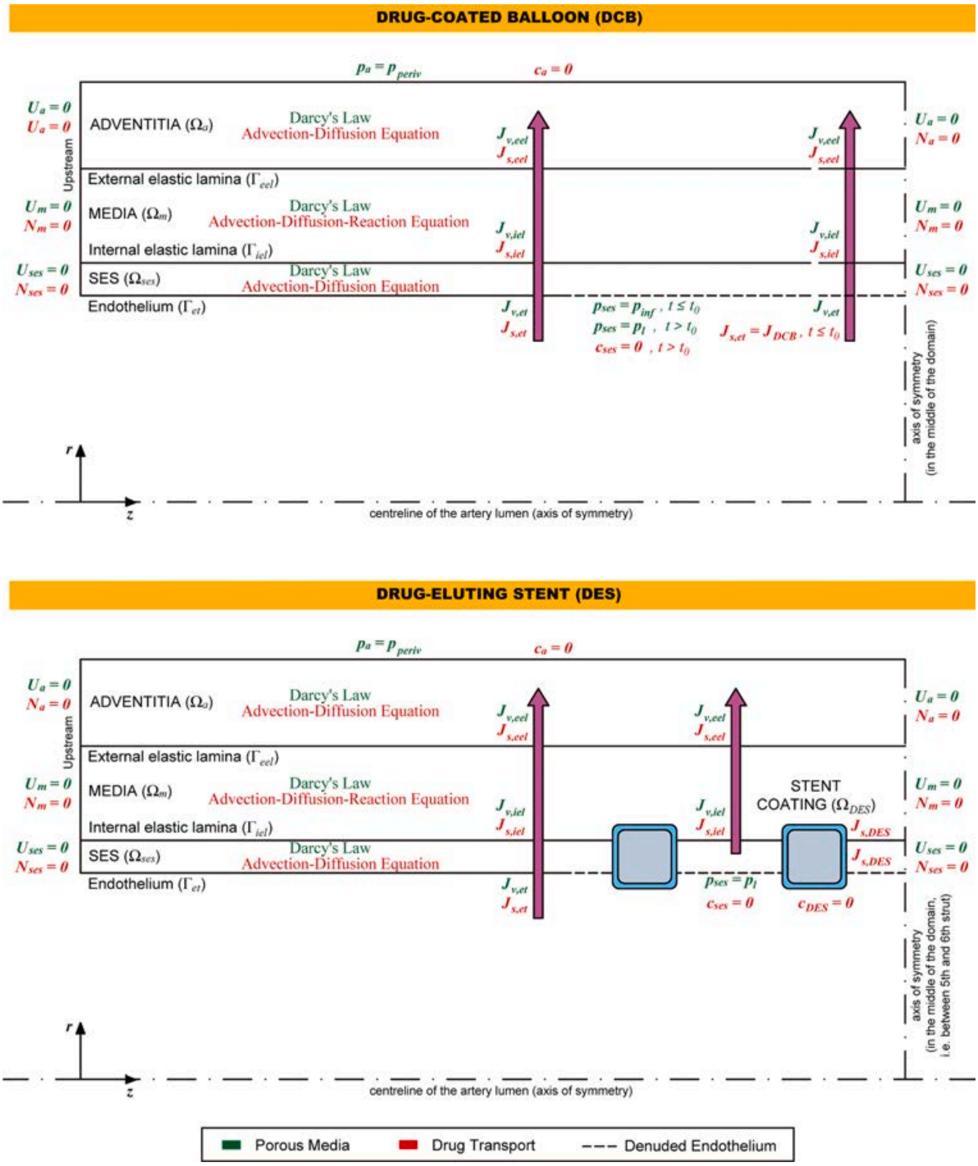

Fig. 3. Schematic summarising the governing equations and boundary conditions involved in the computational models of DCB and DES drug delivery. For notation, please refer to the main text.

meable to the drug ($-\boldsymbol{n}_{DES}\cdot(-D_{DES}\nabla c_{DES}) = 0$). We refer the reader to Fig. 3 for a schematic summarising the governing equations and boundary conditions involved in the computational models of DCB and DES drug delivery.

2.3. Numerical methods

The commercial finite element (FE) package COMSOL Multiphysics 5.6 (COMSOL AB, Burlington, MA, USA) was used to build the mesh and to numerically solve the governing equations described in Section 2 for the different cases considered. The computational analysis for the DCB

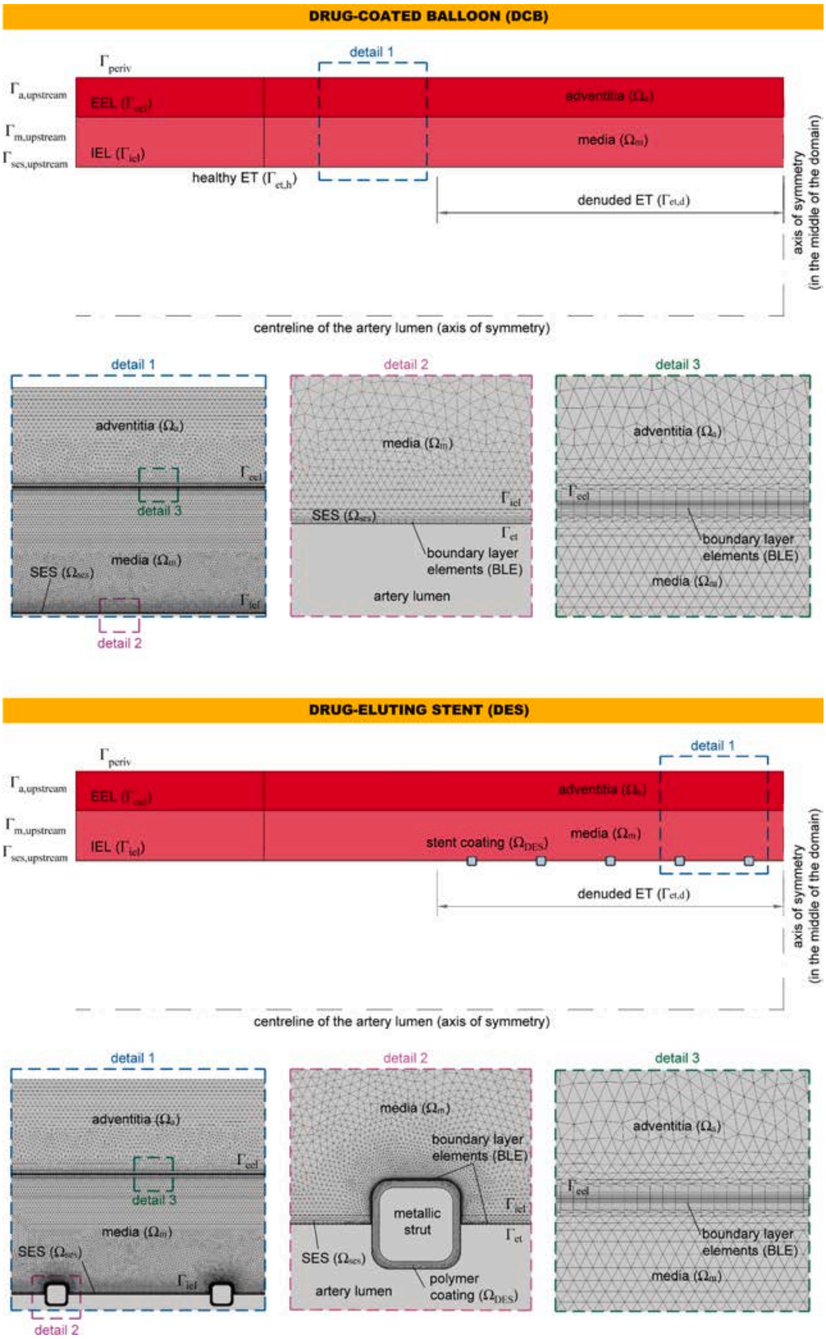

Fig. 4. Detailed view of the Finite Element mesh used in the computations. For notation, please refer to the main text.

cases was conducted in four steps: (1) a stationary analysis of the plasma filtration during inflation; (2) a time-dependent drug transport analysis coupled with the solutions of transmural flow computed in the previous step; (3) a stationary analysis of the plasma filtration post-angioplasty; and (4) a time-dependent drug transport analysis coupled with the solutions of transmural flow computed in the previous step. The computational analysis for the DES cases was conducted in two steps: (1) a stationary analysis of the plasma filtration; (2) a time-dependent drug transport analysis coupled with the solutions of transmural flow computed in the previous step. A sensitivity analysis was carried out in order to evaluate the influence of the mesh and time-step size on the solution. Mesh density and time-step independence was assumed when there was less than 1% difference in the time varying profiles of drug content in the tissue after several mesh and time-step refinements. The computational domains were discretized in space using triangular elements, resulting in an overall mesh varying between approximately 128000 and 594000 elements for the DCB models and between 158000 and 300000 elements for the DES models. The triangular mesh was enhanced with boundary layer elements (BLE) at the endothelium and the external elastic lamina for both DES and DCB cases and, moreover, at the interface of the stent polymeric coating with the tissue for DES cases, in order to smooth the sharp initial condition between the stent polymer and the surrounding domain. The spatial discretization employs quadratic Lagrange elements for the porous media and drug dynamics problems, respectively. Details of the mesh used in the different regions of the computational models are illustrated in Fig. 4.

A Multifrontal Massively Parallel Sparse (MUMPS) direct solver was used to solve the stationary steps with a tolerance for the relative error of the solution of 10^{-3}. The backward differentiation formula (BDF) method was used for the time discretization of the transient steps, with variable order of accuracy between 1 and 5 and variable time-step size, with the maximum time-step size restricted to 1 h. The relative and absolute tolerance was set to 10^{-3} and 10^{-4}, respectively. The resulting system of time-dependent partial differential equations (PDEs) was solved using a Parallel Direct Sparse Solver (PARDISO). Using14 cores of an Intel® Core$^{\mathrm{TM}}$ i9-10940X CPU @ 3.30 GHz processor, the computation time for each of the simulations carried out varied between 2 and 19 h.

2.4. *Summary of investigated cases*

We simulate 5 distinct cases covering DCBs with different drug delivery kinetics, drug doses and drug types and DESs with different drug release kinetics. The various cases considered are summarised in Table 2. Case 5 represents an ‘artificial’ stent where we have adjusted the drug diffusion coefficient in the stent coating and coating thickness to match the mass of drug delivered by 60 s with Case 2 (the high dose SIR DCB). The purpose of simulating Case 5 is to establish if, in principle, it would be possible to design a DES with similar release kinetics to the DCB.

2.5. *Analysis of the results*

In order to facilitate comparison between the various cases simulated (Table 2) we calculate three time-dependent quantities of interest over a period of 30 days. Firstly, drug content (*DC*) quantifies μg drug/g tissue and is a key measure of safety. The *DC* is given by:

$$DC(t) = \sum_i \frac{M_w}{\rho V_i} \int_{V_i} \left(c_i + b_i^s + b_i^{ns}\right) dV_i, \tag{14}$$

where V_i denotes the volume of layer i and ρ is the density of wet arterial tissue. Plotting *DC* over time allows visualisation of the peak drug concentration in the tissue and the time at which this occurs, as well as indicating the ability of the tissue to retain the drug. Secondly, since sustained saturation of specific binding sites (% *SBSS*) has been strongly linked with efficacy (Tzafriri et al., 2012; McKittrick et al., 2019) we compute this quantity via:

$$\%SBSS(t) = \frac{100}{V_m \cdot b^s_{max,m}} \int_{V_m} b^s_m dV_m. \tag{15}$$

Finally, while not directly indicative of safety or efficacy, non-specific binding site saturation (% *NSBSS*) is also computed since it contributes to drug retention within the tissue:

Table 3
List of model parameters related to the arterial tissue.

Parameter	Description	Value	Reference
r_l	Lumen radius	1.5 mm	(Mongrain et al., 2005)
δ_{ses}	Intima thickness	0.01 mm	(Karner et al., 2001)
δ_m	Media thickness	0.5 mm	(Vairo et al., 2010)
δ_a	Adventitia thickness	0.4 mm	(Creel et al., 2000)
p_l	Pressure in the lumen	100 mmHg	(Ai and Vafai, 2006)
p_{inf}	Pressure during DCB application	8 atm	(Anbalakan et al., 2021)
p_{periv}	Pressure in the perivascular tissue	30 mmHg	(Ai and Vafai, 2006)
ρ_p	Plasma density	1060 kg m^{-3}	(Bozsak et al., 2014)
μ_p	Plasma dynamic viscosity	$7.2 \cdot 10^{-4}$ Pa s	(Zunino, 2004)
ϕ_{ses}	Porosity of the intima	0.983	(Ai and Vafai, 2006)
ϕ_m	Porosity of the media	0.258	(Ai and Vafai, 2006)
ϕ_a	Porosity of the adventitia	0.85	(Lovich and Edelman, 1996)
γ_{ses}	Hindrance coefficient in the intima	1	(Escuer et al., 2020)
γ_m	Hindrance coefficient in the media	0.845	(Escuer et al., 2020)
γ_a	Hindrance coefficient in the adventitia	1	(Escuer et al., 2020)
κ_{ses}	Darcy permeability in the intima	$2.2{\cdot}10^{-16}$ m^2	(Ai and Vafai, 2006)
κ_m	Darcy permeability in the media	$2{\cdot}10^{-18}$ m^2	(Zunino, 2004)
κ_a	Darcy permeability in the adventitia	$2{\cdot}10^{-18}$ m^2	(Vairo et al., 2010)
$L_{p,et}$	Hydraulic conductivity of endothelium	$2.2{\cdot}10^{-12}$ m^2 s kg^{-1}	(Bozsak et al., 2014)
$L_{p,iel}$	Hydraulic conductivity of IEL	$2.2{\cdot}10^{-9}$ m^2 s kg^{-1}	(Bozsak et al., 2014)
$L_{p,eel}$	Hydraulic conductivity of EEL	$2.2{\cdot}10^{-9}$ m^2 s kg^{-1}	(Escuer et al., 2020)
ρ	Density of wet arterial tissue	0.983 g ml^{-1}	(Tzafriri et al., 2012)

Table 2
Summary of the different cases considered. (*) denotes the initial drug loading considering the full domain.

Case	Name	Device	Drug	J_{DCB}	D_{DES}	M^0_{DES}	Coating thickness
1	Low Dose SIR DCB	DCB	Sirolimus	Low dose	n/a	n/a	n/a
2	High Dose SIR DCB	DCB	Sirolimus	High dose	n/a	n/a	n/a
3	Low Dose PTX DCB	DCB	Paclitaxel	Low dose	n/a	n/a	n/a
4	Realistic SIR DES	DES	Sirolimus	n/a	1.5×10^{-17} m^{2}s^{-1}	50 μg (*)	8 μm
5	Fast SIR DES	DES	Sirolimus	n/a	1×10^{-13} m^{2}s^{-1}	96.3 μg (*)	1.456 μm

$$\%NSBSS(t) = \frac{100}{V_m \cdot b^{ns}_{max,m}} \int_{V_m} b^{ns}_m dV_m. \tag{16}$$

In addition, we calculate spatial maps of drug distribution at 6 time points between 10 min and 30 days. The values of the various model parameters used in the simulations are included in Tables 3 and 4.

3. Results

3.1. Comparison between different DCB platforms

We start by comparing Case 1 with Case 2, i.e. deployment of SIR coated DCBs following either the low or high dose drug flux expression (Fig. 5a–b). In Fig. 5a (Left) we observe that for the low dose SIR DCB, as the balloon application time is increased, the peak *DC* increases since more drug is delivered to the arterial wall. This is true regardless of whether the lumen pressure for $t \leqslant t_0$ is simulated to be $p = 100$ mmHg or to match the balloon inflation pressure $p = p_{inf}$. However, it is notable that when $p = p_{inf}$ for $t \leqslant t_0$, *DC* declines substantially slower with time, in agreement with (Sarifuddin and Mandal, 2018). The rationale for this is that the increased advective term as a result of increased pressure gradient delivers drug deeper into the arterial wall, meaning that less drug is exposed to the lumen sink following balloon removal. This is more clearly observed in the spatial plots (Supplementary Fig. S2). This result indicates that it is imperative to incorporate the balloon inflation pressure within drug delivery simulations. The aforementioned trends are replicated when considering the high dose SIR DCB (Fig. 5b left). However, the corresponding peak *DC* values are substantially higher (greater than 10-fold) for the high dose SIR DCB compared with those achieved with the low dose SIR DCB and there is only a marginal difference in *DC* when extending the balloon application time from 30 −60 s for the high dose SIR DCB.

For the low dose SIR DCB, the majority of specific binding sites are saturated rapidly (within the first few days) in all cases considered (Fig. 5a right). The higher the DCB application time, the higher % *SBSS* is. Moreover, for the same reasons as described above, when $p = p_{inf}$ for $t \leqslant t_0$, higher % *SBSS* is achieved. This is echoed in the spatial plots of specific bound drug concentration (Supplementary Fig. S3). It is notable that after the early rapid increase in % *SBSS*, the rate of increase proceeds at a significantly slower rate, before reaching a peak and then declining approximately linearly with time over the remainder of the 30 days simulated: in the absence of a sustained source of drug delivery, drug unbinds and is cleared through the tissue via advection and diffusion, without being replenished. In Fig. 5b (right) we observe that the high dose SIR DCB leads to more rapid and higher levels of specific binding site saturation compared with the low dose SIR DCB. In particular, we note that approximately 95–100% *SBSS* is observed for all balloon application times considered. Moreover, the decline of % *SBSS* is slower than for the low dose SIR DCB. In other words, more receptors are saturated for longer with the high dose SIR DCB. Similarly to the low dose SIR DCB case, when $p = p_{inf}$ for $t \leqslant t_0$, higher % *SBSS* is achieved. For each case, %*NSBSS* follows a similar pattern to *DC*: the peak value is reached rapidly within the first day, before a quick decline to very low levels within approximately 15 days, indicating relatively rapid unbinding from non-specific binding sites (Supplementary Fig. S1a-S1b). In each case, %*NSBSS* is markedly lower than %*SBSS*, due to the larger density of non-specific binding sites compared with specific binding sites.

3.2. Comparison between DCBs coated with different drugs

In Fig. 6a–b we examine the influence of varying the drug delivered (either SIR or PTX) from the low dose DCB platform (Case 1 vs Case 3). Having already established the importance of accounting for the increased pressure during balloon inflation, all plots in Fig. 6a–b consider $p = p_{inf}$ for $t \leqslant t_0$. Since the mass of drug delivered is identical by definition, the *DC* peak is the same. However, the differing

Table 4
List of model parameters related to the different drugs considered: sirolimus (SIR) and paclitaxel (PTX).

Parameter	Description	Value SIR	Value PTX	Ref.
D_{ses}	Effective diffusion coefficient in the intima	$1.67 \cdot 10^{-11}$ m^2 s^{-1}	$1.70 \cdot 10^{-11}$ m^2 s^{-1}	(Bozsak et al., 2014)
$D_{m,r}$	Effective radial diffusion coefficient in the media	$7 \cdot 10^{-12}$ m^2 s^{-1}	$2 \cdot 10^{-12}$ m^2 s^{-1}	(Levin et al., 2004)
$D_{m,z}$	Effective axial diffusion coefficient in the media	$4 \cdot 10^{-11}$ m^2 s^{-1}	$5 \cdot 10^{-11}$ m^2 s^{-1}	(Levin et al., 2004)
D_a	Effective diffusion coefficient in the adventitia	$4 \cdot 10^{-12}$ m^2 s^{-1}	$4 \cdot 10^{-12}$ m^2 s^{-1}	(Escuer et al., 2020)
P_{et}	Permeability of ET	$3.6 \cdot 10^{-6}$ m s^{-1}	$3.0 \cdot 10^{-6}$ m s^{-1}	(Bozsak et al., 2014)
P_{iel}	Permeability of IEL	$9.6 \cdot 10^{-6}$ m s^{-1}	$9.8 \cdot 10^{-6}$ m s^{-1}	(Bozsak et al., 2014)
P_{eel}	Permeability of EEL	$9.6 \cdot 10^{-6}$ m s^{-1}	$9.6 \cdot 10^{-6}$ m s^{-1}	(Escuer et al., 2020)
s_{et}	Sieving coefficient in the ET	0.855	0.860	(Bozsak et al., 2014)
s_{iel}	Sieving coefficient in the IEL	1	1	(Bozsak et al., 2014)
s_{eel}	Sieving coefficient in the EEL	1	1	(Escuer et al., 2020)
K^{ns}_d	Non-specific equilibrium dissociation constant	$2.6 \cdot 10^{-3}$ mol m^{-3}	$3.1 \cdot 10^{-3}$ mol m^{-3}	(Rami Tzafriri et al., 2009)
k^{ns}_{on}	Non-specific drug binding rate constant	2 m^3 mol^{-1} s^{-1}	0.17 m^3 mol^{-1} s^{-1}	(Rami Tzafriri et al., 2009; Escuer et al., 2020)
k^{ns}_{off}	Non-specific drug unbinding rate constant	$5.2 \cdot 10^{-3}$ s^{-1}	$5.27 \cdot 10^{-4}$ s^{-1}	(McGinty and Pontrelli, 2016; Escuer et al., 2020)
$b^{ns}_{max,m}$	Non-specific binding site density in the media	0.363 mol m^{-3}	0.117 mol m^{-3}	(Tzafriri et al., 2012; Rami Tzafriri et al., 2009; Díaz et al., 2003)
K^s_d	Specific equilibrium dissociation constant	$2 \cdot 10^{-7}$ mol m^{-3}	$2.5 \cdot 10^{-5}$ mol m^{-3}	(Bierer et al., 1990; Díaz et al., 2003)
k^s_{on}	Specific drug binding rate constant	800 m^3 mol^{-1} s^{-1}	$3.6 \cdot 10^{-3}$ m^3 mol^{-1} s^{-1}	(Wear and Walkinshaw, 2007; Díaz et al., 2003)
k^s_{off}	Specific drug unbinding rate constant	$1.6 \cdot 10^{-4}$ s^{-1}	$9.1 \cdot 10^{-2}$ s^{-1}	(McGinty and Pontrelli, 2016; Díaz et al., 2003)
$b^s_{max,m}$	Specific binding site density in the media	$3.3 \cdot 10^{-3}$ mol m^{-3}	$1.0 \cdot 10^{-2}$ mol m^{-3}	(Tzafriri et al., 2012; Díaz et al., 2003)
M_w	Molecular weight	914.2 g mol^{-1}	853.9 g mol^{-1}	(Levin et al., 2004)

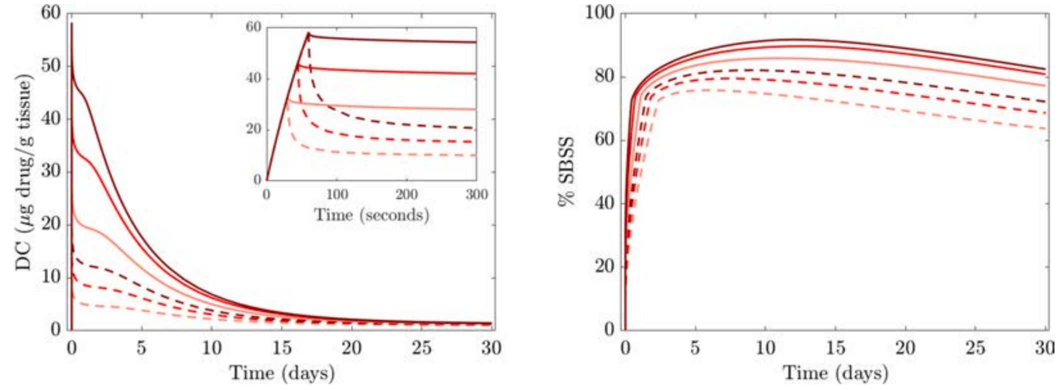

(a) Case 1: Low Dose SIR DCB

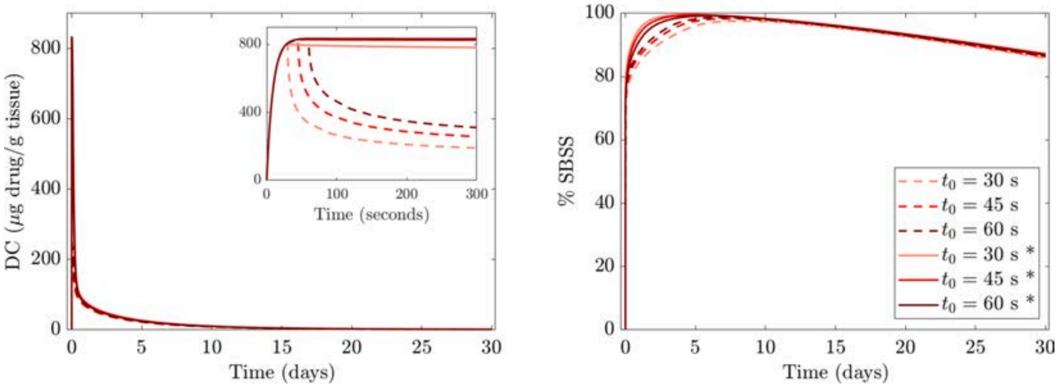

(b) Case 2: High Dose SIR DCB

Fig. 5. Comparison between (a) Case 1 (Low Dose SIR DCB) and (b) Case 2 (High Dose SIR DCB). LEFT: Drug Content (*DC*) vs time. RIGHT: % *SBSS* vs time. (*) denotes pressure increased over lesion to $p = p_{inf}$ for $t \leq t_0$ to match balloon inflation pressure.

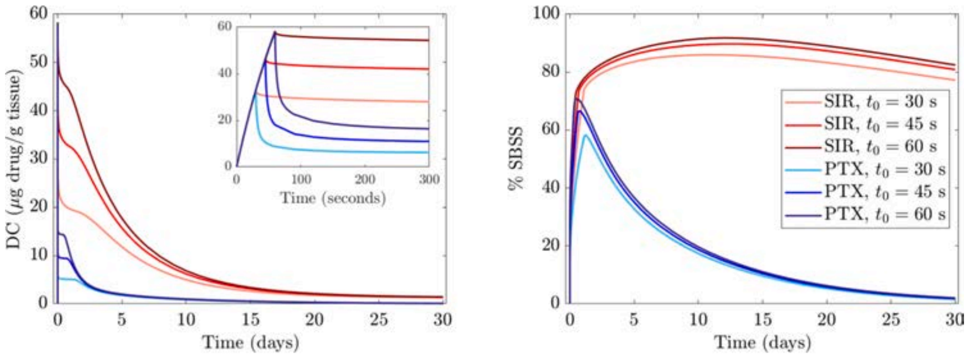

(a)

(b)

Fig. 6. Comparison between Case 1 (Low Dose SIR DCB) and Case 3 (Low Dose PTX DCB). (a): Drug Content (*DC*) vs time. (b) % *SBSS* vs time. In all cases $p = p_{inf}$ for $t \leq t_0$ to match balloon inflation pressure.

physiochemical properties of PTX gives rise to substantially quicker decline in *DC* levels within the arterial wall, compared with SIR (Fig. 6a). This is reflected in the % *SBSS* plot (Fig. 6b), where we observe lower peak specific receptor saturation values, and significantly faster decline of % *SBSS* for the PTX DCB compared with the SIR DCB. In other words, with the same delivery kinetics, in our simulations SIR is retained within the tissue for longer than PTX. This is a direct consequence of the differing physio-chemical properties of the drugs that we have obtained from the literature (we refer the reader to the Limitations section for discussion on this). In each case, there is a small increase in % *SBSS* with increased duration of balloon application. Regardless of which drug is used, %*NSBSS* never comes close to 100% saturation, reaching peaks of approximately 30% and 25% for the low dose SIR DCB and low dose PTX DCB, respectively (Supplementary Fig. S1c).

3.3. Comparison between DCB and DES

In Fig. 7a–b we compare the results for (i) the low dose SIR DCB; (ii) the high dose SIR DCB; (iii) the realistic SIR stent providing sustained drug release and; (iv) an artificial fast SIR stent whose properties have been tailored to match the drug influx from the high dose SIR DCB. As expected, we observe a significantly higher *DC* peak (greater than 10-fold) with the high dose SIR DCB and fast SIR DES compared with the realistic SIR DES and the low dose SIR DCB (Fig. 7a). Moreover, the peak occurs earlier for the rapid delivery configurations (low dose SIR DCB, high dose SIR DCB, and fast SIR DES), compared with the more sustained release from the realistic SIR DES. Despite achieving a higher peak *DC*, the low dose SIR DCB, high dose SIR DCB and fast SIR DES result in rapid decline of *DC* to the extent that within a few days, they fall below the realistic SIR DES *DC* value and stay there for the remainder of the 30 days simulated. In other words, the realistic SIR DES results in a higher *DC* value for a greater portion of the 30 days. However, it is noted that, despite the similar drug influx from the high dose SIR DCB and fast SIR DES, the decline from the peak *DC* is notably slower for the high dose SIR DCB, likely as a consequence of the increased pressure during balloon application. It is enlightening to examine the spatial plots of free drug concentration for the low dose SIR DCB and the realistic SIR DES (Fig. 8). These plots highlight the rapid free drug delivery to the tissue, followed by relatively fast clearance through the tissue, for the DCB case compared with the slower and more sustained drug delivery of the DES. Also evident from these plots is the higher free drug concentrations at later times for the DES, with the DCB resulting in higher free drug concentrations at early times. Due to the heterogeneous delivery of drug in the case of the DES, free drug concentrations between struts remain very low for all times simulated. On the other hand, the homogeneous delivery of drug from the DCB ensures little axial variation in the free drug concentrations along the length of the lesion.

All cases considered achieve high levels of specific binding site saturation relatively rapidly, within the first day (approx. 75%–95%) (Fig. 7b). It is notable that the %*SBSS* curves of the high dose SIR DCB and fast SIR DES are almost identical, with each reaching higher values than the realistic SIR DES and the low dose SIR DCB. However, while the high dose SIR DCB and fast SIR DES achieve higher levels of % *SBSS* in the short term, with these levels declining steadily between approximately day 5 to day 30, the realistic SIR DES %*SBSS* level rises steadily over time, reaching approximately 100 % by 30 days. The spatial plots of specific bound drug concentration (Fig. 9) reflect these results. However, the spatial plots reveal that at later times, lower values of %*SBSS* for the case of the DCB are likely driven by lower drug concentrations at the lumen interface, as a direct result of the lack of a sustained drug source. With the exception of the realistic SIR DES, all cases considered rapidly reach their peak %*NSBSS* (of approximately 30 − 75%) before a decline to near negligible levels over a period of about 15 days (Supplementary Fig. S1d). In contrast, the realistic SIR DCB achieves a significantly lower %*NSBSS* peak of approximately 20%, which is delayed with respect to the other cases (occurring at around day 5). However, %*NSBSS* declines at a substantially slower rate with values of around 8 −20% maintained for the remainder of the 30 days simulated.

3.4. Limitations

We wish to emphasise that, like all computational studies, there are a number of simplifications in this work. We reiterate that we have employed a simplified 2D-axisymmetric geometry which does not account for the presence of an atherosclerotic lesion, whose geometry and composition will vary from patient-to-patient. Moreover, tissue deformation as a result of DCB or DES deployment has not been considered. In our preliminary simulations, we employed the fluid dynamics equations that are typically used within the context of endovascular device drug transport simulations. In reality, blood does not always behave as a Newtonian fluid, and pulsatile flow would be a more accurate description than steady-flow. Notwithstanding, each of these features, which introduce additional complexity, have previously been shown to have a limited influence on drug concentrations within the arterial wall. We have gleaned parameter values from across the (large) literature in this field, the limitations of which we have previously discussed (Escuer et al., 2021). In particular we note that while a full set of binding parameters are available for SIR (Tzafriri et al., 2012), we have not been able to locate within the literature a full set of binding parameters (specific and non-specific) for PTX and have, therefore, been forced to calculate these from different sources. Regardless of the drug in question, to the best of our knowledge, there is no experimental data available in the literature that would allow one to impose different binding site densities within the different layers of the arterial wall. We further wish to reiterate that our model assumes that a negligible amount of DCB coating adheres to the arterial wall during application. If a sizeable portion of the coating adheres to the tissue, a feature likely to be highly dependent on the excipient/drug formulation, then this may act as a

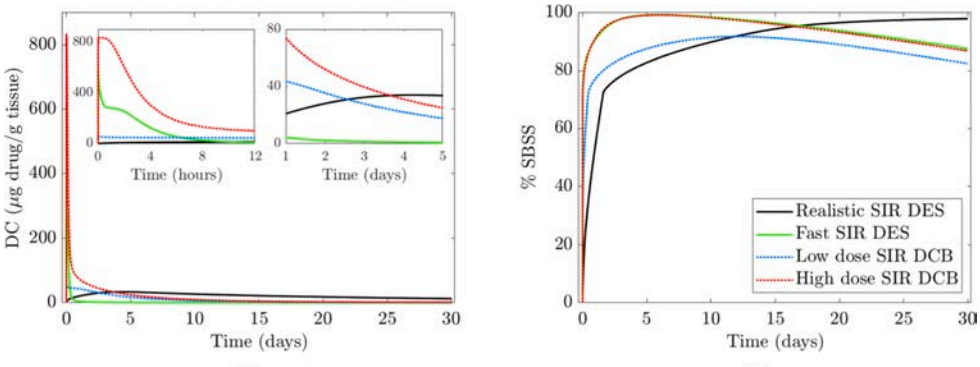

(a)

(b)

Fig. 7. Comparison between Case 1 (Low Dose SIR DCB), Case 2 (High Dose SIR DCB), Case 4 (Realistic SIR DES) and Case 5 (Fast SIR DCB). (a): Drug Content (*DC*) vs time. (b): % *SBSS* vs time. In all cases $p = p_{inf}$ for $t \leq t_0$ to match balloon inflation pressure.

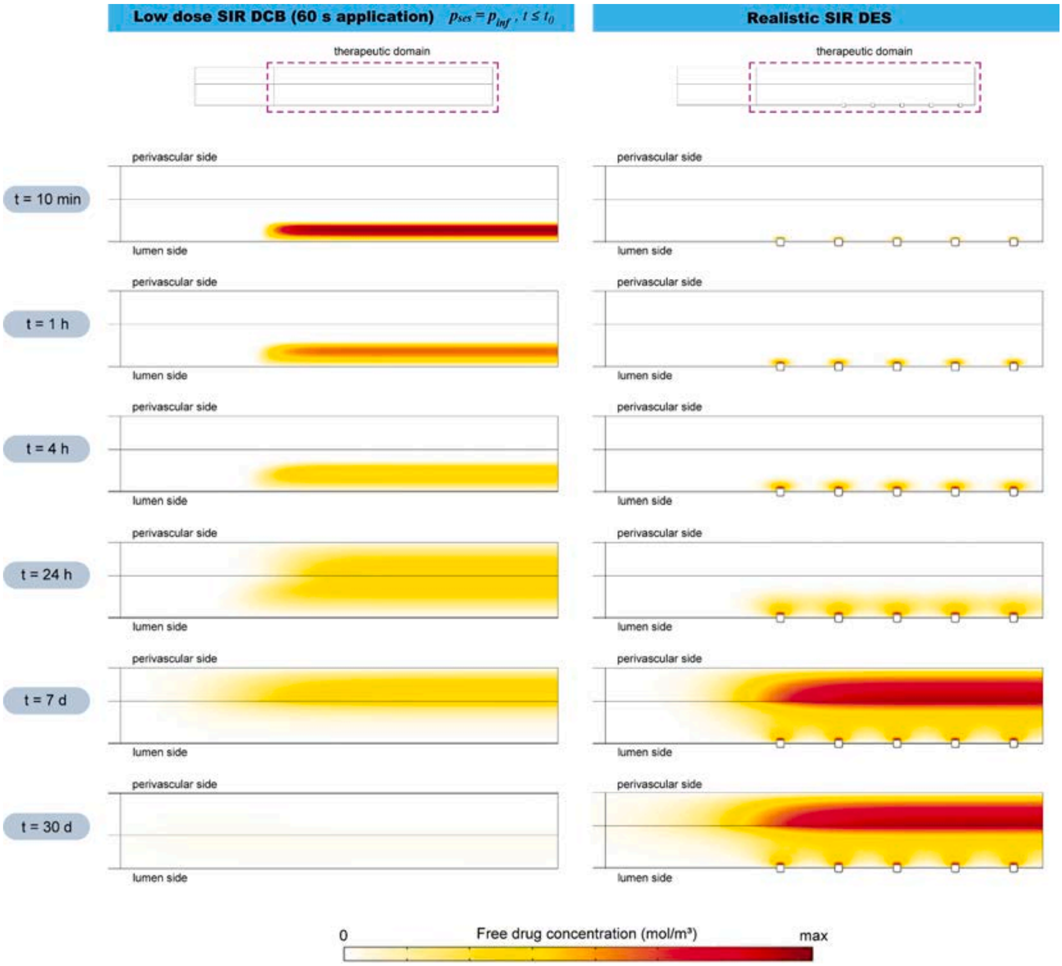

Fig. 8. Low dose SIR DCB vs realistic SIR DES spatial free drug concentration plots for $t = 10$ min, 1 h, 4 h, 24 h, 7 days and 30 days. For details of the max value in the scale, please refer to Table S1.

reservoir that would allow drug to be delivered to the arterial wall for far longer than the DCB application time. Finally, a key assumption underlying our model is that vessel wall remodelling does not significantly influence the transport and distribution of drug.

4. Discussion

DCBs and DESs give rise to vastly different drug delivery kinetics. The former necessitates fast delivery while the latter enables more sustained release. Each platform allows for either low or high drug loading. Existing literature suggests that sustaining drug release is more important than increasing dose, at least for SIR DESs (Tzafriri et al., 2012). However, results from recent clinical trials of DCBs suggest that rapid drug release may, in certain circumstances, still be effective (Jeger et al., 2018). Moreover, existing literature highlights that the optimal drug release profile may be drug-dependent (Bozsak et al., 2014; Bozsak et al., 2015). Despite significant efforts over the past two decades, the optimal drug and release profile to successfully counteract restenosis remains ill-defined. Computational models, such as the one presented here, provide a platform for investigating spatio-temporal drug concentrations that are achieved in the arterial wall when different drugs and drug platforms with varying release kinetics are deployed. This, in turn, enables calculation and comparison of key indices related to safety (*DC*) and efficacy (%*SBSS*). In this paper, we have simulated drug delivery from DCBs and DESs, encompassing different drugs, doses and release kinetics. We now reiterate the key findings and their potential consequences.

Firstly, our results have highlighted that it is imperative to incorporate within the simulations the elevated pressure in the lumen during balloon application. This leads to deeper delivery of drug, higher drug retention and increased levels of specific binding site saturation, when compared with simulations that utilise a fixed lumen pressure for all time. Increasing the duration of DCB application from 30–60 s leads to higher *DC* and %*SBSS*. However, the relative increase in these values depends strongly on the DCB dose and release kinetics. In other words, the potential benefit of a DCB longer application time is dependent on the DCB configuration (drug, drug dose and excipient properties) and may therefore be more beneficial for some DCBs than for others. Our work has uncovered differences between SIR and PTX DCBs. Our results indicate that, assuming the same dose and release kinetics, SIR is retained within the tissue for longer than PTX, at least for the parameter values simulated.

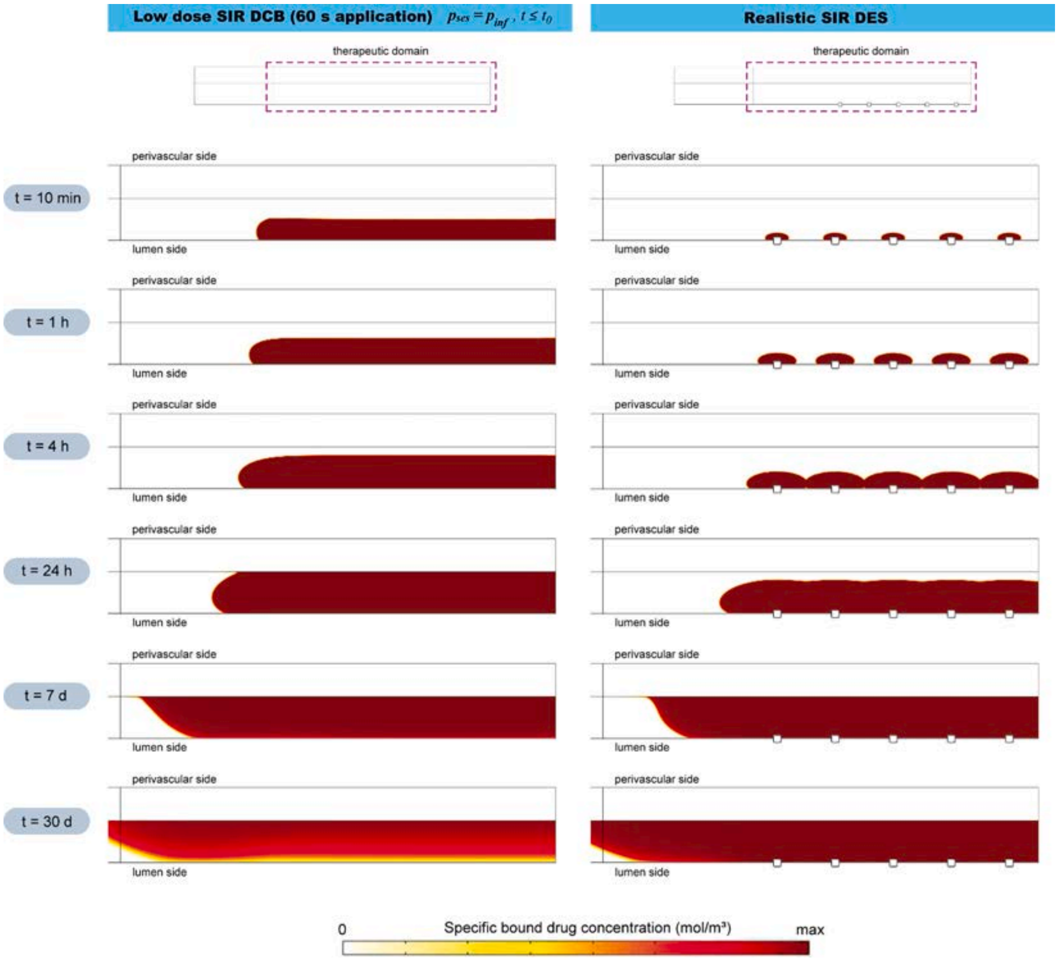

Fig. 9. Low dose SIR DCB vs realistic SIR DES spatial specifically bound drug concentration plots for $t = 10$ min, 1 h, 4 h, 24 h, 7 days and 30 days. For details of the max value in the scale, please refer to Table S1.

The relatively rapid decline of *DC* values for the high dose SIR DCB, coupled with the high %*SBSS* levels suggests that the initial drug loading on the high dose SIR DCB may be too high: in other words, a lower initial drug dose could potentially give rise to similar levels of efficacy, while potentially easing any concerns regarding the high initial *DC* peak. On the other hand, the more prolonged decline of *DC* for the low dose SIR DCB, coupled with the less than ideal %*SBSS* levels suggests that the initial drug loading could be increased somewhat to achieve potentially greater efficacy, while potentially giving rise to *DC* peaks that are within safety margins. It is interesting to compare the peak *DC* achieved with these DCBs with existing in vivo experimental data. In (McKittrick et al., 2019), mean *DC* following SIR release from a low dose and high dose SIR DES was reported to range from approximately 5–10 μg/g tissue while in (Tzafriri et al., 2012), mean *DC* following SIR release from CYPHER and NEVO prototype DESs ranged from approximately 15–20 μg/g. However, as is common in the experimental literature, these peak measurements correspond to the first time point considered, 1 day, which is substantially later than the simulated peak for the low dose and high dose DCBs considered here. Grube and Buellesfield (Grube and Buellesfeld, 2006) do provide an earlier measurement time point of 1 h when considering release of a different compound, Biolimus A9™, from the BioMatrix™ stent platform. The mean *DC* peak at 1 h is reported to be approximately 600 μg/g, dropping to around 100 μg/g by 1 day. While each of these studies utilised porcine in vivo models, there are likely to be differences in the precise details of the experimental protocols. Availability of experimental data of *DC* following in vivo DCB deployment is more limited. Radke et al. (2011) consider a PTX DCB for coronary application and report a mean *DC* value of approximately 150 μg/g at 30 min post-deployment, which decreases to around 100 μg/g by 1 day and further reduces to around 100 μg/g by 7 days. Finally, Gongora et al. (Gongora et al., 2015) consider three PTX DCBs for peripheral applications (Ranger, In.Pact Admiral and Lutonix). They report mean *DC* peaks ranging from approximately 50–60 μg/g at 4 h, which drop to approximately 5–20 μg/g by 1 day and further drop to around 1–10 μg/g by 7 days. As well as possible differences in experimental protocols, the different anatomical location of the DCB deployment is likely to play a role. Thus, it appears that the *DC* values obtained in the present study are broadly in line with the existing literature, providing confidence in the simulations. Unfortunately, %*SBSS* is extremely difficult, if not impossible, to measure in vivo and we are not aware of any such measurements in the literature that would enable us to compare the values we have achieved in our simulations.

Returning to the direct comparison between DCBs and DESs, if saturating more specific binding sites earlier is most important, then each DCB considered offers an advantage over the realistic SIR DES simulated. However, if maintaining high levels of %*SBSS* towards and beyond 30 days is desired, then the realistic SIR DES would be preferred. By simulating an artificial fast SIR DES, we have demonstrated that if the safety and efficacy markers of the SIR DCBs simulated are acceptable, but a permanent structure is preferred, then it may be possible to design a new class of fast-release DES whose release kinetics are matched to those of a DCB.

Taken together, our findings suggest that there may exist a DCB configuration, in terms of drug loading and release rate, that gives rise to sufficiently similar safety and efficacy results as current commercial DESs such as the stent platform considered here. Future work should explore the use of an optimisation framework to attempt to infer DCB drug, dose and release rate, as well as procedural aspects such as balloon inflation pressure and application time, that give rise to *DC* values that fall within the therapeutic window, while maximising %*SBSS* for the period of arterial healing. Moreover, it may be worth investigating DCB and DES delivery within a single platform in an attempt to get the 'best of both worlds'.

Declaration of Competing Interest

We declare that one of our authors (Andre Fensterseifer Schmidt) has received a financial contribution towards his student fees from Biosensors International. This has been declared on the manuscript itself.

Moreover, in terms of possible reviewers, while we have cited the works **Prof Elazer Edelman and co-worker Dr Rami Tzafriri** extensively in this work, we are conflicted with this research group through a new jointly funded Centre between University of Glasgow and MIT, entitled "SofTMechMP", EPSRC grant number EP/S030875/1.

Acknowledgements

This work was funded by the Spanish Ministry of Economy, Industry and Competitiveness through research project number PID2019-107517RB-I00; the Department of Industry and Innovation (Government of Aragon) through research group Grant No. T24-20R (Fondo Social Europeo); and the Carlos III Health Institute (ISCIII) through the CIBER initiative. Dr. McGinty acknowledges funding provided by EPSRC (Grant No. EP/S030875/1 and EP/T017899/1).

Appendix A. Supplementary material

Supplementary data associated with this article can be found, in the online version, at https://doi.org/10.1016/j.ijpharm.2022.121742.

References

Ai, Lisong, Vafai, K., 2006. A coupling model for macromolecule transport in a stenosed arterial wall. Int. J. Heat Mass Transf. 49 (9–10), 1568–1591.

Anbalakan, Karthic, Wei Toh, Han, Ying Ang, Hui, Buist, Martin Lindsay, Leo, Hwa Liang, 2021. Assessing the influence of atherosclerosis on drug coated balloon therapy using computational modelling. Eur. J. Pharmaceut. Biopharmaceut., vol. 158, pp. 72–82.

Bierer, Barbara E., Mattila, Petri S., Standaert, Robert F., Herzenberg, Leonard A., Burakoff, Steven J., Crabtree, Gerald, Schreiber, Stuart L., 1990. Two distinct signal transmission pathways in t lymphocytes are inhibited by complexes formed between an immunophilin and either fk506 or rapamycin. Proc. Natl. Acad. Sci., 87(23), 9231–9235.

Bozsak, Franz, Chomaz, Jean-Marc, Barakat, Abdul I., 2014. Modeling the transport of drugs eluted from stents: physical phenomena driving drug distribution in the arterial wall. Biomech. Model. Mechanobiol. 13 (2), 327–347.

Bozsak, Franz, Gonzalez-Rodriguez, David, Sternberger, Zachary, Belitz, Paul, Bewley, Thomas, Chomaz, Jean-Marc, Barakat, Abdul I, 2015. Optimization of drug delivery by drug-eluting stents. PLoS One 10 (6), e0130182.

Byrne, Robert A., Joner, Michael, Kastrati, Adnan, 2015. Stent thrombosis and restenosis: what have we learned and where are we going? the andreas grüntzig lecture esc 2014. Eur. Heart J. 36 (47), 3320–3331.

Byrne, Robert A., Serruys, Patrick W., Baumbach, Andreas, Escaned, Javier, Fajadet, Jean, James, Stefan, Joner, Michael, Oktay, Semih, Jüni, Peter, Kastrati, Adnan, et al., 2015. Report of a european society of cardiology-european association of percutaneous cardiovascular interventions task force on the evaluation of coronary stents in europe: executive summary. Eur. Heart J. 36 (38), 2608–2620.

Chang, Gary H., Azar, Dara A., Lyle, Chimera, Chitalia, Vipul C., Shazly, Tarek, Kolachalama, Vijaya B., 2019. Intrinsic coating morphology modulates acute drug transfer in drug-coated balloon therapy. Scient. Rep. 9 (1), 1–10.

Colombo, Monika, Corti, Anna, Berceli, Scott, Migliavacca, Francesco, McGinty, Sean, Chiastra, Claudio, 2021. 3d modelling of drug-coated balloons for the treatment of calcified superficial femoral arteries. Plos One 16 (10), e0256783.

Cortese, Bernardo, Bertoletti, Allesandra, 2011. Paclitaxel coated balloons for coronary artery interventions: A comprehensive review of preclinical and clinical data. Int. J. Cardiol. 161, 4–12.

Creel, Christopher J., Lovich, Mark A., Edelman, Elazer R., 2000. Arterial paclitaxel distribution and deposition. Circ. Res. 86 (8), 879–884.

Díaz, José Fernando, Barasoain, Isabel, Andreu, José Manuel, 2003. Fast kinetics of taxol binding to microtubules effects of solution variables and microtubule-associated proteins. J. Biol. Chem. 278 (10), 8407–8419.

Escuer, Javier, Cebollero, Martina, Pe na, Estefanía, McGinty, Sean, Martínez, Miguel A., 2020. How does stent expansion alter drug transport properties of the arterial wall? J. Mech. Behav. Biomed. Mater., page 103610.

Escuer, Javier, Aznar, Irene, McCormick, Christopher, Peña, Estefanía, McGinty, Sean, Martinez, Miguel A., 2021. Influence of vessel curvature and plaque composition on drug transport in the arterial wall following drug-eluting stent implantation. Biomech. Model. Mechanobiol. 20 (2), 767–786.

Formaggia, Luca, Quarteroni, Alfio, Veneziani, Allesandro, 2010. Cardiovascular Mathematics: Modeling and simulation of the circulatory system, volume 1. Springer Science & Business Media.

Gongora, Carlos A., Shibuya, Masahiko, Wessler, Jeffrey D., McGregor, Jenn, Tellez, Armando, Cheng, Yanping, Conditt, Gerard B., Kaluza, Greg L., Granada, Juan F., 2015. Impact of paclitaxel dose on tissue pharmacokinetics and vascular healing: a comparative drug-coated balloon study in the familial hypercholesterolemic swine model of superficial femoral in-stent restenosis. JACC: Cardiovasc. Intervent. 8 (8), 1115–1123.

Grube, Eberhard, Buellesfeld, Lutz, 2006. Biomatrix biolimus a9-eluting coronary stent: a next-generation drug-eluting stent for coronary artery disease. Exp. Rev. Med. Dev. 3 (6), 731–741.

Heilmann, Torsten, Richter, Christian, Noack, Sabine, Post, Heiko, Mahnkopf, Dirk, mittag, Antje, Thiele, Holger, Figulla, Hans-Reiner, 2010. Drug release profiles of different drug-coated balloon platforms. Eur. Cardiol., 6(4):40–4.

Hwang, Chao-Wei, Edelman, Elazer R., 2002. Arterial ultrastructure influences transport of locally delivered drugs. Circ. Res. 90 (7), 826–832.

Hwang, Chao-Wei, David, Wu., Edelman, Elazer R., 2001. Physiological transport forces govern drug distribution for stent-based delivery. Circulation 104 (5), 600–605.

Hwang, Chao-Wei, David, Wu., Edelman, Elazer R., 2003. Impact of transport and drug properties on the local pharmacology of drug-eluting stents. Int. J. Cardiovasc. Intervent. 5 (1), 7–12.

Jain, Ankur, McGinty, Sean, Pontrelli, Giuseppe, Zhou, Long, 2022. Theoretical modeling of endovascular drug delivery into a multilayer arterial wall from a drug-coated balloon. Int. J. Heat Mass Transf. 187, 122572.

Jeger, Raban V., Farah, Ahmed, Ohlow, Marc-Alexander, Mangner, Norman, Möbius-Winkler, Sven, Leibundgut, Gregor, Weilenmann, Daniel, Wöhrle, Jochen, Richter, Stefan, Schreiber, Matthias, et al., 2018. Drug-coated balloons for small coronary artery disease (basket-small 2): an open-label randomised non-inferiority trial. The Lancet, 392(10150), 849–8568.

Karner, Gerhard, Perktold, Karl, Zehentner, Hans Peter, 2001. Computational modeling of macromolecule transport in the arterial wall. Comput. Methods Biomech. Biomed. Eng. 4 (6), 491–504.

Kedem, Ora, Katchalsky, Aharon, 1958. Thermodynamic analysis of the permeability of biological membranes to non-electrolytes. Biochim. Biophys. Acta 27, 229–246.

Kolachalama, Vijaya B., Pacetti, Stephen D., Franses, Joseph W., Stankus, John J., Zhao, Hugh Q., Shazly, Tarek, Nikanorov, Alexander, Schwartz, Lewis B., Tzafriri, Abraham R., Edelman, Elazer R., 2013. Mechanisms of tissue uptake and retention in zotarolimus-coated balloon therapy. Circulation 127 (20), 2047–2055.

Lee, Dae-Hyun, de la Torre Hernandez, Jose M., 2018. The newest generation of drug-eluting stents and beyond. Eur. Cardiol. Rev., 13(1):54.

Levin, Andrew D., Vukmirovic, Neda, Hwang, Chao-Wei, Edelman, Elazer R., 2004. Specific binding to intracellular proteins determines arterial transport properties for rapamycin and paclitaxel. Proc. Natl. Acad. Sci. USA, 101(25), 9463–9467.

Levitt, David G., 1975. General continuum analysis of transport through pores. i. proof of onsager's reciprocity postulate for uniform pore. Biophys. J . 15 (6), 533–551.

Lovich, Mark A., Edelman, Elazer R., 1996. Computational simulations of local vascular heparin deposition and distribution. Am. J. Physiol.-Heart Circul. Physiol. 271 (5), H2014–H2024.

Mandal, Prashanta Kumar, Sarifuddin, Kolachalama, Vijaya B., 2016. Computational model of drug-coated balloon delivery in a patient-specific arterial vessel with heterogeneous tissue composition. Cardiovasc. Eng. Technol., 7(4):406–419.

McGinty, Sean, 2014. A decade of modelling drug release from arterial stents. Math. Biosci. 257, 80–90.

McGinty, Sean, Pontrelli, Giuseppe, 2016. On the role of specific drug binding in modelling arterial eluting stents. J. Math. Chem. 54 (4), 967–976.

McKittrick, Craig M., McKee, Sean, Kennedy, Simon, Oldroyd, Keith, Wheel, Marcus, Pontrelli, Giuseppe, Dixon, Simon, McGinty, Sean, McCormick, Christopher, 2019. Combining mathematical modelling with in vitro experiments to predict in vivo drug-eluting stent performance. J. Controlled Release 303, 151–161.

McQueen, Alistair, Escuer, Javier, Aggarwal, Ankush, Kennedy, Simon, McCormick, Christopher, Oldroyd, Keith, McGinty, Sean, 2021. Do we really understand how drug eluted from stents modulates arterial healing? Int. J. Pharm. 601, 120575.

Meyer, Guy, Merval, Regine, Tedgui, Alain, 1996. Effects of pressure-induced stretch and convection on low-density lipoprotein and albumin uptake in the rabbit aortic wall. Circ. Res. 79 (3), 532–540.

Mongrain, Rosaire, Leask, Richard, Brunette, Jean, Faik, Iam, Bulman-Feleming, Neil, Nguyen, T., 2005. Numerical modeling of coronary drug eluting stents. Stud. Health Technol. Inform., 113:443–458.

Perkins, Laura E.L., Boeke-Purkis, Katrin H., Wang, Qing, Stringer, Steven K., Coleman, Leslie A., 2009. Xience v™ everolimus-eluting coronary stent system: A preclinical assessment. J. Intervent. Cardiol. 22, S28–S40.

Radke, Peter W., Joner, Michael, Joost, Alexander, Byrne, Robert A., Hartwig, Sonja, Bayer, Gerd, Steigerwald, Kristin, Wittchow, Eric, 2011. Vascular effects of paclitaxel following drug-eluting balloon angioplasty in a porcine coronary model: the importance of excipients. EuroIntervention, 7(6):730–737.

Rami Tzafriri, A., Levin, Andrew D., Edelman, Elazer R., 2009. Diffusion-limited binding explains binary dose response for local arterial and tumour drug delivery. Cell Prolif. 42 (3), 348–363.

Roth, Gregory A., Abate, Degu, Abate, Kalkidan Hassen, Abay, Solomon M., Abbafati, Cristiana, Abbasi, Nooshin, Abbastabar, Hedayat, Abd-Allah, Foad, Abdela, Jemal, Abdelalim, Ahmed, et al., 2018. Global, regional, and national age-sex-specific mortality for 282 causes of death in 195 countries and territories, 1980–2017: a systematic analysis for the global burden of disease study 2017. The Lancet, 392 (10159), 1736–1788.

Sarifuddin, Mandal, Prashanta Kumar, 2018. Effect of interstitial fluid flow on drug-coated balloon delivery in a patient-specific arterial vessel with heterogeneous tissue composition: A simulation study. Cardiovasc. Eng. Technol., 9(2):251–267.

Scheller, Bruno, Hehrlein, Christoph, Bocksch, Wolfgang, Rutsch, Wolfgang, Haghi, Dariush, Dietz, Ulrich, Böhm, Michael, Speck, Ulrich, 2006. Treatment of coronary in-stent restenosis with a paclitaxel-coated balloon catheter. N. Engl. J. Med. 355 (20), 2113–2124.

Sojitra, Prakash, Yazdani, Saami, Otsuka, Fumiyuki, Doshi, Manish, Kolodgie, Frank, Virmani, Renu, 2013. Crt-123. a novel nano particle sirolimus delivery via coated balloon. JACC: Cardiovasc. Intervent. 6 (2 Suppl S), S40.

Tzafriri, Abraham R, Adam Groothuis, G., Price, Sylvester, Edelman, Elazer R., 2012. Stent elution rate determines drug deposition and receptor-mediated effects. J. Controlled Release 161 (3), 918–926.

Tzafriri, Abraham R., Parikh, Sahil A., Edelman, Elazer R., 2019. Taking paclitaxel coated balloons to a higher level: Predicting coating dissolution kinetics, tissue retention and dosing dynamics. J. Controlled Release 310, 94–102.

Tzafriri, Abraham R., Muraj, Benny, Garcia-Polite, Fernando, Salazar-Martín, Antonio G., Markham, Peter, Zani, Brett, Spognardi, Anna, Albaghdadi, Mazen, Alston, Steve, Edelman, Elazer R., 2020. Balloon-based drug coating delivery to the artery wall is dictated by coating micro-morphology and angioplasty pressure gradients. Biomaterials 260, 120337.

Vairo, Giuseppe, Cioffi, Margherita, Cottone, Riccardo, Dubini, Gabriele, Migliavacca, Francesco, 2010. Drug release from coronary eluting stents: a multidomain approach. J. Biomech. 43 (8), 1580–1589.

Wear, Martin A., Walkinshaw, Malcolm D., 2007. Determination of the rate constants for the fk506 binding protein/rapamycin interaction using surface plasmon resonance: An alternative sensor surface for ni2+–nitrilotriacetic acid immobilization of his-tagged proteins. Anal. Biochem. 371 (2), 250–252.

Zunino, Paolo, 2004. Multidimensional pharmacokinetic models applied to the design of drug-eluting stents. Cardiovasc. Eng.: An Int. J. 4 (2), 181–191.

Supplementary material for "Mathematical modelling of endovascular drug delivery: balloons versus stents"

Javier Escuer[1], André Fensterseifer Schmidt[2], Estefanía Peña[1,3], Miguel A. Martínez[1,3], Sean McGinty[2,4,*]

S1. Preliminary model

S1.1. Modelling blood flow

In this preliminary model, blood was modelled as an incompressible Newtonian fluid governed by the steady Navier-Stokes equations and the continuity equation:

$$\rho_b(\boldsymbol{u}_l \cdot \nabla)\boldsymbol{u}_l = -\nabla p_l + \mu_b \nabla^2 \boldsymbol{u}_l, \quad \nabla \cdot \boldsymbol{u}_l = 0, \tag{S.1}$$

where $\boldsymbol{u}_l$ and p_l are the velocity vector field and the pressure field of the blood flow in the lumen, respectively, and ρ_b and μ_b are the density and the dynamic viscosity of the blood, respectively. At the inlet of the lumen, $\Gamma_{l,inlet}$, a fully developed parabolic velocity profile was prescribed:

$$w_{l,inlet} = u_{max}\left(1 - \left(\frac{r}{r_l}\right)^2\right), \tag{S.2}$$

where w_l is the axial component of the blood velocity in the lumen; u_{max} is the centerline velocity for a typical value of the Reynolds number ($Re_l = \rho_b u_0 (2r_l)/\mu_b$) in the coronary artery of 400 corresponding to laminar flow [1]; r is the radial position, u_0 is the mean velocity and; r_l is the internal radius of the artery. A constant pressure of 100 mmHg was considered at the lumen outlet, $\Gamma_{l,outlet}$ [2]. Moreover, the no-slip condition ($w_l = 0$) was prescribed at the endothelium, Γ_{et} [3–5].

S1.2. Modelling drug transport within the lumen

Drug transport inside the arterial lumen was modelled as a time-dependent advection-diffusion process:

$$\frac{\partial c_l}{\partial t} + \boldsymbol{u}_l \cdot \nabla c_l = \nabla \cdot (\boldsymbol{D}_l \nabla c_l), \tag{S.3}$$

---

[*] Corresponding author: Email address: sean.mcginty@glasgow.ac.uk.

[1] Aragón Institute for Engineering Research (I3A), University of Zaragoza, Spain

[2] Division of Biomedical Engineering, University of Glasgow, Glasgow, UK.

[3] Biomedical Research Networking Center in Bioengineering, Biomaterials and Nanomedicine (CIBER-BBN), Spain

[4] Glasgow Computational Engineering Centre, Division of Infrastructure and Environment, University of Glasgow, Glasgow, UK.

where $c_l\ (r, z, t)$ is the drug concentration within the fluid domain; $\boldsymbol{D}_l$ is the isotropic diffusivity of the drug in the blood and; $\boldsymbol{u}_l$ is the blood flow velocity calculated by Eq. (S.1). A zero drug concentration boundary condition is applied at the lumen inlet, $c_l = 0$, and an outflow condition, $-\boldsymbol{n}_l \cdot (-\boldsymbol{D}_l \nabla c_l) = 0$, is applied at the outlet.

S1.3. Model simplification

The preliminary simulations detailed above revealed that the pressure varied from 100 mmHg by less than 1% across the entire lumen/wall interface. Thus we imposed a constant pressure of 100 mmHg at this interface. Moreover, the drug concentration within the lumen was found to be several orders of magnitude lower than in the tissue, justifying the imposition of a sink boundary condition at the lumen. Taken together, these simplifications allowed the entire domain to be halved due to symmetry. For the DCB cases, the symmetry plane was placed at the centre of the lesion, while for the DES cases, the symmetry plane was located mid-way between the 5th and 6th struts.

S2. Supplemental equations

S2.1. Kedem-Katchalsky equations for fluid flux

Endothelium (ET), internal and external elastic laminae (IEL and EEL, respectively) are treated as semipermeable membranes and the fluid flux across them, $J_{v,j}$, is described by the Kedem-Katchalsky equations [6]. Neglecting the osmotic contribution as an approximation [1, 4, 5], the Kedem-Katchalsky equations for fluid flux can be simplified as:

$$J_{v,j} = L_{p,j} \Delta p_j, \tag{S.4}$$

where the subscript $j = \{et, iel, eel\}$ denotes the semipermeable membranes considered: the lumen-SES interface (et), the SES-media interface (iel) and the media-adventitia interface (eel), respectively; $L_{p,j}$ is the membrane hydraulic conductivity and; Δp_j the pressure drop across each semipermeable membrane. Therefore, the volume flux J_v for each membrane can be formulated as follows:

$$J_{v,et} = L_{p,et} \Delta p_{et} = L_{p,et}(p_l - p_{ses}), \tag{S.5}$$

$$J_{v,iel} = L_{p,iel} \Delta p_{iel} = L_{p,iel}(p_{ses} - p_m), \tag{S.6}$$

$$J_{v,eel} = L_{p,eel} \Delta p_{eel} = L_{p,eel}(p_m - p_a), \tag{S.7}$$

where l, ses, m and a denote the lumen, subendothelial space, media and adventitia, respectively.

S2.2. Kedem-Katchalsky equations for solute flux

Discontinuity of solute flux across the semipermeable membranes, $J_{s,j}$, is also governed by the Kedem-Katchalsky equations [6]:

$$J_{s,j} = P_j \Delta c_j + s_j \bar{c}_j J_{v,j}, \tag{S.8}$$

where P_j is the permeability of each semipermeable membrane; Δc_j is the solute concentration difference; s_j is the sieving coefficient and; $\bar{c}_j$ is the weighted average concentration on either side of the corresponding membrane computed as [4, 5, 7]:

$$\bar{c}_{et} = \frac{1}{2}(c_l + c_{ses}) + \frac{s_{et} J_{v,et}}{12 P_{et}}(c_l - c_{ses}), \tag{S.9}$$

$$\bar{c}_{iel} = \frac{1}{2}(c_{ses} + c_m) + \frac{s_{iel} J_{v,iel}}{12 P_{iel}}(c_{ses} - c_m), \tag{S.10}$$

$$\bar{c}_{eel} = \frac{1}{2}(c_m + c_{adv}) + \frac{s_{eel} J_{v,eel}}{12 P_{eel}}(c_m - c_{adv}). \tag{S.11}$$

Therefore, the solute flux J_s for each membrane can be written as follows:

$$J_{s,et} = P_{et}(c_l - c_{ses}) + s_{et}\bar{c}_{et} J_{v,et}, \tag{S.12}$$

$$J_{s,iel} = P_{iel}(c_{ses} - c_m) + s_{iel}\bar{c}_{iel} J_{v,iel}, \tag{S.13}$$

$$J_{s,eel} = P_{eel}(c_m - c_a) + s_{eel}\bar{c}_{eel} J_{v,eel}. \tag{S.14}$$

S3. Supplemental figures

S3.1. Non-specific binding site saturation $\%NSBSS$

Figures S1a-S1d display the results for $\%NSBSS$ as calculated from Eq. 16 of the main text. For a description of the results please refer to the main text.

S3.2. Spatial drug concentration plots

Figures S2-S5 show spatial drug distribution for a variety of different cases.

S4. Supplemental tables

The maximum values of local concentrations in each region of the arterial tissue at six different time points for the low dose SIR DCB and the realistic DES are shown in Table S1.

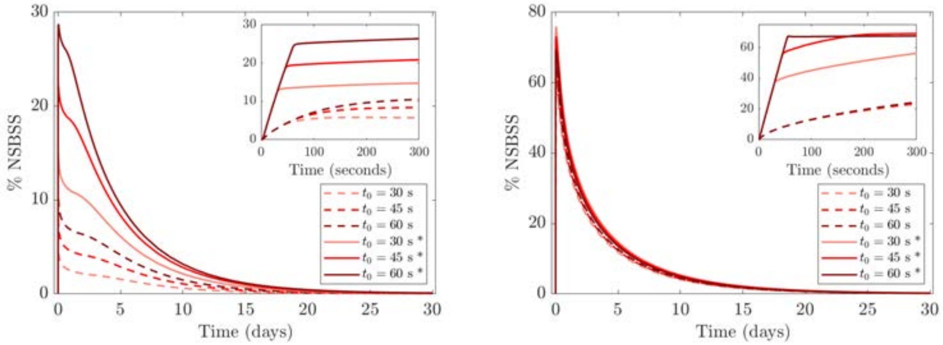

(a) Case 1: Low Dose SIR DCB

(b) Case 2: High Dose SIR DCB

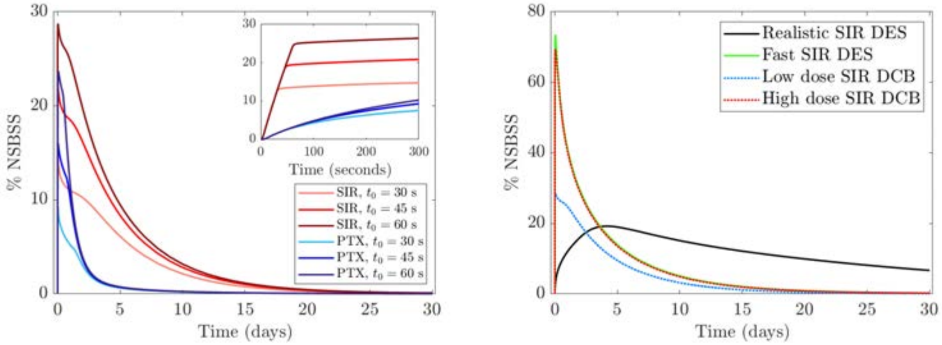

(c) Case 1 vs Case 3: Low Dose SIR vs PTX DCB

(d) Cases 1 vs 2 vs 4 vs 5

Figure S1: Comparison between $\%NSBSS$ for the different cases considered. in plots (a) and (b), * denotes lumen pressure increased to $p = p_{inf}$ for $t \leq t_0$ to match balloon inflation pressure. In plots (c) and (d) all results show $p = p_{inf}$ for $t \leq t_0$.

Figure S2: Low dose SIR DCB spatial free drug concentration plots for $t = 10$ min, 1 h, 4 h, 24 h, 7 days and 30 days. LEFT: $p_{ses} = p_{inf}$ for $t \le 60s$. RIGHT: $p_{ses} = p_l$ for $t \le 60s$. For details of the max value in the scale, please refer to Table S1.

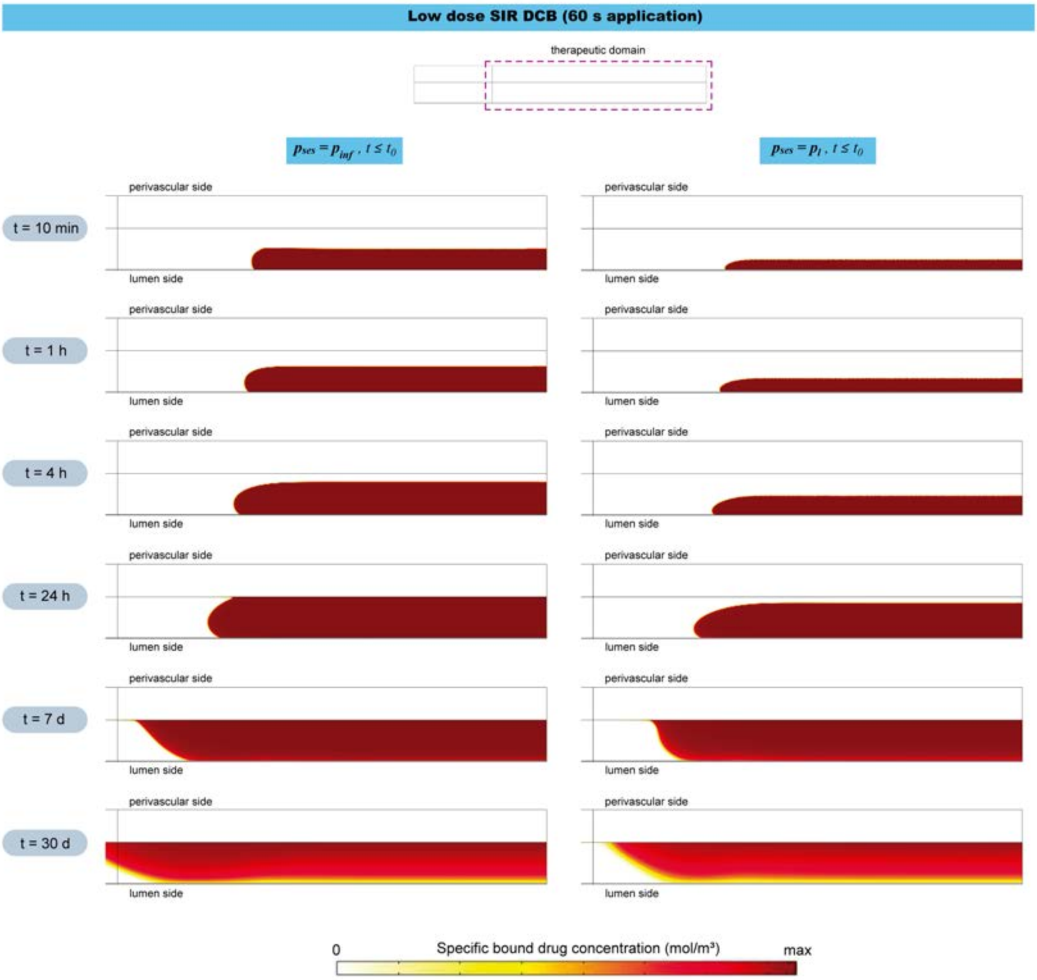

Figure S3: Low dose SIR DCB spatial specifically bound drug concentration plots for t = 10 min, 1 h, 4 h, 24 h, 7 days and 30 days. LEFT: $p_{ses} = p_{inf}$ for $t \leq 60s$. RIGHT: $p_{ses} = p_l$ for $t \leq 60s$. For details of the max value in the scale, please refer to Table S1.

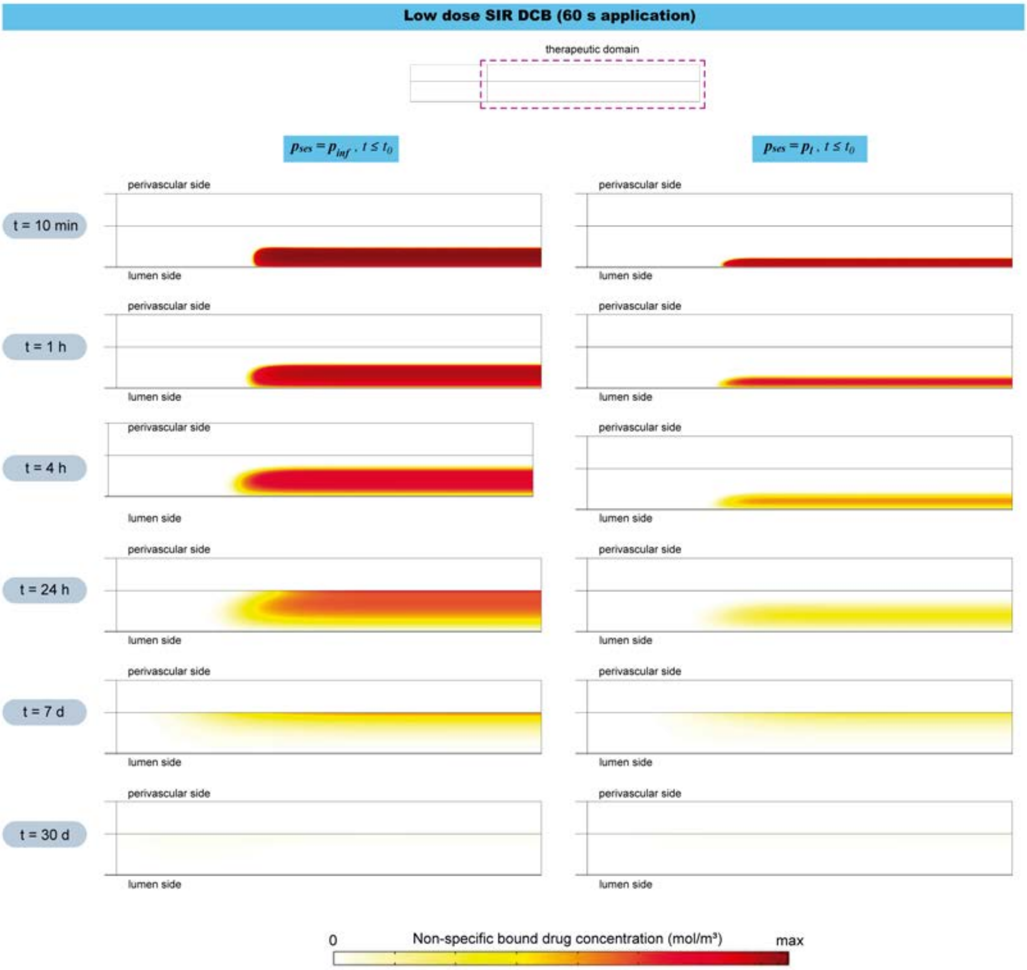

Figure S4: Low dose SIR DCB spatial non-specifically bound drug concentration plots for $t = 10$ min, 1 h, 4 h, 24 h, 7 days and 30 days. LEFT: $p_{ses} = p_{inf}$ for $t \leq 60s$. RIGHT: $p_{ses} = p_l$ for $t \leq 60s$. For details of the max value in the scale, please refer to Table S1.

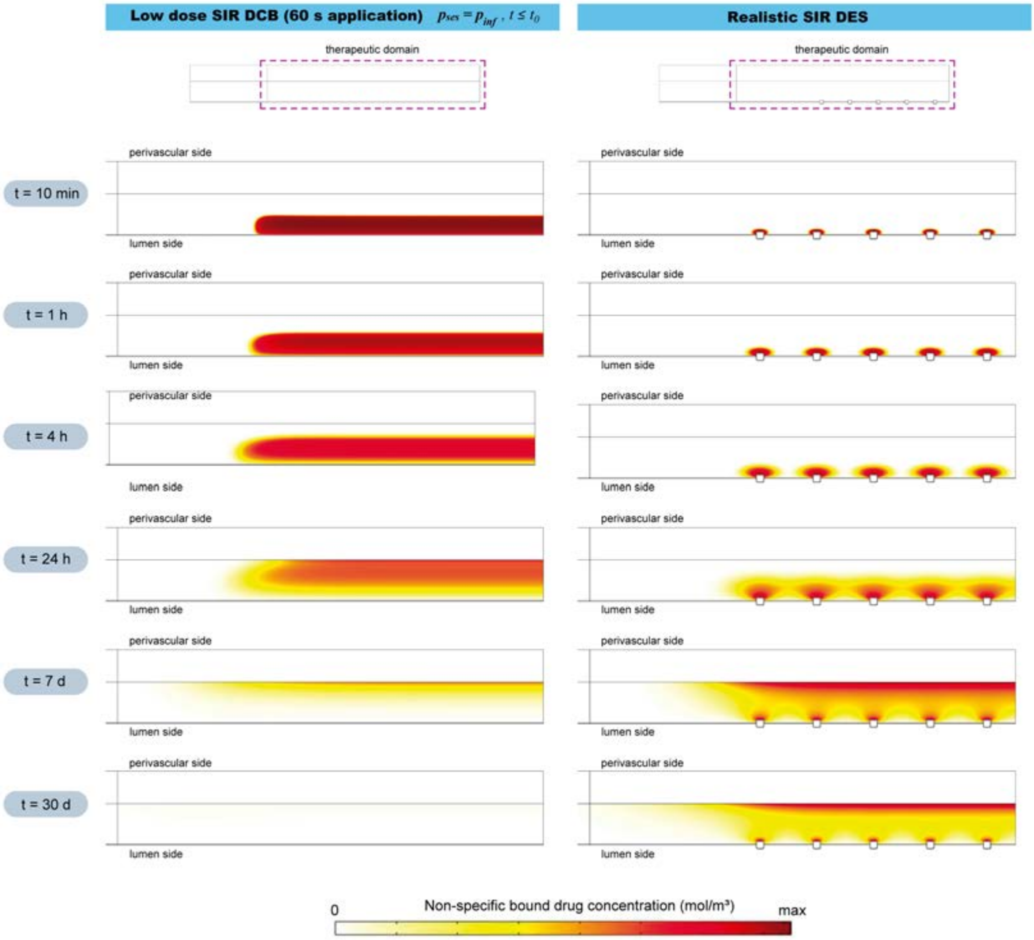

Figure S5: Low dose SIR DCB vs realistic SIR DES spatial non-specifically bound drug concentration plots for $t = 10$ min, 1 h, 4 h, 24 h, 7 days and 30 days. For details of the max value in the scale, please refer to Table S1.

Low dose SIR DCB (60 s application), with $p = p_{inf}$ for $t \leq t_0$

	t = 10 min	t = 1 h	t = 4 h	t = 24 h	t = 7 d	t = 30 d
Free drug in the SES (c_{ses})	$3.07 \cdot 10^{-3}$	$6.07 \cdot 10^{-4}$	$1.58 \cdot 10^{-4}$	$1.82 \cdot 10^{-5}$	$4.50 \cdot 10^{-7}$	$4.42 \cdot 10^{-8}$
Free drug in the media (c_m)	$8.51 \cdot 10^{-2}$ (*)	$1.71 \cdot 10^{-2}$	$6.63 \cdot 10^{-3}$	$2.80 \cdot 10^{-3}$	$1.04 \cdot 10^{-3}$	$1.11 \cdot 10^{-5}$
S Bound drug in the media (b_m^s)	$3.30 \cdot 10^{-3}$ (*)	$3.30 \cdot 10^{-3}$ (*)	$3.30 \cdot 10^{-3}$ (*)	$3.30 \cdot 10^{-3}$ (*)	$3.30 \cdot 10^{-3}$ (*)	$3.30 \cdot 10^{-3}$ (*)
NS Bound drug in the media (b_m^{ns})	$3.52 \cdot 10^{-1}$ (*)	$3.15 \cdot 10^{-1}$	$2.60 \cdot 10^{-1}$	$1.88 \cdot 10^{-1}$	$1.04 \cdot 10^{-1}$	$1.56 \cdot 10^{-3}$
Free drug in the adventitia (c_a)	$5.26 \cdot 10^{-26}$	$2.61 \cdot 10^{-22}$	$6.99 \cdot 10^{-16}$	$2.80 \cdot 10^{-3}$	$1.04 \cdot 10^{-3}$	$1.11 \cdot 10^{-5}$

Low dose SIR DCB (60 s application), with $p = p_l$ for $t \leq t_0$

	t = 10 min	t = 1 h	t = 4 h	t = 24 h	t = 7 d	t = 30 d
Free drug in the SES (c_{ses})	$2.95 \cdot 10^{-3}$	$4.70 \cdot 10^{-4}$	$1.19 \cdot 10^{-4}$	$1.21 \cdot 10^{-5}$	$2.08 \cdot 10^{-7}$	$2.44 \cdot 10^{-8}$
Free drug in the media (c_m)	$2.60 \cdot 10^{-2}$	$5.51 \cdot 10^{-3}$	$2.29 \cdot 10^{-3}$	$7.28 \cdot 10^{-4}$	$4.78 \cdot 10^{-4}$	$6.92 \cdot 10^{-6}$
S Bound drug in the media (b_m^s)	$3.30 \cdot 10^{-3}$ (*)	$3.30 \cdot 10^{-3}$ (*)	$3.30 \cdot 10^{-3}$ (*)	$3.30 \cdot 10^{-3}$ (*)	$3.30 \cdot 10^{-3}$ (*)	$3.21 \cdot 10^{-3}$
NS Bound drug in the media (b_m^{ns})	$3.31 \cdot 10^{-1}$	$2.47 \cdot 10^{-1}$	$1.70 \cdot 10^{-1}$	$7.95 \cdot 10^{-2}$	$5.64 \cdot 10^{-2}$	$9.64 \cdot 10^{-4}$
Free drug in the adventitia (c_a)	$2.35 \cdot 10^{-35}$	$3.69 \cdot 10^{-33}$	$1.05 \cdot 10^{-28}$	$7.49 \cdot 10^{-14}$	$4.78 \cdot 10^{-4}$	$6.92 \cdot 10^{-6}$

Realistic SIR DES ($M_0 = 50$ μg, $D_{DES} = 1.5 \cdot 10^{-17}$ m^2 s^{-1}, $L_{poly} = 8$ μm)

	t = 10 min	t = 1 h	t = 4 h	t = 24 h	t = 7 d	t = 30 d
Free drug in the SES (c_{ses})	$1.06 \cdot 10^{-2}$	$4.92 \cdot 10^{-3}$	$2.53 \cdot 10^{-3}$	$1.04 \cdot 10^{-3}$	$3.86 \cdot 10^{-4}$	$1.15 \cdot 10^{-4}$
Free drug in the media (c_m)	$5.04 \cdot 10^{-2}$	$2.82 \cdot 10^{-2}$ (*)	$1.58 \cdot 10^{-2}$ (*)	$6.79 \cdot 10^{-3}$ (*)	$2.48 \cdot 10^{-3}$ (*)	$7.46 \cdot 10^{-4}$ (*)
S Bound drug in the media (b_m^s)	$3.30 \cdot 10^{-3}$ (*)	$3.30 \cdot 10^{-3}$ (*)	$3.30 \cdot 10^{-3}$ (*)	$3.30 \cdot 10^{-3}$ (*)	$3.30 \cdot 10^{-3}$ (*)	$3.30 \cdot 10^{-3}$ (*)
NS Bound drug in the media (b_m^{ns})	$3.45 \cdot 10^{-1}$	$3.33 \cdot 10^{-1}$ (*)	$3.11 \cdot 10^{-1}$ (*)	$2.62 \cdot 10^{-1}$ (*)	$1.77 \cdot 10^{-1}$ (*)	$8.09 \cdot 10^{-2}$ (*)
Free drug in the adventitia (c_a)	$8.51 \cdot 10^{-43}$	$3.25 \cdot 10^{-37}$	$2.03 \cdot 10^{-31}$	$1.43 \cdot 10^{-16}$	$2.34 \cdot 10^{-3}$	$7.00 \cdot 10^{-4}$

Table S1: Maximum local concentrations of SIR in each layer of the arterial wall for three different scenarios ((i) Low dose SIR DCB with $p = p_{inf}$ for $t \leq t_0$ (ii) Low dose SIR DCB with $p = p_l$ for $t \leq t_0$ (iii) Realistic SIR DES), at six different times points after device deployment. In each column of the table corresponding to a different time, the overall maximum (across the three scenarios) free drug, specific bound drug and non-specific bound concentrations are indicated with (*). These values correspond to the max values in the scale bar of the spatial concentration plots. Note that in some columns the same maximum specific bound drug concentration is reached in more than one of the scenarios.

References

[1] Luca Formaggia, Alfio Quarteroni, and Allesandro Veneziani. *Cardiovascular Mathematics: Modeling and simulation of the circulatory system*, volume 1. Springer Science & Business Media, 2010.

[2] Lisong Ai and K Vafai. A coupling model for macromolecule transport in a stenosed arterial wall. *International Journal of Heat and Mass Transfer*, 49(9-10):1568–1591, 2006.

[3] Giuseppe Vairo, Margherita Cioffi, Riccardo Cottone, Gabriele Dubini, and Francesco Migliavacca. Drug release from coronary eluting stents: a multidomain approach. *Journal of Biomechanics*, 43(8):1580–1589, 2010.

[4] Franz Bozsak, Jean-Marc Chomaz, and Abdul I Barakat. Modeling the transport of drugs eluted from stents: physical phenomena driving drug distribution in the arterial wall. *Biomechanics and Modeling in Mechanobiology*, 13(2):327–347, 2014.

[5] Javier Escuer, Martina Cebollero, Estefanía Peña, Sean McGinty, and Miguel A Martínez. How does stent expansion alter drug transport properties of the arterial wall? *Journal of the Mechanical Behavior of Biomedical Materials*, page 103610, 2020.

[6] Ora Kedem and Aharon Katchalsky. Thermodynamic analysis of the permeability of biological membranes to non-electrolytes. *Biochimica et Biophysica Acta*, 27:229–246, 1958.

[7] David G Levitt. General continuum analysis of transport through pores. i. proof of onsager's reciprocity postulate for uniform pore. *Biophysical Journal*, 15(6):533–551, 1975.

3.4 Work 4: Mathematical modelling of the restenosis process after stent implantation

In this work, a novel 2D continuum mathematical model is presented to describe the complex restenosis process following the stent implantation into a coronary artery. The biological species considered to play a key role in restenosis development are growth factors (GFs), matrix metalloproteinases (MMP), extracellular matrix (ECM), smooth muscle cells (SMCs) and endothelial cells (ECs). Diffusion–reaction equations are used for modelling the mass balance between species in the arterial tissue. Experimental data from the literature have been used in order to estimate model parameters. Moreover, a sensitivity analysis has been performed to study the influence of varying the model parameters on the evolution of the biological species. Our results demonstrate that this computational model qualitatively captures the key characteristics of the lesion growth and the healing process within an artery subjected to non-physiological mechanical forces. Our results also suggest that the arterial wall response is driven by the damage area, smooth muscle cell proliferation and the collagen turnover among other factors.

INTERFACE

royalsocietypublishing.org/journal/rsif

Research

Cite this article: Escuer J, Martínez MA, McGinty S, Peña E. 2019 Mathematical modelling of the restenosis process after stent implantation. J. R. Soc. Interface 16: 20190313. http://dx.doi.org/10.1098/rsif.2019.0313

Received: 6 May 2019
Accepted: 15 July 2019

Subject Category:
Life Sciences–Engineering interface

Subject Areas:
biomechanics, computational biology

Keywords:
restenosis, stent, in-stent restenosis, coronary artery, diffusion–reaction equations, continuum models

Author for correspondence:
Estefanía Peña
e-mail: fany@unizar.es

Electronic supplementary material is available online at http://dx.doi.org/10.6084/m9.figshare.c.4586102.

THE ROYAL SOCIETY
PUBLISHING

Mathematical modelling of the restenosis process after stent implantation

Javier Escuer[1], Miguel A. Martínez[1,2], Sean McGinty[3] and Estefanía Peña[1,2]

[1]Applied Mechanics and Bioengineering Group (AMB), Aragón Institute of Engineering Research (I3A), University of Zaragoza, Zaragoza, Spain
[2]Biomedical Research Networking Centre in Bioengineering, Biomaterials and Nanomedicine (CIBER-BBN), Spain
[3]Division of Biomedical Engineering, University of Glasgow, Glasgow, UK

SM, 0000-0002-2428-2669; EP, 0000-0002-0664-5024

The stenting procedure has evolved to become a highly successful technique for the clinical treatment of advanced atherosclerotic lesions in arteries. However, the development of in-stent restenosis remains a key problem. In this work, a novel two-dimensional continuum mathematical model is proposed to describe the complex restenosis process following the insertion of a stent into a coronary artery. The biological species considered to play a key role in restenosis development are growth factors, matrix metalloproteinases, extracellular matrix, smooth muscle cells and endothelial cells. Diffusion–reaction equations are used for modelling the mass balance between species in the arterial wall. Experimental data from the literature have been used in order to estimate model parameters. Moreover, a sensitivity analysis has been performed to study the impact of varying the parameters of the model on the evolution of the biological species. The results demonstrate that this computational model qualitatively captures the key characteristics of the lesion growth and the healing process within an artery subjected to non-physiological mechanical forces. Our results suggest that the arterial wall response is driven by the damage area, smooth muscle cell proliferation and the collagen turnover among other factors.

1. Introduction

Cardiovascular diseases (CVDs) are the leading cause of mortality in the world. In Europe, 3.9 million deaths a year are attributed to CVDs, with coronary heart disease (CHD) and stroke the primary culprits [1]. CHD is characterized by the development of atherosclerotic plaque, consisting of deposits of cholesterol and other lipids, calcium and macrophages, within the arterial wall. This causes a progressive reduction in the lumen available for the blood flow (stenosis), hardening and loss of elasticity of the arterial tissue.

The use of endovascular devices such as stents and balloons to treat advanced atherosclerotic lesions is now commonplace in the clinic. However, one of the major limitations of these interventions is the development of restenosis [2–7]. Restenosis is understood to comprise three main mechanisms: elastic recoil (in the short term), vessel remodelling and neointimal hyperplasia (in the longer term). The first and second mechanisms are typical in the case of balloon angioplasty, whereas stent deployment usually promotes the formation of neointimal hyperplasia, associated with smooth muscle cell (SMC) migration and proliferation and extracellular matrix (ECM) deposition [7]. Coronary revascularization now generally involves the use of a stent in more than 70% of cases, leading to reduced restenosis rates in comparison to balloon angioplasty alone. With the advent of drug-eluting stents (DES), the incidence of restenosis has been dramatically reduced to approximately less than 10–12% of all angioplasties [8]. However, DES do not completely remove this problem. Since the precise mechanisms behind restenosis after stenting, so-called in-stent restenosis (ISR), are still not fully understood, it therefore remains a significant clinical challenge to predict which patients will develop ISR.

© 2019 The Author(s) Published by the Royal Society. All rights reserved.

Escuer J., Martínez M.A., McGinty S., Peña E. (2019).
Journal of the Royal Society Interface 16(157), 20190313.
JIF (2019) = 3.748 (Q2: 19/71 Multidisciplinary Sciences).

INTERFACE

royalsocietypublishing.org/journal/rsif

Research

Cite this article: Escuer J, Martínez MA, McGinty S, Peña E. 2019 Mathematical modelling of the restenosis process after stent implantation. *J. R. Soc. Interface* **16**: 20190313. http://dx.doi.org/10.1098/rsif.2019.0313

Received: 6 May 2019
Accepted: 15 July 2019

Subject Category:
Life Sciences–Engineering interface

Subject Areas:
biomechanics, computational biology

Keywords:
restenosis, stent, in-stent restenosis, coronary artery, diffusion–reaction equations, continuum models

Author for correspondence:
Estefanía Peña
e-mail: fany@unizar.es

Electronic supplementary material is available online at http://dx.doi.org/10.6084/m9.figshare.c.4586102.

THE ROYAL SOCIETY
PUBLISHING

Mathematical modelling of the restenosis process after stent implantation

Javier Escuer[1], Miguel A. Martínez[1,2], Sean McGinty[3] and Estefanía Peña[1,2]

[1]Applied Mechanics and Bioengineering Group (AMB), Aragón Institute of Engineering Research (I3A), University of Zaragoza, Zaragoza, Spain
[2]Biomedical Research Networking Center in Bioengineering, Biomaterials and Nanomedicine (CIBER-BBN), Spain
[3]Division of Biomedical Engineering, University of Glasgow, Glasgow, UK

SM, 0000-0002-2428-2669; EP, 0000-0002-0664-5024

The stenting procedure has evolved to become a highly successful technique for the clinical treatment of advanced atherosclerotic lesions in arteries. However, the development of in-stent restenosis remains a key problem. In this work, a novel two-dimensional continuum mathematical model is proposed to describe the complex restenosis process following the insertion of a stent into a coronary artery. The biological species considered to play a key role in restenosis development are growth factors, matrix metalloproteinases, extracellular matrix, smooth muscle cells and endothelial cells. Diffusion–reaction equations are used for modelling the mass balance between species in the arterial wall. Experimental data from the literature have been used in order to estimate model parameters. Moreover, a sensitivity analysis has been performed to study the impact of varying the parameters of the model on the evolution of the biological species. The results demonstrate that this computational model qualitatively captures the key characteristics of the lesion growth and the healing process within an artery subjected to non-physiological mechanical forces. Our results suggest that the arterial wall response is driven by the damage area, smooth muscle cell proliferation and the collagen turnover among other factors.

1. Introduction

Cardiovascular diseases (CVDs) are the leading cause of mortality in the world. In Europe, 3.9 million deaths a year are attributed to CVDs, with coronary heart disease (CHD) and stroke the primary culprits [1]. CHD is characterized by the development of atherosclerotic plaque, consisting of deposits of cholesterol and other lipids, calcium and macrophages, within the arterial wall. This causes a progressive reduction in the lumen available for the blood flow (stenosis), hardening and loss of elasticity of the arterial tissue.

The use of endovascular devices such as stents and balloons to treat advanced atherosclerotic lesions is now commonplace in the clinic. However, one of the major limitations of these interventions is the development of restenosis [2–7]. Restenosis is understood to comprise three main mechanisms: elastic recoil (in the short term), vessel remodelling and neointimal hyperplasia (in the longer term). The first and second mechanisms are typical in the case of balloon angioplasty, whereas stent deployment usually promotes the formation of neointimal hyperplasia, associated with smooth muscle cell (SMC) migration and proliferation and extracellular matrix (ECM) deposition [7]. Coronary revascularization now generally involves the use of a stent in more than 70% of cases, leading to reduced restenosis rates in comparison to balloon angioplasty alone. With the advent of drug-eluting stents (DES), the incidence of restenosis has been dramatically reduced to approximately less than 10–12% of all angioplasties [8]. However, DES do not completely remove this problem. Since the precise mechanisms behind restenosis after stenting, so-called in-stent restenosis (ISR), are still not fully understood, it therefore remains a significant clinical challenge to predict which patients will develop ISR.

© 2019 The Author(s) Published by the Royal Society. All rights reserved.

Experimental studies have established a strong correlation between the level of arterial injury caused by the device and the following neointimal thickness and lumen diameter reduction at the stented area [9,10]. Novel stent designs and stent-deployment protocols that minimize induced vascular injury are therefore needed. However, the optimum stent design and the ideal drug release strategy still remain in question despite technological advances [11].

Complementary to the wide variety of experimental studies, computational analysis has emerged as a useful method for designing new medical devices in order to minimize ISR. In the last two decades, many computational models of stent deployment have been developed to study the stress–strain level that the device induces within the arterial wall [12–15]. Several mathematical and numerical models have also been developed to try to understand drug release from stents and subsequent redistribution in the arterial tissue [16–20]. Less attention, however, has been directed to modelling the biological response to treatment.

In recent years, mechanobiological models have emerged to relate mechanics to the complex biological response. These have primarily made use of discrete agent-based models (ABMs) or cellular automata (CA) methods, in some cases combining with finite-element analysis. For example, Zahedmanesh *et al.* developed an ABM to investigate the dynamics of SMCs in vascular tissue engineering scaffolds [21] and an ABM of ISR which allows a quantitative evaluation of the ECM turnover after stent-induced vascular injury [22]; Boyle *et al.* demonstrated that nonlinear growth could be simulated with a cell-centred model [23] and simulated ISR by modelling a combination of injury and inflammation with SMCs represented as discrete agents [24,25]; and Keshavarzian *et al.* [26] developed a mechanobiological model of arterial growth and remodelling. Evans *et al.* [27] highlighted the importance of using a multiscale approach to describe computationally the main physical and biological processes implicated in ISR, introducing the concept of the complex autonoma (CxA) models, based on a hierarchical aggregation of coupled CA and ABMs. Tahir *et al.* [28] focused on the initial phase after stenting and developed a cellular Potts model from which they hypothesized that deeper stent deployment allows easier migration of SMCs into the lumen. Most recently, Zun *et al.* [29] presented a three-dimensional multiscale model of ISR with blood flow simulations coupled to an agent-based SMC proliferation model and demonstrated qualitative agreement with *in vivo* porcine data. In the aforementioned examples, discrete models attempted to represent individual cells in the form of a lattice governed by a set of rules, in contrast to the continuum approach where the evolution of populations of cells and other species such as growth factors (GFs) are described through partial differential equations (PDEs).

In terms of continuum models, Rachev *et al.* [30] proposed a theoretical continuum model to describe the main mechanisms of the coupled deformation and stress-induced arterial tissue thickening observed at the regions close to an implanted stent, comparing the results obtained with experimental data documented in the available literature [31]. However, this phenomenological model does not take into account, for example, the mechanisms implicated in the SMC proliferation or the ECM synthesis. Other continuum mathematical biological models typically comprise a series of coupled diffusion–reaction equations for describing the biological interaction between several species. Such models have been developed to describe phenomena such as neointimal hyperplasia formation [32], atherosclerotic plaque formation [33–36], fibrotic tissue formation surrounding medical implants [37,38] and, more recently, ISR [39] and arterial physiopathology [40]. In contrast to discrete models where cell behaviour is usually described by a set of rules, continuum models offer a mechanistic description, featuring physical parameters which may in principle be measured. In addition, continuum models often have a lower computational cost than ABMs, and naturally allow for modelling diffusion of species and coupling with the mechanical aspects of the problem.

In this paper, we develop a model that allows us to simulate the restenosis process following the insertion of a stent into a coronary artery. The key novelty of our model is that it adopts a continuum approach to describe the sequence of events following damage to the arterial wall, and is therefore formulated in terms of densities/concentrations of a number of important species. This is advantageous because it allows us to assess how the evolution of the various species affects the overall healing process, and more importantly, how variations in the associated parameters and initial conditions influence the process. Diffusion–reaction equations are used for modelling the mass balance between biological species in the arterial wall. The main species considered to play a key role in the process are SMCs, endothelial cells (ECs), matrix-degrading metalloproteinases (MMPs), GFs and ECM. The parameters used in the model to define the biological interaction between the different species have been adapted from experimental data available in the literature. Unlike any of the existing continuum models, we are able to simulate the time-course response of six different biological species involved in ISR after the initial mechanical damage, while at the same time simulating tissue growth. Our primary aim is to gain insight into the physical mechanisms of tissue remodelling post-stenting. Simulating patient-specific cases is beyond the scope of this work: historically, mathematical and computational models in the stents domain have been formulated in idealized scenarios to gain insight before moving onto more realistic patient-specific geometries. With this in mind, we employ a simplified geometry. Notwithstanding, we do compare our results to clinical data and use our model to assess the impact of geometric variations on the final outcome through consideration of a series of commercial stents as well as different inter-strut distances and levels of strut embedment, thereby enabling us to relate our findings to stent design.

2. Governing equations and model assumptions

ISR is an immeasurably complex multiscale system involving a large number of species and an intricate cascade of biological processes (figure 1). Indeed, much of the biology is still unknown. Due to its complexity, in this model we include only what we believe are the predominant species and processes. Specifically, we consider three types of cells (contractile and synthetic SMCs and ECs) and three extracellular components (GFs, MMPs and ECM). We consider the following behaviour: cell types can proliferate, migrate, differentiate and die (apoptosis) while the extracellular components can be

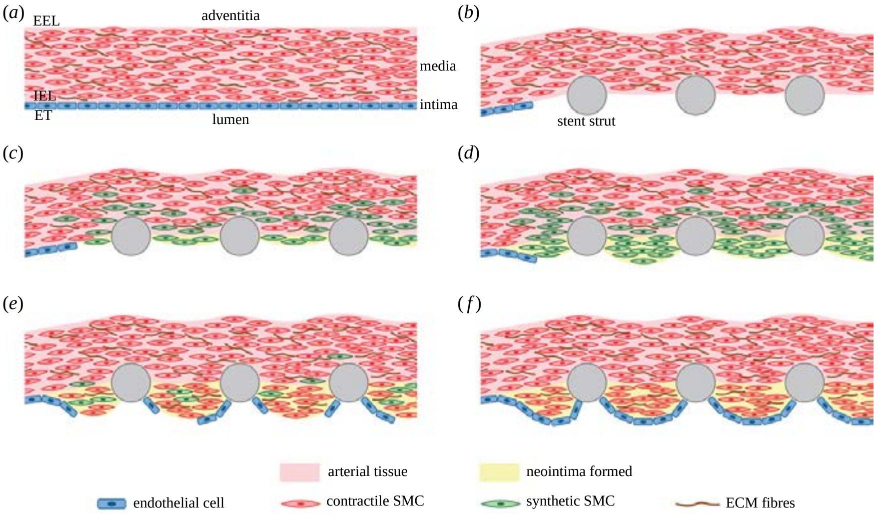

Figure 1. Schematic of ISR. In summary, prior to stent deployment, SMCs exist in a quiescent and contractile phenotype predominantly in the media layer of the tissue and ECs populate the uninjured arterial wall (*a*). After stent deployment (*b*), endothelial denudation, atherosclerotic plaque compression (often with dissection into the media and occasionally adventitia), and unphysiological stretch of the entire artery occur [7]. Platelets are then deposited at the injured area and GFs are released. Local increases in stationary mechanical strain, which occurs following stenting, lead to up-regulation of MMP by SMCs and degradation of collagen in the ECM. Endothelial damage and denudation, among multiple factors, lead to the phenotype switch of medial SMCs from a contractile to a synthetic state [3]. Synthetic SMCs proliferate in response to GFs [24] first in the media and then these begin to migrate towards the injured area (*c*,*d*). Simultaneously, ECs migrate from the lateral edge of the damaged blood vessel surface [2] (*e*). Moreover, synthetic SMCs secrete ECM components, such as collagen and proteoglycans, which constitute the neointimal lesion [24]. Between two and three weeks after the stenting procedure, synthetic SMCs begin to revert to the contractile phenotype [2]. Neointima typically increases up to three months after the procedure, with little change to six months and a gradual reduction between six months to three years [6] (*e*,*f*). (Online version in colour.)

produced or degraded. Since the processes considered take place predominantly in the intima and media layers, in the following model the arterial wall refers to these layers, with the adventitia considered as the outer boundary. Furthermore, blood flow in the lumen and plasma filtration in the tissue have not been included. We refer the reader to §5 for a full discussion of the limitations of this work.

2.1. Material model

An isotropic hyperelastic constitutive model based on a Yeoh strain energy function (SEF) [41] was considered to describe the stress–strain response of the arterial wall. We assume the same mechanical response for the intima and the media layer. Assuming incompressibility of the tissue, the Yeoh SEF can be written as

$$\Psi = c_{10}(I_1 - 3) + c_{20}(I_1 - 3)^2 + c_{30}(I_1 - 3)^2, \tag{2.1}$$

where $c_{10} = 17.01$ kPa, $c_{20} = -73.42$ kPa and $c_{30} = 414.95$ kPa are the hyperelastic material constants and I_1 is the first strain invariant of the Cauchy–Green deformation tensor. The coefficients of the hyperelastic model were identified from fitting the experimental results obtained from Holzapfel *et al.* [42] in specimens of human coronary arteries for the media layer in the circumferential direction using the software for calibration of hyperelastic material models (HyperFit, www.hyperfit.wz.cz).

The stent is modelled as an elasto-plastic material with a Young's modulus of $E = 200$ GPa, Poisson's ratio of $\nu = 0.28$ (representative of biomedical grade stainless steel alloy 316L) and plasticity described by isotropic hardening J_2 flow theory with the tensile stress–strain curves taken from the literature, including a yield strength of 264 MPa and an ultimate tensile strength of 584 MPa at an engineering plastic strain of 0.247 [15].

2.2. Initial estimation and evolution of the damage

Although not completely elucidated, the stimulus triggering the cascade of inflammatory events leading to neointimal formation appears to come from the endothelial damage caused immediately after balloon dilatation and stent placement [43]. We do not explicitly account for all of the mechanical factors that initiate the process which leads to vessel injury and endothelial dysfunction. Following Zahedmanesh *et al.* [22], we assign a level of injury to the arterial wall, d, in a continuous range from 0 to 1. Due to the absence of reliable mechanical data in the literature on the stress–strain levels known to cause arterial injury, the experimental data of *in vitro* tensile tests up to failure of 13 human left anterior descending coronary arteries [42] were used to obtain a qualitative estimation of the damage in the tissue. In particular, we define a piecewise linear function to prescribe the initial arterial damage as a function of von Mises stress, σ_{vm}, calculated by a finite-element (FE) simulation of the stent expansion:

$$d_0 = \begin{cases} 0 & \text{if } \sigma_{\mathrm{vm}} \le \sigma_{\mathrm{vm,inf}} \\ \frac{\sigma_{\mathrm{vm}} - \sigma_{\mathrm{vm,inf}}}{\sigma_{\mathrm{vm,sup}} - \sigma_{\mathrm{vm,inf}}} & \text{if } \sigma_{\mathrm{vm,inf}} < \sigma_{\mathrm{vm}} < \sigma_{\mathrm{vm,sup}} \\ 1 & \text{if } \sigma_{\mathrm{vm}} \ge \sigma_{\mathrm{vm,sup}}, \end{cases} \tag{2.2}$$

where d_0 is the initial damage in the tissue due to the stent placement. This function assigns a value of zero for the damage in areas of the arterial wall in which von Mises stress is lower than $\sigma_{\mathrm{vm,inf}}$ and a value of 1 for the damage in those regions in which von Mises stress exceeds $\sigma_{\mathrm{vm,sup}}$ (figure 2).

Moreover, damage, d, is assumed to decrease continuously with time at a rate directly proportional to the MMP concentration, c_{mmp} [24]. The damage evolution equation is therefore

$$\frac{\partial d}{\partial t} = \underbrace{-k_{\mathrm{deg},d}\, d c_{\mathrm{mmp}}}_{\text{Degradation}}, \tag{2.3}$$

where d is a continuous function of space and time, $d(r, z, t)$, to describe the damage level, $k_{\mathrm{deg},d}$ is the degradation rate of damage and $c_{\mathrm{mmp}}(r, z, t)$ is the concentration of MMP. Equation (2.3) may be considered as a simple description of healing.

2.3. Species evolution

2.3.1. Growth factors

After mechanical arterial injury, platelets, leucocytes and SMCs, among others, release several types of GFs: platelet-derived GF (PDGF), epidermal GF (EGF), insulin-like GF (IGF), transforming GF (TGF) and fibroblast GF (FGF) [2,3,5,7]. However, since their specific roles in the inflammatory phase are not completely understood [2], the term GF includes the combined action of all of them. Denoting the concentration of GFs in the arterial wall by $c_{\mathrm{gf}}(r, z, t)$, and assuming an initial value of $c_{\mathrm{gf},0}$ [44], their behaviour is modelled as follows:

$$\frac{\partial c_{\mathrm{gf}}}{\partial t} + \underbrace{\nabla\cdot(-D_{\mathrm{gf}}\nabla c_{\mathrm{gf}})}_{\text{Random motion}} = \underbrace{k_{\mathrm{prod,gf}}\, d\left(1 - \frac{c_{\mathrm{gf}}}{c_{\mathrm{gf,th}}}\right)}_{\text{Production}} \underbrace{- k_{\mathrm{deg,gf}}(c_{\mathrm{gf}} - c_{\mathrm{gf},0})}_{\text{Degradation}}. \tag{2.4}$$

We are assuming that the GFs experience random motion (i.e. diffusion). Although the diffusion coefficient, D_{gf}, may in general depend on position, we take it here to be constant [32]. The right-hand side of equation (2.4) considers a dynamic balance between degradation and production. GF production is assumed to follow logistic growth: the concentration increases proportionally to the production rate, $k_{\mathrm{prod,gf}}$, and level of damage, d, until some threshold value, $c_{\mathrm{gf,th}}$, is reached. To simplify the mathematical model, we consider that vascular damage is the only trigger of GF production. Degradation, on the other hand, is assumed to occur at a constant rate, $k_{\mathrm{deg,gf}}$, and in proportion to the 'distance' from the initial value.

2.3.2. Matrix-degrading metalloproteinases

Human MMPs are a family of 26 members of zinc-dependent proteolytic enzymes which are considered to be the normal and physiologically relevant mediators of ECM degradation [45,46]. Given that MMP-2 cleaves a wider range of ECM constituents [22], the term MMP specifically refers to MMP-2 in this model. ECs, SMCs, fibroblasts and infiltrating inflammatory cells are able to produce MMPs. In this work, we assume that mechanical damage resulting from stenting upregulates MMP production only by SMCs [46], while at the same time MMP is reduced at a constant rate [24]. The MMP evolution equation is defined as follows:

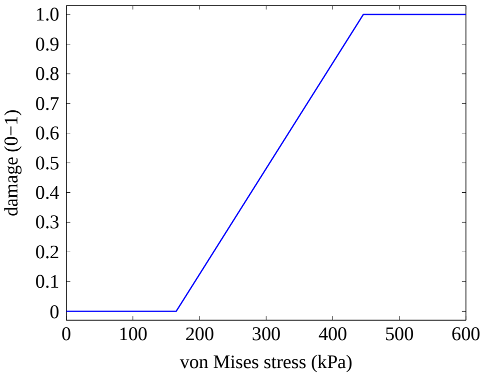

Figure 2. Initial damage as a function of von Mises stress in the arterial wall. In this work, the value selected for the inferior limit of the von Mises stress is 165 kPa, corresponding to three times the value of the physiological circumferential tension calculated by Laplace's Law, for a given blood pressure of 100 mmHg (13.3 kPa). For the superior limit of the von Mises stress, a value of 446 kPa was chosen, based on the mean value of the ultimate tensile stresses for the media layer in the circumferential direction reported by Holzapfel *et al.* [42]. (Online version in colour.)

$$\begin{aligned}\frac{\partial c_{\mathrm{mmp}}}{\partial t} &+ \underbrace{\nabla\cdot(-D_{\mathrm{mmp}}\nabla c_{\mathrm{mmp}})}_{\text{Random motion}} \\ &= \underbrace{(k_{\mathrm{prod1,mmp}} c_{\mathrm{csmc}} + k_{\mathrm{prod2,mmp}} c_{\mathrm{ssmc}}) d\left(1 - \frac{c_{\mathrm{mmp}}}{c_{\mathrm{mmp,th}}}\right)}_{\text{Production}} \\ &\quad \underbrace{- k_{\mathrm{deg,mmp}}(c_{\mathrm{mmp}} - c_{\mathrm{mmp},0})}_{\text{Degradation}},\end{aligned} \tag{2.5}$$

where c_{mmp} is the concentration of MMPs, D_{mmp} is the diffusion coefficient to simulate the random movement of MMP molecules, $k_{\mathrm{prod1,mmp}}$ and $k_{\mathrm{prod2,mmp}}$ are the production rates of MMPs by contractile and synthetic SMCs, respectively, and $k_{\mathrm{deg,mmp}}$ is the constant degradation rate of MMPs. The parameter $c_{\mathrm{mmp},0}$ represents the initial concentration of MMP in the tissue [47], while $c_{\mathrm{mmp,th}}$ is the threshold MMP concentration.

2.3.3. Extracellular matrix

The ECM is the non-cellular component of the arterial wall that provides physical scaffolding for the cellular constituents and is responsible for cell–matrix interactions [48], playing a crucial role in the development of the pathogenesis of restenosis. In particular, ECM components are involved in the regulation of SMC phenotype: degradation of ECM after stenting promotes the transition of SMCs from a quiescent/contractile to an active/synthetic phenotype, whereas its synthesis leads to the opposite [49]. In this work, the behaviour of ECM has been directly related to the behaviour of collagen which constitutes the major component of mature restenotic tissue [7]. For this reason, collagen is assumed to be the only component of the ECM in our model. Collagen is secreted by synthetic SMCs [2] and degraded at a rate proportional to the amount of MMPs [7,24], so its behaviour can be defined as follows:

$$\frac{\partial c_{\mathrm{ecm}}}{\partial t} = \underbrace{k_{\mathrm{prod,ecm}} c_{\mathrm{ssmc}} \left(1 - \frac{c_{\mathrm{ecm}}}{c_{\mathrm{ecm,th1}}}\right)}_{\text{Production}} \\ \underbrace{- k_{\mathrm{deg,ecm}} (c_{\mathrm{mmp}} - c_{\mathrm{mmp,0}}) \left(1 - \frac{c_{\mathrm{ecm,th2}}}{c_{\mathrm{ecm}}}\right)}_{\text{Degradation}}, \qquad (2.6)$$

where $c_{\mathrm{ecm}}(r, z, t)$ is the concentration of collagen, which is produced at a rate $k_{\mathrm{prod,ecm}}$ and degraded at a degradation rate $k_{\mathrm{deg,ecm}}$. The initial concentration of collagen is $c_{\mathrm{ecm,0}}$ [47]. We assume that the natural synthesis of collagen is equal to the age-related degradation rate, therefore these terms have not been taken into account in this equation. Moreover, we assume that ECM kinetics are dominated by production and degradation and that random motion of ECM is negligible.

2.3.4. Contractile smooth muscle cells

SMCs are the most prominent cell type found in intimal hyperplasia. In our model, SMCs can exist in one of two phenotypes: contractile or synthetic. Before stent implantation, SMCs are in a quiescent/contractile phenotype (do not proliferate or synthesize matrix) within the uninjured tissue. We can define the behaviour of the contractile SMCs as

$$\frac{\partial c_{\mathrm{csmc}}}{\partial t} = \underbrace{-k_{\mathrm{diff,csmc}} c_{\mathrm{csmc}} K_{\mathrm{ssmc,ecm}}}_{\text{Differentiation from cSMC to sSMC}} + \underbrace{k_{\mathrm{diff,ssmc}} c_{\mathrm{ssmc}} K_{\mathrm{csmc,ecm}}}_{\text{Differentiation from sSMC to cSMC}}, \qquad (2.7)$$

where $c_{\mathrm{csmc}}(r, z, t)$ is the contractile SMC concentration, $k_{\mathrm{diff,csmc}}$ is the differentiation rate from contractile SMCs to synthetic SMCs, $k_{\mathrm{diff,ssmc}}$ is the differentiation rate from synthetic SMCs to contractile SMCs and $K_{\mathrm{csmc,ecm}}$ and $K_{\mathrm{ssmc,ecm}}$ (figure 3) are functions defined to modulate the SMC differentiation as a function of the ECM concentration:

$$K_{\mathrm{ssmc,ecm}} = -\left(\mathrm{e}^{-((c_{\mathrm{ecm,th}}/c_{\mathrm{ecm}})-1)-|(c_{\mathrm{ecm,th}}/c_{\mathrm{ecm}})-1|} - 1\right) \qquad (2.8)$$

and

$$K_{\mathrm{csmc,ecm}} = -\left(\mathrm{e}^{-((c_{\mathrm{ecm}}/c_{\mathrm{ecm,th}})-1)-|(c_{\mathrm{ecm}}/c_{\mathrm{ecm,th}})-1|} - 1\right). \qquad (2.9)$$

In this model, contractile SMCs may differentiate into synthetic SMCs and vice-versa. The function $K_{\mathrm{ssmc,ecm}}$ contributes to the emergence of the synthetic phenotype, so when $c_{\mathrm{ecm}} < c_{\mathrm{ecm,th}}$ the function $K_{\mathrm{ssmc,ecm}}$ takes positive values, SMCs are activated and switch to a synthetic phenotype starting to migrate, proliferate and synthesize ECM, while if $c_{\mathrm{ecm}} \geqslant c_{\mathrm{ecm,th}}$ then $K_{\mathrm{ssmc,ecm}}$ is equal to zero (no differentiation). On the other hand, $K_{\mathrm{csmc,ecm}}$ contributes to the emergence of the contractile phenotype, so when $c_{\mathrm{ecm}} \leqslant c_{\mathrm{ecm,th}}$ then $K_{\mathrm{csmc,ecm}}$ is zero and if $c_{\mathrm{ecm}} > c_{\mathrm{ecm,th}}$ the function $K_{\mathrm{csmc,ecm}}$ takes a positive value and synthetic SMCs switch back to the contractile phenotype. At the beginning of the simulation $c_{\mathrm{ecm}} = c_{\mathrm{ecm,th}}$ so $K_{\mathrm{ssmc,ecm}}$ and $K_{\mathrm{csmc,ecm}}$ are both equal to zero. We assume that contractile SMCs are initially present only in the media, and at a density of $c_{\mathrm{csmc,0}}$ [50]. Random motion is not taken into account for this cell type since contractile SMCs are considered quiescent and do not migrate. Moreover, contractile SMCs are considered unresponsive to GFs [2].

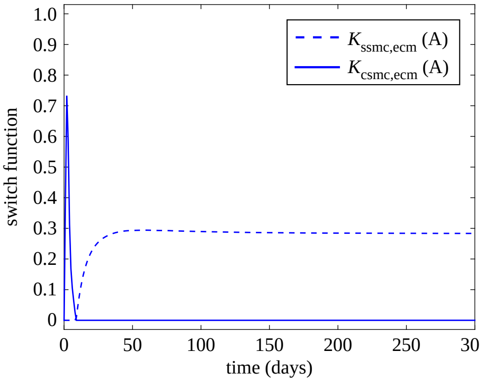

Figure 3. Behaviour of the switch functions defined by equations (2.8) and (2.9). (Online version in colour.)

2.3.5. Synthetic smooth muscle cells

The synthetic SMC evolution equation is as follows:

$$\frac{\partial c_{\mathrm{ssmc}}}{\partial t} + \underbrace{\nabla \cdot (-D_{\mathrm{ssmc}} \nabla c_{\mathrm{ssmc}})}_{\text{Random motion}} = \underbrace{k_{\mathrm{diff,csmc}} c_{\mathrm{csmc}} K_{\mathrm{ssmc,ecm}}}_{\text{Differentiation from cSMC to sSMC}} \\ - \underbrace{k_{\mathrm{diff,ssmc}} c_{\mathrm{ssmc}} K_{\mathrm{csmc,ecm}}}_{\text{Differentiation from sSMC to cSMC}} + \underbrace{k_{\mathrm{prolif,ssmc}} (c_{\mathrm{gf}} - c_{\mathrm{gf,0}})}_{\text{Proliferation}} \\ - \underbrace{k_{\mathrm{apop,ssmc}} c_{\mathrm{ssmc}}}_{\text{Apoptosis}}, \qquad (2.10)$$

where $c_{\mathrm{ssmc}}(r, z, t)$ is the synthetic SMC concentration, D_{ssmc} is the diffusion coefficient of synthetic SMCs in order to simulate the migration process, $k_{\mathrm{prolif,ssmc}}$ is the proliferation rate of synthetic SMCs in response to GFs and $k_{\mathrm{apop,ssmc}}$ is the apoptosis rate at which synthetic SMCs die. The initial density of synthetic SMCs in the arterial wall, $c_{\mathrm{ssmc,0}}$, is assumed to be equal to zero [38].

2.3.6. Endothelial cells

Along with SMCs, ECs constitute the main cell type within the vasculature. ECs perform a wide variety of significant functions, e.g. cell migration and proliferation, remodelling, apoptosis and the production of different biochemical substances [51], as well as the control of vascular function [52]. Moreover, most of the mechanical responses to flow in the arterial wall, such as shear stress and stretch, directly affect ECs indicating that these cells have specific mechanotransducers capable of transforming mechanical forces into biological responses. A thin single layer of ECs forms the endothelium, which in normal conditions, besides being a permeability barrier between the blood flow and the arterial wall, promotes vasodilatation and suppresses intimal hyperplasia by inhibiting inflammation, thrombus formation and SMC proliferation and migration [53]. However, at sites of injury caused by the stent, the endothelium is denuded [7]. This de-endothelization is considered to be one of the most important mechanisms contributing to restenosis [54]. In this work, it is assumed that the endothelium is denuded between stent struts, considering that only a small amount of cells survive in this region. The behaviour of the ECs may be modelled as

$$\frac{\partial c_{\mathrm{ec}}}{\partial t}+\underbrace{\nabla\cdot(-D_{\mathrm{ec}}\nabla c_{\mathrm{ec}})}_{\text{Random motion}}=\underbrace{k_{\mathrm{prolif,ec}}c_{\mathrm{ec}}\left(1-\frac{c_{\mathrm{ec}}}{c_{\mathrm{ec,0}}}\right)}_{\text{Proliferation}},\tag{2.11}$$

where $c_{\mathrm{ec}}(r, z, t)$ is the density of the endothelial cells, D_{ec} is the diffusion coefficient of the ECs to simulate their migration from the lateral edge of the damage blood vessel surface [2] and $k_{\mathrm{prolif,ec}}$ is the EC proliferation rate. ECs can exist only in the intima or subendothelial spaces (SES). The initial concentration of ECs is assumed to be near to zero at sites where the SES is injured and $c_{\mathrm{ec,0}}$ [55] at the intact SES. In order to ensure a tractable mathematical model, the equation which governs the behaviour of the ECs is assumed to be independent of the rest of the presented coupled PDEs.

2.4. Tissue growth

We follow the continuum framework for growth of biological tissue developed by Garikipati *et al.* [56] to describe the tissue growth that leads to restenosis. This formulation considers mass transport and mechanics coupled due to the kinematics of volumetric growth. Accordingly, the balance of mass in the system must satisfy

$$\frac{\partial \rho_o^i}{\partial t}=\Pi_i-\nabla\cdot\boldsymbol{M}_i,\tag{2.12}$$

where the index i is used to indicate an arbitrary species; ρ_o^i are the concentrations of the species as mass per unit volume in the reference configuration; Π_i are the sources/sinks related to migration, proliferation, differentiation and apoptosis of the cells and synthesis and degradation of the substances; and $\boldsymbol{M}_i$ are the mass fluxes of the i arbitrary species. The operators $\nabla(\bullet)$ and $\nabla\cdot(\bullet)$ denote the gradient operator and the divergence of a vector in the reference configuration, respectively. The total material density of the tissue (ρ_o) is the sum of all the individual species concentrations (ρ_o^i), i.e. $\rho_o=\sum_i \rho_o^i$. These densities, ρ_o^i, evolve if local volumetric changes take place as a result of mass transport and inter-conversion of species. That implies that the total density in the reference configuration, ρ_o, also changes with time, i.e. as species concentration increases, the material of a species swells, and conversely, shrinks as concentration decreases [56]. Assuming that these volumetric changes are locally isotropic, we can define the following growth deformation gradient tensor: $\boldsymbol{F}_g^i=(\rho_o^i)/(\rho_{\mathrm{orig}}^i)\boldsymbol{I}$, where ρ_{orig}^i represents the original density of a species in the reference configuration and $\boldsymbol{I}$ is the isotropic tensor of second order. Taking this into consideration, under the small strain hypothesis we can write

$$\nabla\cdot\boldsymbol{v}^i=\frac{\rho_o^i}{\rho_{\mathrm{orig}}^i},\tag{2.13}$$

where $\boldsymbol{v}$ is the velocity of the material points [36]. Since the primary components of restenotic tissue are ECs, SMCs and collagen (here represented by ECM), we neglect volume contributions from the other species. Therefore, the isotropic growth that leads restenosis can be finally determined as

$$\nabla\cdot\boldsymbol{v}=\frac{\partial\Delta c_{\mathrm{ec}}}{\partial t}V_{\mathrm{ec}}+\frac{\partial\Delta c_{\mathrm{smc}}}{\partial t}V_{\mathrm{smc}}+\frac{\partial\Delta c_{\mathrm{ecm}}}{\partial t}\frac{1}{\rho_{\mathrm{ecm}}},\tag{2.14}$$

where Δc_{ec}, Δc_{smc} and Δc_{ecm} are the variations of concentrations of ECs, both contractile and synthetic SMCs and ECM, respectively, with respect to the initial concentration of these species before the restenosis process initiation. The parameters V_{ec} and V_{smc} are the volume of an EC and an SMC, respectively, and ρ_{ecm} is the collagen density (table 3). To calculate the volume of the individual cells, the shape of the ECs is assumed to be spherical [22] and the SMC shape is assumed to be ellipsoidal or spindle-shaped [57]. Therefore, the volume of each cell type may be estimated as follows:

$$V_{\mathrm{ec}}=\frac{4}{3}\pi r_{\mathrm{ec}}^3\tag{2.15}$$

and

$$V_{\mathrm{smc}}=\frac{4}{3}\pi r_{\mathrm{smc}}^2 l_{\mathrm{smc}},\tag{2.16}$$

where r_{ec} is the typical radius of an EC, and r_{smc} and l_{smc} are the typical radius and the length of an SMC, respectively as shown in table 3. This growth process has been defined following the method described for the development of atherosclerotic plaque in [36] and the fibrosis process after the implantation of an inferior vena cava filter in [38], respectively.

3. Computational model

3.1. Model geometry

A two-dimensional axisymmetric geometry corresponding to an idealized representation of a straight stented coronary artery segment is considered in all simulations (figure 4*a*). The baseline computational geometry (table 1) is similar to that introduced by Mongrain *et al.* [16], also employed by Vairo *et al.* [18] and modified by Bozsak *et al.* [19] to study the stent drug release and redistribution in the arterial wall. In order to be able to relate our findings to stent design, we also assess the impact of geometric variations on the final outcome. Specifically, we consider geometrical parameters for three commercial stents, Resolute (Medtronic), Xience (Abbott Vascular) and Biomatrix (Biosensors), whose strut dimensions were obtained from Byrne *et al.* [59], as well as varying the numbers of struts (n_s), inter-strut spacing (ISS), expansion diameter and level of strut embedment. In total, 9 different geometrical configurations are simulated, as summarized in table 2.

3.2. Boundary conditions

The following boundary conditions were applied to the arterial wall mechanical model: (a) at the lumen–arterial wall interface, $\Gamma_{\mathrm{et},i}$ and $\Gamma_{\mathrm{et},d}$, a constant pressure of 100 mmHg is used to simulate *in vivo* physiological conditions and (b) a displacement of 0.2 mm of the stent struts domain, Ω_s, against the wall is prescribed in order to achieve an extra dilatation of the vessel that is usual in stenting techniques. For the biological species evolution, flux and concentration continuity at the SES–media interface, Γ_{iel}, is prescribed. A zero flux boundary condition, $-\boldsymbol{n}\cdot(-D_j\nabla c_j)=0$, where $\boldsymbol{n}$ is the unit normal vector to the corresponding exterior boundary and j denotes each layer of the arterial tissue, was applied at the following boundaries: lumen–wall interface, struts–wall interface, Γ_s,

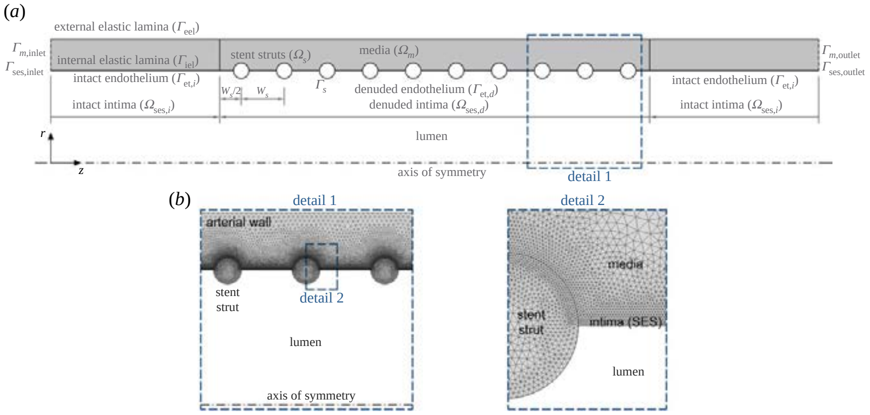

Figure 4. (*a*) Baseline model geometry. The arterial wall is modelled as a multilayer structure distinguishing two different domains: intima and media layer. The adventitia is not modelled as a distinct layer but rather as a boundary condition at the outer surface of the media. The initial luminal radius, r_l, and the thickness of each wall layer, δ_j, in the unloaded geometry of the vessel are listed in table 1, based on typical physiological values found in the literature. The stent implanted in the arterial wall is represented by 10 circular struts each of 0.125 mm radius, r_s, half-embedded in the tissue and located 0.7 mm centre-to-centre distance, w_s, simulating a small lesion of 7 mm. We note that the problem is actually symmetrical about the *r*-axis, i.e. half way between the 5th and 6th struts. (*b*) Details of the FE mesh of the computational model. (Online version in colour.)

Table 1. List of parameters related to the geometry of the baseline model.

parameter	description	value (mm)	reference
r_l	lumen initial radius	1.2	[58]
δ_{ses}	intima thickness	0.01	[19]
δ_m	media thickness	0.5	[17]
r_s	strut radius	0.125	[16]
w_s	interstrut distance	0.7	[16]

arterial wall inlet, $\Gamma_{j,\mathrm{inlet}}$, and outlet, $\Gamma_{j,\mathrm{outlet}}$, and outer surface of the media, Γ_{eel}, in case of GFs, MMPs, ECM and SMCs or SES–media interface in case of EC. All computational boundaries and domains are shown in figure 4 for the baseline model.

3.3. Numerical methods

The commercial software package COMSOL Multiphysics 5.3 (COMSOL AB, Burlington, MA, USA) was used to create the computational geometry and to solve numerically, by means of the finite element method (FEM), the mechanobiological model detailed in §2, which is composed of three coupled systems: (1) a steady system which simulates the mechanical expansion of the stent used for the estimation of the level of damage within the tissue, (2) a transient PDE system which simulates the temporal evolution of the biological species in the arterial wall and, finally, (3) a stationary mechanical analysis to simulate the tissue growth that leads to restenosis. The computational domains (stent struts, intima and media) were meshed using quadratic Lagrange triangular elements, resulting in an overall fine mesh with approximately 150 000 elements (figure 4*b*). A mesh sensitivity analysis was carried out in order to investigate the model mesh independence, testing a series of meshes with different mesh densities. Mesh independence was obtained when there was less than 2% change in the mean concentration of the biological species within the arterial wall for successive mesh refinements. The time-advancing scheme used in the transient problem was a backward differentiation formula with variable order of accuracy varying from one to five and variable time stepping. Both stationary and transient problems were solved using a direct linear solver (MUMPS) with relative and absolute tolerance assigned at 10^{-4} and 10^{-3}, respectively.

3.4. Model parameters

Reference values of the parameters included in the governing equations are summarized in table 3. They correspond to the rates of production, degradation, proliferation and differentiation, the diffusion coefficients of the biological species, the initial concentrations and the threshold values taken into account. Wherever possible, the model input parameters were derived directly from experimental data available in the literature, but in some cases estimation was necessary to ensure that the evolution of the species was broadly consistent with the time-course of restenosis described in some experimental studies [2,3,5,7].

3.5. Sensitivity analysis

A sensitivity analysis of the 28 parameters indicated in table 1 was performed in order to evaluate the effect of varying each input parameter involved on the evolution of the restenosis process and to test the robustness of the results of the computational model. This is of particular importance because of the absence of a complete set of experimental data and the variability seen in many of the parameters. Computations were carried out for four different values for each parameter apart from the reference value, RV, which is shown in table 3. The first two values were considered ± half the reference value of the selected parameter and the other two were

Table 2. List of cases simulated to relate our findings to stent design. The last column refers to the ratio of the lumen diameter after stent expansion to the lumen diameter before stent expansion.

case	stent model	strut shape	strut size (μm)	ISS (mm)	n_s	Emb. config. (%)	ratio
0	baseline model	circular	250	0.7	10	50	1.1
1	Resolute (Medtronic)	circular	91	0.7	10	50	1.1
2	Xience (Abbott)	square	81	0.7	10	50	1.1
3	Biomatrix (Biosensors)	square	120	0.7	10	50	1.1
4	baseline model	circular	250	1.4	5	50	1.1
5	baseline model	circular	250	1.0	7	50	1.1
6	baseline model	circular	250	0.5	14	50	1.1
7	baseline model	circular	250	0.7	10	25–75	1.1
8	baseline model	circular	250	0.7	10	50	1.2

given by increasing and decreasing by one order of magnitude, as can be seen in table 4.

4. Results and discussion

The cascade of events occurring within the arterial wall after the stenting procedure and the consequent response of all the biological species are detailed in this section. The level of damage, local concentrations of GFs, MMPs and ECM and local densities of the SMCs and ECs have been evaluated over time at different points of the computational domain, shown in figure 5*a*, in order to show the restenosis evolution and the stability of the model. Points A and C are located close to a central stent strut in the media and in the denuded SES between struts, respectively. Points B and D are situated far away from the stented area in the media and SES, respectively. Moreover, in order to study the evolution of the solute dynamics in the stented domain, where the behaviour of the system will be more affected by the level of damage in the tissue, the distribution of all the species at five different times of the simulation is shown.

4.1. Quantification of damage

The deformed baseline computational geometry is shown in figure 5*a*. The final radii after deployment in the stented and unstented domain were 1.7 mm and 1.5 mm, respectively. Moreover, the total wall thickness was reduced to approximately 0.4 mm in the stented area. Figure 5*b* displays the von Mises stress distribution in the arterial wall. The scaling of the stress and the corresponding quantification of the initial damage has been performed is detailed in §3.2.

4.2. Damage evolution for the baseline model

The local evolution of damage at points A and B is shown in figure 6*a*. At point B, the level of damage is equal to zero at every time, demonstrating that the model does not evolve over time in regions distant from the device. For this reason, local concentrations of substances and local densities of cells at points located far away from the damage caused by the stent remain approximately constant with time. At point A, the level of damage in the tissue decays exponentially with time until the healing process is complete. Figure 6*b* shows the distribution of the damage in the stented domain over time. Initially, the highest level of damage is found close to the stent struts and to the regions between the struts, where the endothelium has been denuded. As time proceeds, damage decreases continuously to zero in the radial and longitudinal directions towards the adventitial boundary and the unstented domain, respectively. The literature suggests that wound healing is variable in duration. Comparing with our results it can be observed that, from day 90, damage is essentially negligible across the entire baseline computational domain, indicating that the healing process is largely complete in agreement with the classical healing response documented in Forrester *et al.* [2]. This healing process is mainly governed by the evolution of the concentration of MMP as observed in equation (2.3) coupled with the remaining diffusion–reaction equations.

4.3. Evolution of the species for the baseline model

The results for the GF evolution are shown in figures 7*a* and 8*a*. At damaged vascular sites (point A), the local concentration of GFs initially increases abruptly peaking approximately between two and three weeks after stent implantation. Following this peak, the concentration decays exponentially over time returning to the physiological baseline value, contributing to the stabilization of the synthetic SMCs, in agreement with the temporal sequence of GF expression documented in Forrester *et al.* [2]. As the GF production depends directly on damage (equation (2.4)), at points far from the stented area (point B), the concentration of GFs does not vary over time.

Figures 7*b* and 8*b* show the evolution over time for the MMPs. At the beginning of the simulation the initial concentration of MMP is set to a homeostatic value of $3.83 \times 10^{-7}\,\mathrm{mol\,m^{-3}}$ [47]. The local concentration of MMP at point A starts increasing, mainly due to its production by the synthetic SMCs, until reaching its maximum value at day 9, which is consistent with the time course of expression of MMP-2 observed by Bendenck *et al.* [60]. As MMP synthesis depends directly on the level of damage in the tissue, which continues decreasing over time, the effect of the degradation term of equation (2.7) is greater than the effect of the production term and, therefore, the concentration of MMPs starts decreasing until reverting to its normal physiological levels [61].

Table 3. List of parameters related to the biological model.

parameter	description	value	reference
rates			
$k_{\text{deg},d}$	damage degradation	$0.5\ \text{m}^3\ \text{mol}^{-1}\ \text{s}^{-1}$	estimated
$k_{\text{prod,gf}}$	GF production	$8 \times 10^{-13}\ \text{mol m}^{-3}\ \text{s}^{-1}$	estimated
$k_{\text{deg,gf}}$	GF degradation	$1.27 \times 10^{-6}\ \text{s}^{-1}$	[24–65]
$k_{\text{prod1,mmp}}$	MMP production by cSMC	$3 \times 10^{-26}\ \text{mol cell}^{-1}\ \text{s}^{-1}$	adapted from [22]
$k_{\text{prod2,mmp}}$	MMP production by sSMC	$6 \times 10^{-26}\ \text{mol cell}^{-1}\ \text{s}^{-1}$	adapted from [22]
$k_{\text{deg,mmp}}$	MMP degradation	$4.63 \times 10^{-6}\ \text{s}^{-1}$	[24]
$k_{\text{prod,ecm}}$	ECM production by sSMC	$2.157 \times 10^{-11}\ \text{g cell}^{-1}\ \text{s}^{-1}$	[36]
$k_{\text{deg,ecm}}$	ECM degradation	$2 \times 10^{3}\ \text{s}^{-1}$	estimated
$k_{\text{diff,csmc}}$	cSMC differentiation	$5 \times 10^{-7}\ \text{s}^{-1}$	[23–36]
$k_{\text{diff,ssmc}}$	sSMC differentiation	$2.314 \times 10^{-6}\ \text{s}^{-1}$	[23]
$k_{\text{prolif,ssmc}}$	sSMC proliferation by GF	$2.5 \times 10^{13}\ \text{cell mol}^{-1}\ \text{s}^{-1}$	estimated
$k_{\text{apop,ssmc}}$	sSMC apoptosis	$2.2 \times 10^{-10}\ \text{s}^{-1}$	[66]
$k_{\text{prolif,ec}}$	EC proliferation	$10^{-6}\ \text{s}^{-1}$	adapted from [67]
diffusion coefficients			
D_{gf}	GFs	$2.6 \times 10^{-11}\ \text{m}^2\ \text{s}^{-1}$	[32]
D_{mmp}	matrix metalloproteinases	$1.2 \times 10^{-12}\ \text{m}^2\ \text{s}^{-1}$	[68]
D_{ecm}	ECM	neglected	[36]
D_{csmc}	cSMCs	neglected	[36]
D_{ssmc}	synthetic smooth muscle cells	$1.85 \times 10^{-13}\ \text{m}^2\ \text{s}^{-1}$	[69]
D_{ec}	ECs	$8 \times 10^{-14}\ \text{m}^2\ \text{s}^{-1}$	[32]
initial concentrations			
$c_{\text{gf,0}}$	GF initial concentration	$3.48 \times 10^{-7}\ \text{mol m}^{-3}$	[44]
$c_{\text{mmp,0}}$	MMP initial concentration	$3.83 \times 10^{-7}\ \text{mol m}^{-3}$	[47]
$c_{\text{ecm,0}}$	ECM initial concentration	$6.67\ \text{mol m}^{-3}$	[47]
$c_{\text{csmc,0}}$	cSMC initial concentration	$3.16 \times 10^{13}\ \text{cell m}^{-3}$	[50]
$c_{\text{ssmc,0}}$	sSMC initial concentration	$0\ \text{cell m}^{-3}$	[38]
$c_{\text{ec,0}}$	EC initial concentration	$5 \times 10^{11}\ \text{cell m}^{-3}$	[55]
threshold values			
$c_{\text{gf,th}}$	GF threshold concentration	$10 \times c_{\text{gf,0}}$	estimated
$c_{\text{mmp,th}}$	MMP threshold concentration	$10 \times c_{\text{mmp,0}}$	estimated
$c_{\text{ecm,th}}$	ECM threshold	$c_{\text{ecm,0}}$	[38]
$c_{\text{ecm,th1}}$	ECM superior threshold	$1.5 \times c_{\text{ecm,0}}$	estimated
$c_{\text{ecm,th2}}$	ECM inferior threshold	$0.1 \times c_{\text{ecm,0}}$	estimated
growth model			
r_{ec}	EC radius	$17.87\ \mu\text{m}$	[22]
r_{smc}	SMC radius	$3.75\ \mu\text{m}$	[57]
l_{smc}	SMC length	$115\ \mu\text{m}$	[57]
ρ_{ecm}	ECM density	$1\ \text{g ml}^{-1}$	[47]

The collagen variation over time is shown in figures 7*c* and 8*c*. At early times post-deployment, the local concentration of ECM at point A is degraded as a consequence of the increase of MMPs until reaching a minimum value of $4.02\ \text{mol m}^{-3}$ after 2 days. From this point, its concentration starts increasing over time, mainly because of the differentiation of the contractile SMCs and the proliferation of the synthetic SMCs, producing neointimal thickening in the weeks after injury [7] until an equilibrium value of approximately $7.8\ \text{mol m}^{-3}$ is reached at approximately day 50.

Figures 7*d*, 8*d* and 7*e*, 8*e* illustrate the evolution of the contractile and synthetic SMCs, respectively. At the beginning of the process, the local density of the contractile SMCs at point A decreases due to the differentiation into a synthetic phenotype until reaching a minimum value of $2.85 \times 10^{13}\ \text{cell m}^{-3}$ one to two weeks after the stenting procedure. Meanwhile,

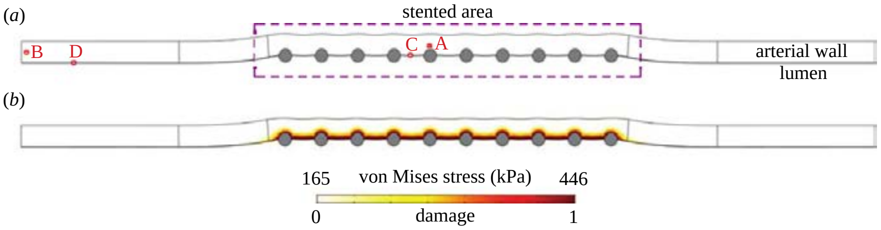

Figure 5. (*a*) Deformed computational geometry and (*b*) von Mises stress distribution and corresponding quantification of the initial damage in the arterial wall. Points A and C are located close to a central stent strut in the media and in the denuded SES between struts, respectively. Points B and D are situated far away from the stented area in the media and SES, respectively. (Online version in colour.)

Table 4. List of cases with the corresponding parameter values computed in the sensitivity analysis. (*) Note that due to the reference value of $c_{\mathrm{ssmc},0}$ in case 22 being equal to zero, the strategy for varying parameters had to be adjusted. Points A and C are located close to a central stent strut in the media and in the denuded SES between struts, respectively. Points B and D are situated far away from the stented area in the media and SES, respectively.

case	parameter	unit	RV/10	RV/2	RV	2 RV	10 RV
01	$k_{\mathrm{deg,d}}$	$\mathrm{m^3\,mol^{-1}\,s^{-1}}$	0.05	0.25	0.5	1	5
02	$k_{\mathrm{prod,gf}}$	$\mathrm{mol\,m^{-3}\,s^{-1}}$	8×10^{-14}	4×10^{-13}	8×10^{-13}	1.6×10^{-12}	8×10^{-12}
03	$k_{\mathrm{deg,gf}}$	$\mathrm{s^{-1}}$	1.27×10^{-7}	6.35×10^{-7}	1.27×10^{-6}	2.54×10^{-6}	1.27×10^{-5}
04	$k_{\mathrm{prod1,mmp}}$	$\mathrm{mol\,cell^{-1}\,s^{-1}}$	3×10^{-27}	1.5×10^{-26}	3×10^{-26}	6×10^{-26}	3×10^{-25}
05	$k_{\mathrm{prod2,mmp}}$	$\mathrm{mol\,cell^{-1}\,s^{-1}}$	6×10^{-27}	3×10^{-26}	6×10^{-26}	1.2×10^{-25}	6×10^{-25}
06	$k_{\mathrm{deg,mmp}}$	$\mathrm{s^{-1}}$	4.63×10^{-7}	2.31×10^{-6}	4.63×10^{-6}	9.26×10^{-6}	4.63×10^{-5}
07	$k_{\mathrm{prod,ecm}}$	$\mathrm{g\,cell^{-1}\,s^{-1}}$	2.15×10^{-12}	1.07×10^{-11}	2.15×10^{-11}	4.31×10^{-11}	2.15×10^{-10}
08	$k_{\mathrm{deg,ecm}}$	$\mathrm{s^{-1}}$	2×10^{2}	1×10^{3}	2×10^{3}	4×10^{3}	2×10^{4}
09	$k_{\mathrm{diff,csmc}}$	$\mathrm{s^{-1}}$	5×10^{-8}	2.5×10^{-7}	5×10^{-7}	10^{-6}	5×10^{-6}
10	$k_{\mathrm{diff,ssmc}}$	$\mathrm{s^{-1}}$	2.31×10^{-7}	1.15×10^{-6}	2.31×10^{-6}	4.62×10^{-6}	2.31×10^{-5}
11	$k_{\mathrm{prolif,ssmc}}$	$\mathrm{cell\,mol^{-1}\,s^{-1}}$	2.5×10^{12}	1.25×10^{13}	2.5×10^{13}	5×10^{13}	2.5×10^{14}
12	$k_{\mathrm{apop,ssmc}}$	$\mathrm{s^{-1}}$	2.2×10^{-11}	1.1×10^{-10}	2.2×10^{-10}	4.4×10^{-10}	2.2×10^{-9}
13	$k_{\mathrm{prolif,ec}}$	$\mathrm{s^{-1}}$	10^{-7}	5×10^{-7}	10^{-6}	2×10^{-6}	10^{-5}
14	D_{gf}	$\mathrm{m^2\,s^{-1}}$	2.6×10^{-12}	1.3×10^{-11}	2.6×10^{-11}	5.2×10^{-11}	2.6×10^{-10}
15	D_{mmp}	$\mathrm{m^2\,s^{-1}}$	1.2×10^{-13}	6×10^{-13}	1.2×10^{-12}	2.4×10^{-12}	1.2×10^{-11}
16	D_{ssmc}	$\mathrm{m^2\,s^{-1}}$	1.85×10^{-14}	9.26×10^{-13}	1.85×10^{-13}	3.7×10^{-13}	1.85×10^{-12}
17	D_{ec}	$\mathrm{m^2\,s^{-1}}$	8×10^{-15}	4×10^{-14}	8×10^{-14}	1.6×10^{-13}	8×10^{-13}
18	$c_{\mathrm{gf},0}$	$\mathrm{mol\,m^{-3}}$	3.48×10^{-8}	1.74×10^{-7}	3.48×10^{-7}	6.96×10^{-7}	3.48×10^{-6}
19	$c_{\mathrm{mmp},0}$	$\mathrm{mol\,m^{-3}}$	3.83×10^{-8}	1.91×10^{-7}	3.83×10^{-7}	7.66×10^{-7}	3.83×10^{-6}
20	$c_{\mathrm{ecm},0}$	$\mathrm{mol\,m^{-3}}$	0.667	3.335	6.67	13.33	66.7
21	$c_{\mathrm{csmc},0}$	$\mathrm{cell\,m^{-3}}$	3.16×10^{12}	1.58×10^{13}	3.16×10^{13}	6.32×10^{13}	3.16×10^{14}
22*	$c_{\mathrm{ssmc},0}$	$\mathrm{cell\,m^{-3}}$	0 (RV)	3.16×10^{12}	1.58×10^{13}	3.16×10^{13}	—
23	$c_{\mathrm{ec},0}$	$\mathrm{cell\,m^{-3}}$	5×10^{10}	2.5×10^{11}	5×10^{11}	$1{\cdot}10^{12}$	5×10^{12}
24	$c_{\mathrm{gf,th}}$	$\mathrm{mol\,m^{-3}}$	3.48×10^{-7}	1.74×10^{-6}	3.48×10^{-6}	6.96×10^{-6}	3.48×10^{-5}
25	$c_{\mathrm{mmp,th}}$	$\mathrm{mol\,m^{-3}}$	3.83×10^{-7}	1.91×10^{-6}	3.83×10^{-6}	7.66×10^{-6}	3.83×10^{-5}
26	$c_{\mathrm{ecm,th}}$	$\mathrm{mol\,m^{-3}}$	0.667	3.335	6.67	13.33	66.7
27	$c_{\mathrm{ecm,th1}}$	$\mathrm{mol\,m^{-3}}$	1	5	10	20	100
28	$c_{\mathrm{ecm,th2}}$	$\mathrm{mol\,m^{-3}}$	0.067	0.333	0.667	1.333	6.67

the synthetic SMCs are immediately activated and start proliferating in the media [3]. The local density of synthetic SMCs increases to a value of $3.92\times10^{12}\,\mathrm{cell\,m^{-3}}$ between two and three weeks after injury [3], coinciding in time with the peak in the concentration of GFs and demonstrating that locally produced GFs are a major stimulus for SMC migration and proliferation, in agreement with Forrester *et al.* [2]. After this time, synthetic SMCs begin to revert back to the contractile phenotype. This process continues over several months and is paralleled by a change in the

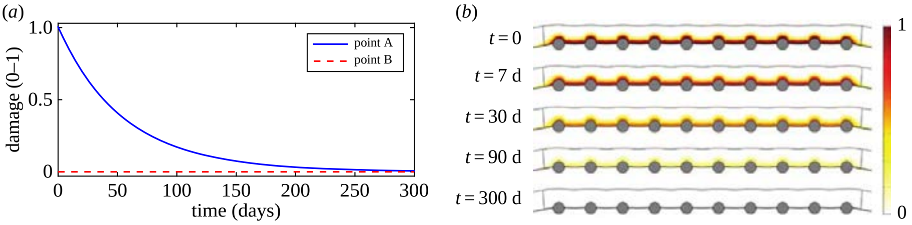

Figure 6. Local evolution of the damage over time at two different points within the media (*a*) and distribution of damage in the stented area of the arterial wall at five different times after stent implantation (*b*). Point A and point B are located close to a central stent strut and far away from the effect of the stent in the media, respectively. (Online version in colour.)

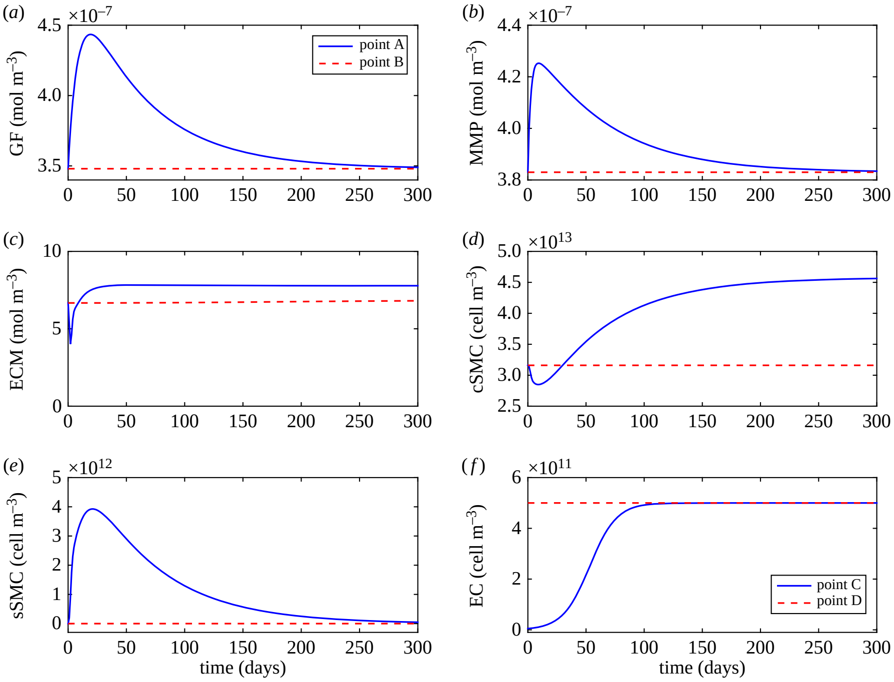

Figure 7. Time-varying local concentration/density profiles of (*a*) GFs, (*b*) MMPs, (*c*) ECM, (*d*) contractile SMCs, (*e*) synthetic SMCs and (*f*) ECs at two different points within the arterial wall. Points A and C are located close to a central stent strut in the media and in the denuded SES between struts, respectively. Points B and D are situated far away from the stented area in the media and SES, respectively. (Online version in colour.)

ECM [2]. It can be noted that the evolution in the concentration of the ECM components, mainly collagen, plays a key role in SMC differentiation, as discussed in §2.3.3, since when the ECM concentration is sufficiently low, synthetic SMCs appear, and when it is sufficiently high, contractile SMCs appear.

ECs only exist within the intima and their behaviour is governed mainly by proliferation and migration. The time-varying local density profiles of this cell type are shown in figure 7*f*. It can be seen that at points where the endothelium has been denuded by the stent (i.e. point C), ECs start proliferating at the beginning of the restenotic process. Between days 100 and 150, they cease proliferation, reaching, at approximately day 180, an equilibrium density of 5×10^{11} cell m^{-3} [55] along the length of the SES, corresponding to homeostatic conditions and in agreement with the temporal response described by Forrester *et al.* [2]. It can be considered then that the endothelium has been completely restored. However, after this time restenotic events continue since both SMC proliferation/migration and ECM deposition do not necessarily cease at this time.

4.4. Sensitivity analysis

The results for the sensitivity analysis performed involving those parameters that have the greatest influence on the behaviour of the system are shown in figures 9 and 10. The discussion is included in the electronic supplementary material.

4.5. Tissue growth

The volumetric growth of new tissue into the lumen of the vessel in response to the mechanical injury caused by the medical device after 300 days is shown in figure 11,

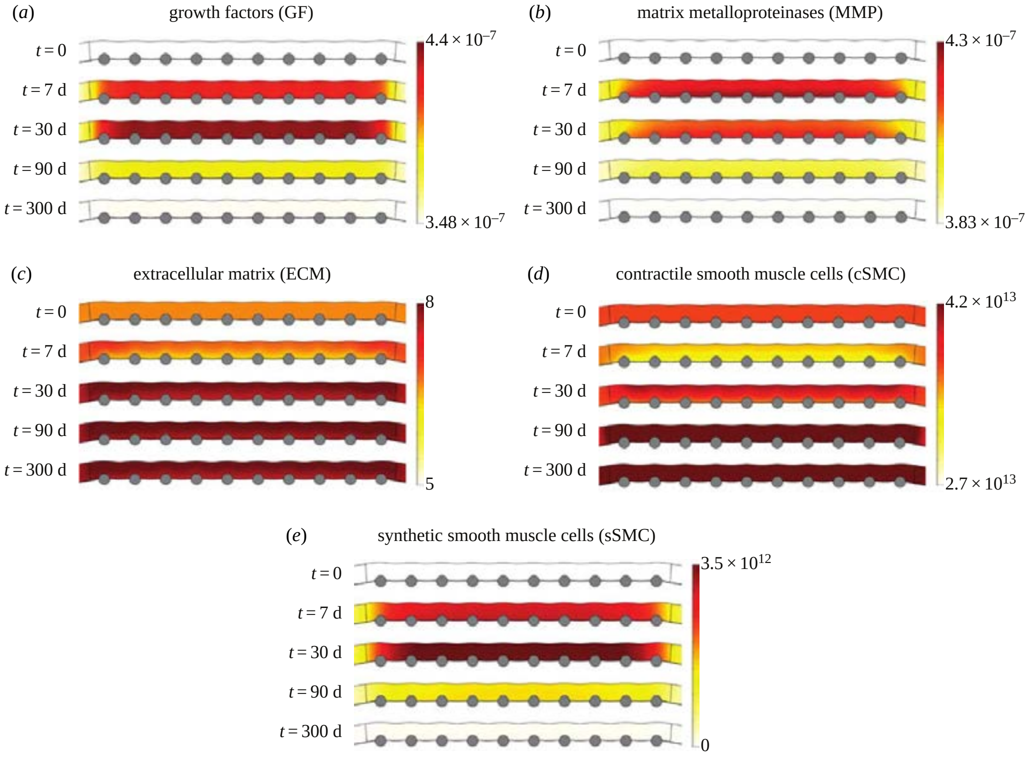

Figure 8. (*a–e*) Evolution of the distribution of all biological species in the media layer of the arterial wall at different times of the simulation. The substance concentration and cell density are shown in mol m^{-3} and cell m^{-3}, respectively. (Online version in colour.)

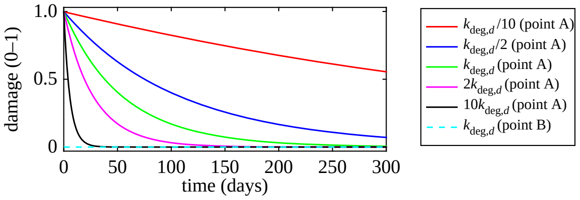

Figure 9. Influence of varying damage degradation rate on the evolution of the damage. Refer to the electronic supplementary material for a discussion. (Online version in colour.)

for the baseline model. It should be noticed that the restenotic tissue grows considerably between struts. The degree of occlusion can be measured in terms of the diameter or area of restenosis [62]. In this work, the change in the cross-sectional area of the model is used as a measure of measuring arterial restenosis. The percentage of stenosis is calculated as $(1 - A_r/A_{\mathrm{ref}}) \cdot 100$, where A_r and A_{ref} are the area of the lesion and of the reference site, respectively. Therefore, the resulting degree of restenosis after 300 days is approximately 25% for the baseline set of parameters simulated in broad agreement with the clinical data presented in Nobuyoshi *et al.* [63].

4.6. Impact of geometric variations on tissue growth

In figure 12, we consider the impact of different geometric configurations on the % restenosis for the various cases considered in table 2. The model produces different levels of restenosis depending on the geometric parameters, and our results are in qualitative agreement with clinical observations. Specifically, the results of our simulations show that % restenosis:

- — increases with increasing strut diameter;
- — decreases with an increase in inter-strut spacing;
- — increases with an increase in lumen expansion diameter;
- — depends on the strut embedment configuration.

5. Limitations

We would like to emphasize that there are a number of limitations in this work, as we now discuss.

5.1. Validation

Whilst the continuum approach that we have adopted is advantageous in that it allows us to assess how the evolution

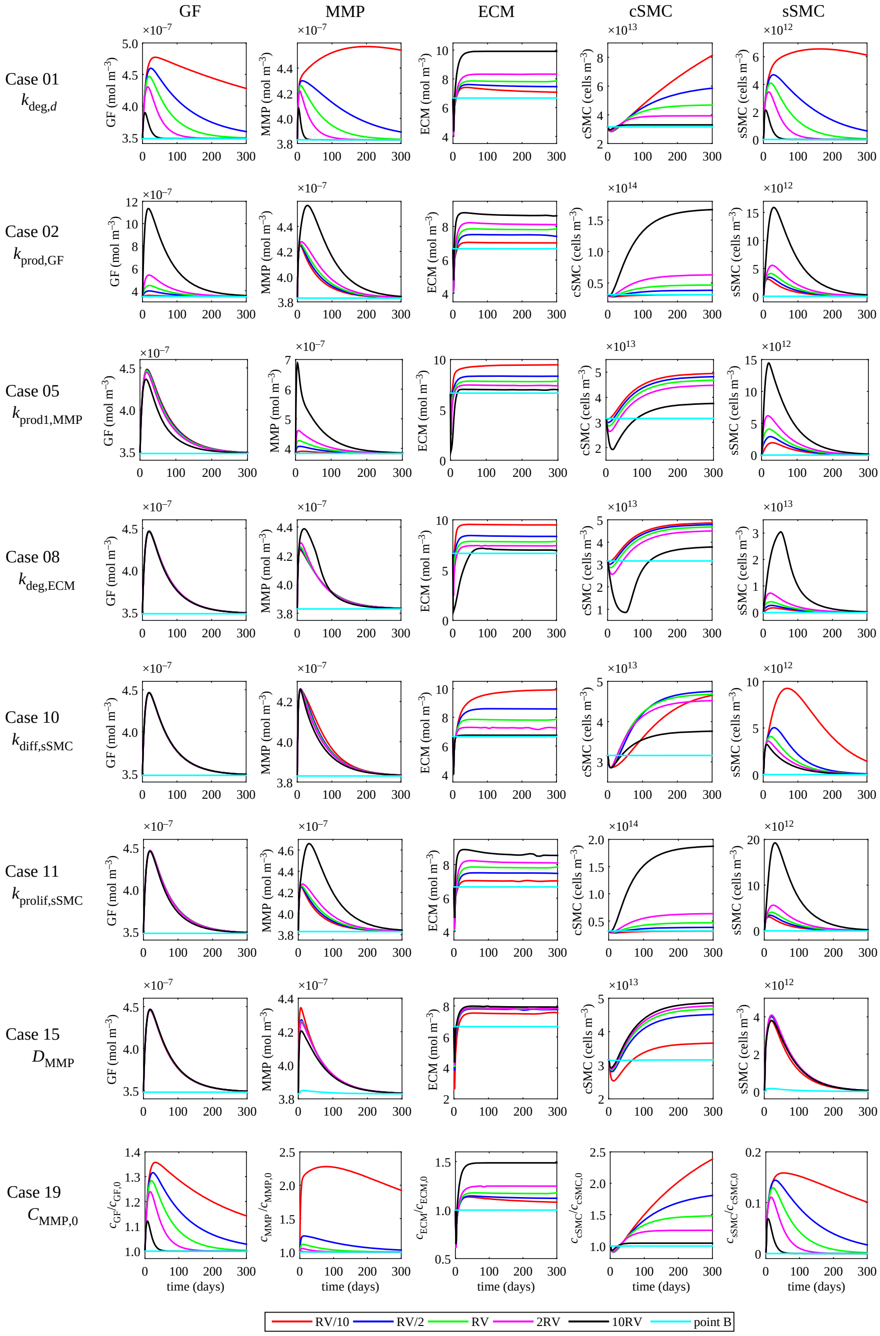

Figure 10. Key results from the sensitivity analysis. The plots show the effect of varying several parameters on the concentration of GFs, MMPs and ECM as well as the density of contractile and synthetic SMCs for eight different cases. Computations were carried out for four different values for each parameter apart from the reference value, RV, which is shown in table 3. The values of 2RV and RV/2 were considered ± half the RV of the selected parameter; 10RV and RV/10 were given by increasing and decreasing by one order of magnitude the RV (table 4). The results shown for point B correspond exclusively to the RV (baseline model). Refer to the electronic supplementary material for a discussion. (Online version in colour.)

of the various species affects the overall healing process, the disadvantage is that it is extremely difficult to measure spatiotemporal cellular densities and GF concentrations experimentally. Certainly, we are not aware of how such validation may be obtained *in vivo*. In short, we do not believe that the data currently exist to validate the predictions of

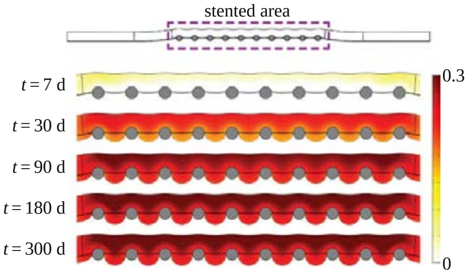

Figure 11. Evolution of the volumetric growth at different times of the simulation for the baseline model. (Online version in colour.)

the model at the level of individual concentrations/densities in space and in time. Therein lies the major advantage of the continuum model proposed here, i.e. the ability to simulate the evolution of species which we cannot get insight into from *in vivo* experiments. Notwithstanding, we have compared our results to restenosis data (at the tissue level) and have shown that our model is in broad agreement with what is seen in the clinic.

5.2. Flow modelling

We acknowledge that there is a known link between the level of shear stress and restenosis. Indeed, most haemodynamics models that assess different stent designs and patient-specific geometries set out to predict quantities such as wall shear stress (WSS), oscillatory shear index and time-averaged WSS, because these can be related to clinical outcome. Keller *et al.* [64], for example, investigated the correlation between mechanical and fluid stresses and the magnitude of restenosis, and found that while a linear correlation is not obtained when these stimuli are considered separately, there is a closer correlation when the combined action of these stimuli is considered. While such correlations are useful for providing insight into the influence of force on restenosis, what is less clear is precisely *how* the transmission of fluid forces affects the behaviour of the cells and other species involved in the healing response. The most sophisticated model of restenosis to date [29] does include the effects of flow, but in in an indirect way. Specifically, Zun *et al.* assume that neointimal growth is dictated by nitric oxide (NO) production, which is governed by average WSS. Therefore, Zun *et al.* calculate WSS from a steady laminar flow simulation and pass this to their biological solver, where the level of NO dictates the ensuing biological response through a set of rules. In the absence of data resolving the underlying physics of how the transmission of force generated by flow affects the healing process *in vivo*, the influence of flow has been neglected in the present analysis. Certainly, the force generated by flow would influence the parameters of our model: in this sense, the sensitivity analysis could be seen to indirectly incorporate the effects of varying flow.

5.3. Geometry

Concerning the geometry of the FE model, a two-dimensional axisymmetric geometry corresponding to an idealized representation of a straight segment of a healthy coronary artery has been considered in this study. This could be improved using more realistic geometries of the artery, such as coronary arteries with curvature, bifurcations, the presence of atherosclerotic plaque or derived directly from three-dimensional patient-specific geometries. However, such models would considerably increase the cost of the numerical simulations and are left for future work.

5.4. Damage modelling

In this work, following the approach presented by Zahedmanesh *et al.* [22], the modelling of the initial damage in the tissue after stenting is considered in a very simple way, which is based on the ultimate tensile stress–stretch response for each layer of human coronary arteries [42]. However, to our knowledge, there is no experimental data published in the literature which directly relate the levels of stress–strain due to stent deployment to the arterial wall injury and the sequence of events associated such as GF and MMP production, synthesis, number of proliferating SMCs, etc.

5.5. Model parameters and biological species

The biological parameters involved in this model were obtained from a wide range of *in vivo* and *in vitro* experiments from the published literature on different blood vessels from human and animal models. However, due to the important structural and functional differences between arteries [48], these parameters could vary from artery-to-artery, species-to-species and patient-to-patient, or even from one lesion to another in the same patient. Additionally, some of these parameters have had to be estimated to be consistent with the time course of the restenosis process found in different studies [2–5,7]. Moreover, all the parameters have been taken as constant and uniform through the whole artery, but in fact they are very likely to change during the process. Finally, only the most important biological species have been taken into account. Other species involved in the coronary restenosis process such as platelets, monocytes, different classes of GFs (PDGF, EGF, IGF, TGF, FGF), mesenchymal cells, fibroblasts, collagen subtypes, proteoglycans, fibronectin, etc., have been grouped or omitted. Moreover, only the main biological processes have been considered in this model. Other processes such as activation and migration of the mesenchymal stem cells, release of GFs by fibroblasts or ECM synthesis by ECs were not included.

6. Conclusion

A mathematical and computational model which successfully captures the main characteristics of the restenosis process after stent implantation in a healthy coronary artery has been presented in this work. A continuum approach has been taken into account for modelling the behaviour of the different biological species involved in ISR, resulting in a PDE system of several coupled diffusion–reaction equations, solved numerically by means of the FEM. Mechanical damage, which is quantitatively estimated as a function of the von Mises stress levels obtained in the arterial wall after a FE simulation of the stent expansion, is considered as the stimulus needed to start the process.

Our results confirm that ISR depends on multiple factors, with the ECM dynamics and SMC proliferation the primary contributors to its pathogenesis. In addition to this, the sensitivity analysis carried out for the different model parameters,

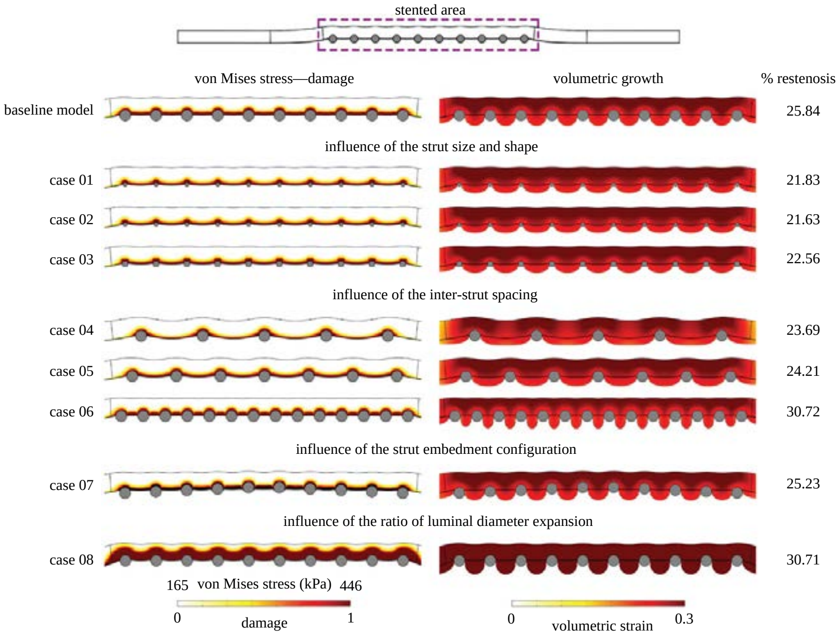

Figure 12. The impact of different geometric configurations (table 2) on von Mises stress distribution and volumetric growth after 300 days. (Online version in colour.)

as well as providing information on the stability of the model, provides us with an understanding of how changes in one parameter will affect the behaviour of the whole system. The value of $k_{\mathrm{deg},d}$ has a significant impact on the healing rate. Moreover, it was shown that the rates of production, degradation, differentiation and proliferation taken into account highly affect the local levels of concentration/density of the species involved in the process and the temporal response of the system. The apoptosis rate of synthetic SMCs, diffusion coefficients and initial conditions also influence the evolution of the model, although to a lesser extent.

In conclusion, in spite of the simplifications and limitations we have discussed, the model developed is able to capture some of the underlying mechanisms and patterns of ISR. Moreover, the results obtained are in good agreement with clinical hypotheses relating to ISR occurrence. Therefore, this model can be considered as a step forward to a better understanding of this phenomenon.

Data accessibility. The data associated with this paper consist of the mathematical models and their numerical solution as detailed in the text.

Authors' contributions. Conceived and designed the study: M.A.M., S.M. and E.P. Development of mathematical model: J.E., M.A.M., S.M. and E.P. Computational implementation of model: J.E. Writing, review and editing: J.E., M.A.M., S.M. and E.P.

Competing interests. We declare we have no competing interests.

Funding. The authors gratefully acknowledge funding provided by the Spanish Ministry of Economy, Industry and Competitiveness under research project number DPI2016-76630-C2-1-R and grant no. BES-2014-069737.

References

1. Wilkins E, Wilson L, Wickramasinghe K, Bhatnagar P, Leal J, Luengo-Fernandez R, Burns R, Rayner M, Townsend N. 2017 *European cardiovascular disease statistics*, p. 192. Brussels, Belgium: European Heart Network.
2. Forrester JS, Fishbein M, Helfant R, Fagin J. 1991 A paradigm for restenosis based on cell biology: clues for the development of new preventive therapies. *J. Am. Coll. Cardiol.* **17**, 758–769. (doi:10.1016/S0735-1097(10)80196-2)
3. Bauters C, Isner JM. 1997 The biology of restenosis. *Prog. Cardiovasc. Dis.* **40**, 107–116. (doi:10.1016/S0033-0620(97)80003-5)
4. Libby P, Tanaka H. 1997 The molecular bases of restenosis. *Prog. Cardiovasc. Dis.* **40**, 97–106. (doi:10.1016/S0033-0620(97)80002-3)
5. Welt FG, Rogers C. 2002 Inflammation and restenosis in the stent era. *Arterioscler. Thromb. Vasc. Biol.* **22**, 1769–1776. (doi:10.1161/01.ATV.0000037100.44766.5B)
6. Bennett MR. 2003 In-stent stenosis: pathology and implications for the development of drug eluting stents. *Heart* **89**, 218–224. (doi:10.1136/heart.89.2.218)
7. Costa MA, Simon DI. 2005 Molecular basis of restenosis and drug-eluting stents. *Circulation* **111**, 2257–2273. (doi:10.1161/01.CIR.0000163587.36485.A7)
8. Buccheri D, Piraino D, Andolina G, Cortese B. 2016 Understanding and managing in-stent restenosis: a review of clinical data, from pathogenesis to treatment. *J. Thorac. Dis.* **8**, E1150–E1162. (doi:10.21037/jtd.2016.10.93)
9. Schwartz RS *et al.* 1992 Restenosis and the proportional neointimal response to coronary artery injury: results in a porcine model. *J. Am. Coll. Cardiol.* **20**, 1284–1293. (doi:10.1016/0735-1097(92)90389-5)
10. Kornowski R, Hong MK, Tio FO, Bramwell O, Wu H, Leon MB. 1998 In-stent restenosis: contributions of

inflammatory responses and arterial injury to neointimal hyperplasia. *J. Am. Coll. Cardiol.* **31**, 224–230. (doi:10.1016/S0735-1097(97)00450-6)

11. McHugh P, Barakat A, McGinty S. 2016 Medical stents: state of the art and future directions. *Ann. Biomed. Eng.* **44**, 274–275. (doi:10.1007/s10439-015-1526-x)
12. Migliavacca F, Petrini L, Massarotti P, Schievano S, Auricchio F, Dubini G. 2004 Stainless and shape memory alloy coronary stents: a computational study on the interaction with the vascular wall. *Biomech. Model. Mechanobiol.* **2**, 205–217. (doi:10.1007/s10237-004-0039-6)
13. Zahedmanesh H, Kelly DJ, Lally C. 2010 Simulation of a balloon expandable stent in a realistic coronary artery: determination of the optimum modelling strategy. *J. Biomech.* **43**, 2126–2132. (doi:10.1016/j.jbiomech.2010.03.050)
14. García A, Peña E, Martínez M. 2012 Influence of geometrical parameters on radial force during self-expanding stent deployment. Application for a variable radial stiffness stent. *J. Mech. Behav. Biomed. Mater.* **10**, 166–175. (doi:10.1016/j.jmbbm.2012.02.006)
15. Conway C, McGarry J, McHugh P. 2014 Modelling of atherosclerotic plaque for use in a computational test-bed for stent angioplasty. *Ann. Biomed. Eng.* **42**, 2425–2439. (doi:10.1007/s10439-014-1107-4)
16. Mongrain R, Leask R, Brunette J, Faik I, Bulman-Feleming N, Nguyen T. 2005 Numerical modeling of coronary drug eluting stents. *Stud. Health Technol. Inform.* **113**, 443–458.
17. Migliavacca F, Gervaso F, Prosi M, Zunino P, Minisini S, Formaggia L, Dubini G. 2007 Expansion and drug elution model of a coronary stent. *Comput. Methods Biomech. Biomed. Eng.* **10**, 63–73. (doi:10.1080/10255840601071087)
18. Vairo G, Cioffi M, Cottone R, Dubini G, Migliavacca F. 2010 Drug release from coronary eluting stents: a multidomain approach. *J. Biomech.* **43**, 1580–1589. (doi:10.1016/j.jbiomech.2010.01.033)
19. Bozsak F, Chomaz JM, Barakat AI. 2014 Modeling the transport of drugs eluted from stents: physical phenomena driving drug distribution in the arterial wall. *Biomech. Model. Mechanobiol.* **13**, 327–347. (doi:10.1007/s10237-013-0546-4)
20. McGinty S, Pontrelli G. 2016 On the role of specific drug binding in modelling arterial eluting stents. *J. Math. Chem.* **54**, 967–976. (doi:10.1007/s10910-016-0618-7)
21. Zahedmanesh H, Lally C. 2012 A multiscale mechanobiological modelling framework using agent-based models and finite element analysis: application to vascular tissue engineering. *Biomech. Model. Mechanobiol.* **11**, 363–377. (doi:10.1007/s10237-011-0316-0)
22. Zahedmanesh H, Van Oosterwyck H, Lally C. 2014 A multi-scale mechanobiological model of in-stent restenosis: deciphering the role of matrix metalloproteinase and extracellular matrix changes. *Comput. Methods Biomech. Biomed. Eng.* **17**, 813–828. (doi:10.1080/10255842.2012.716830)
23. Boyle C, Lennon AB, Early M, Kelly D, Lally C, Prendergast P. 2010 Computational simulation methodologies for mechanobiological modelling: a cell-centred approach to neointima development in stents. *Phil. Trans. R. Soc. A* **368**, 2919–2935. (doi:10.1098/rsta.2010.0071)
24. Boyle CJ, Lennon AB, Prendergast PJ. 2011 In silico prediction of the mechanobiological response of arterial tissue: application to angioplasty and stenting. *J. Biomech. Eng.* **133**, 081001. (doi:10.1115/1.4004492)
25. Boyle CJ, Lennon AB, Prendergast PJ. 2013 Application of a mechanobiological simulation technique to stents used clinically. *J. Biomech.* **46**, 918–924. (doi:10.1016/j.jbiomech.2012.12.014)
26. Keshavarzian M, Meyer CA, Hayenga HN. 2017 Mechanobiological model of arterial growth and remodeling. *Biomech. Model. Mechanobiol.* **17**, 1–15. (doi:10.1007/s10237-017-0946-y)
27. Evans DJ *et al.* 2008 The application of multiscale modelling to the process of development and prevention of stenosis in a stented coronary artery. *Phil. Trans. R. Soc. A* **366**, 3343–3360. (doi:10.1098/rsta.2008.0081)
28. Tahir H, Niculescu I, Bona-Casas C, Merks R, Hoekstra A. 2015 An in silico study on the role of smooth muscle cell migration in neointimal formation after coronary stenting. *J. R. Soc. Interface* **12**, 20150358. (doi:10.1098/rsif.2015.0358)
29. Zun P, Anikina T, Svitenkov A, Hoekstra A. 2017 A comparison of fully-coupled 3D in-stent restenosis simulations to *in-vivo* data. *Front. Physiol.* **8**, 284. (doi:10.3389/fphys.2017.00284)
30. Rachev A, Manoach E, Berry J, Moore Jr J. 2000 A model of stress-induced geometrical remodeling of vessel segments adjacent to stents and artery/graft anastomoses. *J. Theor. Biol.* **206**, 429–443. (doi:10.1006/jtbi.2000.2143)
31. Hoffmann R, Mintz GS, Dussaillant GR, Popma JJ, Pichard AD, Satler LF, Kent KM, Griffin J, Leon MB. 1996 Patterns and mechanisms of in-stent restenosis: a serial intravascular ultrasound study. *Circulation* **94**, 1247–1254. (doi:10.1161/01.CIR.94.6.1247)
32. Budu-Grajdeanu P, Schugart RC, Friedman A, Valentine C, Agarwal AK, Rovin BH. 2008 A mathematical model of venous neointimal hyperplasia formation. *Theor. Biol. Med. Modell.* **5**, 2. (doi:10.1186/1742-4682-5-2)
33. Calvez V, Ebde A, Meunier N, Raoult A. 2009 Mathematical modelling of the atherosclerotic plaque formation. *ESAIM: Proc.* **28**, 1–12. (doi:10.1051/proc/2009036)
34. Ibragimov A, Ritter L, Walton JR. 2010 Stability analysis of a reaction-diffusion system modeling atherogenesis. *SIAM J. Appl. Math.* **70**, 2150–2185. (doi:10.1137/08073490X)
35. El Khatib N, Génieys S, Kazmierczak B, Volpert V. 2012 Reaction–diffusion model of atherosclerosis development. *J. Math. Biol.* **65**, 349–374. (doi:10.1007/s00285-011-0461-1)
36. Cilla M, Peña E, Martínez MA. 2014 Mathematical modelling of atheroma plaque formation and development in coronary arteries. *J. R. Soc. Interface* **11**, 20130866. (doi:10.1098/rsif.2013.0866)
37. Su J, Gonzales HP, Todorov M, Kojouharov H, Tang L. 2011 A mathematical model for foreign body reactions in 2D. *Int. J. Comput. Math.* **88**, 610–633. (doi:10.1080/00207161003640035)
38. Nicolás M, Peña E, Malvè M, Martínez M. 2015 Mathematical modeling of the fibrosis process in the implantation of inferior vena cava filters. *J. Theor. Biol.* **387**, 228–240. (doi:10.1016/j.jtbi.2015.09.028)
39. Fereidoonnezhad B, Naghdabadi R, Sohrabpour S, Holzapfel G. 2017 A mechanobiological model for damage-induced growth in arterial tissue with application to in-stent restenosis. *J. Mech. Phys. Solids* **101**, 311–327. (doi:10.1016/j.jmps.2017.01.016)
40. Marino M, Pontrelli G, Vairo G, Wriggers P. 2017 A chemo-mechano-biological formulation for the effects of biochemical alterations on arterial mechanics: the role of molecular transport and multiscale tissue remodelling. *J. R. Soc. Interface* **14**, 20170615. (doi:10.1098/rsif.2017.0615)
41. Yeoh OH. 1993 Some forms of the strain energy function for rubber. *Rubber Chem. Technol.* **66**, 754–771. (doi:10.5254/1.3538343)
42. Holzapfel GA, Sommer G, Gasser CT, Regitnig P. 2005 Determination of layer-specific mechanical properties of human coronary arteries with nonatherosclerotic intimal thickening and related constitutive modeling. *Am. J. Physiol. Heart Circ. Physiol.* **289**, H2048–H2058. (doi:10.1152/ajpheart.00934.2004)
43. Jukema JW, Verschuren JJ, Ahmed TA, Quax PH. 2012 Restenosis after PCI. Part 1: pathophysiology and risk factors. *Nat. Rev. Cardiol.* **9**, 53–62. (doi:10.1038/nrcardio.2011.132)
44. McLaren J, Prentice A, Charnock-Jones D, Smith S. 1996 Vascular endothelial growth factor (VEGF) concentrations are elevated in peritoneal fluid of women with endometriosis. *Hum. Reprod.* **11**, 220–223. (doi:10.1093/oxfordjournals.humrep.a019023)
45. Matrisian LM. 1992 The matrix-degrading metalloproteinases. *Bioessays* **14**, 455–463. (doi:10.1002/bies.950140705)
46. Newby AC. 2006 Matrix metalloproteinases regulate migration, proliferation, and death of vascular smooth muscle cells by degrading matrix and non-matrix substrates. *Cardiovasc. Res.* **69**, 614–624. (doi:10.1016/j.cardiores.2005.08.002)
47. Sáez P, Peña E, Martínez MÁ, Kuhl E. 2013 Mathematical modeling of collagen turnover in biological tissue. *J. Math. Biol.* **67**, 1765–1793. (doi:10.1007/s00285-012-0613-y)
48. Robertson AM, Watton PN. 2013 Mechanobiology of the arterial wall. In *Modeling of transport in biological media* (eds SM Becker, AV Kuznetsov), pp. 275–347. New York, NY: Elsevier.
49. Thyberg J, Blomgren K, Roy J, Tran PK, Hedin U. 1997 Phenotypic modulation of smooth muscle cells after arterial injury is associated with changes in the distribution of laminin and fibronectin. *J. Histochem. Cytochem.* **45**, 837–846. (doi:10.1177/002215549704500608)

50. Tracy RE. 1997 Declining density of intimal smooth muscle cells as a precondition for atheronecrosis in the coronary artery. *Virchows Arch.: Eur. J. Pathol.* **430**, 155–162. (doi:10.1007/BF01008037)
51. Chien S. 2007 Mechanotransduction and endothelial cell homeostasis: the wisdom of the cell. *Am. J. Physiol. Heart Circ. Physiol.* **292**, H1209–H1224. (doi:10.1152/ajpheart.01047.2006)
52. Michiels C. 2003 Endothelial cell functions. *J. Cell. Physiol.* **196**, 430–443. (doi:10.1002/jcp.10333)
53. Marx SO, Totary-Jain H, Marks AR. 2011 Vascular smooth muscle cell proliferation in restenosis. *Circ.: Cardiovasc. Interv.* **4**, 104–111. (doi:10.1161/CIRCINTERVENTIONS.110.957332)
54. Kipshidze N, Dangas G, Tsapenko M, Moses J, Leon MB, Kutryk M, Serruys P. 2004 Role of the endothelium in modulating neointimal formation: vasculoprotective approaches to attenuate restenosis after percutaneous coronary interventions. *J. Am. Coll. Cardiol.* **44**, 733–739. (doi:10.1016/s0735-1097(04)01083-6)
55. Farcas MA, Rouleau L, Fraser R, Leask RL. 2009 The development of 3-D, *in vitro*, endothelial culture models for the study of coronary artery disease. *Biomed. Eng. Online* **8**, 30. (doi:10.1186/1475-925X-8-30)
56. Garikipati K, Arruda E, Grosh K, Narayanan H, Calve S. 2004 A continuum treatment of growth in biological tissue: the coupling of mass transport and mechanics. *J. Mech. Phys. Solids* **52**, 1595–1625. (doi:10.1016/j.jmps.2004.01.004)
57. Martini FH, Nath JL, Bartholomew EF. 2014 *Fundamentals of anatomy and physiology*, 10th edn. Harlow, UK: Pearson.
58. Dodge Jr JT, Brown BG, Bolson EL, Dodge HT. 1992 Lumen diameter of normal human coronary arteries. Influence of age, sex, anatomic variation, and left ventricular hypertrophy or dilation. *Circulation* **86**, 232–246. (doi:10.1161/01.CIR.86.1.232)
59. Byrne RA, Joner M, Kastrati A. 2015 Stent thrombosis and restenosis: what have we learned and where are we going? The Andreas Grüntzig Lecture ESC 2014. *Eur. Heart J.* **36**, 3320–3331. (doi:10.1093/eurheartj/ehv511)
60. Bendeck MP, Zempo N, Clowes AW, Galardy RE, Reidy MA. 1994 Smooth muscle cell migration and matrix metalloproteinase expression after arterial injury in the rat. *Circ. Res.* **75**, 539–545. (doi:10.1161/01.RES.75.3.539)
61. George SJ, Zaltsman AB, Newby AC. 1997 Surgical preparative injury and neointima formation increase MMP-9 expression and MMP-2 activation in human saphenous vein. *Cardiovasc. Res.* **33**, 447–459. (doi:10.1016/S0008-6363(96)00211-8)
62. Ota H, Takase K, Rikimaru H, Tsuboi M, Yamada T, Sato A, Higano S, Ishibashi T, Takahashi S. 2005 Quantitative vascular measurements in arterial occlusive disease. *Radiographics* **25**, 1141–1158. (doi:10.1148/rg.255055014)
63. Nobuyoshi M, Kimura T, Nosaka H, Mioka S, Ueno K, Yokoi H, Hamasaki N, Horiuchi H, Ohishi H. 1988 Restenosis after successful percutaneous transluminal coronary angioplasty: serial angiographic follow-up of 229 patients. *J. Am. Coll. Cardiol.* **12**, 616–623. (doi:10.1016/S0735-1097(88)80046-9)
64. Keller BK, Amatruda CM, Hose DR, Gunn J, Lawford PV, Dubini G, Migliavacca F, Narracott AJ. 2014 Contribution of mechanical and fluid stresses to the magnitude of in-stent restenosis at the level of individual stent struts. *Cardiovasc. Eng. Technol.* **5**, 164–175. (doi:10.1007/s13239-014-0181-y)
65. Sherratt J, Murray J. 1991 Mathematical analysis of a basic model for epidermal wound healing. *J. Math. Biol.* **29**, 389–404. (doi:10.1007/BF00160468)
66. Rossi F, Casalini T, Raffa E, Masi M, Perale G. 2012 Bioresorbable polymer coated drug eluting stent: a model study. *Mol. Pharm.* **9**, 1898–1910. (doi:10.1021/mp200573f)
67. Schwartz RS, Chu A, Edwards WD, Srivatsa SS, Simari RD, Isner JM, Holmes DR. 1996 A proliferation analysis of arterial neointimal hyperplasia: lessons for antiproliferative restenosis therapies. *Int. J. Cardiol.* **53**, 71–80. (doi:10.1016/0167-5273(95)02499-9)
68. Collier IE, Goldberg GI. 2015 Dynamics and mechanism of substrate recognition by matrix metalloproteases. In *Matrix metalloproteinase biology* (eds I Sagi, JP Gaffney), pp. 23–40.
69. Lally C, Prendergast P. 2006 Simulation of in-stent restenosis for the design of cardiovascular stents. In *Mechanics of biological tissue* (eds GA Holzapfel, RW Ogden), pp. 255–267. Berlin, Germany: Springer.

Supplementary Online Material for Mathematical Modelling of the Restenosis Process after Stent Implantation

Javier Escuer[1] · **Miguel A. Martínez**[1,2] · **Sean McGinty**[3] · **Estefanía Peña**[1,2]

This file includes:

- S1. Discussion related to Figures 9 and 10 of the sensitivity analysis
- S2. Supplemental figures related to the sensitivity analysis

S1 Discussion related to Figures 9 and 10 of the sensitivity analysis

A sensitivity analysis of the 28 parameters indicated in Table 3 of the main text was performed in order to evaluate the effect of varying each input parameter involved on the evolution of the restenosis process and to test the robustness of the results of the computational model. This is of particular importance because of the absence of a complete set of experimental data and the variability seen in many of the parameters. However, only those parameters whose variation showed the greatest impact on the results have been included in the main text. The discussion corresponding to those figures is detailed in this section.

Local variations of GFs, MMPs, ECM and SMCs at point A, located close to a central stent strut in the media, are illustrated in Fig. 10 for 8 different cases. The results shown for point B correspond exclusively to the baseline model. The variables of the system damage, d, and local density of endothelial cells, c_{ec}, do not experience large changes with the variation of the parameters, so the results corresponding to these variables have not been included in this work.

The damage degradation rate, $k_{deg,d}$, is an estimated parameter from experimental data directly proportional to the healing rate of the tissue. As can be seen in Fig. 9 of the main text, for high values of $k_{deg,d}$, the level of damage in the arterial wall decreases more rapidly and consequently the healing process is accelerated. The reference value for this parameter has been calibrated according to experimental data that shows that the damage caused by the device implantation is restored after approximately 300 days. The

---

[1] Applied Mechanics and Bioengineering Group (AMB), Aragón Institute of Engineering Research (I3A), University of Zaragoza, Zaragoza, Spain.
[2] Biomedical Research Networking Center in Bioengineering, Biomaterials and Nanomedicine (CIBER-BBN), Spain.
[3] Division of Biomedical Engineering, University of Glasgow, Glasgow, UK.

impact of this parameter on the evolution of the biological species is studied in Case 01. When $k_{deg,d}$ is decreased, we observe an increase in the local maximum concentrations of GFs, MMPs and of the local densities of SMC and a slowing down of the temporal response of these species, representing a longer time to reach their maximum and the final equilibrium. However, reduced equilibrium concentrations are shown for the ECM components when $k_{deg,d}$ decreases. It is important to highlight that when the healing process is faster ($k_{deg,d}$ higher), the concentration levels of ECM components in the tissue are also higher, and this ultimately leads to an increased tissue growth.

When $k_{prod,gf}$ is varied, Case 02, a general rise in the local concentrations and densities of all the species is observed when the value of this parameter is increased. Furthermore, we observe a reduction in the initial degradation of the ECM and in the differentiation of the contractile SMCs into the synthetic phenotype with increasing values of this parameter. Therefore, the increase observed in the local density of synthetic SMCs with $k_{prod,gf}$ is mainly due to their proliferation by the action of GFs. Similar behaviour of the system is observed when the impact of the synthetic SMCs proliferation rate by the GFs, $k_{prolif,ssmc}$ (Case 11) is analysed. A very similar response can also be obtained by varying the initial concentration of MMP, $c_{mmp,0}$, in Case 19. It should be noted that in this case the normalized local concentrations and densities, $c_j/c_{j,0}$, were represented in order to establish comparisons with the other cases simulated.

On the one hand, when the MMP production rate by the contractile SMCs, $k_{prod1,mmp}$, is modified in Case 05, an increase in the local concentration of MMPs and in the local density of synthetic SMC is observed at point A when the parameter value rises. Moreover, the instant in which the peaks appear in their time-varying profiles is independent of the value for these species. On the other hand, the local concentration of GFs, ECM and the local density of contractile SMC at point A is reduced if the value of $k_{prod1,mmp}$ increases. Furthermore, an increase in the initial degradation of the ECM and in the differentiation of the contractile SMC into the synthetic phenotype, can be noted when the value of this parameter increases, resulting in lower restenotic growth at the end of the simulation. Similar responses are observed when the ECM degradation rate, $k_{deg,ecm}$ (Case 08) is varied.

In Case 10, small changes are observed in the temporal response of GFs and MMPs when varying the differentiation rate from synthetic to contractile SMCs, $k_{diff,ssmc}$, is analysed. However, for the rest of the species considered, the changes are notable. In general, local concentrations and densities of ECM and SMCs increase when the value of this parameter decreases. However, the variation of $k_{diff,ssmc}$ does not affect the level of the initial degradation of the ECM or the amount of contractile SMCs differentiated into synthetic phenotype. In case of synthetic SMCs, when $k_{diff,ssmc}$ increases a slower response is observed in the time-varying local density profiles, meaning that they take longer to revert to the contractile phenotype.

In general, the variation of the diffusion coefficients does not generate relevant changes in the time-varying profiles for most of the species. In Case 15, as a representative example of the effect of varying the diffusivity, the influence of the variation of the MMP diffusion coefficient, D_{mmp}, is shown. It can be noted that D_{mmp} has virtually no effect on GFs and synthetic SMCs and only slightly affects the local concentrations of MMPs and ECM components. However, a decrease in the density of contractile SMCs at point A is observed when the MMP diffusivity decreases.

We note the appearance of possible numerical instabilities when observing the time-varying concentration profiles of ECM, which is the substance most sensitive to changes in many of the parameters. This is primarily due to numerical issues caused by the reduction of the shape function order used in the discretization of the FE mesh only in the sensitivity analysis, in order to achieve faster computational times. However, these issues do not affect the global behaviour of the system and the general conclusions of this section.

S2 Suplemental figures related to the sensitivity analysis

Here, the results for the rest of the cases simulated are shown.

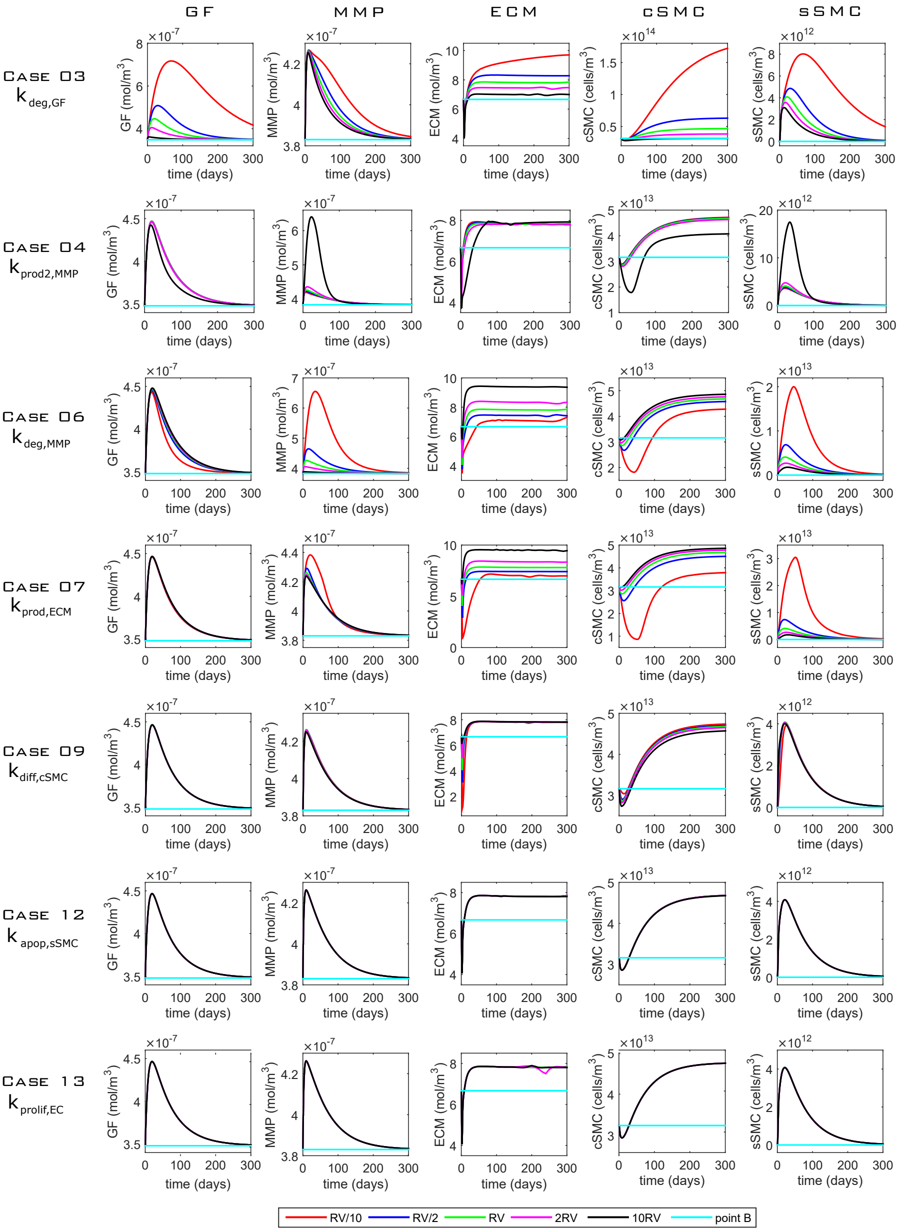

Fig. S1: Supplemental results from the sensitivity analysis related to the rates. The plots show the effect of varying several rates on the concentration of GFs, MMPs and ECM as well as the density of contractile and synthetic SMCs. Computations were carried out for four different values for each parameter apart from the reference value, RV, which is shown in Table 3 of the main text. The values of 2RV and RV/2 were considered ± half the RV of the selected parameter; 10RV and RV/10 were given by increasing and decreasing by one order of magnitude the RV (see Table 4 of the main text). The results shown for point B correspond exclusively to the RV (baseline model).

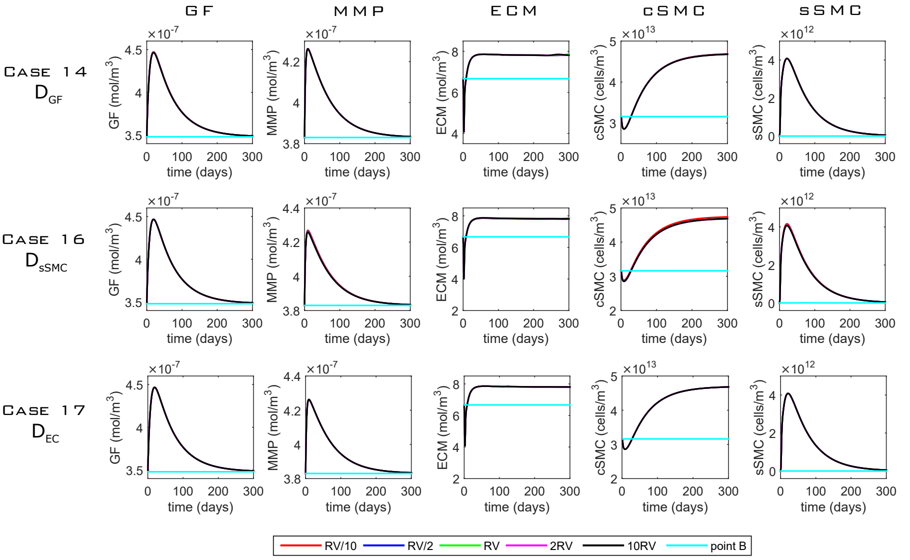

Fig. S2: Supplemental results from the sensitivity analysis related to the diffusion coefficients. The plots show the effect of varying several diffusivities on the concentration of GFs, MMPs and ECM as well as the density of contractile and synthetic SMCs. Computations were carried out for four different values for each parameter apart from the reference value, RV, which is shown in Table 3 of the main text. The values of 2RV and RV/2 were considered ± half the RV of the selected parameter; 10RV and RV/10 were given by increasing and decreasing by one order of magnitude the RV (see Table 4 of the main text). The results shown for point B correspond exclusively to the RV (baseline model).

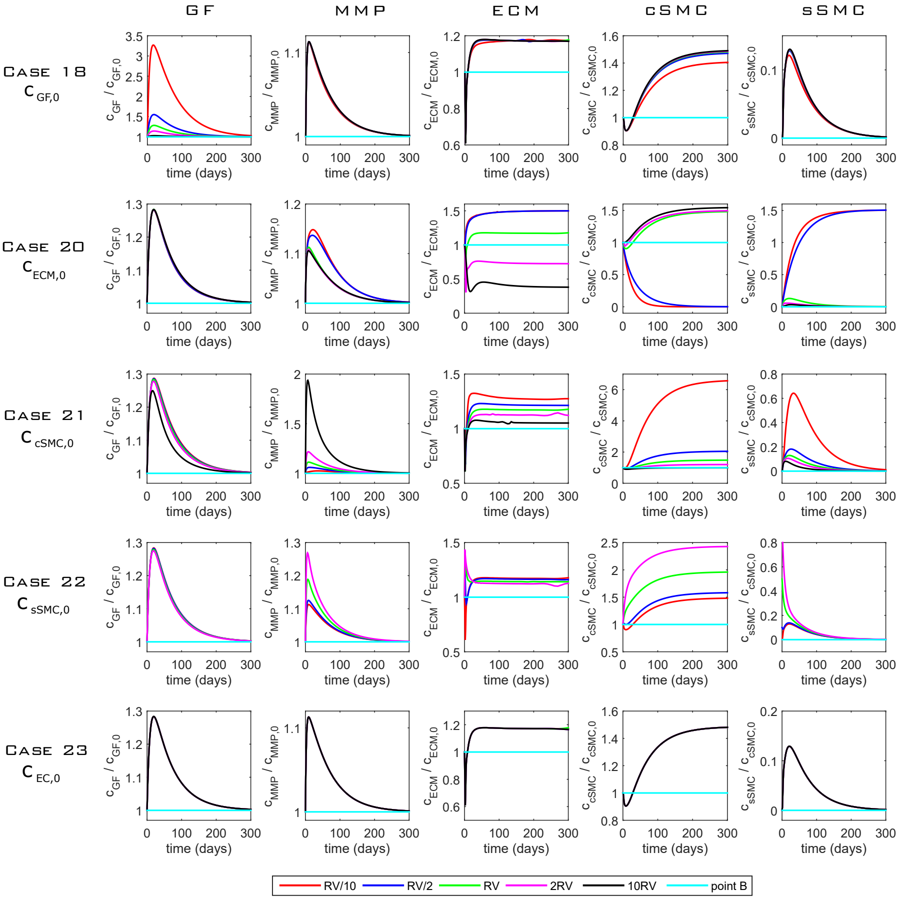

Fig. S3: Supplemental results from the sensitivity analysis related to the initial concentrations. The plots show the effect of varying several initial conentrations on the concentration of GFs, MMPs and ECM as well as the density of contractile and synthetic SMCs. Computations were carried out for four different values for each parameter apart from the reference value, RV, which is shown in Table 3 of the main text. The values of 2RV and RV/2 were considered ± half the RV of the selected parameter; 10RV and RV/10 were given by increasing and decreasing by one order of magnitude the RV (see Table 4 of the main text). The results shown for point B correspond exclusively to the RV (baseline model).

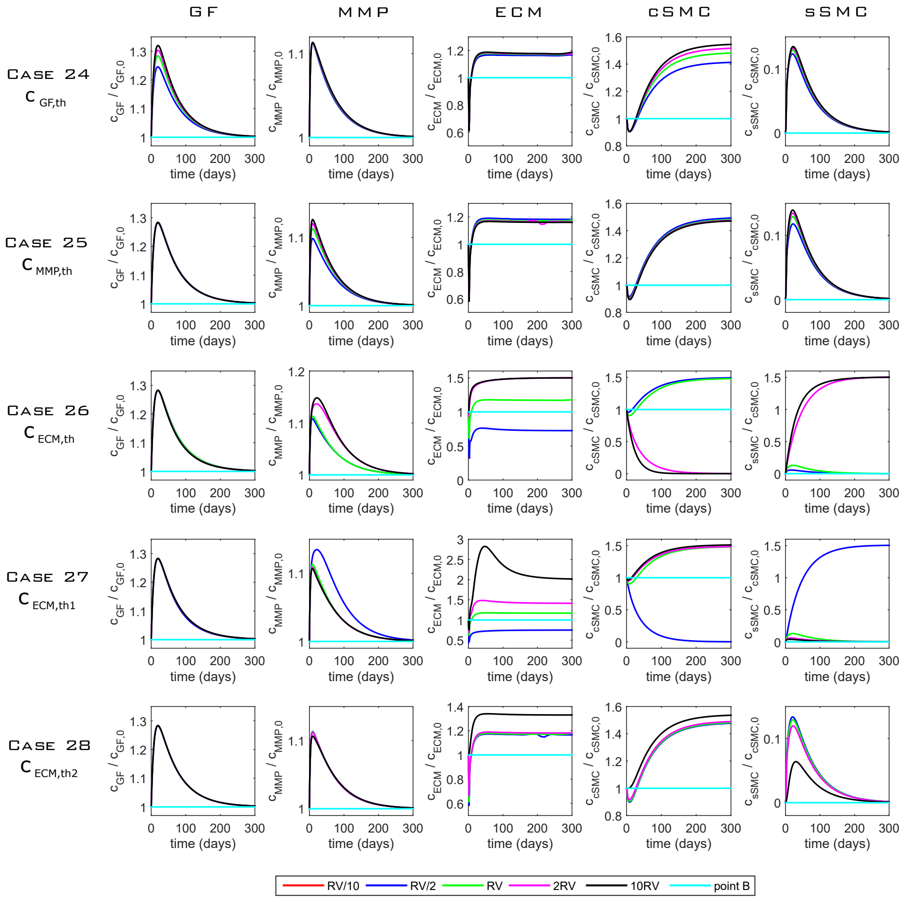

Fig. S4: Supplemental results from the sensitivity analysis related to the threshold values. The plots show the effect of varying the threshold values on the concentration of GFs, MMPs and ECM as well as the density of contractile and synthetic SMCs. Computations were carried out for four different values for each parameter apart from the reference value, RV, which is shown in Table 3 of the main text. The values of 2RV and RV/2 were considered ± half the RV of the selected parameter; 10RV and RV/10 were given by increasing and decreasing by one order of magnitude the RV (see Table 4 of the main text). The results shown for point B correspond exclusively to the RV (baseline model).

CHAPTER 4

Discussion

As this Thesis is presented as a compendium of publications, each work contains a thorough discussion and comparison with the existing literature. Therefore, this chapter summarizes the main achievements, conclusions and the future questions that arise from this work. Contributions to national and international conferences, research stays and different collaborations derived from the work developed in this Thesis are also included in this chapter.

Contents

4.1 Original contributions

The main original contributions of this thesis are listed below:

Work 1: How does stent expansion alter drug transport properties of the arterial wall?

- A comprehensive *in silico* model to analyse the effect of stent mechanical expansion on the drug transport properties of a multilayer arterial wall, described as an anisotropic, hyperelastic material, was developed. We established relationships between mechanical force generated through device expansion and alteration in diffusion within the arterial wall and performed simulations to elucidate the impact of such alterations in spatio-temporal drug release and tissue uptake.
- The impact of local drug concentrations in tissue, which are linked to the biological effect of the substance, was analysed in order to assess whether drug concentrations locally are at therapeutic (and not toxic) levels. This analysis is also relevant for the design of effective drug delivery modalities.
- This research allows to establish a methodology to link computational models focused on drug transport from endovascular devices and computational models focused on studying the mechanical expansion and interaction between the device and vessel. Therefore, it allows to include the effect of tissue deformation and stress caused by stent expansion in drug transport models.

Work 2: Influence of vessel curvature and plaque composition on drug transport in the arterial wall following drug-eluting stent implantation

- An exhaustive computational model was developed to analyse the impact of the variability of the coronary artery geometry on drug transport in the blood flow and in the arterial tissue through a series of simulations to elucidate the effect of arterial curvature on spatio-temporal drug uptake within tissue.
- The influence of the atherosclerotic plaque heterogeneity on the overall drug distribution was also investigated.

Work 3: Endovascular drug delivery: balloons versus stents

- A comprehensive model of DCB delivery, transport and retention to date was developed. The model consider a 2D-axisymmetric geometry and incorporates two nonlinear phases of binding (specific and non-specific) and the influence of advection within a multilayer arterial wall.

- This framework was used to:
  - Simulate drug delivery from different types of balloon platform.
  - Explore the influence of DCB application time.
  - Elucidate the importance on release kinetics of elevated pressure during DCB application.
  - Compare DCB delivery of two different drugs (sirolimus and paclitaxel).
  - Compare simulations of DESs vs DCBs to explore if there are any potential benefits, in terms of safety and efficacy, of treating small de novo lesions with a DCB vs a DES.

Work 4: Mathematical modelling of the restenosis process after stent implantation

- A mathematical and computational model which successfully captures the key characteristics of the restenosis process after stent implantation in a coronary artery was developed. The key novelty of this model is that a continuum approach is taken into account to describe the cascade of events following damage to the arterial wall due to stenting procedure, and is therefore formulated in terms of densities/concentrations of a number of important species. This is advantageous because it allows us to assess how the evolution of the various species affects the overall healing process, and more importantly, how variations in the associated parameters and initial conditions influence the process.

- Unlike any of the existing continuum models, we are able to simulate the time-course response of six different biological species (growth factors, matrix-degrading metalloproteinases, extracellular matrix, both contractile and synthetic smooth muscle cell and endothelial cells) involved in ISR after the initial mechanical damage, while at the same time simulating tissue growth.

- A sensitivity analysis of all parameters involved in the ISR model was performed in order to evaluate the effect of varying each input parameter involved on the evolution of the restenosis process and to test the robustness of the results of the computational model. This is of particular importance because of the absence of a complete set of experimental data and the variability observed in the literature in many of the parameters.

- This restenosis model was used to assess the impact of geometric configurations on the final outcome through consideration of a series of commercial stents as well as different inter-strut distances and levels of strut embedment, thereby enabling us to relate our findings to stent design.

4.2 Conclusions

The main conclusions drawn from this Thesis, based on the computational studies performed, are presented in this section.

Work 1: How does stent expansion alter drug transport properties of the arterial wall?

- Our findings demonstrated that mechanical expansion can have an influence on the effective diffusion coefficients of drugs in arterial tissue, with the overall influence on drug transport through the arterial wall dependent on the radial Peclet number that is derived from these diffusion coefficients.
- The effect of stent expansion on drug transport in the arterial tissue is dependent not only on the specific layer in question (intima, media or adventitia), but also on the particular drug (sirolimus vs paclitaxel). Generally speaking, the effect of mechanical expansion is more prominent in the case of paclitaxel, particularly so in the adventitia layer of the arterial wall.
- Current computational models of drug transport eluted from DES typically make use of drug diffusion coefficients that have been derived from static tissue experiments (i.e. not subjected to mechanical expansion). Therefore, these models are likely to be under- or over-estimating drug transport and retention in arterial tissue.
- Our findings may also be of importance to other forms of localised arterial drug delivery, such as through DCBs. The key difference with DCBs would appear to be a time-varying dependence on drug transport parameters, coinciding with inflation and deflation of the balloon.

Work 2: Influence of vessel curvature and plaque composition on drug transport in the arterial wall following drug-eluting stent implantation

- Arterial curvature leads to the asymmetric distribution of drug in the arterial wall, with the level of asymmetry highly dependent on the level of curvature. Specifically, with increasing curvature, more of the drug ‘partitions’ into the inner wall. This asymmetric distribution, as a result of fluid forces, is likely to be exacerbated in more realistic patient-specific geometries. The implication of this finding for stent manufacturers is that care should be taken when considering the drug loading on the stent, since this asymmetric drug distribution could, in theory at least, result in insufficient drug concentrations reaching the outer wall, while the concentrations reaching the inner wall could be too high. The consequence for the patient could well be asymmetric neointimal growth as part of the healing process.

- Lipidic atherosclerotic plaques give rise to higher drug concentrations than fibrotic plaques, while calcified plaques are impenetrable to drug. The impenetrability of calcified plaque has potentially important implications and, if large enough in extent, may act as a significant barrier to drug reaching the arterial tissue where proliferating and migrating cells reside.
- The presence of plaque in the arterial wall, regardless of the composition of the core, can slightly delay receptor saturation in the tissue, a quantity that has widely been associated with efficacy [Tzafriri et al., 2012; McKittrick et al., 2019].
- Plaque can act as a source of drug (i.e. as a reservoir of drug) ensuring that decline in receptor saturation is significantly reduced compared with the healthy wall case. The implication is that in diseased states, binding sites may well be saturated for longer, i.e. patients receive an effective drug dose for longer.
- Arterial curvature and atherosclerotic plaque composition have important influences on the spatio-temporal distribution of drug in tissue, with potential implications in terms of effectiveness of the treatment. Stent manufacturers are advised to consider that a ‘one-size-fits-all’ stent drug dose may not be adequate for all patients, and could, at least in part, be contributing to differences in outcome from patient to patient that are observed clinically. Since the majority of the existing computational models tend to neglect these features, they are also likely to be under- or over-estimating drug uptake and redistribution in arterial tissue.

Work 3: Endovascular drug delivery: balloons versus stents

- Our results highlighted that it is imperative to incorporate within the DCB simulations the elevated pressure in the lumen during balloon application. This leads to deeper delivery of drug, higher drug retention and increased levels of specific binding site saturation, when compared with simulations that utilise a fixed lumen pressure for all time.
- The drug content (DC) values obtained in this study are broadly in line with the existing literature [McKittrick et al., 2019; Tzafriri et al., 2012; Grube and Buellesfeld, 2006; Gongora et al., 2015; Radke et al., 2011], providing confidence in the simulations.
- Assuming the same drug dose and release kinetics in a DCB, sirolimus is retained within the tissue for longer than paclitaxel, at least for the parameter values simulated which are based on data from the literature.

- Regarding the direct comparison between DCBs and DESs, if saturating more specific binding sites earlier is most important, then each DCB considered offers an advantage over the realistic sirolimus DES simulated. However, if maintaining high levels of %SBSS towards and beyond 30 days is desired, then the realistic sirolimus DES would be preferred.
- By simulating an artificial fast sirolimus DES, we have demonstrated that if the safety and efficacy markers of the sirolimus DCBs simulated are acceptable, but a permanent structure is preferred, then it may be possible to design a new class of fast-release DES whose release kinetics are matched to those of a DCB.
- There may exist a DCB configuration, in terms of drug loading and release rate, that gives rise to sufficiently similar safety and efficacy results as current commercial DESs existing in the market such as the stent platform considered here.

Work 4: Mathematical modelling of the restenosis process after stent implantation

- The restenosis model developed in this Thesis was able to capture some of the underlying mechanisms and patterns of ISR.
- The sensitivity analysis carried out for the different model parameters provide information on the stability of the model and an understanding of how changes in one parameter will affect the behaviour of the whole system. The value of the damage degradation constant had a significant impact on the healing rate. Moreover, results shown that the rates of production, degradation, differentiation and proliferation taken into account highly affect the local levels of concentration/density of the species involved in the process and the temporal response of the system. The apoptosis rate of synthetic SMCs, diffusion coefficients and initial conditions also influenced the evolution of the model, although to a lesser extent.
- The results of the simulations have shown that % restenosis increases with increasing strut size; decreases with an increase in inter-strut spacing; increases with an increase in lumen expansion diameter; and depends on the strut embedment configuration.
- The comparison of the results to restenosis experimental data (at the tissue level) from the literature has shown that the developed model is in broad agreement with clinical hypotheses relating to ISR occurrence.
- This model gave important insights into the dynamics of ISR and can be considered as a step forward to a better understanding of this complex biological process. A further coupling between the ISR model and the drug transport models

could be an important step forward in the design of personalised endovascular devices much more efficient and safe.

4.3 Future lines

Considering the works developed in this Thesis and taking into account its conclusions and limitations, different lines of action for future works are proposed in this section.

- To study the influence of deformation in other key parameters involved in drug transport (e.g. porosity and permeability). Possibly further experimental studies may be needed to analyse the dependence of these parameters.
- Coupling between solid mechanics and drug transport models in 3D, extending the 2D approach developed in this Thesis to idealised three-dimensional vessel geometries, where the complex realistic stent geometry can be considered. To analyse the effect of the mechanical expansion of different stent designs on drug transport and retention in the arterial tissue (Fig. 4.1).
- Concerning the geometries of the finite element models developed in this Thesis, 2D and 2D-axisymmetric geometries corresponding to idealized representations of straight segments of coronary arteries have been considered. This could be improved using more realistic geometries of arteries such as bifurcations or directly 3D patient-specific geometries obtained from medical images. A more sophisticated model of plaque could be also devised to take into account its complicated structure.
- In terms of modelling drug transport within the stent coating, in line with the vast majority of models in the literature, a simple diffusion model was considered in this work. However, depending on the particular stent, drug and coating under consideration, more complex nonlinear models that accounts for the combined effects of diffusion, dissolution and solubility in the polymer coating may be required in order to describe drug release from the stent.
- Future work should explore the use of an optimisation framework to attempt to infer DCB drug, dose and release rate, as well as procedural aspects such as balloon inflation pressure and application time, that give rise to total drug content values that fall within the therapeutic window, while maximising the percentage of the specific binding sites saturated for the period of arterial healing.
- Development of a more complex ISR model including other biological agents (e.g. platelets, monocytes, different classes of growth factors (PDGF, EGF, IGF, TGF, FGF), mesenchymal cells, fibroblasts, collagen subtypes, proteoglycans,

fibronectin, etc.) and other processes (e.g. activation and migration of the mesenchymal stem cells, release of GFs by fibroblasts or ECM synthesis by ECs, etc.) involved in the restenosis process. The increasing of the complexity of the growth model could allow us to provide more precise information about the restenosis process. However, more data is needed to make the model more accurate.

- The modelling of the initial mechanical damage in the tissue after stenting considered in this Thesis is based on the ultimate tensile stress–stretch response for each layer of the wall observed in human coronary arteries [Holzapfel et al., 2005a]. A more complex modelling of this initial stimulus needed to start the ISR process is proposed as a new line of future work.
- To our knowledge, there is no experimental data published in the literature which directly relate the levels of stress–strain due to device deployment to the arterial wall injury and the cascade of events associated. Moreover, it should be taken into account the difficulty of founding experimental parameters and constant values to feed the mechanobiological model of ISR. Therefore, the development of own experimental tests in order to obtain these data is also proposed.
- In general, future efforts must be focused on the calibration and validation of the computational models with experimental/patient-specific cases.

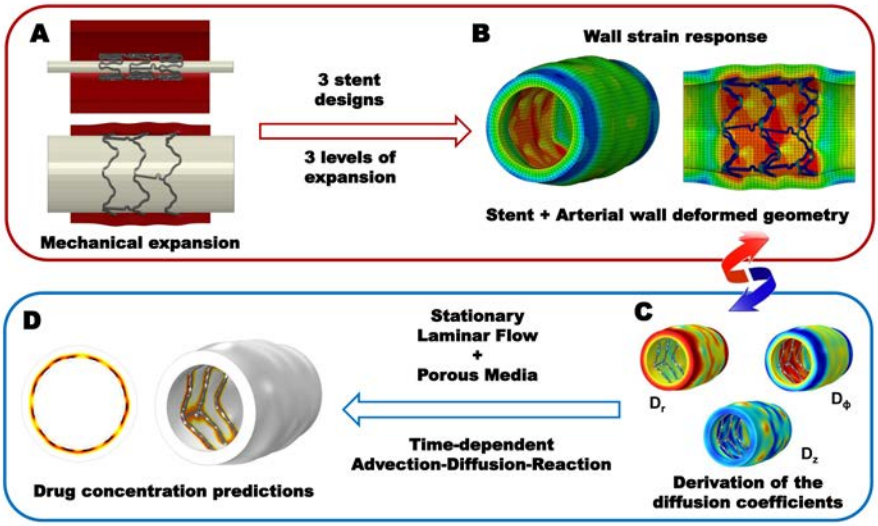

Figure 4.1. *On-going work. Coupling solid mechanics and drug transport in 3D.*

4.4 Conferences

With the view to expanding the work developed on this Thesis and encouraging the transmission of the knowledge acquired, the following communications have been presented during the project duration:

1. **Escuer J.**, Peña E., Pina E., Martínez M.A. Analysis of the influence of plaque composition and geometry on drug transport from drug eluting stents. Submitted to *27th Congress of the European Society of Biomechanics (ESB2022).* Porto (Portugal), June 2022.
2. McQueen A., **Escuer J.**, Fensterseifer Schmidt A., Aggarwal A., Kennedy S., McCormick C., Olroyd K., McGinty S. *In silico* modelling of in-stent restenosis subject to spatiotemporal delivery of drug. Submitted to *7th International Conference on Computational and Mathematical Biomedical Engineering (CMBE22).* Milano (Italy), June 2022.
3. Fensterseifer Schmidt A., **Escuer J.**, McGinty S. *In silico* modelling of endovascular drug delivery. *Mathematical modelling and control for healthcare and biomedical systems (MCHBS2021 Virtual Workshop).* Roma (Italy), September 2021.
4. McQueen A., **Escuer J.**, Aggarwal A., Kennedy S., McCormick C., Olroyd K., McGinty S. Preliminary approaches to understand how anti-proliferative drug modulate in-stent restenosis. *Mathematical modelling and control for healthcare and biomedical systems (MCHBS2021 Virtual Workshop).* Roma (Italy), September 2021.
5. **Escuer J.**, Peña E., Martínez M.A., McGinty S. Endovascular drug delivery: stents versus balloons. *26th Congress of the European Society of Biomechanics (ESB2021).* Milano (Italy), July 2021.
6. **Escuer J.**, Aznar I., McCormick C., Peña E., McGinty S, Martínez M.A.. How does vessel curvature and plaque composition affect the distribution in tissue of drug eluted from stents? *26th Congress of the European Society of Biomechanics (ESB2021).* Milano (Italy), July 2021.
7. **Escuer J.**, McGinty S., Peña E., Martínez M.A., Conway C. Coupling solid mechanics & drug transport in 3D for drug-eluting stent analysis. *25th Congress of the European Society of Biomechanics (ESB2019).* Vienna (Austria), July 2019.
8. **Escuer J.**, Martínez M.A., McGinty S., Peña E. A computational mechanobiological model to simulate the in-stent restenosis process. *25th Congress of the European Society of Biomechanics (ESB2019).* Vienna (Austria), July 2019.

9. **Escuer J.**, Peña E., McGinty S., Martínez M.A. How does mechanical expansion of endovascular devices alter drug transport properties of the arterial wall? *VI Jornada de Doctorandos del Programa de Doctorado en Ingeniería mecánica (PDIM).* Zaragoza (Spain), June 2019.

10. **Escuer J.**, Aznar I., Peña E., Martínez M.A. How does vessel curvature influence drug release from DES and drug transport in arterial tissue? *VIII Jornada Jóvenes Investigadores Instituto de Investigación en Ingeniería de Aragón* (Aragón Institute for Engineering Research, I3A). Zaragoza (Spain), June 2019.

11. Martínez M.A, **Escuer J.**, McGinty S., Peña E. A continuum-approach model to numerically simulate the in-stent restenosis process. *First Colloquium of the Spanish Theoretical and Applied Mechanics Society (STAMS2019).* Madrid (Spain), March 2019.

12. **Escuer J.**, Peña E., Martínez M.A, McGinty S. Elucidating the importance of drug-dissolution and specific binding in a 2D model of arterial drug-eluting stent (DES). *Virtual Physiological Human Conference (VPH2018).* Zaragoza (Spain), September 2018.

13. **Escuer J.**, Peña E., Martínez M.A, McGinty S. Effect of drug dissolution and specific-binding on DES modeling. A computational study. *Modelling & Experiments in Drug Delivery Systems (MEDDS).* Glasgow (UK), September 2018.

14. **Escuer J.**, Cebollero M., Peña E., McGinty S., Martínez M.A. Numerical Modelling of the Combined Effect of Mechanical Deployment and Drug Delivery in Endovascular Devices. *13th World Congress in Computational Mechanics (WCCM2018).* New York (USA), July 2018.

15. **Escuer J.**, Cebollero M., Peña E., McGinty S., Martínez M.A. Computational modelling of the effect of mechanical expansion on drug delivery from endovascular devices. *18th World Congress of Biomechanics (WCB2018).* Dublin (Ireland), July 2018.

16. **Escuer J.**, Aznar I., Peña E., Martínez M.A. Influence of curvature of the vessel on the drug transport phenomenon from DES devices. *18th World Congress of Biomechanics (WCB2018).* Dublin (Ireland), July 2018.

17. **Escuer J.**, Scullion B., McCormick C., Martínez M.A, McGinty S. On the influence of non-uniform binding site density in determining arterial drug distribution following stent−based delivery. *18th World Congress of Biomechanics (WCB2018).* Dublin (Ireland), July 2018.

18. **Escuer J.**, Peña E., McGinty S., Martínez M.A. Computational analysis of the influence of dissolution-diffusion and specific binding on drug transport in

the arterial wall following stent-based delivery. *VII Jornada Jóvenes Investigadores Instituto de Investigación en Ingeniería de Aragón* (Aragón Institute for Engineering Research, I3A). Zaragoza (Spain), June 2018.

19. **Escuer J.**, Peña E., Martínez M.A. Numerical modeling of drug transport in arterial wall from drug delivery intravascular devices. *23rd Congress of the European Society of Biomechanics (ESB2017).* Seville (Spain), July 2017.

20. **Escuer J.**, Martínez M.A, Peña E. Mechanobiological model of the restenosis process after stent implantation. *23rd Congress of the European Society of Biomechanics (ESB2017).* Seville (Spain), July 2017.

21. **Escuer J.**, Martínez M.A, Peña E. Mathematical and numerical modeling of restenosis after DES implantation. *VI Jornada Jóvenes Investigadores Instituto de Investigación en Ingeniería de Aragón* (Aragón Institute for Engineering Research, I3A). Zaragoza (Spain), June 2017.

22. **Escuer J.**, Peña E., Martínez M.A. Numerical modeling of drug transport in healthy and pathological arterial wall. *12th World Congress on Computational Biomechanics (WCCM16).* Seoul (Republic of Korea), July 2016.

23. **Escuer J.**, Peña E., Martínez M.A. Drug transport in arteries in healthy and pathological conditions. Numerical modeling and experimental validation. *22nd Congress of the European Society of Biomechanics (ESB2016).* Lyon (France), July 2016.

24. **Escuer J.**, Peña E., Martínez M.A. Computational modeling of drug transport from drug-eluting stents in arterial wall. *7th Summer School on Biomechanics of Soft Tissues: Multiscale Modeling, Simulation and Applications.* Graz (Austria), July 2016.

25. **Escuer J.**, Peña E., Martínez M.A. Numerical simulation of drug transport in arterial wall under healthy and atherosclerotic conditions. *19th European Conference on Mathematics for Industry (ECMI2016).* Santiago de Compostela (Spain), June 2016.

26. **Escuer J.**, Peña E., Martínez M.A. Modelo multicapa para el estudio de difusión de fármacos en arterias a través de dispositivos intravasculares. *V Jornada Jóvenes Investigadores Instituto de Investigación en Ingeniería de Aragón* (Aragón Institute for Engineering Research, I3A). Zaragoza (Spain), May 2016.

27. **Escuer J.**, Peña E., Martínez M.A. Modelo numérico de transporte convectivo-difusivo del paclitaxel en la pared arterial y validación experimental. *V Reunión del Capítulo Nacional Español de la Sociedad Europea de Biomecánica* (European Society of Biomechanics, ESB). Madrid (Spain), November 2015.

28. **Escuer J.**, Peña E., Martínez M.A. Estudio computacional y validación experimental de la difusión del paclitaxel en arterias. *XXXIII Congreso Anual de la Sociedad Española de Ingeniería Biomédica (CASEIB2015).* Madrid (Spain), November 2015.

4.5 Stays in Research Institutions

Two research stays have been done during the development of this Thesis:

1. University of Glasgow (Glasgow, Scotland, United Kingdom), under the supervision of Dr. Sean McGinty. [September-December, 2017]
2. National University of Ireland Galway (Galway, Ireland), under the supervision of Dr. Claire Conway. [September-December, 2018]

4.6 Other works related to this Thesis

4.6.1 Publications in journals

Firstly, works in which the PhD candidate has participated as co-author, and have already been published, have been included in this subsection:

- McQueen A., Escuer J., Aggarwal A., Kennedy S., McCormick C., Oldroyd K., McGinty S. (2021). Do we really understand how drug eluted from stents modulates arterial healing? *International Journal of Pharmaceutics*, 601:120575. https://doi.org/10.1016/j.ijpharm.2021.120575.
  JIF (2020): 5.875 (Q1: 37/276 Pharmacology & Pharmacy).

There are also some articles in preparation to be submitted soon to different scientific journals:

- Escuer J., Pina E., Martínez M.A, Peña E. How does the geometry and plaque composition influence tissue uptake and retention of drug eluted from stents? *In preparation.*
- Escuer J., McGinty S., Peña E., Martínez M.A., Conway C. Coupling solid mechanics & drug transport in 3D for drug-eluting stent analysis. *In preparation.*
- McQueen A., Escuer J., Fensterseifer-Schmidt A., Aggarwal A., Kennedy S., McCormick C., Oldroyd K., McGinty S. Mathematical modelling of restenosis subject to the spatiotemporal delivery of drug. *In preparation.*

4.6.2 Final Master's Projects

The following Final Master's Projects, directly related with the scope of this Thesis, have been supervised during this period:

- Estudio de la difusión de fármacos desde dispositivos intravasculares en una geometría paciente-específica. Author: Mario Lamas Rodríguez. Supervisors: Miguel Ángel Martínez Barca and Javier Escuer Gracia. University of Zaragoza. December 2018.
- Infuencia de la curvatura arterial en la eficiencia de dispositivos intravasculares de liberación de fármacos. Author: Irene Aznar Lou. Supervisors: Miguel Ángel Martínez Barca and Javier Escuer Gracia. University of Zaragoza. December 2017.
- Modelo computacional acoplado de la expansión mecánica de dispositivos intravasculares y liberación de fármaco asociada. Author: Martina Cebollero Burgués. Supervisors: Miguel Ángel Martínez Barca and Javier Escuer Gracia. University of Zaragoza. September 2017.

4.6.3 Final Degree's Projects

The following Final Degree's Project, also directly related with the scope of this Thesis, has been supervised during this period:

- Influencia de la geometría y composición de la placa de ateroma en el transporte de fármacos en la pared arterial liberados desde un stent coronario. Author: Estela Pina Clos. Supervisors: Estefanía Peña Baquedano and Javier Escuer Gracia. University of Zaragoza. September 2020.

4.7 Funding

Financial support for this research was provided by the Spanish Ministry of Economy and Competitiveness through research projects DPI2013-44391-P and DPI2016-76630-C2-1-R; the Department of Industry and Innovation of the Government of Aragón through the research grant T24-17R (Fondo Social Europeo) and research project LM-P121-18 and; the Instituto de Salud Carlos III (Carlos III Health Institute, ISCIII) through the CIBER-BBN initiative. Concurrently, the author gratefully acknowledges research support from the Spanish Ministry of Economy and Competitiveness for the specific financial support through the individual grant BES-2014-069737 and the mobility fellowships EEBB-I-17-12605 and EEBB-I-18-13000, which provided the opportunity to conduct two research stays.

APPENDIX

A

Resumen y conclusiones en español

Este Apéndice contiene un extenso resumen en castellano que incluye las contribuciones originales, las principales conclusiones y las líneas de desarrollo futuro derivadas de la realización de esta Tesis, cumpliendo con el Artículo 3.2 del Acuerdo de 25 de junio de 2020, del Consejo de Gobierno de la Universidad, por el que se aprueba el Reglamento sobre Tesis Doctorales de la Universidad de Zaragoza-

A.1 Motivación

Las enfermedades cardiovasculares (ECVs) siguen siendo la principal causa de mortalidad en el mundo [Tsao et al., 2022; Timmis et al., 2022]. En Europa, aproximadamente 4,1 millones de muertes (aproximadamente 2,2 millones de muertes en mujeres y 1,9 millones de muertes en hombres) fueron atribuidas a las ECVs, en el año más reciente de datos disponibles (2019), siendo las enfermedades coronarias, 38% de todas las muertes debidas a ECVs en mujeres y 44% en hombres, y los accidentes cerebrovasculares (ACVs), 26% de todas las muertes debidas a ECVs en mujeres y 21% en hombres, los principales responsables [Timmis et al., 2022]. En 2015, la Red Europea del Corazón estimó que las ECVs costaron a la economía de la Unión Europea (UE) unos 210.000 millones de euros. Esta estimación del coste económico de las ECVs a la sociedad sigue siendo la más reciente que existe en los países de la UE. En el caso particular de España, en 2020 se produjeron 493.776 muertes, 75.073 más que en 2019 (un 17,9% más) debido principalmente a la pandemia de COVID-19. Las ECVs se mantuvieron un año más como primera causa de muerte con un 24.3% del total de fallecidos, seguido de los tumores (22.8%). Las enfermedades infecciosas, que incluyen los casos de COVID-19 identificados y sospechosos, fueron la tercera causa de muerte en nuestro país (16.4%).

La aterosclerosis es la principal causa de cardiopatía isquémica y está caracterizada por la anormal acumulación de colesterol y otro lípidos, macrófagos, tejido conectivo, calcio y otras sustancias en el interior de los vasos sanguíneos, provocando un estrechamiento progresivo de la luz del vaso (estenosis) que conduce a una reduucción parcial o total del flujo sanguíneo que circula a través de las arterias coronarias hacia el corazón. Además, la posible rotura de una de estas placsa ateroscleróticas puede dar lugar a la formación de coágulos (trombos) que, dirigidos hacia órganos diana como el corazón o el cerebro, pueden provocar infartos de miocardio, accidentes cerebrovasculares o incluso la muerte [Libby et al., 2002].

Las principales alternativas terapéuticas que existen hoy en día para tratar estas lesiones ateroscleróticas son el tratamiento farmacológico y el control estricto de los factores de riesgo, la cirugía convencional (invasiva) y las técnicas intravasculares (angioplastia con balón con o sin stent), en las que un dispositivo protésico se introduce en la arteria mediante un catéter sin la necesidad de realizar una intervención convencional. La angioplastia coronaria transluminal percutánea (ACTP) o intervención coronaria percutánea (ICP), se realizaba inicialmente sin la inserción de un stent [Dotter and Judkins, 1964; Grüntzig, 1978]. En una angioplastia con balón, el dispositivo se lleva al lugar donde se encuentra estrechamiento del vaso a través de un catéter insertado en la arteria. El balón se infla a alta presión durante unos segundos comprimiendo la placa aterosclerótica y expandiendo el vaso, restaurando el tamaño del lumen arterial y, por tanto, mejorando el flujo sanguíneo (revascularización). Después, el dispositivo se recupera de nuevo mediante un cateterismo. Sin embargo, su éxito se ha visto obstaculizado por las limitaciones inherentes al cierre agudo del vaso y al retroceso elástico a corto plazo, y a la remodelación vascular negativa (retroceso tardío) y la proliferación neointimal a largo plazo [Bauters and Isner, 1997].

Por lo tanto, los stents coronarios se desarrollaron para superar estas limitaciones, mediante el andamiaje de la arteria dilatada por el balón y la prevención del retroceso tardío. La gran mayoría de los procedimientos de ICP que se realizan en la actualidad consisten en la angioplastia con balón y la implantación de un stent [Iqbal et al., 2013]. Sin embargo, a pesar de las notables mejoras clínicas, la trombosis aguda del stent, junto con el aumento de la hiperplasia neointimal y la remodelación tardía del vaso que da lugar a la nueva complicación de la reestenosis intra-stent (RIS), se siguen señalando como las principales limitaciones de esta técnica [Alfonso et al., 2014]. De hecho, el seguimiento clínico a medio y largo plazo de los pacientes con stents metálicos sin recubrimiento implantados reveló unas tasas de RIS considerables del 20 al 30% [Hoffmann et al., 1996]. Esto llevó a varios intentos de minimizar las tasas de reestenosis optimizando el rendimiento del stent en términos de diseño geométrico, métodos de fabricación, materiales, procedimiento de implantación y métodos de expansión. Cuando estas actualizaciones mecánicas no resolvieron los problemas de reestenosis encontrados con los stents metálicos desnudos, los investigadores consideraron soluciones farmacológicas mediante el uso de stents recubiertos con sustancias antiproliferativas, también llamados stents farmacoactivos (SFAs).

Con la llegada de los stents liberadores de fármacos, la incidencia de reestenosis se ha reducido drásticamente [Buccheri et al., 2016]. Sin embargo, a pesar del revolucionario éxito en la reducción de las tasas de RIS y de los eventos clínicos asociados, el uso de SFAs recubiertos con polímeros permanentes no ha demostrado ser una solución definitiva para el tratamiento de la enfermedad coronaria. Su permanencia en la arteria se asocia a un retraso en la cicatrización del vaso y a un riesgo de trombosis, y, además, la mayoría de los pacientes tienen que recibir un tratamiento antiplaquetario dual caro y prolongado [Byrne et al., 2015b]. Además, si se produce RIS, no es factible retirar el stent original e insertar uno nuevo en el mismo lugar, lo que complica la estrategia de revascularización, conduciendo a muchos grupos clínicos a considerar el uso de balones recubiertos de fármacos como una alternativa atractiva a los SFAs para el tratamiento de la enfermedad coronaria en determinadas condiciones anatómicas. En particular, los balones farmacoactivos (BFAs) pueden utilizarse en el tratamiento de la RIS cuando no es factible insertar otro SFA [Scheller et al., 2006]. Además, los BFAs son cada vez más interesantes en el contexto del tratamiento de pequeñas lesiones de novo [Jeger et al., 2018]. Una ventaja clave de la implantación de un BFA frente a un SFA es que no tienen permanencia. Sin embargo, esto puede ser potencialmente una desventaja, ya que el breve período de aplicación asociado a los BFA presenta solamente una corta ventana para la administración del fármaco.

Como complemento a la gran variedad de estudios fisiológicos y clínicos, el uso del modelado y la simulación computacional (*in silico*) para los dispositivos endovasculares ha surgido como una potente técnica que puede contribuir a abordar algunas de las limitaciones de los a menudo difíciles y costosos análisis experimentales, con modelos centrados en diferentes áreas: mecánica estructural y dinámica de fluidos computacional, cinética de liberación del fármaco, captación y posterior redistribución en el tejido arterial y respuesta de cicatrización del tejido arterial. La relativa flexibilidad de los métodos numéricos para llevar a cabo estudios paramétricos de las distintas variables que intervienen en el diseño de los dispositivos endovasculares puede traducirse en una reducción de tiempo y costes en cuanto al diseño y la fabricación del dispositivo. Para modelar la interacción del dispositivo con la pared arterial, las propiedades biomecánicas del tejido deben ser perfectamente conocidas. En el ámbito fisiológico, los modelos constitutivos intentan captar el comportamiento (visco)elástico de los tejidos cardiovasculares, incorporando a su definición matemática parámetros relacionados con la estructura. También hay que tener en cuenta que durante algunas intervenciones quirúrgicas, como la angioplastia coronaria, las cargas a las que se somete el tejido vascular durante las intervenciones quirúrgicas son muy superiores a las correspondientes a las condiciones fisiológicas, por lo que las simulaciones numéricas deben considerar las teorías de daño y (visco)plasticidad, entre otras.

Por lo tanto, son necesarios mayores esfuerzos para desarrollar modelos más avanzados de dispositivos endovasculares implantados en arterias en condiciones sanas y patológicas para una mejor comprensión de su rendimiento y que puedan ayudar a diseñar dispositivos endovasculares personalizados mucho más eficientes y seguros.

Estos modelos deben tener en cuenta todos los rasgos mecánicos y de comportamiento que los caracterizan, de forma que sean lo más realistas posible. Esta es la principal motivación de esta Tesis.

A.2 Objetivos y metodología

Partiendo de la motivación expuesta en el apartado anterior, el objetivo principal de esta Tesis es avanzar en el desarrollo de nuevos modelos matemáticos y computacionales para el estudio del transporte y retención de fármacos desde dispositivos endovasculares en el tejido arterial con el fin de comprender mejor su rendimiento.

Además del objetivo general expuesto, se detallan algunos de los objetivos parciales que se han ido cumpliendo durante el desarrollo de esta Tesis doctoral:

- Desarrollo de nuevos modelos computacionales de flujo de fluidos (sangre y plasma) y transporte de fármacos liberados desde diferentes dispositivos endovasculares (stent y balón) en arterias coronarias sanas, utilizando una herramienta comercial de cálculo por el Método de Elementos Finitos (MEF) como COMSOL Multiphysics (COMSOL AB, Burlington, MA, USA). Los modelos incorporan dos fases (específica y no específica) no lineales de unión del fármaco al tejido arterial e incluyen la influencia de la difusión y la convección en la pared arterial, considerada multicapa y anisótropa.
- Análisis de la influencia de la expansión mecánica de un stent en las propiedades de transporte de fármacos de la pared arterial para establecer relaciones entre la deformación mecánica generada por la expansión del dispositivo y la alteración de la difusión y convección en el tejido. Realización de simulaciones para dilucidar el impacto de dichas alteraciones en la liberación espacio-temporal del fármaco y en los perfiles de captación del fármaco por el tejido.
- Estudio del impacto de la variabilidad de la geometría de la arteria coronaria en el transporte de fármaco en el flujo sanguíneo y en el tejido arterial, realizando una serie de simulaciones para elucidar el efecto de la curvatura arterial en la captación espacio-temporal del fármaco en el tejido.
- Investigación del efecto de la composición heterogénea de la placa aterosclerótica en la distribución global del fármaco en la pared del vaso.
- Simulación de la administración de fármacos desde diferentes tipos de plataformas de balones, explorando la influencia del tiempo de aplicación del balón farmacoactivo e intentando dilucidar la importancia que tiene en la cinética de liberación la elevada presión a la que se somete el vaso durante la aplicación del dispositivo.
- Comparación de simulaciones de stents y balones liberadores de fármacos con el fin de explorar si existe algún beneficio potencial, en términos de seguridad y

eficacia, a la hora de tratar pequeñas lesiones de novo con un balón frente a un stent.

- Análisis del efecto de la elección del fármaco (sirolimus y paclitaxel) en los dispostivos intravasculares.
- Establecimiento de una metodología para el modelado del proceso de reestenosis tras la implantación de un stent (reestenosis intra-stent, RIS) con el fin de comprender mejor las especies y los procesos biológicos implicados. Diseño y desarrollo de un modelo matemático y computacional continuo basado en ecuaciones de reacción-difusión que capture con éxito las principales características de la RIS en una arteria coronaria.

Para alcanzar los objetivos indicados, a lo largo del desarrollo de esta Tesis se ha adoptado la siguiente metodología de trabajo:

- Planteamiento del problema.
- Elección de los principales efectos físicos a modelar en los diferentes problemas planteados: transporte de fármacos liberados desde los dispositivos endovasculares en vasos sanos y patológicos, expansión mecánica de los dispositivos intravasculares y crecimiento reestenótico intra-stent.
- Elección de las ecuaciones matemáticas adecuadas para reproducir los efectos físicos a simular.
- Revisión de los modelos matemáticos y computacionales existentes en la literatura relacionados con la temática de esta Tesis que han servido de base para los nuevos modelos desarrollados por el investigador. Selección de los aspectos válidos para nuestra problemática y modificación de los elementos necesarios de los modelos existentes.
- Ajuste de los parámetros de los modelos desarrollados utilizando datos experimentales, principalmente de la literatura existente.
- Implementación de los modelos computacionales en softwares comerciales de elementos finitos como COMSOL Multiphysics (COMSOL AB, Burlington, MA, USA) y ABAQUS (Dassault Systèmes Simulia Corp., Johnston, RI, USA).
- Aplicación de los modelos computacionales desarrollados para obtener respuestas a las principales cuestiones clínicas planteadas. Por ejemplo, análisis de la influencia de diferentes fármacos, análisis del impacto de los fármacos en diferentes concentraciones y en diferentes tipos de vasos, comparación del efecto de la liberación de fármacos desde diferentes dispositivos endovasculares (stent y balón), acoplamiento de modelos mecánicos y de transporte de fármacos, entre otros.
- Obtención de conclusiones clínicas basadas en los resultados numéricos obtenidos.

A.3 Estructura de la Tesis

Esta Tesis se presenta como un compendio de publicaciones y el presente documento cumple, por tanto, con los requisitos establecidos por la Universidad de Zaragoza tras el Acuerdo de 25 de junio de 2020 del Consejo de Gobierno de la Universidad, por el que aprueba el Reglamento sobre Tesis Doctorales de la Universidad de Zaragoza, y donde se contemplan las tesis desarrolladas como compendio de publicaciones (Artículo 20). De acuerdo con esto, en la página inicial del documento se ha especificado que la Tesis desarrollada es un compendio de publicaciones y se han enumerado las referencias completas de cada uno de los trabajos que constituyen el cuerpo de la Tesis.

El presente documento consta de la siguiente estructura:

- En el **Capítulo 1** se presenta la motivación, los objetivos de la investigación y el esquema de la estructura de la Tesis.
- En el **Capítulo 2** se exponen las principales características del sistema vascular. Se hace especial hincapié en la descripción de la estructura de la pared vascular de las arterias grandes y medianas, así como en su clasificación en función de su papel fisiológico y su composición. También se presentan las características mecánicas más relevantes de los vasos sanguíneos. Se ofrece una revisión del estado del arte en la modelización cardiovascular. En particular, se presentan las leyes constitutivas más utilizadas en el modelado de la pared de los vasos sanguíneos. Además, se expone una visión general de la importancia de los problemas clínicos estudiados en este trabajo y de las principales técnicas de tratamiento. El capítulo se completa con una descripción general del estado del arte de la modelización matemática y computacional en la investigación de dispositivos intravasculares. Todos estos conceptos son importantes para entender los resultados y el alcance de esta Tesis.
- El **Capítulo 3** incluye los trabajos que componen el compendio de publicaciones.
- Finalmente, en el **Capítulo 4** se ofrece una discusión global de este trabajo. También se describen las aportaciones originales de esta Tesis, así como las conclusiones específicas de cada uno de los trabajos desarrollados y una perspectiva de las futuras líneas de trabajo.

Para finalizar, se incluye un Apéndice con un amplio resumen del trabajo desarrollado en castellano.

A.4 Contribuciones originales

Dado que esta Tesis se presenta como un compendio de publicaciones, cada trabajo contiene una exhaustiva discusión y comparación con la literatura existente. Por ello, en este capítulo se resumen los principales logros y conclusiones alcanzadas, así como las líneas futuras que se derivan de esta investigation. También se incluyen en este capítulo las contribuciones a Jornadas y Congresos nacionales e internacionales, las estancias de investigación realizadas en centros internacionales y las diferentes colaboraciones derivadas del trabajo desarrollado en esta Tesis.

A continuación, se enumeran las principales aportaciones originales de esta Tesis.

Trabajo 1: ¿Cómo altera la expansión del stent las propiedades de transporte de fármacos de la pared arterial?

- Se desarrolló un completo modelo computacional para analizar el efecto de la expansión mecánica del stent en las propiedades de transporte de fármacos de la pared arterial, considerada multicapa y descrita como un material anisótropo e hiperelástico. Se establecieron relaciones entre la fuerza mecánica generada por la expansión del dispositivo y la alteración de la difusión en la pared arterial, y se realizaron simulaciones numéricas para dilucidar el impacto de tales alteraciones en la liberación espacio-temporal del fármaco desde el dispositivo y la subsecuente retención en el tejido.
- Se analizó el impacto de las concentraciones locales del fármaco en el tejido arterial, que están relacionadas con el efecto biológico de la sustancia antiproliferativa considerada, para evaluar si las concentraciones de fármaco a nivel local se encuentran dentro de unos niveles terapéuticos (y no tóxicos). Este análisis también es relevante para el diseño de modalidades más eficaces de administración de fármacos.
- Esta investigación permitió establecer una metodología para vincular modelos computacionales centrados en el transporte de fármacos desde dispositivos intravasculares con modelos computacionales centrados en el estudio de la expansión mecánica y la interacción entre el dispositivo y el vaso sanguíneo.

Trabajo 2: Influencia de la curvatura del vaso sanguíneo y de la composición de la placa de ateroma en el transporte de fármacos en la pared arterial tras la implantación de un stent liberador de fármacos.

- Se desarrolló un modelo computacional para analizar el impacto de la variabilidad de la geometría de la arteria coronaria en el transporte del fármaco en el flujo sanguíneo y en el tejido arterial mediante una serie de simulaciones para dilucidar el efecto de la curvatura arterial en la captación espacio-temporal del fármaco dentro del tejido.

- Se investigó la influencia de la heterogeneidad de la placa aterosclerótica en la distribución global del fármaco en el tejido.

Trabajo 3: Administración de fármacos mediante dispositivos intravasculares: comparativa balones vs stents

- Se ha desarrollado un detallado modelo de liberación, transporte y retención de balón farmaco. El modelo considera una geometría 2D-axisimétrica e incorpora dos fases no lineales de unión (específica y no específica) y la influencia de la advección dentro de una pared arterial multicapa.
- Este marco ha sido utilizado para:
  - Simular la administración de fármacos desde diferentes tipos de plataformas de balones.
  - Explorar la influencia del tiempo de aplicación del balón farmacoactivo.
  - Dilucidar la importancia de la cinética de liberación considerando el aumento de presión en el vaso existente durante la aplicación del balón.
  - Comparar la aplicación de dos fármacos diferentes (sirolimus y paclitaxel).
  - Comparar simulaciones de stent farmacoactivo frente a balón farmacoactivo con el objetivo de explorar si existe algún beneficio potencial, en términos de seguridad y eficacia, para tratar pequeñas lesiones de novo con un balón frente tratarlas con un stent.

Trabajo 4: Modelado matemático del proceso de reestenosis tras la implantación de un stent.

- Se ha desarrollado un modelo matemático y computacional que capta con éxito las características clave del proceso de reestenosis tras la implantación de un stent en una arteria coronaria. La principal novedad de este modelo es que se tiene en cuenta un enfoque continuo para describir la cascada de acontecimientos que siguen al daño producido en la pared arterial debido al procedimiento de implantación de un stent y, por tanto, se formula en términos de densidades/concentraciones de una serie de especies biológicas. Esto es muy ventajoso ya que nos permite evaluar cómo la evolución de las distintas especies biológicas consideradas afecta al proceso global de cicatrización y, lo que es más importante, cómo las variaciones de los parámetros asociados y las condiciones iniciales influyen en el proceso.

- A diferencia de cualquiera de los modelos continuos existentes hasta la fecha de publicación de este trabajo, el modelo es capaz de predecir la respuesta temporal de seis especies biológicas diferentes (factores de crecimiento, metaloproteasas, componentes de matriz extracelular, células musculares lisas contráctiles y sintéticas y células endoteliales) que intervienen en la RIS tras el daño mecánico inicial producido durante la implantación, simulando al mismo tiempo el crecimiento de tejido restenótico.
- Se realizó un análisis de sensibilidad de todas las variables implicadas en el modelo de RIS para evaluar el efecto de la variación de cada uno de los parámetros de entrada implicados en la evolución del proceso de reestenosis y de cara a comprobar la robustez de los resultados obtenidos con el modelo computacional. Esto es de especial importancia debido a la ausencia de un conjunto completo de datos experimentales y a la gran variabilidad observada en la literatura en muchos de los parámetros del modelo.
- Este modelo de RIS se utilizó además para evaluar el impacto de diferentes configuraciones geométricas del dispositivo en el resultado final mediante la consideración en las simulaciones realizadas de una serie de stents comerciales, así como de diferentes distancias de separación entre los struts del stent y diferentes niveles de incrustación de los mismos, permitiendo relacionar los hallazgos encontrados con el diseño del dispostivo intravascular.

A.5 Conclusiones

En esta sección se presentan las principales conclusiones extraídas de esta Tesis, basadas en los estudios computacionales realizados.

Trabajo 1: ¿Cómo altera la expansión del stent las propiedades de transporte de fármacos de la pared arterial?

- Los principales hallazgos encontrados demostraron que la expansión mecánica del dispositivo puede influir en los coeficientes de difusión efectivos de los fármacos en el tejido arterial, y que la influencia global en el transporte de fármacos a través de la pared depende del número de Peclet radial que se deriva de estos coeficientes de difusión.
- El efecto de la expansión del stent sobre el transporte de fármacos en el tejido arterial depende no sólo de la capa específica en cuestión (íntima, media o adventicia), sino también del fármaco concreto (sirolimus frente a paclitaxel). En general, el efecto de la expansión mecánica es más importante en el caso del paclitaxel, especialmente en la adventicia.

- Los modelos computacionales existentes de transporte de fármacos eluidos desde stents suelen utilizar coeficientes de difusión de fármacos derivados de experimentos tisulares estáticos (es decir, no sometidos a expansión mecánica). Por lo tanto, es probable que estos modelos estén subestimando o sobreestimando (dependiendo del caso) el transporte y la retención de fármacos en el tejido arterial.
- Nuestros resultados también pueden ser importantes para otras formas de administración arterial localizada de fármacos, como los balones farmacoactivos. La diferencia clave con los balones farmacoactivos parece ser una dependencia variable en el tiempo de los parámetros de transporte del fármaco, coincidiendo con el tiempo de aplicación del dispostivo intravascular.

Trabajo 2: Influencia de la curvatura del vaso sanguíneo y de la composición de la placa de ateroma en el transporte de fármacos en la pared arterial tras la implantación de un stent liberador de fármacos.

- La curvatura arterial conduce a la distribución asimétrica del fármaco en la pared arterial y el nivel de asimetría depende, en gran medida, del nivel de curvatura. En concreto, al aumentar la curvatura la arterial, una mayor parte del fármaco se acumula en la pared interna del vaso sanguíneo. Es probable que esta distribución asimétrica, como resultado de las fuerzas del fluido, se vea exacerbada en geometrías más realistas (paciente-específicas). La implicación de este hallazgo para los fabricantes de stents es que se debe tener especial cuidado al considerar la carga de fármacos en el dispositivo, ya que esta distribución asimétrica del fármaco podría, al menos en teoría, dar lugar a concentraciones insuficientes de fármacos que lleguen a la pared externa del vaso, mientras que las concentraciones que llegan a la pared interna podrían ser demasiado altas, superando incluso el umbral de toxicidad. La consecuencia para el paciente podría ser un crecimiento neointimal asimétrico como parte del proceso de curación tras la implantación del dispositivo.
- Las placas ateroscleróticas lipídicas dan lugar a concentraciones de fármacos más elevadas que las placas fibróticas, mientras que las placas calcificadas son impenetrables al fármaco por naturaleza. La impenetrabilidad de la placa calcificada tiene implicaciones potencialmente importantes y, si su extensión es lo suficientemente grande, puede actuar como una barrera significativa impidiendo que el fármaco llegue al tejido arterial donde residen las células musculares lisas que proliferan y migran.
- La presencia de placa de ateroma en la pared arterial, independientemente de la composición del núcleo, puede retrasar ligeramente la saturación de los receptores específicos en el tejido, una variable que ha sido habitualmente relacionada con la eficacia [Tzafriri et al., 2012; McKittrick et al., 2019].

- La placa puede actuar como una fuente de fármaco (en realidad, como un reservorio de fármaco) asegurando que la disminución de la saturación del receptor se reduce significativamente en comparación con el caso de la pared sana. La implicación es que, en estados avanzados de enfermedad, los sitios de unión pueden estar saturados durante más tiempo, es decir, los pacientes reciben una dosis efectiva de fármaco durante más tiempo.
- Tanto la curvatura arterial como la composición de la placa aterosclerótica influyen de forma significativa en la distribución espacio-temporal del fármaco en el tejido, con posibles implicaciones en la eficacia del tratamiento. Se aconseja a los fabricantes de endoprótesis que tengan en cuenta que una dosis de fármaco para endoprótesis de 'talla única' puede no ser adecuada para todos los pacientes, y podría, al menos en parte, estar contribuyendo a los diferentes resultados de un paciente a otro que se observan clínicamente. Dado que la mayoría de los modelos computacionales existentes hasta la fecha tienden a ignorar estas características, también es probable que subestimen o sobreestimen la captación y redistribución del fármaco en el tejido arterial.

Trabajo 3: Administración de fármacos mediante dispositivos intravasculares: comparativa balones vs stents

- Los resultados obtenidos ponen de manifiesto que es imprescindible incorporar en los modelos de balones farmacoactivos la elevada presión a la que está sometido el vaso durante el tiempo de aplicación del dispositivo. Esto conduce a una mayor y más rápida penetración del fármaco en el tejido, a una mayor retención del mismo y a mayores niveles de saturación de los stios de unión específicos (receptores), en comparación con las simulaciones que utilizan una presión fija en el lumen durante todo el tiempo.
- Los valores de contenido total de fármaco en el tejido obtenidos en este estudio coinciden ampliamente con las observaciones experimentales recogidas en la literatura existente [McKittrick et al., 2019; Tzafriri et al., 2012; Grube and Buellesfeld, 2006; Gongora et al., 2015; Radke et al., 2011], proporcionando confianza en las simulaciones realizadas.
- Suponiendo la misma dosis de fármaco y la misma cinética de liberación para un balón farmacoactivo, el sirolimus se retiene en el tejido durante más tiempo que el paclitaxel, al menos para los valores de los parámetros simulados que se basan en datos experimentales de la literatura.
- En cuanto a la comparación directa entre los balones y los stents farmacoactivos, si lo más importante es saturar antes los sitios de unión específicos, cada uno de los balones considerados ofrece una cierta ventaja sobre el stent recubierto con sirolimus simulado. Sin embargo, si lo que se desea es mantener unos niveles

elevados de porcentaje de sitios de unión específicos saturas más allá de los 30 días considerados, entonces es preferible el stent farmacoactivo.

- Al simular una liberación de fármaco rápida artificial (no realista) desde un stent farmacoactivo recubierto con sirolimus, se ha demostrado que si los marcadores de seguridad y eficacia de los balones recubiertos con sirolimus simulados son aceptables pero se prefiere un dispositivo intravascular permanente como el stent, entonces puede ser posible diseñar una nueva clase de stents farmacoactivos de liberación rápida cuya cinética de liberación se ajuste a la de un balón liberador de fármacos.
- Puede existir una configuración de balón farmacoactivo, en términos de carga de fármaco y de tasa de liberación, que dé lugar a resultados de seguridad y eficacia suficientemente similares a los de los actuales stents farmacoactivos comerciales disponibles en el mercado.

Trabajo 4: Modelado matemático del proceso de reestenosis tras la implantación de un stent.

- El modelo de reestenosis desarrollado en esta Tesis fue capaz de capturar algunos de los mecanismos y patrones subyacentes más importantes de la RIS.
- El análisis de sensibilidad realizado para los distintos parámetros del modelo proporciona información sobre la estabilidad del mismo y permite comprender cómo los cambios en un parámetro afectan al comportamiento de todo el sistema. El valor de la constante de degradación del daño tuvo un impacto muy significativo en la tasa de curación. Además, los resultados mostraron que las constantes de producción, degradación, diferenciación y proliferación tenidas en cuenta afectan en gran medida a los niveles locales de concentración/densidad de las especies implicadas en el proceso de RIS y a la respuesta temporal del sistema. La tasa de apoptosis de las células musculares lisas sintéticas, los coeficientes de difusión y las condiciones iniciales también influyeron en la evolución del modelo, aunque en menor medida.
- Los resultados obtenidos han demostrado que el porcentaje de reestenosis aumenta con el aumento del tamaño de los struts del stent, disminuye con el aumento de la distancia entre los struts, aumenta con el aumento del diámetro de expansión del lumen arterial y depende de la configuración geométrica de los struts del dispositivo.
- La comparación de los resultados obtenidos frente a datos experimentales de reestenosis existentes en la literatura (a nivel del tejido), demuestra que coinciden ampliamente con las hipótesis clínicas relativas a la aparición de la RSI.

- El modelo mecanobiológico desarrollado ha proporcionado información importante sobre la dinámica de la RIS y puede considerarse un paso adelante hacia una mejor comprensión de este complejo proceso biológico. Un mayor acoplamiento entre el modelo de RIS y los modelos de transporte de fármacos podría ser un importante paso adelante en el diseño de dispositivos intravasculares personalizados mucho más eficaces.

A.6 Líneas futuras

Considerando los trabajos desarrollados en esta Tesis y teniendo en cuenta sus conclusiones y limitaciones, en este apartado se proponen algunas posibles líneas de investigación para llevar a cabo en el futuro y que permitirán mejorar los resultados obtenidos y ampliar los conocimientos adquiridos:

- Estudiar la influencia de la deformación en otros parámetros clave implicados en el transporte de fármacos (por ejemplo, la porosidad y la permeabilidad).
- Con respecto a las geometrías de los modelos de elementos finitos desarrollados en esta Tesis, generalmente se han considerado geometrías 2D y 2D-axisimétricas correspondientes a representaciones idealizadas de segmentos rectos de arterias coronarias. En alguno de los modelos presentados también se han considerado geometrías 2D correspondientes a segmentos curvos de arteria y con presencia de placa de ateroma. Esto podría mejorarse utilizando geometrías más realistas de vasos (aunque siempre ligeramente idealizadas), como pueden ser bifurcaciones o directamente geometrías 3D específicas del paciente obtenidas a partir de imágenes médicas. Un modelo más sofisticado de la placa de ateroma también podría concebirse para tener en cuenta su complicada estructura.
- En cuanto al modelado de la liberación de fármacos desde el recubrimiento del stent, en línea con la gran mayoría de los modelos existentes en la literatura que consideran un recubrimiento permanente del stent (correspondientes a los stents farmacoactivos de primera y segunda generación), se ha considerado un modelo de difusión lineal simple. Sin embargo, dependiendo del stent, el fármaco y el recubrimiento en cuestión, pueden ser necesarios modelos no lineales más complejos que tengan en cuenta los efectos combinados de la difusión, la disolución y la solubilidad en el recubrimiento polimérico para describir la liberación del fármaco del stent, o incluso otros fenómenos como la degradación o la erosión (fenómenos propios de la nueva generación de stents farmacoactivos).
- Los futuros trabajos deberían explorar el uso de un marco de optimización para intentar inferir el fármaco, la dosis y la tasa de liberación del balón liberador de fármaco, así como de diferentes aspectos del procedimiento como la presión

de inflado del balón y el tiempo de aplicación, que den lugar a valores de contenidos de fármacos en el tejidos que se encuentren dentro de la ventana terapéutica, maximizando al mismo tiempo el porcentaje de sitios de unión específicos saturados durante el periodo de cicatrización arterial.

- Desarrollo de un modelo de reestenosis intra-stent más complejo que incluya otros agentes biológicos (por ejemplo, plaquetas, monocitos, diferentes clases de factores de crecimiento (PDGF, EGF, IGF, TGF, FGF), células mesenquimales, fibroblastos, subtipos de colágeno, proteoglicanos, fibronectina, etc.) y otros procesos (por ejemplo, la activación y la migración de las células madre mesenquimales, la liberación de factores de crecimiento por los fibroblastos o la síntesis de matriz extracelular por las células endoteliales, etc.) que intervienen en el proceso de reestenosis. El aumento de la complejidad del modelo de crecimiento proporcionaría información más precisa sobre el proceso de reestenosis. Sin embargo, se necesitan más datos para que el modelo sea más preciso.
- La modelización del daño mecánico inicial en el tejido después de la colocación de un stent que se considera en esta tesis se basa en la respuesta de tensión última-estiramiento para cada capa de la pared observada en las arterias coronarias humanas [Holzapfel et al., 2005a]. Se propone como nueva línea de trabajo futura una modelización más compleja de este estímulo inicial necesario para iniciar el proceso de RIS.
- Hasta la fecha, no hay datos experimentales publicados en la literatura que relacionen directamente los niveles de tensión-deformación debidos a la expansión del dispositivo con la lesión de la pared arterial y la cascada de eventos asociados. Además, hay que tener en cuenta la dificultad de encontrar parámetros experimentales y constantes para alimentar el modelo mecanobiológico de la RIS. Por ello, se propone también el desarrollo de pruebas experimentales propias para la obtención de estos datos.

A.7 Contribuciones a congresos

Con el fin de ampliar el trabajo desarrollado en esta Tesis y fomentar la transmisión de los conocimientos adquiridos durante este periodo, se han presentado las siguientes comunicaciones a congresos y jornadas nacionales e internacionales:

1. **Escuer J.**, Peña E., Pina E., Martínez M.A. Analysis of the influence of plaque composition and geometry on drug transport from drug eluting stents. Submitted to *27th Congress of the European Society of Biomechanics (ESB2022).* Oporto (Portugal), Junio 2022.
2. McQueen A., **Escuer J.**, Fensterseifer Schmidt A., Aggarwal A., Kennedy S., McCormick C., Olroyd K., McGinty S. *In silico* modelling of in-stent restenosis

subject to spatiotemporal delivery of drug. Submitted to *7th International Conference on Computational and Mathematical Biomedical Engineering (CMBE22).* Milán (Italia), Junio 2022.

3. Fensterseifer Schmidt A., **Escuer J.**, McGinty S. *In silico* modelling of endovascular drug delivery. *Mathematical modelling and control for healthcare and biomedical systems (MCHBS2021 Virtual Workshop).* Roma (Italia), Septiembre 2021.
4. McQueen A., **Escuer J.**, Aggarwal A., Kennedy S., McCormick C., Olroyd K., McGinty S. Preliminary approaches to understand how anti-proliferative drug modulate in-stent restenosis. *Mathematical modelling and control for healthcare and biomedical systems (MCHBS2021 Virtual Workshop).* Roma (Italia), Septiembre 2021.
5. **Escuer J.**, Peña E., Martínez M.A., McGinty S. Endovascular drug delivery: stents versus balloons. *26th Congress of the European Society of Biomechanics (ESB2021).* Milán (Italia), Julio 2021.
6. **Escuer J.**, Aznar I., McCormick C., Peña E., McGinty S, Martínez M.A.. How does vessel curvature and plaque composition affect the distribution in tissue of drug eluted from stents? *26th Congress of the European Society of Biomechanics (ESB2021).* Milán (Italia), Julio 2021.
7. **Escuer J.**, McGinty S., Peña E., Martínez M.A., Conway C. Coupling solid mechanics & drug transport in 3D for drug-eluting stent analysis. *25th Congress of the European Society of Biomechanics (ESB2019).* Viena (Austria), Julio 2019.
8. **Escuer J.**, Martínez M.A., McGinty S., Peña E. A computational mechanobiological model to simulate the in-stent restenosis process. *25th Congress of the European Society of Biomechanics (ESB2019).* Viena (Austria), Julio 2019.
9. **Escuer J.**, Peña E., McGinty S., Martínez M.A. How does mechanical expansion of endovascular devices alter drug transport properties of the arterial wall? *VI Jornada de Doctorandos del Programa de Doctorado en Ingeniería mecánica (PDIM).* Zaragoza (España), Junio 2019.
10. **Escuer J.**, Aznar I., Peña E., Martínez M.A. How does vessel curvature influence drug release from DES and drug transport in arterial tissue? *VIII Jornada Jóvenes Investigadores del Instituto de Investigación en Ingeniería de Aragón (I3A).* Zaragoza (España), Junio 2019.
11. Martínez M.A, **Escuer J.**, McGinty S., Peña E. A continuum-approach model to numerically simulate the in-stent restenosis process. *First Colloquium of the Spanish Theoretical and Applied Mechanics Society (STAMS2019).* Madrid (España), Marzo 2019.

12. **Escuer J.**, Peña E., Martínez M.A, McGinty S. Elucidating the importance of drug-dissolution and specific binding in a 2D model of arterial drug-eluting stent (DES). *Virtual Physiological Human Conference (VPH2018).* Zaragoza (España)), Septiembre 2018.

13. **Escuer J.**, Peña E., Martínez M.A, McGinty S. Effect of drug dissolution and specific-binding on DES modeling. A computational study. *Modelling & Experiments in Drug Delivery Systems (MEDDS).* Glasgow (Reino Unido), Septiembre 2018.

14. **Escuer J.**, Cebollero M., Peña E., McGinty S., Martínez M.A. Numerical Modelling of the Combined Effect of Mechanical Deployment and Drug Delivery in Endovascular Devices. *13th World Congress in Computational Mechanics (WCCM2018).* New York (EEUU), Julio 2018.

15. **Escuer J.**, Cebollero M., Peña E., McGinty S., Martínez M.A. Computational modelling of the effect of mechanical expansion on drug delivery from endovascular devices. *18th World Congress of Biomechanics (WCB2018).* Dublin (Irlanda), Julio 2018.

16. **Escuer J.**, Aznar I., Peña E., Martínez M.A. Influence of curvature of the vessel on the drug transport phenomenon from DES devices. *18th World Congress of Biomechanics (WCB2018).* Dublin (Irlanda), Julio 2018.

17. **Escuer J.**, Scullion B., McCormick C., Martínez M.A, McGinty S. On the influence of non-uniform binding site density in determining arterial drug distribution following stent−based delivery. *18th World Congress of Biomechanics (WCB2018).* Dublin (Irlanda), Julio 2018.

18. **Escuer J.**, Peña E., McGinty S., Martínez M.A. Computational analysis of the influence of dissolution-diffusion and specific binding on drug transport in the arterial wall following stent-based delivery. *VII Jornada Jóvenes Investigadores del Instituto de Investigación en Ingeniería de Aragón (I3A).* Zaragoza (España), Junio 2018.

19. **Escuer J.**, Peña E., Martínez M.A. Numerical modeling of drug transport in arterial wall from drug delivery intravascular devices. *23rd Congress of the European Society of Biomechanics (ESB2017).* Sevilla (España), Julio 2017.

20. **Escuer J.**, Martínez M.A, Peña E. Mechanobiological model of the restenosis process after stent implantation. *23rd Congress of the European Society of Biomechanics (ESB2017).* Sevilla (España), Julio 2017.

21. **Escuer J.**, Martínez M.A, Peña E. Mathematical and numerical modeling of restenosis after DES implantation. *VI Jornada Jóvenes Investigadores del Instituto de Investigación en Ingeniería de Aragón (I3A).* Zaragoza (España), Junio 2017.

22. **Escuer J.**, Peña E., Martínez M.A. Numerical modeling of drug transport in healthy and pathological arterial wall. *12th World Congress on Computational Biomechanics (WCCM16).* Seúl (República de Korea), Julio 2016.

23. **Escuer J.**, Peña E., Martínez M.A. Drug transport in arteries in healthy and pathological conditions. Numerical modeling and experimental validation. *22nd Congress of the European Society of Biomechanics (ESB2016).* Lyon (Francia), Julio 2016.

24. **Escuer J.**, Peña E., Martínez M.A. Computational modeling of drug transport from drug-eluting stents in arterial wall. *7th Summer School on Biomechanics of Soft Tissues: Multiscale Modeling, Simulation and Applications.* Graz (Austria), Julio 2016.

25. **Escuer J.**, Peña E., Martínez M.A. Numerical simulation of drug transport in arterial wall under healthy and atherosclerotic conditions. *19th European Conference on Mathematics for Industry (ECMI2016).* Santiago de Compostela (España), Junio 2016.

26. **Escuer J.**, Peña E., Martínez M.A. Modelo multicapa para el estudio de difusión de fármacos en arterias a través de dispositivos intravasculares. *V Jornada Jóvenes Investigadores del Instituto de Investigación en Ingeniería de Aragón (I3A).* Zaragoza (España), Mayo 2016.

27. **Escuer J.**, Peña E., Martínez M.A. Modelo numérico de transporte convectivo-difusivo del paclitaxel en la pared arterial y validación experimental. *V Reunión del Capítulo Nacional Español de la Sociedad Europea de Biomecánica* (European Society of Biomechanics, ESB). Madrid (España), Noviembre 2015.

28. **Escuer J.**, Peña E., Martínez M.A. Estudio computacional y validación experimental de la difusión del paclitaxel en arterias. *XXXIII Congreso Anual de la Sociedad Española de Ingeniería Biomédica (CASEIB2015).* Madrid (España), Noviembre 2015.

A.8 Estancias de investigación

Durante el desarrollo de esta Tesis se han realizado dos estancias en centros de investigación:

1. University of Glasgow (Glasgow, Escocia, Reino Unido), bajo la supervisión del Dr. Sean McGinty. Septiembre-Diciembre, 2017.

2. National University of Ireland Galway (Galway, Ireland), bajo la supervisión de la Dr. Claire Conway. Septiembre-Diciembre, 2018.

A.9 Otros trabajos relacionados con la temática de la Tesis

A.9.1 Publicaciones en revistas científicas

En primer lugar, en esta subsección se han incluido los trabajos ya publicados en los que el investigador ha participado como coautor de los mismos:

- McQueen A., Escuer J., Aggarwal A., Kennedy S., McCormick C., Oldroyd K., McGinty S. (2021). Do we really understand how drug eluted from stents modulates arterial healing? *International Journal of Pharmaceutics*, 601:120575. https://doi.org/10.1016/j.ijpharm.2021.120575.
  JIF (2020): 5.875 (Q1: 37/276 Pharmacology & Pharmacy).

También existen varios artículos en preparación que se enviarán próximamente a diferentes revistas científicas:

- Escuer J., Pina E., Martínez M.A, Peña E. How does the geometry and plaque composition influence tissue uptake and retention of drug eluted from stents? *En preparación.*
- Escuer J., McGinty S., Peña E., Martínez M.A., Conway C. Coupling solid mechanics & drug transport in 3D for drug-eluting stent analysis. *En preparación.*
- McQueen A., Escuer J., Fensterseifer-Schmidt A., Aggarwal A., Kennedy S., McCormick C., Oldroyd K., McGinty S. Mathematical modelling of restenosis subject to the spatiotemporal delivery of drug. *En preparación.*

A.9.2 Trabajos Fin de Máster (TFMs)

Durante este periodo se han dirigido los siguientes Trabajos Fin de Máster, directamente relacionados con el ámbito de esta Tesis:

- Estudio de la difusión de fármacos desde dispositivos intravasculares en una geometría paciente-específica. Autor: Mario Lamas Rodríguez. Directores: Miguel Ángel Martínez Barca y Javier Escuer Gracia. Universidad de Zaragoza. Diciembre 2018.
- Infuencia de la curvatura arterial en la eficiencia de dispositivos intravasculares de liberación de fármacos. Autora: Irene Aznar Lou. Directores: Miguel Ángel Martínez Barca y Javier Escuer Gracia. Universidad de Zaragoza. Diciembre 2017.

- Modelo computacional acoplado de la expansión mecánica de dispositivos intravasculares y liberación de fármaco asociada. Autora: Martina Cebollero Burgués. Directores: Miguel Ángel Martínez Barca y Javier Escuer Gracia. Universidad de Zaragoza. Septiembre 2020.

A.9.3 Trabajos Fin de Grado (TFGs)

Durante este periodo se ha dirigido el siguiente Trabajo Fin de Grado, también directamente relacionado con el ámbito de esta Tesis:

- Influencia de la geometría y composición de la placa de ateroma en el transporte de fármacos en la pared arterial liberados desde un stent coronario. Autora: Estela Pina Clos. Directores: Estefanía Peña Baquedano y Javier Escuer Gracia. Universidad de Zaragoza. Septiembre 2020.

A.10 Financiación

Esta investigación ha contado con el apoyo del Ministerio de Economía y Competitividad a través de los proyectos de investigación DPI2013-44391-P y DPI2016-76630-C2-1-R; del Departamento de Industria e Innovación del Gobierno de Aragón a través de la beca de investigación T24-17R (Fondo Social Europeo) y del proyecto de investigación LM-P121-18 y; del Instituto de Salud Carlos III (ISCIII) a través de la iniciativa CIBER-BBN. Al mismo tiempo, el autor agradece el apoyo a la investigación del Ministerio de Economía y Competitividad español por el apoyo a través de la beca individual BES-2014-069737 y las becas de movilidad EEBB-I-17-12605 y EEBB-I-18-13000, que proporcionaron la oportunidad de realizar dos estancias de investigación en University of Glasgow (Glasgow, Escocia, Reino Unido) en 2017 y National University of Ireland Galway (Galway, Irlanda) en 2018.

Bibliography

Abizaid, A. and Costa Jr, J. R. (2010). New drug-eluting stents: an overview on biodegradable and polymer-free next-generation stent systems. *Circulation: Cardiovascular Interventions*, 3(4):384–393.

Abraham, J., Gorman, J., Sparrow, E., Stark, J., and Kohler, R. (2013). A mass transfer model of temporal drug deposition in artery walls. *International Journal of Heat and Mass Transfer*, 58(1-2):632–638.

Alastrué, V., Martinez, M., Doblaré, M., and Menzel, A. (2009). Anisotropic micro-sphere-based finite elasticity applied to blood vessel modelling. *Journal of the Mechanics and Physics of Solids*, 57(1):178–203.

Alfonso, F., Byrne, R. A., Rivero, F., and Kastrati, A. (2014). Current treatment of in-stent restenosis. *Journal of the American College of Cardiology*, 63(24):2659–2673.

Anbalakan, K., Toh, H. W., Ang, H. Y., Buist, M. L., and Leo, H. L. (2021). Assessing the influence of atherosclerosis on drug coated balloon therapy using computational modelling. *European Journal of Pharmaceutics and Biopharmaceutics*, 158:72–82.

Ang, H., Ng, J., Bulluck, H., Wong, P., Venkatraman, S., Huang, Y., and Foin, N. (2018). Fundamentals of bioresorbable stents. In *Functionalised Cardiovascular Stents*, pages 75–97. Elsevier.

Arruda, E. M. and Boyce, M. C. (1993). A three-dimensional constitutive model for the large stretch behavior of rubber elastic materials. *Journal of the Mechanics and Physics of Solids*, 41(2):389–412.

Axel, D. I., Kunert, W., Göggelmann, C., Oberhoff, M., Herdeg, C., Küttner, A., Wild, D. H., Brehm, B. R., Riessen, R., Köveker, G., et al. (1997). Paclitaxel inhibits arterial smooth muscle cell proliferation and migration in vitro and in vivo using local drug delivery. *Circulation*, 96(2):636–645.

Bauters, C. and Isner, J. M. (1997). The biology of restenosis. *Progress in Cardiovascular Diseases*, 40(2):107–116.

Bentzon, J. F., Otsuka, F., Virmani, R., and Falk, E. (2014). Mechanisms of plaque formation and rupture. *Circulation Research*, 114(12):1852–1866.

Bergel, D. H. (1960). *The visco-elastic properties of the arterial wall.* PhD thesis, Queen Mary University of London.

Boland, E. L., Grogan, J. A., and McHugh, P. E. (2019). Computational modelling of magnesium stent mechanical performance in a remodelling artery: Effects of multiple remodelling stimuli. *International Journal for Numerical Methods in Biomedical Engineering*, 35(10):e3247.

Bom, M. J., Van Der Heijden, D. J., Kedhi, E., Van Der Heyden, J., Meuwissen, M., Knaapen, P., Timmer, S. A., and Van Royen, N. (2017). Early detection and treatment of the vulnerable coronary plaque: can we prevent acute coronary syndromes? *Circulation: Cardiovascular Imaging*, 10(5):e005973.

Bonetti, P., Lerman, L., Napoli, C., and Lerman, A. (2003). Statin effects beyond lipid lowering—are they clinically relevant? *European Heart Journal*, 24(3):225–248.

Boyle, C., Lennon, A. B., Early, M., Kelly, D., Lally, C., and Prendergast, P. (2010). Computational simulation methodologies for mechanobiological modelling: a cell-centred approach to neointima development in stents. *Philosophical Transactions of the Royal Society of London A: Mathematical, Physical and Engineering Sciences*, 368(1921):2919–2935.

Boyle, C. J., Lennon, A. B., and Prendergast, P. J. (2011). In silico prediction of the mechanobiological response of arterial tissue: application to angioplasty and stenting. *Journal of Biomechanical Engineering*, 133(8):081001.

Boyle, C. J., Lennon, A. B., and Prendergast, P. J. (2013). Application of a mechanobiological simulation technique to stents used clinically. *Journal of Biomechanics*, 46(5):918–924.

Bozsak, F., Chomaz, J.-M., and Barakat, A. I. (2014). Modeling the transport of drugs eluted from stents: physical phenomena driving drug distribution in the arterial wall. *Biomechanics and Modeling in Mechanobiology*, 13(2):327–347.

Bozsak, F., Gonzalez-Rodriguez, D., Sternberger, Z., Belitz, P., Bewley, T., Chomaz, J.-M., and Barakat, A. I. (2015). Optimization of drug delivery by drug-eluting stents. *PLoS One*, 10(6):e0130182.

Buccheri, D., Piraino, D., Andolina, G., and Cortese, B. (2016). Understanding and managing in-stent restenosis: a review of clinical data, from pathogenesis to treatment. *Journal of Thoracic Disease*, 8(10):E1150.

Budu-Grajdeanu, P., Schugart, R. C., Friedman, A., Valentine, C., Agarwal, A. K., and Rovin, B. H. (2008). A mathematical model of venous neointimal hyperplasia formation. *Theoretical Biology and Medical Modelling*, 5(1):1–9.

Byrne, R. A., Joner, M., Alfonso, F., and Kastrati, A. (2014). Drug-coated balloon therapy in coronary and peripheral artery disease. *Nature Reviews Cardiology*, 11(1):13–23.

Byrne, R. A., Joner, M., and Kastrati, A. (2015a). Stent thrombosis and restenosis: what have we learned and where are we going? The Andreas Grüntzig Lecture ESC 2014. *European Heart Journal*, 36(47):3320–3331.

Byrne, R. A., Serruys, P. W., Baumbach, A., Escaned, J., Fajadet, J., James, S., Joner, M., Oktay, S., Jüni, P., Kastrati, A., et al. (2015b). Report of a European Society of Cardiology - European Association of Percutaneous Cardiovascular Interventions task force on the evaluation of coronary stents in Europe: executive summary. *European Heart Journal*, 36(38):2608–2620.

Calvez, V., Ebde, A., Meunier, N., and Raoult, A. (2009). Mathematical modelling of the atherosclerotic plaque formation. In *ESAIM: Proceedings*, volume 28, pages 1–12. EDP Sciences.

Camenzind, E., Steg, P. G., and Wijns, W. (2007). A cause for concern. *Circulation*, 115(11):1440–1455.

Canham, P. B., Finlay, H. M., Dixon, J. G., Boughner, D. R., and Chen, A. (1989). Measurements from light and polarised light microscopy of human coronary arteries fixed at distending pressure. *Cardiovascular Research*, 23(11):973–982.

Caputo, M., Chiastra, C., Cianciolo, C., Cutrì, E., Dubini, G., Gunn, J., Keller, B., Migliavacca, F., and Zunino, P. (2013). Simulation of oxygen transfer in stented arteries and correlation with in-stent restenosis. *International Journal for Numerical Methods in Biomedical Engineering*, 29(12):1373–1387.

Cardamone, L., Valentin, A., Eberth, J., and Humphrey, J. (2009). Origin of axial prestretch and residual stress in arteries. *Biomechanics and Modeling in Mechanobiology*, 8(6):431–446.

Carew, T. E., Vaishnav, R. N., and Patel, D. J. (1968). Compressibility of the arterial wall. *Circulation Research*, 23(1):61–68.

Casarin, S., Berceli, S. A., and Garbey, M. (2017). Linking gene dynamics to vascular hyperplasia–toward a predictive model of vein graft adaptation. *PLoS One*, 12(11):e0187606.

Cheng, J. and Zhang, L. T. (2019). Simulation of vessel tissue remodeling with residual stress: An application to in-stent restenosis. *International Journal of Smart and Nano Materials*, 10(1):11–27.

Chiastra, C., Wu, W., Dickerhoff, B., Aleiou, A., Dubini, G., Otake, H., Migliavacca, F., and LaDisa Jr, J. F. (2016). Computational replication of the patient-specific stenting procedure for coronary artery bifurcations: From oct and ct imaging to structural and hemodynamics analyses. *Journal of Biomechanics*, 49(11):2102–2111.

Chuong, C. and Fung, Y. (1983). Three-dimensional stress distribution in arteries. *Journal of Biomechanical Engineering*, 105(3):268–274.

Chuong, C. and Fung, Y. (1984). Compressibility and constitutive equation of arterial wall in radial compression experiments. *Journal of Biomechanics*, 17(1):35–40.

Chuong, C.-J. and Fung, Y.-C. (1986). Residual stress in arteries. In *Frontiers in Biomechanics*, pages 117–129. Springer.

Cilla, M., Peña, E., and Martínez, M. A. (2014). Mathematical modelling of atheroma plaque formation and development in coronary arteries. *Journal of The Royal Society Interface*, 11(90):20130866.

Colombo, M., Corti, A., Berceli, S., Migliavacca, F., McGinty, S., and Chiastra, C. (2021). 3D modelling of drug-coated balloons for the treatment of calcified superficial femoral arteries. *Plos one*, 16(10):e0256783.

Conway, C., McGarry, J., Edelman, E., and McHugh, P. (2017). Numerical simulation of stent angioplasty with predilation: an investigation into lesion constitutive representation and calcification influence. *Annals of Biomedical Engineering*, 45(9):2244–2252.

Conway, C., McGarry, J., and McHugh, P. (2014). Modelling of atherosclerotic plaque for use in a computational test-bed for stent angioplasty. *Annals of Biomedical Engineering*, 42(12):2425–2439.

Conway, C., Sharif, F., McGarry, J., and McHugh, P. (2012). A computational test-bed to assess coronary stent implantation mechanics using a population-specific approach. *Cardiovascular Engineering and Technology*, 3(4):374–387.

Cortese, B. and Bertoletti, A. (2012). Paclitaxel coated balloons for coronary artery interventions: a comprehensive review of preclinical and clinical data. *International Journal of Cardiology*, 161(1):4–12.

Cortese, B., Granada, J. F., Scheller, B., Schneider, P. A., Tepe, G., Scheinert, D., Garcia, L., Stabile, E., Alfonso, F., Ansel, G., et al. (2016). Drug-coated balloon treatment for lower extremity vascular disease intervention: An international positioning document. *European Heart Journal*, 37(14):1096–1103.

Corti, A., Colombo, M., Migliavacca, F., Matas, J. F. R., Casarin, S., and Chiastra, C. (2021). Multiscale computational modeling of vascular adaptation: A systems biology approach using agent-based models. *Frontiers in Bioengineering and Biotechnology*, 9.

Corti, A., Colombo, M., Rozowsky, J. M., Casarin, S., He, Y., Carbonaro, D., Migliavacca, F., Rodriguez Matas, J. F., Berceli, S. A., and Chiastra, C. (2022). A predictive multiscale model of in-stent restenosis in femoral arteries: linking haemodynamics and gene expression with an agent-based model of cellular dynamics. *Journal of the Royal Society Interface*, 19(188):20210871.

Costa, M. A. and Simon, D. I. (2005). Molecular basis of restenosis and drug-eluting stents. *Circulation*, 111(17):2257–2273.

Creel, C. J., Lovich, M. A., and Edelman, E. R. (2000). Arterial paclitaxel distribution and deposition. *Circulation Research*, 86(8):879–884.

Cutrì, E., Zunino, P., Morlacchi, S., Chiastra, C., and Migliavacca, F. (2013). Drug delivery patterns for different stenting techniques in coronary bifurcations: A comparative computational study. *Biomechanics and Modeling in Mechanobiology*, 12(4):657–669.

DeBakey, M. E., Lawrie, G. M., and Glaeser, D. H. (1985). Patterns of atherosclerosis and their surgical significance. *Annals of Surgery*, 201(2):115.

Demiray, H. (1972). A note on the elasticity of soft biological tissues. *Journal of Biomechanics*, 5(3):309–311.

Demiray, H., Weizsäcker, H. W., Pascale, K., and Erbay, H. (1988). A stress-strain relation for a rat abdominal aorta. *Journal of Biomechanics*, 21(5):369–374.

Denny, W. J. and Walsh, M. T. (2014a). Numerical modelling of mass transport in an arterial wall with anisotropic transport properties. *Journal of Biomechanics*, 47(1):168–177.

Denny, W. J. and Walsh, M. T. (2014b). Numerical modelling of the physical factors that affect mass transport in the vasculature at early time periods. *Medical Engineering & Physics*, 36(3):308–317.

d'Errico, M., Sammarco, P., and Vairo, G. (2015). Analytical modeling of drug dynamics induced by eluting stents in the coronary multi-layered curved domain. *Mathematical Biosciences*, 267:79–96.

Diodato, M. and Chedrawy, E. G. (2014). Coronary artery bypass graft surgery: the past, present, and future of myocardial revascularisation. *Surgery Research and Practice*, 2014.

Dobrin, P. B. and Rovick, A. A. (1969). Influence of vascular smooth muscle on contractile mechanics and elasticity of arteries. *American Journal of Physiology-Legacy Content*, 217(6):1644–1651.

Dotter, C. T. and Judkins, M. P. (1964). Transluminal treatment of arteriosclerotic obstruction: Description of a new technic and a preliminary report of its application. *Circulation*, 30(5):654–670.

El Khatib, N., Génieys, S., Kazmierczak, B., and Volpert, V. (2012). Reaction–diffusion model of atherosclerosis development. *Journal of Mathematical Biology*, 65(2):349–374.

Escuer, J., Aznar, I., McCormick, C., Peña, E., McGinty, S., and Martinez, M. A. (2021). Influence of vessel curvature and plaque composition on drug transport in the arterial wall following drug-eluting stent implantation. *Biomechanics and Modeling in Mechanobiology*, 20(2):767–786.

Escuer, J., Cebollero, M., Peña, E., McGinty, S., and Martínez, M. A. (2020). How does stent expansion alter drug transport properties of the arterial wall? *Journal of the Mechanical Behavior of Biomedical Materials*, page 103610.

Escuer, J., Martínez, M. A., McGinty, S., and Peña, E. (2019). Mathematical modelling of the restenosis process after stent implantation. *Journal of the Royal Society Interface*, 16(157):20190313.

Escuer, J., Schmidt, A. F., Peña, E., Martínez, M. A., and McGinty, S. (2022). Mathematical modelling of endovascular drug delivery: balloons versus stents. *International Journal of Pharmaceutics*, page 121742.

Evans, D. J., Lawford, P. V., Gunn, J., Walker, D., Hose, D., Smallwood, R., Chopard, B., Krafczyk, M., Bernsdorf, J., and Hoekstra, A. (2008). The application of multiscale modelling to the process of development and prevention of stenosis in a stented coronary artery. *Philosophical Transactions of the Royal Society of London A: Mathematical, Physical and Engineering Sciences*, 366(1879):3343–3360.

Feenstra, P. H. and Taylor, C. A. (2009). Drug transport in artery walls: A sequential porohyperelastic-transport approach. *Computer Methods in Biomechanics and Biomedical Engineering*, 12(3):263–276.

Fereidoonnezhad, B., Naghdabadi, R., Sohrabpour, S., and Holzapfel, G. A. (2017). A mechanobiological model for damage-induced growth in arterial tissue with application to in-stent restenosis. *Journal of the Mechanics and Physics of Solids*, 101:311–327.

Ferreira, J. A., Gonçalves, L., Naghipoor, J., de Oliveira, P., and Rabczuk, T. (2017). The influence of atherosclerotic plaques on the pharmacokinetics of a drug eluted from bioabsorbable stents. *Mathematical Biosciences*, 283:71–83.

Ferreira, J. A., Gonçalves, L., Naghipoor, J., de Oliveira, P., and Rabczuk, T. (2018). The effect of plaque eccentricity on blood hemodynamics and drug release in a stented artery. *Medical Engineering & Physics*, 60:47–60.

Filipovic, N., Teng, Z., Radovic, M., Saveljic, I., Fotiadis, D., and Parodi, O. (2013). Computer simulation of three-dimensional plaque formation and progression in the carotid artery. *Medical & Biological Engineering & Computing*, 51(6):607–616.

Fischman, D. L., Leon, M. B., Baim, D. S., Schatz, R. A., Savage, M. P., Penn, I., Detre, K., Veltri, L., Ricci, D., Nobuyoshi, M., et al. (1994). A randomized comparison of coronary-stent placement and balloon angioplasty in the treatment of coronary artery disease. *New England Journal of Medicine*, 331(8):496–501.

Formaggia, L., Minisini, S., and Zunino, P. (2010). Modeling polymeric controlled drug release and transport phenomena in the arterial tissue. *Mathematical Models and Methods in Applied Sciences*, 20(10):1759–1786.

Frangos, S. G., Gahtan, V., and Sumpio, B. (1999). Localization of atherosclerosis: role of hemodynamics. *Archives of Surgery*, 134(10):1142–1149.

Fruchart, J.-C., Nierman, M. C., Stroes, E. S., Kastelein, J. J., and Duriez, P. (2004). New risk factors for atherosclerosis and patient risk assessment. *Circulation*, 109(23_suppl_1):III–15.

Fung, Y. (1983). On the foundations of biomechanics. *Journal of Applied Mechanics*, 50:1003–1009.

Fung, Y., Fronek, K., and Patitucci, P. (1979). Pseudoelasticity of arteries and the choice of its mathematical expression. *American Journal of Physiology-Heart and Circulatory Physiology*, 237(5):H620–H631.

Fung, Y. C. (1993). *Biomechanics: Mechanical properties of living tissues*. Springer Science & Business Media.

García, A., Peña, E., and Martínez, M. (2012). Influence of geometrical parameters on radial force during self-expanding stent deployment. application for a variable radial stiffness stent. *Journal of the Mechanical Behavior of Biomedical Materials*, 10:166–175.

Garg, S. and Serruys, P. W. (2010). Coronary stents: current status. *Journal of the American College of Cardiology*, 56(10S):S1–S42.

Gasser, T. C. (2017). Aorta. In *Biomechanics of Living Organs*, pages 169–191. Elsevier.

Gasser, T. C. (2021). Conduit vessels. In *Vascular Biomechanics*, pages 233–304. Springer.

Gasser, T. C., Ogden, R. W., and Holzapfel, G. A. (2006). Hyperelastic modelling of arterial layers with distributed collagen fibre orientations. *Journal of the Royal Society Interface*, 3(6):15–35.

Gierig, M., Wriggers, P., and Marino, M. (2021). Computational model of damage-induced growth in soft biological tissues considering the mechanobiology of healing. *Biomechanics and Modeling in Mechanobiology*, 20(4):1297–1315.

Gijsen, F. J., Migliavacca, F., Schievano, S., Socci, L., Petrini, L., Thury, A., Wentzel, J. J., van der Steen, A. F., Serruys, P. W., and Dubini, G. (2008). Simulation of stent deployment in a realistic human coronary artery. *Biomedical Engineering Online*, 7(1):23.

Gongora, C. A., Shibuya, M., Wessler, J. D., McGregor, J., Tellez, A., Cheng, Y., Conditt, G. B., Kaluza, G. L., and Granada, J. F. (2015). Impact of paclitaxel dose on tissue pharmacokinetics and vascular healing: a comparative drug-coated balloon study in the familial hypercholesterolemic swine model of superficial femoral in-stent restenosis. *JACC: Cardiovascular Interventions*, 8(8):1115–1123.

Gray, W. A. and Granada, J. F. (2010). Drug-coated balloons for the prevention of vascular restenosis. *Circulation*, 121(24):2672–2680.

Grube, E. and Buellesfeld, L. (2006). Biomatrix® Biolimus A9®-eluting coronary stent: A next-generation drug-eluting stent for coronary artery disease. *Expert review of medical devices*, 3(6):731–741.

Grüntzig, A. (1978). Transluminal dilatation of coronary-artery stenosis. *The Lancet*, 311(8058):263.

Gundiah, N., Ratcliffe, M. B., and Pruitt, L. A. (2009). The biomechanics of arterial elastin. *Journal of the Mechanical Behavior of Biomedical Materials*, 2(3):288–296.

Hackam, D. G. and Anand, S. S. (2003). Emerging risk factors for atherosclerotic vascular disease: a critical review of the evidence. *Journal of the American Medical Association*, 290(7):932–940.

He, R., Zhao, L., Silberschmidt, V. V., and Liu, Y. (2020). Mechanistic evaluation of long-term in-stent restenosis based on models of tissue damage and growth. *Biomechanics and Modeling in Mechanobiology*, 19(5):1425–1446.

Heldman, A. W., Cheng, L., Jenkins, G. M., Heller, P. F., Kim, D.-W., Ware Jr, M., Nater, C., Hruban, R. H., Rezai, B., Abella, B. S., et al. (2001). Paclitaxel stent coating inhibits neointimal hyperplasia at 4 weeks in a porcine model of coronary restenosis. *Circulation*, 103(18):2289–2295.

Herrington, W., Lacey, B., Sherliker, P., Armitage, J., and Lewington, S. (2016). Epidemiology of atherosclerosis and the potential to reduce the global burden of atherothrombotic disease. *Circulation Research*, 118(4):535–546.

Hoffmann, R., Mintz, G. S., Dussaillant, G. R., Popma, J. J., Pichard, A. D., Satler, L. F., Kent, K. M., Griffin, J., and Leon, M. B. (1996). Patterns and mechanisms of in-stent restenosis: a serial intravascular ultrasound study. *Circulation*, 94(6):1247–1254.

Holzapfel, G. A. (2006). Determination of material models for arterial walls from uniaxial extension tests and histological structure. *Journal of Theoretical Biology*, 238(2):290–302.

Holzapfel, G. A. (2008). Collagen in arterial walls: biomechanical aspects. In *Collagen*, pages 285–324. Springer.

Holzapfel, G. A., Gasser, T. C., and Ogden, R. W. (2000). A new constitutive framework for arterial wall mechanics and a comparative study of material models. *Journal of Elasticity and the Physical Science of Solids*, 61(1-3):1–48.

Holzapfel, G. A., Gasser, T. C., and Stadler, M. (2002). A structural model for the viscoelastic behavior of arterial walls: continuum formulation and finite element analysis. *European Journal of Mechanics-A/Solids*, 21(3):441–463.

Holzapfel, G. A. and Ogden, R. W. (2010). Constitutive modelling of arteries. *Proceedings of the Royal Society A: Mathematical, Physical and Engineering Sciences*, 466(2118):1551–1597.

Holzapfel, G. A. and Ogden, R. W. (2018). Biomechanical relevance of the microstructure in artery walls with a focus on passive and active components. *American Journal of Physiology-Heart and Circulatory Physiology*, 315(3):H540–H549.

Holzapfel, G. A., Sommer, G., Auer, M., Regitnig, P., and Ogden, R. W. (2007). Layer-specific 3d residual deformations of human aortas with non-atherosclerotic intimal thickening. *Annals of Biomedical Engineering*, 35(4):530–545.

Holzapfel, G. A., Sommer, G., Gasser, C. T., and Regitnig, P. (2005a). Determination of layer-specific mechanical properties of human coronary arteries with nonatherosclerotic intimal thickening and related constitutive modeling. *American Journal of Physiology-Heart and Circulatory Physiology*, 289(5):H2048–H2058.

Holzapfel, G. A., Stadler, M., and Gasser, T. C. (2005b). Changes in the mechanical environment of stenotic arteries during interaction with stents: computational assessment of parametric stent designs. *Journal of Biomechanical Engineering*, 127(1):166–180.

Holzapfel, G. A. and Weizsäcker, H. W. (1998). Biomechanical behavior of the arterial wall and its numerical characterization. *Computers in Biology and Medicine*, 28(4):377–392.

Horner, M., Joshi, S., Dhruva, V., Sett, S., and Stewart, S. (2010). A two-species drug delivery model is required to predict deposition from drug-eluting stents. *Cardiovascular Engineering and Technology*, 1(3):225–234.

Hossain, S. S., Hossainy, S. F., Bazilevs, Y., Calo, V. M., and Hughes, T. J. (2012). Mathematical modeling of coupled drug and drug-encapsulated nanoparticle transport in patient-specific coronary artery walls. *Computational Mechanics*, 49(2):213–242.

Humphrey, J. and Na, S. (2002). Elastodynamics and arterial wall stress. *Annals of Biomedical Engineering*, 30(4):509–523.

Humphrey, J. and Rajagopal, K. (2002). A constrained mixture model for growth and remodeling of soft tissues. *Mathematical models and methods in applied sciences*, 12(03):407–430.

Humphrey, J. D. (1995). Mechanics of the arterial wall: review and directions. *Critical Reviews in Biomedical Engineering*, 23(1-2).

Humphrey, J. D. (2002). *Cardiovascular Solid Mechanics: Cells, Tissues, and Organs*. Springer Science & Business Media.

Hwang, C.-W. and Edelman, E. R. (2002). Arterial ultrastructure influences transport of locally delivered drugs. *Circulation Research*, 90(7):826–832.

Hwang, C.-W., Wu, D., and Edelman, E. R. (2001). Physiological transport forces govern drug distribution for stent-based delivery. *Circulation*, 104(5):600–605.

Hwang, C.-W., Wu, D., and Edelman, E. R. (2003). Impact of transport and drug properties on the local pharmacology of drug-eluting stents. *International Journal of Cardiovascular Interventions*, 5(1):7–12.

Hwang, M., Garbey, M., Berceli, S. A., and Tran-Son-Tay, R. (2009). Rule-based simulation of multi-cellular biological systems—a review of modeling techniques. *Cellular and Molecular Bioengineering*, 2(3):285–294.

Ibragimov, A., Ritter, L., and Walton, J. R. (2010). Stability analysis of a reaction-diffusion system modeling atherogenesis. *SIAM Journal on Applied Mathematics*, 70(7):2150–2185.

INE (2021). Deaths according to cause of death. Year 2020. Instituto Nacional de Estadística.

Iqbal, J., Gunn, J., Serruys, P. W., et al. (2013). Coronary stents: historical development, current status and future directions. *British Medical Bulletin*, 106(1):193–211.

Iyer, R., Kuriakose, A. E., Yaman, S., Su, L.-C., Shan, D., Yang, J., Liao, J., Tang, L., Banerjee, S., Xu, H., et al. (2019). Nanoparticle eluting-angioplasty balloons to treat cardiovascular diseases. *International Journal of Pharmaceutics*, 554:212–223.

Jain, A., McGinty, S., Pontrelli, G., and Zhou, L. (2022). Theoretical modeling of endovascular drug delivery into a multilayer arterial wall from a drug-coated balloon. *International Journal of Heat and Mass Transfer*, 187:122572.

Jeger, R. V., Eccleshall, S., Wan Ahmad, W. A., Ge, J., Poerner, T. C., Shin, E.-S., Alfonso, F., Latib, A., Ong, P. J., Rissanen, T. T., et al. (2020). Drug-coated balloons for coronary artery disease: Third report of the international dcb consensus group. *Cardiovascular Interventions*, 13(12):1391–1402.

Jeger, R. V., Farah, A., Ohlow, M.-A., Mangner, N., Möbius-Winkler, S., Leibundgut, G., Weilenmann, D., Wöhrle, J., Richter, S., Schreiber, M., et al. (2018). Drug-coated balloons for small coronary artery disease (basket-small 2): An open-label randomised non-inferiority trial. *The Lancet*, 392(10150):849–856.

Kalita, P. and Schaefer, R. (2008). Mechanical models of artery walls. *Archives of Computational Methods in Engineering*, 15(1):1–36.

Karanasiou, G. S., Papafaklis, M. I., Conway, C., Michalis, L. K., Tzafriri, R., Edelman, E. R., and Fotiadis, D. I. (2017). Stents: biomechanics, biomaterials, and insights from computational modeling. *Annals of Biomedical Engineering*, 45(4):853–872.

Kedem, O. and Katchalsky, A. (1958). Thermodynamic analysis of the permeability of biological membranes to non-electrolytes. *Biochimica et Biophysica Acta*, 27:229–246.

Keshavarzian, M., Meyer, C. A., and Hayenga, H. N. (2018). Mechanobiological model of arterial growth and remodeling. *Biomechanics and Modeling in Mechanobiology*, 17(1):87–101.

Kiousis, D. E., Gasser, T. C., and Holzapfel, G. A. (2007). A numerical model to study the interaction of vascular stents with human atherosclerotic lesions. *Annals of Biomedical Engineering*, 35(11):1857–1869.

Kolachalama, V. B., Pacetti, S. D., Franses, J. W., Stankus, J. J., Zhao, H. Q., Shazly, T., Nikanorov, A., Schwartz, L. B., Tzafriri, A. R., and Edelman, E. R. (2013). Mechanisms of tissue uptake and retention in zotarolimus-coated balloon therapy. *Circulation*, 127(20):2047–2055.

Kolandaivelu, K., O'Brien, C. C., Shazly, T., Edelman, E. R., and Kolachalama, V. B. (2015). Enhancing physiologic simulations using supervised learning on coarse mesh solutions. *Journal of The Royal Society Interface*, 12(104):20141073.

Lally, C., Dolan, F., and Prendergast, P. (2005). Cardiovascular stent design and vessel stresses: A finite element analysis. *Journal of Biomechanics*, 38(8):1574–1581.

Lally, C. and Prendergast, P. (2006). Simulation of in-stent restenosis for the design of cardiovascular stents. In *Mechanics of Biological Tissue*, pages 255–267. Springer.

Lawton, R. W. (1954). The thermoelastic behavior of isolated aortic strips of the dog. *Circulation Research*, 2(4):344–353.

Lee, D.-H. and de la Torre Hernandez, J. M. (2018). The newest generation of drug-eluting stents and beyond. *European Cardiology Review*, 13(1):54.

Levin, A. D., Vukmirovic, N., Hwang, C.-W., and Edelman, E. R. (2004). Specific binding to intracellular proteins determines arterial transport properties for rapamycin and paclitaxel. *Proceedings of the National Academy of Sciences of the United States of America*, 101(25):9463–9467.

Li, S., Lei, L., Hu, Y., Zhang, Y., Zhao, S., and Zhang, J. (2019). A fully coupled framework for in silico investigation of in-stent restenosis. *Computer Methods in Biomechanics and Biomedical Engineering*, 22(2):217–228.

Libby, P., Ridker, P. M., and Maseri, A. (2002). Inflammation and atherosclerosis. *Circulation*, 105(9):1135–1143.

Lillie, M., Shadwick, R., and Gosline, J. (2010). Mechanical anisotropy of inflated elastic tissue from the pig aorta. *Journal of Biomechanics*, 43(11):2070–2078.

MacNeill, B. D., Lowe, H. C., Takano, M., Fuster, V., and Jang, I.-K. (2003). Intravascular modalities for detection of vulnerable plaque: current status. *Arteriosclerosis, thrombosis, and vascular biology*, 23(8):1333–1342.

Maes, L., Cloet, A.-S., Fourneau, I., and Famaey, N. (2021). A homogenized constrained mixture model of restenosis and vascular remodelling after balloon angioplasty. *Journal of the Royal Society Interface*, 18(178):20210068.

Mandal, A. P. and Mandal, P. K. (2018). Distribution and retention of drug through an idealised atherosclerotic plaque eluted from a half-embedded stent. *International Journal of Dynamics and Control*, 6(3):1183–1193.

Mandal, P. K., Sarifuddin, and Kolachalama, V. B. (2016). Computational model of drug-coated balloon delivery in a patient-specific arterial vessel with heterogeneous tissue composition. *Cardiovascular Engineering and Technology*, 7(4):406–419.

Manjunatha, K., Behr, M., Vogt, F., and Reese, S. (2022a). Finite element modelling of in-stent restenosis. In *Current Trends and Open Problems in Computational Mechanics*, pages 305–318. Springer.

Manjunatha, K., Behr, M., Vogt, F., and Reese, S. (2022b). A multiphysics modeling approach for in-stent restenosis: Theoretical aspects and finite element implementation. *arXiv preprint arXiv:2204.02301*.

Marino, M., Pontrelli, G., Vairo, G., and Wriggers, P. (2017). A chemo-mechano-biological formulation for the effects of biochemical alterations on arterial mechanics: the role of molecular transport and multiscale tissue remodelling. *Journal of The Royal Society Interface*, 14(136):20170615.

Martin, D. M. and Boyle, F. J. (2011). Drug-eluting stents for coronary artery disease: a review. *Medical Engineering & Physics*, 33(2):148–163.

Marx, S. O., Jayaraman, T., Go, L. O., and Marks, A. R. (1995). Rapamycin-fkbp inhibits cell cycle regulators of proliferation in vascular smooth muscle cells. *Circulation Research*, 76(3):412–417.

McCormick, C. (2018a). Overview of cardiovascular stent designs. In *Functionalised Cardiovascular Stents*, pages 3–26. Elsevier.

McCormick, C. (2018b). Polymer-free drug-eluting stents. In *Functionalised Cardiovascular Stents*, pages 57–74. Elsevier.

McFadden, E. P., Stabile, E., Regar, E., Cheneau, E., Ong, A. T., Kinnaird, T., Suddath, W. O., Weissman, N. J., Torguson, R., Kent, K. M., et al. (2004). Late thrombosis in drug-eluting coronary stents after discontinuation of antiplatelet therapy. *The Lancet*, 364(9444):1519–1521.

McGinty, S. (2010). *Stents and arterial flows*. PhD thesis, University of Strathclyde.

McGinty, S. (2014). A decade of modelling drug release from arterial stents. *Mathematical Biosciences*, 257:80–90.

McGinty, S., McKee, S., McCormick, C., and Wheel, M. (2015a). Release mechanism and parameter estimation in drug-eluting stent systems: analytical solutions of drug release and tissue transport. *Mathematical Medicine and Biology: a Journal of the IMA*, 32(2):163–186.

McGinty, S., McKee, S., Wadsworth, R. M., and McCormick, C. (2010). Modelling drug-eluting stents. *Mathematical Medicine and Biology: a journal of the IMA*, 28(1):1–29.

McGinty, S. and Pontrelli, G. (2015). A general model of coupled drug release and tissue absorption for drug delivery devices. *Journal of Controlled Release*, 217:327–336.

McGinty, S. and Pontrelli, G. (2016). On the role of specific drug binding in modelling arterial eluting stents. *Journal of Mathematical Chemistry*, 54(4):967–976.

McGinty, S., Vo, T. T., Meere, M., McKee, S., and McCormick, C. (2015b). Some design considerations for polymer-free drug-eluting stents: a mathematical approach. *Acta Biomaterialia*, 18:213–225.

McKavanagh, P., Zawadowski, G., Ahmed, N., and Kutryk, M. (2018). The evolution of coronary stents. *Expert Review of Cardiovascular Therapy*, 16(3):219–228.

McKittrick, C., Kennedy, S., Oldroyd, K., McGinty, S., and McCormick, C. (2016). Modelling the impact of atherosclerosis on drug release and distribution from coronary stents. *Annals of Biomedical Engineering*, 44(2):477–487.

McKittrick, C. M., McKee, S., Kennedy, S., Oldroyd, K., Wheel, M., Pontrelli, G., Dixon, S., McGinty, S., and McCormick, C. (2019). Combining mathematical modelling with in vitro experiments to predict in vivo drug-eluting stent performance. *Journal of Controlled Release*, 303:151–161.

McNaught, A. D., Wilkinson, A., et al. (1997). *Compendium of chemical terminology*, volume 1669. Blackwell Science Oxford.

McQueen, A., Escuer, J., Aggarwal, A., Kennedy, S., McCormick, C., Oldroyd, K., and McGinty, S. (2021). Do we really understand how drug eluted from stents modulates arterial healing? *International Journal of Pharmaceutics*, 601:120575.

Melly, L., Torregrossa, G., Lee, T., Jansens, J.-L., and Puskas, J. D. (2018). Fifty years of coronary artery bypass grafting. *Journal of Thoracic Disease*, 10(3):1960.

Migliavacca, F., Gervaso, F., Prosi, M., Zunino, P., Minisini, S., Formaggia, L., and Dubini, G. (2007). Expansion and drug elution model of a coronary stent. *Computer Methods in Biomechanics and Biomedical Engineering*, 10(1):63–73.

Migliavacca, F., Petrini, L., Massarotti, P., Schievano, S., Auricchio, F., and Dubini, G. (2004). Stainless and shape memory alloy coronary stents: a computational study on the interaction with the vascular wall. *Biomechanics and Modeling in Mechanobiology*, 2(4):205–217.

Mongrain, R., Faik, I., Leask, R. L., Rodés-Cabau, J., Larose, É., and Bertrand, O. F. (2007). Effects of diffusion coefficients and struts apposition using numerical simulations for drug eluting coronary stents. *Journal of Biomechanical Engineering*, 129(5):733–742.

Mongrain, R., Leask, R., Brunette, J., Faik, I., Bulman-Feleming, N., and Nguyen, T. (2005). Numerical modeling of coronary drug eluting stents. *Studies in Health Technology and Informatics*, 113:443–458.

Mooney, M. (1940). A theory of large elastic deformation. *Journal of Applied Physics*, 11(9):582–592.

Morlacchi, S. and Migliavacca, F. (2013). Modeling stented coronary arteries: where we are, where to go. *Annals of biomedical engineering*, 41(7):1428–1444.

Morris, P. D., Iqbal, J., Chiastra, C., Wu, W., Migliavacca, F., and Gunn, J. P. (2018). Simultaneous kissing stents to treat unprotected left main stem coronary artery bifurcation disease; stent expansion, vessel injury, hemodynamics, tissue healing, restenosis, and repeat revascularization. *Catheterization and Cardiovascular Interventions*, 92(6):E381–E392.

Mortier, P., Holzapfel, G. A., De Beule, M., Van Loo, D., Taeymans, Y., Segers, P., Verdonck, P., and Verhegghe, B. (2010). A novel simulation strategy for stent insertion and deployment in curved coronary bifurcations: comparison of three drug-eluting stents. *Annals of Biomedical Engineering*, 38(1):88–99.

Moses, J. W., Leon, M. B., Popma, J. J., Fitzgerald, P. J., Holmes, D. R., O'Shaughnessy, C., Caputo, R. P., Kereiakes, D. J., Williams, D. O., Teirstein, P. S., et al. (2003). Sirolimus-eluting stents versus standard stents in patients with stenosis in a native coronary artery. *New England Journal of Medicine*, 349(14):1315–1323.

Neumann, F.-J., Sousa-Uva, M., Ahlsson, A., Alfonso, F., Banning, A. P., Benedetto, U., Byrne, R. A., Collet, J.-P., Falk, V., Head, S. J., et al. (2019). 2018 esc/eacts guidelines on myocardial revascularization. *European Heart Journal*, 40(2):87–165.

Nezami, F. R., Athanasiou, L. S., and Edelman, E. R. (2021). Endovascular drug-delivery and drug-elution systems. In *Biomechanics of Coronary Atherosclerotic Plaque*, pages 595–631. Elsevier.

Nicolás, M., Peña, E., Malvè, M., and Martínez, M. (2015). Mathematical modeling of the fibrosis process in the implantation of inferior vena cava filters. *Journal of Theoretical Biology*, 387:228–240.

Nobuyoshi, M., Kimura, T., Nosaka, H., Mioka, S., Ueno, K., Yokoi, H., Hamasaki, N., Horiuchi, H., and Ohishi, H. (1988). Restenosis after successful percutaneous transluminal coronary angioplasty: serial angiographic follow-up of 229 patients. *Journal of the American College of Cardiology*, 12(3):616–623.

Nolan, D. and McGarry, J. (2016). On the compressibility of arterial tissue. *Annals of Biomedical Engineering*, 44(4):993–1007.

Nolan, D. R. and Lally, C. (2018). An investigation of damage mechanisms in mechanobiological models of in-stent restenosis. *Journal of Computational Science*, 24:132–142.

Nordmann, A. J., Briel, M., and Bucher, H. C. (2006). Mortality in randomized controlled trials comparing drug-eluting vs. bare metal stents in coronary artery disease: a meta-analysis. *European Heart Journal*, 27(23):2784–2814.

Oberhoff, M., Herdeg, C., Baumbach, A., and Karsch, K. R. (2002). Stent-based antirestenotic coatings (sirolimus/paclitaxel). *Catheterization and cardiovascular interventions*, 55(3):404–408.

O'Brien, C. C., Kolachalama, V. B., Barber, T. J., Simmons, A., and Edelman, E. R. (2013). Impact of flow pulsatility on arterial drug distribution in stent-based therapy. *Journal of controlled release*, 168(2):115–124.

O'Connell, B. M., McGloughlin, T. M., and Walsh, M. T. (2010). Factors that affect mass transport from drug eluting stents into the artery wall. *Biomedical Engineering Online*, 9(1):15.

Ogden, R. W. (1972). Large deformation isotropic elasticity–on the correlation of theory and experiment for incompressible rubberlike solids. *Proceedings of the Royal Society of London. A. Mathematical and Physical Sciences*, 326(1567):565–584.

Patel, J., Sheehan, V., and Gurk-Turner, C. (2003). Ezetimibe (zetia): a new type of lipid-lowering agent. In *Baylor University Medical Center Proceedings*, volume 16, pages 354–358. Taylor & Francis.

Peña, J. A., Martínez, M. A., and Peña, E. (2015). Layer-specific residual deformations and uniaxial and biaxial mechanical properties of thoracic porcine aorta. *Journal of the Mechanical Behavior of Biomedical Materials*, 50:55–69.

Pericevic, I., Lally, C., Toner, D., and Kelly, D. J. (2009). The influence of plaque composition on underlying arterial wall stress during stent expansion: the case for lesion-specific stents. *Medical Engineering & Physics*, 31(4):428–433.

Pleouras, D. S., Sakellarios, A. I., Tsompou, P., Kigka, V., Kyriakidis, S., Rocchiccioli, S., Neglia, D., Knuuti, J., Pelosi, G., Michalis, L. K., et al. (2020). Simulation of atherosclerotic plaque growth using computational biomechanics and patient-specific data. *Scientific Reports*, 10(1):1–14.

Pontrelli, G. and de Monte, F. (2007). Mass diffusion through two-layer porous media: an application to the drug-eluting stent. *International Journal of Heat and Mass Transfer*, 50(17-18):3658–3669.

Pontrelli, G. and de Monte, F. (2009). Modeling of mass dynamics in arterial drug-eluting stents. *Journal of Porous Media*, 12(1).

Pontrelli, G. and de Monte, F. (2010). A multi-layer porous wall model for coronary drug-eluting stents. *International Journal of Heat and Mass Transfer*, 53(19-20):3629–3637.

Poon, M., Marx, S. O., Gallo, R., Badimon, J. J., Taubman, M. B., Marks, A. R., et al. (1996). Rapamycin inhibits vascular smooth muscle cell migration. *The Journal of Clinical Investigation*, 98(10):2277–2283.

Prabhu, S. and Hossainy, S. (2007). Modeling of degradation and drug release from a biodegradable stent coating. *Journal of Biomedical Materials Research Part A*, 80(3):732–741.

Rachev, A., Manoach, E., Berry, J., and Moore Jr, J. (2000). A model of stress-induced geometrical remodeling of vessel segments adjacent to stents and artery/graft anastomoses. *Journal of Theoretical Biology*, 206(3):429–443.

Radke, P. W., Joner, M., Joost, A., Byrne, R. A., Hartwig, S., Bayer, G., Steigerwald, K., and Wittchow, E. (2011). Vascular effects of paclitaxel following drug-eluting balloon angioplasty in a porcine coronary model: the importance of excipients. *EuroIntervention*, 7(6):730–737.

Rafieian-Kopaei, M., Setorki, M., Doudi, M., Baradaran, A., and Nasri, H. (2014). Atherosclerosis: process, indicators, risk factors and new hopes. *International Journal of Preventive Medicine*, 5(8):927.

Rhodin, J. A. (1980). Architecture of the vessel wall. *Vascular smooth muscle*, pages 1–31.

Ridker, P. M., Stampfer, M. J., and Rifai, N. (2001). Novel risk factors for systemic atherosclerosis: a comparison of c-reactive protein, fibrinogen, homocysteine, lipoprotein (a), and standard cholesterol screening as predictors of peripheral arterial disease. *Jama*, 285(19):2481–2485.

Rivlin, R. and Saunders, D. (1951). Large elastic deformations of isotropic materials vii. Experiments on the deformation of rubber. *Philosophical Transactions of the Royal Society of London. Series A, Mathematical and Physical Sciences*, 243(865):251–288.

Rivlin, R. S. (1948). Large elastic deformations of isotropic materials iv. Further developments of the general theory. *Philosophical Transactions of the Royal Society of London. Series A, Mathematical and Physical Sciences*, 241(835):379–397.

Roach, M. R. and Burton, A. C. (1957). The reason for the shape of the distensibility curves of arteries. *Canadian Journal of Biochemistry and Physiology*, 35(8):681–690.

Robertson, A. M. and Watton, P. N. (2013). Mechanobiology of the arterial wall. *Modeling of transport in biological media. Elsevier, New York*, pages 275–347.

Rossi, F., Casalini, T., Raffa, E., Masi, M., and Perale, G. (2012). Bioresorbable polymer coated drug eluting stent: a model study. *Molecular Pharmaceutics*, 9(7):1898–1910.

Sarifuddin and Mandal, P. K. (2018). Effect of interstitial fluid flow on drug-coated balloon delivery in a patient-specific arterial vessel with heterogeneous tissue composition: A simulation study. *Cardiovascular Engineering and Technology*, 9(2):251–267.

Scheller, B., Hehrlein, C., Bocksch, W., Rutsch, W., Haghi, D., Dietz, U., Böhm, M., and Speck, U. (2006). Treatment of coronary in-stent restenosis with a paclitaxel-coated balloon catheter. *New England Journal of Medicine*, 355(20):2113–2124.

Scheller, B., Hehrlein, C., Bocksch, W., Rutsch, W., Haghi, D., Dietz, U., Böhm, M., and Speck, U. (2008). Two year follow-up after treatment of coronary in-stent restenosis with a paclitaxel-coated balloon catheter. *Clinical Research in Cardiology*, 97(10):773–781.

Scheller, B., Speck, U., Abramjuk, C., Bernhardt, U., Böhm, M., and Nickenig, G. (2004). Paclitaxel balloon coating, a novel method for prevention and therapy of restenosis. *Circulation*, 110(7):810–814.

Schiavone, A. and Zhao, L. (2016). A computational study of stent performance by considering vessel anisotropy and residual stresses. *Materials Science and Engineering: C*, 62:307–316.

Schiavone, A., Zhao, L., and Abdel-Wahab, A. A. (2014). Effects of material, coating, design and plaque composition on stent deployment inside a stenotic artery-finite element simulation. *Materials Science and Engineering: C*, 42:479–488.

Schömig, A., Dibra, A., Windecker, S., Mehilli, J., Suárez de Lezo, J., Kaiser, C., Park, S.-J., Goy, J.-J., Lee, J.-H., Di Lorenzo, E., et al. (2007). A meta-analysis of 16 randomized trials of sirolimus-eluting stents versus paclitaxel-eluting stents in patients with coronary artery disease. *Journal of the American College of Cardiology*, 50(14):1373–1380.

Serruys, P. W., Chevalier, B., Dudek, D., Cequier, A., Carrié, D., Iniguez, A., Dominici, M., van der Schaaf, R. J., Haude, M., Wasungu, L., et al. (2015). A bioresorbable everolimus-eluting scaffold versus a metallic everolimus-eluting stent for ischaemic heart disease caused by de-novo native coronary artery lesions (absorb ii): An interim 1-year analysis of clinical and procedural secondary outcomes from a randomised controlled trial. *The Lancet*, 385(9962):43–54.

Serruys, P. W., De Jaegere, P., Kiemeneij, F., Macaya, C., Rutsch, W., Heyndrickx, G., Emanuelsson, H., Marco, J., Legrand, V., Materne, P., et al. (1994). A comparison of balloon-expandable-stent implantation with balloon angioplasty in patients with coronary artery disease. *New England Journal of Medicine*, 331(8):489–495.

Serruys, P. W., Kutryk, M. J., and Ong, A. T. (2006). Coronary-artery stents. *New England Journal of Medicine*, 354(5):483–495.

Serruys, P. W., Silber, S., Garg, S., Van Geuns, R. J., Richardt, G., Buszman, P. E., Kelbæk, H., Van Boven, A. J., Hofma, S. H., Linke, A., et al. (2010). Comparison of zotarolimus-eluting and everolimus-eluting coronary stents. *New England Journal of Medicine*, 363(2):136–146.

Sigwart, U., Puel, J., Mirkovitch, V., Joffre, F., and Kappenberger, L. (1987). Intravascular stents to prevent occlusion and re-stenosis after transluminal angioplasty. *New England Journal of Medicine*, 316(12):701–706.

Sojitra, P., Yazdani, S., Otsuka, F., Doshi, M., Kolodgie, F., and Virmani, R. (2013). Crt-123. a novel nano particle sirolimus delivery via coated balloon. *JACC: Cardiovascular Interventions*, 6(2 Suppl S):S40.

Sommer, G., Regitnig, P., Kältringer, L., and Holzapfel, G. A. (2010). Biaxial mechanical properties of intact and layer-dissected human carotid arteries at physiological and supraphysiological loadings. *American Journal of Physiology-Heart and Circulatory Physiology*, 298(3):H898–H912.

Sotomi, Y., Onuma, Y., Collet, C., Tenekecioglu, E., Virmani, R., Kleiman, N. S., and Serruys, P. W. (2017). Bioresorbable scaffold: the emerging reality and future directions. *Circulation Research*, 120(8):1341–1352.

Sousa, J. E., Costa, M. A., Abizaid, A., Abizaid, A. S., Feres, F., Pinto, I. M., Seixas, A. C., Staico, R., Mattos, L. A., Sousa, A. G., et al. (2001a). Lack of neointimal proliferation after implantation of sirolimus-coated stents in human coronary arteries: A quantitative coronary angiography and three-dimensional intravascular ultrasound study. *Circulation*, 103(2):192–195.

Sousa, J. E., Costa, M. A., Abizaid, A. C., Rensing, B. J., Abizaid, A. S., Tanajura, L. F., Kozuma, K., Van Langenhove, G., Sousa, A. G., Falotico, R., et al. (2001b). Sustained suppression of neointimal proliferation by sirolimus-eluting stents: one-year angiographic and intravascular ultrasound follow-up. *Circulation*, 104(17):2007–2011.

Sousa, J. E., Serruys, P. W., and Costa, M. A. (2003a). New frontiers in cardiology: drug-eluting stents: Part i. *Circulation*, 107(17):2274–2279.

Sousa, J. E., Serruys, P. W., and Costa, M. A. (2003b). New frontiers in cardiology: drug-eluting stents: Part ii. *Circulation*, 107(18):2383–2389.

Spencer, A. (1971). Part III. theory of invariants. *Continuum Physics*, 1:239–353.

Stefanini, G. G., Byrne, R. A., Serruys, P. W., de Waha, A., Meier, B., Massberg, S., Jüni, P., Schömig, A., Windecker, S., and Kastrati, A. (2012). Biodegradable polymer drug-eluting stents reduce the risk of stent thrombosis at 4 years in patients undergoing percutaneous coronary intervention: A pooled analysis of individual patient data from the isar-test 3, isar-test 4, and leaders randomized trials. *European Heart Journal*, 33(10):1214–1222.

Stefanini, G. G. and Holmes Jr, D. R. (2013). Drug-eluting coronary-artery stents. *New England Journal of Medicine*, 368(3):254–265.

Stefanini, G. G., Taniwaki, M., and Windecker, S. (2014). Coronary stents: novel developments. *Heart*, 100(13):1051–1061.

Stone, G. W., Midei, M., Newman, W., Sanz, M., Hermiller, J. B., Williams, J., Farhat, N., Mahaffey, K. W., Cutlip, D. E., Fitzgerald, P. J., et al. (2008). Comparison of an everolimus-eluting stent and a paclitaxel-eluting stent in patients with coronary artery disease: a randomized trial. *Journal of the American Medical Association*, 299(16):1903–1913.

Stone, G. W., Rizvi, A., Newman, W., Mastali, K., Wang, J. C., Caputo, R., Doostzadeh, J., Cao, S., Simonton, C. A., Sudhir, K., et al. (2010). Everolimus-eluting versus paclitaxel-eluting stents in coronary artery disease. *New England Journal of Medicine*, 362(18):1663–1674.

Su, J., Gonzales, H. P., Todorov, M., Kojouharov, H., and Tang, L. (2011). A mathematical model for foreign body reactions in 2D. *International Journal of Computer Mathematics*, 88(3):610–633.

Taber, L. A. and Perucchio, R. (2000). Modeling heart development. *Journal of Elasticity and The Physical Science of Solids*, 61(1):165–197.

Tahir, H., Bona-Casas, C., and Hoekstra, A. G. (2013). Modelling the effect of a functional endothelium on the development of in-stent restenosis. *PLoS One*, 8(6):e66138.

Tahir, H., Bona-Casas, C., Narracott, A. J., Iqbal, J., Gunn, J., Lawford, P., and Hoekstra, A. G. (2014). Endothelial repair process and its relevance to longitudinal neointimal tissue patterns: comparing histology with in silico modelling. *Journal of The Royal Society Interface*, 11(94):20140022.

Tahir, H., Hoekstra, A. G., Lorenz, E., Lawford, P. V., Hose, D. R., Gunn, J., and Evans, D. J. (2011). Multi-scale simulations of the dynamics of in-stent restenosis: impact of stent deployment and design. *Interface Focus*, 1(3):365–373.

Tahir, H., Niculescu, I., Bona-Casas, C., Merks, R., and Hoekstra, A. (2015). An in silico study on the role of smooth muscle cell migration in neointimal formation after coronary stenting. *Journal of the Royal Society Interface*, 12:20150358.

Takamizawa, K. and Hayashi, K. (1987). Strain energy density function and uniform strain hypothesis for arterial mechanics. *Journal of Biomechanics*, 20(1):7–17.

Tarbell, J. M. (2003). Mass transport in arteries and the localization of atherosclerosis. *Annual Review of Biomedical Engineering*, 5(1):79–118.

Tepe, G., Laird, J., Schneider, P., Brodmann, M., Krishnan, P., Micari, A., Metzger, C., Scheinert, D., Zeller, T., Cohen, D. J., et al. (2015). Drug-coated balloon versus standard percutaneous transluminal angioplasty for the treatment of superficial femoral and popliteal peripheral artery disease: 12-month results from the IN. PACT SFA randomized trial. *Circulation*, 131(5):495–502.

Tepe, G., Zeller, T., Albrecht, T., Heller, S., Schwarzwälder, U., Beregi, J.-P., Claussen, M. C. D., Oldenburg, A., Scheller, B., and Speck, U. (2008). Local delivery of paclitaxel to inhibit restenosis during angioplasty of the leg. *New England Journal of Medicine*, 358(7):689–699.

Thomas, M. R. and Lip, G. Y. (2017). Novel risk markers and risk assessments for cardiovascular disease. *Circulation Research*, 120(1):133–149.

Timmis, A., Vardas, P., Townsend, N., Torbica, A., Katus, H., De Smedt, D., Gale, C. P., Maggioni, A. P., Petersen, S. E., Huculeci, R., et al. (2022). European society of cardiology: cardiovascular disease statistics 2021. *European Heart Journal*, 43(8):716–799.

Tomberli, B., Mattesini, A., Baldereschi, G. I., and Di Mario, C. (2018). A brief history of coronary artery stents. *Revista Espanola de Cardiologia (English ed.)*, 71(5):312–319.

Tortora, G. J. and Derrickson, B. H. (2018). *Principles of anatomy and physiology.* John Wiley & Sons.

Treloar, L. (1943a). The elasticity of a network of long-chain molecules. I. *Transactions of the Faraday Society*, 39:36–41.

Treloar, L. (1943b). The elasticity of a network of long-chain molecules. II. *Transactions of the Faraday Society*, 39:241–246.

Tsao, C. W., Aday, A. W., Almarzooq, Z. I., Alonso, A., Beaton, A. Z., Bittencourt, M. S., Boehme, A. K., Buxton, A. E., Carson, A. P., Commodore-Mensah, Y., et al. (2022). Heart disease and stroke statistics—2022 update: A report from the american heart association. *Circulation*, 145(8):e153–e639.

Tzafriri, A. R., Garcia-Polite, F., Li, X., Keating, J., Balaguer, J.-M., Zani, B., Bailey, L., Markham, P., Kiorpes, T. C., Carlyle, W., et al. (2018). Defining drug and target protein distributions after stent-based drug release: Durable versus deployable coatings. *Journal of Controlled Release*, 274:102–108.

Tzafriri, A. R., Groothuis, A., Price, G. S., and Edelman, E. R. (2012). Stent elution rate determines drug deposition and receptor-mediated effects. *Journal of Controlled Release*, 161(3):918–926.

Tzafriri, A. R., Levin, A. D., and Edelman, E. R. (2009). Diffusion-limited binding explains binary dose response for local arterial and tumour drug delivery. *Cell Proliferation*, 42(3):348–363.

Tzafriri, A. R., Parikh, S. A., and Edelman, E. R. (2019). Taking paclitaxel coated balloons to a higher level: Predicting coating dissolution kinetics, tissue retention and dosing dynamics. *Journal of Controlled Release*, 310:94–102.

Vairo, G., Cioffi, M., Cottone, R., Dubini, G., and Migliavacca, F. (2010). Drug release from coronary eluting stents: a multidomain approach. *Journal of Biomechanics*, 43(8):1580–1589.

Vaishnav, R. N. and Vossoughi, J. (1983). Estimation of residual strains in aortic segments. In *Biomedical Engineering II*, pages 330–333. Elsevier.

Vaishnav, R. N., Young, J. T., and Patel, D. J. (1973). Distribution of stresses and of strain-energy density through the wall thickness in a canine aortic segment. *Circulation Research*, 32(5):577–583.

Valanis, K. and Landel, R. F. (1967). The strain-energy function of a hyperelastic material in terms of the extension ratios. *Journal of Applied Physics*, 38(7):2997–3002.

VanderLaan, P. A., Reardon, C. A., and Getz, G. S. (2004). Site specificity of atherosclerosis: site-selective responses to atherosclerotic modulators. *Arteriosclerosis, Thrombosis, and Vascular Biology*, 24(1):12–22.

Vito, R. P. and Dixon, S. A. (2003). Blood vessel constitutive models—1995–2002. *Annual Review of Biomedical Engineering*, 5(1):413–439.

Vo, T. T., Morgan, S., McCormick, C., McGinty, S., McKee, S., and Meere, M. (2018). Modelling drug release from polymer-free coronary stents with microporous surfaces. *International Journal of Pharmaceutics*, 544(2):392–401.

Wagenseil, J. E. and Mecham, R. P. (2009). Vascular extracellular matrix and arterial mechanics. *Physiological Reviews*, 89(3):957–989.

Wang, S. and Vafai, K. (2015). Analysis of low density lipoprotein (ldl) transport within a curved artery. *Annals of biomedical engineering*, 43(7):1571–1584.

Ward, N. C., Watts, G. F., and Eckel, R. H. (2019). Statin toxicity: mechanistic insights and clinical implications. *Circulation Research*, 124(2):328–350.

Watson, M. G., Byrne, H. M., Macaskill, C., and Myerscough, M. R. (2018). A two-phase model of early fibrous cap formation in atherosclerosis. *Journal of Theoretical Biology*, 456:123–136.

Watson, M. G., Byrne, H. M., Macaskill, C., and Myerscough, M. R. (2020). A multiphase model of growth factor-regulated atherosclerotic cap formation. *Journal of Mathematical Biology*, 81(2):725–767.

Wessely, R., Schömig, A., and Kastrati, A. (2006). Sirolimus and paclitaxel on polymer-based drug-eluting stents: similar but different. *Journal of the American College of Cardiology*, 47(4):708–714.

WHO (2007). *Prevention of cardiovascular disease: guidelines for assessment and management of total cardiovascular risk*. World Health Organization.

Williams, C. L., Hayman, L. L., Daniels, S. R., Robinson, T. N., Steinberger, J., Paridon, S., and Bazzarre, T. (2002). Cardiovascular health in childhood: a statement for health professionals from the committee on atherosclerosis, hypertension, and obesity in the young (ahoy) of the council on cardiovascular disease in the young, american heart association. *Circulation*, 106(1):143–160.

Windecker, S., Serruys, P. W., Wandel, S., Buszman, P., Trznadel, S., Linke, A., Lenk, K., Ischinger, T., Klauss, V., Eberli, F., et al. (2008). Biolimus-eluting stent with biodegradable polymer versus sirolimus-eluting stent with durable polymer for coronary revascularisation (leaders): a randomised non-inferiority trial. *The Lancet*, 372(9644):1163–1173.

Wingerd, B. D. (2009). *Medical Terminology Complete!* Pearson.

Yeoh, O. H. (1990). Characterization of elastic properties of carbon-black-filled rubber vulcanizates. *Rubber Chemistry and Technology*, 63(5):792–805.

Yeoh, O. H. (1993). Some forms of the strain energy function for rubber. *Rubber Chemistry and Technology*, 66(5):754–771.

Zahedmanesh, H., Kelly, D. J., and Lally, C. (2010). Simulation of a balloon expandable stent in a realistic coronary artery: Determination of the optimum modelling strategy. *Journal of Biomechanics*, 43(11):2126–2132.

Zahedmanesh, H. and Lally, C. (2012). A multiscale mechanobiological modelling framework using agent-based models and finite element analysis: application to vascular tissue engineering. *Biomechanics and Modeling in Mechanobiology*, 11(3):363–377.

Zahedmanesh, H., Van Oosterwyck, H., and Lally, C. (2014). A multi-scale mechanobiological model of in-stent restenosis: deciphering the role of matrix metalloproteinase and extracellular matrix changes. *Computer Methods in Biomechanics and Biomedical Engineering*, 17(8):813–828.

Zhao, S., Wu, W., Samant, S., Khan, B., Kassab, G. S., Watanabe, Y., Murasato, Y., Sharzehee, M., Makadia, J., Zolty, D., et al. (2021). Patient-specific computational simulation of coronary artery bifurcation stenting. *Scientific reports*, 11(1):1–17.

Zheng, Y. (2018). Bioabsorbable metallic stents. *Functionalised Cardiovascular Stents*, pages 99–134.

Zhou, Q. and Liao, J. K. (2010). Pleiotropic effects of statins–basic research and clinical perspectives–. *Circulation Journal*, 74(5):818–826.

Zhu, X. and Braatz, R. D. (2014). Modeling and analysis of drug-eluting stents with biodegradable plga coating: Consequences on intravascular drug delivery. *Journal of Biomechanical Engineering*, 136(11):111004.

Zhu, X. and Braatz, R. D. (2015). A mechanistic model for drug release in plga biodegradable stent coatings coupled with polymer degradation and erosion. *Journal of Biomedical Materials Research Part A*, 103(7):2269–2279.

Zun, P., Anikina, T., Svitenkov, A., and Hoekstra, A. (2017). A comparison of fully-coupled 3D in-stent restenosis simulations to in-vivo data. *Frontiers in Physiology*, 8:284.

Zun, P., Narracott, A., Chiastra, C., Gunn, J., and Hoekstra, A. (2019). Location-specific comparison between a 3D in-stent restenosis model and micro-ct and histology data from porcine in vivo experiments. *Cardiovascular Engineering and Technology*, 10(4):568–582.

Zun, P., Svitenkov, A., and Hoekstra, A. (2021). Effects of local coronary blood flow dynamics on the predictions of a model of in-stent restenosis. *Journal of Biomechanics*, 120:110361.

Zunino, P. (2004). Multidimensional pharmacokinetic models applied to the design of drug-eluting stents. *Cardiovascular Engineering: An International Journal*, 4(2):181–191.

Zunino, P., D'Angelo, C., Petrini, L., Vergara, C., Capelli, C., and Migliavacca, F. (2009). Numerical simulation of drug eluting coronary stents: mechanics, fluid dynamics and drug release. *Computer Methods in Applied Mechanics and Engineering*, 198(45-46):3633–3644.